Templated synthesis of novel molecules and materials using 1,4-disubstituted-1,2,3-triazole supramolecular building blocks

Eoin P. McCarney, B.A. (Mod.)

December 2017

University of Dublin

Trinity College

Based on research carried out under the direction of
Prof. Thorfinnur Gunnlaugsson

A thesis submitted to the School of Chemistry, University of Dublin, Trinity College for the degree of Doctor of Philosophy

Declaration

I declare that this thesis for the degree of Doctor of Philosophy has not been submitted as an exercise for a degree at this or any other university. Except where duly acknowledged, all work described herein is original and has been carried out by the author. I agree to deposit this thesis in the University's open access institutional repository or allow the library to do so on my behalf, subject to Irish Copyright Legislation and Trinity College Library conditions of use and acknowledgement.

_____

Eoin P. McCarney

Abstract

This thesis, entitled "Templated synthesis of novel molecules and materials using 1,4-disubstituted-1,2,3-triazole supramolecular building blocks", describes the facile synthetic modification of the 1,4-disubstituted-1,2,3-triazole motif in the development and characterisation of new ligands and their various discrete and polymeric supramolecular systems.

Chapter 1 introduces the most recent advances from the literature involving the supramolecular chemistry of the 1,4-disubstituted-1,2,3-triazole. Particular attention is paid to 2,6-bis(1,2,3-triazol-4-yl)pyridine and 2-(1,2,3-triazol-4-yl)pyridine moieties. The applications of these motifs in the formation of various functional systems such as metallo-supramolecular gels, porous coordination polymers and mechanically interlocked systems is summarised.

Chapter 2 details the successful synthetic modification of the 2,6-bis(1,2,3-triazol-4-yl)pyridine core and characterisation of several new metal-chelating systems.

Chapter 3 describes the formation of several *f*-metal templated supramolecular systems using the newly synthesised range of ligands. This study is extended to investigating the formation of highly luminescent metallo-supramolecular gels and the study of their interesting healable properties.

Chapter 4 focuses on the *d*-metal templated synthesis of several coordination polymer materials using the divergent metal binding ability of one of the newly developed ligand systems. The porous systems developed are investigated for the uptake of specific guests in the development of luminescent materials.

Chapter 5 discusses the pre-organisation ability of several 2,6-bis(1,2,3-triazol-4-yl)pyridine systems for the formation of self-templating mechanically interlocked molecules.

Chapter 6 presents a coordination chemistry study into the *d*-metal binding selectivity of a subtly unsymmetric 1,4-disubstituted-1,2,3-triazole ligand containing two possible coordination sites.

Chapter 7 provides detailed experimental procedures. References are provided in Chapter 8 and supplementary data and spectra are presented in several Appendices.

Acknowledgements

First and foremost, I would like to thank my PhD supervisor Prof. Thorri Gunnlaugsson for the great opportunity I was given to work in his research group. Little did I know six years ago when I approached him to enquire about a summer internship in his lab that I would do my final year research project in his group and also be submitting a PhD thesis in the same group. His generosity in both giving his resources, in providing inspirational personal references and his unwavering enthusiasm in chemistry encouraged me to challenge myself. The opportunities I received to write, present internationally and to compete with some of the best young chemists in global competitions are special things that I hold very dear and I'm very thankful for all his support in these endeavors. Not to mention not judging me and the offering of an understanding glass of whiskey as late-morning paper-writing perk-ups following particularly heavy nights.

Secondly, I would like to thank the research group, past and present. Down through the years, you have maintained a very special environment where you selflessly give time and help and patience, to each other and visitors, in overcoming lab issues, tackling tedious synthesis and other offerings of advice which were crucial for me, personally, starting off. I was inspired by this ability of the group to help and I hope I have helped in turn, for my part, and the cycle continues down the line for the betterment of the young scientists to come. The spirit of comradery the group fosters in the birthday tea-breaks, secret santas and other nights out (yes, drinky poohs…) were things I always looked forward to and made my time here very enjoyable. A very sincere thanks to the thoughtfulness I received from all, following my accident. I will never forget it; it was truly appreciated during a horrible time.

A special word of thanks to Joe Byrne, my academic uncle but also one of my proudest sons. He was the perfect mentor to have starting off during my final year research project. If he had not been as involved, the project would not have been such a success and I most likely wouldn't have continued with my studies. Even having left the group, Joe remains ever reliable to answer questions and continue to impart his knowledge.

I want to say thank you so much to Oxana Kotova, the group's matriarch, who's lightest of touches commands order and her good nature and kind leadership has ensured a smooth running and remarkably productive research group for many years.

Massive thanks to Chris Hawes for his indispensable expertise and selfless sharing of the wealth of his crystallographic knowledge, without whom, the complex topologies and subtle unsymmetries would not be described so accurately or eloquently. His manuscript

corrections urged me to write less in a way that sounds like a presenter of an after-school kid's tv-show, advice I will try to transfer to my future literary works. I wish him all the best in his bright future in Keele University who I hope appreciate the gem they have gained.

Thanks Steve for his photophysicality, Sachi for his "Is it?" and his SEMs, Jason for his spatula and whose diamond calfs are a constant reminder not to skip leg-day, Fergus (sorry for the naphthalimides) DermyEspandrAmy, Sam for his genius, Durham nerd-camp pal Hannah, **btp** buddy Izzy, Bruno for not being a muesli, June, in advance for making Werner great again, Anna for her anions, Gearoid for the goss, Niamh for treating my old desk with reverence, Adam, Raju and Ema for…. eh, you're good lads too. Anyone I've forgotten I'll buy you a pint.

I would like to thank all esteemed members of the formidable Thorri's Hammers. Alas, I have failed in my captaincy in bringing the Cup home for the last time. But, the silverware comes second to those palpable moments when unassuming characters produced performances which made my spirit leap with pride and those moments when the team captured the hearts and minds of an entire department.

I would like thank the three undergraduate students, Neil, Billy and Mairéad who I had the pleasure to mentor during their final year research projects. The outstanding work of at least two of my students comprise a substantial portion of the material presented in this thesis which is testament to the level of pride I have for their hard work and success. Thanks again to Thorri for giving me this trusted and privileged opportunity to teach these excellent scientists who I know will have bright futures ahead of them.

Thanks to all the technical staff, in particular, Brendan for his training of me in X-ray Crystallography, John, Manuel, Martin, Gary, Patsy and Tom. Thanks to all my collaborators: Jon, Miguel, Gavin, Matthias, Kevin, Salvador, Wolfgang and many more. Thanks to the Irish Research Council and Science Foundation Ireland for the financial support.

Thanks to my family, Paddy and Marian, Miriam and Niall, you are my role models, who have encouraged me all the way. I endeavour to measure up to your outstanding example and I hope I make you proud.

Bjørn you are one of the best friends I will ever make and I am very thankful I had you as a flat-mate for four years. Good luck to you Son of Odin.

List of Abbreviations

Å	angstrom (1×10^{-10} m)
app	apparent
β	global stability constant
bpy	2,2′-bipyridine
btp	2,6-bis(1,2,3-triazol-4-yl)pyridine
tp	2-(1,2,3-triazol-4-yl)pyridine
br s	broad singlet
CD	circular dichroism
COSY	correlation spectroscopy
CPL	circularly polarised luminescence
CuAAC	copper(I)-catalysed alkyne–azide ‘click’ reaction
CV	cyclic voltammetry
δ	chemical shift (NMR)
d	doublet
DEPT	distortionless enhancement by polarization transfer
DFT	density functional theory
DIC	*N*,*N*′-diisopropylcarbodiimide
DMAP	4-dimethylaminopyridine
DMSO	dimethylsulfoxide
DMF	*N*,*N*-dimethylformamide
dpa	dipicolinic acid; pyridine-2,6-dicarboxylic acid
EDTA	ethylenediaminetetraacetic acid
eq.	equivalent(s)
ESI^+/ESI^-	electrospray ionisation (positive/negative mode)
EtOAc	ethyl acetate
SEM	scanning elctron microscopy
FT-IR	Fourier-transform infrared spectrometry
Gly	glycine
hr	hour
HMBC	heteronuclear multiple-bond correlation spectroscopy
HOMO	highest occupied molecular orbital
HRMS	high resolution mass spectrometry

HSQC	heteronuclear single quantum coherence spectroscopy
IR	infrared
ISC	inter-system crossing
J	NMR coupling constant
K	Formation equilibrium constant
λ	wavelength
LMCT	ligand-to-metal charge transfer
Ln(III)	trivalent lanthanide(III) ion
LUMO	lowest unoccupied molecular orbital
m	multiplet
MALDI	matrix-assisted laser desorption/ionisation
MLCT	metal-to-ligand charge transfer
ML*n*	1:*n* metal-to-ligand assembly, where *n* = 1,2,3.
MRI	magnetic resonance imaging
m/z	mass-to-charge ratio
NHC	*N*-heterocyclic carbene
NMR	nuclear magnetic resonance
NOE	nuclear Overhauser effect
Φ	total luminescence quantum yield
PET	photoinduced electron transfer
ppm	parts per million
Ph	phenyl
Bn	benzyl
pyr	pyridyl
q	quartet
q	metal-bound water molecules, i.e. ‘hydration state’
qt	quaternary (carbon)
quin	quintet
RCM	ring-closing metathesis
ROESY	rotational Overhauser effect spectroscopy
rt	room temperature
s	singlet
S_0	singlet ground state
S_1	singlet excited state

SEM	scanning electron microscopy
st	stretching vibration mode (IR)
τ	lifetime
t	triplet
T_1	triplet excited state
TBA	tetrabutylammonium
TEM	transmission electron microscopy
Tg	3,6,9-trioxadec-1-yl
THF	tetrahydrofuran
TMS	trimethylsilane/trimethylsilyl
TOCSY	total correlation spectroscopy
tris	tris(hydroxymethyl)aminomethane
Trp	tryptophan
terpy	2,2':6',2''-terpyridine
UV-vis	ultra-violet–visible
Fluor.	Fluorescence
Phosph.	Phosphorescence
Eu(III)	Europium(III)
Tb(III)	Terbium(III)
L	Ligand
Ln(III)	Lanthanide ion
MALDI	Matrix assisted laser desorption/ionisation
M:L	Metal : ligand
PPh_3	Triphenylphosphine
R	Arbitrary functional group
RBF	Round-bottom flask

Table of Contents

1 Introduction 1

1.1 Scope of Thesis 2

1.2 Supramolecular Self-Assembly 2

1.3 The 1,2,3-triazole and 'Click' Chemistry 3

1.4 Click triazoles as chelating ligands 5

1.4.1 Bidentate ligands 5
1.4.2 Bidentate ligands containing the 1,4-disubstituted-1,2,3-triazole motif 6
1.4.3 Terdentate Ligands 8
1.4.4 Terdentate **btp** ligand origins and significance 11

1.5 Btp metal coordination 12

1.5.1 Copper 14
1.5.2 Zinc 15
1.5.3 Silver 16
1.5.4 Platinum 17
1.5.5 Iridium 18
1.5.6 Rhodium 19
1.5.7 Ruthenium 19
1.5.8 **Btp**:Lanthanide containing complexes and supramolecular systems 22
1.5.9 Triazolylidene **btp** metal coordination through C4 position 25

1.6 Recent btp advances in the Gunnlaugsson Group 27

1.7 Anions 31

1.8 Other recent btp advances 33

1.9 Synthetic strategies for the facile variability of 1,4-disubstituted-1,2,3-triazoles. 34

1.9.1 Azides 35
1.9.2 Alkynes 36

1.10 Supramolecular Polymers 37

1.10.1 Supramolecular Gels 38
1.10.2 Metal-organic frameworks (MOFs) 45

1.11 Mechanically interlocked systems 48

1.12 Work described in this thesis 52

2 Facile synthetic variation of the 4-pyridyl position of the btp motif towards ligands with increased functionality 53

2.1 Introduction 54

2.2 Synthetic procedures for functionalisation of the btp 4-pyridyl position ... 54

2.3 Synthesis and characterisation of 4-pyridyl functionalised btp ligands 56
2.4 Synthesis of btp ligands modified at the 4-pyridyl position with amino functionality 64
2.5 Synthesis of ditopic btp ligand 98 66
2.6 Synthesis of lipophilic btp ligand functionalised at the 4-pyridyl position 67
2.7 Conclusions 70
3 Metal templated self-assembly of btp ligands and the formation of healable Ln(III) luminescent metallogels 73
3.1 Introduction 74
3.2 Photophysical properties of the Ln(III) ions 75
3.3 Formation and characterisation of Ln(III) complexes 79
3.4 Binding studies of btp ligands with Ln(III) using spectroscopic techniques 86
3.5 Formation of supramolecular metallogels 92
3.6 Formation of Ln(III) luminescent metallogels from Eu($H_3$84)$_3$ and Tb($H_3$84)$_3$ complexes 95
3.7 Gel Rheology 101
3.8 Rheological Measurements of btp derived supramolecular gels 103
3.9 Towards mixed Ln(III) luminescent white-light emitting metallogels 106
3.10 Summary of preliminary results from An(III) extraction studies with lipophilic derivatised btp ligand 108
3.11 Conclusions 110
3.12 Future Work 111
4 Crystalline coordination polymers derived from tri-carboxylic acid btp tecton $H_3$84 towards functional MOF materials 113
4.1 Introduction 114
4.2 Structural analysis of btp ligand H384 and Na384-derived coordination polymer network 115
4.3 Synthesis and structural studies of *poly*-[Cu$_3$84$_2$)]·(DMF)$_{3.3}$ (100) 120
4.4 Thermal Analysis of 100 123
4.5 Synthesis and structural studies of *poly*-[Zn$_7$84$_6$]·((CH$_3$)$_2$NH$_2$)$_4$·(H$_2$O)$_{45}$ (101) 124

4.6 Identification of the charge balancing $(CH_3)_2NH_2^+$ cation 129
4.7 Thermal and gas adsorption studies 130
4.8 Modelled solvent channel occupancies for 101 132
4.9 Crystal structure of impurity phase *poly*-[Zn(H84)] 133
4.10 Cation exchange experiment. 135
4.11 Spectroscopic monitoring of Ln(III) exchange and sensitisation studies. 139
4.12 Conclusions and Future Work 144
5 Study of the pre-organisation requirements for the formation of self-templated 2,6-bis(1,2,3-triazol-4-yl)pyridine [2]catenanes 146
5.1 Introduction 147
5.2 Structural features of previous btp ligands in [2]catenane formation 147
5.3 Synthesis and characterisation of chiral btp olefins 103R/S 149
5.3.1 Investigation into self-templating of **103R/S** in solution by ^{1}H NMR spectroscopy and mass spectrometry 152
5.4 RCM of chiral btp olefins 103R/S 154
5.5 ^{1}H NMR threading experiment 160
5.6 Chiroptical spectroscopic characterisation of btp ligands 103R/S, 109R/S, 110R/S and [2]catenanes 111R/S 163
5.7 Epimerisation of chiral centre 167
5.8 Synthesis and characterisation of btp olefin 104 functionalised at the 4-pyridyl position 170
5.9 RCM of btp olefin 104 functionalised at the 4-pyridyl position 172
5.10 Synthesis and characterisation of olefin-derivatised btp ligands 105 and 106 175
5.10.1 Investigation into self-templating of **105** and **106** in solution by ^{1}H NMR spectroscopy and mass spectrometry 179
5.10.2 RCM of **btp** olefins **105** and **106** 181
5.11 Synthesis and characterisation of olefin-derivatised btp ligands 107 and 108 183
5.12 Investigation into self-templating of 107 and 108 in solution by ^{1}H NMR spectroscopy and mass spectrometry 185
5.12.1 RCM of btp olefins **107** and **108** 186
5.13 Discussion 190
5.14 Anion recognition by [2]catenane and macrocycles 193

5.15 Chiroptical probing of Ln(III)-directed formation of luminescent supramolecular gels 197
5.16 Conclusions 200
5.17 Future work 202
6 Synthesis and structural studies of the subtly unsymmetric 1,4-di(2-pyridyl)-1,2,3-triazole ligand and its transition metal complexes 204
6.1 Introduction 205
6.2 Synthesis and structural studies of 124 206
6.3 Synthesis and self-assembly studies of $[Cu124_2]PF_6$ 211
6.4 Crystallographic Study of $[Cu124_2]PF_6$ 212
6.5 Synthesis and structural studies of $[Ag124_2]SbF_6$ 214
6.6 Synthesis and structural study of $[Co124_2(NO_3)_2]$ 218
6.7 Synthesis and crystallographic study of Pt(II) phases derived from 124 220
6.8 Photophysical studies of complexes in solution 226
6.9 Discussion 227
6.10 Conclusion 229
6.11 Final Future Perspectives 229
6.12 Final Summary 231
7 Experimental 234
7.1 General Experimental Details 235
7.1.1 Materials and Methods 235
7.1.2 X-ray Crystallography 236
7.1.3 Photophysical measurements 237
7.1.4 Spectrophotometric titrations and binding constants 237
7.1.5 Microscopy and Rheological studies of the gels 238
7.2 Synthetic Procedures 238
7.2.1 Synthesis of ligands discussed in Chapter 2 238
7.2.2 Synthesis of complexes discussed in Chapter 3 249
7.2.3 Preparation of supramolecular gels derived from **H_384** 250
7.2.4 Preparation of coordination polymer materials derived from **H_384** presented in Chapter 4 251
7.2.5 Synthesis of compounds presented in Chapter 5 252
8 References 271
9 Appendices 288
9.1 Appendix A (NMR) 289
9.2 Appendix B (Mass Spectrometry) 339

9.3 Appendix C (Spectroscopy) 341

9.4 Appendix D (Thermogravimetric Analysis) 353

9.5 Appendix E (Crystallography) 355

9.5.1 Powder XRD.....362
9.5.2 Crystallographic Refinement details.....363

1 Introduction

1.1 Scope of Thesis

The goal of this PhD project was to study the coordination chemistry of modified 1,4-disubstituted-1,2,3-triazole containing ligands, from discrete metal complexes to coordination polymers, with a focus on generating functional supramolecular systems and materials. It is desired to gain an in-depth understanding of the self-assembly behaviour of this versatile hetereoaromatic functional group with a range of cationic metal guests. Labile and inert transition metals and *f*-block lanthanide metals will be explored in the study of the resulting diverse metallo-supramolecular architectures. The functional properties of the systems generated will be further investigated. Particular attention will be devoted to the synthesis and study of gels and porous coordination polymers as well as the self-assembly behaviour responsible for the self-templation of interlocked systems.

1.2 Supramolecular Self-Assembly

Supramolecular chemistry has been at the cornerstone in the development of novel systems leading to the growth of nanotechnology in the last decade. In the context of supramolecular chemistry, 'self-assembly' describes a process whereby a system of pre-existing components form an organised system, or pattern, as a result of local interactions between the components. The fundamental interactions of this process consist of various non-covalent interactions between molecules, such as hydrogen bonding, π–π stacking and metal–ligand coordination interactions. The formation of complex and functional molecular structures, triggered by the use of metal directing templates[1] and self-assemblies, is highly topical in both medicinal chemistry[2-3] and material science.[4-6] The use of metal ions is particularly attractive for the generation of novel structures as their coordination requirement and pre-organisation facilitates the incorporation of geometrical directionality as well as function, when coupled with careful ligand design. Examples of this, which are of particular interest, are the trivalent lanthanide (Ln(III)) ions,[7] such as europium (Eu(III)) and terbium (Tb(III)), and transition metals such as cobalt, copper, zinc, cadmium, ruthenium and silver. When combining a conformationally adaptable ligand precursor with a labile metal ion's energetically preferred coordination geometry, structurally diverse supramolecular architectures can be created.[8] Both discrete molecules and infinite coordination polymers, such as metal organic frameworks (MOFs) can be generated.[8] In the case of transition metal ions, a diverse range of coordination geometries can be accessed, such as tetrahedral (*e.g.* Cu(I)),

square planar (*e.g.* Pt(II)), and pseudo octahedral (*e.g.* Ru(II) and Fe(II)) and various bipyramidal coordination polyedra (*e.g.* Cu(II) and Zn(II)). Ln(III) ions possess higher coordination numbers (9-12) allowing access to complex polyhedra such as trigonal prismatic and square antiprismatic.[8]

The objective of this PhD project was to develop a number of novel ligands incorporating the 1,4-disubstituted-1,2,3-triazole motif either in the form of the 2,6-bis(1,2,3-triazol-4-yl)pyridine (**btp**)† tridentate framework or based on the bidentate 2-(1,2,3-triazol-4-yl)pyridine (**tp**) motif in order to explore the self-assembly behaviour of these heterocyclic derivatives, either in the case of self-templation or in the presence of *d*- and *f*-metal ion centres. The advantage of these ligand structures is that they can be rationally modified to accommodate other functionality and structural units. This allows participation in additional macromolecular interactions, altering both the overall structural complexity and function of the resulting supramolecular self-assemblies. The properties of the resulting discrete metal complexes, extended polymer materials and mechanically interlocked systems were to be studied in the solid and solution state and their potential function investigated.

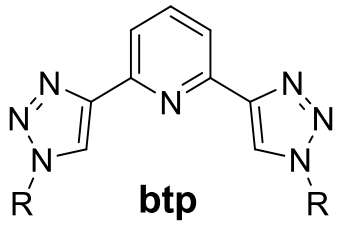

btp

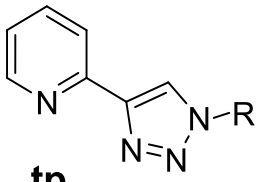

tp

1.3 The 1,2,3-triazole and 'Click' Chemistry

The 1,2,3-triazole is a nitrogen rich heterocycle which has become ubiquitous in the literature in recent years due to its ease of synthetic preparation, *via* the azide-alkyne 1,3-dipolar cycloaddition (or the 1,3-Huisgen cycloaddition),[9] and also due to its metal coordination ability, amongst many other uses. The copper catalysed variation of the 1,3-Huisgen cycloaddition, the Copper(I)-catalysed Azide-Alkyne Cycloaddition (CuAAC) has shown great potential as a dependable reaction with a wide scope of substrates. Sharpless *et al.*[10] developed the CuAAC reaction as regiospecific and high yielding, exclusively giving 1,4-disubstituted-1,2,3-triazole products. The azide-alkyne triazole version of Huisgen's [2+3] cycloaddition, although non-classical due to its non-concerted nature, has been described by Sharpless as the 'cream of the crop'.[11] Despite concern over the safety of azides,[12] chemists have given these transformations special attention over the years. Both the

† The **btp** motif has also been called by other names in the literature, such as 'tripy' (Schubert *et al.*) and 'bitapy' (Kakuchi *et al.*). The term 'clickate' has also been used by Hecht *et al.*

azide and alkyne groups present a wide range of advantages as substrates for the CuAAC reaction, such as stability in the presence of the nucleophiles, electrophiles and solvents; 1,3-dipolar reagents that have this quality are particularly rare. Both can easily be derivatised[13] and this will be discussed in detail in Section 1.9. Another advantage of this reaction is it can be carried out in aqueous media.[14] Sharpless and co-workers gave an insight into the mechanistic pathway of this process, through the use of DFT calculations, see Scheme 1.1(A).[15] This mechanism was later revised, see Scheme 1.1(B), as the postulated monometallic cupra-cycle would represent an unfavourably strained structure possessing excessive electron density.[16] The rate-limiting step, the transient formation of the bimetallic six-membered metallacycle was corroborated by a $^{63}Cu/^{65}Cu$ crossover experiment.[17] This mechanism also explained the regiospecificity of the reaction in the preference for Cu(I) π coordination at the α-carbon of the acetylide which directed a nucleophilic attack of the β-carbon at the azide terminus.

The majority of reported uses of the CuAAC reaction have not taken advantage of the coordinative abilities of the 1,2,3-triazole motif, rather employing it as a linker between other functional building blocks. This is the case for applications, particularly in biological, biochemical and carbohydrate research, wherein it has a physicochemical resemblance to the amide functional group due to its relative planarity, strong dipole moment and hydrogen bond donor and acceptor properties.[18-19] There are also many review articles covering the use of CuAAC chemistry in the construction of dendrimers and polymeric architectures,[20] and in the construction of higher order interlocked supramolecular structures.[21] With regard to the CuAAC reaction featuring in the supramolecular arena, the 'active metal template' strategy, pioneered by Leigh *et al.* was utilised in the templated synthesis of [2]catenanes[22]

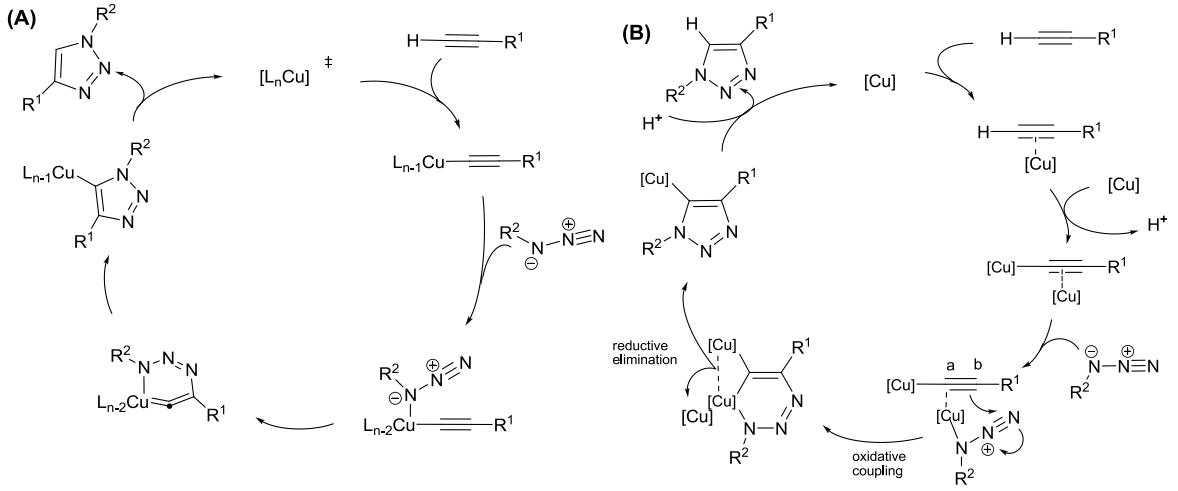

Scheme 1.1 CuAAC mechanism: (A) Original postulated mechanism,[15] (B) Revised Mechanism.[16-17]

and [2]rotaxanes;[23-25] some examples of which will be discussed in detail in Section 1.11. With regard to metal coordination, there have been several recent reviews of metal-chelating systems synthesised using the CuAAC reaction.[26-28] Schibli *et al.* described the installation of triazolyl metal chelating sites into molecules in a single step using the CuAAC reaction as the 'click to chelate' approach.[29] As a result of the recent explosion of interest in incorporating "click-triazoles" into chelating units, a review of the coordination properties of the 1,4-disubstituted-1,2,3-triazole will be discussed in detail with respect to the **btp** and **tp** binding motifs.

1.4 Click triazoles as chelating ligands

There are competing factors which must be taken into account when considering any self-assembly process. Metal complexation results in a decrease in hydration when a solvated metal is involved, resulting in favourable increased entropy of the system, which, thus, favours the complexation process. Conversely, dehydration is endothermic, *i.e.* bond formation between the cation and the ligand often does not compensate for this unfavourable energy contribution, thus in order for the Gibbs free energy change to favour complexation, the overall binding process is generally entropically driven. With this in mind, it is common to make use of polydentate ligands for building a coordination environment around *d*- and *f*-metals. The polydentate ligands at the core of this research project will be discussed in the following sections, with particular attention paid to bidentate and terdentate ligands comprising the 1,4-disubstituted-1,2,3-triazole and their recent appearances in the literature. The facile introduction of a wide range of functional groups renders them versatile and readily tunable and gives them an advantage over more classical analogues, namely 2,2'-bipyridine (**bpy**) and 2,2':6,2"-terpyridine (**terpy**). Before discussing the 1,4-disubstituted-1,2,3-triazole, a brief review of the bidentate and terdenetate ligands which paved the way for the "click-triazole" as a chelating motif will be looked at in the following section.

1.4.1 Bidentate ligands

The bidentate heterocyclic **bpy** and its derivatives have been the focus of widespread attention due to their remarkable coordination chemistry.[30-31] Their stability in both aqueous solution and to atmospheric oxygen ensures both their synthesis and storage life are not affected by ambient conditions.[32] Their strong *d*-metal binding behaviour arises from the two pyridyl nitrogen σ-dative interactions which are complemented by the overlap between

the *d*-orbitals of transition metal ions under coordination and the electron deficient aromatic π-system. Following the first synthesis of **bpy** and its iron complexation by Blau *et al.*[33] a large range of substituted **bpy** ligands has found use in many systems, giving rise to intriguing progress in areas such as luminescent molecular sensors[34-35] and photo-activated species through coordination to an appropriate transition metal, such as Ru(II).[31,36-37] The potential for further functionalisation of **bpy** through multi-step reaction pathways has been extensively explored.[38-40] The similarities of this class of bidentate ligands with certain 1,4-disubstituted-1,2,3-triazole derivatives have also been investigated thoroughly. Despite being more stable than their 'clicked' analogues[41] the power of the 1,4-disubstituted-1,2,3-triazole motif, for instance, is that a wide range of substrates can be introduced in a single step using the CuAAC reaction, through azide substitution of alkyl and aryl halides[42-43] as well as the diazo transfer of amines.[44] This will be discussed further in section 1.9. The bidentate **tp** analogue of **bpy** is very topical and has been developed relatively recently. This will be explored in the next sections paying particular attention to the coordination chemistry behaviour.

1.4.2 Bidentate ligands containing the 1,4-disubstituted-1,2,3-triazole motif

Bidentate ligands containing the 1,4-disubstituted-1,2,3-triazole unit are the most common subclass of "click-triazole" motif found in the literature. Of these the bidentate 2-(1,2,3-triazol-4-yl)pyridine motif (**tp**) and 2-(1,2,3-triazol-1-yl)pyridine (**tp'**) feature frequently (Figure 1.1). However, only examples relating to the coordination chemistry of such bidentate binding units will be included in the following discussion for succinctness.

The **tp** family of chelating ligands have been investigated for their relatively easy functionalisation in contrast to their **bpy** analogues. This class of 1,4-disubstituted-1,2,3-

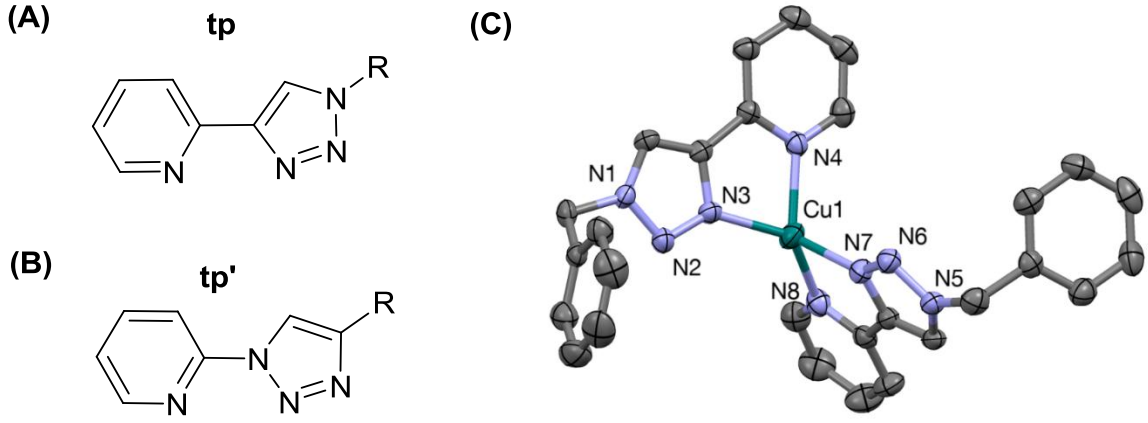

Figure 1.1 (A) **tp** (B) **tp'** (C) Crystal structure of [Cu**1**$_2$]BF_4 coordination complex. Thermal ellipsoids at 50% probability and hydrogen atoms and counterion omitted for clarity.[41]

triazole derivatives displays **bpy**-like *N-N* five membered chelation and the transition metal derived complexes show a decreased stability compared to those of **bpy**.[41] Fleischel *et al.* demonstrated the similarities of the [Cu**1**$_2$]BF$_4$ complex in the solid state , see Figure 1.1(C) with the analogous [Cu(**bpy**)$_2$]$^+$ complex. Similarities were observed through oxidation by O_2 and cyclic voltammetry experiments. The coordination polyhedra geometries and metal ligand bond lengths with Cu(I) and Ag(I) correlated closely with **bpy**. Interest has continued to grow in the incorporation of this type of ligand motif into coordination polymers and discrete polynuclear assemblies due to their intriguing architectures and potential applications as materials in catalysis, separation technology and biomedical applications[45] (*e.g.* drug delivery, sensors, in electronic and magnetic devices).[46-47]

Crowley *et al.* have recently employed facile one-pot CuAAC methods for the generation of **tp** and **tp'** ligands and examined their coordination properties with copper(II), silver(I), palladium(II), platinum(II), gold(I), and gold(III) ions.[42,48-53] In the case of one particular study, the stability of "regular" (*reg*) binding **tp** complexes over "inverse" (*inv*) binding **tp'** complexes with various metal ions was investigated, Figure 1.2.[54] The *reg* binding, demonstrated by the octahedral complex [Ru**1**(**bpy**)$_2$]$^+$, is so called, as the coordination of the metal ions occurs through the more electron rich proximal *N3* nitrogen atom. In the case of the *inv* binding, demonstrated by the octahedral complex [Ru**2**(**bpy**)$_2$]$^+$, the medial *N3*

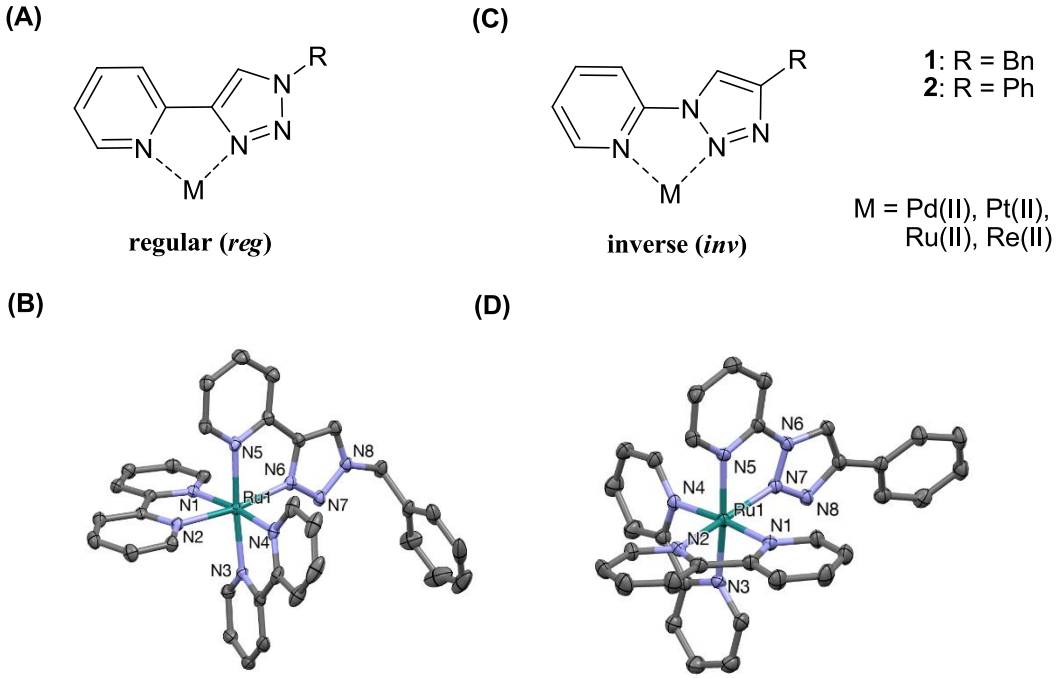

Figure 1.2 (A) The **tp** with regular (*reg*) binding pocket for metal ion (M) chelation and (B) the corresponding [Ru**1**(**bpy**)$_2$]$^+$ crystal structure.[54] (C) The **tp'** with inverse (*inv*) binding pocket and (D) the corresponding [Ru**2**(**bpy**)$_2$]$^+$ crystal structure.[54] Thermal ellipsoids displayed at 50% probability and counterions and hydrogen atoms omitted for clarity.

nitrogen adjacent to two electron-withdrawing nitrogen atoms is affected by a stronger inductive effect, and hence, is a weaker σ donor relative to the proximal nitrogen which is connected to a nitrogen atom and a less electron-withdrawing carbon atom.[54-55] Crowley *et al.* demonstrated this more pronounced stability of the *reg* complex comprising the **tp** isomer through ligand exchange studies and density functional theory (DFT) calculations. This will be explored in Chapter 6 to demonstrate that the typically active bidentate coordination functionality inherent in 1,4-disubstituted-1,2,3-triazoles favours binding through the *reg* binding pocket even when both *reg* and *inv* metalation sites are simultaneously present in the ligand scaffold.[55]

As in the case of the bidentate **tp** motif being explored extensively as a **bpy** analogue in recent times, another class of 1,4-disubstituted-1,2,3-triazole containing ligand has served as a readily derivatised **terpy** substitute. The terdentate two triazole containing **btp** binding motif, which comprised the core of the work conducted during this research project, will be discussed in detail in the next sections but firstly a brief overview of related terdentate ligand coordination systems which preceded it will be conducted.

1.4.3 Terdentate Ligands

Terdentate pyridine-centred ligands have found use in many areas of coordination and supramolecular chemistry, as well as in the design of catalysts and magnets with applications being found in photochemical and optoelectronic devices.[27] Of the most well studied terdentate ligands, dipicolinic acid (**H_2dpa**) and **terpy** have featured frequently in recent years, Figure 1.3. The **H_2dpa** motif chelates metal ions in its deprotonated form (**dpa**) through the pyridyl nitrogen and two carboxylate oxygen atoms. Bünzli, Piguet, Chauvin and co-workers have been interested in the **dpa** terdentate binding motif as metallo-supramolecular templates with Ln(III) ions and their photophysical and photochemical properties.[7,56] Chauvin *et al*. described the synthesis of a range of Ln(III)-directed self-assembly bundles using **dpa** derivatised ligands with 1:3 metal:ligand (M:L) stoichiometry.[57] They also demonstrated the use of Cs_3[Ln(**dpa**)$_3$] complexes as standards

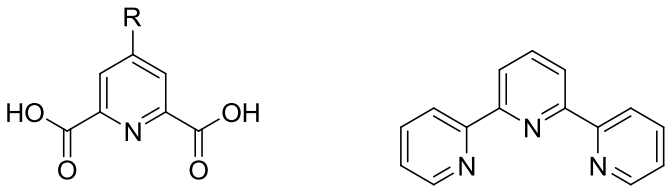

R = H **H_2dpa** **terpy**

Figure 1.3 – Terdentate ligands **H_2dpa** and **terpy**.

for luminescent quantum yield determination.[58-59] Work on this family of complexes was also intended to emphasise the extent of fine-tuning achievable for luminescent Ln(III) systems. The dependency of the photophysical properties on the nature of the appended ligand substituents was demonstrated by the remarkable tuning of the quantum yield efficiency of the Ln(III) centred emission by varying the substituent R of the **dpa** 4-pyridyl position, Figure 1.3.[57]

In related work, the Gunnlaugsson group has formed very stable and intricate luminescent 1:3 Ln(III):ligand self-assembled bundles[60-63] in which three chiral pyridyldiamide terdentate chelating ligands, **3**, were arranged around a Eu(III) centre in a chiral helical manner. The naphthalene derivative,[60] shown in Figure 1.4, was dubbed the 'Trinity Sliotar'. This class of compounds has since been derivatised with varying R' groups giving rise to Ln(III) self-assembled bundles,[61-66] helicates,[63-64,67] Langmuir-Blodgett monolayers[68] and mechanically interlocked systems.[64,69] These systems were further derivatised through the incorporation of other functional groups at the 4-pyridyl position.[70-71] Recently, Kotova *et al.* combined the coordination ability of the **dpa** motif with that of the **terpy** motif in the generation of white light emitting (WLE) solution-based discrete heterometallic lanthanide-directed self-assembly complexes.[72] An introductory review of the most prevalent terdentate ligand in the literature, **terpy** will be presented.

The **terpy** terdentate heterocyclic moiety, Figure 1.2, has been thoroughly studied and continues to appear in many areas of coordination chemistry[73-75] with both *d*-metal ions,[76-81] particularly with respect to the photophysical applications of its Ru(II) complexes,[27,34,82] and Ln(III) ions.[3,34,83] **Terpy** commonly forms achiral $[M(\mathbf{terpy})_2]^{2+}$ pseudo-octahedral complexes, with transition metals ions like Ru(II)[73,84] and Os(II),[73] see Figure 1.5(A). The symmetry of these prevent the need for resolving enantiomers, such as those formed with **bpy** of the formula $[M(\mathbf{bpy})_3]^{2+}$. The dileptic complex shown in Figure 1.5(A) displays the planar **terpy** ligands in a mutually orthogonal orientation. Also, metal:ligand (M:L) stoichiometries can also be controlled as demonstrated by the crystal structure of the monoleptic $[Ru(\mathbf{terpy})Cl_2(DMSO)]$ shown in Figure 1.5(B).[85] **Terpy** has been shown to be

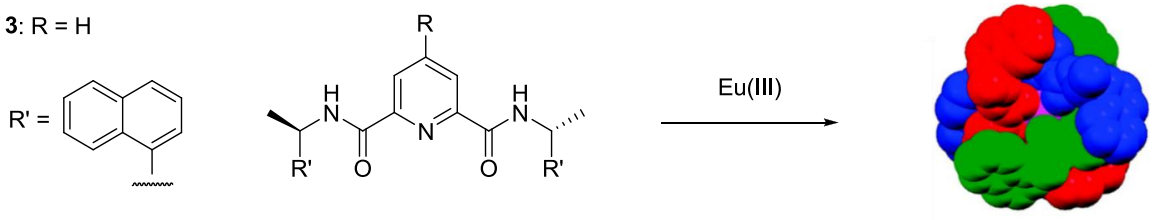

Figure 1.4 Dpa amide derivative, **3**. The crystal structure of the self-assembly bundle formed when **3** reacts with Eu(III), so-called the Trinity Sliotar.[60]

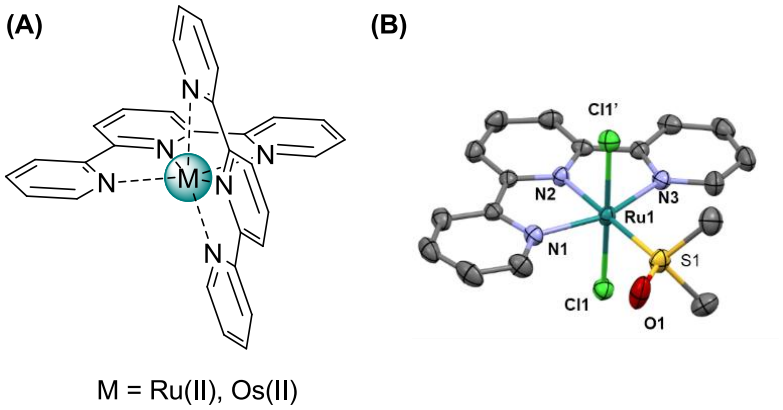

Figure 1.5 (A) Pseudo-octahedral structure of dileptic $[M(\mathbf{terpy})_2]^{2+}$ with M = Ru(II), Os(II)[73-75] and (B) crystal structure of monoleptic $[Ru(\mathbf{terpy})Cl_2(DMSO)]$.[85] Thermal ellipsoids at 50% probability and hydrogen atoms and disordered contributor omitted for clarity.

an efficient Ln(III) chelator binding the metal ion in a 1:3 M:L stoichiometric fashion with widespread use in the study of fluorescent complexes for biomedical applications.[3] **Terpy** coordination has also extended to the development of functional soft materials using various metal cross-linkers possessing multitopic binding motifs. For example, Kotova *et al.* reported the tritopic tris-**terpy** ligand **4**, possessing the tripodal 1,3,5-benzene tricarboxamide core, Figure 1.6.[86] This has been shown to form supramolecular gels with *d*-metal ions[87] and luminescent gels when cross-linked with Eu(III). which when doped with halide salts leads to the formation of single crystal salt nanowires through a diffusion-driven base growth mechanism upon drying of the gel matrix.[88]

Furthermore, Terech *et al.* reported the tritopic bis-**terpy** cyclam ligand **5** which when bound to Ni(II) formed a supramolecular gel possessing self-healing capabilities.[80] Related multitopic metal binding systems will be discussed in more detail in relation to designing functional supramolecular metallogels in section 1.10.1. It is evident from the examples above that **terpy** is a versatile binding motif and continues to be used in the generation of supramolecular coordination polymers,[77] supramolecular gels,[4,86] and other areas of

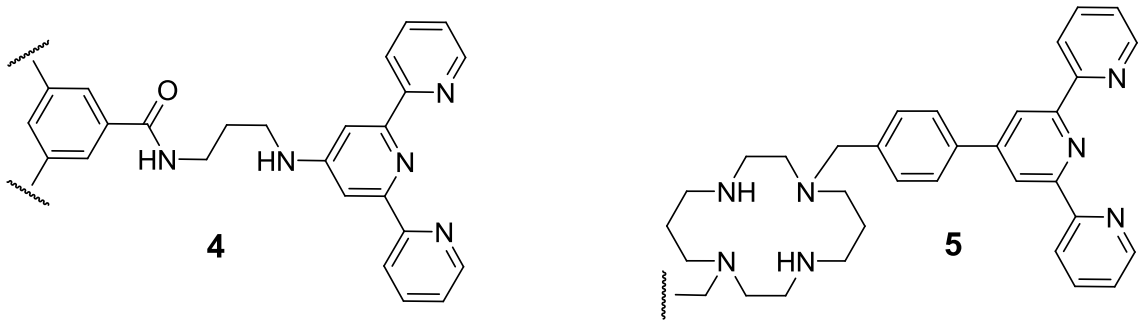

Figure 1.6 Tripodal tris-**terpy** ligand structure **4** and tritopic bis-**terpy** ligand **5** which have both been shown to form supramolecular metallogels through cross-linking of Eu(III) ions and Ni(II) ions respectively.

materials research, but also finds value in many other disciplines including medicinal chemistry[78] and in ion sensors[89-90] amongst others.[79,91] The motif has certain drawbacks, such as difficult synthesis.[92-95] Gaining efficient and convenient access to an alternative terdentate chelating motif possessing similar coordination properties to **terpy** is one of the main advantages the 1,4-disubstituted-1,2,3-triazole has over other terdentate motifs. In the next section, a brief introduction of how the 1,4-disubstituted-1,2,3-triazole features in terdentate binding motifs will be presented including the fortuitous origin of the **btp** chelating unit.

1.4.4 Terdentate btp ligand origins and significance

Although there are several instances of terdentate ligands containing one 1,4-disubstituted-1,2,3-triazoles[96-97] this section will be concerned with the aforementioned **btp** binding motif, Figure 1.7. **Btp** contains one central pyridyl unit and two 1,4-disubstituted-1,2,3-triazole containing units is a member of a family of terdentate pyridine-centred heteroaromatic ligands and has been shown to form stable coordination complexes with both transition metal and Ln(III) ions.[98-99]

The motif was first reported by Fokin *et al.* using CuAAC in an effort to develop efficient Cu(I) stabilising ligands for reaction rate enhancement of the same reaction type.[100] As part of this work, **btp** ligand **6**, functionalised at the *N1* triazolyl position with a benzyl group, alongside many other compounds developed, proved to be less efficient than the **TBTA** ligand in providing the necessary stabilisation of the catalytic Cu(I). Nevertheless, the resemblance of **btp** to **terpy** and the prospect of introducing many functional groups through the choice of azide using CuAAC could be harnessed for developing libraries of ligands possessing terdentate binding behaviour. Future ligand modifications and functionalisations are often desired which is one of the main reasons why **btp** continues to appear in areas in

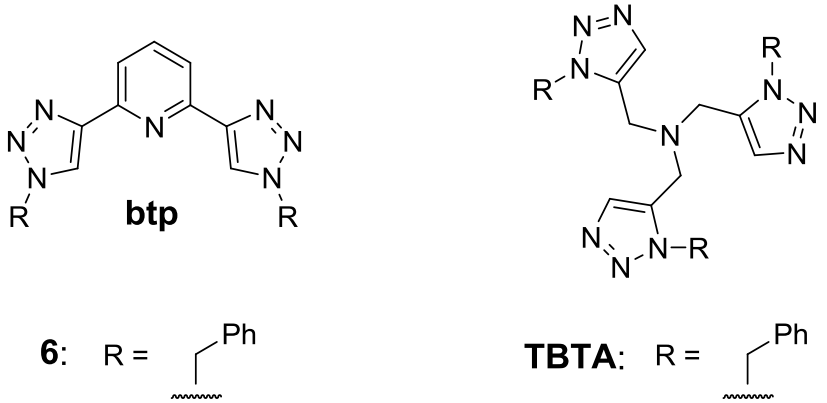

Figure 1.7 First reported **btp** ligand **6** and **TBTA** developed for Cu(I) stabilisation for CuAAC reaction rate enhancement.

chemistry once dominated by **terpy**. Flood *et al.* were the first to take advantage of the potential of this motif as a terdentate ligand for metal ion coordination.[98] An overview of the metal coordination and self-assembly behaviour of the **btp** motif will now be presented, with relevance to its structure, versatility and efficacy in coordination chemistry.

1.5 Btp metal coordination

Before delving into the library of metal complexes and supramolecular systems which exist through **btp** coordination chemistry it is worth taking note of the interesting conformational changes the **btp** system can undergo depending on the chemical and electrostatic environment within which it is placed. Unbound **btp**, and in the presence of anions, displays the triazole moieties *anti–anti* (or 'kinked') conformation with respect to the pyridyl nitrogen atom,[27,42 101-103] see Figure 1.8. Several crystal structures have already been reported displaying this *anti-anti* conformation.[104-110] This is due to energetically favourable electrostatic interactions as the repulsion between the lone pairs of the adjacent proximal triazolyl nitrogen atoms and pyridyl nitrogen atom destabilises the alternative *syn–syn* conformation. This *anti-anti* behaviour is reminiscent of the strong preference of **bpy**, **terpy** and various aza-arenes for adopting an *anti* conformation. This was exploited by Lehn and co-workers through the "helicity codon" approach in generating helical structures.[111] Hecht *et al.* designed analogous **btp** foldamers, **7**, which demonstrated the same chiral helicity, arising from the *anti-anti* conformational preference, induced by solvophobic effects and π-π stacking interactions, see Figure 1.9. The helicates were shown to undergo chiral inversion in the presence of an achiral halide ion. Hecht *et al.* realised that this made **btp** ideally suited for integration into larger macromolecular architectures; the resulting systems displayed a strong response to external stimuli, *e.g.* pH[108] and the presence of metal ions. Thus, **btp**-derivatives adopted helical conformations due to these favourable *anti-anti* orientation in various solvents, but upon metal chelation and switching to *syn-syn* conformation (Figure 1.8) led to cross-linked gels imparting various functions, *e.g.* magnetic (Fe(II)/(III)) or emissive (Eu(III)) materials.[112] A thorough discussion of the function of **btp** as an efficient

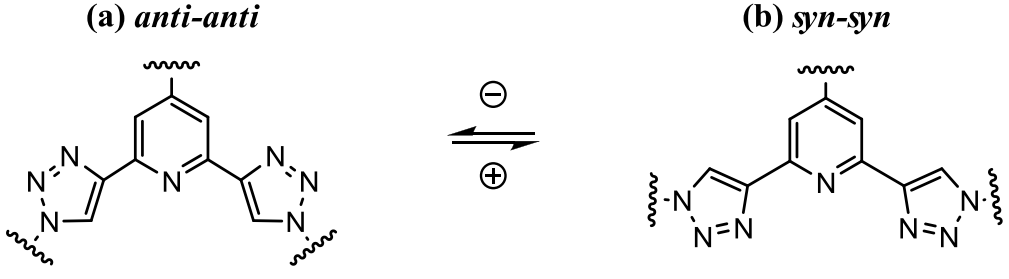

Figure 1.8 Conformational changes of the **btp** motif.

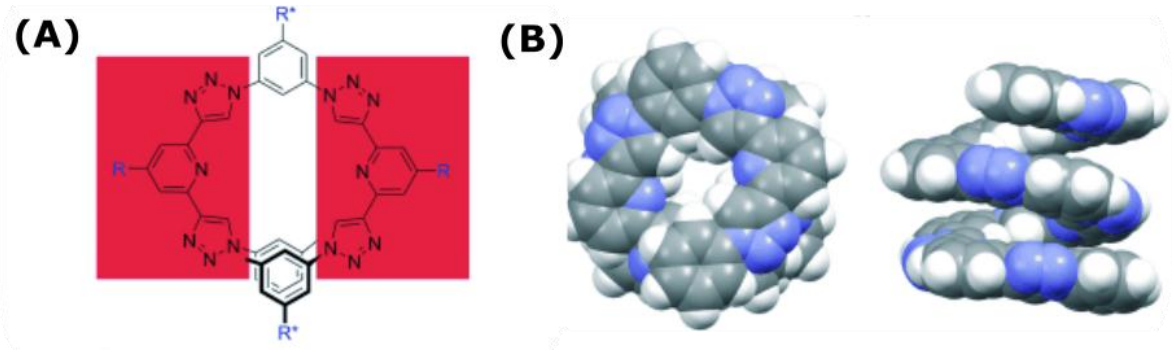

Figure 1.9 (A) Foldamer **7** helicity based on conformational preference for *anti-anti* **btp** where R, R' are polar side chains. (B) Space filling model of helical structure with side chains omitted for clarity. Figure reproduced from Ref.[101] Copyright 2008: Wiley

metal chelating motif will now be carried out.

The coordination chemistry of **btp** ligands has recently been reviewed at length by Byrne *et al*.[27] Others have focused more generally on the coordination chemistry of "click" triazoles.[12] With regard to specific examples from the literature, it comes as no surprise that **btp** shares metal chelation properties with the much studied **terpy** motif.[3,27,34,76-83] Their similar bond lengths and angles with Ru(II) (determined by X-ray diffraction analysis) is very apparent in Figure 1.10. A close comparison can be made between monoleptic Ru(II) **btp** complexes and their [Ru(**terpy**)Cl_2(DMSO)] analogues, which will be discussed in section 1.5.7. As previously stated, coordination of the **btp** terdentate motif with metal ions results in a dramatic conformational switching about the freely rotating *C*-*C* pyridine-triazole bond. The *syn–syn* (or 'extended') conformation facilitates metal ion chelation through the N_3 motif. This conformation dominates in the presence of a cation, such as metal ions or a proton. It has also been evidenced by nuclear Overhauser effect (NOE) NMR studies wherein it was found that, upon protonation of **btp**, interactions between the triazolyl

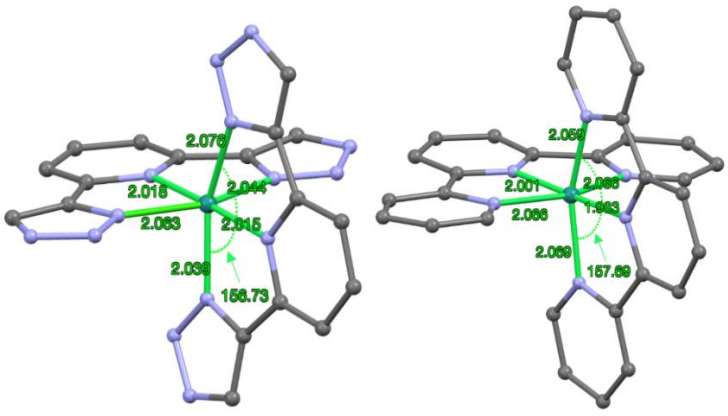

Figure 1.10 Comparison of the coordination dimensions between similar pseudo-octahedral Ru(II) complexes of **btp**[98] and **terpy**[49] from X-ray diffraction analysis. Bond lengths given in Ångstroms (Å) and bond angles given in degrees (°).

and pyridyl proton resonances are significant, indicative of the *syn-syn* arrangement of the adjacent heterocyclic rings.[103,105] The same interactions are not observed in the absence of a protonating agent in which case it is expected that the **btp** adopts the *anti-anti* conformation which is supported by observing a lack of through-space interactions between the pyridyl and triazolyl hydrogens. This conformational switching effect is common in the literature with crystal structure reports of **btp** chelation of Ni(II),[113] Fe(II),[98,105,114] Pt(II),[113,115-116] Pd(II),[117] Ir(III),[113] and Pb(II).[118] These examples will not be discussed, having been reviewed at length, previously.[119] Highly relevant examples, including more recent reports, of **btp** coordination chemistry with a selection of *d*- and *f*-metals will be explored in the coming sections, divided up according to metal.

1.5.1 Copper

Sankararaman *et al.* demonstrated the conformational switching upon complexing Cu(II) using the **btp** ligand **6**, synthesised by Fokin *et al.*[100] X-ray diffraction analysis of single crystals were obtained of the solitary ligand **6** and of the [Cu**6**(BF_4)(C_5H_5N)(H_2O)]BF_4 pseudo-octahedral complex, Figure 1.11.[120] The change from *anti-anti* to *syn-syn* upon complexation of Cu(II) was evidenced by observing the proximal triazolyl nitrogens, *N3* and *N4*, which rotated about the pyridyl-triazolyl *C-C* bond. The authors reported a decrease in the ligand fluorescence upon complexation. Using **6**, Crowley *et al.* reported a [Cu**6**Cl_2] complex wherein the metal centre adopted a distorted square pyramidal coordination polyhedron.[42] It is worth noting this range of Cu(II) coordination geometries affordable when elucidating the structures of Cu(II):**btp** complexes, which will be discussed in Chapter 4.

The most recent report of copper:**btp** interactions was published by Boratyński *et al.*

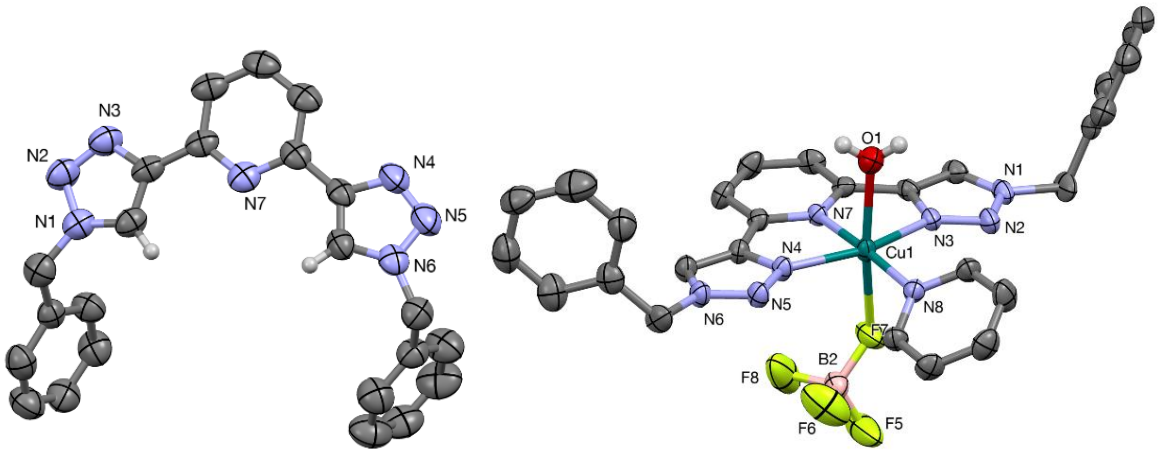

Figure 1.11 Molecular structures of ligand **6** displaying **btp** *anti-anti* conformation and [Cu**6**(BF_4)(C_5H_5N)(H_2O)]BF_4 complex displaying **btp** *syn-syn* conformation.[120] Thermal ellipsoids at 50% probability and hydrogen atoms and second counterion omitted for clarity.

following the efficient synthesis of chiral ligand **8** equipped with a Cinchona alkaloid moiety.[121] It was investigated whether these could be used as effective ligands for asymmetric copper-catalysed Michael additions. It was shown that the presence of the chiral Cinchona linker was responsible for effective chirality transfer. Gałęzowska *et al*., using the same ligand, then reported the formation of Cu(II) complexes and through obtaining mass spectrometry data concluded that complexes with Cu(**btp**)$_2$ stoichiometries were formed.[122] However, it was only through assumption, regarding preferred binding geometry of the metal ion, that they could claim the Cinchona part remained unbound and available for other potential bio-activity.

Recently, Kraft e*t al.* reported the synthesis of sugar-derived **btp** ligands[123] which achieved medium enantioselectivity as Cu(I) stabilizing ligands in asymmetric alkynylations of *N*-arylimines in a chosen model reaction *i.e.* the Cu(I)-catalyzed addition of phenylacetylene to *N*-benzylideneaniline producing chiral *N*-(1,3-diphenylprop-2-yn-1-yl)aniline. It was concluded that these preliminary results showed that the ligands reported could be useful for metal-catalyzed stereoselective reactions.

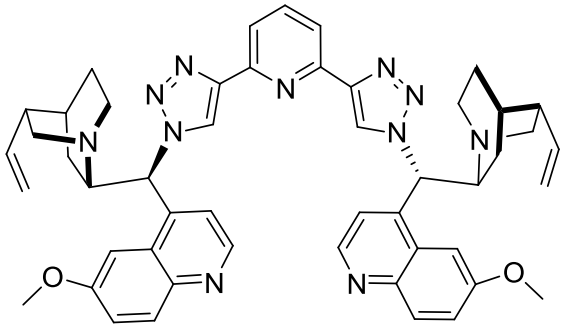

8

1.5.2 Zinc

The role of **btp** in complexing Zn(II) will be of major significance in the development of structurally diverse MOFs (Chapter 4), therefore a review of appropriate Zn(II) **btp** coordination will now be presented. Zhu *et al.* reported the crystal structure of dileptic pseudo-octahedral [Zn**9**$_2$](ZnCl$_4$) in the solid state, see Figure 1.12(A).[118] The dilepic complex also formed predominantly in solution, based on ^{1}H NMR studies and isothermal titration calorimetry, despite the anticipated formation of the monoleptic zinc:**9** (1:1) complex based on previously reported structures. The crystal structure of the monoleptic complex [Zn**10**Br$_2$],[99] see Figure 1.12(B), in which the Zn(II) coordination sphere was described as being a distorted square pyramidal geometry with a structural parameter (τ) = 0.46[124] was reported by Hecht *et al.* In related work, Meudtner and Hecht reported the

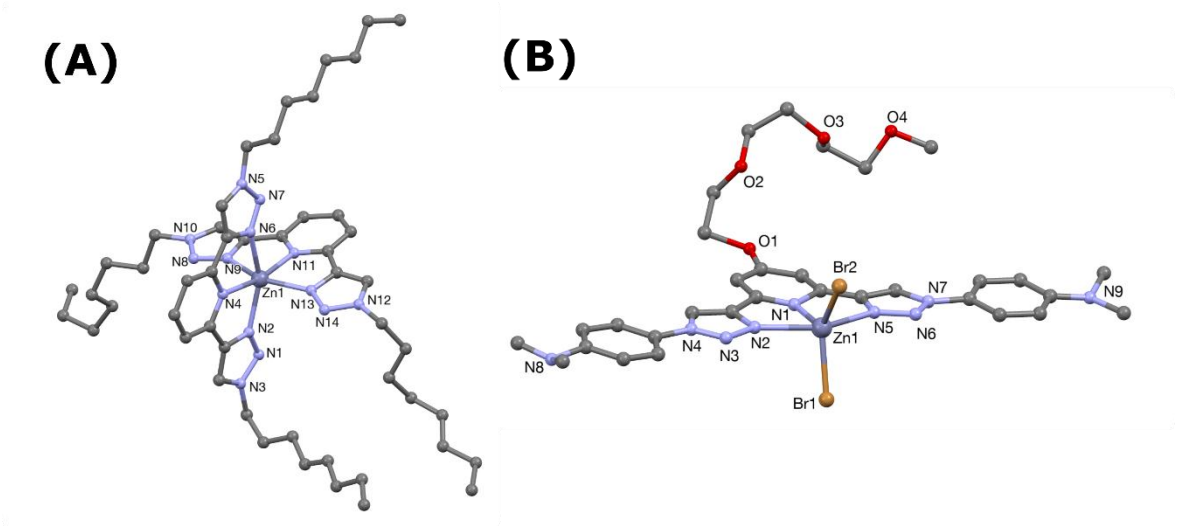

Figure 1.12 Molecular structures of (A) dileptic [Zn**9**$_2$](ZnCl$_4$) complex[118] and (B) monoleptic [Zn**10**Br$_2$][99] complexes. Solvent molecules, hydrogen atoms and counterions omitted for clarity.

formation of metallo-supramolecular crosslinked gels upon addition of Zn(II) to *poly*-**btp** helical foldamers of the same family as that of **7**.[112] Similarly, supramolecular metallogels were also produced by Yuan *et al.* upon addition of Zn(CF$_3$SO$_3$)$_2$ solutions to **btp**-containing polymers in 1:2 stoichiometric ratio.[125] The metallogels formed were robust enough to be picked up and placed under bending and compressive strain and also displayed self-healing behaviour. These metal cross-linked gel systems will be discussed further in Section 1.10.1, alongside other examples.

1.5.3 Silver

Another kinetically labile metal which has been studied for its coordination with multi-dentate Lewis basic ligands is silver. Its lability arises due to a d^{10} electronic configuration and, as a result, Ag(I) can accommodate a range of coordination geometry numbers ranging from 2 to 6 which can give rise to unexpected results. Such properties have been the reason behind the utilisation of Ag(I) ions in the design of metallo- supramolecular systems.[126]

Crowley *et al.* have demonstrated such behaviour with several 1,4-disubstituted-1,2,3-triazole[51] and **btp** derivatives[42] in the generation of an intertwined tetrameric architecture involving each ligand of **6** coordinated to three of the four Ag(I) centres, Figure 1.13.[42] Each metal adopts a distorted tetrahedral coordination polyhedron through the bidentate binding of a pyridyl nitrogen atom and proximal nitrogen atom of one of the triazoles while the second triazole unit of the ligand is coordinated, in a bridging fashion, to two adjacent Ag(I) ions using both the proximal nitrogen atom and the less-electron-rich medial nitrogen atom. The intriguing system is further stabilised through several π–π interactions between the

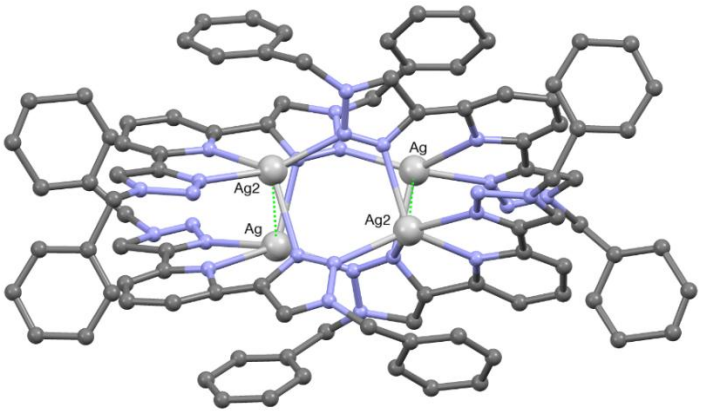

Figure 1.13 Molecular structure of tetrameric $[Ag_4\mathbf{6}_4](SbF_6)_4$. Argentophilic interaction displayed in green. Hydrogen atoms, solvent molecules and counterions omitted for clarity.[42]

ligand aryl groups alongside argentophilic interactions. This species was not only a consequence of crystal packing but also existed in solution as evidenced by ^{1}H NMR studies. **Btp** self-assembly with Ag(I) is an example of how a labile metal centre can facilitate the generation of structurally diverse architectures which would not be attainable using more rigid building blocks. The coordination chemistry of **btp** is extended with more inert heavier metals like platinum, iridium, rhodium and ruthenium.

1.5.4 Platinum

There have been several reports of Pt(II):**btp** complexes which have been summarised by Byrne *et al.* in a recent review.[27,113,115-116] Since then, there have been two further publications concerning the classical N_3 coordination of **btp** to Pt(II) with another reporting the preparation of Pt(II) complexes of mesoionic *N*-heterocyclic carbenes[127] (Section 1.5.9). Schulze *et al.* have reported the synthesis of soluble Pt(II)-containing polymers **11** based on a 4-pyridyl functionalised ethynyl **btp** ligand, Figure 1.14.[128] The polymer exhibited good film-forming ability and alongside observed solid-state emission, the authors claim these polymer systems possess high potential for integration into optoelectronic devices.

De Cola *et al.* reported the synthesis of monocationic Pt(II) complexes containing neutral

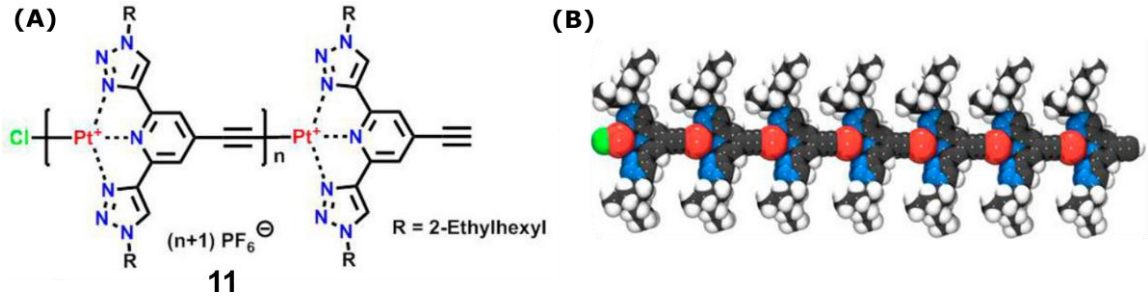

Figure 1.14 (A) **Btp** derived polyplatinyne **11** (B) spacefill model of the metalloploymer. Figure reproduced from Ref.[128] Copyright 2017: American Chemical Society.

btp derivatives, one of which consists of a bulky adamantyl group **12** and the other possessing a planar phenyl moiety **13**. Monoanionic ancillary ligands (Cl^- and CN^-) coordinating the Pt(II) centre resulted in different photophysical properties *i.e.* non-luminescent and luminescent, respectively, at room temperature. The steric nature of the ligand substituents also had an effect on the structural variation of the crystal packing with [Pt**12**CN]PF_6, [Pt**13**Cl]PF_6 and [Pt**13**CN]PF_6 all displaying Pt(II)···Pt(II) interactions in the solid state. This was in contrast to [Pt**12**Cl]PF_6 which did not show the same interactions due to the combined factors of the steric bulk of the adamantyl group and the diminished π-accepting nature of the Cl^- compared to that of the CN^- which helped induce such inter-metal interactions.

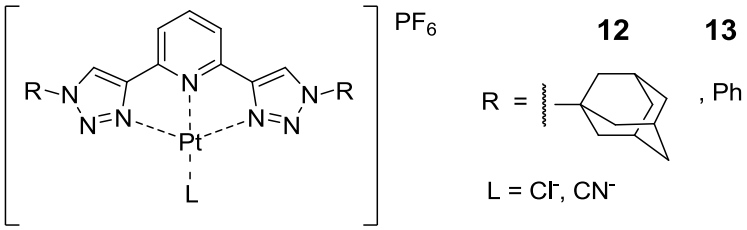

1.5.5 Iridium

Several articles of **btp**:Ir(III) complexes have been reported to date.[113] More recently, however, Prokop *et al.* reported the synthesis of two **btp** ligands, **14** and **15**, functionalised with the glucose sugar moiety,[129] for Ir(III) complex formation in the development of analogous **terpy**-platinum complexes which have shown promise as effective anticancer agents due to their good DNA-binding properties.[130] From cytotoxicity and cell targeting studies of Burkitt-like lymphoma cells it was concluded that the **terpy**:Ir(III) analogues had higher activity in relation to cell-death induction relative to the Ir(III) complexes of **14** and **15**, therefore the focus of further biological studies were centred on the **terpy** analogue over the **btp** analogues.

The only other occurrence of **btp**'s classical N_3 complexation of Ir(III) in the literature was reported by Byrne *et al.* The monoleptic [Ir**16**]Cl_3 complex was synthesised in which the

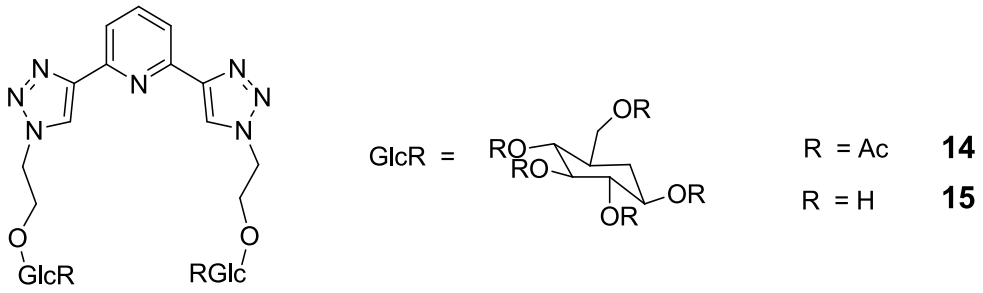

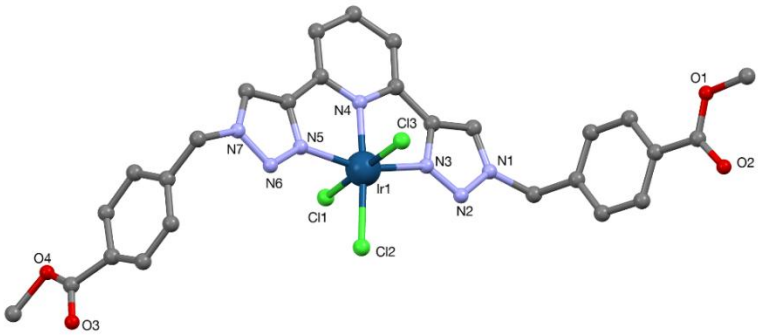

Figure 1.15 Monoleptic [Ir**16**]Cl_3 complex.[113]

crystal structure analysis showed an octahedral N_3Cl_3 coordination environment, Figure 1.15.[113] As part of this work the coordination, photophysical and electrochemical behaviour of **btp** with several *d*- metal ions was investigated, the results of which will be discussed in more detail in Section 1.6.

1.5.6 Rhodium

Yam *et al.* have recently used **btp** ligand **17**, as was first reported by Flood *et al.*,[98] in the synthesis of new Rh(I) complexes and study of their supramolecular assembly in order to gain more fundamental understanding of noncovalent metal···metal interactions.[131] Varying the concentration and temperature induced self-aggregation assembly behaviour *via* Rh(I)···Rh(I) interactions, π···π stacking and hydrophobic···hydrophobic interactions between the alkyl chains. This was evidenced by the increased intensity of an absorption band at 883 nm in the UV-vis absorption spectra assigned to trimeric species in solution.

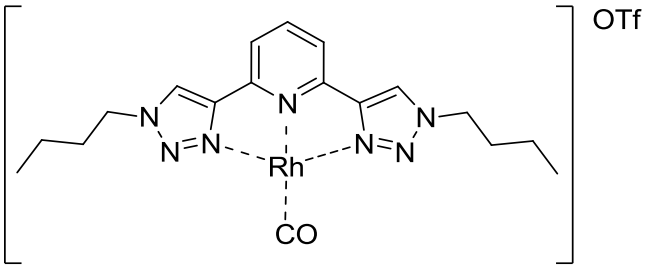

[Rh**17**(CO)]OTf

1.5.7 Ruthenium

Beginning with the most recent reports, Kakuchi *et al.* extended their work on the development of 3-arm and 4-arm star-branched polystyrene Ru(II):**btp** complexes using the "Click-to-Chelate" approach[132] by achieving synthesis of 3-arm, up as far as 12-arm starshaped poly(styrene oxide) (PSO) Ru(II) complexes. They achieved this by combining **btp** ligands **18**, **19** and **20** possessing PSO substituents within which each had varying number (x = 1-3) of side-arms.[133] The authors claim that this approach using **btp** as the

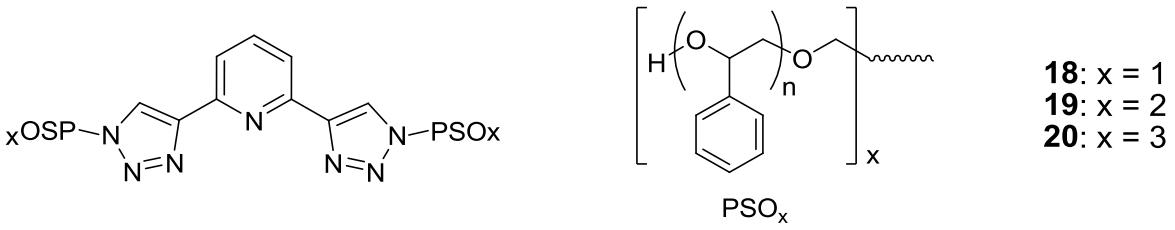

chelating motif achieved sophisticated metal-templated synthesis of macromolecules and could be used as a powerful tool for such polymer designs in the future. This non-covalent approach was particularly valuable in the synthesis of polymers with arm number greater than four as it offered more control than covalent approaches such as the core-first ring-opening polymerisation of styrene oxide (SO).

There is an extensive collection of reports featuring the coordination of Ru(II) using **btp** with interest stemming from the photophysical and electrochemical properties of the resulting complexes.[98,113,115,134] Flood and co-workers investigated if **btp** ligand **21** could form stable coordination compounds with Ru(II) amongst other metals.[98] The dilpetic [Ru**21**$_2$]$(PF_6)_2$ complex was characterised by single crystal X-ray diffraction analysis which displayed a distorted octahedral coordination geometry, Figure 1.16(A). The coordination and optical properties of these complexes were concluded to be similar to their **terpy** analogues,[75] while subtle differences in the electronic properties in relation to higher energy excited states of the **btp** moiety were observed.

Hecht and co-workers also reported dileptic Ru(II) **btp** complexes and also monoleptic Ru(II) complexes possessing asymmetric coordination spheres.[99] The crystal structure of [Ru**22**Cl_2(DMSO)] showed a distorted octahedral coordination geometry with the ligand binding in a tridentate manner; the axial sites were occupied by two chlorido ligands and

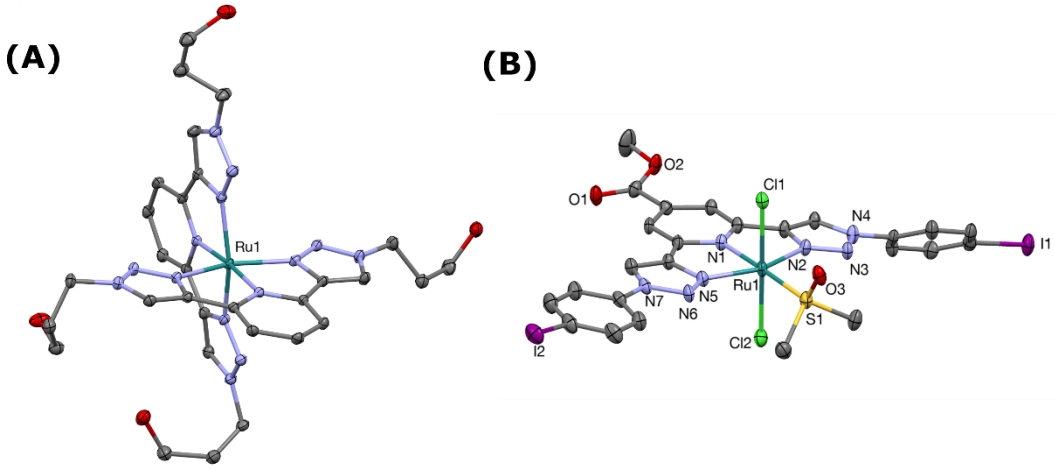

Figure 1.16 (A) Molecular structure of dilpetic [Ru**21**$_2$]$(PF_6)_2$ complex.[98] (B) Molecular structure of monoleptic [Ru**22**Cl_2(DMSO)].[99] Thermal ellipsoids at 50% probability and hydrogen atoms and counterions omitted for clarity.

finally the DMSO molecule was binding equatorially through the sulfur atom, Figure 1.16(B). Once again, the overall structural parameters of the complex were very similar to the corresponding **terpy** complex, *i.e.* [Ru(**terpy**)Cl_2(DMSO)].[85] This article showcased the ability to efficiently functionalise **btp** with different substituents in a modular fashion, which will be discussed in more detail in Section 1.9. A variety of **btp** ligands were synthesised with variability at the triazolyl *N1* aryl arms and at the 4-pyridyl position, for example, **22** consisted of a 4-iodophenyl substituent at the triazolyl *N1* position and a methyl ester group at the 4-pyridyl position. The influence the electron-withdrawing and electron donating groups at these positions had on the properties of the complexes was investigated.[99] Cyclic Voltammetry (CV) measurements demonstrated strong changes in the redox behaviour of the Ru(II) complexes depending on the coordinating ligand, particularly, the electron-donating or -withdrawing properties of the substituent at the 4-pyridyl position of the **btp** ligand. The stronger electron-donating effect of substituents showed lower oxidation potentials.

Schubert *et al.* reported the synthesis of π-conjugated ditopic **btp** ligands **23** and **24** with which coordination to Ru(II) complexes resulted in the formation of metallo-supramolecular polymers.[134] These systems, when imaged using atomic force microscopy (AFM) and transmission electron microscopy (TEM) methods, displayed rod-like structures and possessed good film-forming properties when drop-casted, suggesting their potential use in printable photovoltaic devices due to their optoelectronic properties endowed by the Ru(II) component.

As these last two examples demonstrate, the functionalisation of **btp** using divergent binding groups shows the potential scope for the development of materials systems such as coordination polymers. Endowing these systems with the metal's properties is desirable for applications in various devices. The photophysical and electrochemical properties of Ru(II) explain the popularity of this metal with material chemists and coordination chemists.

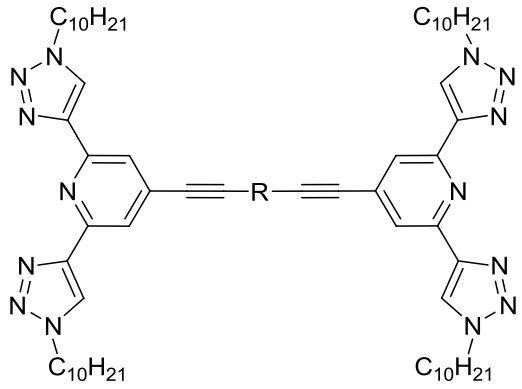

R = **23**

R = **24**

Another class of metals possessing rich photophysical properties are the lanthanides. The coordination chemistry of **btp** with valency three lanthanide (Ln(III)) ions will be examined in the next section.

1.5.8 Btp:Lanthanide containing complexes and supramolecular systems

There exists a plethora of Ln(III) hosting molecules whose behavioural diversity rationally affects macromolecular interactions, changing both the overall structural complexity and function of the resulting supramolecular self-assemblies. The rich variety of possibilities of Ln(III) ion-incorporated supramolecular systems has been explored by Bünzli, Piguet, Mazzanti, Chauvin and the Gunnlaugsson group to name but a few, and it has been shown that these systems offer potential for functionalisation, with demonstrated uses as, for example, luminescent probes and sensors for specific analytes.[56,135-137] It is with growing momentum that Ln(III) ions have been used to template the formation of a variety of supramolecular systems,[56,135-136,138-145] acting as guests for linear polydentate ligands and macrocyclic receptors. As Ln(III) ions are densely charged Lewis acids, a terdentate σ donor Lewis base containing chelating motif such as **btp** is a good choice for satisfying their coordination requirements.

Flood and co-workers, who demonstrated the formation of stable coordination complexes between **btp** ligands and *d*-metals ions,[98] were also the first to characterise the formation of stable complexes with Eu(III) through single crystal X-ray diffraction analysis. The molecular structure of [Eu**17**$_3$](ClO$_4$)$_3$ (Figure 1.17) shows the necessity for three terdentate ligands of **17** to satisfy the high coordination numbers of Eu(III). The complex displays tricapped trigonal prismatic geometry and the overall tris-chelated **btp** complex is more

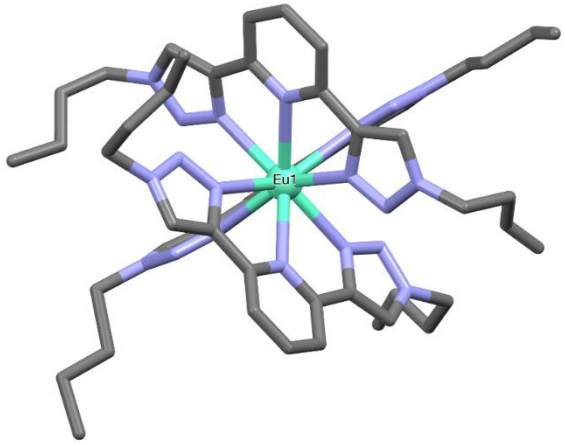

Figure 1.17 X-ray crystal structure of [Eu**17**$_3$](ClO$_4$)$_3$ viewed 'edge-on' relative to one of the **btp** ligands. Hydrogen atoms and counterions omitted for clarity.[98]

isotropic than its tris-**terpy** counterpart complex.[146] Inter ligand steric hindrance is minimised by the 1,2,3-triazole rings, resulting in almost planarity of each **btp** core with each of the three ligands mutually orthogonal to each other. In contrast the mean planes defined by each pyridyl ring of a **terpy** ligand in the $[Eu(\mathbf{terpy})_3](ClO_4)_3$ counterpart are tilted at an angle of between 12° and 26° to the adjacent ring, predominantly due to intra-ligand lone-pair repulsion consistent with a more ionic type of bonding between **terpy** and the Eu(III) centre. The **btp** motif of **17** also demonstrated sensitisation of the Eu(III) radiative states thus giving rise to the characteristic line-like emission in the red region of the spectrum when excited with UV radiation and a concomitant quenching of the ligand fluorescence through intersystem crossing (ISC) *via* the triplet state of **17**. Hecht and co-workers reported the synthesis of another **btp** containing tris-complex showing a similar X-ray crystal structure with Eu(III).[105] There has been one other Eu(III) **btp** crystal structure reported to date as will be presented in the coming section.

Btp ligands have featured with increasing frequency of late in new solvent extraction processes for the removal of transuranium elements (TRU), for example actinides (An) such as neptunium, plutonium, americium, and curium. These TRU are produced in nuclear fuel during reactor operation from neutron capture by uranium-235/238 and are themselves radioactive[147], therefore, efficient and selective removal of harmful TRU from waste mixtures is fundamental in the effort to close the nuclear fuel cycle, thus solving the environmental issues related to the management of existing nuclear waste. Some recent reports will now be presented.

Panak *et al.* have recently reported the time-resolved laser fluorescence spectroscopy for the formation of complexes of Cm(III) and Eu(III) with hydrophilic **btp** ligand **21**[98] functionalised at the *N1* position of the triazole with propan-1-ol,[148] Figure 1.18. The aim of the study was to investigate **btp** derivatives in order to obtain more stable complexes for

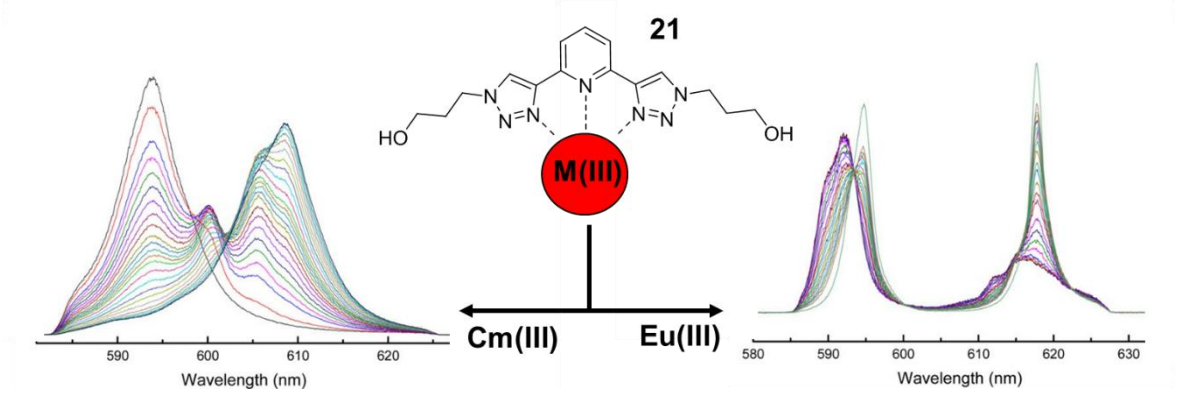

Figure 1.18 Fluorescence spectroscopy responses using **21** for determining selectivity of Cm(III) over Eu(III). Figure reproduced from Ref.[148] Copyright 2017: American Chemical Society.

optimum extraction conditions for the An/Ln separation process.

Casnati *et al.* have reported that hydrophilic **btp** ligands **25**, **26** and **27**, endowed with high trivalent actinide (An(III)) selectivity in the presence of large amounts of Ln(III) ions, are exceptional candidates for advanced separation processes in the treatment of radioactive waste.[149] The increasing number of OH groups at the periphery of the **btp** motif ensured solubility in aqueous media. This resulted in considerable increases in Am(III) extraction into water. The extraction process involved competing with TODGA-based organic solutions containing 99.9% of An(III) and Ln(III) ions, which had been previously co-extracted from aqueous phase feeds similar in composition to those coming from the PUREX (Plutonium URanium Extraction Process) raffinate *i.e.* high level nuclear waste. The authors believe that this new hydrophilic **btp** extraction system and related systems could contribute to the effective treatment of dangerous nuclear waste in the coming years.

A complexation study of *p*-tolyl functionalised **btp** ligand **28** with Ln(III) ions and An(III) ions was carried out using single-crystal X-ray diffraction and time-resolved laser fluorescence spectroscopy.[150] Crystal structures of Eu(III) and Sm(III) were isostructural displaying the tricapped trigonal prismatic geometry of analogous compounds with the **btp** motif and *p*-tolyl substituent of each ligand displaying essentially co-planarity, Figure 1.19. The composition and stability of Cm(III):**28** and Eu(III):**28** complexes formed in solution and the resulting global stability constants were obtained through analysis of the changing luminescence with respect to metal concentration of the two systems. The study showed a higher selectivity performance for Cm(III) over Eu(III) on account of the larger values of log β_3 for Cm(III): log β_3 [Cm**28**$_3$] = 14.0 ± 0.3 and log β_3 [Eu**28**$_3$] = 10.3 ± 0.2.

Taking advantage of the luminescent properties of the Ln(III) ions through the complexation with sensitising chelating motifs such as **btp** has given rise to many new and interesting systems, as has just been presented, with much potential for application in a wide realm of fields. It has also been shown that the Ln(III) ions have also demonstrated uses in

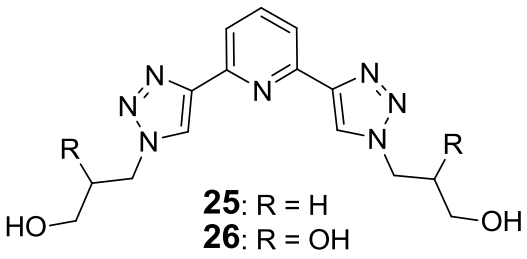

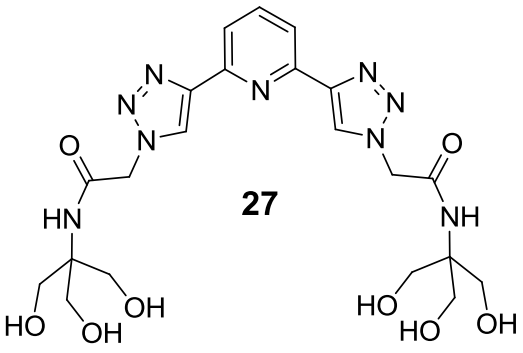

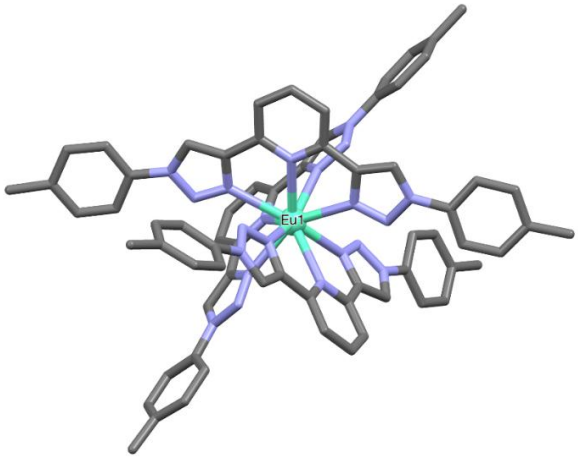

Figure 1.19 Crystal structure of [Eu**28**$_3$](OTf)$_3$ complex with hydrogen atoms and triflate counterions omitted for clarity.[150]

materials chemistry, endowing functional soft matter with dynamic mechanical properties. This will be discussed in more detail using additional examples in the context of supramolecular gels in Section 1.10.1.

The classical N_3 *syn-syn* binding conformation has been the feature of all the metal complexes with **btp** discussed up to this point. However, one last metal binding mode of the **btp** motif will be explored in the next section with reference to the latest appearances in the literature. This arises upon formation of bis(1,2,3-triazole-5-ylidene)pyridine wherein coordination through the *C4* triazolyl position occurs.

1.5.9 Triazolylidene btp metal coordination through C4 position

Hwang *et al.* recently reported the preparation of platinum complexes of mesoionic *N*-heterocyclic carbenes[127] based on a **btp**-like pyridine-bridged bis(1,2,3-triazole-5-ylidene) ligand **29**, methylated at the triazole *N3* position and functionalised at the triazole *N1* position with bulky 2,4,6-trimethylphenyl substituents, see Figure 1.20(A). This ligand was first reported by Schubert *et al.* in the preparation of bis(terdentate) Ru(II) complexes[151] and further functionalised by Berlinguette *et al.* for anchoring stabilised Ru(II) sensitisers to TiO_2 semiconductor surfaces[152] for application in dye sensitised solar cells. The monoleptic complexes were of the type [Pt**29**L]A (where the counterion A = Cl or PF_6 in the cases where the auxiliary ligand L = Cl or CN and A = PF_6 when L = CH_3CN). A crystal structure of [Pt**29**Cl]PF_6 was obtained displaying the *anti-anti* ligand conformation necessary for metal chelation to occur, now that the triazolyl proximal nitrogen (labelled *N2* and *N7*) is methylated and electron density now resides on the deprotonated *C4*. It was found that the CH_3CN and CN bound complexes exhibited vapochromic responses attractive for chemo

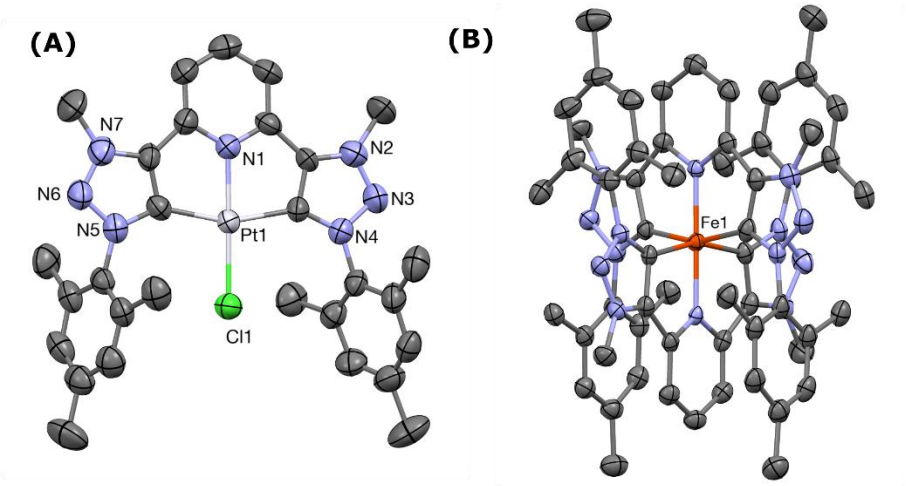

Figure 1.20 (A) Crystal structure of complex [Pt**29**Cl]PF_6 (atom labelling according to CIF).[127] (B) Crystal structure of [Fe**29**$_2$](Fe_2Cl_6O). Thermal ellipsoids displayed at 50% probability with hydrogen atoms, counterions and solvent molecules omitted for clarity.

sensing applications for volatile organic vapour detection. Using the same ligand **29**, Matsubara *et al.* reported the synthesis of an example of a dileptic iron complex [Fe**29**$_2$](PF_6)$_2$. A crystal structure was obtained upon anion exchange of the PF_6^- anion with a (μ-oxo)bis[trichloroferrate(III)] ($[Fe_2Cl_6O]^{2-}$) counterion, see Figure 1.20(B).[153] A crystal structure of the isopropyl derivative ligand **30** was also reported in the same article. In related work, Matsubara *et al.* reported the synthesis of a bimetallic Cu(I) complex with ligand **30**, from a dimeric Ag(I) precursor (Figure 1.21).[154] Interestingly, the isopropyl groups stabilised the Ag(I) dimer in contrast to the tetrameric Ag(I) analogue reported by Schubert *et al.* when **29** is used instead.[151]

A collection of similar **btp** based carbene ligands have been complexed with Ir(III) in the development of blue or green electroluminescent dopants for organic optoelectronic devices, Figure 1.22. This work has been patented by Cheil Industries, Inc., S. Korea.[155] A range of

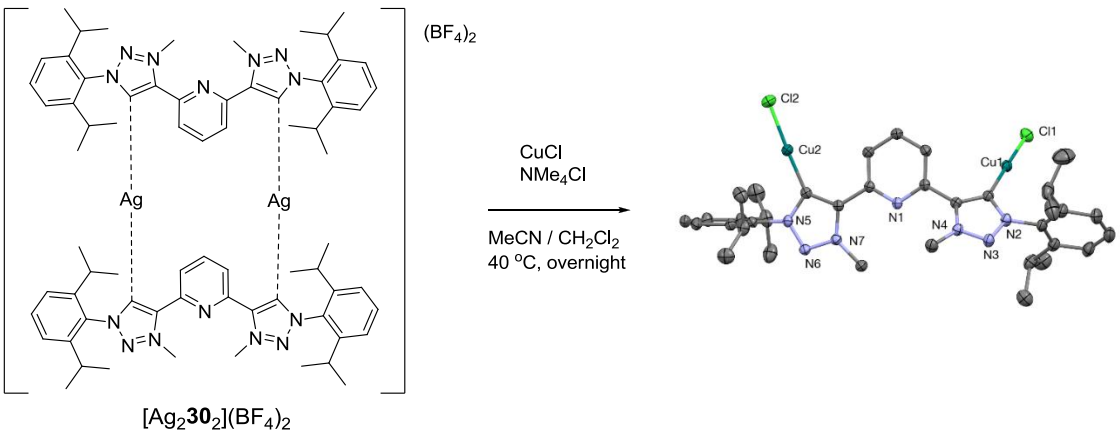

Figure 1.21. [Ag_2**30**$_2$](BF_4)$_2$ dimer precursor and synthesis of [Cu_2**30**Cl_2]. Thermal ellipsoids displayed at 50% probability with hydrogen atoms and solvent molecules omitted for clarity.

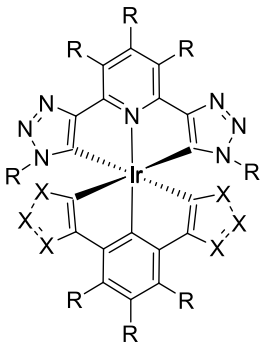

31

Figure 1.22 General structure diagram for a range of **btp** based Ir(III) complexes for use as electro-luminescent dopants in organic optoelectronic devices. X = N, NR, CR *etc.*; R = H, D, halogen, cyano, hydroxy, C1-C20 alkyl chains *etc.*[155]

Ir(III) complexes **31** were reported with varying substituents X = N, NR, CR *etc.*; R = H, D, halogen, cyano, hydroxy, C1-C20 length alkyl chains *etc.*

1.6 Recent btp advances in the Gunnlaugsson Group

As was discussed earlier, Byrne *et al.* conducted structural studies of **btp** ligands chelating various *d*-metals using **btp** ligand **16**.[113] The coordination, photophysical and electrochemical studies of Ru(II):**btp** complexes using ligands **16** and its hydrolysed analogue **32** was also carried out. When **32** was complexed with Ru(II) it gave rise to the formation of metallo-supramolecular gels. The crystal structure of the [Ru**32**$_2$](PF$_6$)Cl complex gives an insight into the short range molecular arrangements comprising the metallo-supramolecular gel, Figure 1.23. The packing in the crystal structure displays intermolecular hydrogen bonding interactions between the carboxylic acid termini which hydrogen bond to water and ethanol molecules. There is also a non-classical hydrogen bonding interaction between one carboxylic acid group and a chloride ion which is itself involved in a hydrogen bonding interaction with the *CH* of one triazole ring. This example

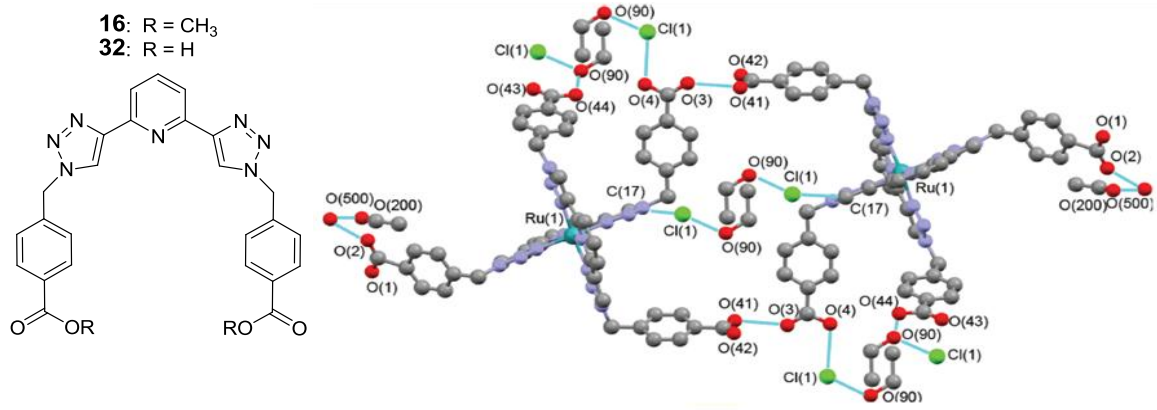

Figure 1.23 Btp ligands **16** and **32**. X-ray crystal structure of (Ru**32**$_2$](PF$_6$)Cl showing the various supra-molecular interactions also observed in supramolecular gel formation. Figure reproduced from Ref.[113] Copyright 2013: Royal Society of Chemistry.

demonstrated the solid state interactions likely to contribute to the formation of supramolecular gels. The use of X-ray diffraction analysis for gaining an insight into the short range order of gel systems developed over the course of this research thesis will contribute to our understanding of their structure on the molecular scale. Similar gel based systems will be discussed in more detail in Section 1.10.1.

Bradberry *et al.* went on to use **32** alongside the **H$_2$dpa** derivative, **33**, in reporting a molecular logic gate mimic comprised of outputs arising from the use of Ln(III)- and ligand-centred emissions (Figure 1.24).[70] This system represents one of only a few examples to date of the use of sensitising luminescent 4*f* ions as outputs in molecular logic. The encapsulation of complexes within a polymer organogel gave luminescence changes in response to the inputs [H^+] and [F^-]. The (0,0) state involved the green and red phosphorescence from Tb**32**$_3$ and Eu**33**$_3$, respectively. The (1,0) state was achieved by acidification which gave rise to an increase in the Eu(III) emission intensity through the PET effect of **33**. The (0,1) state was brought about through addition of fluoride causing a decrease in both the Tb(III) and Eu(III) emission intensities through dissociation of the Tb**32**$_3$ complex and deprotonation of the already protonated Eu**33**$_3$, respectively. The (1,1) state was accessed by addition of both acid and fluoride resulting in an enhanced Eu(III) emission and loss of Tb(III) alongside an increase in the **btp** ligand **32** fluorescence.

In other work, the **btp** ligand **32** was further functionalised with a selection of amino acids, Gly, Ala, Phe, and Trp methyl esters, to give amide derivatives **34** which were then used in the study of the Ln(III) directed self-assembly of highly luminescent supramolecular bundles.[112] This work was undertaken with a view to introducing biologically relevant and chiral moieties into such ligands, however, the complexes dissociated in aqueous media. These derivatives were shown to form stable, emissive Ln(III) complexes in organic solvents

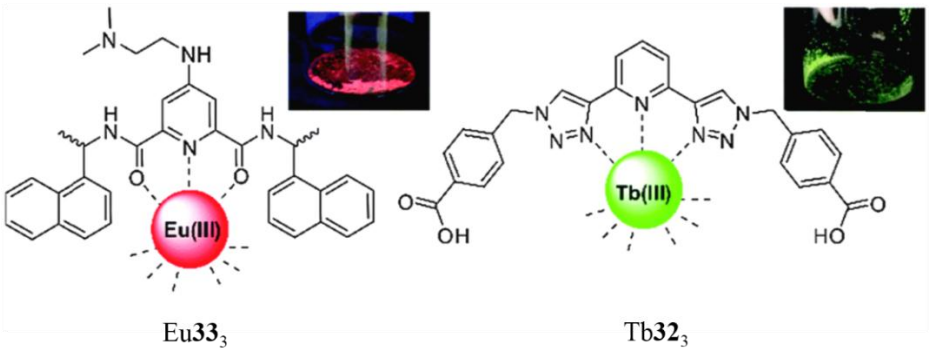

Figure 1.24 Structures of ligands **32** and **33** and their complexes [Tb**32**$_3$] and [Eu**33**$_3$]. (Inset) Coloured emission arising from complexes under UV irradiation at λ = 254 nm. Figure reproduced from Ref.[70] Copyright 2015: Royal Society of Chemistry.

such as DMSO, possessing millisecond time range radiative excited states. Their photophysical properties in organic solutions were used to determine global stability constants of the self-assembly equilibria. Quantum yields for the Tb(III) complex emission of 46−70% in CH_3CN solution were measured, reflecting the efficient energy sensitisation of the Tb(III) complexes by the **btp** 'antenna'. By comparison, the Eu(III) complexes displayed less high quantum yields of 0.3−3%. It was concluded that the more efficient Tb(III) radiative state sensitisation was as a result of the better energy match with the **btp** triplet state. This was determined through low temperature phosphorescence emission measurements of the Gd(II) complex of **16**. This article demonstrated that introducing functionality at the aryl terminal positions did little to perturb the self-assembly behaviour with Ln(III) ions as evidenced by the comparable speciation equilibria species formed, calculated global stability constants and quantum yields of luminescence. In the case of α−amino acids: Gly, Ala, Phe, derivatives. The Trp functionalised cases showed a less efficient quantum yield of luminescence in both Eu(III) and Tb(III) complexes.

By introducing methyl functionality closer to the **btp** chelating core, as seen for **35**, in the form of methine chiral centres at the former methylene position (X), additional useable chiroptical spectroscopic properties were endowed on the **btp** system.[156] Byrne e*t al.* was able to monitor the self-assembly of ligand (*S,S)* and (*R,R*) entantiomers, **35S** and **35R**, respectively, with Eu(III) and Tb(III) using Circular Dichroism (CD) titrations upon addition of aliquots of Ln(III) metal solution to a solution of the ligand. Significant changes occurred in the CD spectra including an intense Cotton effect, giving rise to a bisignate CD couplet of the same sign as each respective ligand. Circular polarised luminescence (CPL) of the complexes was also measured with each pair of enantiomers displaying signals of equal magnitude and opposite sign for each band characteristic of a specific *f-f* electronic transition, thus demonstrating that the chirality of the ligands was transferred to the Ln(III) complexes. This was one of the first utilisations of CD titrations for probing the metal-directed self-

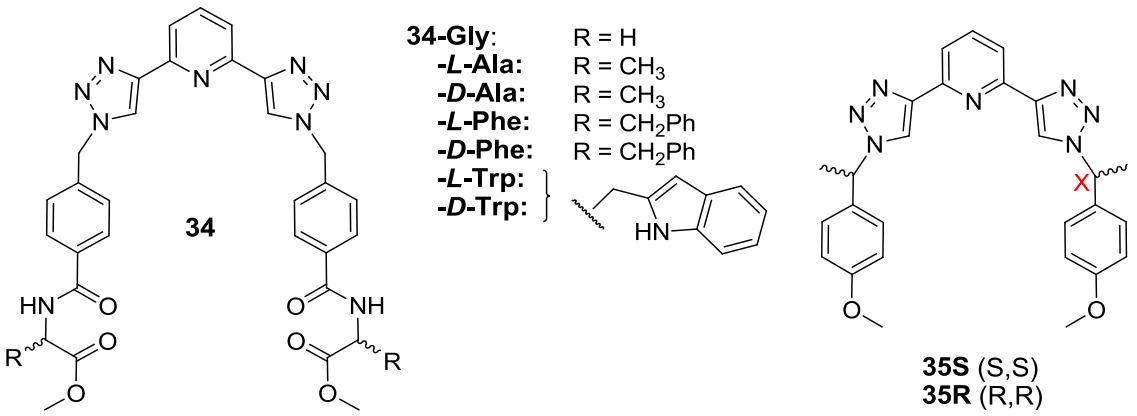

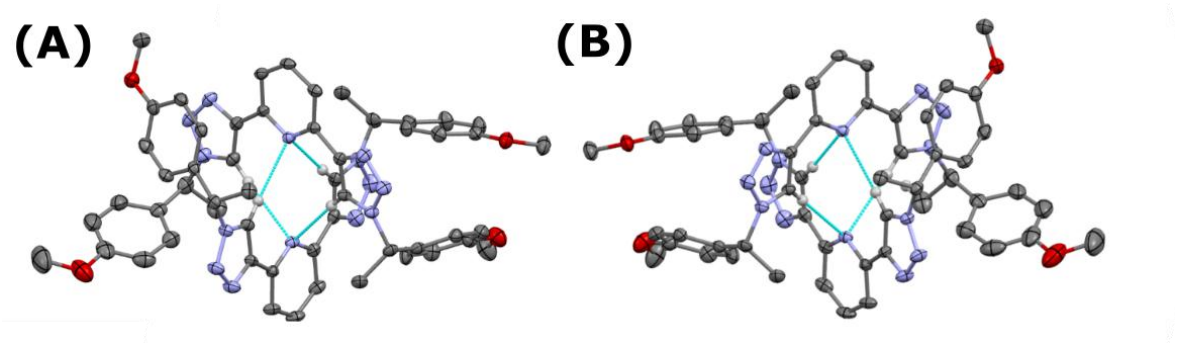

Figure 1.25 (A) X-ray crystal structures of **35S** and (B) **35R** enantiomers.[156] Thermal ellipsoids displayed at 50% probability with hydrogen atoms not involved in hydrogen bonding omitted for clarity.

assembly of supramolecular systems. Crystal structures of both enantiomers, **35S** and **35R**, were obtained which displayed interesting dimerisation of the ligands in the solid state through a self-templation effect, Figure 1.25. This phenomenom arises due to the acidic nature of the triazolyl *CH*s, which sees each triazolyl CH on each **btp** involved in a non- classical hydrogen bonding interaction with the pyridyl nitrogen of the other dimeric **btp**. As expected the opposite enantiomer displays mirroring behaviour.

Byrne *et al.* expanded on this work in achieving successful and high yielding synthesis of self-templated [2]catenanes **36a-c**.[102] The crystal structure demonstrates the self-assembly was made possible through a combination of non-classical **btp** hydrogen bonding interactions, as in the case of **35S** and **35R**, and also amide hydrogen bonding interactions, Figure 1.26. Details of the synthesis and properties of these, and analogous, mechanically interlocked systems will be discussed in more detail in Section 1.11. The structural nature of these [2]catenane hosts also exhibited a pronounced selectivity for the anion recognition

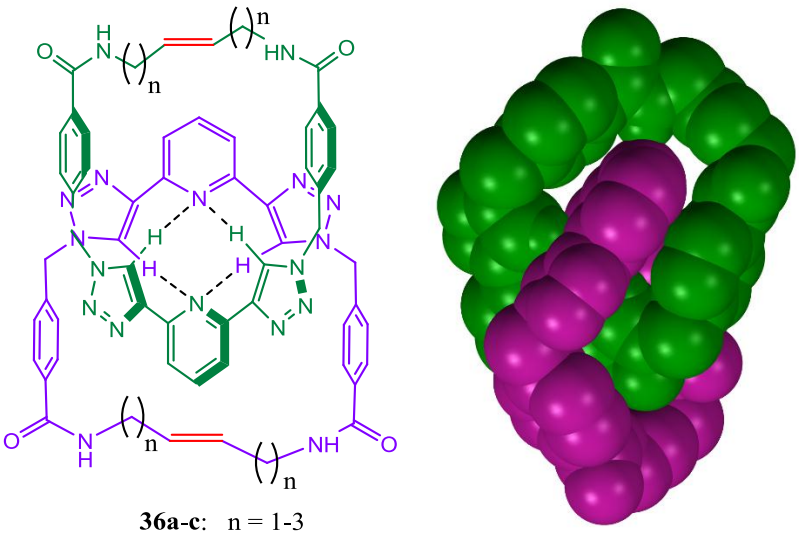

36a-c: n = 1-3

Figure 1.26 [2]Catenanes **36a-c** and spacefill representation of crystal structure showing interlocked nature.[102]

of $H_2PO_4^-$ through the same interactions necessary for self-templation. With this in mind, a discussion of an interesting artefact of the *anti-anti* conformation of **btp** ligands and its dual ability to facilitate coordination with anions form the next section.

1.7 Anions

1,2,3-Triazoles have the ability to interact with anions *via* the triazolyl *CH*.[157] This is as a result of the three electronegative nitrogen atoms situated adjacent to each other which sets up a large dipole, the axis of which is almost collinear with the *C-H* bond. The electron density deficiency on the opposite, carbon-centred, side of the ring, strongly polarises the *C-H* bond making it capable of engaging with anions, *via* hydrogen bonding. **Btp**'s *anti-anti* conformation arises also as an artefact of the close proximity of the pyridyl nitrogen. The resulting cooperativity of more than one pre-organised triazolyl *CH* hydrogen bond donor has resulted in several interesting studies on **btp**'s efficiency as an anion receptor.[102,113,158-160] Some of the most relevant and recent examples will be presented briefly.

Flood *et al.* were the first to investigate the interactions between **btp** derived triazolophane systems **37** and **38** and halide anions.[158] The crystal structure of TBA[**37**$_2$·I] was obtained, however, due to the weak diffraction, the authors can only tentatively suggest the formation of a 'sandwich' complex between **37** and iodide in the solid state, Figure 1.27.

In related work, Wang *et al.* have demonstrated, more recently, the synthesis of another **btp** derived triazolophane **39** for anion complexation applications.[159] The crystal structure of **39** showed the molecules adopting a chair-like conformation in the solid state with an oblique-pillar cavity (Figure 1.28). Again, possessing the *anti-anti* conformation of the triazole units, **39** exhibited selective binding of $H_2PO_4^-$, $HP_2O_7^{3-}$ and HSO_4^- over other

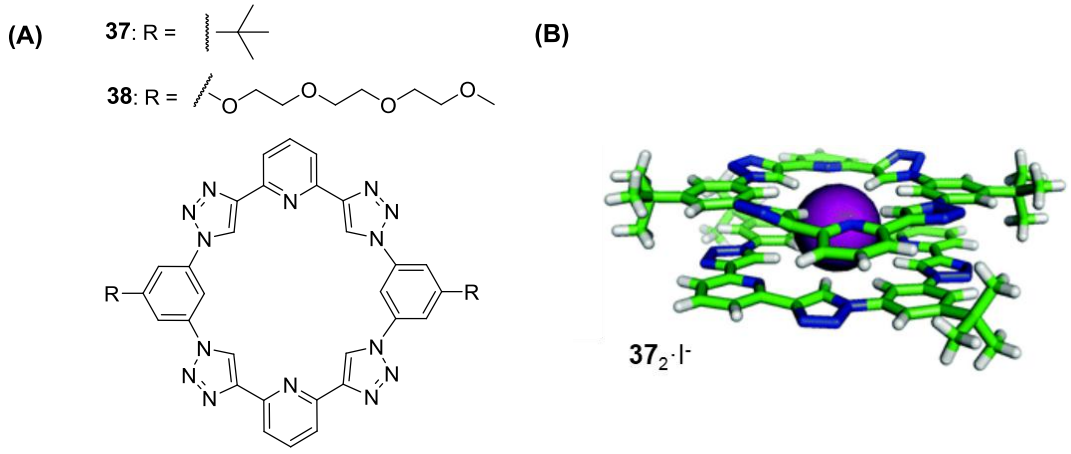

Figure 1.27 (A) **Btp** derived triazolophanes. (B) Molecular structure of TBA[**37**$_2$·I] 'sandwich' complex with counterion omitted. Figure reproduced from Ref.[157] Copyright 2010: Royal Society of Chemistry.

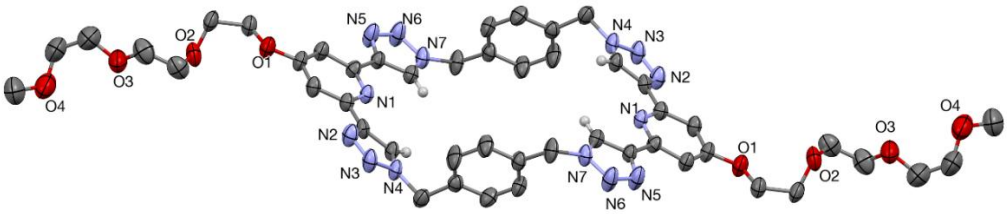

Figure 1.28 Molecular structure of **39**.[159]

anions through ^{1}H NMR titration analysis. Interestingly, the triazolophane, consisting of a benzene instead of a pyridine unit lacked the *anti-anti* conformation required to facilitate anion binding behaviour.

Lacour *et al.* recently reported the functionalisation of **btp** with Tröger's bases at the *N1* position of the triazole, **40** for use as anion-binding organocatalysts for the tritylation of amines and alcohols.[160] In the absence of **40** no reactivity was observed with amine substrates while once **40** was added products were formed in good yields (78% to 89%). Also, in the case of the tritylation of benzyl alcohol, a moderate formation of product in the absence of **40** was reported, increasing from 28% to 84% yield in the presence of **40**. Furthermore, ^{1}H NMR anion binding studies with chloride anions were carried out displaying the largest chemical shift change for the triazolyl *CH* proton resonance. The binding constant obtained for the titration of **40** with chloride was K = 11.5 ± 1.1 M^{-1} with acetone as the solvent. This was lower than the corresponding value for the Tröger's base analogue, possessing a benzene group in place of the pyridine ring, *i.e.* K = 47.9 ± 1.1 M^{-1} rationalised by the potential for repulsion between the pyridyl nitrogen and the anion. A crystal structure of **40** was obtained (Figure 1.29), however, the authors failed to discuss the interesting self-templating dimerisation observed in the solid state as a result of crystal packing factors and also through mutual hydrogen bonding between the triazolyl *CH*s of one

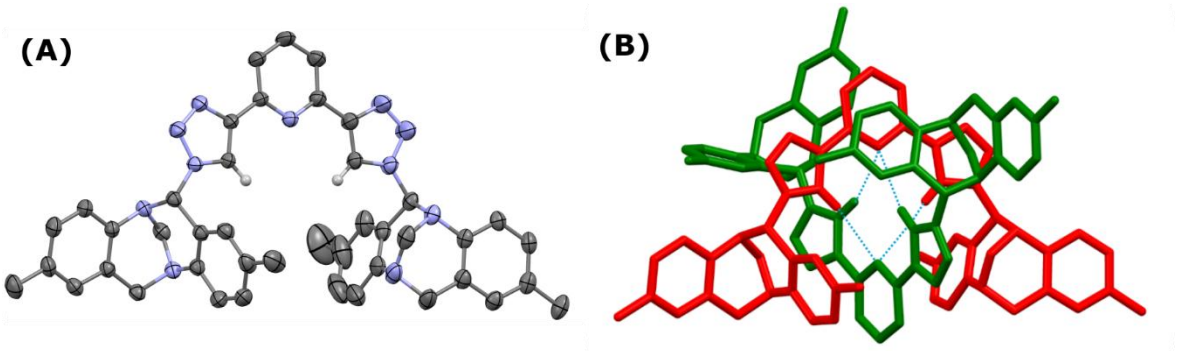

Figure 1.29 (A) Crystal structure of **40** displaying *anti-anti* conformation. Thermal ellipsoids displayed at 50% probability and solvent molecules and certain hydrogens omitted for clarity. (B) Asymmetric unit displays the dimerization of two molecules of **40** through non-classical hydrogen bonding self-templation.

btp and the pyridyl nitrogen of the other **btp** motif. This self-templating **btp** dimer was also observed in the crystal structure of **35S** and **35R** as we saw in Section 1.6.

Byrne *et al.* showed that the structures of the three complexes [Ru**32**$_2$](PF$_6$)Cl, [Ni**16**$_2$](PF$_6$)Cl and [Ir**16]**Cl$_3$ all displayed non-classical hydrogen bonding interactions between the acidic triazolyl *CH* and chloride ions, Figure 1.23.[113] This demonstrated the ability of **btp** to interact with metal ions and anions simultaneously. Presently, however, a thorough review of the most recent reports of **btp** in the literature would not be complete without drawing attention to two other articles concerning new synthetic routes for accessing **btp**-like systems and biological applications of novel **btp** ligands, respectively.

1.8 Other recent btp advances

There are two other recent reports involving **btp** since the publication of the extensive review by Byrne *et al.*[27] which will be included for completion. Dehean *et al.* have recently reported a single-step acid catalysed reaction for rapid assembly of *NH*-1,2,3-triazoles,[161] in the form of symmetrical *NH*-**btp** and also asymmetric *NH*-**tp** derivatives (Scheme 1.2). The metal-free pathway enabled the direct synthesis of a library of these heterocycles, including *NH*-**btp 41** from commercially available acetyl pyridines. The synthetic route required the combination of enolisable ketones and NH$_4$OAc resulting in a transiently generated enamine which underwent a [3+2] cycloaddition reaction with the 4-nitrophenyl azide, as the source of dinitrogen, forming a triazoline as the key intermediate. This had fewer steps than the synthesis of *NH*-1,2,3-triazoles from the respective bromopyridine starting materials,[27] however, the route did not appear to be particularly atom economical as it required the loss of a molecule of 4-nitroaniline in order for aromatisation and the regiospecific formation of the *NH*-1,2,3-triazole **41** to be achieved.

Vidal *et al.* reported the design of glycosyltransferase inhibitors targeting human

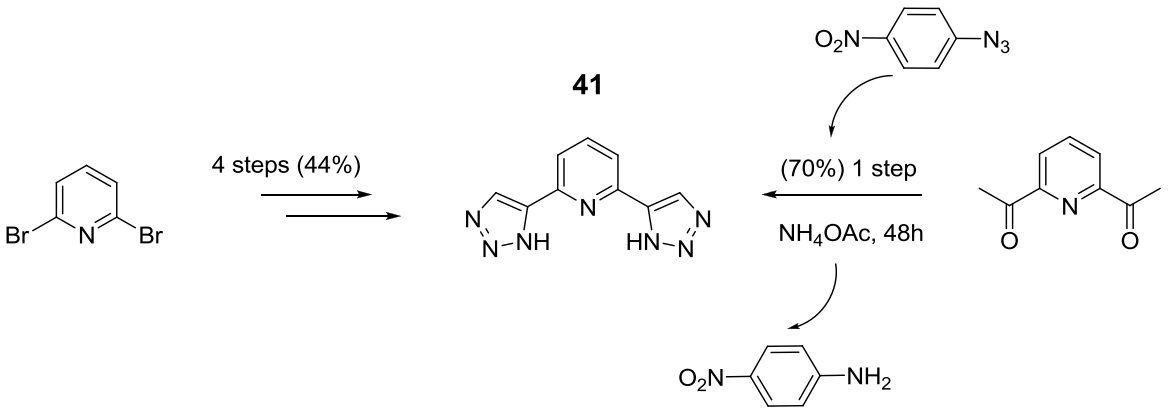

Scheme 1.2. Two synthetic routes towards **41** from (Left) 2,6-dibromopyridine and from (Right) 2,6 diacetylpyridine.[161]

O-GlcNAc transferase by functionalising the **btp** motif asymmetrically with an *N*-acylated glycopyranosyl amine and 2',3'-di-*O*-acetyl-5'-azido-5'-deoxy-uridine, **42**.[162] This article focused on the design of OGT inhibitors as analogues of the natural UDP-GlcNAc substrate by replacing the pyrophosphate surrogate, responsible for poor cell membrane permeation, with a pyridyl moiety. The compounds used in the study provided moderate *in vitro* inhibition of OGT which was explained by the trapping of the inhibitor compounds at the cell membrane. These last two examples demonstrate the newest synthetic methodologies for the synthesis of **btp**, **tp** and other 1,4-disubstituted-1,2,3-triazoles. It is important to be aware of the strategies already reported to date.

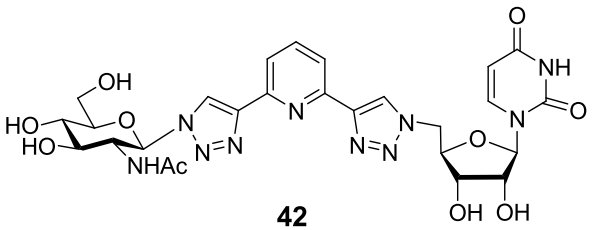

42

1.9 Synthetic strategies for the facile variability of 1,4-disubstituted-1,2,3-triazoles.

The discussion above of **btp**, **tp** and their appearances throughout the field of coordination chemistry has shown that synthetic developments are occurring rapidly and myriads of metallo-supramolecular systems and topological designs are being accessed. Thus, the focus is shifting more towards expanding new methods for functionalising ligands, with facile synthetic approaches that are modular and high-yielding. A challenge facing the use of **bpy** and **terpy** in various applications was successful derivatisation of the pyridyl moieties. In contrast to this, the 1,4-disubstituted-1,2,3-triazole can generally be readily synthesised upon 'clicking' an azide derivative with an alkyne. Either a Cu(I) salt (*e.g.* CuI), or more frequently a Cu(II) salt which is reduced *in situ*, (*e.g.* $CuSO_4 \cdot 5H_2O$), acts as the CuAAC catalyst. Fletcher *et al.* developed a one-pot reaction synthetic procedure,[163-164] whereby it was found that the addition of K_2CO_3 to standard aqueous CuAAC conditions lead to deprotection of the silyl protected alkyne and, followed by CuAAC with the derivatised azide, resulted in the near quantitative formation of 'click' products, Scheme 1.3. In the case of 2,6-bis((trimethylsilyl)ethynyl)pyridine **43**, the result is a **btp** derivatised at the *N1* site of the triazole rings. The derivatisation can be accomplished *via* a wide range of azide and alkyne substrates. The substituted azides are formed through azide substitution of alkyl and aryl halides[42-43] as well as the diazo transfer of amines.[44] The alkyne derivatives are accessed

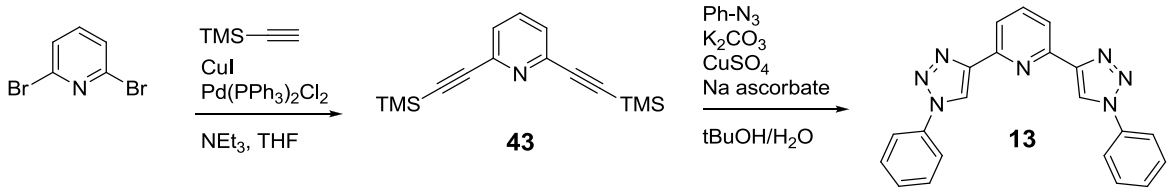

Scheme 1.3 Sonogashira coupling of 2,6-dibromopyridine followed by a one-pot deprotection/ CuAAC synthetic strategy for preparation of ligand **13**.[42]

through Sonogashira coupling of terminal alkynes with an extensive collection of 2,6-dihalopyridines. The generation of these substrates will be looked at more closely in the following sections.

1.9.1 Azides

The versatility of triazolyl substituents is remarkable and, depending on the choice of azide precursor, can include alkyl chains, aryl groups and many other functional groups including porphryins,[105] ferrocenes,[42] polystyrene[132] and carbonate and phosphonate groups (which allow binding to TiO_2 surfaces).[152] For this reason, a number of synthetic routes have been developed where the azide can be generated and 'clicked' *in situ*, in order to avoid isolating the compounds due to their potential explosive nature. For example, Crowley *et al.* have reported a one pot multi-component CuAAC "click" approach[42] whereby sodium azide and an organic halide undergo a substitution reaction forming the appropriate substituted azide, and without isolation of this azide precursor, the relevant alkyne is added at which point CuAAC then proceeds in the presence of the Cu(I) catalyst. Alkyl halides undergo substitution with sodium azide readily at room temperature in a DMF:H_2O (4:1) solvent mixture, however, aryl halides such as bromobenzene, in the synthesis of **13**, require alternative conditions. Several efficient synthetic protocols have been developed in relation to aryl halides, namely, refluxing the aryl halide with NaN_3, CuI, DMEDA and sodium ascorbate in a degassed EtOH/H_2O (7:3) solution for several hours.[42,165]

Another route to obtaining the desired azide precursor is a one pot synthesis from amine starting materials. Diazo transfer reagents have been developed such as the imidazole-1-sulfonyl azide ($ImSO_2N_3$) hydrochloride salt[44] which was first synthesised by Goddard-Borger *et al.* for the conversion of primary amines into azides and the conversion of activated methylene substrates into diazo compounds. The process was further extended by Stonehouse *et al*. in a three-component 'click' reaction,[166] where the azide was formed *in situ* in the presence of a range of alkynes for the formation of various 1,4-disubstituted 1,2,3-triazoles. The synthetic route towards the hydrochloride version of the $ImSO_2N_3$ diazo

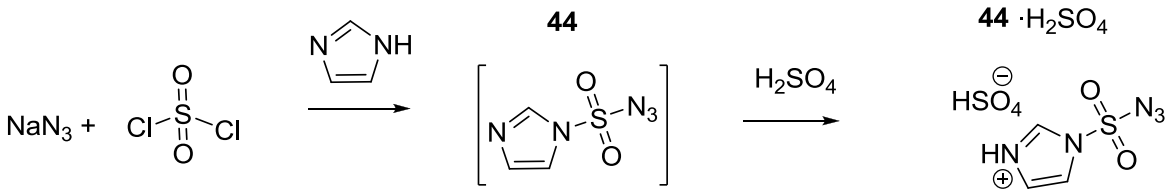

Scheme 1.4. Synthetic route to **44**·H_2SO_4 diazo transfer reagent.[167]

transfer reagent has been reported to be hazardous due to the production of explosive by-products such as sulfonyl diazide and hydrazoic acid.[168] Therefore, the sulfuric acid salt **44**·H_2SO_4 was proposed as a more stable alternative,[167] see Scheme 1.4. Byrne *et al.* made use of Stonehouse *et al.*'s three component 'click' approach using the more robust **44**·H_2SO_4 as a diazo-transfer agent, reporting a new modular and mild synthesis of **btp** enantiomers **35R/S** from chiral amines and the protected alkyne **43**, Figure 1.30.[156] Introduction of chirality into the **btp** core was achieved stereoselectively using α-aryl amine **45** and the stereochemistry of the chiral centre was retained. Byrne *et al.* made use of the dramatic colour changes in order to monitor the course of the multi-step reaction.[156] These chiral ligands were subsequently used to form optically active luminescent self-assembly structures as discussed in Section 1.6.

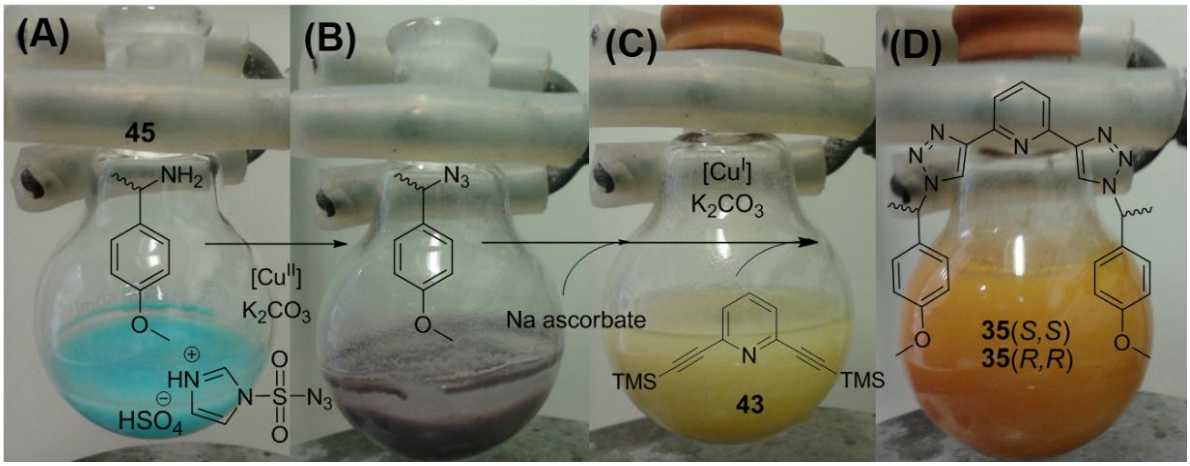

Figure 1.30 Schematic representation of the one-pot diazo-transfer-deprotection-'click' reaction for the synthesis of ligands **35R/S** utilising the colour changes to monitor reaction progress.[156]

1.9.2 Alkynes

Variability of the final 1,4-disubstituted 1,2,3-triazole compound can also be carried out depending on the choice of alkyne. The majority of reported uses of the CuAAC reaction have not taken advantage of the coordinative abilities of the 1,2,3-triazole motif, rather employing it as a linker between other functional building blocks. The alkyne precursors of this nature will not be discussed. Alkynes such as pyridylacetylenes, in particular **43**, will be the focus of the synthetic precursors used to derive the final 1,4-disubstituted-1,2,3-triazole

products reported in this research project. These precursors are readily accessible in a few short steps using conventional synthetic techniques and can be obtained in high yields and purity. The 1,4-disubstituted-1,2,3 click triazole ligands which will be the focus of the work carried out herein, containing terdentate binding sites, such as **btp**, and containing bidentate binding sites, such as **tp**, can be synthesised from 2-((trimethylsilyl)ethynyl)pyridine substrates, **43** and **46**, respectively. Sonogashira coupling can be used to introduce the alkyne functional group in mild conditions with various bromo-[42,105] and chloropyridines.[169] The trimethylsilyl-protected alkynes can then undergo CuAAC according to the one-pot deprotection-'click' route devised by Fletcher *et al. via* the *in situ* generation of deprotecting hydroxide from K_2CO_3 in aqueous solution and forego any purification of the deprotected alkyne.

Several 4-pyridyl substituted pyridylalkyne derivatives have been reported to date. This is an obvious and chemically significant location on the heteroaromatic ring with potential for modifying **btp** ligands. There are several synthetic routes reporting this particular modification and will be discussed in detail in Chapter 2 as a large focus of the work carried out in this research project was the modification of **btp** ligands, such as **16** and **32** developed by Byrne *et al.*[27,70,103,119,170] with additional 4-pyridyl functional groups. Such groups are significant in order to strategically induce the appropriate supramolecular interactions necessary for the controllable generation of functional materials, such as supramolecular polymer systems.

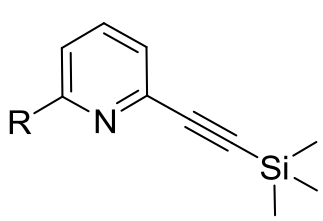

43: R = 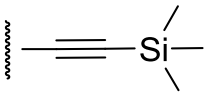

46: R = H

1.10 Supramolecular Polymers

Supramolecular polymers can be defined as any type of assembly formed from one or more molecular components *via* reversible bonds.[171] A few of the main forces to drive supramolecular polymer formation can be in the form of a variety of reversible noncovalent interactions such as multiple hydrogen bonding,[172] host-guest interactions[173] and metal-ligand coordination.[174] As regards metal-ligand coordination, when bridging ligands possessing divergent multitopic binding ability and metal ions are mixed in solution, three main kinds of self-assemblies can be constructed. These are: (i) disordered aggregates with no directional order giving rise to amorphous coordination polymers, (ii) highly ordered

aggregates involving simultaneous long- and short-range order, leading to coordination polymers and metal-organic frameworks (MOFs),[175-176] and finally (iii) soft materials *i.e.* intermediate assemblies with short-range order but no long-range order.[4] As much of the work carried out in this research project is primarily concerned with the **btp** moiety's use as an efficient metal binding host in the generation of supramolecular polymer systems, an overview of the latter two of the three main types of metal-ligand coordination self-assemblies just listed will be carried out *i.e.* soft materials, namely supramolecular gels, and coordination polymers, namely MOFs.

1.10.1 Supramolecular Gels

Currently, there exists a great deal of interest in the development of new supramolecular materials with various functional properties that are different from their monomeric or discrete molecular components.[4] Interest in gels has grown in many scientific disciplines including tissue engineering and wound healing, drug delivery, and also sensing.[4,6] Some examples where development of these materials is ongoing, particularly in relation to metal-containing gels, will be discussed in the following sections. Firstly, a detailed description of what these interesting materials are, how they are formed and the techniques which are used to study their properties will be carried out.

Flory defined a gel as a two-component colloidal dispersion, with a continuous structure and macroscopic dimensions which are permanent on the time scale of the experiment, and is solid-like in its rheological behaviour.[177] There are several denominations of gels ranging from lamellar structures to covalently-polymerised networks.[6,172] However, a supramolecular gel can be described as an aggregation of directionally-dependent three-dimensional structures in solution, self-assembled through non-covalent interactions such as hydrogen bonds, π-π interactions, van der Waals and ionic forces, and metal coordination, *etc*.[6] Ideally, a gel consists of a relatively small amount gelling component (the gelator) and a significant volume of solvent. Upon self-assembly of the gelators into hierarchical structures the solvent molecules are immobilized within the gel matrix. Gels can be classified as *hydrogels* or *organogels*, within which the solvent encapsulated is water or an organic solvent, respectively. Gels possess a relatively disordered nature, the short range order not extending from the molecular to multimicrometer scale and as such it is challenging to understand the structure of the gel. The mechanism of gel formation is a hierarchical process which can be broken down into a primary, secondary, and tertiary structure. The self-assembly process involves the following steps, in which the primary component is the result

of dimerisation of two or more individual gelators, leading to the formation of oligomers through interaction with other dimers, demonstrated using urea-tape as an example in Figure 1.31(A).[172] Other urea dimerising interactions such as extended hydrogen bonding and π–π interactions in the solid state were demonstrated by Pandurangan *et al.* using X-ray crystallography of novel aryl-pyridyl ureas like **47**, see Figure 1.31(B).[178] In selected cases, these ureas formed supramolecular gels with antimicrobial properties against Staphylococcus aureus and/or Escherichia coli. The secondary component in the self-assembly process arises from the extension of these oligomers into polymeric fibril formations of approximately similar width as the molecular building blocks (≈ 1-10 nm), and finally the tertiary process of the cross-linking of fibrils at junction points into fibres (≈ 20-50 nm width) and 'splinters' (≈ 10 μm width, Figure 1.31(C))[178] which interact to give a long range, intertwined network stretching the whole sample. Finally, immobilisation of the solvent in the gel matrix is induced through surface tension. Surface tension effects allow the gel to be stable towards gravitational force when the vessel encasing it is turned upside down. This 'inversion test' is a crude technique typically used to identify whether or not gelation has occurred.[5]

Despite the plethora of gels which have been reported to date,[6,172,179-180] there is a large gap between functional gel design efforts and actual knowledge of the supramolecular structure of the gels, *i.e.* the molecular arrangement of gelator molecules within the gel fibres. Of

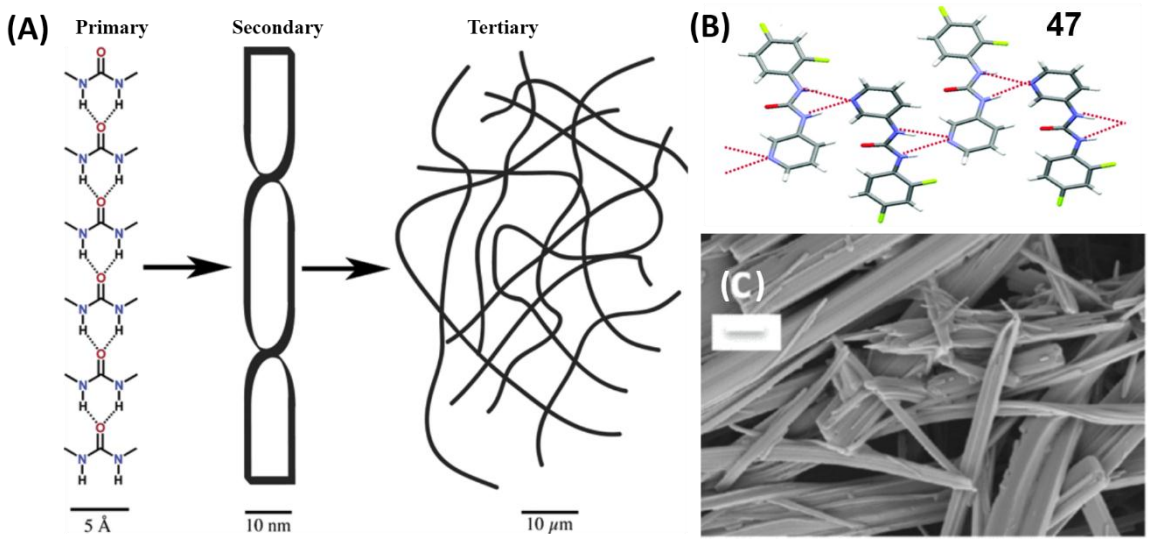

Figure 1.31 (A) Hierarchical assembly process of supramolecular gel formation using urea derivatives as the gelators. Figure reproduced from Ref.[172] Copyright 2004: American Chemical Society. (B) Crystal structure of pyridyl urea **47** displaying oligomeric extended hydrogen bonding interactions. (C) SEM imaging (scale bar at 10 μm) of fibrous morphology of an organogel formed from an aryl-pyridyl urea analogue of **47** in a 4:1 THF:H_2O mixture (1% wt.). Figure reproduced from Ref.[178] Copyright 2014: Royal Society of Chemistry.

fundamental concern is the structure of the gel both on the micro- and nanoscale *i.e.* at the cross-linking junction zones, the fibre-liquid interface and also at the molecular level.[6,172] The macroscopic structure or morphology of these materials can be imaged by Scanning Electron Microscopy (SEM), Cryo-SEM, Transmission Electron Microscopy (TEM), Cryo-TEM, Scanning Tunnelling Electron Microscopy (STEM), and Helium Ion Beam Microscopy (HIBM). Other techniques used to study gels are optical and confocal microscopy, dynamic light scattering (DLS), and SAXS (Small-Angle X-ray Scattering) and SANS (Small-Angle Neutron Scattering).[172] Techniques such as UV-vis/CD absorption can be used to detect changes in the ground state electronic properties in the generation of the supramolecular systems. Luminescence spectroscopic techniques is another very informative tool for gaining insights into the primary structure of the gels.[6,172,181] Ln(III) centred phosphorescence can be very valuable in the characterisation of the metal ion chemical environments within the gel matrix.[182]

The gel rheological behaviour is perhaps its most important defining feature. Rheology[183] is the study of the deformation and flow of matter under the influence of an applied stress. In general terms, when the mechanical properties of a material are under investigation, if the application of a continuous weak stress results in an overall resistance to further deformation, the material is a solid. However, the material is a liquid if flow is observed as a result of the deformation from the applied stress. Gels display both solid-like and liquid-like properties, depending on the strength of the applied stress. Thixotropy is an interesting property in which mechanical stress induces the break-up of the solid gel network, allowing the material to "flow", but the gel's elastic properties recover spontaneously upon release of the force, thus the network reforms over time.[184] This will be discussed in more detail in Chapter 3 in studying the thixotropic properties of the **btp** derived supramolecular gels. Inducing such "self-healing" properties are a particularly topical area of research due to its potential to improve how reliable, useful and long-lived the resulting materials become.[185-188] Gels which have the ability to self-heal are a subset of what are referred to as stimuli-responsive materials. A discussion of the interesting properties of both self-healing and other classes of stimuli-responsive soft materials in the literature will be made in the following section.

1.10.1.1 Stimuli-responsive Gels

The ability of certain stimuli-responsive polymer gels to autonomously heal upon damage are a consequence of the inherent dynamic nature of the non-covalent bonds of which they consist. In general, responsive materials that can change their physical state in response to

physical or chemical stimuli do so through the reorganisation of their molecular make-up upon exposure to an external trigger. Supramolecular gels have been shown to be responsive when external stresses such as ultrasound,[189] light[190] or chemical triggers[86,174,191] are applied. This reversible nature is a vital part of the development of functional gel-based systems. Gels with sensing capabilities are an example of functional responsive materials which undergo a change in spectroscopic, electronic, or magnetic properties upon detection of a particular analyte. The incorporation of metal ions into gels, *i.e.* metallogels, broadens the possibilities for engineering the response of these materials. Coordination-based gels can be endowed with the metal's physicochemical properties, *e.g.* magnetism, colour, rheology, photophysical properties, catalytic activity and redox behaviour. Therefore, there is an increased range of chemical and physical stimuli that these gels can react to in contrast to their non-metal containing counterparts.

There are two types of metallogels generally reported.[5-6,172] Firstly, non-covalently interacting "standalone" coordination complexes linked together in the gel matrix. In this scenario the discrete complexes are joined through other non-covalent interactions. For example, Yan *et al.* reported a series of Pt(II):**terpy** complexes **48a** and **48b** (Figure 1.32) which showed gelation in DMSO, driven by Pt···Pt, π···π and hydrophobic-hydrophobic

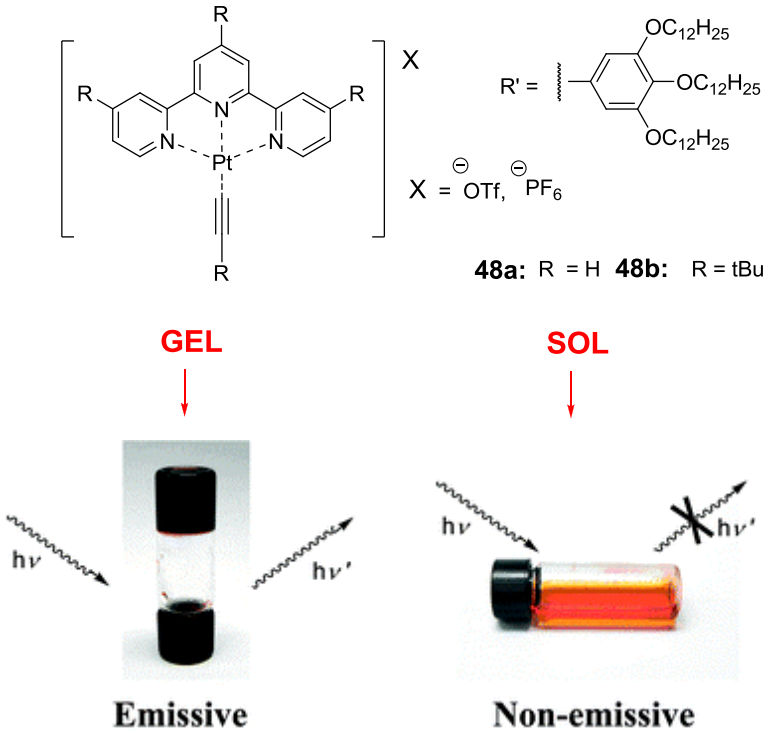

Figure 1.32 Functional metallogels formed from non-covalent interactions where metal-**48a/b** coordination is not central to the formation of the extended gel network. Gel to sol transition results in a colour change and loss of luminescence properties. Figure reproduced from Ref.[192] Copyright 2007: Royal Society of Chemistry.

interactions.[192] Here, the dative coordination bond is a secondary interaction in the assembly design and not involved in linking the gelator molecules together.[6] It was also demonstrated that dramatic colour and emission changes were observed during the sol-gel transition.

Secondly, however, there are gel structures consisting of organic molecules, such as multi-topic ligands with at least two binding sites for metals which facilitate the formation of branched two and three dimensional coordination polymer gel networks.[86] A short review of some examples of functional supramolecular metallogels, beginning with the most recent reports, will be presented in the following section, with a particular focus on autonomously healing systems consisting of the **btp** motif, or analogues thereof, playing the role of the ligating host. Weng *et al.* most recently reported the formation of self-healing metallo-supramolecular polymer gels from **btp** ligand macromolecule **49**. The macromolecule was synthesised *via* chain extension of two components: a CuAAC prepared bis-propene functionalised **btp** ligand which underwent a UV initiated thiol-ene "click" reaction with bis-thiol functionalised polytetrahydrofuran prepolymer linkers culminating in multiple **btp**-units incorporated throughout the polymer backbone, Figure 1.33.[193] Three metallo-supramolecular gel materials formed by separately cross-linking **btp** macromolecule **49** with Eu(III), Tb(III) and Zn(II) displayed self-healing behavior when stacking the three respective metallogels together in a saturated toluene atmosphere for one hour. The resulting joined material composite was then subject to bending and stretching but breakage at the joints was not observed. This work was an extension of similar systems[125,194] which displayed similar

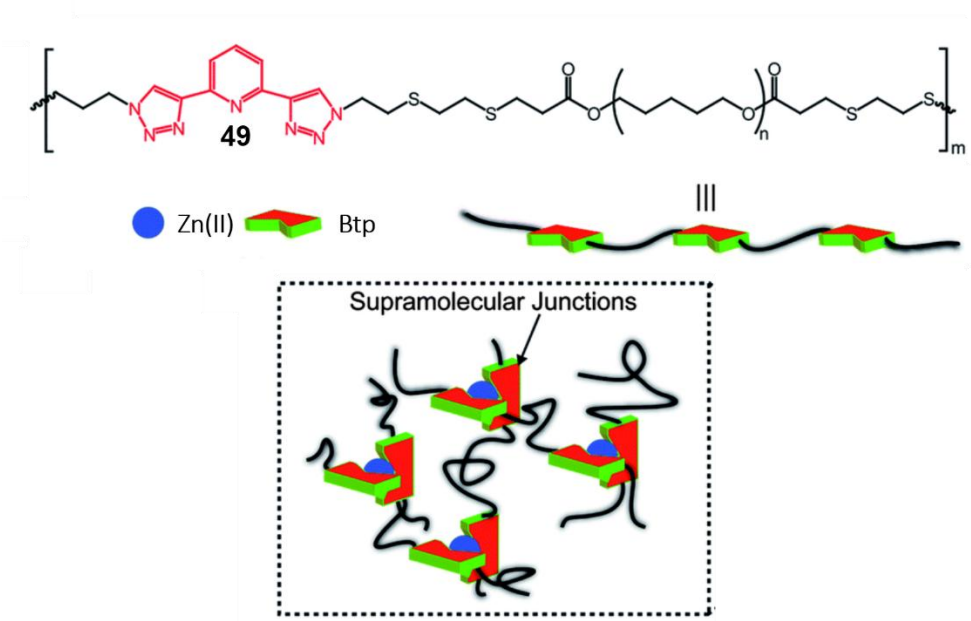

Figure 1.33 Multiple **btp** motifs (represented as bricks) incorporated into ligand macromolecule **49** which coordinate with Zn(II) ions (represented as balls) to form a metallo-supramolecular gel. Figure reproduced from Ref.[193] Copyright 2014: The Royal Society of Chemistry.

self-healing behaviour on account of the metal-**btp** complexation sites. It was rationalised that these cross-linking points were responsible for the healable nature of the final materials which were robust enough to be picked up and placed under bending and compressive strain.[125] The gels demonstrated the thermodynamically stable but kinetically labile nature of the metal:**btp** complexation, a property which is of valuable significance in systems where a fast response is required. These systems also exhibited mechanical properties such as high tensile strength (up to 18 MPa), and exceptional toughness (up to 70 MPa).

There are several other examples of self-healing metallogels which contain metal chelating groups analogous to **btp**. Rowan *et al.* developed ditopic ligand **50** featuring the 2,6-bis(benzimidazol-2-yl)pyridine (**bbp**) binding motif, joined by a penta(ethylene glycol) unit which exhibited linear chain extension binding with either Co(II) and Zn(II) ions.[195] The Zn(II) containing polymeric sequence was also cross-linked with Eu(III) or La(III) giving rise to globular colloidal particles that crystallised followed by phase separation leading to the formation of metallogels, Figure 1.34. The gelation mechanism was investigated using rheological study and techniques mentioned previously, namely, optical and confocal microscopy, DLS, and XRD.[179] This work was further developed using related **bpp** ditopic polymer **51** featuring a low molecular-weight poly(ethylene-co-butylene) linker. Despite being based on weakly coordinating complexes optically healable and exceptionally strong metallo-supramolecular gel networks were formed.[190] Upon exposure to light, the Zn(II)/La(III):**51** complexes comprising the gel cross-links absorbed energy which was converted into heat. The effect of this was the temporary dissociation of Zn(II)/La(III):**51**

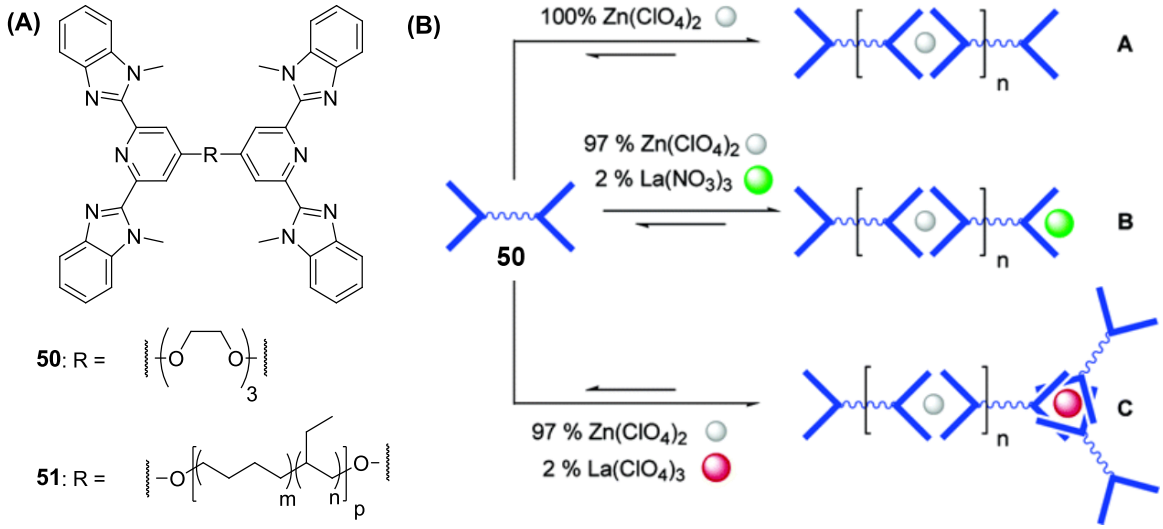

Figure 1.34 (A) Ditopic ligands **50** and **51**. (B) Schematic showing the mixed *f-d* metallogel formations **A-C** with ditopic **bpp** ligand **50**. Figure reproduced from Ref.[179] Copyright 2006: American Chemical Society

cross-links, with subsequent decrease in viscosity of the material, which then recombined, thus healing any defects caused by strains or damage done to the system. In other work, it was shown that upon solvent evaporation of similar Eu(III):**51** based gels, followed by compression moulding, films were formed which displayed appreciable elastomeric mechanical properties.[196] This was not a feature of the dried sample of **51**. The metal ions played a vital role in imparting these film materials with useful functions, namely the ability to be healed, after cutting, by treatment with ultrasound. Various reversible and irreversible mechanically activated reactions were used to study the disassembly process using the characteristic photoluminescent properties of the system.

Finally, Martínez-Calvo *et al.* investigated the role of the guest Ln(III) ion in the formation of highly luminescent metallo-supramolecular gels, from a morphological and rheological perspective using a **dpa** derived multidentate ligand **52** (Figure 1.35).[197] The gelation process used the 1:3 Ln(III):**52** stoichiometric ratio to form pre-organised metal complexes which were then cross-linked through Ln(III)-carboxylate coordination upon additional equivalents of Ln(III). SEM imaging and rheological studies showed that the gels prepared using only Eu(III) or only Tb(III) possessed different morphological and rheological properties to each other, which also differed from those consisting of mixed Eu(III) and Tb(III) in the gel formation. This was despite Eu(III) and Tb(III) having similar coordination properties which would indicate that self-recognition in the individual gels was different from that of the mixed system. The gels showed the ability to self-heal after being cut and allowed to recombine. Futhermore, the luminescent properties of the soft materials could be tuned depending on the Eu(III):Tb(III) stoichiometric ratios used in their synthesis, resulting in a

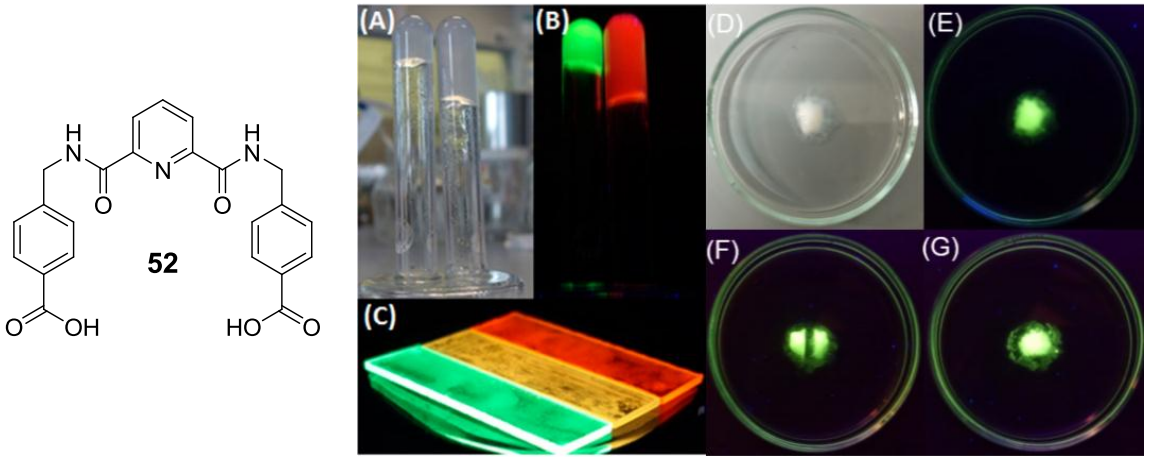

Figure 1.35. **Dpa** amide derivative **52**. (A) Tb(III) metallogel and Eu(III) metallogel in daylight and (C) Luminescence of Eu(III), Tb(III), and mixed Eu(III)/ Tb(III) gels on quartz plates. (D)-(G) Healing experiment of Tb(III) gel with (D) Tb(III) gel in daylight, (E) under UV irradiation, (F) gel after being cut, and (G) self-healing.

variety of luminescent colours.

These articles demonstrate the ability of metallo-supramolecular interactions, through their dynamic nature, to achieve the production self-healing, functional soft materials. The multiple coordinating directionality together with the conformational capability range of similar ligands to those discussed above in the generation of functional soft materials also make them very appealing for the design of new architecturally diverse MOFs possessing desirable functional properties. The importance of functional MOFs based on using 1,4-disubstituted-1,2,3-triazoles, or analogues thereof, as tectons will be discussed in the next section using relevant examples.

1.10.2 Metal-organic frameworks (MOFs)

As mentioned previously, when bridging ligands possessing divergent multitopic binding ability and metal ions are mixed in solution, one of the resulting self-assemblies can be in the form of highly ordered crystalline aggregates involving simultaneous long- and short-range order *i.e.* MOFs (Figure 1.36).[8,176,198] MOFs represent a swiftly advancing research area in chemical and material sciences, continuously intriguing scientists, not only by the extensive range of network topologies obtainable[199-200] but also by their applicable properties,[201] such as catalysis,[202-204] sensing,[205-207] guest encapsulation[208-209] and for gas adsorption and separation.[201,210-216] The most detailed structural information of MOFs is gained from single crystal X-ray diffraction (XRD) analysis,[198] with bulk purity determined using powder XRD and elemental analysis. Even armed with such techniques, often the overall connectivity or topology of a network can be difficult to initially ascertain as a result

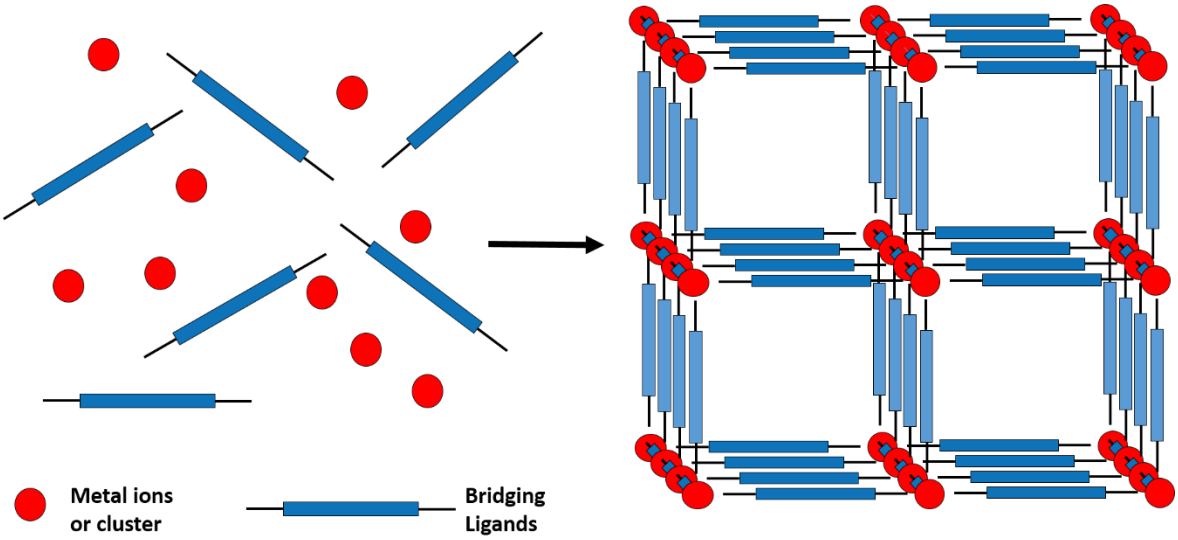

Figure 1.36 Schematic representation of the building block principle behind forming MOFs.

of the vast range of ligand and metal binding modes, particularly in closely packed extended three-dimensional networks. The complicated structure should thus be simplified and described in terms of nodes and links. The node is a structural feature such as a metal, metal cluster or combination of metal and ligand coordination sub-units which are connected together to three or more other nodes *via* links.[217] The links, for example, a bridging ligand, are then the structural components within a network which connect to only two other structural features. Nodes and links are connected through coordination bonds. The structurally diverse topologies displayed in coordination polymers requires the use of nomenclature based on mathematical descriptions of networks, in order to fully describe their connectivity.[218-221]

MOFs can have valuable properties bestowed upon them by the nature of the resulting extended structure in the form of topology, channel size and regularity, and charge distribution *etc*[176] and also by the tectons they consist of. These valuable properties, including luminescence,[222-224] and applications, such as chemical separation,[225] sensing,[205-206,225] and ion exchange,[226-227] amongst others,[228] arise from their ability to absorb and recognise specific guests through various host-guest interactions. The uptake of specific guests by MOFs in the development of luminescent materials has potential for application in fluorescent sensing and in the development of next generation solid-state lighting devices, display technologies, and other lighting applications.[229-230] A few examples of functional MOFs which demonstrate interesting responses to specific guests will be outlined presently.

The terdentate heteroaromatic **btp** motif has frequently been incorporated into amorphous polymers and macromolecules through metal-templated synthesis[27,231-234] as well as in the formation of metallo-supramolecular gels.[27,101,112-113,182] There are no reports of **btp** derived MOFs. In relation to other nitrogen containing heterocycles, there are few reports of MOFs featuring the 1,2,3-triazole motif[235-250] of which fewer are 1,4-disubstituted,[239,248-250] compared to the relative ubiquity of the 1,2,4-triazole motif exploited for such studies.[90,204,209,212,214-215,227,251-254] As a result, this introductory note on MOFs will pay attention to certain relevant examples from the literature which incorporate nitrogen rich heterocycles such as **terpy**, derivatised with carboxylic acid groups.[255] Zhao *et al.* reported the unique chiral interpenetrating structure of a *d-f* heterometallic MOF using **terpy** derived ligand **H53** functionalised at the 4-pyridyl position with a phenylcarboxylic acid motif (Figure 1.37).[256] The mixed trigonal prismatic Tb(III) and square pyramidal Zn(II) centres were linked through bridging CO_3^{2-} anions resulting in chiral helical chains which were themselves connected through **53** *via* the carboxylate binding of the Tb(III), generating an

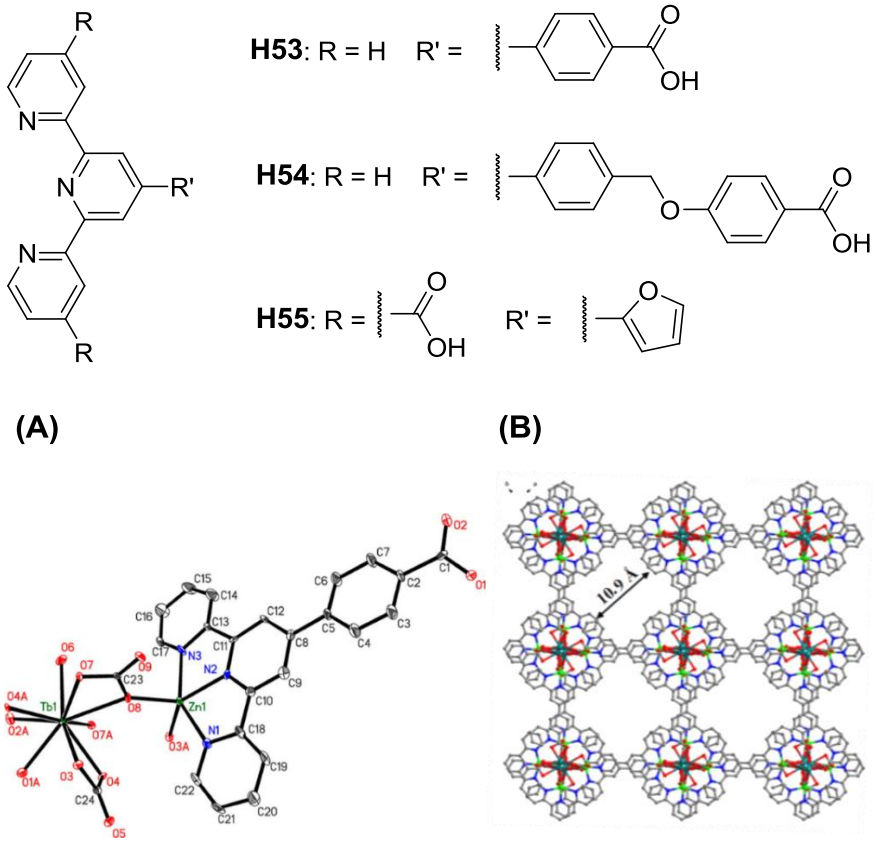

Figure 1.37 (A) Asymmetric unit of *poly*-[TbZn**53**$(CO_3)_2(H_2O)$] with an thermal ellipsoids displayed at 30% probability and hydrogen atoms omitted for clarity. (B) One set of the interpenetrating 3D frameworks comprising the overall MOF viewed along the *c*- axis. Figure reproduced from Ref.[256] Copyright 2015: American Chemical Society.

interpenetrated three dimensional framework. The application of this Tb(III) luminescent MOF for the detection of small organic molecules was investigated, with the authors concluding that formol, acetaldehyde and propanal quenched its phosphorescent emission out of a group of fourteen solvents in total used in the sensing test. **H53** has also featured in articles reporting a Ru(II) complex-incorporated Ti-oxo-cluster based MOF for the photocatalyic production of hydrogen.[257] In addition, they reported a *poly*-[Eu**53**$_3$] MOF which demonstrated fast response and high sensitivity for the detection of Fe(III) ions in aqueous solution or in biological systems.[258]

Paul *et al.* reported a Cu(II) derived MOF using a flexible **terpy**-derived ligand **H54** displaying efficient catalytic properties in water/ionic liquid medium for the single-pot hydrocarboxylation of cyclohexane.[259] The *poly*-[Cu**54**(NO_3)] extended in one dimensional coordination polymer chains through N_3 coordination of the square pyramidal Cu(II) centre and the terminal monodentate carboxylate binding of another ligand **54**, with the remaining axial position occupied by a monodentate nitrate. Sun *et al.* reported a *poly*-($[Zn_2$**55**$_2]\cdot 5H_2O$) MOF which displayed permanent porosity through gas adsorption measurements with N_2,

H_2 and CO_2. It also exhibited strong fluorescence and its ability to sense organic nitro compounds through quenching of the fluorescence intensity was attributed to the uncoordinated carboxylate oxygens facing into the channels.[260]

Conformational adaptability is an important concept of polymeric supramolecular assemblies like MOFs, as is their recognition of a substrate and the resulting response of the system to such an event. These are also important properties of another class of supramolecular assemblies, albeit a more discrete form *i.e.* mechanically interlocked systems. This fascinating area of supramolecular chemistry will be looked at in the next section with reference to recent developments in the literature concerning, in particular, 1,4-disubstituted-1,2,3-triazole containing systems.

1.11 Mechanically interlocked systems

Discrete molecular species comprised of covalent sub-components which are held together, not through direct covalent interactions, but due to the inability of bonds and atoms to pass through one another are said to be mechanically interlocked. A large amount of work has been invested in the investigation of properties of discrete interlocked assemblies possessing mechanical bonds, for example, knots,[261-264] rotaxanes[21,23,25,265-266] and catenanes.[21,261,267-270] The most well-known example of a mechanically interlocked system, coming from the pioneering work of Sauvage *et al.*,[271] is the [*n*]catenane, when two or more macrocycles are threaded through the cavity of one another (where *n* denotes the number of interlocked macrocycles). For successful formation, it is a requirement for two molecules to assemble in close proximity before covalent bond formation between the terminal sites of the open forms of each of the macrocycles (or "clipping") yields irreversibly connected molecules. In order to access these unique and topologically non-trivial molecular species, a range of methodologies have been developed for templating the assembly of such systems. These include metal templation,[21-22,25,263-264,270] hydrogen bonding interactions,[266,272-276] donor acceptor interactions [277-278] and anion coordination.[279-280]

The application of CuAAC 'click' chemistry in catenane and rotaxane synthesis has proved very important over the years, in capping bulky groups at the ends of rotaxane axles[21] but also through the 'active metal template' strategy pioneered by Leigh *et al.*[22-23] CuAAC was utilised in this way whereby the Cu(I) ion templates an already formed macrocycle **56** and a linear precursor molecule **57** in place and simultaneously closes **57** into a macrocycle *via* the formation of a 1,2,3-triazole resulting in [2]catenane **58** (Scheme 1.5). The active metal template can then be scavenged by EDTA/$NH_{3(aq)}$. Goldup *et al.* showed that this strategy

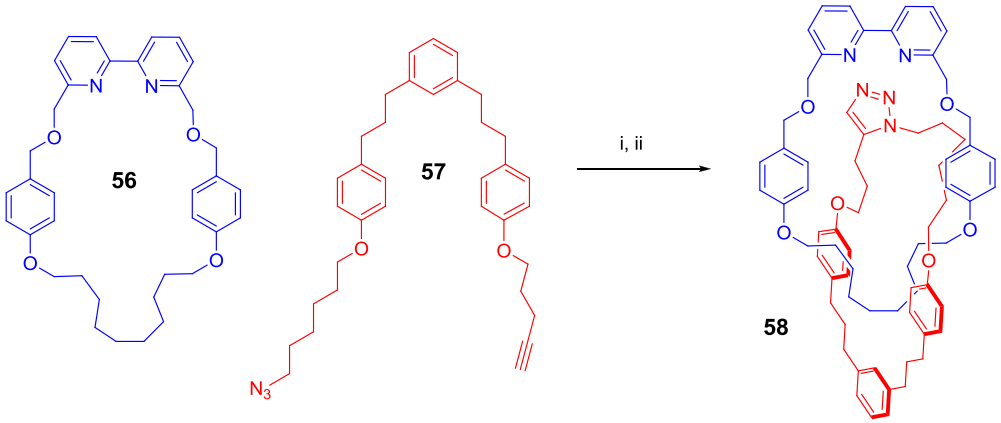

Scheme 1.5 Synthesis of [2]catenane **58**. Reagents and conditions: (i) $[Cu(CH_3CN)_4](PF_6)$, $C_2H_4Cl_2$, 80 °C, 7-21 days. (ii) EDTA, $NH_{3(aq)}$, 49-50% (over two steps).[16]

also worked in the templated synthesis of [2]rotaxanes, where the 1,2,3-triazole containing 'axle' is formed *in situ* by Cu(I) localised within a macrocycle.[23-25] A **btp** incorporated mechanically interlocked system was recently reported by Goldup *et al.* using the active template CuAAC technique for the synthesis of Sauvage-type molecular shuttles.[281] The thread **59** contained a **btp** site and **tp** site (Figure 1.38). It was shown that the various bipyridine macrocycles predominantly occupied the tridentate **btp** station by NMR analysis due to the shift observed of the triazolyl protons. Investigation of the shuttling of the macrocycle between the **btp** and bidentate **tp** station was also carried out, through the addition of diamagnetic metal ions in a Sauvage-style approach.[265]

These examples demonstrate the value of assisted templation for pre-organising precursors before locking them in place mechanically. However, examples of "self-templated" mechanically interlocked molecules formed solely through the use of hydrogen bonding interactions are relatively rare. Notable examples of such "self-templated" structures are the homocircuit [2]catenanes (the interlocked macrocycles are exactly the same) developed by the research groups of Hunter,[272-273] Vögtle,[266] Leigh,[275] and Evans.[276] These systems relied on self-templating amide hydrogen bonding interactions. Also worth noting is that each of

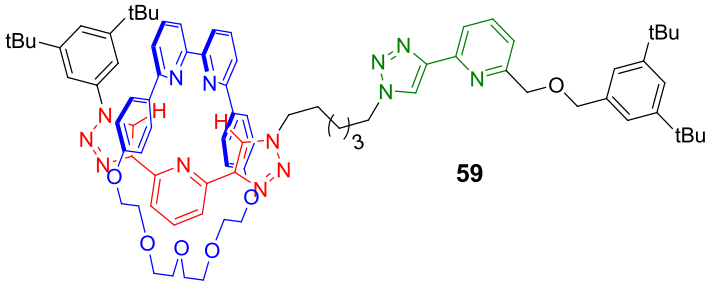

Figure 1.38 Structural represtation of a bi-stable molecular shuttle **59** incorporating **btp** and **tp** sites.[281]

the systems incorporate an isophthaloyldiamide moiety or a closely resembling analogue.

Beginning with the most recently reported, Evans *et al.* detailed the rapid synthesis of an isophthalamide [2]catenane **60**.[276] The X-ray crystal structure supports the hypothesis that the formation of the interlocked molecule is driven by hydrogen bond templation as inter-ring hydrogen bonding is clearly observed, Figure 1.39. In each interlocked macrocycle, the amides of one isophthaloyldiamide motifs are *cis* to each other, forming a bifurcated hydrogen bonding interaction with one amide oxygen of the *trans* oriented isophthaloyldiamide of the other macrocycle. The other interlocked macrocycle sees two hydrogen bonding interactions from each of the isophthaloyldiamide *NH*s to separate oxygen atoms in the polyether chain of its interlocked equivalent. The dynamic behaviour of the system was explored using ^{1}H NMR spectroscopy through varying the solvent composition and the temperature. Increasing the concentration of DMSO-d_6 was shown to disrupt the inter-ring hydrogen bonding increasing the rate of ring rotation. The result was a sharpening of certain proton resonances. At higher temperature, all the proton resonances sharpened as the increased thermal energy of the system competed with hydrogen bonding interactions resulting in faster ring rotation on the NMR timescale.

Going back to the very first report,[272] however, Hunter published the crystal structure[273] of [2]catenane **61** which was formed in a mixture of products *i.e.* dimeric and tetrameric macrocycle derivatives. The two macrocycles which make up **61** are crystallographically symmetry equivalent molecules, Figure 1.40. The same set of bifurcated hydrogen bonds between *cis* isophthaloyldiamide motifs of each macrocycle and the *trans* isophthaloyldiamide motif of the other macrocycle are observed.

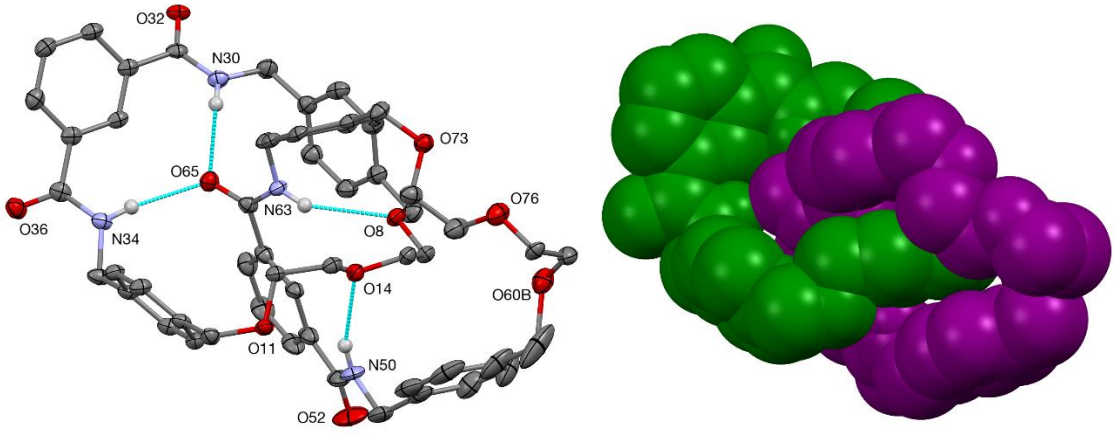

Figure 1.39 X-ray crystal structure of [2]catenane **60**. Ellipsoids displayed at 50% probability and the disordered contributor, solvent molecules and hydrogen atoms (except those involved in hydrogen bonding interactions) omitted for clarity. Labelled atoms as they appear in CIF file.[276] The space fill representation of **60** clearly demonstrates the interlocked nature of the system.

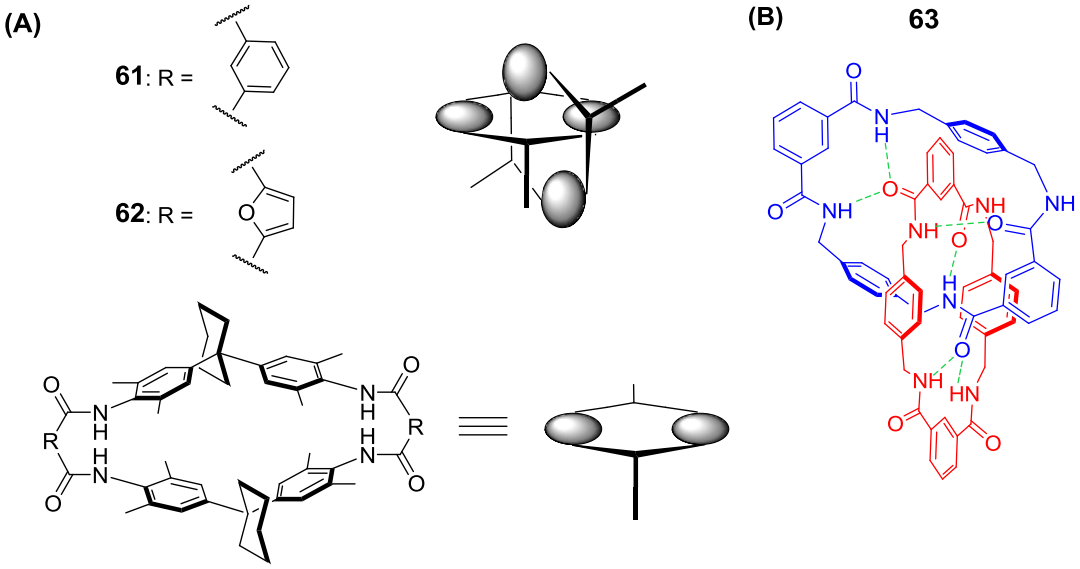

Figure 1.40 (A) Schematic representation of and furanoyl derived [2]catenanes **61** and **62**, respectively. (B) Benzylic isophthaloyldamide [2]catenane **63.**

Vögtle *et al.*, simultaneously reported a similar result with a closely related [2]catenane **62** which differed to **61** only by replacing the benzene ring in the isophthaloyldiamide motif with a furan ring.[266,274] The crystal structure demonstrates the same hydrogen bonding pattern responsible for the self-templated dimerisation, one bifurcated interaction connecting the two *cis* oriented amide *N-H*s with one of the *trans* oriented amide oxygen atoms of the opposite interlocked macrocycle's furanoyl motif. The third hydrogen bond arises as the other *trans* oriented amide oxygen is hydrogen bonded to the *trans* oriented amide *N-H* on the opposite macrocycle. Through symmetry, these three hydrogen bonding interactions are doubled giving a total of six hydrogen bonds observed per [2]catenane in the solid state.

Finally, Leigh *et al.* reported the solid-state structure of a benzylic isophthaloyldiamide [2]catenane **63**.[275] The X-ray crystal structure also supports the proposal that catenane formation is hydrogen bonding templated. π-π stacking interactions may also play a role in the dimerisation assembly. In the same fashion as previous catenane examples, the two macrocyclic rings of each catenane **63** are held through a total of six hydrogen bonds. These self-assembly processes, currently provide the only realistic approach towards such systems. As we saw in Section 1.6 the **btp** containing [2]catenanes **36a-c** were developed by Byrne *et al*. The topologies and dynamic properties of these systems are unique and the pre-organisation requirements for such systems to be synthesised in high yields are worth exploring.

1.12 Work described in this thesis

As discussed above, functionalising the 1,4-disubstituted-1,2,3-triazole motif in the synthesis of chelating ligands such as **btp** and **tp** has led to many significant developments in supramolecular chemistry. Derivatisation of the **btp** heterocyclic unit at the triazolyl *N1* positon has been explored thoroughly in the Gunnlaugsson group. The aims central to the work conducted in this PhD research project are further functionalising the **btp** and **tp** motifs in the development of functional supramolecular systems, from discrete metal complexes to coordination polymers and interlocked molecules.

Chapter 2 will report several facile modifications to the 4-pyridyl position of the **btp** core through the introduction of conjugated functional groups.

Chapter 3 will detail the self-assembly behaviour of the modified **btp** ligands with *f*-metals and the templated formation of metallo-supramolecular gels. An exploration into how these supramolecular systems are formed will be carried out using photophysical measurements, X-ray crystallography and ^{1}H NMR spectroscopy. An investigation of the functional properties of these soft materials will also be carried out using rheological measurements. The preliminary results of binding selectivity studies of **btp** ligands with An/Ln mixtures will also be summarised.

Chapter 4 will focus on the synthesis and structural analysis of several **btp**-derived coordination polymers. The synthesis of MOFs for the uptake of specific guests in the development of luminescent materials will also be investigated.

Chapter 5 will employ self-templating interactions in the formation of mechanically interlocked molecules. The effect of modifying the **btp** motif, at the triazolyl *N1* position and at the 4-pyridyl position, in the formation of self-templated [2]catenanes will be investigated. The interactions of the resulting *anti-anti* pre-organised **btp** systems with anions will also be explored.

Chapter 6 will demonstrate that the typically active bidentate coordination functionality inherent in subtly unsymmetric **tp**-derived ligands favours binding through the *reg* binding pocket even when both *reg* and *inv* metalation sites are simultaneously present in the ligand scaffold.

Chapter 7 will provide detailed experimental procedures. References will be provided in Chapter 8 and supplementary data and spectra will be presented in several Appendices.

2 Facile synthetic variation of the 4-pyridyl position of the btp motif towards ligands with increased functionality

2.1 Introduction

As was stated in Section 1.9, **btp** can be synthetically modified in a wide variety of ways using the initial choice of azide and/or alkyne starting material and also variation of the aromatic **btp** heterocycle. There have been several reports detailing the modification of the 4-pyridyl position of **btp** which is relatively reactive due to its *para* conjugation with the pyridyl nitrogen atom, allowing conventional pyridine chemistry to be used for the introduction of a variety of substituents.[105,110] Furthermore, the newly installed substituent's location relative to the Lewis base nitrogen atom can serve to tune photophysical, electronic and structural properties of the resulting complexes;[57,99] an increase in the degree of conjugation can be achieved by the addition of functional groups in transforming UV-vis absorbing chromophores into ligand building blocks that absorb at longer wavelengths.[57,282] As mentioned in Section 1.5.7, variation of the 4-pyridyl substituents in **22** clearly showed a direct effect on the redox behaviour of the Ru(II) complexes synthesised, opening up potential for the predictable tuning of such properties.[99] However, modification of the 4-pyridyl position can also be used in the design of higher order supramolecular systems and materials through the introduction of 'handles' for further functionalisation. The aim of this chapter is to modify the **btp** core with particular focus on the 4-pyridyl position for the appendage of conjugated substituents towards the design of higher order supramolecular systems and materials. To bring about these transformations several synthetic routes have been reported using commercially available starting materials. The new **btp** ligands developed over the course of this research project were synthesised employing these routes, therefore, the review of such synthetic pathways and their discussion is highly relevant.

2.2 Synthetic procedures for functionalisation of the btp 4-pyridyl position

Hecht *et al.* reported two approaches for the synthesis of 4-pyridyl substituted **btp** 'clickates' **64a**-**g**.[105] Firstly, they took advantage of the 4-pyridyl carboxylic acid group of the citrazinic acid starting material **65** (Scheme 2.1) by introducing carbonyl functionality into the **btp** motif. This route involved the chlorination of **65**, followed by the hydrolysis of the activated acid chloride *in situ* with H_2O to afford **66**. This allowed the introduction of the 3,6,9-trioxadec-1-yl ester functionality **67** followed by Sonogashira coupling, deprotection of the protected alkyne **68** and CuAAC of **69** with a range of azides to produce ligands **64a-g** in 85%-100% yield.

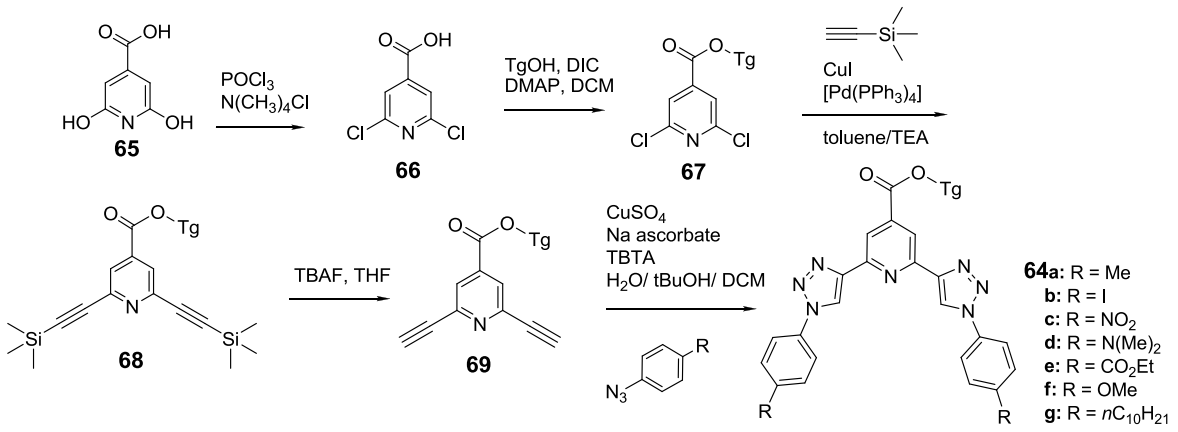

Scheme 2.1 Synthetic route to **btp** 'clickates' **64a-g** functionalised at the 4-pyridyl position with a 3,6,9-trioxadec-1-yl (Tg) ester functionality.[105]

The second approach detailed in the same article commenced with the oxidation of 2,6-dibromopyridine **70** to 2,6-dibromopyridine-*N*-oxide **71** followed by selective nitration at the 4-pyridyl position producing **72** (Scheme 2.2). This was then reduced in order to remove the *N*-oxide, allowing the nitro group of **73** to undergo nucleophilic substitution with deprotonated triethyleneglycol. The resulting 2,6-dibromo-4-(3,6,9-trioxadec-1-yloxy)pyridine **74** underwent Sonogashira coupling giving **75** followed by CuAAC of the deprotected alkyne **76**, as before, with a range of azides yielding ligands **10** and **77a-d**.

Chandrasekar and Chandrasekhar used a similar method for functionalising **btp** motifs at the 4-pyridyl position as Hecht *et al.* reported.[105] However, they extended this by carrying out elegant functional group interconversions after the **btp** core had been constructed in

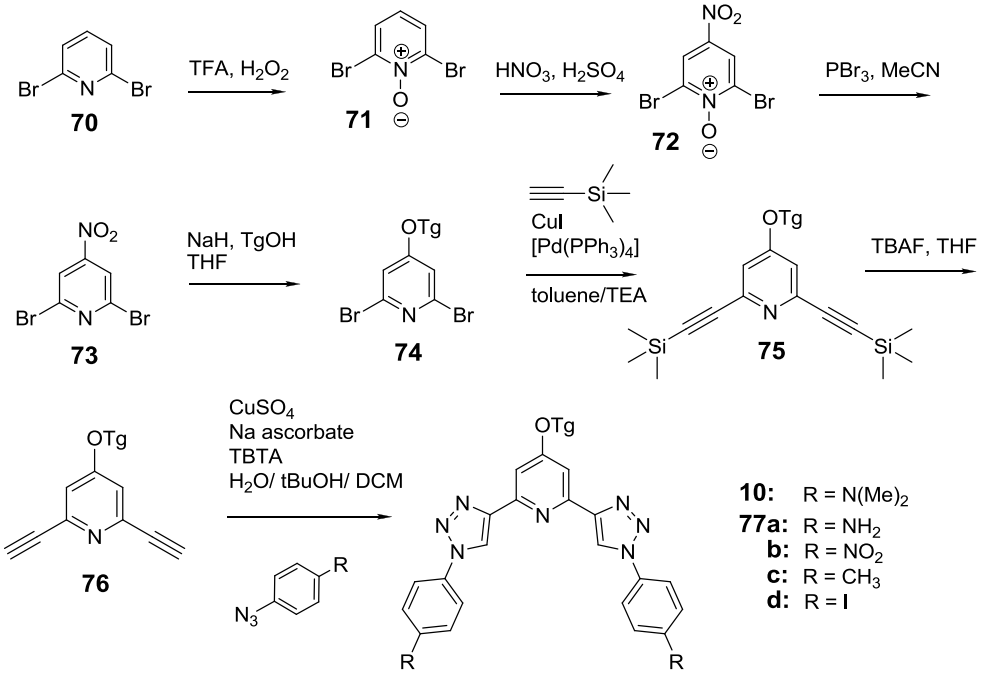

Scheme 2.2 Synthetic route to **10** and **77a-d** functionalised at the 4-pyridyl position with a 3,6,9-trioxadec-1-yloxy group.[105]

order to develop ditopic ligands.[110] Like Hecht *et al.*, the synthetic route began with citrazinic acid **65**, and in a similar fashion[283] they produced **btp** ligand **78** (Scheme 2.3) which had carbonyl functionality in the form of a methyl ester rather than the 3,6,9-trioxadec-1-yl ester **64**. This was hydrolysed to the acid analogue **79**. The carboxylic acid functional group is important for the introduction of or interconversion to a new functionality, a representative example of which was the sequential conversion of the 4-pyridyl carboxylic acid into an acyl azide followed by thermal Curtius rearrangement and subsequent hydrolysis to provide the amino derivative **80** in 78% yield. Diazotisation of the amino group, followed by reaction of the diazonium salt with KI produced the iodide derivative **81** which was in turn reacted with either *bis*(pinacolato)diboron to give a ditopic **btp** ligand **82a**, or aryl boronic acids to introduce ditopic mono- and diphenyl linked **btp** ligands, **82b** and **82c**, respectively.

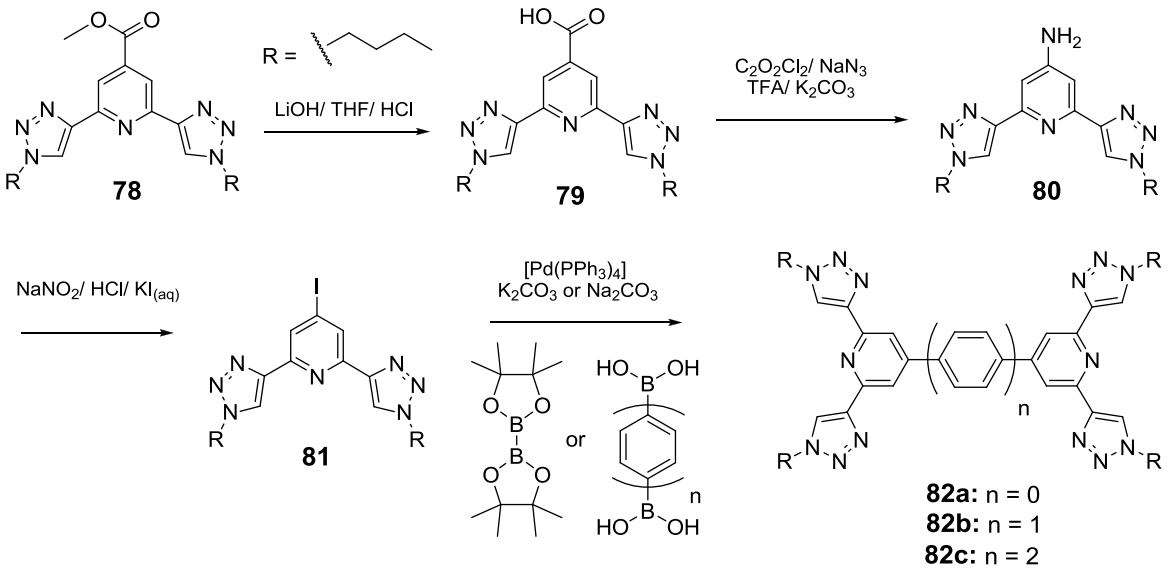

Scheme 2.3 Synthetic route towards ditopic **btp** ligands **82a-c**.[110]

2.3 Synthesis and characterisation of 4-pyridyl functionalised btp ligands

In this chapter, several **btp** containing ligands, analogous to systems **16** and **32** developed by Byrne *et al.*[27,70,103,113,119] were derivatised with carbonyl functional groups at the 4-pyridyl position of the **btp** core. It was envisaged that the tri-methyl ester **btp** ligand **83** would display rich coordination chemistry and good solubility in a range of solvents and the tri-carboxylic acid **btp** $\mathbf{H_3}$**84** (incorporating several divergent metal binding carboxylate functionalities), upon deprotonation would be a potential candidate for a low molecular weight gelator (Chapter 3). It was also envisaged that the incorporation of orthogonal functional groups at the 4-pyridyl position (R') and aryl "arms" (R) in the synthesis of **btp**

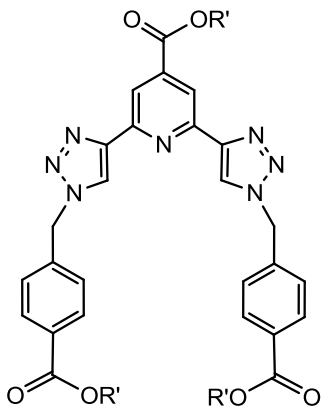

	R'	R
83:	CH_3	CH_3
$H_3$84:	H	H
85:	Bn	CH_3
86:	Bn	H
87:	H	CH_3

ligand **85** would be desirable as orthogonality could then be used to selectively interconvert the carboxylic acid functional groups in **btp** ligands **86** and **87** at the two locations. For example, it will be demonstrated in Chapter 5 that appendage of olefin groups *via* amide coupling with the carboxylic acid moieties on the aryl "arms" of **86** aids in our understanding of the self-assembly formation of 4-pyridyl functionalised homocircuit [2]catenanes. Furthermore, in Section 2.5 of this chapter orthogonal derivatisation of the 4-pyridyl position of **87** is a promising route towards the development of ditopic **btp** ligands.[5,179,196]

Ligand **83** was synthesised *via* a one-pot deprotection/'click' reaction[164] involving methyl-2,6-(bis(trimethylsilyl)acetynyl)isonicotinate **88** and methyl 4-(azidomethyl)benzoate **89**, formed *in situ* from the relevant bromide, according to Scheme 2.4. The first step of the synthesis was the chlorination of the commercially available citrazinic acid **65** using $POCl_3$

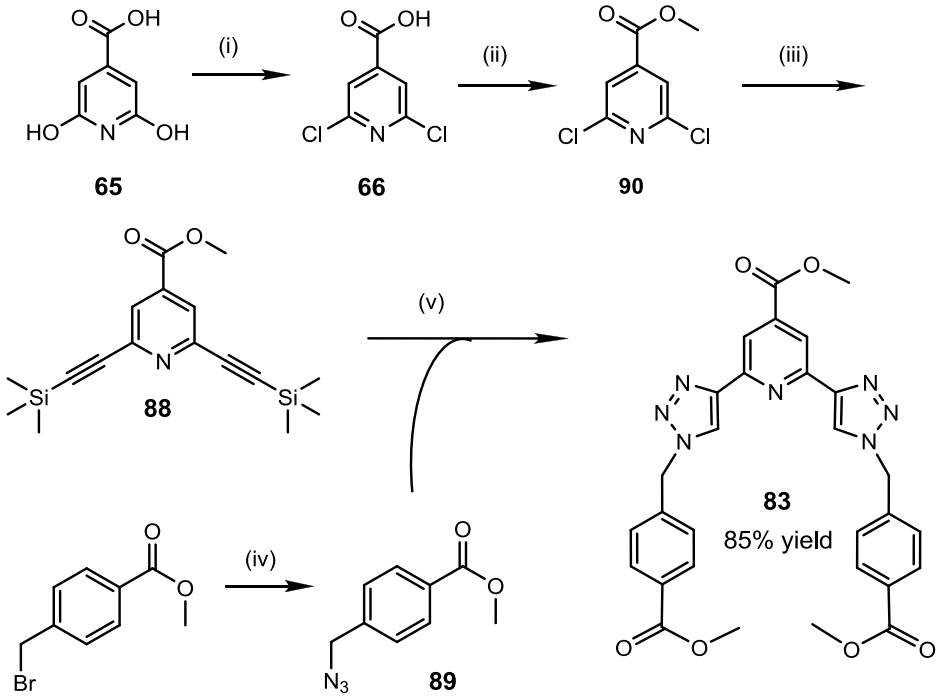

Scheme 2.4 Synthesis of **83**. (i) TBACl, $POCl_3$, 140°C. (ii) MeOH, H^+, 80°C (iii) (1) CuI, $(PPh_3)_2PdCl_2$, Et_3N:THF (1:1), (2) ethynyltrimethylsilane 0°C→70°C, (iv) NaN_3, DMF:H_2O (4:1) rt (v) $CuSO_4{\cdot}5H_2O$, K_2CO_3, Sodium Ascorbate, DMF:H_2O (4:1), rt.

forming the reactive acid chloride intermediate which was quenched with H_2O to afford **66** in 90% yield.[169] This was esterified to **90**[99] and then recrystallised from CH_3OH to afford pure needle-like crystals in 40% yield. From this, the necessary trimethylsilyl-protected alkyne **88** was formed *via* Sonogashira coupling in 72% yield.[99] The relevant azide, **89** was formed *in situ via* nucleophilic substitution of methyl 4-(bromomethyl)benzoate with sodium azide in stirred DMF:H_2O (4:1) solution at room temperature before addition of **88**, degassing and CuAAC. After scavenging the Cu(I) using ligand **83** was isolated upon trituration with cold CH_3OH in 85% yield**.** ^{1}H NMR (600 MHz, $CDCl_3$) was used to characterise this compound (Figure 2.1). The two lowest field resonances, 1 and 2 found at 8.10 ppm and 8.58 ppm were assigned to the triazolyl and pyridylprotons, respectively. The aryl protons, 3 and 4, were found to resonate at 8.00 ppm and 7.31 ppm, respectively. The singlet at 5.62 ppm, 5, was assigned as the CH_2 using DEPT analysis. The two singlets at 3.97 ppm and 3.90 ppm accounted for the methyl protons, 6 and 7, respectively. ^{13}C NMR (151 MHz, $CDCl_3$), HSQC and HMBC allowed the carbon signals to be assigned (Appendix A.1). MALDI$^+$ mass spectrometry analysis displayed a characteristic peak at *m/z* = 568.1968, which corresponded to the *m/z* calculated for $[M+H]^+$. The UV-vis absorption spectrum

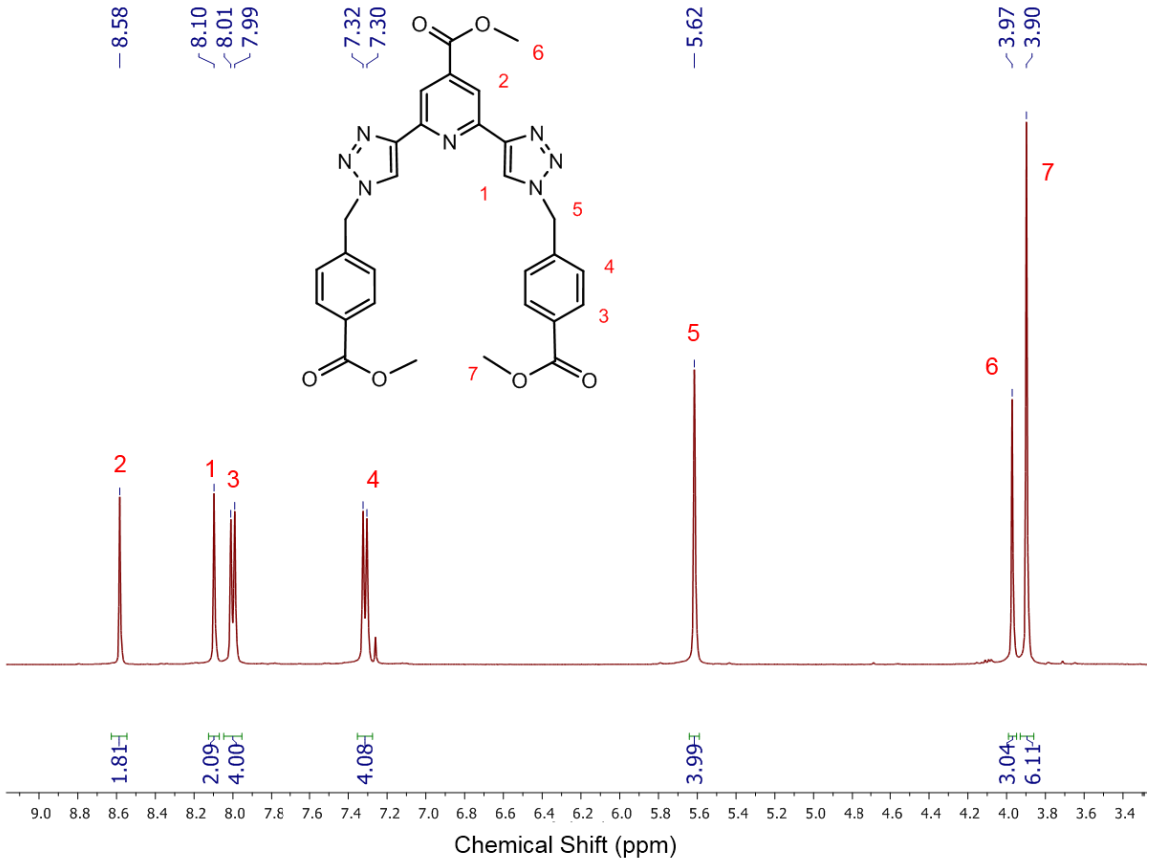

Figure 2.1 ^{1}H NMR spectrum of tri-methyl ester **btp** ligand **83** (600 MHz, $CDCl_3$) with resonances labelled.

demonstrated that the extra degree of conjugation afforded to the **btp** motif and electron withdrawing nature of the methyl ester were manifested in a bathochromic shift in the absorption band assigned to the **btp** n→π* transition, which was red-shifted to 327 nm (ε_{max}=65,000 dm^3 mol^{-1} cm^{-1}) for **83** (Appendix C.1) relative to the corresponding band at 301 nm (ε_{max} = 45,000 dm^3 mol^{-1} cm^{-1}) for its unsubstituted **btp** analogue **16**[103,113,282] The band centred at 236 nm (ε_{max} = 14,000 dm^3 mol^{-1} cm^{-1}) assigned to the π→π* transitions in the aromatic rings remained relatively unchanged compared with 235 nm (ε_{max} = 8,700 dm^3 mol^{-1} cm^{-1}) for **16**. The broad emission band maximum appeared at the longer wavelength of 375 nm relative to 335 nm for **83** and **16**, respectively. The formation of Ln(III) complexes of this ligand and the self-assembly of these systems in CH_3CN will be detailed in Chapter 3. Furthermore, the modification of ligand **83** with long chain alkyl groups at the *N1* triazolyl position and the resulting ligand's self-assembly with Ln(III) ions alongside preliminary results of the study of its An/Ln binding selectivity properties will also be discussed in Chapter 3.

As seen from Section 1.10, there currently exists a great deal of interest in the search for new soft materials with enriched functional properties endowed by the gelator molecules they are comprised of.[4-6] The incorporation of several divergent metal binding carboxylic acid groups was brought about by hydrolysis of the three methyl ester groups of **83**. The corresponding tri-carboxylic acid **btp** ligand **$H_3$84** was obtained in 71% yield by refluxing at 110 ^oC for 24 hours in CH_3OH:$NaOH_{(aq)}$ (1:1). The CH_3OH was removed under reduced pressure and the remaining aqueous fraction was acidified to pH = 4. Interestingly, upon leaving the solution to stand momentarily the mixture's viscosity increased dramatically and a gel-like precipitate was formed. This observation will be discussed further in Chapter 3. The loss of the methyl ester peaks at 3.97 and 3.90 ppm from the ^1H NMR (400 MHz, DMSO-d_6) spectrum confirmed the formation of **$H_3$84** (Figure 2.2). ESI^+ mass spectrometry displayed a characteristic peak at *m/z* = 548.1289 for $[M+Na]^+$. The formation of **$H_3$84** was also confirmed by X-ray diffraction analysis, however, this structure will be discussed in detail in Chapter 4 where its use as a tecton in generating functional porous coordination polymers will be featured.

The introduction of carbonyl functional groups into this series of **btp** ligands **85** and **86** for functionalisation in an orthogonal manner was carried out according to Scheme 2.5. The acid, **66**, was treated with $NaHCO_3$ and benzyl bromide was added in anhydrous DMF before stirring at 70 °C for 17 hours leading to the formation of the benzyl ester **91** in 86% yield. Sonogashira coupling successfully formed the bis-alkyne **92** which wa s purified by

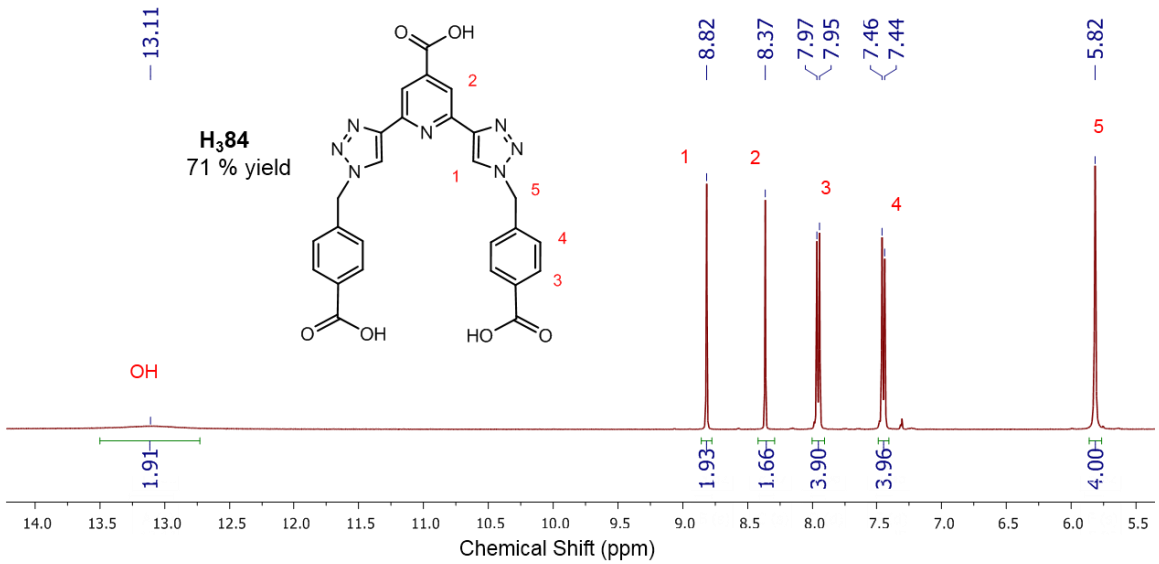

Figure 2.2 ^{1}H NMR spectrum of tri-carboxylic acid **btp** ligand **H$_3$84** (400 MHz, DMSO-d_6) with resonances labelled.

automatic flash chromatography. This was followed by the one-pot CuAAC reaction of **92** with azide **89** which generated the benzyl ester derivatised ligand **85** as an off white powder in excellent yield (84%), isolated in an identical manner to **83**. The ^{1}H NMR (600 MHz, $CDCl_3$) spectrum (Figure 2.3) appeared similar to that of **83** with the obvious difference being the second methylene singlet integrating for 2 protons at 5.43 ppm and the extra

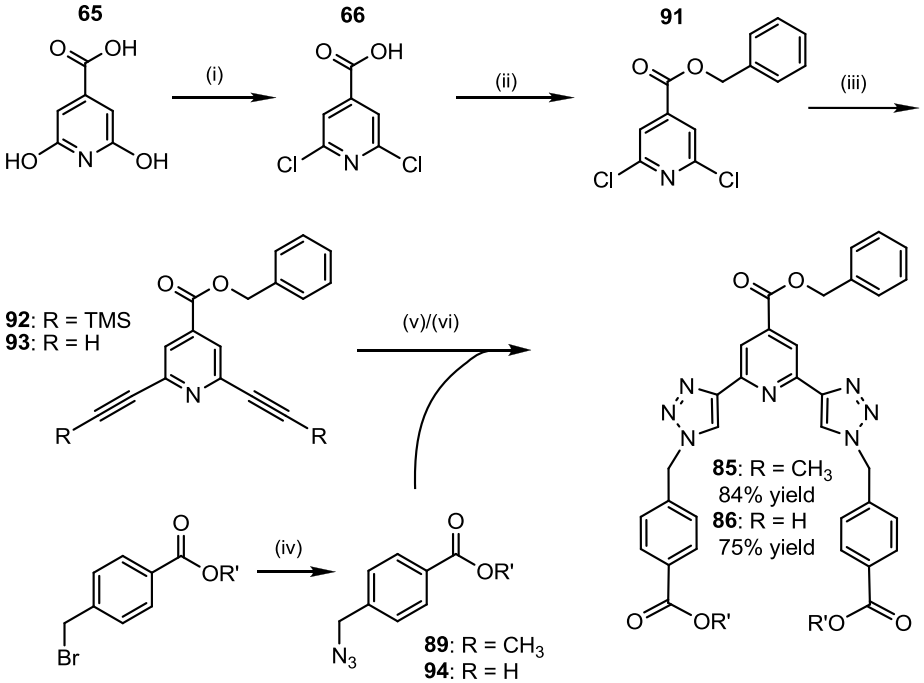

Scheme 2.5 Synthesis of **85** and **86**. (i) TBACl, $POCl_3$, 140°C (ii) BnBr, $NaHCO_3$, DMF, 70°C (iii) CuI, $(PPh_3)_2PdCl_2$, ethynyltrimethylsilane, Et_3N:THF (1:1), 0°C→70°C, (iv) NaN_3, DMF:H_2O (4:1), rt (v) from **89**: $CuSO_4{\cdot}5H_2O$, K_2CO_3, Sodium Ascorbate, DMF:H_2O (4:1), rt. [a] (vi) from **94**: $CuSO_4{\cdot}5H_2O$, Sodium Ascorbate, DMF:H_2O (4:1), rt.

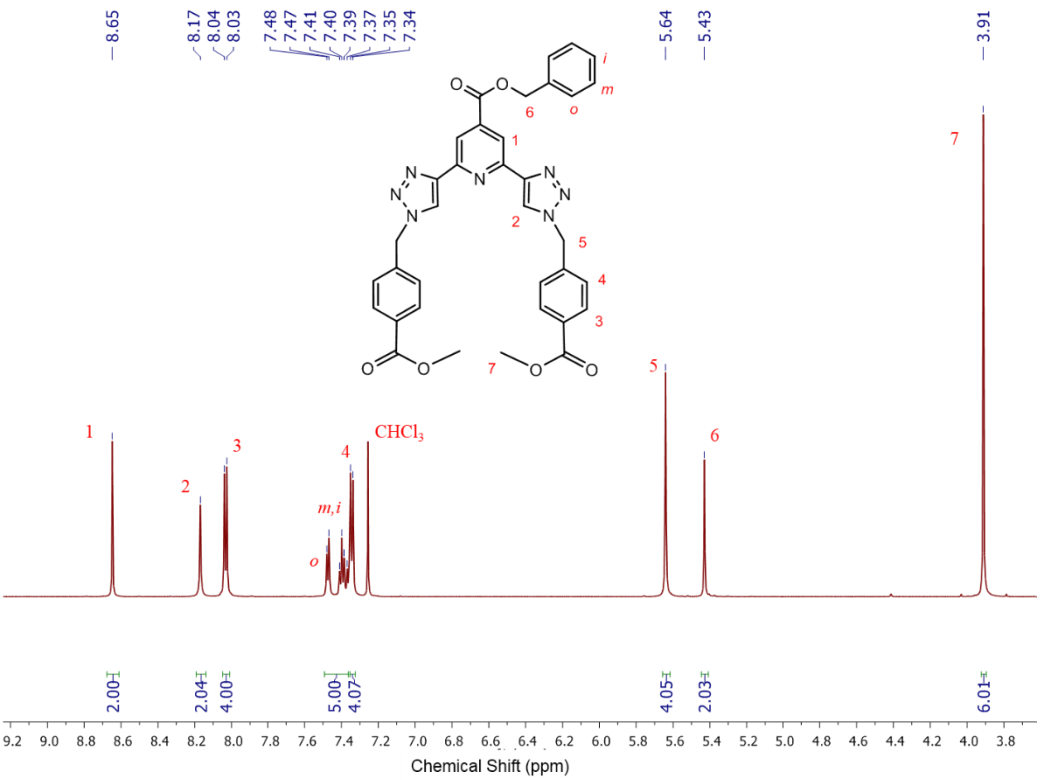

Figure 2.3 ^{1}H NMR spectrum of 4-benzyl ester **btp** ligand **85** (600 MHz, $CDCl_3$) with resonances labelled.

aromatic protons of the benzene ring integrating to 5 as a mutliplet from 7.49-7.36 ppm. Formation of **85** was also confirmed by single crystal X-ray diffraction analysis. Crystal data, data collection, and structure refinement details are summarised in Appendix E, Table E.1). Needle-like single crystals were grown by slow evaporation of a solution consisting of CH_3CN:H_2O (6:1). **Btp** ligand **85** crystallised and the X-ray data was solved and refined in the monoclinic $P2_1$ space group with one crystallographically distinct molecule in the asymmetric unit (Figure 2.4). As seen for other unbound **btp** systems, the *anti-anti* conformation predominates.[104-110] One triazolyl and one pyridyl unit are essentially coplanar with a twist of 28.17(16)° which facilitates a hydrogen bonding interaction between the proximal triazolyl nitrogen atom *N3* and the triaozlyl *CH* of a neighbouring molecule in the *b* axis direction. There is no evidence of **btp**-**btp** dimerisation in the solid state as seen in the cases of **35R**/**S** and **40** in Sections 1.6 and 1.7, respectively. The molecules pack in an interdigitated manner along the *a*-axis, see Figure 2.4(B), as a result of π–π interactions between adjacent aryl "arms", with a mean interplanar distance of *ca.* 3.4 Å. A similar packing diagram has been observed in the solid state in the case of unsubstituted **btp** analogue **16** (Appendix E.3).[113,119] The packing also sees π-π stacking interactions between pyridyl and triazolyl units of adjacent molecules along the *c*-axis with a mean plane to plane

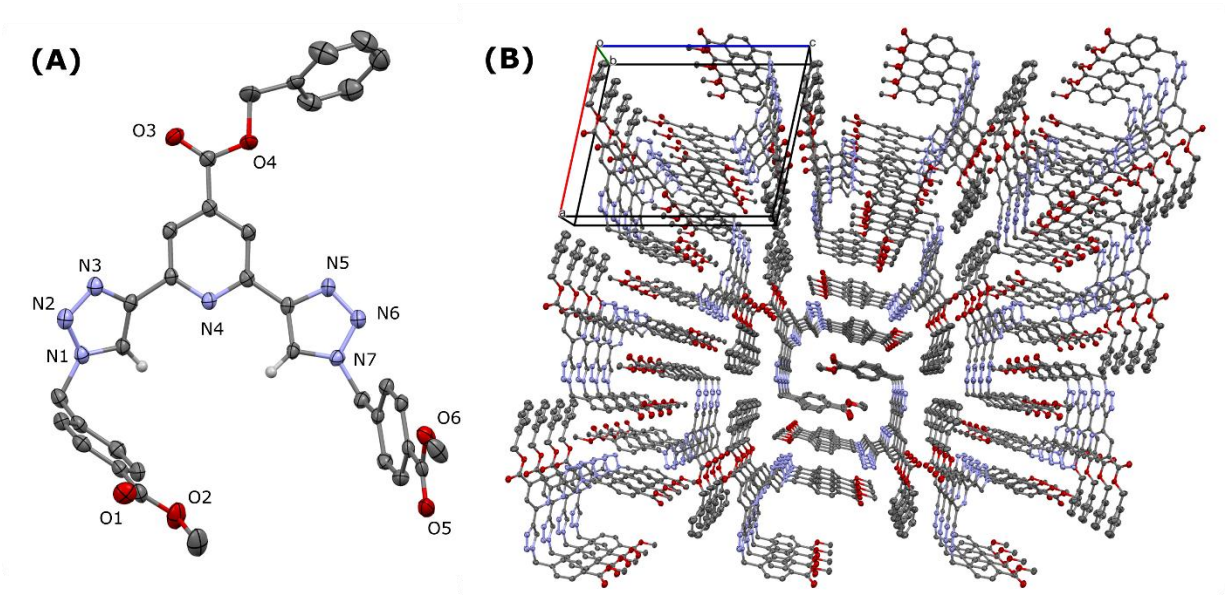

Figure 2.4 (A) Molecular structure of **btp** ligand **85**. (B) The interdigitated packing structure viewed parallel to the *b*-axis. Thermal ellipsoids displayed at 50% probability and disordered contributor omitted for clarity

centroid distance of *ca.* 3.3 Å (Appendix E.4). The benzyl ester moiety's aromatic ring is disordered over two sites and both aryl "arms" are oriented in a *cis* fashion. ESI^+ mass spectrometry also confirmed the formation of the desired ligand as evidenced by a peak at *m/z* = 666.2072, assigned to $[M+Na]^+$ and purity was confirmed by elemental analysis.

By simply varying the choice of azide another benzyl ester derivatised **btp** ligand **86** wasformed displaying orthogonal carbonyl groups at the 4-pyridyl position and aryl "arms", in the form of a benzyl ester and carboxylic acids, respectively (Scheme 2.5). The ligand was formed in 75 % yield using a modified one-pot CuAAC appraoch similar to that of **85** from the deprotected bis-ethynylpyridine **93**, and 4-(azidomethyl)benzoic acid **94**. K_2CO_3 was not added in this synthetic route to **86** as prior deprotection of **92** was carried out using fluoride (see the Experimental Section). Initial attempts of CuAAC towards the formation of **86** using the Fletcher *in situ* deprotection[163] of the trimethylsilyl-protected bis-alkyne **92** in the presence of K_2CO_3 had resulted in trace amounts of benzyl ester hydrolysis. Ligand **86** was fully characterised (see Appendix A.4) and its formation was evidenced by ^1H NMR spectroscopy (Figure 2.5). ESI^- mass spectrometry also confirmed the formation of the desired ligand as evidenced by a peak at *m/z* = 614.1803 *i.e.* $[M-H]^-$. The importance of **86** lies in the ability to attach further functionality using the carboxylic acid groups while keeping the benzyl protecting group intact. Formation of an amide (through amide coupling reactions or an intermediate acid chloride) can introduce further functionality depending on the amine used. This will be demonstrated in Chapter 5 *via* the amide coupling of amino

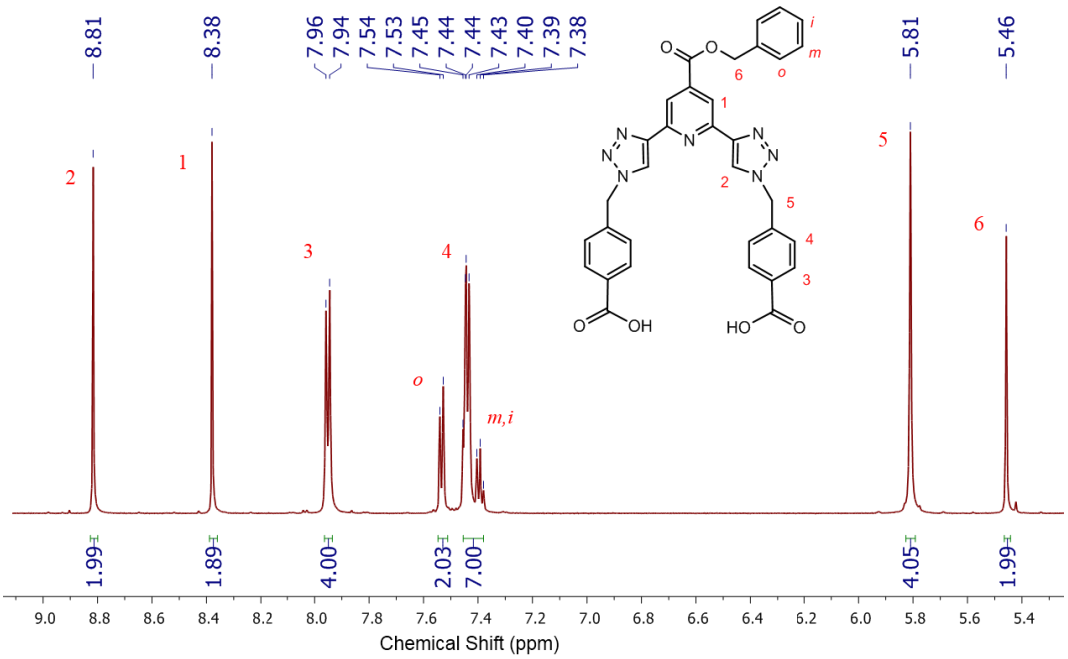

Figure 2.5 ^{1}H NMR spectrum of **btp** ligand **86** (600 MHz, DMSO-d_6) with resonances labelled.

precursors containing olefin groups at these carboxylic acid positions in the study of the formation of **btp**-derived [2]catenanes derivatised at the 4-pyridyl position.

It was envisaged that deprotection of the benzyl ester through hydrogenation would allow access to a reactive 4-pyridyl carbonyl "handle" for further functionalisation. With this in mind, **btp** ligand **87** was orthogonally deprotected upon catalytic hydrogenation with 10% palladium on carbon at 3 bar in a Parr Hydrogenator for 24 hours in EtOH. Filtration through celite gave the desired compound, as a beige solid in 97% yield. This was fully characterised,

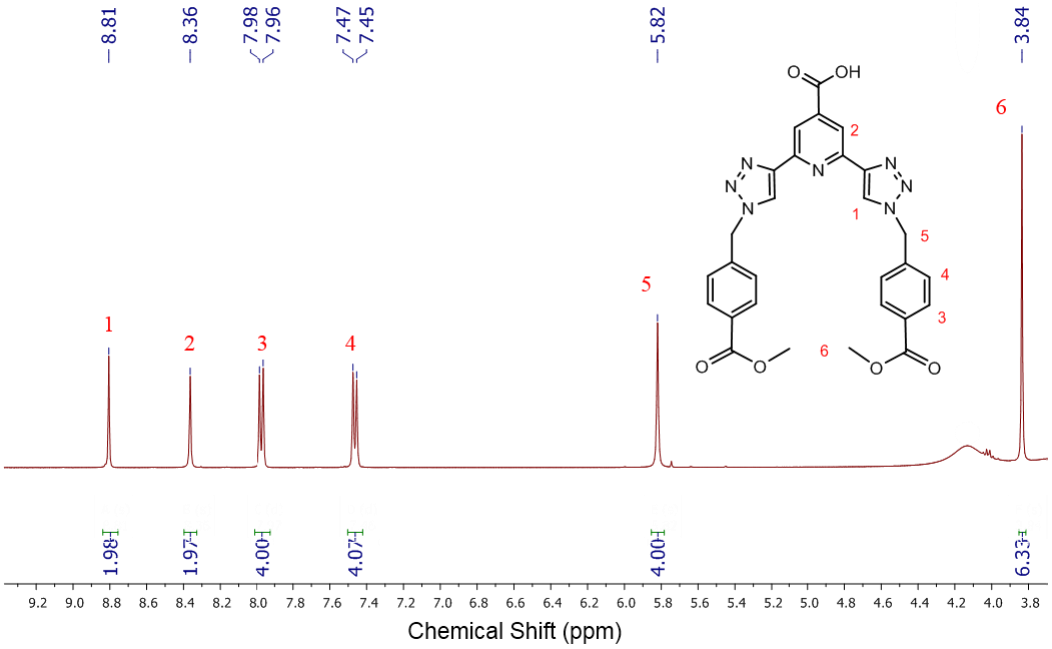

Figure 2.6 ^{1}H NMR spectrum of **btp** ligand **87** (400 MHz, DMSO-d_6) with resonances labelled.

showing characteristic signals and loss of the benzyl protecting group as evidenced by ^{1}H NMR spectroscopy (Figure 2.6). This ligand is an important precursor in the formation of a range of **btp** ligands for the incorporation of further functionality using the electrophilic carboxylic acid "handle" by reacting **87** with a range of nucleophiles. Finally, it was demonstrated that ligands **83**, **$H_3$84** and **87** could be accessed in a one step process from **85** using transesterification, hydrolysis and hydrogenation, respectively.

2.4 Synthesis of btp ligands modified at the 4-pyridyl position with amino functionality

The functionalisation of **btp** with nucleophilic groups was also investigated through the appendage of a conjugated amino group at the 4-pyridyl position. It was envisaged that the nucleophilic amino group could then be used as a "handle" for tuning the structure of the **btp** ligands resulting in a valuable synthetic tool for the potential development of more complex ligand systems. As discussed in Section 2.2, Hecht *et al.* reported the functionalisation of dibromopyridine **70** by oxidation giving 2,6-dibromopyridine-*N*-oxide **71** followed by the selective nitration at the 4-pyridyl position producing **72**, Scheme 2.2.[105] A similar route was adapted for the installation the amino functionality into the **btp** ligand **95** (Scheme 2.6). Reduction of both the *N*-oxide and the nitro groups of **72** using AcOH solution and Fe filings with sonication[284] resulted in the desired formation of **96** in good yield (78%) using an approach reported by Hay *et al.*[105] Sonogashira Coupling installed the

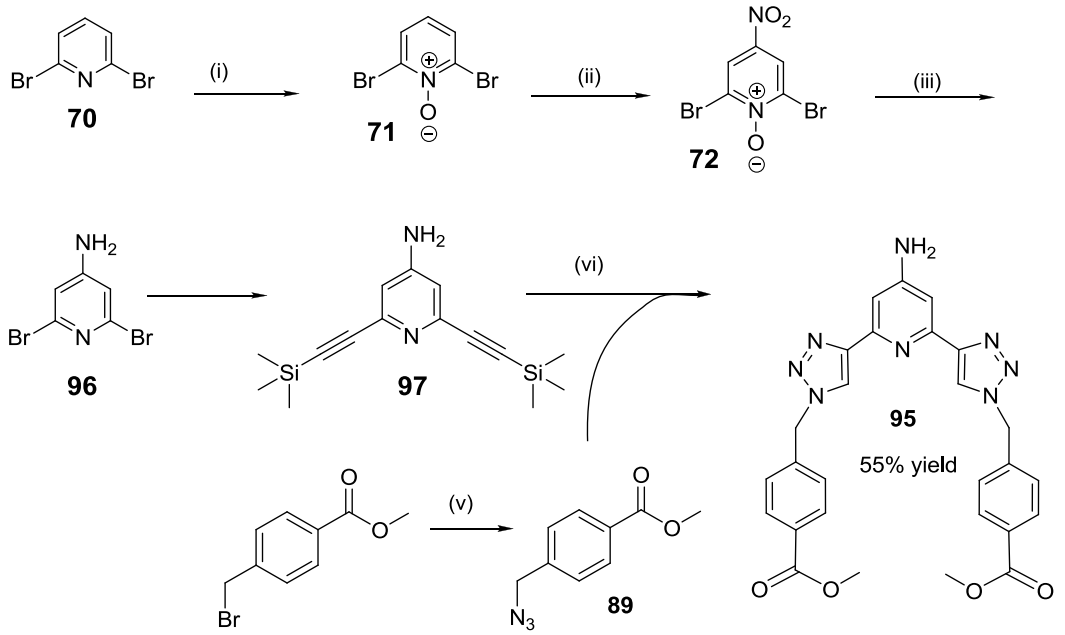

Scheme 2.6 Synthesis of **95**. (i) TFA, H_2O_2, 100°C (ii) HNO_3/H_2SO_4, 60°C (iii) AcOH, Fe, rt (iv) (1) CuI, $(PPh_3)_2PdCl_2$, Et_3N:THF (1:1), (2) ethynyltrimethylsilane, 0°C→70°C (v) NaN_3, DMF:H_2O (4:1), rt (vi) $CuSO_4.5H_2O$, Sodium Ascorbate, K_2CO_3, DMF:H_2O (4:1), rt.

ethynyl moieties **97** in an excellent yield of 84% (after flash chromatography). Bis-alkyne **97** subsequently underwent CuAAc in the same manner as **83** and **85** producing **95** in 55% yield after CH_3OH trituration. The ^1H NMR spectrum of **95** (Figure 2.6), showed broadened NH_2 resonance at 6.34 ppm and significantly shielded pyridyl resonance at 7.21 ppm compared to the corresponding proton signal for the acid **87** which appeared at 8.36 ppm (Figure 2.5). The triazolyl resonance at 8.52 ppm was similarly shielded compared to that of acid **87** which was found at 8.81 ppm. This is indicative of the delocalisation of the amino lone pair into the aromatic **btp** ring. ESI^+ mass spectrometry also confirmed the formation of the desired ligand as evidenced by a peak at *m/z* = 525.2004 *i.e.* $[M+H]^+$. Having successfully introduced an amino moiety to the **btp** motif, it was also investigated if the elegant functional group interconversion demonstrated in Scheme 2.3[110] could be carried out on **87** in an alternative route to forming **95** *via* thermal Curtius rearrangement. Following another synthetic route, reported by Johnson *et al.*,[285] the carboxylic acid **87** was chlorinated using $SOCl_2$/DMF before reacting with (azidoethynyl)trimethylsilane. The intermediate acyl azide was refluxed with added TFA for the Curtius rearrangement step and subsequent hydrolysis of the intermediate isocyanate (which was not isolated) with K_2CO_3 in aqueous CH_3OH provided the amino derivative **95** in 20% yield. With the amino moiety installed, it was next investigated if it possessed sufficient nucleophilicity to undergo further functionalisation such as in the generation of ditopic **btp** ligands.

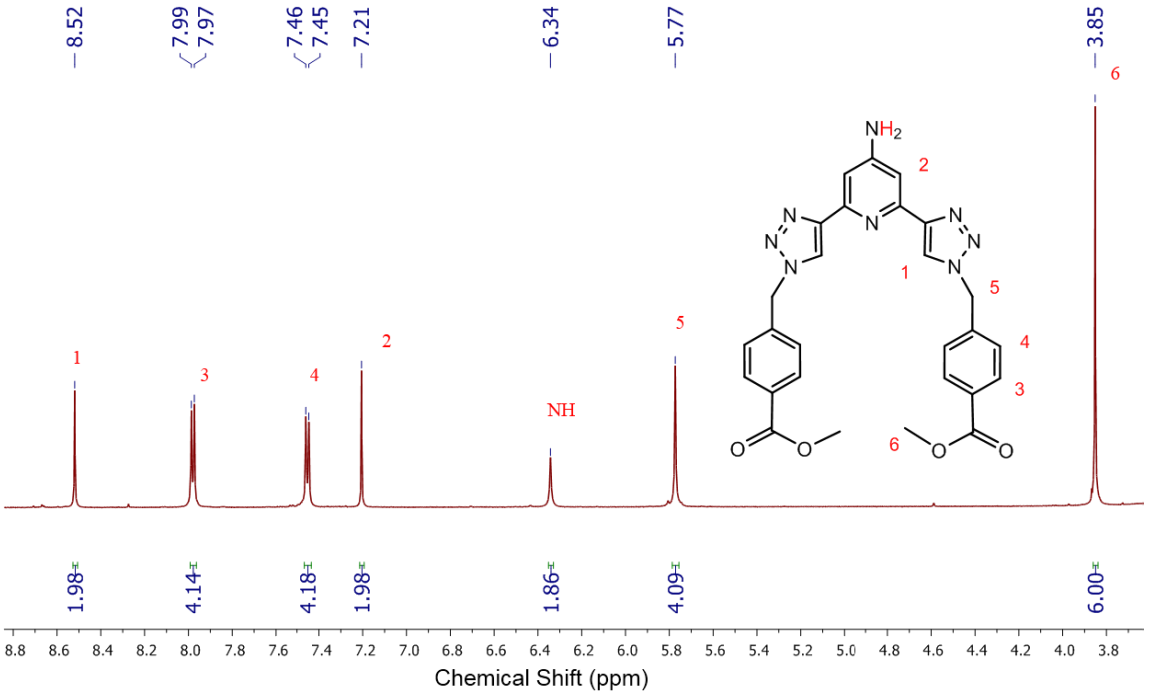

Figure 2.6 ^1H NMR spectrum of amino **btp** ligand **95** (600 MHz, DMSO-d_6) with resonances labelled.

2.5 Synthesis of ditopic btp ligand 98

Ditopic ligands are significant in the formation of supramolecular polymers,[13-14,27-28] as in the case of **btp** ligands **82a-c** (Scheme 2.3),[110] where, upon cross-linking with Eu(III), a 3D polymeric species was generated with a proposed formula of $\{[Eu\mathbf{82}_3](NO_3)_3\}_n$. The authors rationalised this proposal on the expected Eu(III) coordination number 9 on the basis of previously reported structures,[98,105] such as those generated by ditopic **btp** analogues **50** and **51** (Figure 1.34),[179,190,195-196] discussed in Section 1.10.1. It is also worthwhile stating that Schubert *et al.* reported the synthesis of π-conjugated ditopic **btp** ligands **23** and **24**.[134]

The synthesis of ditopic **btp** ligand **98** was carried out *via* the generation of the acid chloride intermediate using $SOCl_2$/DMF from **87**. After distilling off the excess $SOCl_2$ and dissolving the residue in anhydrous toluene, DMAP and Et_3N were added slowly before coupling with amino **btp** ligand **95** at reflux. Following purification by automatic flash chromatography ditopic ligand **98** was obtained in a respectable yield of 45% as evidenced by ^{1}H NMR spectroscopy (Figure 2.7). The subtly unsymmetric nature of **98** was evidenced by two separate resonances for the triazolyl protons at 8.81 ppm and 8.69 ppm, the pyridyl protons at 8.56 ppm and 8.54 ppm and methylene protons at 5.82 ppm and 5.79 ppm.

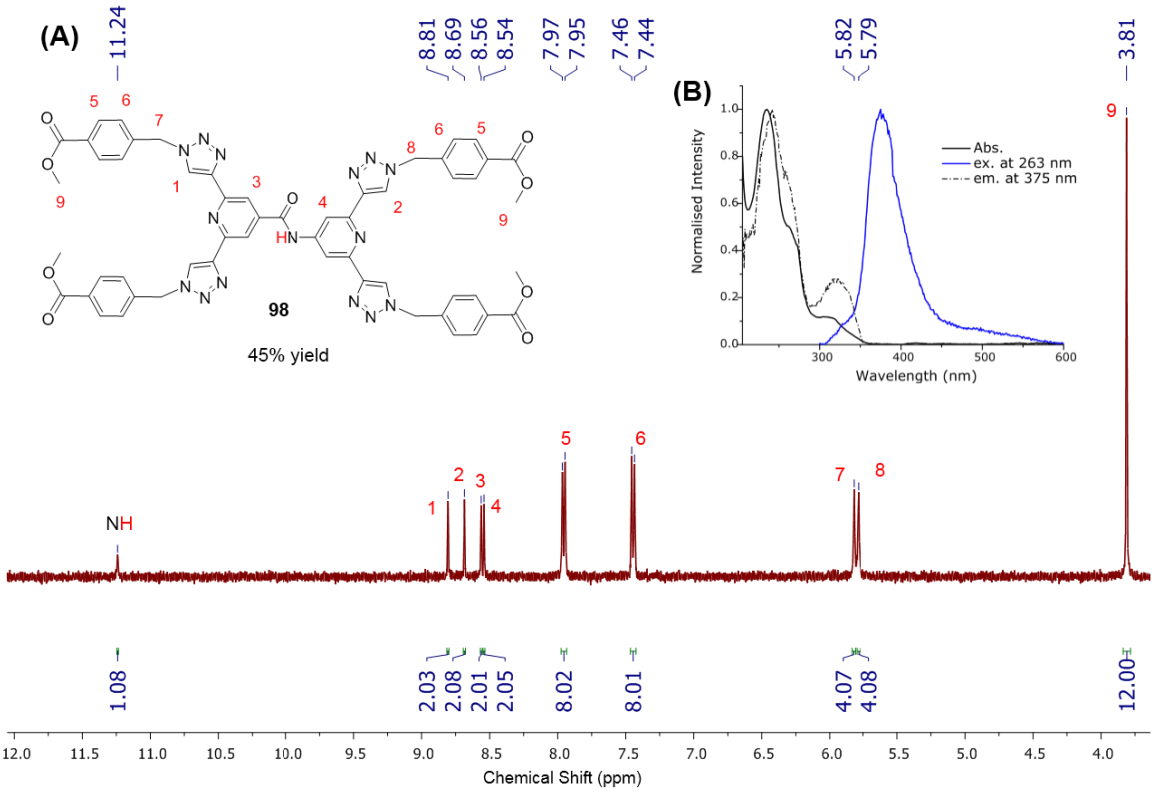

Figure 2.7 (A) ^{1}H NMR spectrum of ditopic **btp** ligand **98** (600 MHz, DMSO-d_6) with resonances labelled. (B) UV-vis absorption, emission and excitation spectra of **btp** ligand **98** in CH_3CN (c=0.01 mM).

Successful formation of **98** was also evidenced by ESI^+ mass spectrometry with a signal at *m/z* = 1004.3721 *i.e.* $[M+H]^+$. The UV-vis absorption spectrum in CH_3CN of **98**, Figure 2.7(B) displayed a blue-shift in the n→π* absorbance band of 14 nm and a small blue-shift in the π→π* band of 2 nm compared to ligand **83**. Excitation at 263 nm gave rise to an emission band centred at 375 nm similar to the corresponding emission of **83**.

This synthesis of **98** is presented as a preliminary result in the development of ditopic **btp** ligands. As such, there is a large scope for the development of a range of ditopic **btp** compounds using the synthetic procedures discussed above. Functionalisation of the aryl "arms" with solubilising groups may enable more facile handling of such large molecular weight compounds for the purpose of studying their self-assembly with Ln(III) ions in an analogous fashion as those reported by Rowan *et al.* using **btp** analogues **50** and **51**.[7b,7c,15a,17]

2.6 Synthesis of lipophilic btp ligand functionalised at the 4-pyridyl position

As discussed in Section 1.5.8, **btp** derivatives have featured with increasing frequency of late in new solvent extraction processes for the removal of transuranium elements (TRU) efficiently and selectively from waste mixtures in the effort to solve the environmental issues related to the management of existing nuclear waste.[98,148] A number of recent reports have appeared detailing the synthesis of **btp** ligands derivatised with hydrophilic groups[98,148-150] in order to improve the extraction of An(III) ions into aqueous media. An alternative approach was pursued in order for the extraction process to take place in non-polar solvents such as CH_2Cl_2. Several **btp** ligands, including **16**, **32**, **83**, **85**, **87** and **95** were tested for their ability to separate Ln(III) ions from An(III) ions in non-polar media, however, the solubility of these complexes were poor under these conditions. This work was carried out in collaboration with Dr. Saptharshi Biswas in the Baker group in Trinity College Dublin's

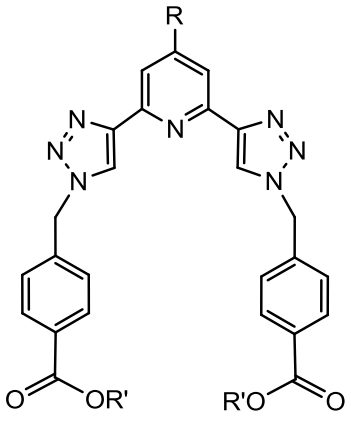

	R	R'
17:	H	CH_3
34:	H	H
83:	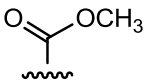	CH_3
85:	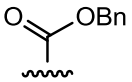	CH_3
87:	H	CH_3
95:	NH_2	CH_3

School of Chemistry. For this reason, the synthesis of **btp** ligand **99** (derivatised at the 4-pyridyl poisiton with a methyl ester), and functionalised with long chain hexadecyl lipophilic groups at the *N1* triazolyl position was carried out according to Scheme 2.7.

As was discussed in Section 1.9, the choice of precursor azide allows for the facile introduction of a wide range of functional groups making **btp** readily tunable at the triazolyl *N1* position. Byrne *et al.* made use of Stonehouse *et al.*'s three component 'click' approach[166] using the $ImSO_2N_3{\cdot}H_2SO_4$ diazo-transfer agent, to convert amines to azides *in situ* in a new modular and mild synthetic route towards **btp** ligands, Figure 1.30.[156] The lipophilic **btp** ligand **99** was synthesised in a two-step one-pot *diazo-transfer-deprotection-'click'* reaction from alkyne **88** and hexadecylamine.[156] In the first step, the relevant azide was formed *in situ* from hexadecylamine through the Cu(II) catalysed diazo transfer reaction in the presence of transfer reagent, $ImSO_2N_3{\cdot}H_2SO_4$ and K_2CO_3. The reaction mixture was cyan in colour initially and upon successful formation of the azide after 15 hours the suspension turned lilac (Figure 1.33, Section 1.9.1).[156] After addition of sodium ascorbate and K_2CO_3 after the mixture was degassed to give a yellow coloured suspension. A solution of **88** in DMF was then added and allowed to stir at room temperature for 24 hours giving rise to an orange suspension upon completion of CuAAC. The reaction mixture was washed with aqueous EDTA/NH_4OH solution, in order to scavenge Cu(II) ions, and then extracted into CH_2Cl_2. After the solvent was removed under reduced pressure, the residue was purified by trituration with cold CH_3OH and **99** was obtained in high purity as confirmed by elemental analysis and in 59% yield.

^{1}H NMR spectroscopy confirmed successful synthesis of the desired lipophilic **btp** ligand (Figure 2.8). The ^{1}H NMR of **99** displayed proton resonance signals associated with the **btp** motif, *i.e.* the pyridyl and triazolyl resonances, appearing at 8.65 ppm and 8.30 ppm. The

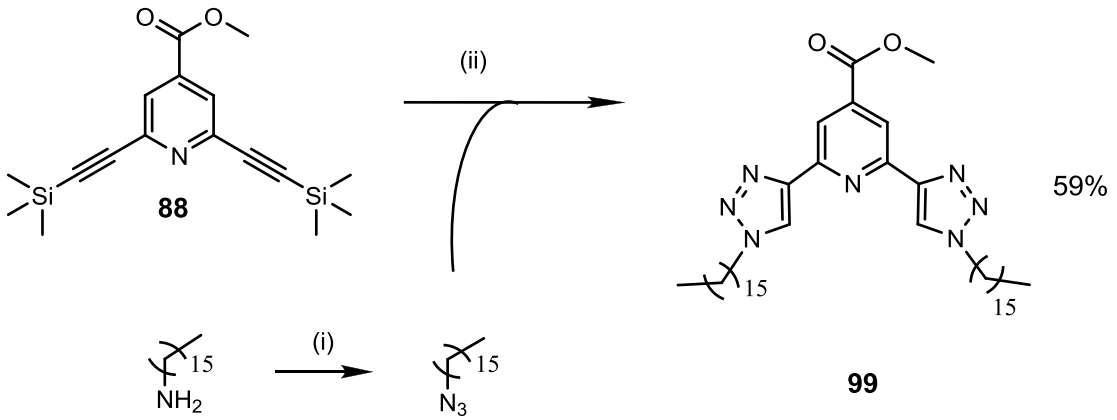

Scheme 2.7 Synthesis of **99**. (i) $CuSO_4{\cdot}5H_2O$, $ImSO_2N_3{\cdot}H_2SO_4$ and K_2CO_3 in CH_3OH, rt, 15 h; (ii) Sodium ascorbate, K_2CO_3, DMF/ tBuOH/ H_2O (5:5:3), rt, 18 h.

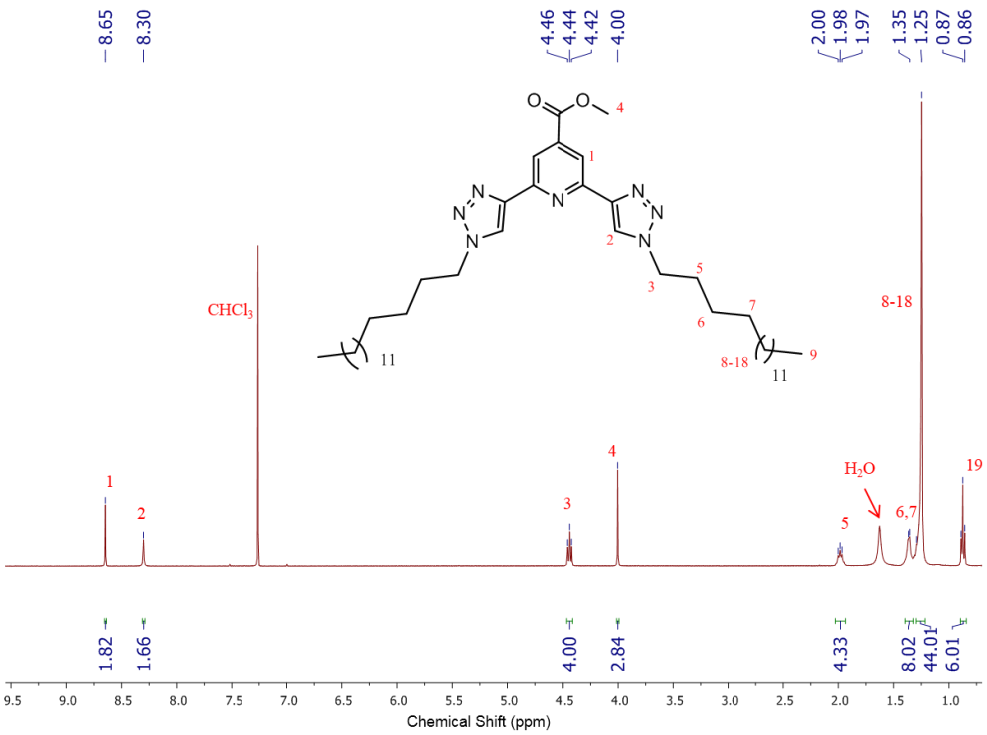

Figure 2.8 ^{1}H NMR spectrum of lipophilic **btp** ligand **99** (400 MHz, $CDCl_3$) with resonances labelled.

methylene protons adjacent to the triazolyl *N1* position can be found as a triplet at 4.44 ppm and the methyl ester protons appeared as a singlet at 4.00 ppm. The aliphatic region contained the remaining expected methylene peaks between 2.00 ppm and 1.25 ppm with the terminal methyl peak of the hexadecyl chain assigned as a tripet at 0.86 ppm.

The solid state structure was also obtained due to the formation of large blocks of colourless crystals, grown by toluene diffusion into CH_2Cl_2:CH_3CN (1:1) solution of **99**. The structure model was solved in the monoclinic crystal system with $P2_1/c$ space group containing one molecule in the asymmetric unit (Figure 3.9). The structure shows the **btp** motif adopting the *anti-anti* arrangement due to the nitrogen lone pair as is often observed in these types of ligand systems.[104-110] The triazolyl and two pyridyl units are essentially coplanar; (the interplanar angle between the mean planes of the each of the triazolyl rings with the pyridyl ring measuring *ca.* 11.3° and 8.6°, respectively). The planar conformation of **btp** facilitates the slipped π-π stacking interactions between molecules along the *c*-axis, in which the main aromatic overlap occurs between the pyridyl moiety of one ligand and the methyl ester moiety of its adjacent stacking partner (the perpendicular distance between the parallel mean planes of molecules is *ca.* 3.4 Å). This arrangement also facilitates the alignement of the lipophilic hexadecyl chains of neighbouring molecules. The hexadecyl chains on each of the arms of the ligand extend outward in the same direction in a *cis* fashion

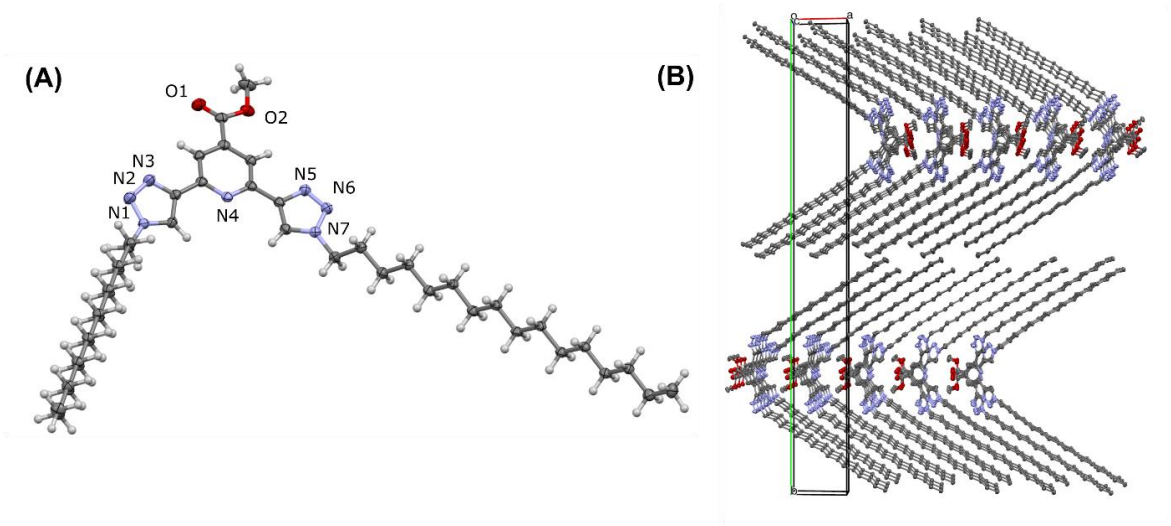

Figure 3.9 (A) Molecular structure of **btp** ligand **99**. (B) Packing diagram viewed parallel to the *c*-axis. Thermal ellipsoids displayed at 50% probability.

from the **btp** and both display *trans* coplanar (straight chain) behaviour with no disorder along the chains.

The self-assembly behaviour of **99** with Ln(III) ions was studied in solution *via* spectroscopic binding titrations which will be presented in the next Chapter and the preliminary results of the investigations using **99** in the Ln(III)/An(III) extraction selectivity studies in collaboration with the Baker group will be briefly summarised.

2.7 Conclusions

Various modifications of the **btp** motif at the 4-pyridyl position through introduction of carbonyl and amino moieties were successfully carried out. A number of new **btp** ligands (**83**, **H$_3$84**, **85**, **86**, **87**, **95**, **98** and **99**) were fully characterised by ^{1}H, ^{13}C NMR and IR spectroscopy, HRMS and CHN. The efficient appendage of a conjugated methyl ester group at the 4-pyridyl position of the **btp** motif was demonstrated in the formation of tri-methyl ester **btp** ligand **83**. Relative to the analogous **btp** ligand **16** developed by Byrne *et al.*[70,113,119] the modification resulted in bathochromic shifts of absorption and emission band maxima of the chromophore. The tri-carboxylic acid **btp H$_3$84**, incorporating several potential divergent metal binding sites was synthesised *via* the hydrolysis of **83**. Orthogonal carbonyl functional groups at the 4-pyridyl position of the **btp** motif and aryl "arms" were introduced efficiently in the synthesis of 4-pyridyl benzyl ester **btp** ligands **85** and **86**. It was demonstrated in the selective deprotection of the benzyl ester group of **85** through catalytic hydrogenation in the formation of 4-pyridyl acid **btp 87** that there is potential for further functionalising these systems in a chemo-orthogonal manner. Derivatisation of the **btp** motif

with a nucleophilic amino moiety in the form of **btp** ligand **95** was demonstrated using two synthetic routes, one of which was the thermal Curtius rearrangement of **87** followed by hydrolysis of the isocyanate intermediate. Orthogonal activation of the 4-pyridyl caroboxylic acid of **87** *via* an intermediate acid chloride and subsequent amide coupling with amino **btp 95** presented a promising route towards the development of ditopic **btp** ligands as evidenced by the reasonably efficient formation of ditopic **btp 98**. The synthesis of lipophilic **btp** ligand **99** functionalised at the 4-pyridyl position with a conjugated methyl ester group was also demonstrated with a view to introducing lipophilic groups in order to increase the solubility of the **btp** motif in non-polar organic media.

There is a large scope for the development of the synthetic methods used in this chapter. For example, the importance of **86** lies in the ability to attach further functionality to the carboxylic acid groups while keeping the benzyl protecting group intact. This will be investigated in detail in the self-templating assembly studies of 4-pyridyl functionalised homocircuit [2]catenanes in Chapter 5. In a similar fashion acid **87** is a potential precursor for the formation of a range of **btp** ligands for the incorporation of further functionality by reacting the electrophilic carboxylic acid "handle" with a range of nucleophiles. For example, introduction of amino acids would affect the formation of artificial 3D-structured "metallo-peptides"[103] and incorporation of *d*-metal chelators such as polypyridyl moieties would allow for the formation of two distinctive supramolecular networks using a mixture of *d*- and *f*-metal ions ((Ru(II) and Ln(III) respectively)[139,286] which could then be used for DNA binding and cellular imaging. Evaluation of the biological applications in biological media such as in cancer cells is also proposed. The synthesis of **98** is presented as a preliminary result in the development of ditopic **btp** ligands possessing divergent metal binding behavior which when cross-linked with metal ions may give rise to the formation of functional metallo-supramolecular polymers.

Byrne *et al.* reported that **32**, the di-carboxylic acid analogue of **H$_3$84**, gave rise to the formation of metallo-supramolecular gels when complexed with Ru(II).[113] With this in mind, **btp** ligand **H$_3$84**'s potential as a low molecular weight gelator will be investigated in the next chapter. Furthermore, the formation of Ln(III) templated luminescent and stimuli-responsive metallogels with ligand **H$_3$84** and the material's properties will be discussed. The solution state self-assembly of the less complex tri-methyl ester **83** ligand system with Ln(III) ions will provide valuable insights into the dynamic processes involved in the synthesis of these complex polymeric materials. This understanding will aid our efforts in controlling the formation of these metallo-supramolecular systems and characterising them, not only on the

macroscopic scale but also at the molecular level. Ligand **$H_3$84** will also be investigated for its use as a multitopic tecton in the generation of functional porous coordination polymers (Chapter 4). The self-assembly of lipophilic **btp** ligand **99** will also be studied in the next chapter as well as a presentation of some preliminary results of an investigation into whether the increased solubility of the **btp** ligand in non-polar solvents such as CH_2Cl_2 will improve the chelating motif's ability to extract *f*-metals from aqueous media. The selectivity of binding of Ln(III) ions over An(III) ions for the development of more efficient and selective removal of TRU from nuclear waste mixtures will also be briefly presented.

3 Metal templated self-assembly of btp ligands and the formation of healable Ln(III) luminescent metallogels

3.1 Introduction

It is with growing momentum that Ln(III) ions have been used to direct the formation of a variety of supramolecular systems,[56,135-136,138-145] as their unique photophysical properties, have shown potential in applications in medicinal diagnostics,[2] optical imaging,[3] light emitting diodes (LEDs), liquid crystals and telecommunications[132] and as dyes in security inks and labels.[287] Ln(III) ions have also featured in the practical development of contrast agents for magnetic resonance imaging (MRI) and luminescent chemosensors for specific analytes[56,135-137] and in the optical imaging of cells.[138] As a consequence of this, there exists a plethora of Ln(III) hosting molecules whose behavioural diversity affects the function of the resulting supramolecular self-assemblies. The features of such Ln(III) hosting ligands usually consists of hard Lewis bases, such as carboxylic acids and nitrogen-containing heterocycles which can simultaneously act a sensitising chromophore in populating the Ln(III) excited state allowing access of the rich photophysical properties of the metals.[3,98-99,140,288]

As discussed in Section 1.5.8, Flood and co-workers, were the first to demonstrate the formation of stable luminescent coordination complexes between **btp** ligands and Eu(III) through single crystal X-ray diffraction analysis.[98] Several other crystal structures have been reported to date[150] and **btp** ligands have featured with increasing frequency of late in new solvent extraction processes for the removal of transuranium elements (TRU), for example trivalent actinides (An(III)) ions.[147-149]

The unique photophysical properties of the Ln(III) ions has made them desirable for the incorporation into functional materials such as gels.[71] Interest in functional gels has grown in many scientific disciplines including tissue engineering and wound healing, drug delivery, and also sensing.[4,6] Supramolecular gels have been shown to be reversibly responsive when external stresses are applied to them with several reports of autonomously healing systems consisting of the **btp** motif, or analogues thereof, playing the role of the ligating host.[86,193,112,125,194] In this chapter, the ability of metallo-supramolecular interactions, through their dynamic nature, to achieve the generation of self-healing, functional gels using **btp** will be investigated and their thixotropic properties studied. It is also the aim of this chapter to take advantage of the luminescent properties of the sensitised Ln(III) ions incorporated into the responsive gel systems, developed herein, in order to bridge the large gap between functional gel design efforts[86,174,189-191,195,197] and actual knowledge of the supramolecular structure of the gels. Despite the plethora of gels which have been reported to date,[6,172,179-

[180] this lack of understanding of the structure-function correlation of gels remains a prominent challenge in the way of property tuning.[184]

As was demonstrated in the previous Chapter 2, the facile variability of **btp** is readily achieved resulting in the convenient development of neutral nitrogen-containing **btp** heterocycle linkers such as ligand **83**, possessing the potential for rich divergent coordination chemistry and also ligand **H$_3$84** through the facile incorporation of divergent metal binding ability in the form of the multiple carboxylate functionality. The characterisation of the thermodynamically prepared complexes of **83**, **H$_3$84**, **85** and **99** with Ln(III) ions alongside the investigation of the corresponding self-assembly behaviour of several of these with Ln(III) ions in solution will be studied. Following this, foreseeing the capability of **H$_3$84** for generating functional soft materials, the gelation studies of **H$_3$84** and the incorporation of Ln(III) ions into the resulting systems will be explored in detail. Some of the key features that make Ln(III) ions desirable as supramolecular scaffold templates, particularly their photophysical properties will now be introduced.

3.2 Photophysical properties of the Ln(III) ions

The Ln(III) ions possess unique photophysical properties, which have led to a lot of interest in recent years.[2-3,132,287] Lanthanides are the elements of atomic numbers 57–71, in the first period of the *f*-block of the periodic table, see Figure 3.1.[56] The most stable lanthanide oxidation state is +3; these ions are hard Lewis acids, possessing relatively high charge densities and have a strong electrostatic nature to their bonding. Therefore, ligand design usually comprises of hard Lewis bases, such as amines, carboxylic acids, hydroxyl groups and nitrogen-containing heterocycles.[3] The Ln(III) ions have a large and varied range of coordination numbers of between 6 and 12, with the most studied ions, Eu(III) and Tb(III), commonly displaying a coordination number of 9.[7] The Ln(III) ions comprising these complexes, upon saturation of their coordination sphere, are protected from vibrational coupling increasing the light absorption profile by 'antenna effects'.[289] The characteristic photophysical features of the ions allow for the monitoring of the self-assembly process in solution *via* relatively simple spectroscopic techniques such as UV-vis absorption, luminescence spectroscopy, especially as NMR techniques can be rendered complicated due to the paramagnetic Ln(III) ions.[290] Upon complexation, the unique emission spectra of the Ln(III) ion may be sufficiently modulated such that complex formation as a function of metal addition to ligand (or *vice versa*) may be evaluated using non-linear regression analysis software such as SPECFIT and ReactLab Equilibria.[21] These software

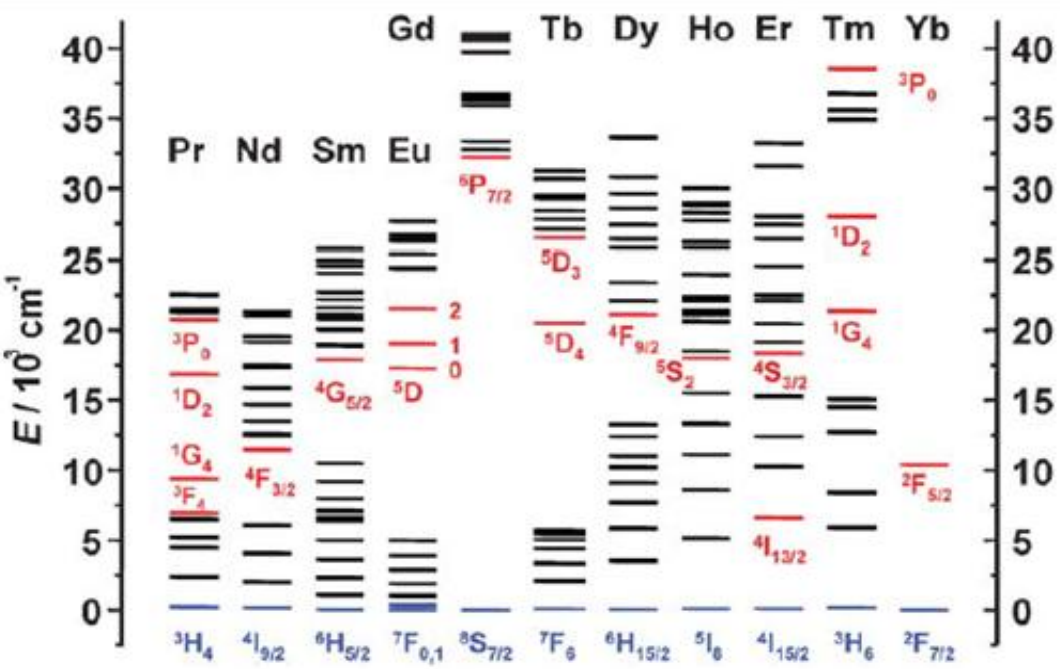

Figure 3.1 Partial energy diagrams for Ln(III) ions (main luminescent levels in red and fundamental levels in blue). Figure reproduced from Ref.[56] Copyright 2005: Royal Society of Chemistry

programs can be used to analyse the experimental binding isotherms observed in both the ground and the excited states, with the view of determining both the speciation and the stability constants for the formation of various self-assembly equilibria in solution.

The unique photophysical properties of Ln(III) ions are beneficial in the sense that the excited states are long-lived, long wavelength emission, sharp characteristic line-like emission bands and large *pseudo*-Stokes shifts.[288] These unique properties of the Ln(III) ions arise from the shielding of the 4*f* orbitals by the $5s^2$ and $5p^6$ orbitals resulting in little vibrational coupling with the environment and as a result they interact only very weakly with ligand orbitals. Emission bands are therefore narrower and ion-specific, leading to relatively pure emission colours.[56,132] Pure *f*→*f* transitions are forbidden and as a result, excited state lifetimes are several orders of magnitude longer than those of the background fluorescence of the biological media, for example.[291] Long lived excited states are useful in sensing as time-gating can overcome drawbacks arising from light scattering and auto-fluorescence[140] while emission beyond tissue absorption wavelengths improves signal quality. Ln(III) ions are being increasingly used as useful reporter groups for monitoring certain chemical reactions and as non-cytotoxic fluorescent probes.[287,292-295]

As direct excitation of Ln(III) emission is not efficient due to the small dipole strength of *f*→*f* transitions, the Ln(III) excited state can be populated alternatively using a sensitising chromophore, ideally with a high absorption coefficient and Förster overlap,[140] through a

process called the 'antenna effect',[140,288] see Figure 3.2(A). The modified Jablonski diagram in Figure 3.2(B)[56] shows the sensitising antenna absorbing electromagnetic radiation, followed by a change in spin multiplicity of the excited state. The energy is then transferred to the Ln(III) centre[289,296] and from there it can be dispersed either by emission of light (luminescence) or *via* a variety of non-radiative deactivation mechanisms. The energy difference between the triplet excited state of the ligand and the accepting level of Ln(III) must be sufficient (>1700 cm^{-1}) such that thermally activated energy back-transfer is minimised.[291]

The efficiency of a given ligand to sensitise the luminescence of a Ln(III) ion is given by:

$$\Phi_{tot} = \eta_{sens}\,\Phi_{Ln}^{Ln} = \eta_{sens}\,\frac{\tau_{obs}}{\tau_{rad}} \qquad \textbf{Equation 1}^{56}$$

where Φ_{tot} is the overall quantum yield of the metal centered luminescence measured upon ligand excitation relative to a standard such as Cs_3[Eu(**dpa**)$_3$] in Tris buffer (with Φ_{tot} = 24±2.5% for Cs_3[Eu(**dpa**)$_3$] under excitation at 279 nm).[58] Φ_{Ln}^{Ln} is the intrinsic quantum yield determined upon direct metal excitation, η_{sens} is the antenna-to-ion energy transfer efficiency and τ_{obs} and τ_{rad} are the observed and radiative lifetimes, respectively. For Eu(III) complexes Φ_{tot} can be measured by relative method to which the absorbance and emission intensity of the sample are compared according to:

$$\Phi_{tot} = \frac{\Phi x}{\Phi r} = \frac{Ex}{Er} \times \frac{Ar(\lambda r)}{Ax(\lambda x)} \times \frac{Ir(\lambda r)}{Ix(\lambda x)} \times \left(\frac{n_x}{n_r}\right)^2 \qquad \textbf{Equation 2}$$

where subscript r – reference and x – sample; E – integrated luminescence intensity; A – absorbance at the excitation wavelength; I – intensity of the excitation light at the same wavelength, n – refractive index of the solution. The estimated error for quantum yield determination using the relative method is ±10%.

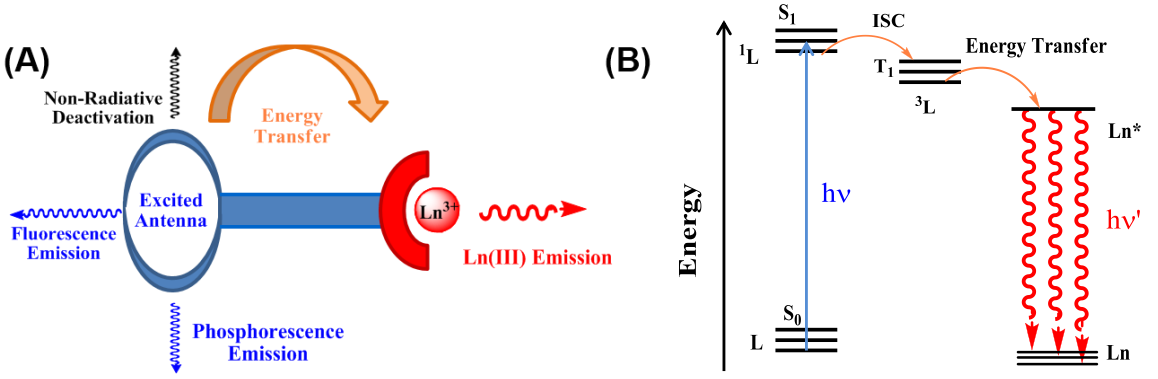

Figure 3.2 (A) The 'Antenna' effect. (B) Simplified Jablonski diagram for Ln(III) absorption–emission process.

Having measured Φ_{tot}, η_{sens} and Φ_{Ln}^{Ln} can be calculated using Equation 1 once τ_{rad} lifetime is obtained. This is achieved using Equation 3:

$$\frac{1}{\tau_{rad}} = A_{MD,0} \times \frac{I_{tot}}{I_{MD}} \times n^3 \qquad \textbf{Equation 3}$$

where n is the refractive index of the solvent, $A_{MD,0}$ is the spontaneous emission probability for the $^5D_0 \rightarrow {}^7F_1$ transition *in vacuo*, $A_{MD,0} = 14.65\ s^{-1}$ and $\frac{I_{tot}}{I_{MD}}$ is the ratio of the total area of the corrected Eu(III) emission spectrum to the area of the $^5D_0 \rightarrow {}^7F_1$ band.[61,297] The value of $A_{MD,0}$ was found from the theoretically calculated dipole strength and with the aid of Judd-Ofelt theory. The $^5D_0 \rightarrow {}^7F_1$ transition in the Eu(III) emission spectrum is the only magnetic dipole transition and has no electric dipole contribution. Therefore, this transition is practically independent of the changes of the Eu(III) coordination environment. The reason τ_R, Φ_{Ln}^{Ln} and η_{sens} are not accessible in the case of Tb(III) is because this metal does not possess a purely magnetic dipole transition like the $^5D_0 \rightarrow {}^7F_1$ in Eu(III).

The quantum yield of the luminescence step (Φ_{Ln}^{Ln}) expresses how well the radiative process compete with non-radiative processes. Φ_{Ln}^{Ln} essentially depends on the energy gap between the lowest lying excited (emissive) state of the metal ion and the highest sublevel of its ground multiplet. The smaller this gap, the easier is its deactivation by non-radiative processes, for instance, through vibrations of bound ligands or solvent molecules, particularly those possessing high energy vibrations such as *O–H*. In this way, the luminescence of Ln(III) ions can be quenched *via* the transfer of energy from the Ln* excited state to solvent molecules, such as H_2O and CH_3OH, through molecular vibrations when these species are inside the coordination sphere. The minimisation of this process can be achieved through the relevant saturation of coordination sites with chelating ligands. The number of metal-bound protic solvent molecules is proportional to the rate of quenching. Horrocks *et al*. developed an equation to estimate the hydration state of a Eu(III) or Tb(III) complex based on the observation that *O–D* isotopic oscillators reduce the excited state lifetimes of Eu* and Tb* to a far lesser extent than *O–H* oscillators.[298-299] This equation was further modified by Parker *et al.*[300] to include the contribution of *N-H* and *C-H* oscillators and the following describes the hydration state of Eu(III) in H_2O and deuterium oxide *i.e.*

$$q^{Eu(III)} = 1.2\left\{\left(\frac{1}{\tau_{H2O}} - \frac{1}{\tau_{D2O}}\right) - 0.25 - 0.075x\right\} \qquad \textbf{Equation 4}$$

where τ is the lifetime of the complex in solution and accounts for the oscillations of water and deuterium oxide bonds. x accounts for the number of *C-H* and *N-H* oscillators directly

bound to the Eu(III) metal. A *q* values of 0 suggests that there are no solvent molecules in the inner coordination sphere which is ideal for systems whose importance rely on their luminescence. By complexing with appropriate multidentate ligands assembled around the metal centre it is expected that the Ln(III) sits in a fully saturated environment, shielded from solvent molecules, with a coordination number of 9, for example through tris-terdentate ligand binding in the case of **btp**. Hence, the expected self-assembly formation is of a 1:3 M-L complex. The formation and characterisation of several **btp**-derived Ln(III) complexes will be presented in the next section.

3.3 Formation and characterisation of Ln(III) complexes

The formation of Ln(III) complexes using several **btp** ligands functionalised at the 4-pyridyl position, discussed in the previous chapter, was explored. All complexes were obtained with the formula $[Ln\mathbf{L}_n](CF_3SO_3)_3$, however, for simplicity will be written as $\mathbf{LnL_n}$ where **Ln** = Eu(III) or Tb(III), **L** is **btp** ligand and *n* = 1-3. The synthesis of **Eu83$_3$**, **Eu(H$_3$84)$_3$**, **Eu85$_3$** and **Eu99$_3$** and their Tb(III) analogues was achieved by reacting the appropriate ligand with either $Eu(CF_3SO_3)_3{\cdot}6H_2O$ or $Tb(CF_3SO_3)_3{\cdot}6H_2O$ in CH_3OH in 1:3 metal:ligand (M:L) stoichiometry under microwave irradiation at 80°C for 60 minutes followed by isolation using precipitation from diethyl ether or toluene diffusion. Eu(III) and Tb(III) complexes were characterised using conventional methods and the data can be found in Appendix A-C. Complexations were also carried out in other solvents, such as CH_3CN and H_2O, but the reactions did not proceed to completion and undesirable precipitation out of solution of the starting materials was observed due to poorer solubility in those solvents.

The characterisation of Ln(III) complexes was carried out in the same manner, therefore, **Eu83$_3$** will be discussed in greatest detail. Formation of the desired 1:3 stoichiometry[98] in 99% yield was confirmed by ^{1}H NMR spectroscopy (400 MHz, CD_3OD) (Figure 3.3) with several trends which coincided with analogous complexes derived from ligands **16**. The most notable differences between the ^{1}H NMR spectrum of the Eu(III) complex and that of the ligand was the large upfield shift of the triazolyl and pyridyl ^{1}H signal resonances, from 8.67 ppm to 7.69 ppm and 8.46 ppm to 5.35 ppm, respectively. This change in chemical shift was particularly pronounced for the pyridyl resonance, indicative of the paramagnetic nature of the Eu(III) core. The two aryl resonances underwent similar shielding, resulting in a change in chemical shift from 8.03 ppm to 7.82 ppm and from 7.47 ppm to 7.23 ppm, respectively. Another clear contrast can be seen in the division of the 4 methylene protons per ligand into two widely spaced doublets at 6.30 ppm and 5.52 ppm. The geminal coupling between the

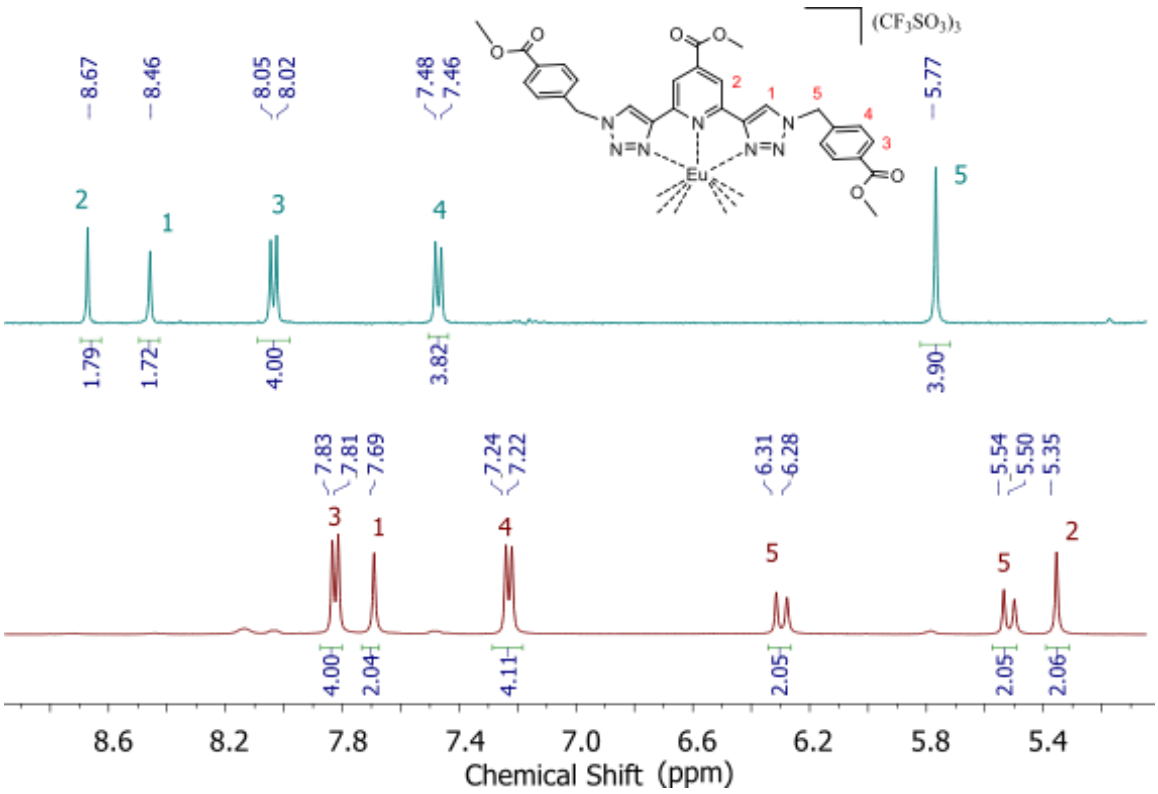

Figure 3.3 ^{1}H NMR (400MHz, CD_3OD) of **83** (top) and **Eu83$_3$** (bottom) showing resonances with greatest chemical shift change.

methylene linker protons (J=14.6 Hz) was indicative of a loss of chemical equivalency between the protons indicative a loss of free rotation about the methylene linker upon complexation. It was also possible to see similar trends in the ^{13}C NMR spectrum of **Eu83$_3$** (400 MHz, CD_3OD) (Appendix A.12), particularly in relation to the dramatic chemical shift decrease from 124.0 ppm to 104.1 ppm and from 117.7 ppm to 86.0 ppm for the 5-triazolyl and 3,5-pyridyl carbon resonances, respectively. Formation of the desired complex was also observed by MALDI-TOF mass spectrometry analysis showing formation of [**Eu83$_3$**-$CF_3SO_3^-$]$^+$ with *m/z* of 2152.3796. The measured isotopic distribution pattern corresponded to the calculated distribution for [**Eu83$_3$**-$CF_3SO_3^-$]$^+$ (Appendix B.1). Furthermore, solid state characterisation of **Eu83$_3$** was carried out using single crystal X-ray diffraction analysis at 150 K. Colourless single crystals of **Eu83$_3$** were successfully grown by ether diffusion into a CH_3CN solution of **Eu83$_3$** over 3 days. The crystallographic data were solved by Dr. Brendan Twamley in the School of Chemistry, University of Dublin and the structure model was refined in the low symmetry triclinic space group $P\bar{1}$. The coordination of three **btp** ligands of **83** around the Eu(III) centre resembled analogous Eu(III):**btp** structures previously reported.[7a,150,25-26] The large coordination number of 9 (N_9) of the metal centre was satisfied with three terdentate ligands oriented around the metal centre (Figure 3.4). The

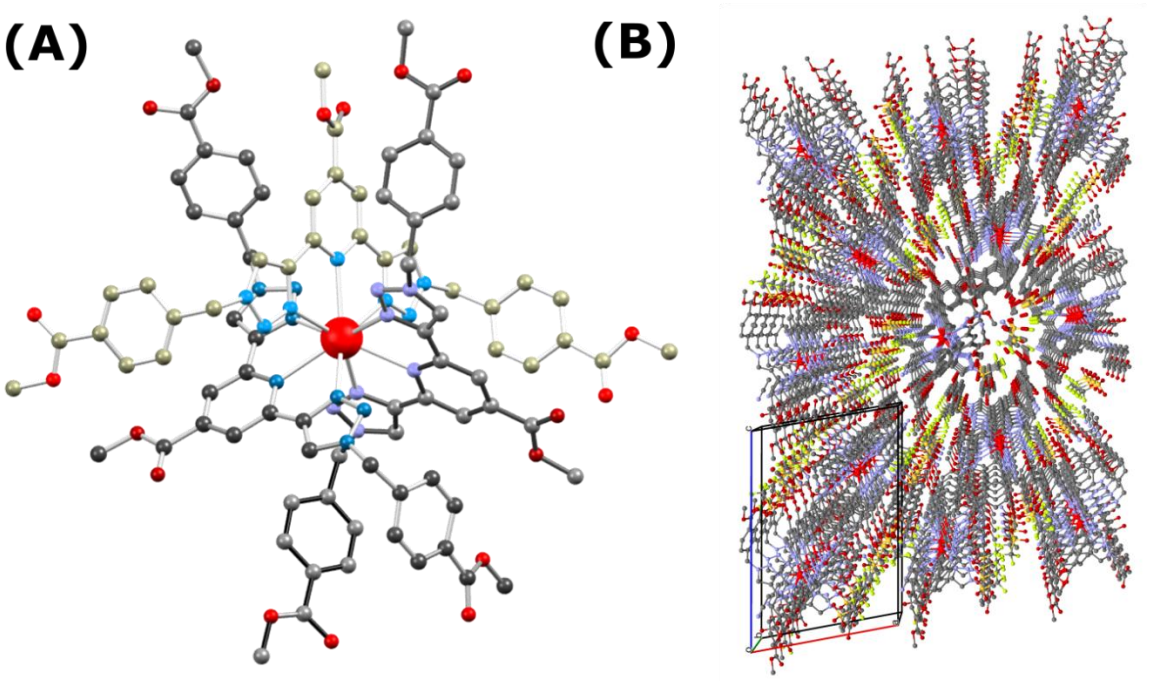

Figure 3.4 (A) Crystal structure of Eu**83**$_3$. Hydrogens, counter-ions and solvent molecules omitted for clarity. (B) Packing diagram for **Eu83**$_3$ viewed parallel to the *b*-axis.

crystal structure showed essential coplanarity of the three ring units of the **btp** motif and the *syn-syn* orientation of the triazole rings necessary for the nitrogen atoms to bind to the metal centre, behaviour supported by similar systems.[7a,150,25-26] The aryl "arms" adopted a *trans* conformation about the methylene linker with π-π interactions between the benzoate arms of neighbouring tris-complexes. This orientation corroborates the observation in the ^{1}H NMR spectrum wherein the methylene proton resonance was split due to the change in chemical environment experienced by each proton per methylene linker arising as a result of its proximity to the paramagnetic Eu(III) centre. It can be concluded from this that the same structure existed in solution. The extended packing is dominated by electrostatic interactions between the tris-complex cation species and the $CF_3SO_3^-$ anions, see Figure 3.4(B). This structure demonstrates the nature in which the ester groups point outwards in a radial fashion from the Eu(III) centre. This conformation of the carbonyl groups in the complex appears ideal for further use as 'linking' points in the generation of novel materials such as gels[197] which will be investigated using the tri-carboxylic acid analogue **Eu(H$_3$84)$_3$** in Section 3.6. The crystal structures of **Y83$_3$** and **Yb83$_3$**, prepared in the same fashion, were found to be isostructural (Appendix E, Table E.2). The same procedure was followed for the thermodynamic formation of Ln(III) complexes of **Tb83$_3$**, **Eu(H$_3$84)$_3$**, **Tb(H$_3$84)$_3$**, **Eu85$_3$**, **Eu99$_3$** and **Tb99$_3$** in respectable yields. Systems involving **H$_3$84** and **85** were more complex and solubility factors were an issue in obtaining full characterisations. For example, broad

signals were obtained from the ^{1}H NMR spectrum of **Eu(H$_3$84)$_3$** (400 MHz, CD_3OD) (Appendix A.14). These showed resonance chemical shifts similar to those for **Eu83$_3$** with the obvious absence of the methyl proton resonances as expected. The broadened nature of the signal resonances was attributed to the possible aggregation of the complexes through a proposed H-bonding network. No such satisfactory NMR characterisations were possible with **Tb(H$_3$84)$_3$**, **Eu85$_3$**, **Eu99$_3$** nor **Tb99$_3$** in either CD_3OD, $CDCl_3$ or CD_3CN as a result of a combination of a lack of solubility and paramagnetic effect of the Ln(III) centre, however, the complexes were characterised using other conventional methods such as HRMS and IR. The photophysical characterisations can be found in Appendix C with selected examples discussed below.

The UV-vis absorption spectrum of all synthesised Eu(III) and Tb(III) complexes in CH_3CN solution showed a hypsochromic shift in the π→π* transition by 2 nm and a bathochromic shift in the n→π* transition by 6 nm relative to that of the unbound ligand for **Eu83$_3$** and **Eu85$_3$**, see Figure 3.5(A)/(B), respectively. Due to the poor solubility of ligand **H$_3$84** in CH_3CN photophysical analysis was carried out in DMSO:CH_3CN (3:97). Upon complexation, **Eu(H$_3$84)$_3$** and **Tb(H$_3$84)$_3$** were soluble in CH_3CN. The complexes of **Eu99$_3$** and **Tb99$_3$** were spectroscopically analysed in CH_2Cl_2:CH_3CN (1:9) solution in order to aid solubility. The UV- vis absorption spectrum showed similar band position trends as those seen for complexes carried out in CH_3CN (Appendix C.4-5). All **btp** ligands were shown to sensitise Ln(III) emission in CH_3CN solution, *via* the 'antenna' effect (Figure 3.2) upon excitation into either of the π→π*or the n→π* bands, with characteristic red and green emission (Figure 3.5/3.6, respectively) clearly visible to the naked eye under irradiation with

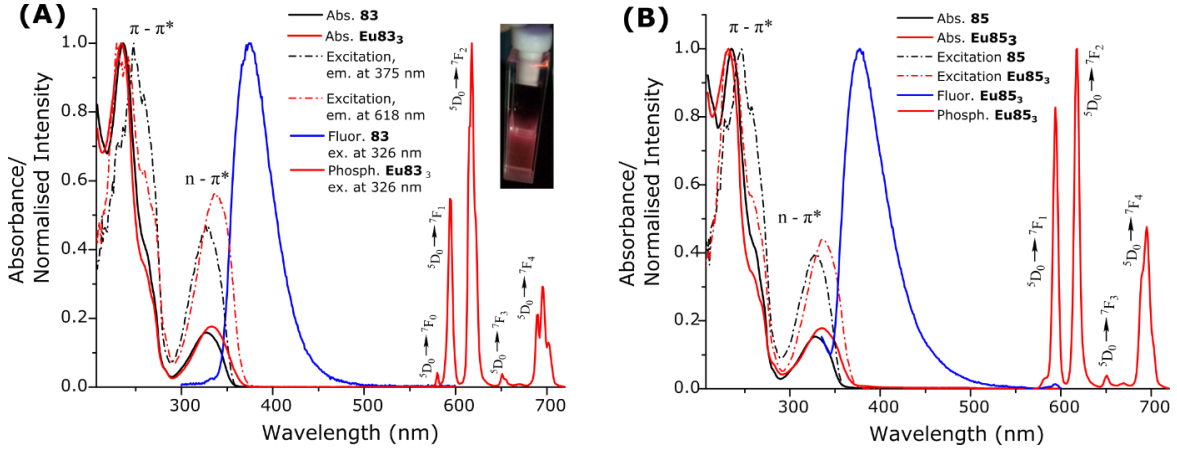

Figure 3.5 UV-vis absorbance, excitation and Ln(III) phosphorescence spectra of (A) **83** and **Eu83$_3$** in CH_3CN solution and (B) **85** and Eu**85**$_3$ in CH_3CN solution (*c*=0.2 mM).; (Inset) photograph of a CH_3CN solution of the **Eu83$_3$** complex under irradiation with UV light.

UV light at 365 nm. Characteristic line-like emission bands were observed at λ = 579, 593, 617, 650 and 694 nm, assigned to the $^5D_0 \rightarrow {}^7F_J$ transitions (J=0–4), for the Eu(III) complexes whereas for the Tb(III) complexes emission bands were observed centred at 490, 545, 585 and 621 nm, assigned to the $^5D_4 \rightarrow {}^7F_J$ transitions (J=6-2). The excitation spectra of the Eu(III) and Tb(III) complexes with emission wavelength held at λ_{em}=618 nm and 490 nm, respectively, had profiles broadly matching the corresponding absorbance spectra. To the naked eye, the Tb(III):**btp** complexes were significantly brighter than the Eu(III):**btp** complexes at the same concentrations (c = 0.2 mM).

This was further confirmed by carrying out luminescence quantum yield (Φ_{tot}) measurements of the complexes; the equations and symbols used in the calculations of all values in Table 3.1 are explained in Section 3.2.[58-59] The values obtained for Φ_{tot} by comparison with the known quantum yield standard, $Cs_3[Eu(\mathbf{dpa})_3]$ in 0.1 M Tris buffer (pH = 7.45), demonstrated **btp**'s low sensitisation of Eu(III), (Φ_{tot} = 2.5-7.4%). **Btp** was a much more efficient sensitiser of the radiative excited state of Tb(III) which was reflected in the values for the Φ_{tot} for the Tb(III) complexes (Φ_{tot} = 58-79%). These values compared closely with those reported by Byrne *et al.* for unsubstituted **btp** ligand **16** with values of Φ_{tot} = 2.4(4)% and 70±12% for the corresponding Eu(III) and Tb(III) complexes, respectively.[103,119] These results demonstrate that these 1:3 complexes display comparable

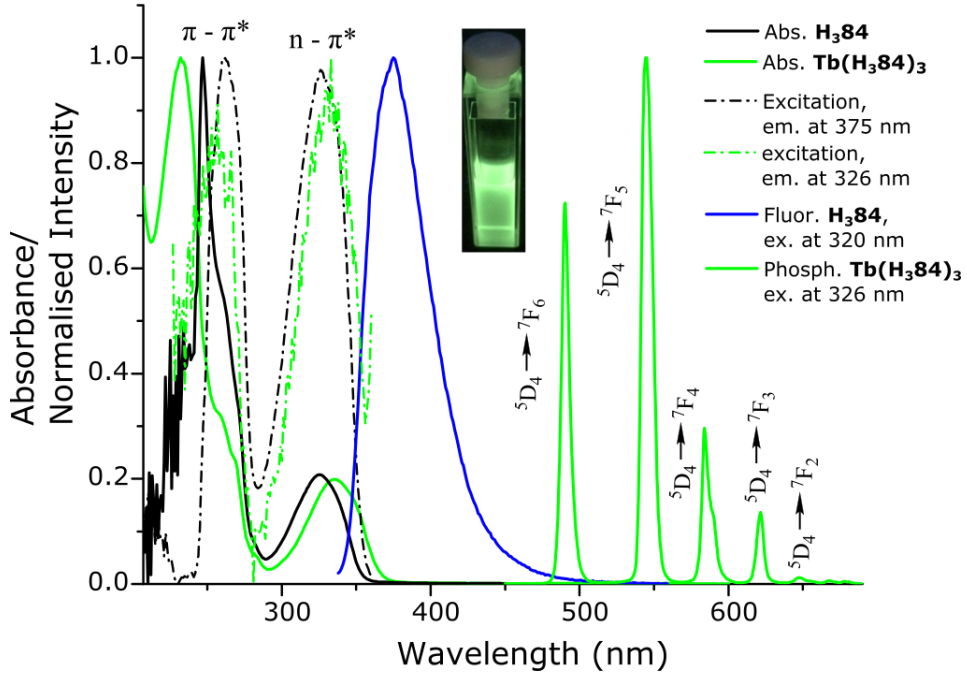

Figure 3.6 UV-vis absorbance, excitation and Ln(III) phosphorescence spectra of **$H_3$84** in DMSO:CH_3CN (3:97) solution and **Tb($H_3$84)$_3$** in CH_3CN solution (c=0.2 mM); (Inset) photograph of a CH_3CN solution of Tb(III) complex under irradiation with UV light. (c = 0.2 mM)

Table 3.1 Antenna-to-ion energy transfer efficiencies (η_{sens}) of Eu(III) complexes calculated from the observed emission spectrum, the observed luminescence lifetime (τ_{obs}) and the experimental overall luminescence quantum yield (Φ_{tot}) upon ligand excitation (λ_{ex} = 279nm). τ_{rad} is the radiative lifetime and Φ_{Ln}^{Ln} is the intrinsic quantum yield. [a] All the complexes obtained with the formula Ln**L**$_n$(CF_3SO_3)$_3$. *Values obtained for Φ_{tot} for **Tb(H$_3$84)$_3$** and for Φ_{tot}, $\tau_{rad,}$ Φ_{Ln}^{Ln} and η_{sens}[61,297] for **Eu(H$_3$84)$_3$** are presented with cation as residual trailing of ligand fluorescence extended into the Ln(III) luminescence range thus affecting I_{tot} for **Tb(H$_3$84)$_3$** and I_{tot}/I_{MD} for **Eu(H$_3$84)$_3$** *i.e.* the ratio of the total area of the corrected Eu(III) emission spectrum to the area of the $^5D_0 \rightarrow {}^7F_1$ band (Appendix C.6).

Complex[a]	Solvent	τ_{obs}, ms	Φ_{tot}, %	τ_{rad}, ms	Φ_{Ln}^{Ln}, %	η_{sens}, %
Eu83$_3$	CH_3CN	3.2	4.8(8)	9.1	35.1	13.8
Eu83$_3$	CH_3OH	1.7	2.5(4)	10.3	16.7	15.2
Eu(H$_3$84)$_3$*	CH_3OH	1.4	7(1)	14.5	10	77.5
Eu99$_3$	CH_2Cl_2:CH_3CN (1:9)	3.1	2.7(5)	10.6	29.5	9.1
Tb83$_3$	CH_3CN	1.8	67±12	N/A	N/A	N/A
Tb83$_3$	CH_3OH	1.6	58±10	N/A	N/A	N/A
Tb(H$_3$84)$_3$*	CH_3OH	1.3	67±12	N/A	N/A	N/A
Tb99$_3$	CH_2Cl_2:CH_3CN (1:9)	1.9	79±14	N/A	N/A	N/A

photophysical properties to those reported for analogous derived from **dpa**-derivatives such as **3**, **52** and related systems.[60-61,65-66,197] The effect of changing solvent can be seen in monitoring the changes in values of $\tau_{rad,}$ $\boldsymbol{\Phi_{Ln}^{Ln}}$ and η_{sens}.[61,297] τ_{rad} for **Eu83$_3$** in CH_3CN and on account of the solvent's hydroxyl oscillator which is a more efficient quencher of Ln(III) excited state.[298] This would imply a higher extent of nonradiative deactivation process in the case of CH_3OH. $\boldsymbol{\Phi_{Ln}^{Ln}}$ is less as it is the ratio of τ_{obs}/τ_{rad}. η_{sens} was the same for both solvents as the antenna would be expected to sensitise the Eu(III) centre as efficiently in both solvents since the energy transfer process is usually through the distance dependent Förster mechanism.[140]

Lifetimes and hydration states of complexes were determined at the low concentration of 0.05 mM and the higher concentration of 0.2 mM in H_2O and D_2O. At the lower concentration, the radiative decay curves were bi-exponential in nature from which the relative percentages of 1:3 M:L complex and 1:2 M:L complex could be determined (Table 3.2). The *q* values (calculated using Equation 4 in Section 3.2) for **Eu83$_3$**, **Eu(H$_3$84)$_3$** and **Eu85$_3$** agreed with the predicted value of zero[298] suggesting no solvent molecules were present in the coordination sphere of Eu(III) and formation of fully coordinated 1:3 M:L

Table 3.2 Observed lifetimes, τ_{obs}, (λ_{ex} = 326 nm), % species and calculated *q* values. [a] All the complexes obtained with the formula Eu**L**$_n$$(CF_3SO_3)_3$ at 0.05 mM. [b] in H_2O [c] in D_2O

Complex[a]	τ_{obs}[b], ms	τ_{obs}[c], ms	% species[b]	% species[c]	q_{value}
Eu83$_3$	1.6(1)	1.8(1)	71.3	76.2	-0.2(5)
Eu83$_2$	0.4(1)	0.5(1)	28.7	23.8	0.4(5)
Eu(H$_3$84)$_3$	1.7(1)	2.5(1)	76.7	100	-0.1(5)
Eu(H$_3$84)$_2$	0.5(1)	-	23.3	-	1.5(5)
Eu85$_3$	2.6(2)	2.1(2)	95.8	81.1	-0.4
Eu85$_2$	0.6(2)	0.6(2)	4.2	18.9	-0.2

complexes. Also in abundance were 1:2 species, **Eu83$_2$** and **Eu(H$_3$84)$_2$**, possessing between one and two solvent molecules within the coordination sphere. This may be explained by partial dissociation of the complex and the freeing of one of the **btp** ligands,[301] thus giving rise to the lower observed lifetime of the **EuL$_2$** species through the quenching effect of the OH oscillators which was summarised in Section 3.2. It is worth noting that there was no dissociation of **Eu(H$_3$84)$_3$** in D_2O at the lower concentration of 0.05 mM. Almost quantitative retention of the 1:3 M:L stoichiometry for **Eu85$_3$** was observed in H_2O (0.05 mM) but dissociation was observed in D_2O. As the solutions became more concentrated there was no observed dissociation into a mixture of 1:3 and 1:2 species. The higher concentration solutions for each Eu(III) complex showed the presence of 1:3 M:L complex exclusively and no dissociation into a mixture of 1:3 and 1:2 was observed. The lifetimes of the 1:3 M:L species at the higher concentrations matched the corresponding lifetimes at the lower concentrations as expected.

It was concluded that there existed a concentration dependence of the stability of **EuL$_3$** complexes with dissociation occurring at low concentration in H_2O and D_2O. This was also the case in CH_3OH, therefore care was exercised to maintain sufficiently high concentrations of Eu(III):**btp** complexes in order to control the speciation. Low concentration kinetic self-assembly behaviour of **83** and **85** with Eu(III) in CH_3CN was next investigated through titration studies in order for the global stability constants for the various equilibria and speciation distribution to be calculated using non-linear regression analysis.

3.4 Binding studies of btp ligands with Ln(III) using spectroscopic techniques

Having synthesised a number of thermodynamically prepared Ln(III):**btp** complexes, low concentration self-assembly studies by titration of specific aliquots of a stock solution of $Ln(CF_3SO_3)_3$ to solutions of **btp** ligands were performed. The changes in the UV-vis absorption and the emission spectra were monitored.

UV-vis absorbance spectra of ligand **83** in CH_3CN (c=1x10^{-5} M), recorded at 21 ^{o}C, showed bands centred at λ_{max} = 236 nm and 327 nm and excitation at either band wavelength gave rise to strong fluorescence emission at λ_{max} = 375 nm, as discussed in Section 2.2. The appearance of Ln(III)-centred emission and changes in the absorption and fluorescence spectra were employed to ascertain the stability and stoichiometry of the solution self-assembly equilibria as a function of Eu(III) equivalents (eq.) added. The titrations were repeated until satisfactorily reproducible results were obtained at least three times. Upon gradual addition of Eu(III) the n→π* band of **83** centred at 327 nm experienced a significant hyperchromic effect and red-shift with corresponding blue-shift of the π→π* transition, see Figure 3.7(A), indicative of the self- assembly of **83** with Eu(III) and the formation of an isosbestic point at 325 nm was observed. At approximately 0.33 eq. of added metal, some residual ligand emission was still present, see Figure 3.7(B). Fluorescence became fully quenched at 0.5 eq. of Eu(III). This quenching of the ligand fluorescence was characteristic of the radiative population of the Eu(III) excited state by energy transfer *via* ISC from the **btp** "antenna" giving rise to Eu(III) emission.[70,103,156] The characteristic emission bands at λ_{max} = 580, 595, 617, 650 and 695 nm corresponded to the radiative deactivation of the Eu(III) $^5D_0$ energy level to the ^7F_J (J = 0-4, respectively), see Figure 3.8. The observed growth in

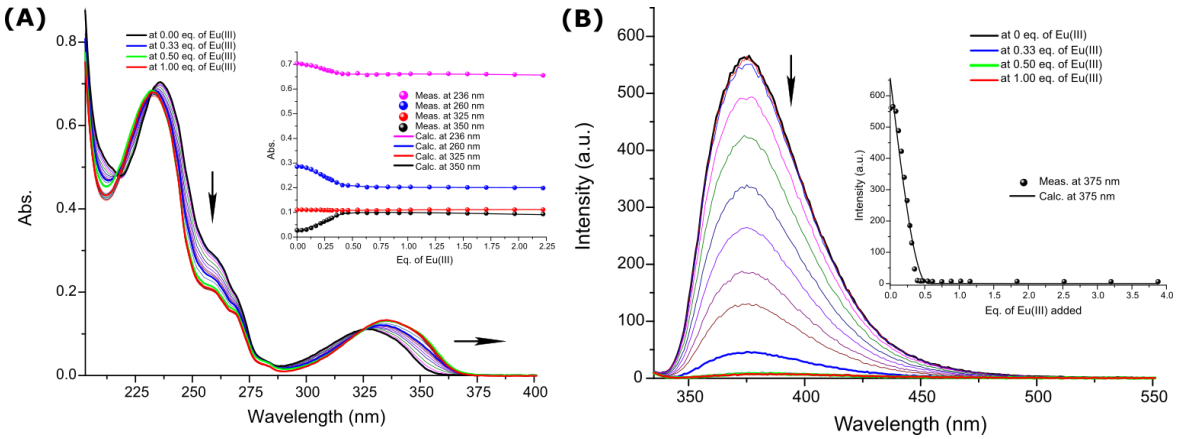

Figure 3.7 (A) UV-Vis and (B) Fluorescence titration of **83** (c = 1x10^{-5} M) upon addition of $Eu(CF_3SO_3)_3$ 0→4 eq. in CH_3CN solution at 20.9^{o}C. (Insets) Experimental binding isotherms and their corresponding fits.

intensity of the J = 0 band corresponded to the initial formation of the 1:3 M:L species. Analysis of the binding isotherm at the J = 0 band-maximum's wavelength (λ = 580 nm) showed the emission intensity reached a maximum at 0.33 eq. of added Eu(III) (Appendix C.7). This and the splitting pattern of the J = 2 band at the same eq. were suggestive of a single chemical species with C_3 symmetry.[60-61,65,103,137,197,299] These photophysical observations coincide with the geometrical properties of the Eu(III) centre as seen in the crystal structure of **Eu83$_3$**. The molecular structure of **Eu83$_3$** showed that the N_9 coordination sphere formed a distorted triaugmented trigonal prism (Appendix E.1), a polyhedron normally associated with D_{3h} site symmetry. Such variations between the solid and the solution state structures, having previously been observed in our group,[60-61,197] allow for the symmetry adjustment (C_3 is a subgroup of D_{3h}). Furthermore, upon addition of 0.33 eq. Eu(III) the self-assembly in CH_3CN solution displayed a phosphorescence pattern with relative intensities and band splits that matched the phosphorescence spectrum of the thermodynamically formed **Eu83$_3$** complex (Appendix C.8). These findings indicated that the self-assembly species in solution at 0.33 eq. of Eu(III) corresponded to the 1:3 M:L complex characterised by X-ray crystallography. As the eq. of Eu(III) increased, there was an observed change in intensity of the hypersensitive J = 2 transition along with the change in bands' splitting patterns, demonstrating a reorientation in the coordination environment

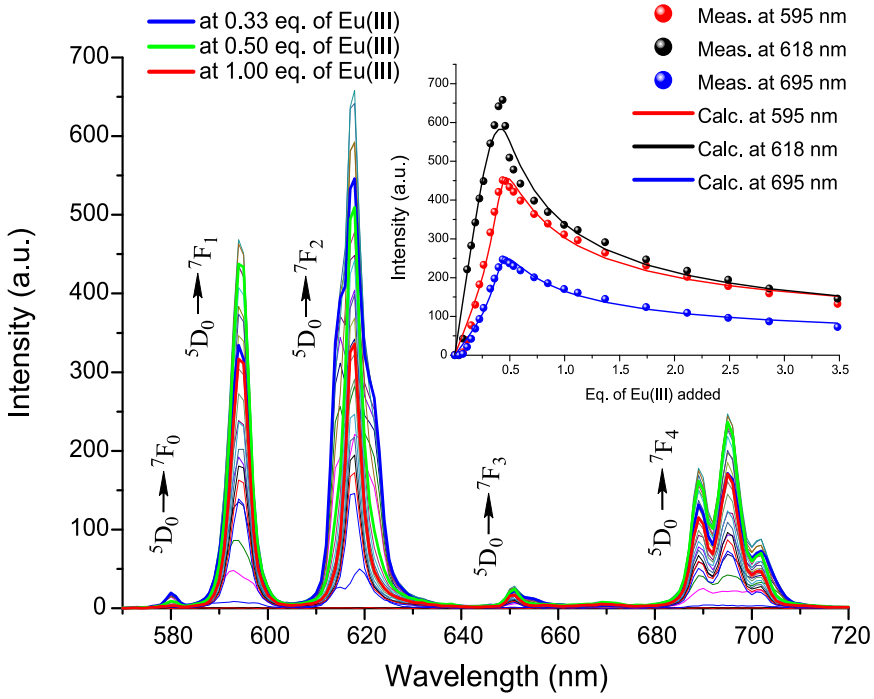

Figure 3.8 Changes in Eu(III) luminescence spectra of **83** (c = 1x10^{-5} M) upon addition of $Eu(CF_3SO_3)_3$ from 0–3.5 eq. recorded in CH_3CN. (Inset) Experimental binding isotherms and their corresponding fits.

of the Eu(III) metal centre,[299] indicative of various equilibrium species existing simultaneously. As the self-assembly dynamics were complicated, a more powerful tool was required for its investigation.

SPECFIT[302] and ReactLab Equilibria,[303] non-linear regression analysis programs, were used to analyse the experimental binding isotherms and fit them using calculated models in order to determine the speciation distribution in solution and global stability constants of the Eu(III):**83**$_n$ (*n*=1-3) self-assembly equilibrium species. The calculated binding isotherms for the various Eu(III):**83**$_n$ self-assembly species showed good correlation to the experimental data, see Figure 3.7/3.8 (Insets). The good fit provided a reliable model for understanding the self-assembly of **83** with Eu(III) at low concentration. The speciation distribution was calculated for all three titrations. The diagram shown in Figure 3.9(A) was calculated using the changes in the UV-vis spectra as the ligand ground state electronic environment was shown to be more sensitive to perturbations caused by the addition of the Eu(III) ion compared to the changes that occurred in the corresponding fluorescence and phosphorescence titration spectra. The speciation distribution diagrams for the fluorescence and phosphorescence titrations are found in Appendix C16. The calculated speciation distribution diagram showed that, at 0.33 Eu(III) eq., the 1:3 M:L species was present in 92 % abundance. The speciation diagram allows a more effective interpretation of the trends seen in the phosphorescence spectra of the titration experiment. In particular, the binding isotherms of the J = 1-4 bands showed a continued increase in intensity up to 0.5 eq. of Eu(III) after which a sharp decrease was observed. The intuitive observation would have been maximum intensity occurring at 0.33 eq. of Eu(III) as was observed in the case of the

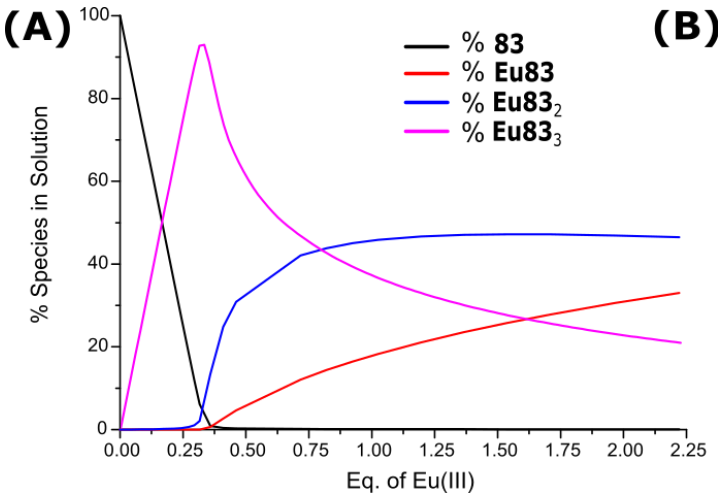

(B)

Eu + **83** ⇌ Eu**83**

Eu + 2 x **83** ⇌ Eu**83**$_2$

Eu + 3 x **83** ⇌ Eu**83**$_3$

log β	**Eu83**	**Eu83$_2$**	**Eu83$_3$**
UV-vis	7.4	15.3(2)	22.9(3)
Fluor.	8.0	17.0	22.5(3)
Phos.	8.4(1)	16.2(2)	22.3(2)

Figure 3.9 (A) Speciation distribution for titration of **83** with Eu(III) calculated from UV-vis titration. (B) Modelled self-assembly equilibria and corresponding calculated global stability constants for the self-assembly of **83** with Eu(III) in CH_3CN

J = 0 band. This would imply 100% formation of 1:3 M:L species at the 0.33 eq. point. However, there was still 8% of the total speciation comprised by unbound ligand which also explains the fact that fluorescence was not fully quenched at the 0.33 eq. point. As more Eu(III) was added up to 0.5 eq., all of ligand **83** came to sensitise the Eu(III) excited state resulting in maximum band intensity and fully quenched fluorescence. This model allowed the global stability constants of the Eu(III):$\mathbf{83}_n$ (n=1-3) equilibrium species to be calculated, see Figure 3.9(B). The stability constants for the phosphorescence titration were found to be $log\ \beta_{1:3}$ = 22.3(2), $log\ \beta_{1:2}$ = 16.2(2) and $log\ \beta_{1:1}$ = 8.4(1) for the 1:3, 1:2 and 1:1 M:L species, respectively, values of which were similar to those of **16**,[103] **34**,[103] **35**[156] and analogous systems in CH_3CN[61-63,144] and higher than such systems in CH_3OH.[61,304] All three values for the stability constants were allowed to converge freely when fitting the phosphorescence titration, however, when fitting the UV-vis and fluorescence titrations certain restrictions were applied in order that convergence upon a plausible value for the stability constant could be achieved. This was done by simply fixing certain values for the stability constants for certain self-assembly species. Two constants were fixed for the fluorescence and one for the UV-vis titration data (the values for $log\beta$ with no associated errors in Figure 3.9). The high stability constants showed the formation of thermodynamically stable systems.

A similar titration experiment was carried out for **83** analogue, **85**, with Eu(III). UV-vis absorption spectra of the ligand **85** in CH_3CN (c = 1x10^{-5} M) recorded at 21 ^{o}C, showed bands centred at λ_{max} = 236 nm (ε_{236} = 69,000 $M^{-1}cm^{-1}$) and 327 nm (ε_{327} = 11,000 $M^{-1}cm^{-1}$). These larger values for molar extinction coefficients were indicative of the benzyl moiety acting as an additional chromophore increasing absorptivity. Excitation at either band maximum gave rise to strong fluorescence emission at λ = 375 nm. The same changes in UV-vis, fluorescence and phosphorescence spectra upon addition of Eu(III) were observed (Appendix C.9-10) For this reason, it is sufficient to simply summarise the main results of the study (Table 3.3). The speciation distribution corresponded to that of **83** (Appendix C.9). In fact, this demonstrated that varying the ester substituent had minimal effects on the self-

Table 3.3 Calculated global stability constants for the self-assembly of **85** with Eu(III) in CH_3CN with λ_{ex} = 325 nm.

Eu + **85** ⇌ Eu**85**

Eu + 2 x **85** ⇌ Eu$\mathbf{85}_2$

Eu + 3 x **85** ⇌ Eu$\mathbf{85}_3$

log β	Eu**85**	Eu$\mathbf{85}_2$	Eu$\mathbf{85}_3$
UV-vis	8.0	16.0	23.1(1)
Fluor.	7.6	16.8	23.9(1)
Phos.	8.8(1)	17.4(2)	23.8(3)

assembly behaviour, albeit, the stability constants were somewhat larger in the case of **85** with Eu(III).

The spectroscopic binding studies were also conducted for lipophilic **btp** ligand **99** in order to monitor its kinetic self-assembly behaviour with Eu(III) and separately with Tb(III) in CH_2Cl_2:CH_3CN (1:9) solution. The photophysical properties of **99** were analysed; the UV-vis absorption spectrum of **99** in CH_2Cl_2:CH_3CN (1:9) (c = 1x10^{-5} M) exhibited bands centred at λ_{max} = 239 nm (ε = 24,000 $M^{-1}cm^{-1}$) and 329 nm (ε = 8,000 $M^{-1}cm^{-1}$), assigned to $\pi\rightarrow\pi^*$ transitions from the aromatic rings and to $n\rightarrow\pi^*$ transitions from the **btp** core, respectively, see Appendix C.5.[103] Excitation at 325 nm gave rise to strong fluorescence emission centred at λ_{max} = 375 nm. As discussed above for **83** and **85**, upon addition of Eu(III) to a solution of **99**, the changes in the UV-vis absorption and the emission spectra were monitored and the same trends in fluorescence quenching and population of the Eu(III) radiative excited state were observed (Appendix C.11, C.13, C.15). The observed lifetime (τ = 3.1 ms) at 0.33 eq. of Eu(III) was indicative of a single chemical species in solution. Such observations coincide with previous reports.[156,197] As expected, the luminescence spectra of **99** at 0.33 eq. of Eu(III) and that of **Eu99$_3$** in solution coincided closely (Appendix C.17).

In the case of the Tb(III) titration the same trends in ground state perturbations and fluorescence quenching were observed (Appendix C.12, C.14) and sensitisation of the Tb(III) excited state was manifested in the observed metal centred emission at 490, 545, 584, 620, 646, 666 and 677 nm assigned to the $^5D_4\rightarrow{}^7F_J$: J = 6-0 transitions, respectively (Figure 3.10).

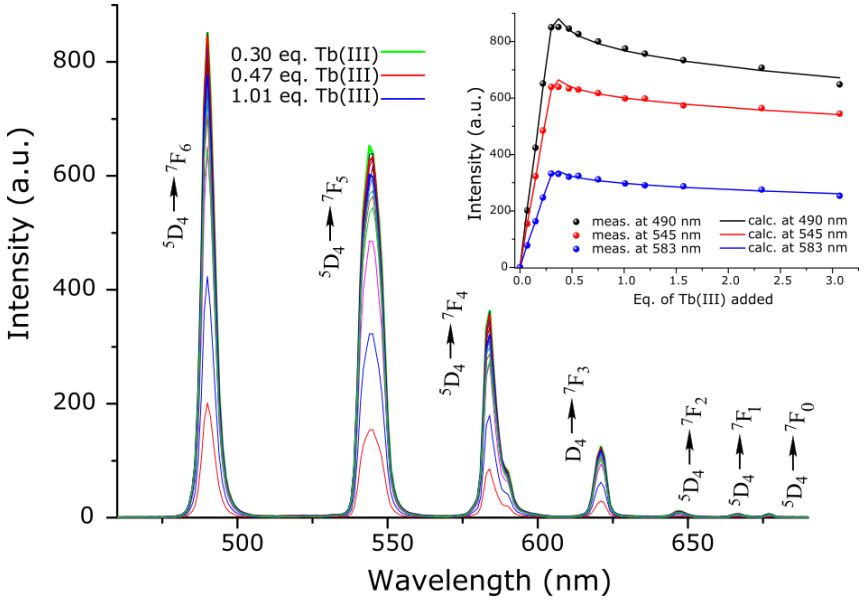

Figure 3.10 Changes in Tb(III) luminescence spectra of **99** (c = 1x10^{-5} M) upon addition of $Tb(CF_3SO_3)_3$ from 0→3 eq. recorded in CH_3CN. (Inset) Experimental binding isotherms.

There was an initial increase in peak intensity up to a max. at 0.33 eq. of Tb(III) added. However, it was clear that there was less of a decrease in intensity of the band transitions as the concentration of Tb(III) was increased compared to that observed for the corresponding titration of **99** with Eu(III) (Appendix C.15) and as was seen above in the case of **83** and **85**.

Nonlinear regression analysis software was used to determine both the speciation distribution and the stability constants for the formation of the Eu(III):**99**$_n$ and Tb(III):**99**$_n$ (n=1-3) equilibria, respectively. The binding isotherms were best fitted to 1:3, 1:2 and 1:1 M:L equilibria in the case of Eu(III) The global stability constants were determined and are summarised in Figure 3.11. These high values compare well with those observed for **83** and **85** above, and related systems.[61,66,197] The Tb(III) titration was also fitted using ReactLab, however, a physically meaningful model could only be determined for the 1:3 M:L and 1:2 M:L equilibria species. Initially, there was growth in the abundance of the 1:3 M:L species up to a maximum of 60% of the overall speciation at 0.33 eq. of Tb(III) added, see Figure 3.11(A). Further addition of Tb(III) gives rise to a majority of the 1:2 M:L species which remained constant for the remainder of the titration. It is possible that the data could only be fit to the 1:3 M:L and 1:2 M:L equilibria model as a result of the substantially larger Φ_{tot} values of the self-assembly species (Φ_{tot} = 79±14% for **Tb99$_3$**); the increase in concentration of a less emissive 1:1 M:L species may be less readily detected.

To conclude, several Ln(III) complexes with **btp** ligands **83**, **H$_3$84** and **85** and **99** functionalised at the 4-pyridyl position with carbonyl groups in the form of esters and carboxylic acids, were characterised and photophysical analysis demonstrated the formation of luminescent 1:3 M:L complexes, the coordination spheres of which

(A)

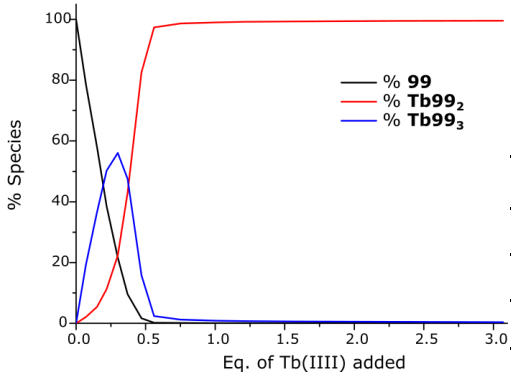

(B)

Eu + **99** ⇌ **Eu99**

Eu + 2 x **99** ⇌ **Eu99$_2$**

Eu + 3 x **99** ⇌ **Eu99$_3$**

(C)

Tb + 2 x **99** ⇌ **Tb99$_2$**

Tb + 3 x **99** ⇌ **Tb99$_3$**

log β	**Eu99**	**Eu99$_2$**	**Eu99$_3$**	**Tb99$_2$**	**Tb99$_3$**
UV-vis	8	16	21.8(1)	16.2	22.1(2)
Fluor.	8.0	16.2(2)	24.0(2)	16.8	23.6(2)
Phos.	7.4(1)	16.7(1)	24.9(2)	15.6	23.9(3)

Figure 3.11 (A) Speciation distribution diagram calculated using ReactLab from UV-vis absorption spectral changes of **99** in CH_2Cl_2:CH_3CN (1:9) (c = 1x10^{-5} M) upon addition of $Tb(CF_3SO_3)_3$. (B) Modelled self-assembly equilibria of **99** with Eu(III) and (C) Tb(III) in CH_2Cl_2:CH_3CN (1:9) with corresponding calculated global stability constants.

were fully saturated. The self-assembly of ester **btp** ligands **83**, **85** and **99** with Eu(III) and Tb(III) was studied and found to give rise to thermodynamically stable systems with high global stability constants. Early stage preliminary results of the An(III)/Ln(III) separation studies with lipophilic **btp** ligand **99** will be presented in Section 3.10. Having explored the spectroscopic binding behaviour of several **btp** ligands upon addition of Eu(III), at low concentrations, the possibility of using the **btp** derivatives developed herein for the formation of Ln(III) templated soft-materials, *i.e* at higher concentrations, was investigated.

3.5 Formation of supramolecular metallogels

For supramolecular gel formation to be successful, the use of weak intermolecular or metal coordination interactions is of critical importance.[6,196,305-307] Hence, the methyl esters of **83** were hydrolysed to the tri-carboxylic derivative **H$_3$84** as a potential candidate for a low molecular weight gelator.[80,172,308] It was foreseen that the semi-flexible **btp** derived ligand possessing the divergent binding behaviour of both the terdentate **btp** motif and the three carboxylic acid moieties would function as 'bridging points' through metal coordination and also through hydrogen bonding interactions (*e.g.* carboxylic dimerisation). Initially, the use of the ligand **H$_3$84** alone in the formation of soft matter was explored. Studies into controlling the self-assembly of Ln(III) templated luminescent metallogels and their mechanical properties alongside the tuning their emission properties will be presented in the following sections.

Although the ultimate goal of designing ligand **H$_3$84** was the development of supramolecular structures and materials, the discovery of the gelation behaviour of **H$_3$84** was in fact serendipitous. Compound **H$_3$84** formed a hydrogel in aqueous solution, see Figure 3.13(A), upon acidification to pH = 4 of the reaction mixture after hydrolysis of

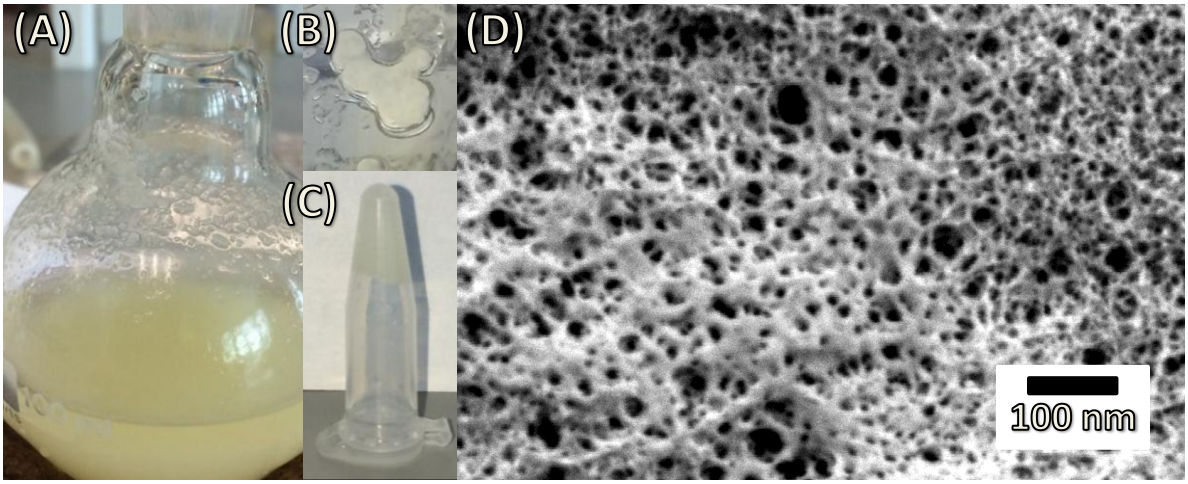

Figure 3.12 Crude hydrogel from **H$_3$84** (A) discovery in RBF, (B) magnified, (C) inversion test, (D) SEM image displaying densely packed fibrous morphology (scale bar 100 nm).

83 (as mentioned in Section 2.3). After acidification and leaving this mixture to stand for 30 minutes the solution increased in viscosity and a soft gel-like precipitate had formed. The sample, the concentration of which was unknown, was stable to flow under the influence of gravity as evidenced by the inversion test, see Figure 3.12(C). The sample was imaged using SEM by Dr. Savyasachi AJ in the Gunnlaugsson group and a densely packed fibrous morphology was apparent.

Several attempts were made at reproducing the gelation using minimal **btp** gelator **$H_3$84** in order to gain an accurate weight percentage (wt. %) of gelator with respect to solvent. Various final acidities were experimented with ($1 < pH < 6$) all forming the off-white 'cotton' like material, from the initially basic solution, that upon standing settled as a soft hydrogel material. Alternatively, it was found that centrifugation at 3500 rpm for 5 minutes, was effective for collecting the gel. The hydrogel with a wt. % of *ca.* 2% (determined by thermogravimetric analysis (TGA), see Appendix D.1) was reproducibly formed through deprotonation of **$H_3$84** (3 mg) in dilute aqueous NaOH solution, (1 mL, pH 8) which fully solubilised the ligand as its sodium salt **$Na_3$84**. Addition of dilute $HCl_{(aq)}$ until pH~6 until the first instances of the soft gel-like precipitate appeared and allowing the mixture to settle over the course of five minutes before decanting off the excess solvent gave rise to the formation of a homogenous hydrogel. This gel was more translucent than the initial serendipitously formed sample. Under irradiation at 365 nm, weak blue fluorescence indicative of the **btp** ligand was visible to the naked eye, see Figure 3.13(B). This gel was imaged using SEM by Dr. Savyasachi AJ, see Figure 3.13(A), in order to study the effect the lower concentration in the sample preparation had on its morphology. The hydrogel displayed a fibrous nature with strands arranged in a tightly packed "spaghetti-like" form. The fibre strands were on average 20-50 nm wide and clearly distinct from neighbouring strands in contrast to the initial sample, see Figure 3.12(D). In the neutralisation process, NaCl was formed and what appeared to be crystals of NaCl were growing on the surface of the gel, see Figure 3.13(C). A similar effect has been reported previously in the Gunnlaugsson group,[88] however, in the reported case, NaCl was forming nano-wires as opposed to crystals of less defined shape.

Attempts at forming an analogous hydrogel by an identical method, but using $TBAOH_{(aq)}$ instead of $NaOH_{(aq)}$ as the solubilising media were carried out. Although there was some observations of gel-like precipitate forming upon acidification, the material was not very robust nor was it particularly resistant to flow when the inversion test was carried out. The significance of the Na^+ ion for the cross-linking of the more robust hydrogel can be

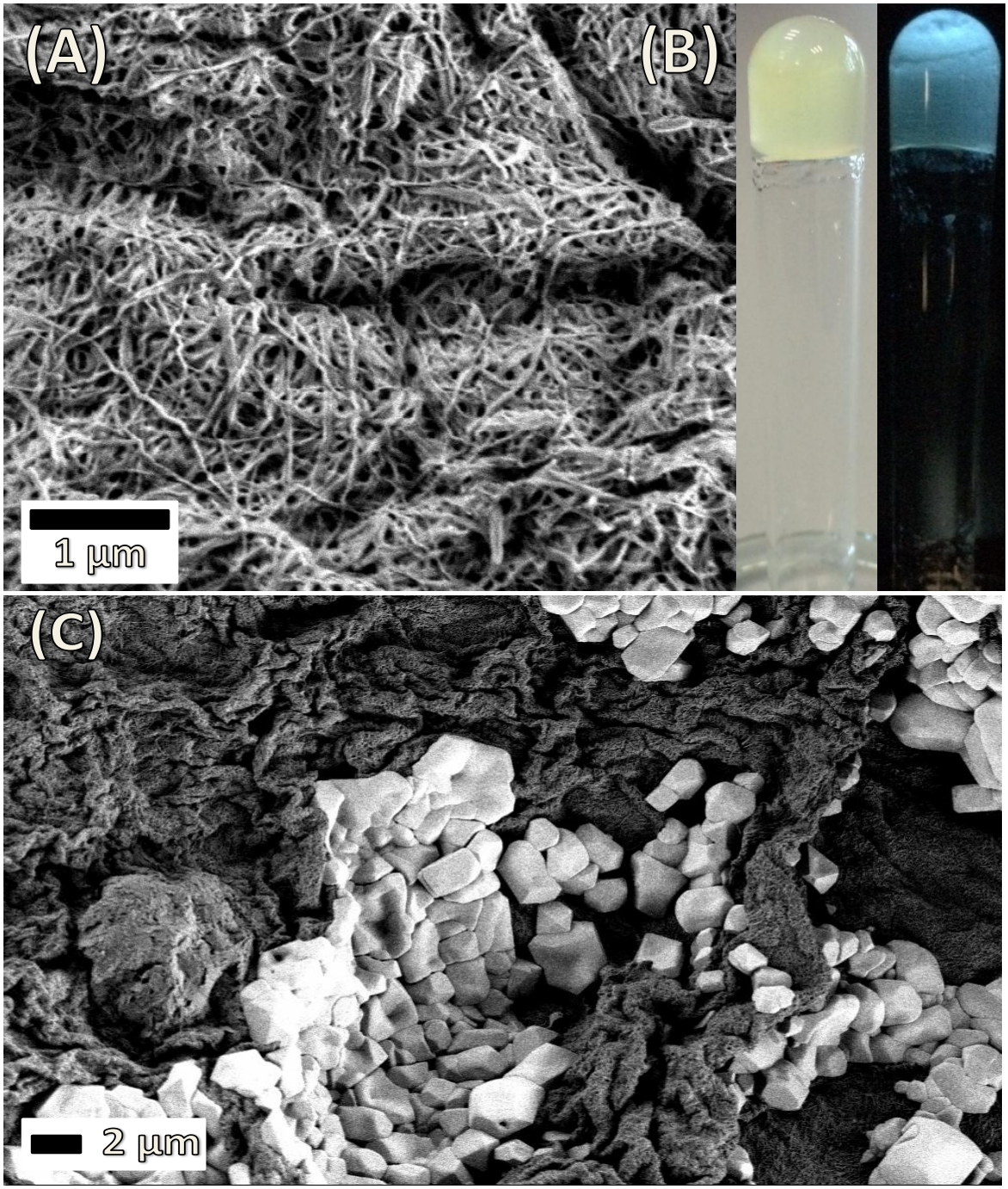

Figure 3.13 (A) SEM image of dried out hydrogel from **$H_3$84** displaying an extended interpenetrated network of fibres (scale bar 1 μm); (B) inversion test demonstrating hydrogel's resistance to flow under gravity. (in daylight and under UV lamp at 365 nm); (C) NaCl deposits on hydrogel surface.

rationalised as follows. In the case of the gel formed using $TBAOH_{(aq)}$, the polar carboxylate groups were highly solvated in the aqueous media, but upon protonation of the groups in the acidification of the mixture, the gelation process was dominated by hydrophobic effects.[6,180,305] Hence, directional hydrogen bonding interactions involving carboxylic acid cyclic dimers culminated in an extended 3D network. The less robust nature of this hydrogel suggests that the Na^+ ions were necessary for the cross-linking of the gelator

molecules through metal-ligand coordination in the formation of a more robust hydrogel system. This process still required the hydrophobic effects brought about by acidification suggesting that Na^+ coordination was occurring simultaneously alongside dimerising carboxylic acid moieties through hydrogen bonding interactions, in the formation of the gel network. A superposition of both supramolecular interactions in the formation of the stable gel was proposed.

An insight into these molecular arrangements of the gelators inside the robust hydrogel matrix was obtained through single crystal X-ray crystallographic analysis of both the *poly*-[**$Na_3$84**] coordination polymer and ligand **$H_3$84**. Metallo-supramolecular gelation shares several commonalities with a crystallisation event, however, it is proposed that crystal growth is only occurring in one dimension in gels.[309] These crystal structures will be discussed in detail in Chapter 4 in relation to the use of **$H_3$84** as a tecton in generating functional porous coordination polymers. Investigations into endowing functional properties to soft materials formed with the tri-carboxylic acid **$H_3$84** ligand will be presented in the next section.

3.6 Formation of Ln(III) luminescent metallogels from Eu($H_3$84)$_3$ and Tb($H_3$84)$_3$ complexes

As we have seen in Section 1.10.1, coordination-based gels can be endowed with the metal's physicochemical properties, *e.g.* magnetism, colour, rheology and photophysical properties. It was this project's goal to impart the materials formed herein with such useful functions, in this case, the interesting photophysical properties of the Ln(III) ions as well the investigation of the material properties of the resulting systems. The incorporation of luminescent groups into gels is an effective design strategy, particularly if the luminescent component, for example a metal ion, is central to the cross-linking gelation process. Their integration is a useful tool for evaluating the molecular arrangement within the material *via* spectroscopic techniques. It was envisaged that this could be achieved when the gelling components consisted of luminescent Ln(III) ions which would allow elucidation of the metal coordination environment at the cross-linking zones through the perturbation of the radiative excited state. Sensitised Eu(III) centres can have emission spectra in which the ratio between emission bands are sensitive to the Ln(III) coordination environment.[299,310] The information gained from the relative band's intensities and splitting patterns can allow an insight to be gained into the site symmetry[23b] of the luminescent Eu(III) ion when correlated with other techniques such as X-ray diffraction analysis. Furthermore, radiative

lifetime studies of the Ln(III) excited state can be used to determine the degree of saturation of the coordination environment.

Having investigated the ability of ligand **$H_3$84** to form hydrogels, the formation of metallogels from complexes **Eu($H_3$84)$_3$** and **Tb($H_3$84)$_3$** was then investigated. It was envisaged, as in the case of the hydrogel, that the nine carboxylic acid moieties of the tris-complexes, **Eu($H_3$84)$_3$** and **Tb($H_3$84)$_3$**, would function as 'bridging points' through carboxylic dimerisation or through the use of 'bridging' metal ions, such as cross-linking Ln(III) ions. This was done in a two-step one-pot procedure[197] (details can be found in the Experimental Section) for all metallogels which will be discussed in terms of the Eu(III)-containing metallogel for succinctness and is represented in schematic form in Figure 3.14. A CH_3OH solution of the **Eu($H_3$84)$_3$** complex was prepared as before in Section 3.3 by microwave irradiation, see Figure 3.14(A). This was then treated with three equivalents of $Eu(CH_3COO)_3$. Upon solvation of the $Eu(CH_3COO)_3$ and subsequent deprotonation of the carboxylic acid moieties, a white fluffy gel-like precipitate was generated indicative of gelation, see Figure 3.14(B). This mixture was irradiated again in the microwave for 30 minutes at 80 ^oC giving rise to the formation of a soft off-white gel-like precipitate upon cooling to room temperature. The mixture was allowed to settle over the course of two hours whereupon the metallogel was formed, or alternatively, it could be isolated by

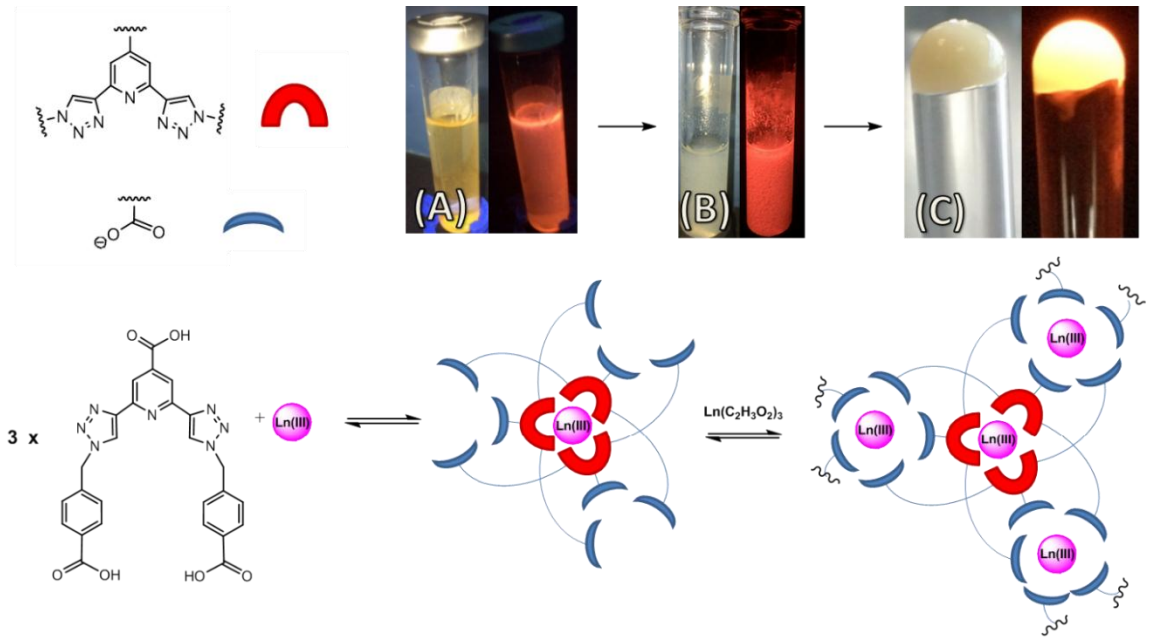

Figure 3.14 Schematic representation of formation of Ln(III) luminescent metallogel demonstrated from precursor **Eu($H_3$84)$_3$** complex. (A) Formation of the precursor **Eu($H_3$84)$_3$** by microwave irraditaion. (B) Addition of the $Eu(CH_3COO)_3$ gel-initiator. (C) Centrifugation and decanting of the supernatent yielded the luminescent metallogel. (Photographs taken in daylight and under UV lamp at 365 nm).

centrifugation, see Figure 3.14(C). The metallogel was highly luminescent to the naked-eye under UV irradiation at 365 nm with characteristic red Eu(III) emission.

TGA analysis of the metallogel showed a loss in mass of *ca.* 95% arising from the methanol content giving it a *ca.* 5 wt. % (Appendix D.2). The gel was also shown to be robust and easily applicable to surfaces, where it was applied on a quartz slide (Figure 3.15(B)) which was then used for spectroscopic analysis. This showed that the emission spectra closely matched that observed for the **Eu(H$_3$84)$_3$** complex in solution for the ΔJ = 1, 2 and 3, while the ΔJ = 4 was structurally identical, but of lesser intensity, see Figure 3.15(C). However, unlike that seen for the **Eu(H$_3$84)$_3$** complex in solution, the ΔJ = 0 was observed in the gel-phase suggesting that a different coordination environment was being added to the system consistent with the cross-linking Eu(III) through the carboxylate moieties. This was supported by comparing the gel's UV-vis absorption spectrum to that of the **Eu(H$_3$84)$_3$** complex in solution, see Figure 3.15(A). Band positions remained constant but a sharp hypochromic effect on π→π* band indicated the Eu(III) interaction with the deprotonated carboxylate groups of **Eu84$_3$** in the gel phase.

In order to characterise the newly formed Eu(III) environment observed in the formation of the metallogel, lifetime studies at different stages of the gelation process were conducted (Table 3.4). Firstly, the radiative decay of the precursor **Eu(H$_3$84)$_3$** complex luminescence in CH_3OH solution was found to be monoexponential with a lifetime τ of 1.4(1) ms. To this was added 2 eq. of $Eu(CH_3COO)_3$, followed by microwave irradiation and isolation of the metallogel. This was done in order to determine the lifetime of the still luminescent supernatant which was also shown to be monoexponential with τ = 1.4(1) ms, indicative of discrete **Eu(H$_3$84)$_3$** complex in solution. Further addition of 1 eq. $Eu(CH_3COO)_3$ was

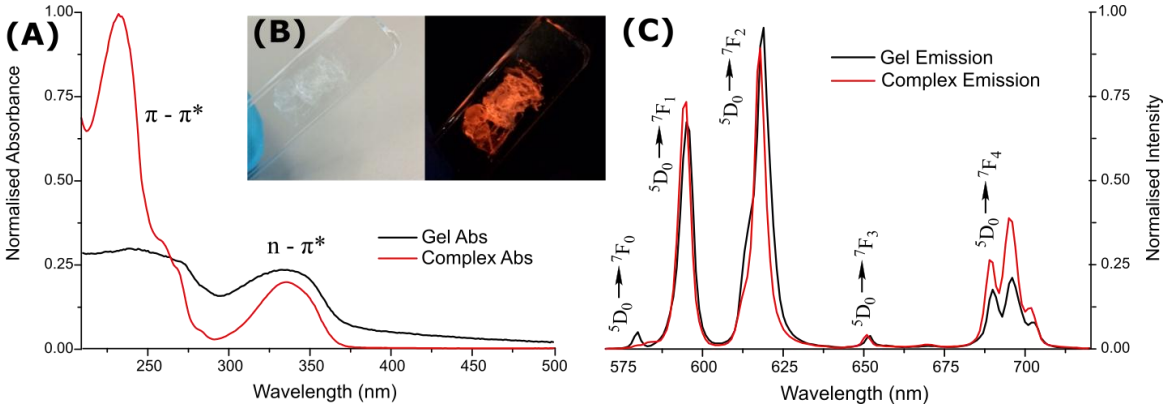

Figure 3.15 (A) UV-vis absorption spectra of **Eu(H$_3$84)$_3$** complex (c = 1x10^{-5} M, CH_3OH, rt) and metallogel. (B) Metallogel applied to quartz slide (in daylight and under UV irradiation at 365 nm). (C) Phosphorescence spectra of **Eu(H$_3$84)$_3$** complex (c = 1x10^{-5} M, CH_3OH, rt) metallogel.

Table 3.4 Observed lifetimes, τ_{obs}, (λ_{ex}=326 nm, λ_{em}=618 nm). [a] Monoexponential decay curve of radiative lifetime in CH_3OH reaction solution after first microwave irradiation. [b] Monoexponential decay curve of radiative lifetime in CH_3OH supernatant after 2 eq. of $Eu(CH_3COO)_3$ added, followed by microwave irradiation and decanting from metallogel. [c] Biexponential decay curve of radiative lifetime after application of metallogel to quartz slide.

Species	τ_{obs}, ms	τ_{obs}, ms
Eu(H$_3$84)$_3$ [a]	1.4(1)	-
Eu(H$_3$84)$_3$ [b]	1.4(1)	-
Metallogel [c]	1.3(1)	0.50(5)

required to collect the maximum amount of metallogel removing any luminescent precursor **Eu(H$_3$84)$_3$** complex from the supernatant. Thus, in total, it required 3 equivalents of $Eu(CH_3COO)_3$ to achieve maximum amount of metallogel and also totally remove luminescent **Eu(H$_3$84)$_3$** complex from the solution. From this the formula *poly*-[**Eu$_3$(Eu84$_3$)**] was proposed for the metallogel. Lifetimes of the metallogel showed biexponential radiative decay indicative of the two Eu(III) environments. A long lived species (τ= 1.3(1) ms) characteristic of the fully saturated **Eu84$_3$** centre and a shorter lived species (τ = 0.50(5) ms) indicative of the cross-linking Eu(III) centres. It can be inferred that Eu(III) from the acetate salt was responsible for the bridging of neighbouring **Eu84$_3$** tris-complexes through the three carboxylate "arms" of the deprotonated **84**, thus forming the extended 3D network culminating in the gel material. As was discussed in Section 1.10.1, this has been reported for **dpa**-derivative **52** in the formation of analogous metallogels.[197] The fact that the metallogel contained two exclusive Eu(III) environments, which were characterised photophysically, suggests that the gel is forming according to the schematical representation depicted in Figure 3.14. It can be concluded that two-step one-pot metallogel formation is a reproducible and highly controlled method of forming functional soft materials which can be readily characterised at the molecular level.

The systematic investigations into the self-assembly behaviour of tri-methyl ester **83**, particularly in relation to crystallography of the **Eu83$_3$** and its luminescence spectroscopy, was valuable in gaining an insight into the molecular arrangement of gelator in the Ln(III) luminescent soft material *poly*-[**Eu$_3$(Eu84$_3$)**]. The correlations between the observed lifetimes of **Eu83$_3$** in CH_3OH, of **Eu(H$_3$84)$_3$** in CH_3OH, of related tris-terdentate Ln(III) gelating systems[197] and the observed lifetimes at the different stages of the gelation process also allowed several meaningful interpretations about the molecular arrangement inside the gel matrix to be made. In terms of the macroscopic properties, several techniques such as

SEM microscopy and rheology studies were used in its analysis. The rheology experiments will be discussed in Section 3.8 after discussing the formation and characterisation of the Tb(III) metallogel analogue using the same two-step one-pot procedure.

Having demonstrated that **btp** was a remarkable sensitiser for Tb(III) with Φ_{tot} between 58% and 79% (Table 3.1) it was a logical step to create the Tb(III) analogue of the luminescent metallogel. The Tb(III) metallogel was also shown to be highly luminescent to the naked-eye under UV irradiation at 365 nm with characteristic green Tb(III) emission, see Figure 3.16(C). TGA analysis of the metallogel showed a similar loss in mass of *ca.* 95% arising from the methanol content giving it a *ca.* 5 wt. % (Appendix D.3). The gel applied on a quartz slide as before, see Figure 3.17(B), which was then used in its spectroscopic analysis. As the Tb(III) radiative state is less sensitive to the coordination environment compared with the Eu(III) radiative state[61,297] the emission spectra of the luminescent gel closely matched that observed for the **Tb(H$_3$84)$_3$** complex in solution for the ΔJ = 6-2, Figure 3.17(C). As seen in the case of Eu(III), the UV-vis absorption spectrum of the gel suggested that cross-linking Tb(III) was occurring through the carboxylate moieties, see Figure 3.17(A). Band positions remained constant but a sharp hypochromic effect on $\pi \rightarrow \pi^*$ band indicated the Tb(III) interaction with the deprotonated carboxylate groups **Tb84$_3$** in the gel phase. The newly formed Tb(III) environment observed in the metallogel was characterised photophysically by radiative lifetime studies in the same way as before at different stages of the gelation process were conducted (Table 3.5). The radiative decay of the **Tb(H$_3$84)$_3$** complex luminescence in CH_3OH solution was found to be monoexponential with τ = 1.3(1) ms. Lifetimes of the metallogel showed biexponential radiative decay indicative of the two Tb(III) environments, a long lived species (τ = 1.1(1) ms) characteristic

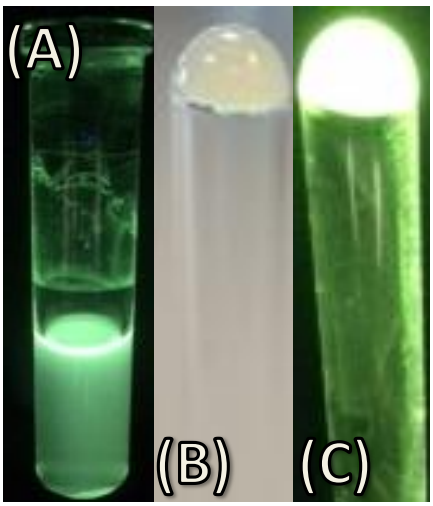

Figure 3.16 (A) **Tb(H$_3$84)$_3$** in CH_3OH prior to $Tb(CH_3COO)_3$ addition. Metallogel (B) in daylight and (C) under UV irradiation at λ_{ex} = 365 nm.

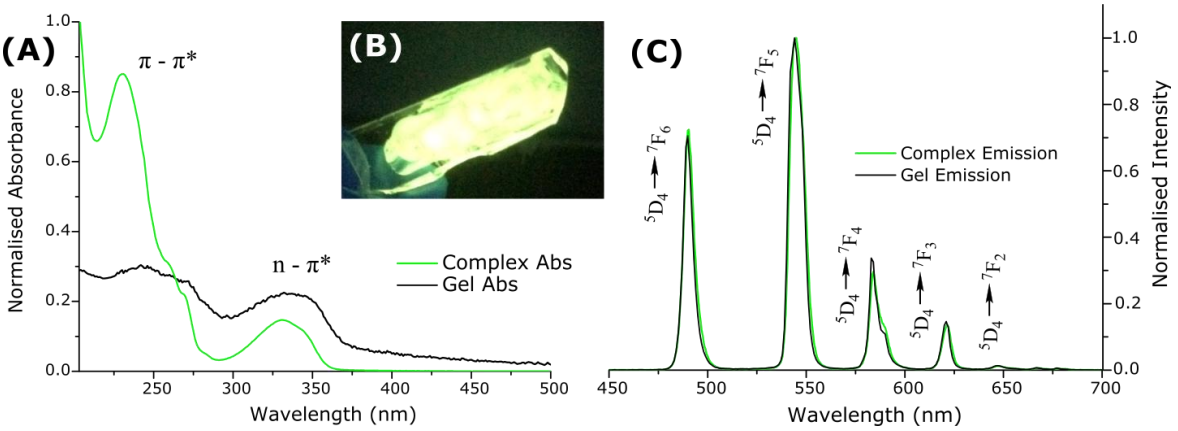

Figure 3.17 (A) UV-vis absorption spectra of **Tb(H$_3$84)$_3$** complex (*c*= 1x10^{-5} M, CH_3OH, rt) and metallogel. (B) Metallogel applied to quartz slide (under UV irradiation at 365 nm). (C) Phosphorescence spectra of **Tb(H$_3$84)$_3$** complex (*c* = 1x10^{-5} M, CH_3OH, rt) metallogel.

Table 3.5 Observed lifetimes, τ_{obs}, (λ_{ex}=326 nm, λ_{em}=580 nm). [a] Monoexponential decay curve of radiative lifetime in CH_3OH reaction solution after first microwave irradiation. [b] Monoexponential decay curve of radiative lifetime in CH_3OH supernatant after 2 eq. of $Tb(CH_3COO)_3$ added, followed by microwave irradiation and decanting from metallogel. [c] Biexponential decay curve of radiative lifetime after application of metallogel to quartz slide.

Species	τ_{obs}, ms	τ_{obs}, ms
Tb(H$_3$84)$_3$ [a]	1.3(1)	-
Tb(H$_3$84)$_3$ [b]	1.3(1)	-
Metallogel [c]	1.1(1)	0.50(5)

of the fully saturated **Tb84$_3$** centre and a shorter lived species (τ = 0.50(5) ms) indicative of the cross-linking Tb(III) centres.

It was investigated if variation of the Ln(III) ion would have an effect on the morphology of the metallogel systems. SEM imaging of the Eu(III) and Tb(III) metallogels demonstrated that incorporation of the Ln(III) ions formed materials with different morphology (Figure 3.18) to that of the hydrogel formed from **H$_3$84** (Figure 3.13). The SEM imaging of the Ln(III)- containing metallogels showed a more condensed structure for both, which lacked the enriched fibrous network seen for the hydrogel of the ligand. The effect of incorporating the different cross-linking metal components on the material properties of the metallo-supramolecular gels were investigated.

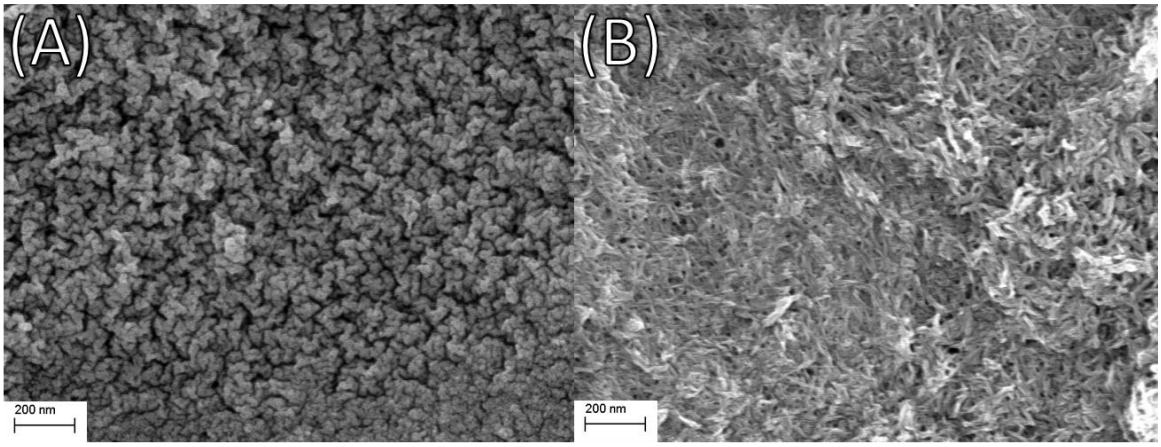

Figure 3.18 SEM images of dried out metallogels of (A) *poly*-[**Eu$_3$(Eu84$_3$)**] and (B) *poly*-[**Tb$_3$(Tb84$_3$)**] (scale bar 200 nm).

3.7 Gel Rheology

As remarked in Section 1.10.1, a gel's rheological behaviour is one of its most important defining features. Using rheology as a tool for exploring structure-function correlations in complex supramolecular systems is indispensable.[184] A thorough analysis of the rheological properties of supramolecular gels can be obtained through studying the soft material's response to applied stress wherein thixotropic behaviour can be identified. Gels that are thick and viscous, under static conditions can flow or see a decrease in their viscosity when external mechanical stresses such as shaking or shearing are applied. The ability of certain stimuli-responsive supramolecular gels to autonomously heal upon damage is a consequence of their thixotropic properties and such "self-healing" materials are a particularly topical area of research.[185-188] Therefore, a background of the theory behind the rheological studies carried out in this research project will be presented briefly.

Under weak stress, a material's elastic and viscous properties can be observed and measured. This range of stress strength being applied to the sample is referred to as the viscoelastic regime. At high stress, the material can begin to flow upon exceeding an associated 'yield stress' or threshold.[6] In very simple terms, a material is classified as elastic when its deformation is proportional to an applied force or stress and a material is categorised as viscous if the rate of deformation is proportional to the force or stress. Viscoelastic materials such as gels exhibit some of both characteristics. There are various set-ups used to study gel rheology (parallel plates, concentric cylinders, cone-and-plate, *etc.*), all of which involve spreading a thin layer of gel between a stationary and a movable component which are moved back and forth relative to one another in an oscillating fashion, see Figure 3.19.[311] This process can create shear stress, for example, resulting in strain being placed on the

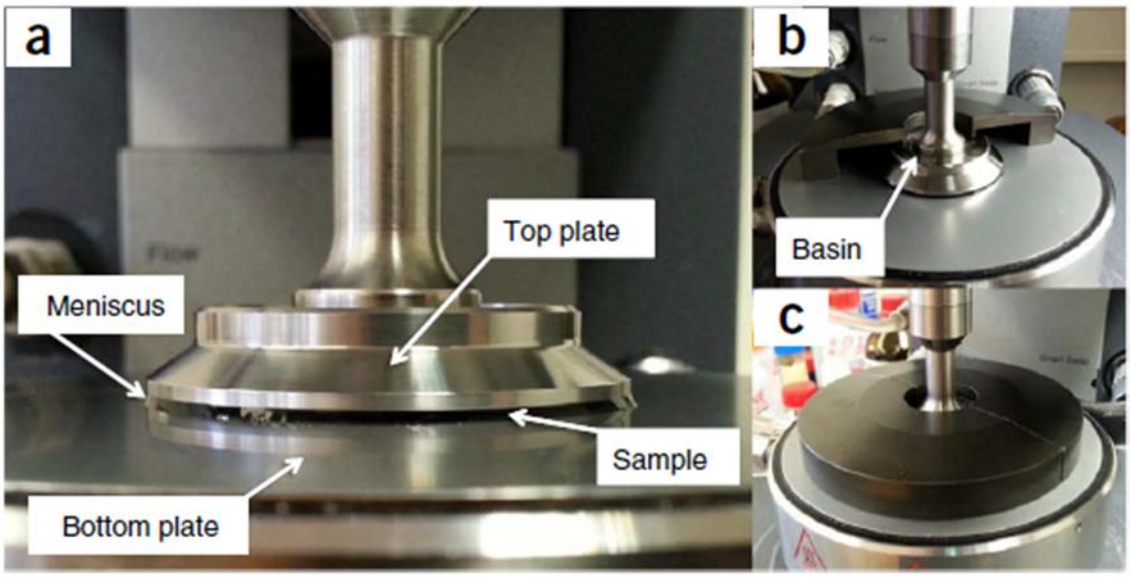

Figure 3.19. A rheometer applies an oscillatory stress to the sample between the plates. Figure reproduced from Ref.[311] Copyright 2014: Nature Publishing Group.

sample between the plates. The complex dynamic modulus (G) is used to quantify the stress-strain relationship, Equation 5.[6,172,183]

$$G = G' + iG' \qquad \textbf{Equation 5}$$

The elastic storage modulus (G′) and elastic loss modulus (G″), representing the solid-like or elastic behaviour and the liquid-like or viscous behaviour, respectively, contribute to the complex modulus, the units of which are in Pascals (Pa). Certain meaningful characteristics of the gel system can be obtained by plotting these variables against the oscillatory frequency, the imposed stress, temperature, and gelator concentration *etc*.

For better understanding of the mechanical properties of gel materials, there are several main rheological studies commonly carried out. The viscoelastic regime is probed by changing the frequency of oscillation of the apparatus while maintaining a constant minimum stress amplitude such that G′ and G″ are independent of the applied stress , see Figure 3.20(A). If G′ is independent of the oscillatory frequency and at least one order of magnitude greater than G″ (due to its solid-like behaviour) up to a particular yield point then the material can be classified as a gel.[6] Another experiment looks at non-linear behaviour of G′ and G″ which arises when larger values of stress amplitudes are varied at constant frequency. Below a particular value of shear stress, called the yield stress, G′ remains constant, however, upon exceeding this yield stress, G′ begins to quickly decrease in value and G″ gains in value, suggesting a breakdown of the extended network as a consequence of external force, see Figure 3.20(B). When the value of G″ exceeds that of G′ the liquid-like component of the complex modulus predominates and the material begins to flow. The

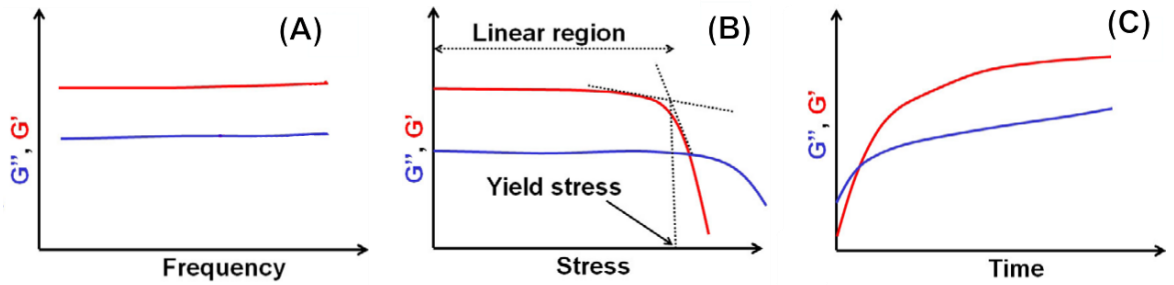

Figure 3.20 Graphical representation of rheological experiments on soft viscoelastic material performed at a constant temperature in the linear region: (A) Frequency sweep at constant shear stress; (B) Determination of yield shear stress and linear region at constant frequency; (C) Recoverability of moduli over time after the release of shear applied. Figure reproduced from Ref.[184] Copyright 2017: WILEY-VCH Verlag.

recoverability of the gels can be studied also using rheological experimental setups by imposing alternating high and low strain amplitudes above and below the yield strain, respectively, and monitoring the effect on the moduli values, see Figure 3.20(C).

3.8 Rheological Measurements of btp derived supramolecular gels

For better understanding of the mechanical properties of the **btp**-derived hydrogel and Ln(III) metallogel materials, rheological studies (strain and frequency sweeps) were performed in collaboration with Dr. Gavin Ryan in the Möbius Group in the Sami Nasr Institute of Advanced Materials (SNIAM), School of Physics, University of Dublin. The strain sweeps for the gels were carried out initially in order to probe the linear viscoelastic regime (Figure 3.21). At low strain amplitudes, the mechano-response of the three gel systems was solid-like; the storage modulus G′ remained constant until the yield strain was reached at which point G′ decreased below G″ indicating a crossover to a liquid-like regime such that the gels started to flow. The hydrogel had a storage modulus of about 0.8 kPa in the linear regime while G′ for the Eu(III) and Tb(III) metallogels were 1.0 kPa and 1.1 kPa, respectively. The yield points were found to occur at 17%, 22% and 26% strain for the ligand hydrogel and

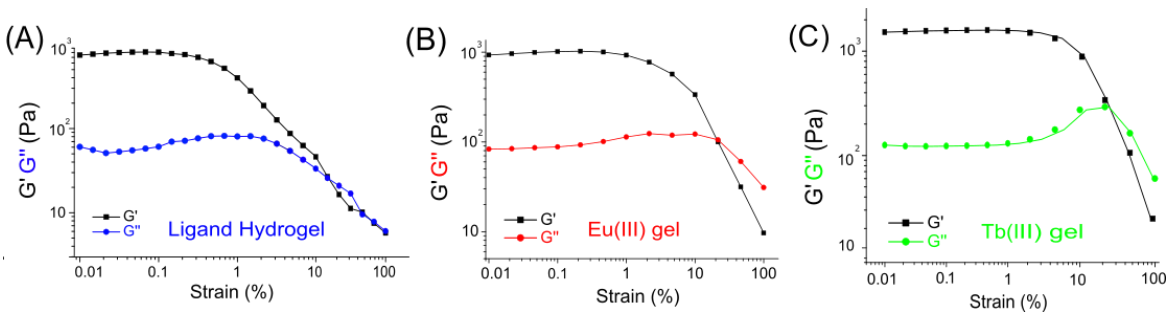

Figure 3.21 Oscillatory rheology strain dependence measurements of the storage modulus G′(■) and loss modulus G″(●) carried out at a f = 1 Hz for (A) the ligand hydrogel (B) the Eu(III) metallogel and (C) the Tb(III) metallogel.

Eu(III) and Tb(III) metallogels, respectively.

Little frequency dependence of the storage and loss moduli was observed in the linear viscoelastic region for all three gel systems and as was seen for the corresponding strain sweeps, the mechano-response of the ligand hydrogel, see Figure 3.22(A) and those of the Eu(III) and Tb(III) metallogels, see Figure 3.22(B)/(C), were solid-like with G′ greater than G″ by an order of magnitude for all three systems, thus fulfilling the definition of a gel.[6] As the frequency of oscillation increased, the loss modulus G″ was observed to approach G′. This effect was seen less dramatically for the Eu(III) and Tb(III) metallogels at high frequencies. The storage moduli values for the Eu(III) and Tb(III) metallogels in the linear viscoelastic regime were G′ = 1 kPa and 1.1 kPa, respectively. However, the ligand hydrogel in this linear regime had a different value of G′ = 0.2 kPa, a decrease from 0.8 kPa indicating that the moduli values had not recovered spontaneously following exceeding its yield point during the strain dependence measurements. This suggested that the mechano-responsiveness of the ligand hydrogel was different to those of the Ln(III)-containing metallogels. This was further investigated through the action of applying a repeating shear stress to the individual gel systems and analysis of the time evolution of the moduli values upon release of the shear stress.

The recovery properties of the gels were tested by imposing alternating strain amplitudes of 20% and 0.1% at a constant 1 Hz oscillation frequency. Both the Eu(III) and Tb(III) metallogels went from liquid-like (G″ > G′) to solid-like (G′ > G″) behaviour with a quick recovery of the original moduli values of within 100 seconds and 50 seconds, respectively, consistently over consecutive runs, see Figure 3.23(B)/(C). This demonstrated that the Ln(III)-containing metallogels were self- healing.[6,182,184,197] The same smooth recovery of G′ and G″ was not observed for the ligand hydrogel, see Figure 3.23(A), as the moduli values were observed to decrease with every successive application of the shear stress. This

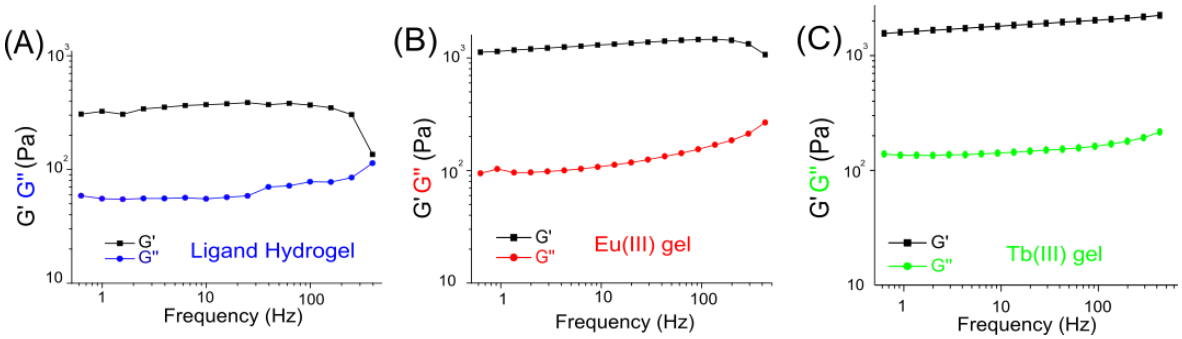

Figure 3.22 Oscillatory rheology frequency sweeps measurements of the storage modulus G′(■) and loss modulus G″(●) carried out at 0.1% strain amplitude for (A) the ligand hydrogel, (B) the Eu(III) metallogel and (C) the Tb(III) metallogel.

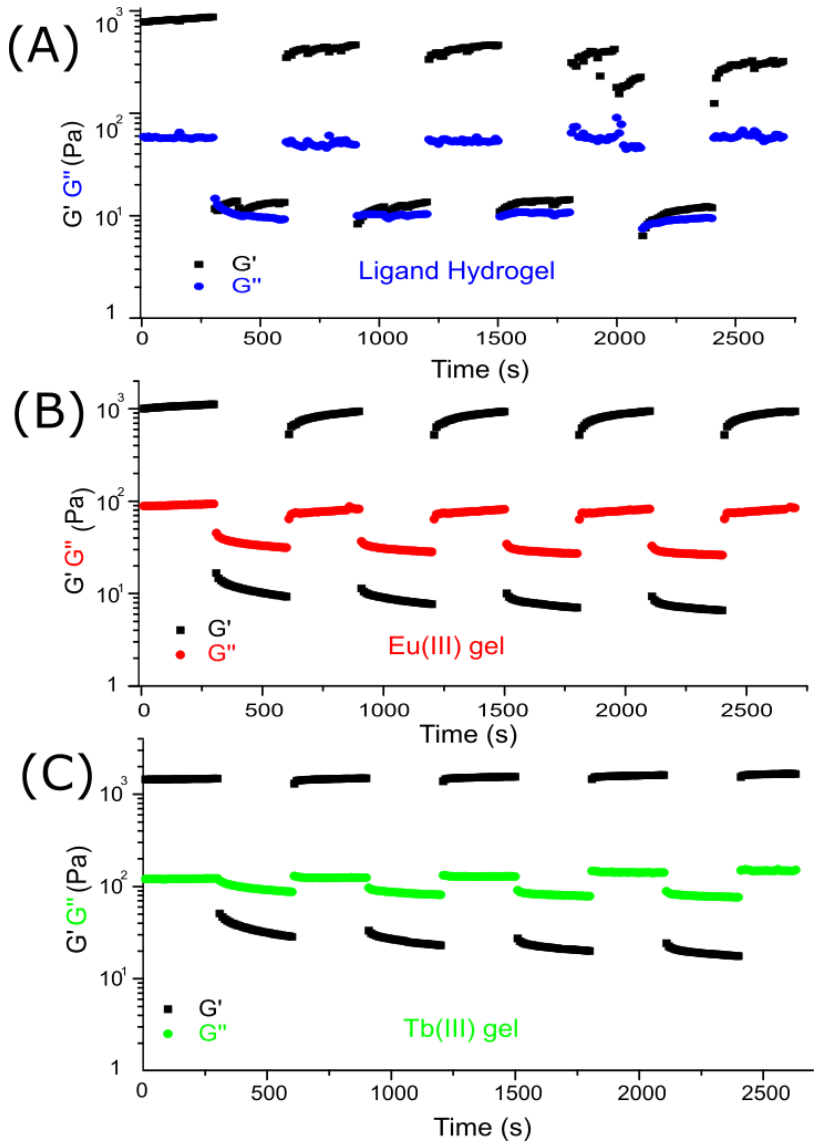

Figure 3.23 Oscillatory rheology time evolution recovery of the storage modulus G′(●) and loss modulus G″(●) test for (A) the ligand hydrogel, (B) the Eu(III) metallogel and (C) the Tb(III) metallogel with alternating strain amplitudes of 20% and 0.1% at f = 1 Hz.

explains the decrease from 0.8 kPa to 0.2 kPa observed between Figure 3.21(A) and Figure 3.22(A) following the strain dependence measurements and at the start of the frequency sweep.

The following rationale is proposed to account for the difference in thixotropic behaviour of the Ln(III)-containing metallogels and the ligand hydrogel. In the case of the Ln(III) metallogel the Ln(III) ions which were 'bridging' between neighbouring tris-complexes were not fully saturated as evident from the radiative lifetime studies. Therefore, when a carboxylate-Ln(III) bond was broken there was an increased possibility of the carboxylate recombining with a vacant Ln(III) coordination site and re-establishing a supramolecular cross-linking interaction. As a result, the Ln(III) metallogels showed more pronounced

healing ability as the G′, G″ values consistently recovered over consecutive application and removal of the shear stress. In the case of the ligand hydrogel, each Na^+ ion cannot be bound by as many carboxylate binding groups at a time, thus, limiting the rate of reformation.

It can be concluded that the viscoelastic properties of the three supramolecular gels compared to those commonly seen for a cross-linked polymer system.[179,183-184] All the systems discussed above, consisted of specific junction zones comprised by metal-carboxylate coordination which were breakable under shear, however, it can be suggested that the difference in the rheologybehaviour is due to the effect of the Ln(III) ions acting as a cross-linker in the formation of the extended 3D network for both the Eu(III) and Tb(III) metallogel systems. Incorporation of the Ln(III) ion results in the formation of stronger materials, less subject to aging and better capable to autonomously heal upon damage.

3.9 Towards mixed Ln(III) luminescent white-light emitting metallogels

It was envisaged that the pronounced luminescence observed upon irradiation of the Ln(III)-containing metallogels could be tuned by varying the stoichiometries of Eu(III) and Tb(III) used in their synthesis[197] with a view to generate white light emitting (WLE) gels. WLE emitting materials have shown potential in the development of next generation solid-state lighting applications, full colour flat-panel electroluminescent displays, and liquid crystal display back-lighting sources.[230,312-313] In order to successfully develop an ideal WLE system, the Commission Internationale de l'Eclairage (CIE) requires that the three primary colors of red, green and blue are present with appropriate intensities spanning the visible spectrum of light *i.e.* between 400 nm and 700 nm culminating in coordinates on a CIE diagram in the region of (0.31, 0.33).[230] Such systems have been reported in a variety of forms such as covalent[314] and supramolecular co-polymers,[315] rare earth doped upconversion materials,[230,316] heterometallic Ln(III) solution based assemblies,[72] MOFs[223-224,317-318] and supramolecular gels.[319]

In this research project, pure WLE emitting gels with CIE coordinates in the region of (0.31, 0.33) were not successfully generated, however, the results of the attempts will be summarised briefly. The synthesis of the mixed gels was carried out in a similar manner as the pure Eu(III) and pure Tb(III) metallogels from Section 3.6. The mixed Ln(III) nature was introduced, for example, by addition of $Tb(CH_3COO)_3$ to a solution of **Eu(H$_3$84)$_3$** in CH_3OH which was then stirred under microwave irradiation to promote cross-linking induced gelation as before. This resulted in the formation of a pale yellow luminescent gel-like precipitate, see Figure 3.24(C) which when allowed to settle formed the mixed *poly-*

[**Tb$_3$(Eu84$_3$)**] gel, see Figure 3.24(D). The gel was analysed photophysically with a similar UV-vis absorption profile as was seen for the pure Eu(III) and pure Tb(III) analogues, see Figure 3.24(A). The fluorescence spectrum showed strong scattering from the thinly spread gel sample on a quartz slide which was centred around 350 nm. Ln(III) centred luminescence was also observed with bands corresponding to both Tb(III) and Eu(III) emission observed, see Figure 3.24(A). Spectral analyses to obtain CIE coordinates were performed using a CIE coordinate calculator running on Mathlab®.[72] The gel displayed CIE coordinates of (0.36, 0.41) corresponding to a pale yellow colour, see Figure 3.24(F). The *poly*-[**Tb$_3$(Eu84$_3$)**] gel possessed CIE coordinates which, out of the mixed Ln(III) gels analysed, were in closest proximity to the idealised WLE coordinates. The mixed gel analogue, *poly*-[**Eu$_3$(Tb84$_3$)**], displayed a more pronounced orange coloured emission, see Figure 3.24(B). Several attempts were made at tuning the colour output of other mixed Ln(III) metallogels by varying the stoichiometries of Eu(III)/Tb(III) acetate cross-linkers used in the synthesis of the gels

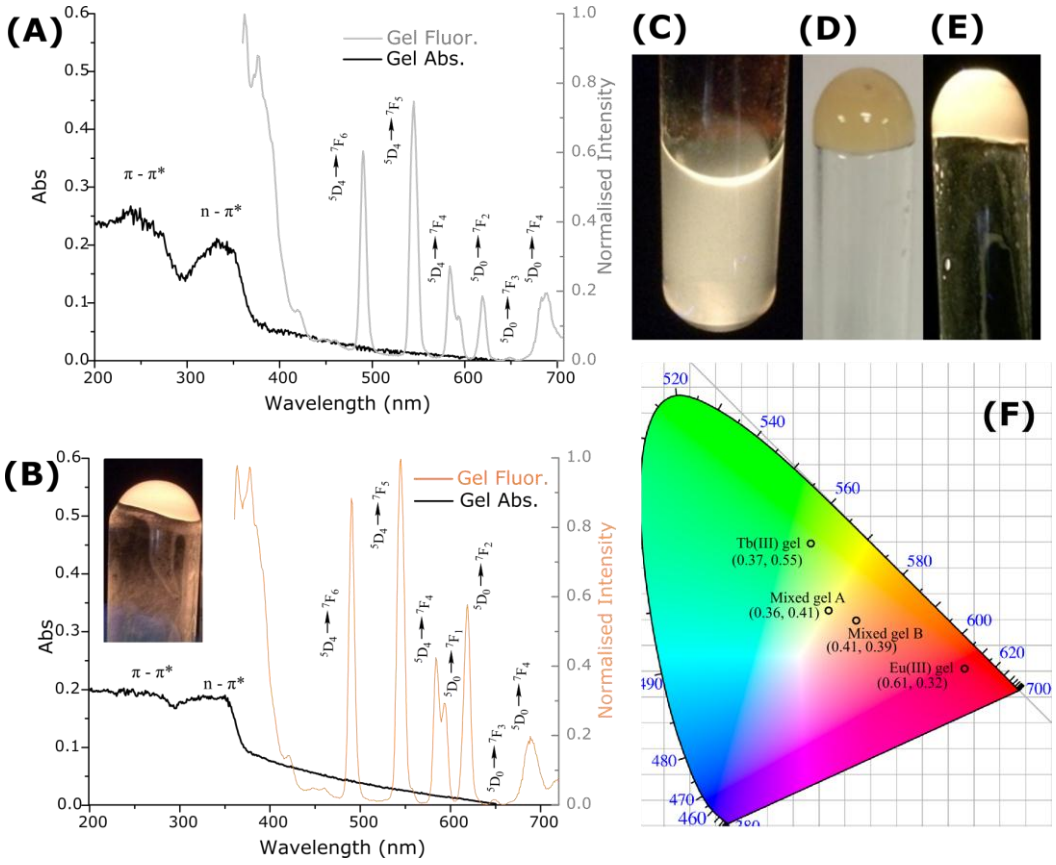

Figure 3.24 UV-vis absorption and fluorescence emission spectra (λ_{ex} = 326 nm) for mixed Eu(III)/Tb(III) metallogels: (A) *poly*-[**Tb$_3$(Eu84$_3$)**] and (B) *poly*-[**Eu$_3$(Tb84$_3$)**]; (Inset (B)) Photograph of *poly*-[**Eu$_3$(Tb84$_3$)**] under UV irradiation at 365 nm. (C) CH_3OH reaction mixture containing *poly*-[**Tb$_3$(Eu84$_3$)**] before and (D) after gelation in daylight and (E) under UV irradiation at 365 nm. (F) CIE-1931 chromaticity diagram plotting coordinates of Tb(III) gel, Eu(III) gel and mixed gels.

and also by mixing solutions of varying stoichiometric ratios of the tris-complexes **Eu(H$_3$84)$_3$** and **Tb(H$_3$84)$_3$** (Appendix C.21) before cross-linking with Eu(III)/Tb(III) acetates. It was found that the formation of mixed gels by cross-linking with Eu(CH$_3$COO)$_3$ gave rise to more orange emitting gels and cross-linking with Tb(CH$_3$COO)$_3$ gave rise to the more pale yellow emitting gels. Varying the excitation wavelength did not change the colour output of the luminescent gels, in contrast to other solution based systems which achieved pure WLE behaviour reported in the Gunnlaugsson Group.[72] The scattering observed in the fluorescence spectrum alongside the lack of a blue emitting chromophore hindered the ability to produce the desired WLE gels. For this reason, the systems were not investigated further.

3.10 Summary of preliminary results from An(III) extraction studies with lipophilic derivatised btp ligand

As discussed in Section 1.5.8, **btp** derivatives have featured frequently in the development of new solvent extraction processes for selectively removing TRU from nuclear waste.[98,148] The chemistry of **btp** derivatives and the corresponding diazine analogues[320] have gathered significant attention for the coordination of the minor An(III) ions (particularly Am(III) and Cm(III) ions) selectively over the Ln(III) ions. This is followed by the subsequent solvent extraction into organic phases.[147,321] The reason for the selectivity is not currently known, but thought to be due to the favoured energy overlap of the π* orbitals of the pyridine with the *f*-orbitals on the An(III),[322] but other factors may be at play.[323] As discussed in Section 1.5.8, a number of reports have outlined the synthesis of hydrophilic **btp** ligands[98,148-150] in order to improve the extraction of An(III) ions into aqueous media.

More recently switching the selectivity to favour the binding of the Ln(III) ions has been observed upon introducing slight differences in the ligand design.[324] As was presented in Section 2.6, this approach was pursued in the functionalisation of **btp** with lipophilic hexadecyl groups at the triazolyl *N1* position, **99**, in order for the extraction process to take place in non-polar solvents such as CH_2Cl_2. However, it was also planned to investigate whether **99** would preferentially bind Ln(III) ions over An(III) ions. This was carried out, firstly, by examining the reactions of **99** in a CH_2Cl_2 solution when mixed with a solution of ^{241}Am (with radioactivity of 100 Bq) in H_2O were examined. The two solutions were stirred for 3 hours, and following the separation of the solvent phases, the activity of both were determined by γ-spectrometry. In brief, the results showed that the activity in the organic phase (which correlated to the amount of Am(III) extracted) was in all cases *ca.* 4 Bq. This

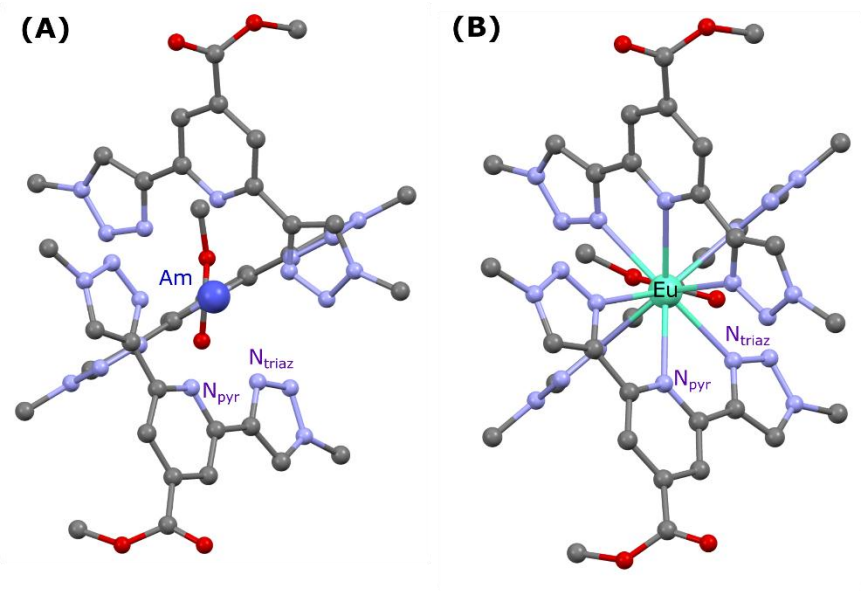

Figure 3.25 Preliminary results from the DFT computational studies of the coordination of **99** to (A) Am(III); (B) Eu(III) using H_2O as the solvent. Substantially larger modelled distances $|N_{pyr}$-*An*| and $|N_{triaz}$-*An*| than for $|N_{pyr}$-*Eu*| and $|N_{triaz}$-*Eu*|.

implied that ligand **99** did not coordinate to Am(III) or that the extraction was not efficient.

This was correlated to DFT calculations carried out by Dr. Satoru Tsushima in the Institute of Resource Ecology in Dresden, Germany using the software package, Gaussian.[325] The models calculated in H_2O for the tris-complexes Am**99**$_3$ and Eu**99**$_3$ (Figure 3.25) showed substantially larger distances $|N_{pyr}$-*Am*| and $|N_{triaz}$-*Am*| than for $|N_{pyr}$-*Eu*| and $|N_{triaz}$-*Eu*|, as summarised in Table 3.6. These results may explain the low activity observed in the organic phase during the Am(III):**99** extraction process, as presumably ligand coordination was so weak that it could not compete with H_2O solvent coordination and as a result the complex was not formed at all. To be convinced of the extraction results, however, a simultaneous extraction of a mixture of Eu(III) and Am(III) should be examined. Facilities wherein ^{152}Eu can be studied are currently being sourced for this endeavour.

Table 3.6 Comparison of Gaussian calculated metal-ligand distances for **99** with Am(III) and Eu(III).

Metal (M)	$\|N_{pyr}$-*M*$\|$/Å	$\|N_{triaz}$-*M*$\|$/Å
Am(III)	2.787-2.834	2.670-2.746
Eu(III)	2.679-2.680	2.575-2.578

3.11 Conclusions

In summary, the self-assembly behaviour of a range of **btp** ligands functionalised at the 4-pyridyl position with Eu(III) and Tb(III) was studied and found to form thermodynamically stable systems. Global stability constants for the 1:3 M:L species in solution were calculated from non-linear regression analysis of the changes in the absorption, fluorescence and Ln(III) centred emission spectra of the ligand upon addition of varying equivalents of Ln(III) ion. X-ray crystallography of **Eu83$_3$** prepared under thermodynamic control showed the formation of a fully saturated Eu(III) centre in 1:3 M:L stoichiometry. It was shown that this structure also existed in solution. Photophysical studies were carried out on all Ln(III) complexes. Lifetimes were measured and hydration states of 1:3 M:L species were found to have *q* values of 0. Luminescence quantum yields of the complexes in CH_3CN and CH_3OH showed values between 2-7% for Eu(III) and 58-79% for Tb(III).

The **btp** ligand **H$_3$84**, possessing three carboxylic acid groups was shown to function as a low molecular weight gelator giving rise to the formation of a hydrogel consisting of a fibrous network encasing aqueous solvent. The corresponding highly luminescent metallogels formed from the tris-complexes, **Eu(H$_3$84)$_3$** and **Tb(H$_3$84)$_3$**, were characterised using SEM imaging which revealed a more compacted morphology in contrast to that of the ligand hydrogel. All gels showed low gelator to solvent ratios with wt. % of *ca.* 2% for the hydrogel and *ca.* 5% for Eu(III) and Tb(III) metallogels. The Ln(III)-containing metallogel cross-linking was investigated through radiative lifetime studies clearly showing two distinct Ln(III) environments present in both Eu(III) and Tb(III) metallogels, consistent with the tris-complexes being bridged through metal-carboxylate coordination interactions. The combination of the observed lifetime measurements with the rheological investigation of the Ln(III) metallogels offered an opportunity to monitor the dynamic behaviour of self-assembly under shear forces and interpret the origin of the interesting thixotropic properties. Both studies combined demonstrated the important role the Eu(III) and Tb(III) ions plays in the formation of these self-healing soft materials, both from the point of view of directing the initial self-assembly formation (*i.e.* 1:3 stoichiometry), as well as in 'bridging' between complexes *via* the carboxylate terminals. The nature of the unsaturated Ln(III) 'bridges' possessing vacant coordination sites meant that bond reformation was occurring upon removal of the shear stress over the course of a short timescale as evidenced by the fast autonomous recovery of the elastic moduli to the equilibrium values observed under static

conditions. The rheological comparison between ligand hydrogel and metallogel demonstrated the Ln(III) ions' utility in soft matter systems.

A challenge for soft material scientists is over-coming the fact that similiar systems have limited lifespans, where damage from constant strain and stress can result in their degradation. The use of high coordination number ions, such as Eu(III) and Tb(III), has the potential for producing soft materials possessing an increased longevity as a consequence of the tris-complex's reversible supramolecular interactions with divergent metal binding ligands. This work represents a step closer to designing a mechano-responsive supramolecular assembly, synthesised with a high degree of control, as the nature of firstly, the structure of the cross-linker at the molecular scale and, secondly, how this endows the observed thixotropic properties on the system are well characterised.

3.12 Future Work

It has been demonstrated in this chapter that conducting a mechanical experiment like rheology on a supramolecular gel can reveal vital information which can allow characterisation of the structure and dynamics of the comprising assemblies.[183-184] Currently, words like "mystery" are still being used to describe the processes involved in the make-up of supramolecular gels.[184] A thorough rheological study complemented with the help of techniques such as small-angle neutron scattering (SANS) is planned for future projects in order to gain a better understanding of the gel structural features. It is envisaged that SANS will permit the probing of the nature of solute-solvent effects in a gel state[6,172,184] as it permits in solution. These are dynamic operations which, it is proposed, play an important role in the cross-linking and formation of fibrils in the hierarchical assembly process discussed in Section 1.10.1.

The varying trends and affinity differences that exist across the Ln(III) series could be used to tune the mechano-responsive properties of analogous metallo-supramolecular gels through the incorporation of other Ln(III) ions in the gel synthesis. Such affinity differences have been demonstrated, for example, in the variability of global stability constants for the formation of ternary Ln(III) complexes involving Eu(III) and Tb(III).[64,144] Also, different solvents, similar to CH_3OH but with higher boiling points, could be used in the synthesis of the gels in order to form soft materials with longer lifetimes as the systems would be less prone to drying out.

Efforts are underway in the Gunnlaugsson group in the incorporation of chirality, in close proximity to the **btp** motif adjacent to the triazolyl *N1* nitrogen atom, a study which would

be interesting in the formation of Ln(III) luminescent metallogels[326] endowed with circularly polarised Ln(III) luminescence.[61,119,156] Furthermore, the potential for the formation of healable materials using ditopic **btp** ligands of the type of 98, presented in Section 2.5,[327] in an analogous fashion to those materials reported by Rowan *et al.*,[179,195] are future routes being considered. It is intended then to explore the functional properties of these self-assemblies (*e.g.* their sensing and imaging abilities), as well as their material properties.

This demonstration of the self-assembly behaviour of several **btp** ligands, functionalised at the 4-pyridyl position of the **btp** motif, with Ln(III) ions, is encouraging in the efforts to design new and chemically useful supramolecular polymer architectures. We will explore the development of porous coordination polymers using **btp** ligand **$H_3$84** with *d*-metal ions such as Cu(II), Zn(II) and the resulting functional properties of the crystalline materials, or so-called MOFs,[6,8,176,207,229,328-330] in the following Chapter.

4 Crystalline coordination polymers derived from tri-carboxylic acid btp tecton $H_3$84 towards functional MOF materials

4.1 Introduction

As remarked in Section 1.10.1 and in Section 3.5, the nature of supramolecular systems produced when divergent multitopic ligands and metal ions are mixed in solution can vary vastly depending on the synthetic conditions used, despite being comprised of the same ligand building blocks or tectons.[8,176,198] It was demonstrated in the previous chapter that when metal ions and ligands possessing divergent binding ability mix in solution one of the self-assembled systems which can arise are coordination polymers, possessing short range order but lacking long range order, some of which are gels.[6] Metallo-supramolecular gelation shares several commonalities with a crystallisation event, however, it is proposed that in the formation of the gel, growth mostly occurs uniaxially.[309] As in gels, the formation of oligomers in the crystallisation of coordination polymers relies on precisely organised intermolecular interactions through recognition of neighbouring molecules. However, as in the case of all crystals, including crystalline coordination polymer materials such as MOFs, crystal packing forces, symmetry effects and conjugation[107,331-332] gain greater significance in the special arrangement of the molecules in the resulting assemblies.

MOFs represent a swiftly advancing research area in chemistry, from the point of view of the extensive functional properties,[201] in applications such as catalysis,[202-204] sensing,[205-207] guest encapsulation[208-209] and for gas adsorption and separation[201,210-216] and the range of network topologies accessible[199-200] in their synthesis. Moving beyond the typical rigid-ligand designs of early reports of porous coordination polymers, so-called MOFs derived from divergent ligands possessing at least one flexible sp^3 linker group, a feature of **btp** tri-carboxylic acid **H$_3$84**, are commonplace.[213,330,333-335] The multiple coordinating directionality[98,105,112-113,182] together with the conformational freedom[27,42,55,102,104-107,113,156] (Scheme 4.1) of semi-rigid ligands like **H$_3$84** make them very appealing for the design of new architecturally diverse MOFs which also possess desirable functional properties. The low-energy bond rotations create a range of bridging geometries facilitating the development of more dynamic or "breathable" systems.[222,228,336] Flexibility in the nodes and/or ligand backbone seems helpful in systems purposed for gas uptake, storage, release and purification,[337-338] prompting some research into the use of flexible linkers instead of the traditional rigid aromatic ligands. This class of semi-rigid ligand can also generate rigid frameworks through increased connectivity in more than two directions.[221] Drawbacks associated with such flexible ligand MOFs[330] include an impeded control over the rational structural predictability of extended network architectures.[176,198] Conformational

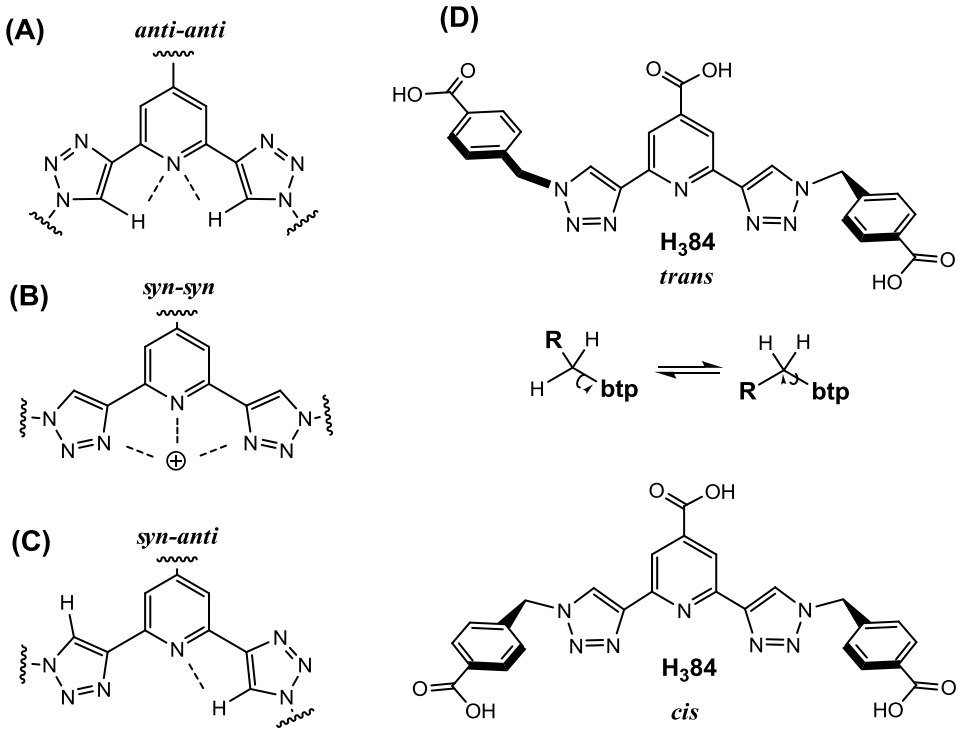

Scheme 4.1 Conformational changes of the (A) unbound and (B) metal chelating **btp** motif and (C) the *syn-anti* conformational possibility. (D) Flexibility in the sp^3 methylene linker through low energy bond rotation.

adaptability of the ligand precursor can be advantageous when combined with a labile metal ion's energetically preferred coordination geometry. This approach can facilitate the generation of structurally diverse MOFs whose architectures would not be attainable from more rigid building blocks.

As stated previously in Section 1.10.2, there are no reports of **btp** derived MOFs, despite the binding motif's frequent incorporation into amorphous polymers and macromolecules[27,231-234] and in the formation of metallo-supramolecular gels.[27,101,112-113,182] Encouraged by this, the exciting possibilities of using the tri-carboxylic acid **btp** ligand **$H_3$84** as a tecton in the generation of functional MOF materials were explored.

4.2 Structural analysis of btp ligand $H_3$84 and $Na_3$84-derived coordination polymer network

It was demonstrated in Section 3.5 that the divergent binding groups possessed by the ligand **$H_3$84** allowed it to function as a low molecular weight gelator through a combination of hydrogen bonding interactions and Na^+-carboxylate coordination. The crystal structures of ligand **$H_3$84** and its sodium salt **$Na_3$84** will next be discussed as these systems have extended hydrogen bonding and coordination polymer properties, respectively, giving rise to their

crystalline make-up. Crystal data, data collection, and structure refinement details are summarised in Appendix E, Table E.3.

The **btp** ligand **H$_3$84** was crystallized by evaporation from CH_3OH. The diffraction data were collected and solved by Dr. Jonathan Kitchen at the University of Southampton and the structure model refined in the monoclinic $P2_1/c$ space group with one molecule in the asymmetric unit (Figure 4.1). Powder X-ray diffraction (PXRD) analysis confirmed phase purity (Appendix E.18). The pyridyl and two triazolyl units are essentially coplanar; the planar conformation of **btp** facilitates the π-π stacking interactions between molecules along the *b*-axis, (the perpendicular distance between the parallel mean planes of **btp** cores is 3.290(3) Å). The benzoic acid arms adopt a *trans*-like conformation relative to the central **btp** core, facilitating packing along the *a* and *b* axes through two pairs of $R_2^2(8)$ cyclic carboxylic acid dimers per molecule[339] (the distances and angles for the two donor-acceptor pairs (D·· A) with distance between one of the donor and acceptor pairs |D···A| of 2.574(4) Å and the corresponding donor-hydrogen-acceptor angle ∠ (*O-H*···*O*) of 173.7(2)°. The other donor-acceptor pair has |D···A| of 2.665(4) Å and ∠ (*O-H*···*O*) of 162.32(15)°. The **btp**

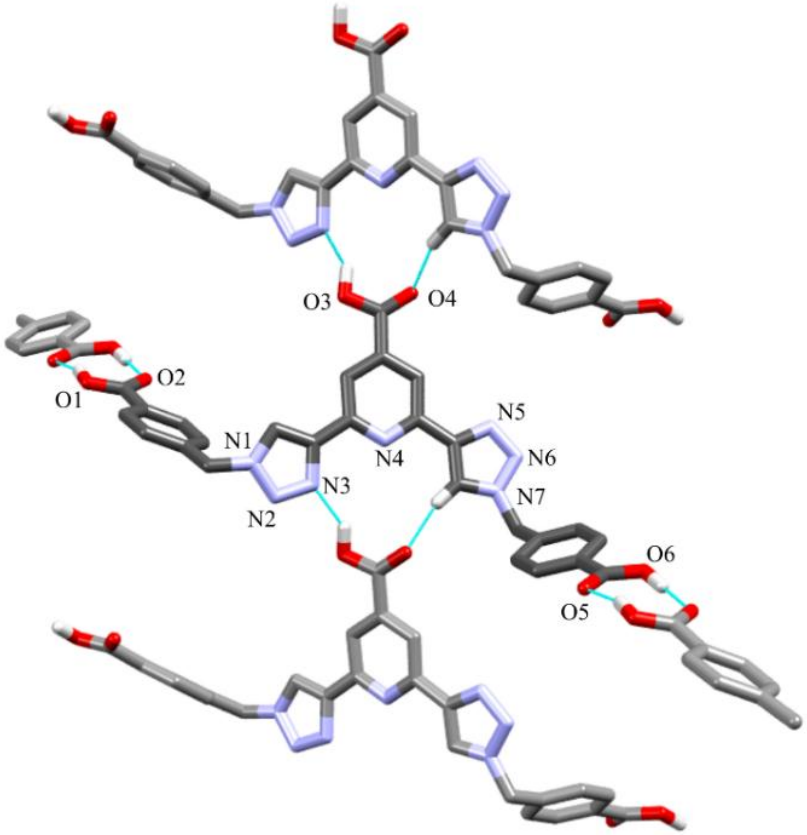

Figure 4.1 X-ray crystal structure of tri-carboxylic acid **btp** ligand **H$_3$84** displaying a three dimensional hydrogen bonded network. Each ligand is connected to four other ligands culminating in a four connecting node. Hydrogen atoms not involved in hydrogen bonding interactions omitted for clarity.

syn-anti orientation facilitates extension of the network in the remaining *c*-axis direction through an $R_2^2(12)$ motif.[339] The proximal nitrogen atom *N3* of one triazole ring faces in towards the pyridyl nitrogen atom as the former acts as a hydrogen bond acceptor for the carboxylic acid oxygen *O3* hydrogen bond donor (|D···A| is 2.668(4) Å, ∠ (*O-H···N*) is 143.78(17)°). Simultaneously, the proximal nitrogen *N5* of the other triazole unit is rotated away from the pyridyl nitrogen atom, resulting in a hydrogen bonding interaction between the triazolyl *C-H* hydrogen bond donor and the 4-pyridyl carboxylic acid oxygen *O4* acceptor (|D···A| is 3.075(4) Å, ∠ (*C-H···O*) is 163.4(2)°). The crystal structure also shows that despite the symmetric nature of the ligand there was no disorder detected over the two triazole ring junctions in the *syn-anti* conformation, each possessing 100% occupancy in their respective orientations throughout the system. This is the first time this **btp** conformation has been observed in the crystalline phase, contrasting with the more common *syn-syn* orientation[27,52,55,98-99,105,113-114,120,182,62,64] adopted when chelation of a metal ion occurs and the *anti-anti* conformation[27,52,55,102,156] which is observed for the unbound ligand.

Each **btp** molecule is connected to four other neighbouring molecules as a result of the hydrogen bonding giving rise to an overall 4-fold interpenetrated 3-dimensional extended structure, see Figure 4.2(B). The nets are described by the **cds** topology, where each **H$_3$84** molecule is defined as a 4-connecting node, see Figure 4.2(A).[340-341] In the idealised **cds** topology, square planar nodes connect to orthogonally-oriented square planar nodes. This is manifested in the crystal structure of **H$_3$84** by an ABAB packing fashion along the *c*-axis with the mean planes defined by the atoms comprising the **btp** moieties in alternating A and B layers twisted relative to each other by an angle of 45.97(15)° (Appendix E.5), as opposed

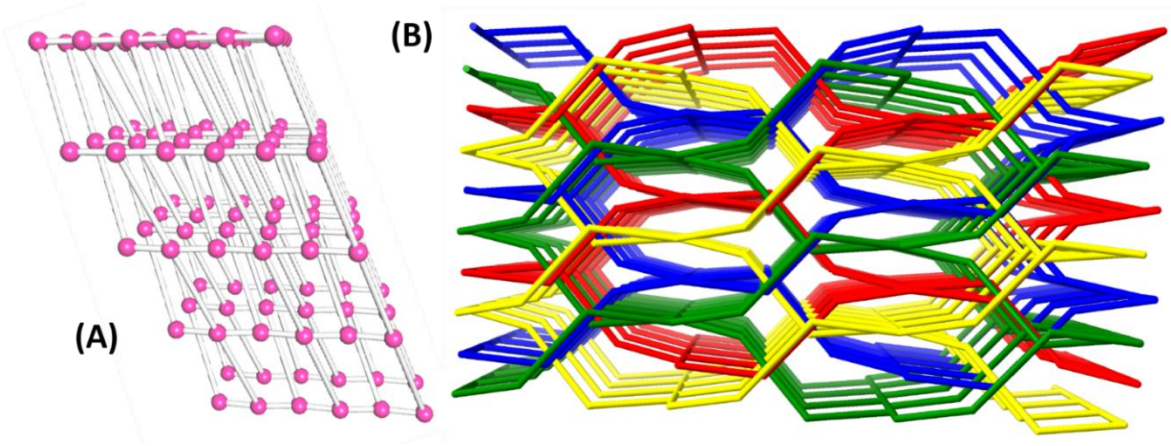

Figure 4.2 (A) Topology diagram for the **cds** network formed by **H$_3$84** with each of the pink spheres representing the 4-connecting nodes defined by **H$_3$84** molecules.[340-341] Interpenetrated networks are omitted for clarity. (B) Simplified rod diagram displaying the four fold interpenetrated hydrogen bonding network in the crystal structure of **H$_3$84**.

to 90° in the idealised **cds** topology.

The study of the solid state structure of **H$_3$84** provides insights into the possible molecular geometry of this compound in the supramolecular hydrogel formed through similar hydrogen bonding interactions as shown in Section 3.5. This is an area in which there is a large gap between design efforts and actual knowledge of the supramolecular structure of the gels within the fibers and at the junction zones.[6,171-172]

In a similar manner, as the presence of Na^+ was required in the formation of a robust hydrogel in Section 3.5, the sodium coordination polymer, *poly*-**Na$_3$84** may also provide further insight into the short range molecular arrangement of the component gelators. The coordination polymer *poly*-**Na$_3$84** was crystallized by evaporation from an aqueous mixture of **H$_3$84** and NaOH. The diffraction data were collected and solved by Dr. Brendan Twamley in the School of Chemistry, Trinity College Dublin and the structure model refined in the monoclinic *C*2/*c* space group which shows half a molecule of the fully deprotonated tri-carboxylate **84** and one crystallographically distinct H_2O molecule coordinating to 1.5 Na^+ atoms in the asymmetric unit. An intricate network comprised of **btp-**Na^+ and carboxylate-Na^+ coordination (Figure 4.3) is revealed extending in three dimensions. Propagation of the coordination polymer parallel to the *a*-axis is facilitated through carboxylate-Na^+ bonds of the aryl "arms" which are oriented *trans* to each other about the methylene linker. The network extends in the perpendicular direction along the *b*-axis *via* coordination of the

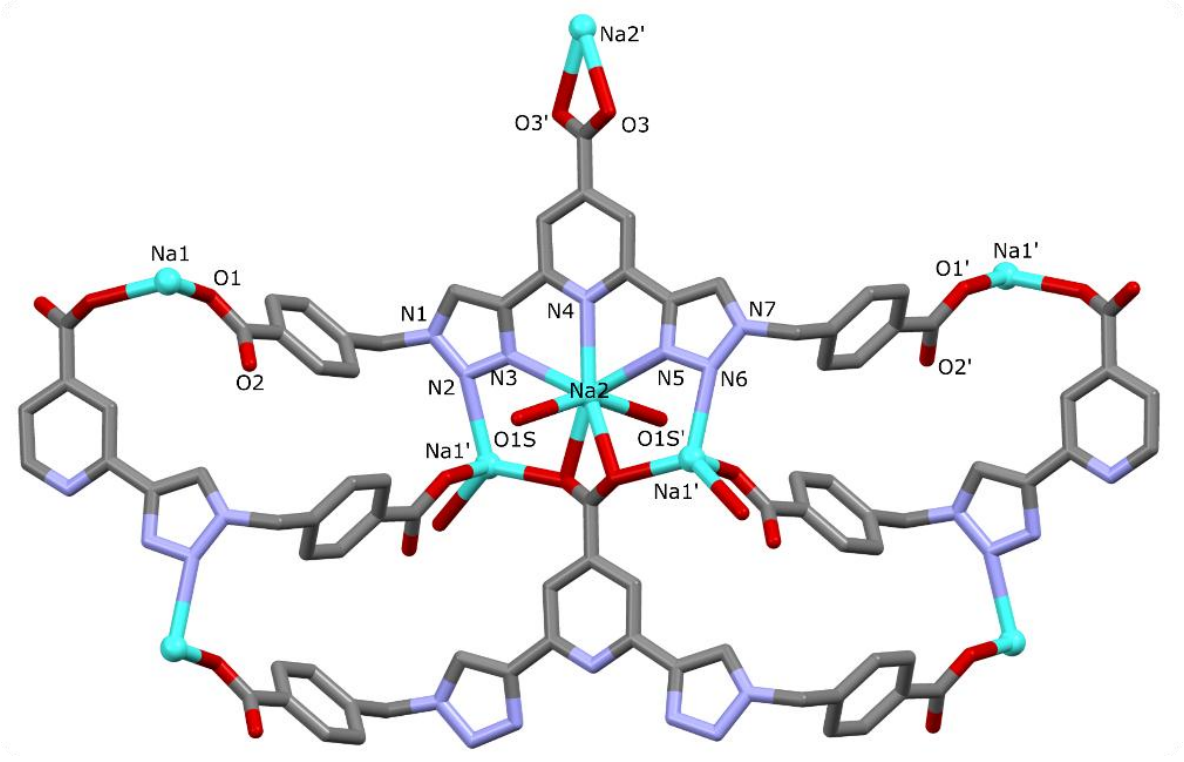

Figure 4.3 Fragment view of the *poly*-**Na$_3$84** coordination polymer.

Na^+ atom through the carboxylate situated at the 4-pyridyl position of **84** and N_3 coordination of the symmetry related Na^+ atom by the *syn-syn* orientation of the **btp** motif. These 2D sheets are connected in the remaining *c* direction through the shared vertices of the two crystallographically distinct sodium environments, *Na1* and *Na2*, which display trigonal bipyramid and *pseudo*-pentagonal bipyramid polyhedron geometries,[8] respectively, as shown in Figure 4.4. The basal vertices of the *Na1* trigonal bipyramidal coordination polyhedron consist of the medial triazolyl nitrogen atom *N6* with a |*Na1-N6*| bond distance of 2.4576(14) Å, the coordination of a H_2O molecule with |*Na1-O1S*| of 2.3708(13) Å, and finally the bridging carboxylate *O3* atom at the 4-pyridyl position of the adjacent ligand **84** with |*Na1-O3*| of 2.2772(11) Å. One of the apices of the trigonal bipyramid consists of the symmetry related bridging carboxylate *O3* atom with the same |*Na1-O3*| as its symmetry equivalent. The remaining apex consists of the monodentate binding carboxylate oxygen *O1* atom of the aryl "arms" with |*Na1-O3*| of 2.2777(11) Å. The *pseudo*-pentagonal bipyramidal geometry of the *Na2* coordination polyhedron is comprised by two symmetry related H_2O molecules situated at both apices with |*Na1-O1S*| of 2.5337(11) Å. The angle

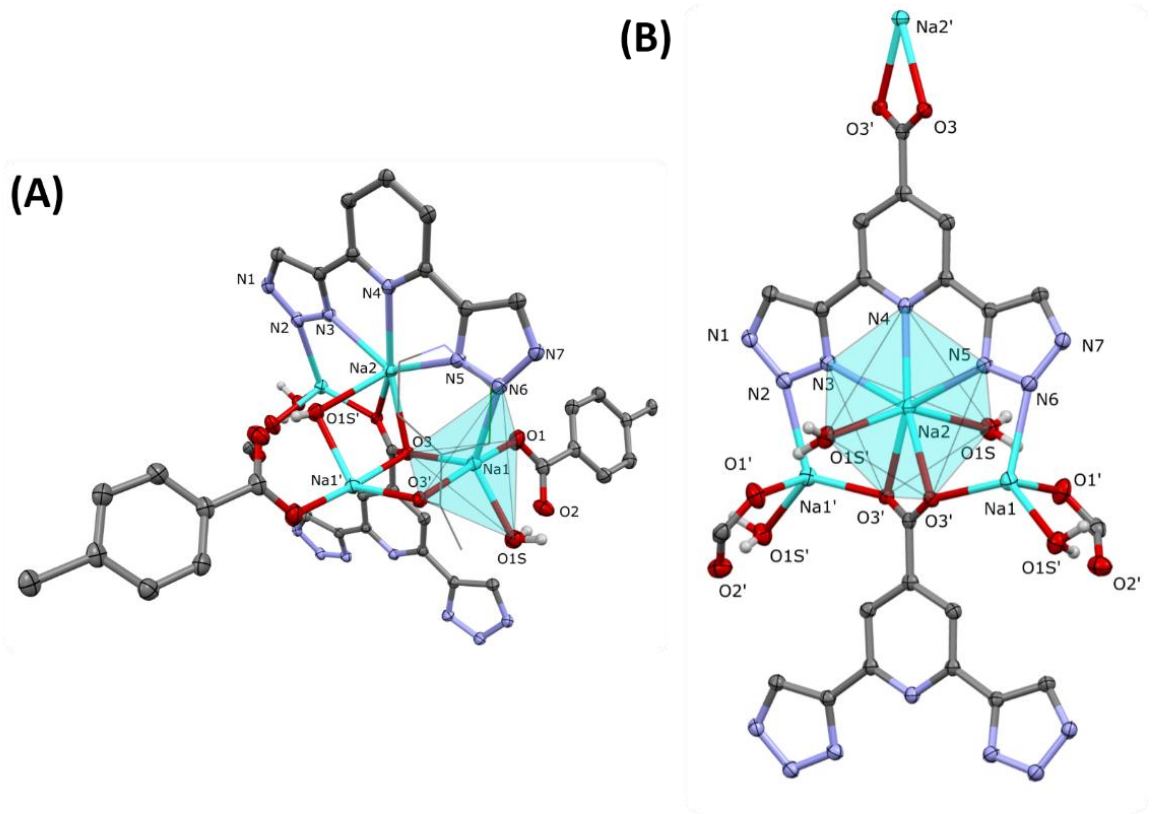

Figure 4.4 The two coordination environments of the Na^+ centres comprised by **btp**, carboxylate and H_2O binding interactions: (A) Trigonal bipyramid *Na1* and (B) pentagonal bipyramidal *Na2*. Thermal ellipsoids are displayed at 50% probability. Hydrogen atoms not attached to H_2O molecules omitted and one pyridyl moiety represented in wireframe for clarity.

∠ (*O1S-Na-O1S*) is 150.96(6)° and each of the hydrogen atoms of the H_2O molecules are involved in a hydrogen bonding interaction with the non-binding carboxylate oxygen atom *O2* of the aryl "arms" of two ligands of **84** with |*O2···O1S*| of 2.6900(14) Å and (∠ (*O-H···O*)) of 169(2)°. This non-binding carboxylate also accepts a hydrogen bond with the triazolyl C-H donor with |*O2···C*$_{triaz}$| of 3.2117(18) Å and (∠ (*C-H···O*)) of *ca.* 172.6°. The terdentate **btp** motif sits in the basal plane of the bipyramid with |*Na2-N4*| of 2.5030(18) Å, |*Na2-N3*| and |*Na2-N3*| of 2.6154(13) Å for the pyridyl nitrogen atom *N4* and the two proximal triazolyl *N3*/*N5* nitrogen atoms, respectively. The remaining two vertices of the *pseudo*-pentagonal bipyramid consist of a chelating bidentate carboxylate binding through oxygen atoms *O3* and *O3*' with |*Na2-N3*| of 2.4918(12) Å. The structure was closely packed and did not exhibit the potential to display permanent porosity, therefore attention was turned to *d*-metal ions such as Cu(II) and Zn(II) whose geometries have been shown to be more suitable for the formation of porous coordination polymers.[8]

4.3 Synthesis and structural studies of *poly*-[Cu$_3$**84**$_2$)]·(DMF)$_{3.3}$ (**100**)

The heating of DMF:H_2O mixtures of **$H_3$84** and *d*-metals in a sealed vial was carried out in the formation of the MOFs described herein. This solvent mixture was used as *in-situ* hydrolysis of the DMF solvent facilitates the generation of dimethylamine[342] which can deprotonate the carboxylic acid groups of **$H_3$84** resulting in the hard lewis base carboxylates suitable for metal ion binding. In this way, green blade-shaped crystals of **100** were obtained upon reaction of **$H_3$84** and copper(II) nitrate hemipentahydrate in a 1 mL mixture of 95:5 DMF:H_2O after heating at 100 °C for 2.5 hours. Phase purity was confirmed using PXRD, see Figure 4.5 and the experimental elemental analysis revealed that the air-dried sample contained 12 H_2O molecules per formula unit. The diffraction data were solved and

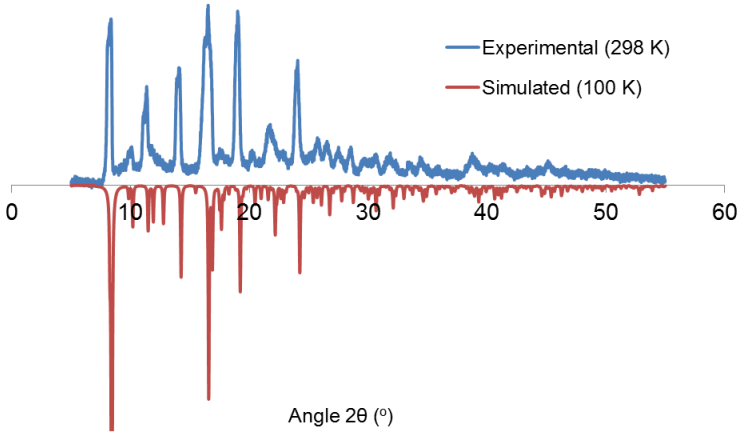

Figure 4.5 X-ray powder diffraction pattern for **100**.

the structure model refined in the tetragonal $I4_1cd$ space group with half of the molecular unit [Cu_3**84**$_2$], shown in Figure 4.6, in the asymmetric unit *i.e.* one fully deprotonated ligand molecule of **84** coordinating 1.5 Cu(II) atoms and also containing two DMF molecules modelled at 0.75 and 0.9 occupancy, respectively (Appendix E.6). The result is a two dimensional coordination polymer extending along the *a* and *b*-axes through metal-ligand coordination with packing in the *c* direction through π-π interactions. There are two Cu(II) coordination environments in the repeat structure: two **btp** ligands can be seen to be coordinating *Cu1 via* the pyridyl nitrogen atom *N4* and the two proximal triazolyl nitrogen atoms *N3* and *N5* (through a *syn-syn* orientation) giving an overall *pseudo*-octahedral N_6 coordination environment. The bite angles ∠ (*N3-Cu1-N4*) and ∠ (*N5-Cu1-N4*) are essentially the same at 78.3(4)° and 78.7(5)°, respectively. The pyridyl-Cu(II) bond length |*N4-Cu1*| is 1.978(8) Å and the corresponding triazolyl bonds lengths measure to be 2.207(12) Å and 2.184(12) Å for |*N3-Cu1*| and |*N5-Cu1*|, respectively. The second Cu(II) environment *Cu2* displays five coordinate geometry that is slightly distorted from square

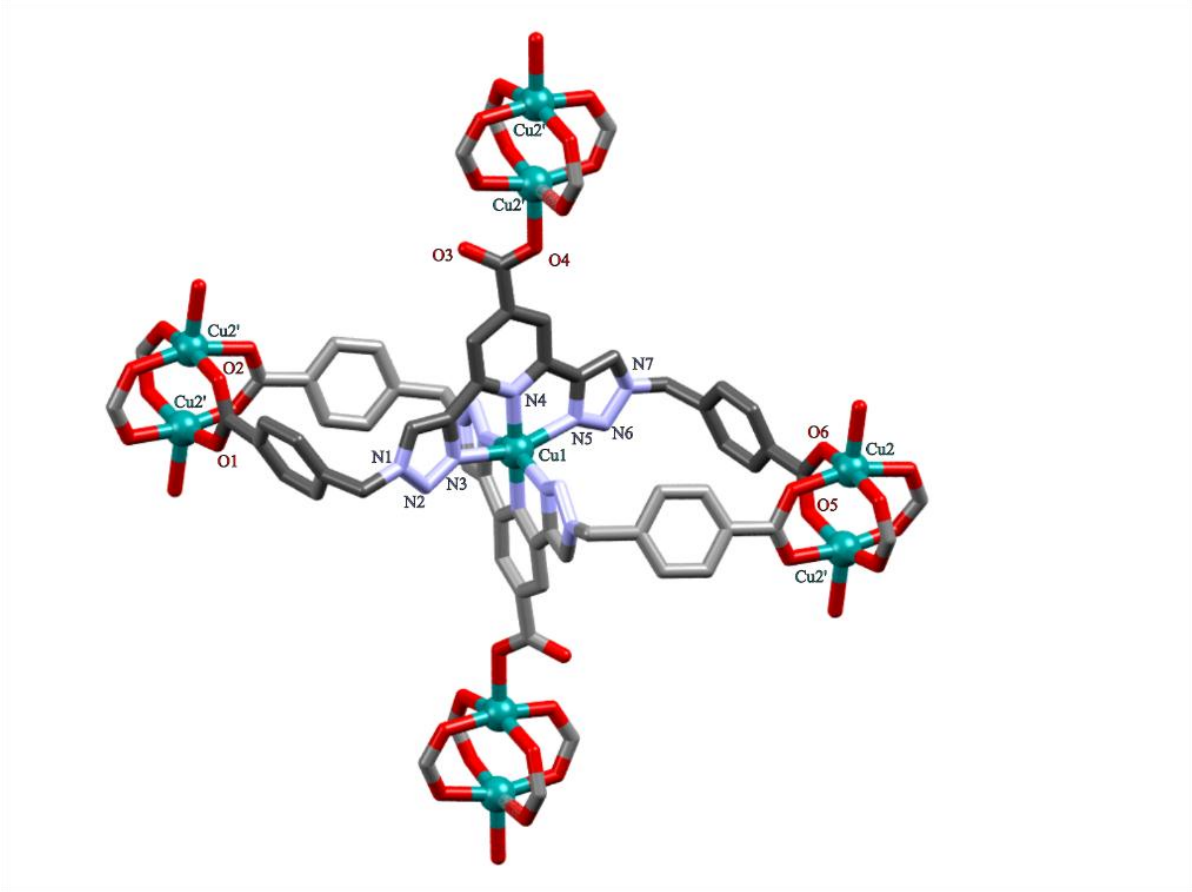

Figure 4.6 X-ray crystal structure of Cu(II) coordination polymer **100** displaying the two unique Cu(II) coordination environments with DMF molecules and hydrogen atoms omitted for clarity. Symmetry code used to generate only completed ligand equivalent atoms (-x, 1-y, +z).

pyramidal ($\tau_5 = 0.18$)[343] within a di-copper paddlewheel cluster through coordination to the aryl "arm" carboxylate groups. Each paddlewheel unit is comprised of only one crystallographically unique copper atom and three unique carboxylate groups. The aryl "arm" carboxylate oxygen atoms *O1*, *O2*, *O5* and *O6* are involved in linking two symmetry equivalent *Cu2* ions in the bridging mode, *μ2-κO:κO'*,[344] at the basal vertices of the square pyramids. The respective bond lengths for |*O1-Cu2'*|, |*O2-Cu2*|, |*O5-Cu2'*| and |*O6-Cu2*| measure to be 1.973(9) Å, 1.941(9) Å, 2.003(9) Å and 1.942(9) Å. The apical site is occupied by the 4-pyridyl carboxylate oxygen atom *O4* through a monodentate binding mode,[345] the bond length being significantly longer (|*O4-Cu2*| is 2.145(6) Å). The non-binding *O3* oxygen atom is involved in a non-classical hydrogen bonding interaction with a carbonyl hydrogen atom of a partially occupied DMF molecule (|D···A| is 3.41(2) Å, ∠ (*C-H···O*) is *ca.* 172.6°).

The topology is best described as a (4,4) net with both the octahedral *Cu1*:**btp** centres and the *Cu2* paddlewheel clusters acting as 4-connecting secondary building units (SBUs), see Figure 4.7(A). The di-copper $[Cu_2(\mu_2\text{-}COO)_4(\kappa^1\text{-}COO)_2]$ moiety can be simplified in this way from an alternative description as a binodal motif. This topology gives rise to the larger solvent channels existing parallel to the *c*-axis, see Figure 4.7(B) with narrower channels remaining in the two orthogonal directions along the *a*- and *b*-axes: the three in total accounting for approximately 12% of the total unit cell volume. The observed two dimensional array is the result of the *trans* conformation adopted by the aryl "arms" about

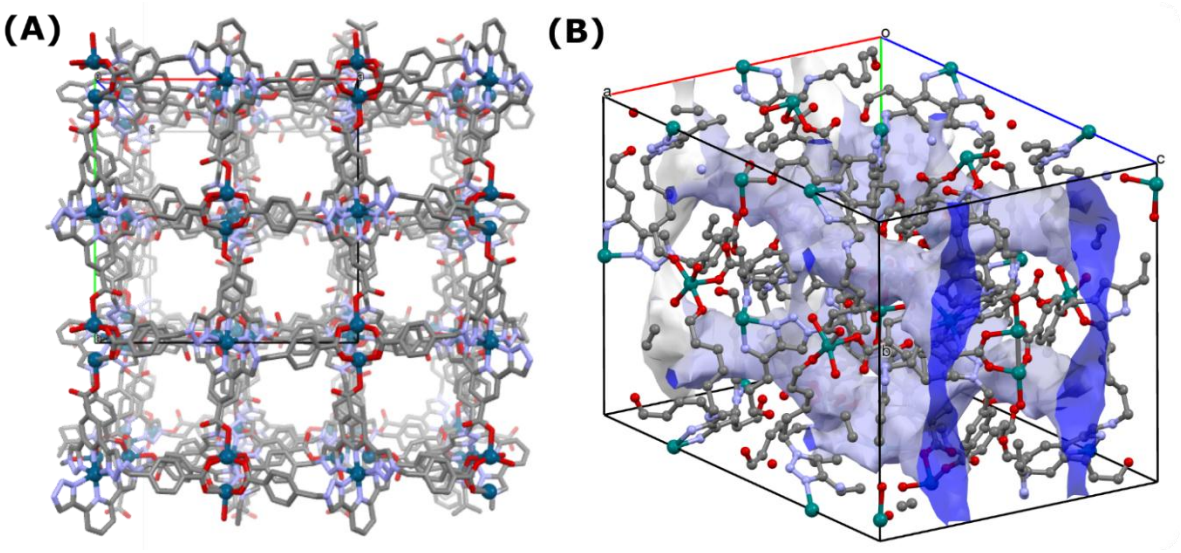

Figure 4.6 (A) Perspective view of the solvent channels that exist along the *c*-axis in the structure of **100**, hydrogen atoms and solvent molecules omitted for clarity. (B) Perspective view of the solvent accessible surface (blue) highlighting the channels that exist in a unit cell with the *b*-axis orientated vertically.

the methylene linker; each one of them facing in essentially directly opposite direction to each other (the dihedral angle between the mean planes defined by the atoms comprising the benzene rings on opposite aryl "arms" of **84** is essentially zero 0.0(6)°). Packing parallel to the *c*-axis is as a result of weak van der Waals and π-π stacking interactions between the benzoate arms and **btp** aromatic rings on adjacent two dimensional layers. These solvent channels visible from the single crystal X-ray diffraction analysis of coordination polymer system **100** indicate promising candidature for permanent porosity, however, there were difficulties in optimizing the synthetic conditions required to reproduce crystalline **100.** The PXRD of the failed attempts showed broad amorphous bands stretching the 2θ range (Appendix E.18). The reason for this remained unclear but one of the proposed causes of this inability to reproduce the synthesis may have been a result of varying degree of H_2O content in the DMF:H_2O solvent mixture, despite measuring out careful ratios of the solvent mixture.[342] Many ratios of DMF:H_2O were used (1:1, 2:1, 4:1, 9:1, 95:5, 98:2, 100:0) but to little avail, following the initial successful synthesis. Various concentrations of reactants were probed by altering the volume of the solvent mixture added (1 mL, 2 mL, 4 mL) and various stoichiometric ratios of metal to ligand were investigated. Different solvents such as DMSO and solvent mixtures including dimethylacetemide:H_2O were also used in the attempts to reform **100**. As a result, a sufficient quantity of material could not be synthesised such that gas adsorption studies could not be carried out in order to determine if **100** retained its structural integrity upon evacuation of the channels or in order to measure its gas uptake. Nevertheless, the as-synthesised sample with which satisfactory phase purity was obtained was analysed by thermal analysis alongside the CH_3CN exchanged sample.

4.4 Thermal Analysis of 100

TGA carried out on an as-synthesised sample of **100** displayed a multistep desolvation profile (Figure 4.8). A gradual loss in mass with increasing temperature was observed between 40 °C and 175 °C which levelled off to a very brief plateau in the region of 200 °C before decomposition began to occur at approximately 250 °C, consistent with the measured melting point (decomp.) of 254-258 °C. A total mass loss of *ca*. 24% wt. in the 40-250 °C range was observed, suggesting the loss of the lattice DMF molecules resolved by single crystal X-ray diffraction analysis. The calculated % wt. for the resolved DMF molecules in the crystal structure of **100** (3.3 molecules per [Cu_3**84**$_2$] unit) is 16.3% suggesting that there was a loss of additional solvent, which could not be resolved crystallographically, from the channels during thermal analysis. A sample was then soaked in CH_3CN for three days before

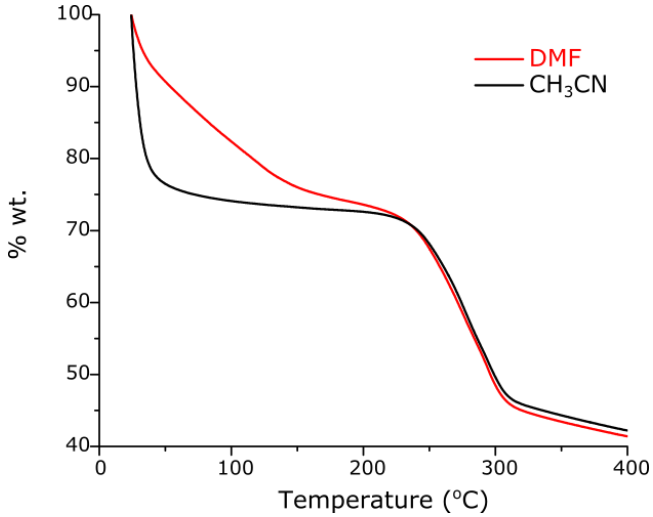

Figure 4.8 TGA of the as-synthesised sample of **100** (red) and CH_3CN exchanged sample (black).

carrying out the same thermal experiment. A rapid loss in mass was observed from the start of the experiment at 25°C as the solvent, presumably CH_3CN, was being rapidly removed from the pores. This mass loss began to plateau at approximately 50 °C until 250 °C totaling a loss of 24% wt. The total mass loss was the same for the CH_3CN exchanged sample of **100** (*ca*. 24% wt.) in the same temperature range (35-210 °C) as the as-synthesised sample of **100**. Despite the difficulties encountered in reproducing the synthetic conditions use to obtain **100**, the formation of the last two examples of Na^+ and Cu(II) coordination polymers with **H$_3$84** were encouraging for the development of functional MOF materials possessing channels suitable for guest uptake. Attempting a similar synthesis using Zn(II) was next carried out.

4.5 Synthesis and structural studies of *poly*-[Zn$_7$**84**$_6$]·((CH$_3$)$_2$NH$_2$)$_4$·(H$_2$O)$_{45}$ (**101**)

In a similar method to that which lead to the formation of **100**, a mixture of faint yellow hexagonal crystals and bright yellow blade-like crystals was obtained upon reaction of **H$_3$84** and zinc(II) nitrate hexahydrate in a mixture of 95:5 DMF:H_2O in a sealed vial heated at 100°C. By optimising the synthesis, such that the zinc(II) nitrate hexahydrate was present in slight excess (1.2 eq.), the hexagonal crystals of coordination polymer with formula *poly*-[Zn$_7$**84**$_6$]·((CH$_3$)$_2$NH$_2$)$_4$·(H$_2$O)$_{45}$, **101**, was exclusively produced in high yield as confirmed by PXRD analysis (Figure 4.9); the reaction being complete after 40 hours. The four $(CH_3)_2NH_2^+$ cations for every Zn$_7$**84**$_6$ repeat unit for charge balance could not be characterised crystallographically. The nature of the cation was instead ascertained using IR and NMR spectroscopy which will be detailed in Section 4.6. The second crystalline phase

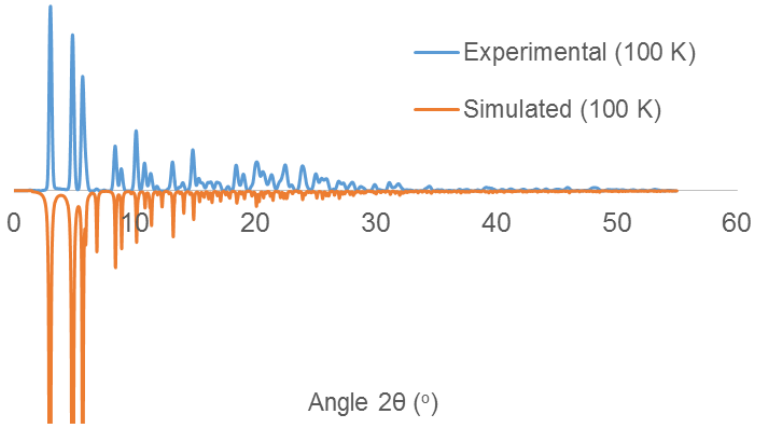

Figure 4.9 X-ray powder diffraction pattern for **101**.

which was present in the initial reaction mixture possessed Zn:**H84** (1:1) stoichiometry. Although this impurity phase (*poly*-[Zn(**H84**)]) could be characterised crystallographically, it was not possible to reproducibly generate the phase selectively. The structural features of *poly*-[Zn(**H84**)] will be presented in Section 4.9.

The structure model for **101** was refined in the cubic $Fd\bar{3}$ space group manifesting as a three dimensional coordination polymer. The asymmetric unit contains one molecule of **84** and two unique zinc sites; one of these sites *Zn1* is present at full crystallographic occupancy, while the other, *Zn2*, occupies a special position, with a total of 1 $^{1}/_{6}$ Zn atoms per molecule of **84** (*i.e.* $Z' = 0.16667$). As a consequence, the extended system is comprised of two distinct coordination environments (Figure 4.10); *Zn1* displays a pseudo trigonal bipyramidal coordination environment as a result of the **btp** *syn-syn* chelation and the binding of two monodentate carboxylate oxygen atoms on the benzyl arms of two adjacent ligands. The

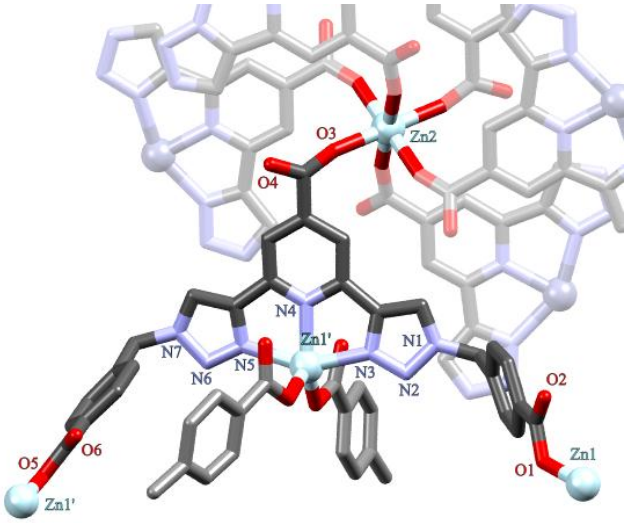

Figure 4.10 Fragment view of the crystal structure of **101** showing the connectivity of the two unique Zn(II) coordination environments.

geometry of *Zn1* shows some deviation from that of an idealized trigonal bipyramid with a value of $\tau_5 = 0.72$.[343] The basal plane of the coordination polyhedron consists of the pyridyl nitrogen atom *N4* and the pair of monodentate carboxylate oxygen atoms, *O1* and *O5*, whereas the apical sites are occupied by the two proximal triazolyl nitrogen atoms, *N3* and *N5*. The bite angles ∠ (*N3-Zn1-N4*) and ∠ (*N4-Zn1-N5*) are 76.6(2)° and 74.4(2)°, respectively. The bond length between the pyridyl nitrogen atom *N4* and *Zn1*, |N4-Zn1|, is 2.081(6) Å and the distances |*N-Zn*| are 2.158(6) Å and 2.206(6) Å for triazole nitrogen atoms *N3* and *N5*, respectively. The bond lengths |*O1- Zn1*| and |*O5-Zn1*| are 1.924(4) Å and 1.937(4) Å, respectively.

The second unique Zn(II) coordination environment, *Zn2*, has octahedral character and is coordinated by six monodentate carboxylate groups. This coordination environment is particularly unusual; crystallographically characterised examples of fully monodentate [Zn(RCOO)$_6$] centers have until now only been reported in homo- or hetero-metallic clusters featuring μ_2-κ*O*;κ*O′* bridging to additional metal ions.[346] This bridging is usually brought about by the formal 4^- charge of the central coordination sphere. However, in the present case, the non-coordinating oxygen atoms are involved in *C-H···O* hydrogen bonding interactions with the nearby triazole *C-H* groups (|*C···O*| is 3.003(9) Å and ∠ (*C-H···O*) is 149.1(4)°), negating their ability to coordinate to an additional cation (Appendix E.8). The octahedral *Zn2* node links six **btp** ligands, each coordinating through the 4-pyridyl carboxylate position. All six metal-ligand bonds are equivalent (|*O1-Zn2*| is 2.087(6) Å), as the *Zn2* atom resides coincident with crystallographic improper rotation axes. The two *C-O* bonds are the same length within error (|*O4-C*| is 1.251(9) Å and |*O3-C*| is 1.232(9) Å) and consistent with a fully ionic carboxylate rather than the more localised bonding mode observed in *Zn1*. A similar hydrogen bonding interaction also occurs involving the non-coordinating oxygen atoms from the *Zn1* coordination sphere with the nearby triazole *C-H*, and is common for **btp**, other 1,2,3-triazole containing and related species[54,347] (|*C···O*| is 3.342(9) Å and ∠ (*C-H···O*) is 161.0(4)°).

The intricate connectivity of **btp** and Zn(II) ions within complex **101** makes a direct comparison of the topology to a known 3-dimensional net challenging. Avoiding the non-trivial trinodal 3,4,6-connected network description arrived at by assigning nodes to each unique metal and ligand, the most sensible topological description was arrived at by assigning a six-connected node to the central octahedral *Zn2* which further encompasses all six of the coordinated ligand molecules and their **btp**-chelated *Zn1* ions, see Figure 4.11(B). With this description, the network 'links' are simply the Zn-carboxylate bonds involving

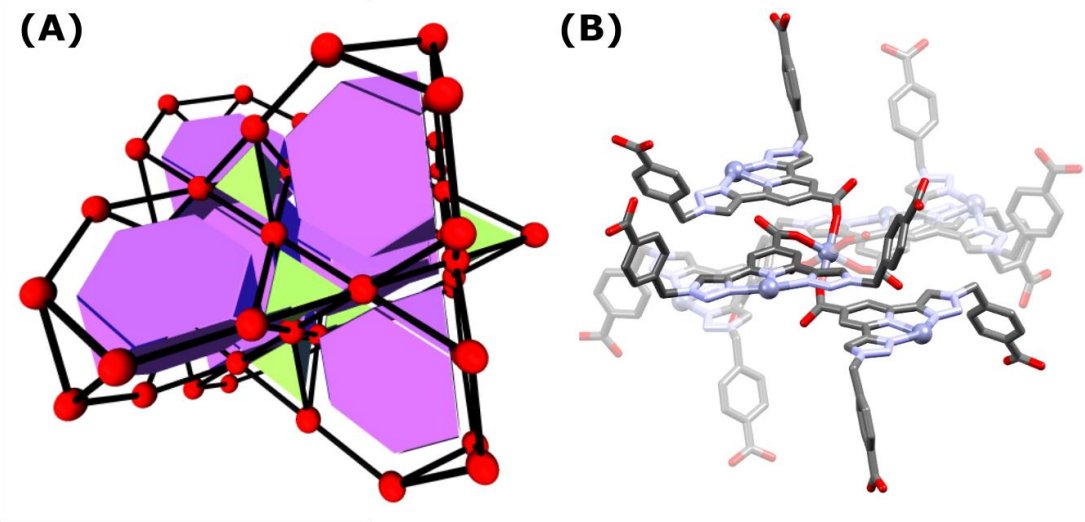

Figure 4.11 (A) Graphical representation of the idealised **crs** topology.[340-341] (B) The fragment view of the six connecting node represented by the red spheres in the **crs** topological diagram.

Zn1, and each of these nodes, as defined above, links to only six others. Any two adjacent nodes are linked to each other by 4 *Zn*-carboxylate links occurring through the pair of symmetry related *Zn1-O1* and *Zn1-O5* bonds, see Figure 4.12(A). The resulting network topology, although somewhat esoteric, is described by the **crs** (cristobalite) net,[340-341] equivalent to the augmented **dia-e** net, see Figure 4.11(A). The six-connecting nodes result in a net of edge-sharing truncated tetrahedra ([$3^4.6^4$], purple) and smaller tetrahedral ([3^4], green).[219-220] No interpenetration was evident in the structure of **101**. The extended structure

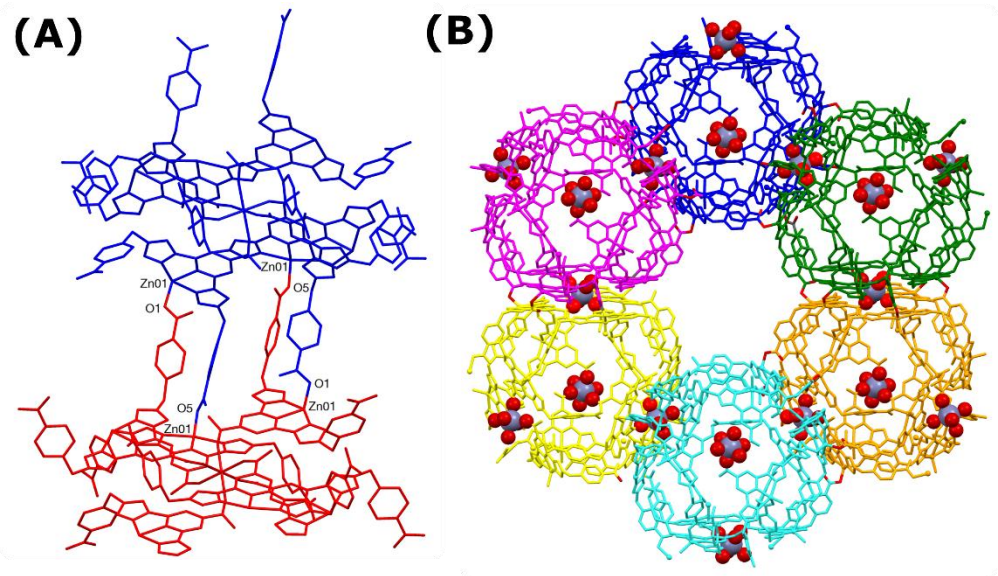

Figure 4.12 (A) Capped stick representation showing 4 Zn-carboxylate links connecting two adjacent nodes in the **crs** topology through the pair of symmetry equivalent *Zn1-O1* and *Zn1-O5* bonds. (B) Rhomboidal cages each connected to 4 other equivalent cages by octahedral *Zn2* centres. The *Zn2* centres shown in space fill representation for clarity.

is dominated by rhomboidal cages connected face-to-face to four equivalent cages by the octahedral *Zn2* centres, see Figure 4.12(B). The remaining two faces, not occupied by Zn2 octahedral sites, are directed into the large solvent channels which exist in all three dimensions, see Figure 4.13(A). A mixture of straight channels and undulated channels are interconnected; the three dimensional network of pores, in total, accounting for approximately 45% of the total unit cell volume, see Figure 4.13(B). It should be noted that, taking into account the $(CH_3)_2NH_2^+$ cations (64 of which per unit cell, which account for only *ca.* 2.5% of the total unit cell volume), the volume of these channels still allows for considerable solvent-accessible volume. These channels are irregular hexagonal in nature and alternate between two distinct sizes *i.e.* approximately 21 Å and 14 Å at their maximum edge-to-edge interatomic distance, respectively (Appendix E.8). The aromatic rings of the aryl carboxylate "arms" dominate the make-up of the edges of the two differing hexagonal channels with the *Zn1* centres positioned at each of the six corners. Following the elucidation of the channel system in the structure of **101**, attention was turned to guest exchange studies which will be discussed in Section 4.7.

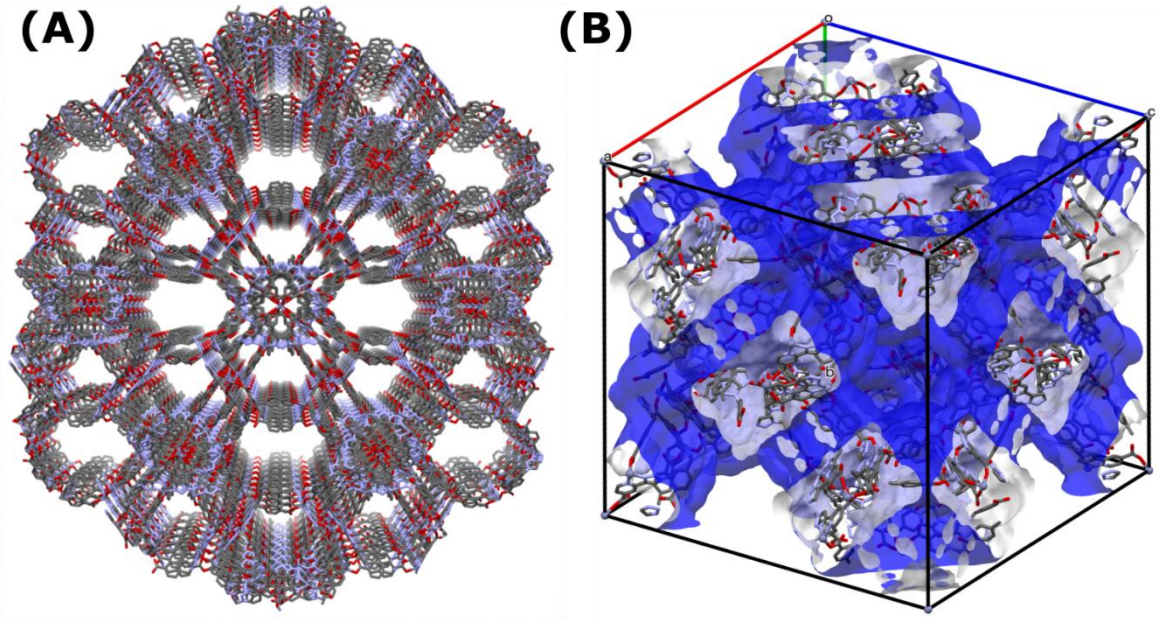

Figure 4.13 (A) Perspective view of the solvent channels in the crystal structure of **101**, hydrogen atoms omitted for clarity. (B) Perspective view of the solvent accessible surface (blue) highlighting the channels that exist in a single unit cell.

4.6 Identification of the charge balancing $(CH_3)_2NH_2^+$ cation

The highly Lewis basic *Zn2* site is the most likely candidate for hydrogen bonding interactions with charge balancing $(CH_3)_2NH_2^+$ cations. Their intractably disordered nature made them impossible to characterise crystallographically. The $(CH_3)_2NH_2^+$ cations most likely originate from *in-situ* hydrolysis of the DMF solvent.[342] The cation was identified using IR (Figure 4.14) and NMR spectroscopy (Figure 4.15); in the IR spectrum of **101** after exchange with CH_3CN, a broad absorbance at 2977 cm^{-1} typical for cationic ammonium *N-H* stretches indicated the presence of $(CH_3)_2NH_2^+$.[348] Digesting the crystals of **101** in deuterated TFA allowed the characteristic $(CH_3)_2NH_2^+$ proton resonances to be seen in the ^1H NMR spectra at 2.89 ppm integrating appropriately. The ratio of the integrals for resonance *e* and for the methyl groups of $(CH_3)_2NH_2^+$ was approximately 4:4 accounting for a **84**:$(CH_3)_2NH_2^+$ 6:4 stoichiometric ratio.

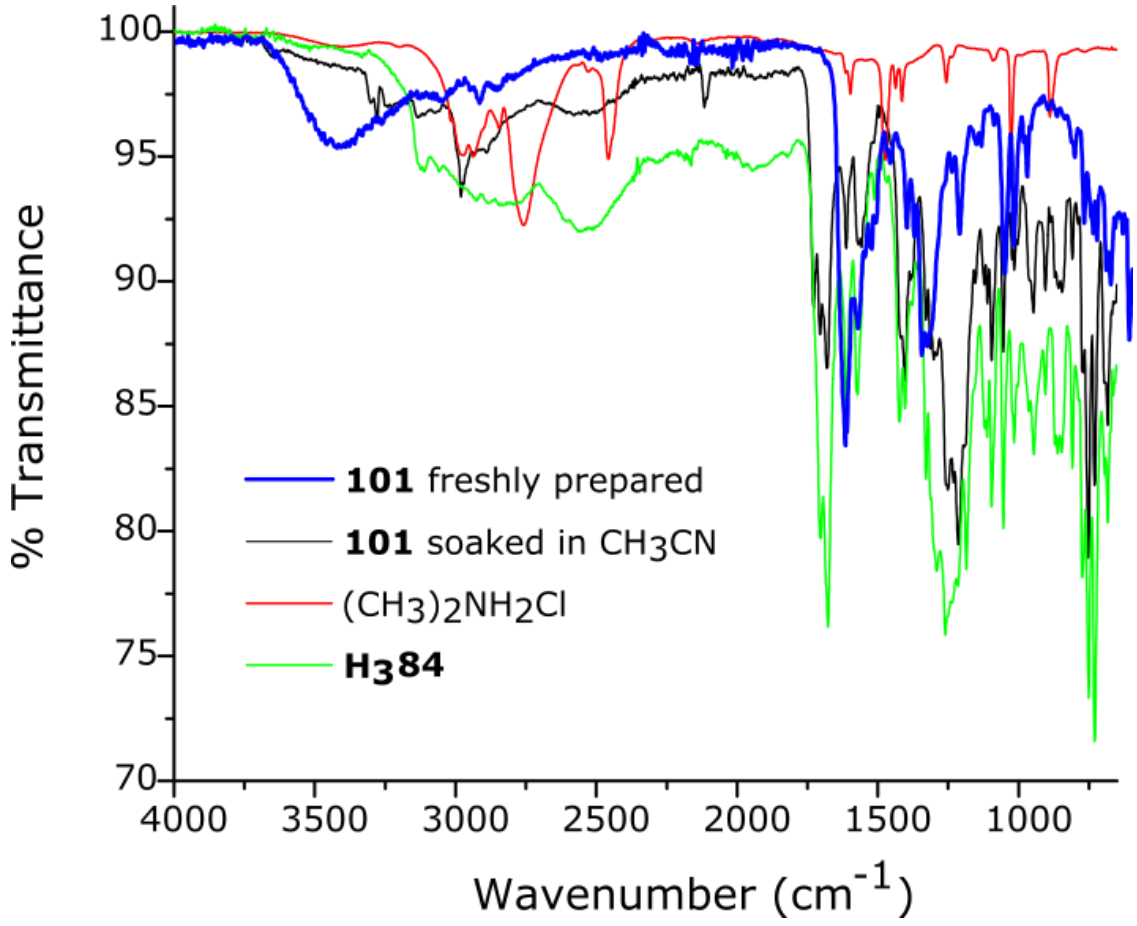

Figure 4.14 IR spectrum comparison between **$H_3$84** (green), H_2NMe_2Cl (red), as-synthesised freshly prepared (blue) and **101** after exchanging with CH_3CN (black). Evidence of a strong broadened NH stretching band in **101** around 3000 cm^{-1} (more easily visible in the CH_3CN exchanged spectrum) is indicative of a $(CH_3)_2NH_2^+$ charge balancing counter-ion.

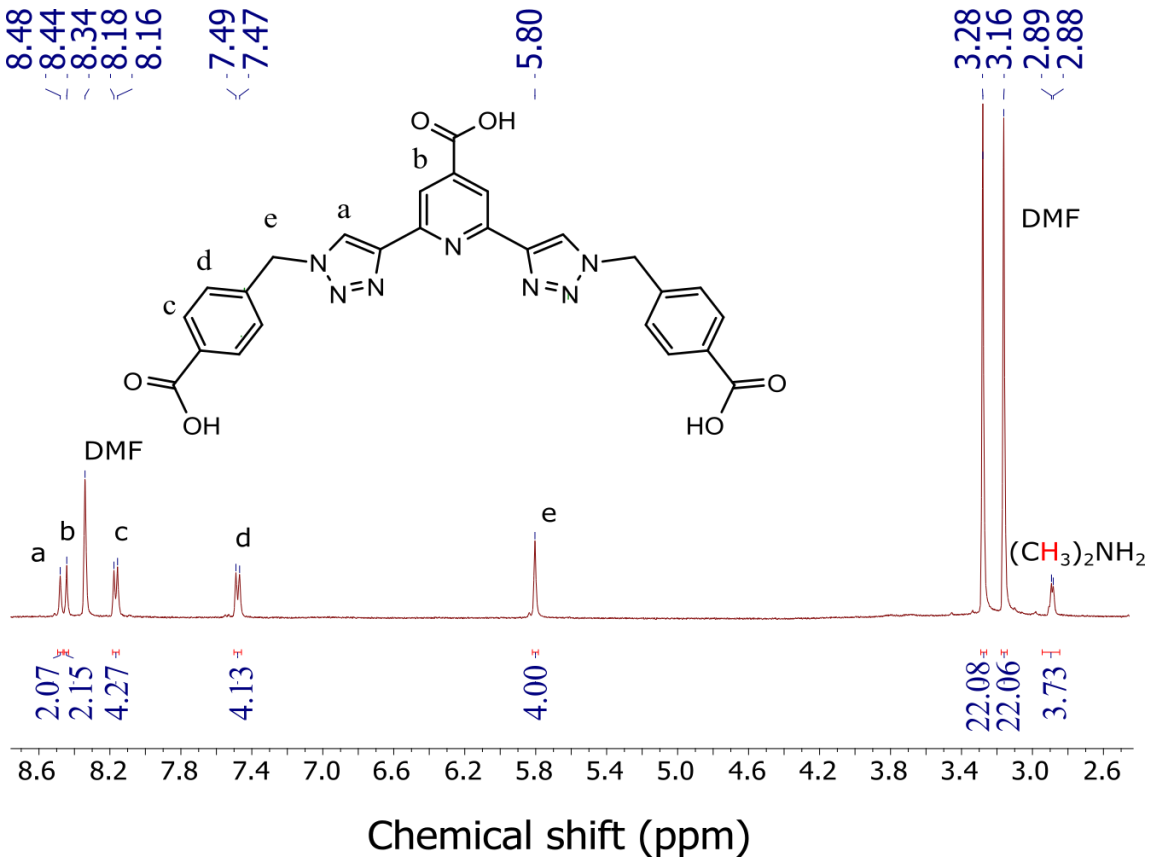

Figure 4.15 ^{1}H NMR (TFA-d_1) of freshly prepared **101** indicating solvent channels comprised of predominantly DMF and the presence of $(CH_3)_2NH_2^+$ cation at 2.88 ppm in appropriate 6:4 **84**:$(CH_3)_2NH_2^+$ ratio.

4.7 Thermal and gas adsorption studies

TGA of freshly isolated **101** revealed a multistep desolvation profile upon heating in a nitrogen atmosphere, see Figure 4.16(A). The freshly prepared, predominantly DMF-filled compound experienced a loss in mass between approximately 60 °C and 120 °C which then flattened at 160 °C between 65% and 61% residual mass before another sharp decrease in mass occurred at 350 °C due to decomposition consistent with the measured metling point of 348−351 °C (decomp). The total loss in mass was approximately 39% (wt.) in the 40-350 °C temperature range. After soaking **101** in CH_3CN, a rapid loss in mass was observed beginning at room temperature and reaching a plateau at approximately 73% residual mass below 100 °C, see Figure 4.16(B). From this data it can be concluded that the lattice solvent molecules in **101** are readily exchanged for the more volatile CH_3CN upon soaking. The effect of exposing a sample of **101** to the atmosphere was also investigated using TGA. The thermal profiles of samples of **101** which had been air dried over the course of four months were strikingly similar, see Figure 4.16(B), and in contrast to a freshly prepared

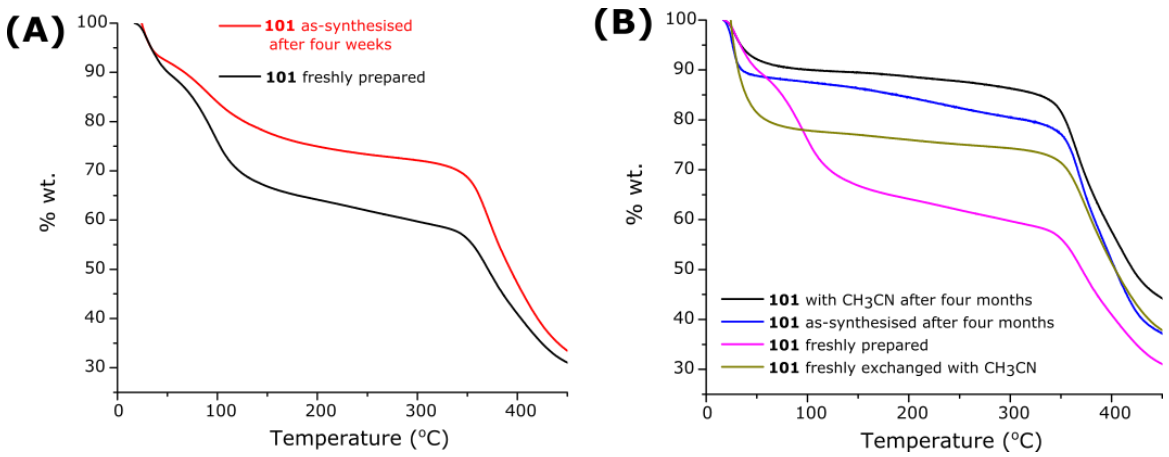

Figure 4.16 (A) TGA of freshly prepared **101** (black) and as-synthesised **101** after four weeks (red). (B) TGA of **101** left in unsealed vials for extended periods displaying gradual exchange of channel solvent molecules with H_2O from atmosphere (blue, black) compared with freshly prepared samples of as-synthesised **101** (magenta) and exchanged with CH_3CN (brown).

sample comprised predominantly of DMF as observed by ^1H NMR of the digested fresh sample (Figure 4.15). There was a more substantial loss in mass for the freshly prepared samples but a lesser loss in residual mass for samples which were air dried indicative of the channel solvent being exchanged with water in the atmosphere. This observation explains why the thermal profiles of **101**, regardless of initial solvent occupying the channels (DMF or CH_3CN), behave similarly after exposure to the atmosphere for an extended period. An intermediate stage of solvent exchange with atmospheric water shows a lesser extent of volatile mass loss, see Figure 4.16(B) due to the shorter four week period of time it was in contact with the atmosphere. This observation that DMF solvent molecules had been exchanged with H_2O molecules was corroborated after elemental analysis on an air-dried sample indicated the presence of water within the channels and could not be suitably fitted allowing to DMF within the channels (found %C 42.73, %H 4.10, %N 14.49, calculated for $[Zn_7\mathbf{84}_6]\cdot(C_2H_8N)_4\cdot(H_2O)_{45}$ *i.e* $C_{164}H_{218}N_{46}O_{81}Zn_7$ %C 42.97, %H 4.78, %N 14.06).

Based on the substantial capacity of **101** for neutral guest molecules, gas adsorption experiments were also carried out by Kevin Byrne in the Schmitt Group at SNIAM, University of Dublin..[216] Following CH_3CN exchange, the sample was activated at 100 °C under dynamic vacuum overnight. Surprisingly, the N_2 (77K), H_2 (77K) and CO_2 (273K) adsorption isotherms showed much lower than expected uptake for the thermally activated material (Figure 4.17), with a maximum loading of ~ 3.75% wt. CO_2 at 1 atm and 278K, and lower loadings for N_2 and H_2. These data suggest that the large and interconnected channels in the as-synthesized material are contracted or collapsed following evacuation. PXRD analysis of the CH_3CN-exchanged material showed a loss of crystallinity after drying

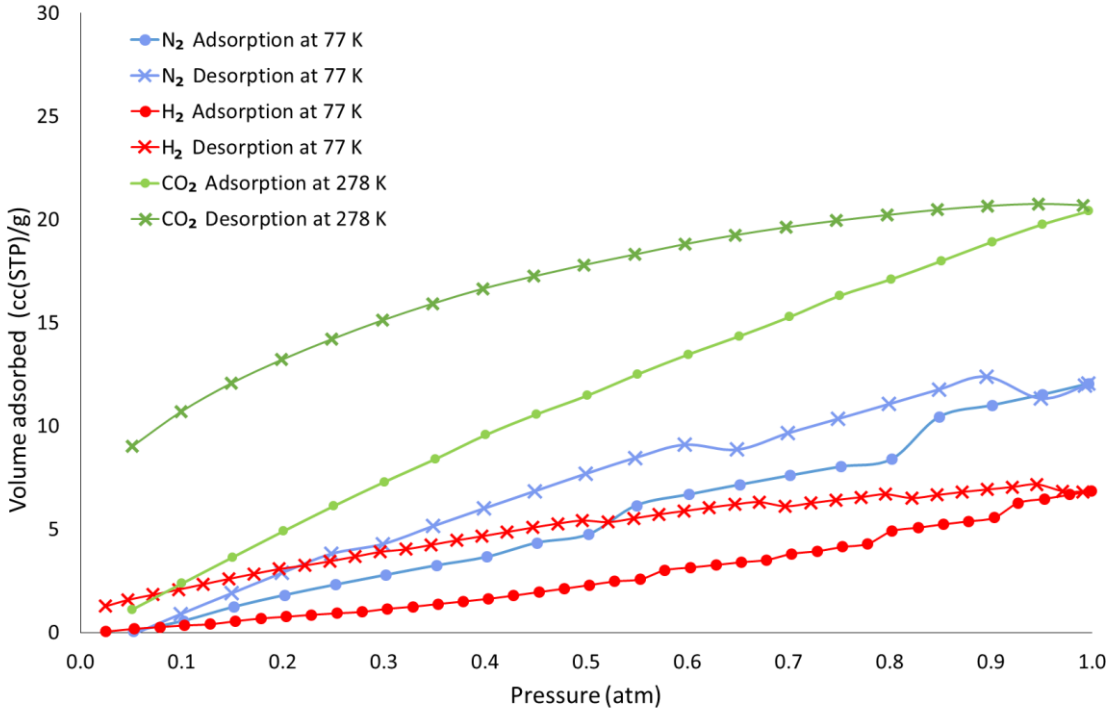

Figure 4.17 Gas adsorption isotherms of **101** after exchange with CH_3CN and activation under dynamic vacuum at 373 K overnight for N_2, H_2 both measured at 77 K and CO_2 measured at 278 K.

(Appendix E.20). This outcome is disappointing for a 3-dimensional framework material; nonetheless, such instability can be rationalised as a consequence of the flexibility of the **btp** ligand supporting the bulk material, and may also be related to the expected lability of the pivotal *Zn2* node. Nevertheless, other forms of guest uptake were investigated as will be presented in Section 4.10.

4.8 Modelled solvent channel occupancies for 101

SQUEEZE[349] generated a value for the electron count for non-localised solvent molecules of 26,955 e^- per unit cell. By including the e^- contribution of the four $(CH_3)_2NH_2^+$ cations, the SQUEEZE value was reduced to 25,227 e^- per unit cell volume. This equated to 631 DMF solvent molecules per unit cell. The observed mass loss from a fresh sample of **101** (TGA: 40-350 °C) was ~37 - 39%, (Figure 4.16(B) (magenta line)). This equated to between 582 and 633 DMF solvent molecules and between 23,290 and 25, 332 e^- per unit cell volume which was in good agreement with the value calculated by SQUEEZE. This was also in good agreement with ^{1}H NMR spectrum of digested freshly prepared sample of **101** in TFA-d_1 (Figure 4.15). Both DMF methyl peaks integrated to 22 protons each relative to the 4 methylene protons per **84** which equated to 44 DMF molecules per $[Zn_7\mathbf{84}_6]$ unit or 704 DMF molecules per unit cell (there are 16 $[Zn_7\mathbf{84}_6]$ formula units per unit cell).

However, the best fit for an air-dried sample by elemental analysis was $[Zn_7\mathbf{84}_6]\cdot((CH_3)_2NH_2)_4\cdot(H_2O)_{45}$, suggesting a void content, in addition to the four $(CH_3)_2NH_2^+$ charge balancing counterions, of 45 H_2O molecules per $Zn_7\mathbf{84}_6$ formula unit. Calculated electron count for these non-localised H_2O solvent molecules was 8896 e^- per unit cell; the discrepancy between this electron count and the electron count provided by SQUEEZE (25,227 e^- per unit cell volume) arose as DMF solvent was exchanged with H_2O solvent on air-drying after several weeks. The calculated volatile mass from elemental analysis corresponding to the 45 H_2O molecules per $Zn_7\mathbf{84}_6$ formula unit was 17.6%, and the observed mass loss (TGA: 40-350 °C) was ~16%, (Figure 4.16(B) (blue line)) which is in good agreement.

Having characterised the dominant phase **101** thoroughly using a range of methods including X-ray diffraction analysis, TGA, IR, ^{1}H NMR, elemental analysis and gas adsorption experiments, the structural nature of the Zn(II)-containing impurity phase will now be presented.

4.9 Crystal structure of impurity phase *poly*-[Zn(H84)]

As discussed in Section 4.5, a mixture of two phases was produced in the initial reaction attempts when $\mathbf{H_3 84}$ and zinc(II) nitrate hexahydrate were reacted in a 1:1 stoichiometric ratio in 95:5 DMF:H_2O at 100 °C. The diffraction data for the impurity phase *poly*-[Zn(**H84**)] were solved in the monoclinic *C2/c* space group revealing a one dimensional coordination polymer (Figure 4.18) with half of the **H84** ligand and one Zn(II) centre in the asymmetric unit (Appendix E.9). The 4-pyridyl carboxylic acid remains protonated such that coordination occurs through the aryl carboxylate moieties and the **btp** unit. The system consists of a single Zn(II) coordination environment which is trigonal bipyramidal, also seen in the case of *Zn1* in the structure of **101**. The polyhedral geometry shows some deviation from that of an idealized trigonal bipyramidal with a value of $\tau_5 = 0.82$ compared with a value of $\tau_5 = 0.72$ for **101**. As before, the basal plane of the coordination polyhedron consists of the pyridyl nitrogen *N4* and the pair of monodentate carboxylate oxygen atoms, *O1* and *O1'*, whereas the apical sites are occupied by the two proximal triazolyl nitrogen atoms, *N3* and *N3'*. The bite angle ∠ (*N3-Zn1-N4*) is 75.40(7)° while the bond length $|N_{pyr}\text{-}Zn|$ is 2.118(4) Å and $|N_{triaz}\text{-}Zn|$ is 2.161(3) Å. The |*O1-Zn1*| bond length measures to be 1.992(2) Å. Extension of the polymer system parallel to the *a*-axis though metal-ligand coordination is evident from the crystal packing. Generation of the linear chain is facilitated through the approximate orthogonal orientation of each aryl carboxylate "arm" in a *trans* manner to the

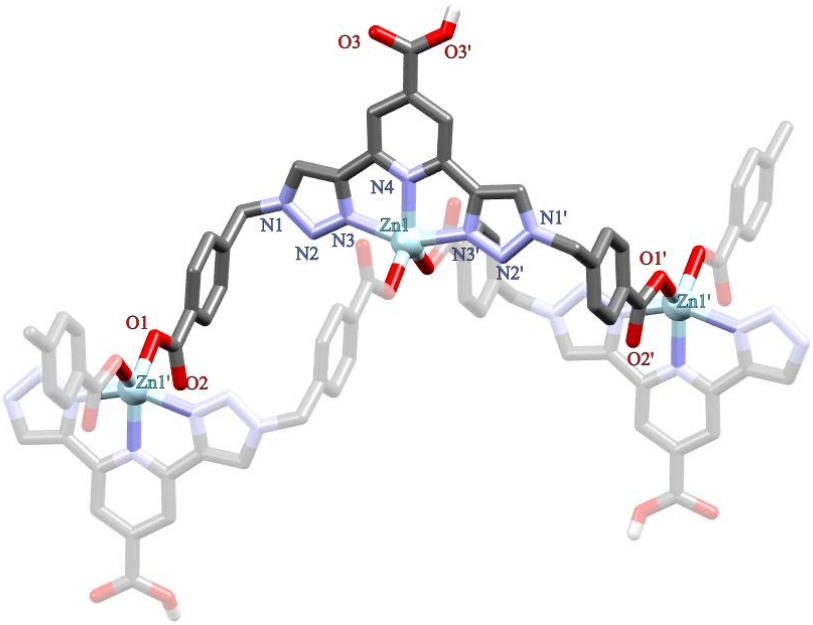

Figure 4.18 Fragment view of the crystal structure of *poly*-[Zn(**H84**)] showing the connectivity of the one unique Zn(II) coordination environment. The carboxylic acid proton's occupancy is distributed equally over the two *O3* and *O3'* atoms.

btp motif about the methylene linker (the dihedral angle between the mean planes defined by the atoms comprising the benzene rings relative to those comprising the **btp** motif is ca. 93°. Packing in the *a*-axis direction is as a result of π-π stacking interactions between the **btp** aromatic rings on adjacent one dimensional chains. Additionally the non-binding carboxylic acid oxygen *O2* is involved in a hydrogen bonding interaction with the triazole *C-H* (|D···A| is 3.089(4) Å, ∠ (C-H···O) is 152.0(2)°) belonging to a neighbouring polymer chain which is inverted through symmetry. Although the direction of the hydrogen bonding is along the *b*-axis, the interaction links adjacent 1-D chains along the *c*-axis. This packing gives rise to the large linear solvent channels, rhomboidal in shape, extending along the *c*-axis (Figure 4.19) accounting for approximately 18% of the total unit cell volume. The carboxylic acid proton which is pointing into a void, is disordered over two symmetry related positions. The diffuse electron density corresponding to a potential hydrogen bonding acceptor could not been modelled and has been treated using the SQUEEZE technique. Further analysis of this phase was not carried out due to difficulties in reproducibly generating the phase selectively. In contrast, the dominant phase **101** could be reliably reproduced in sufficient quantities and excellent purity for further analysis of its functional properties. In particular, the anionic framework of MOF **101** was investigated for its use as a cation exchange matrix.

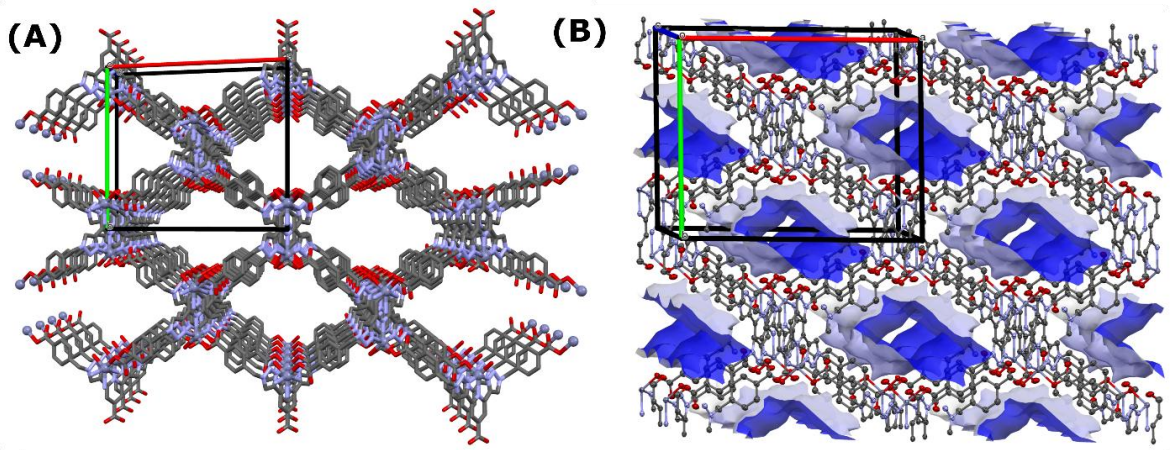

Figure 4.19 (A) Perspective view of the solvent channels that exist along the diagonal in the squeezed structure of *poly*-[Zn(**H84**)], hydrogen atoms omitted for clarity. (B) Perspective view of the solvent accessible surface (blue) highlighting the channels that exist in a 2×2×2 cell with the *b*-axis orientated vertically.

4.10 Cation exchange experiment.

Due to the apparent reduction in free volume of **101** upon evacuation or drying in air, an alternative investigation into the guest uptake properties was undertaken, taking advantage of the anionic framework of **101**. It was found that soaking **101** in concentrated solutions of cationic dyes such as ethidium bromide and methylene blue for 3 days resulted in uptake of the dyes, evident from a color change observed in the individual crystals (Figure 4.20). To confirm that this color change was not simply surface adsorption of the dye, the crystals were soaked with CH_3CN solution for several days until the supernatant ran colorless; after this time no further leeching of dye into the supernatant was observed. The characteristic red color and blue colour of ethidium bromide and methylene blue, respectively, can clearly be seen in the thinner and more transparent crystals whereas the thicker larger crystals appear opaque. The CH_3CN solvent was then replaced with a concentrated stock solution of tetraethylammonium iodide (TEAI) in CH_3CN. Immediately upon addition, the supernatant took on the color of the escaping dye molecules as they were exchanged with the TEA cations. Specific aliquots of the supernatant solution were taken at defined time intervals and the corresponding absorbance was recorded. In each case, the dye-loaded samples showed a release of the respective dye molecule into the supernatant. The absorbance plot and release profile for methylene blue are shown in Figure 4.21. Bands at 204 nm and 247 nm did not undergo any significant changes indicative of the excess TEAI in the solution mixture, while the bands at 293 nm and 655 nm increased in absorbance as the methylene blue guest molecules were liberated from the solid **101**. The concentration increased substantially until between 90 and 120 minutes after the TEAI solution was added and at this point no

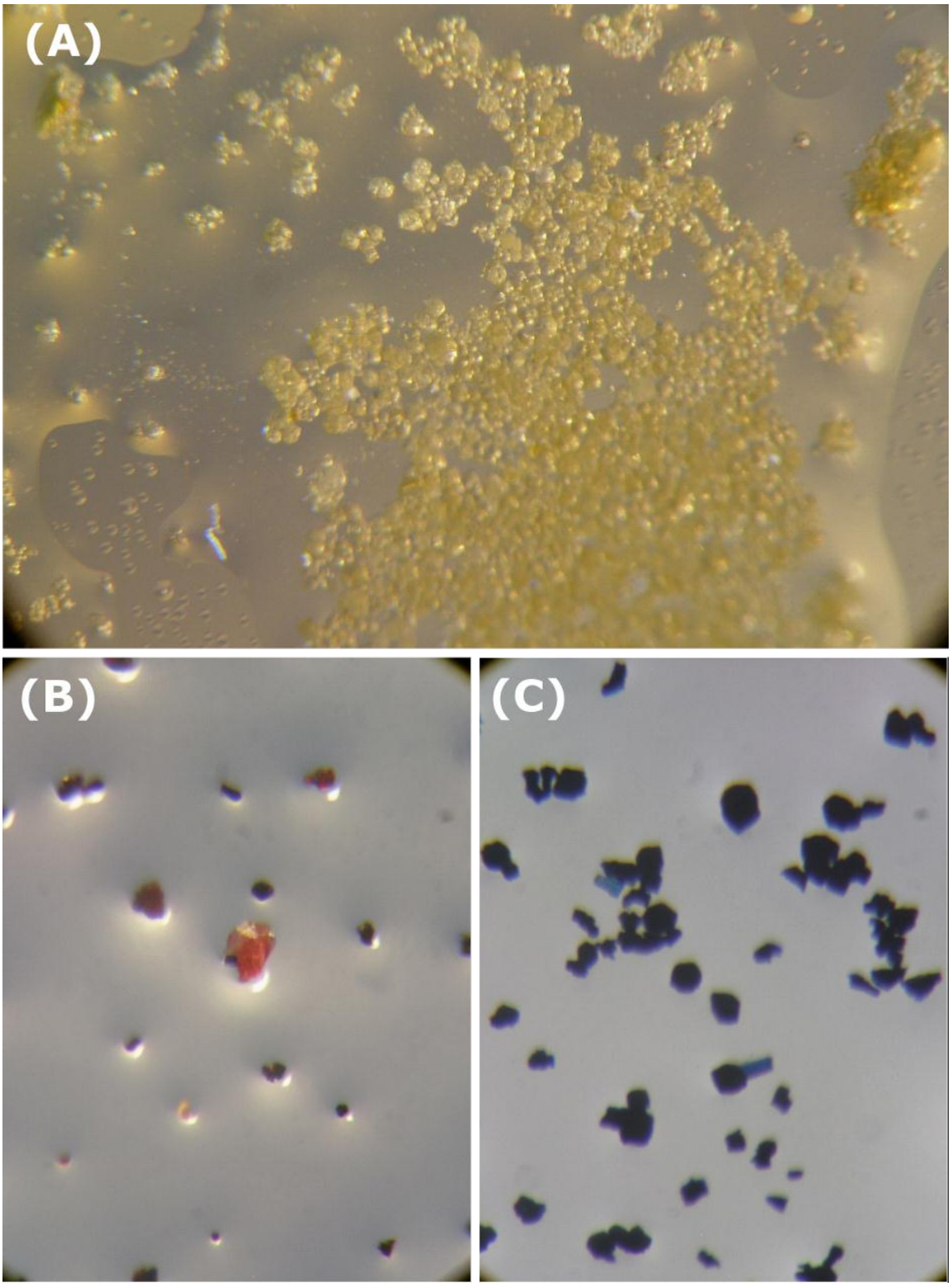

Figure 4.20 Optical microscope photographs of crystals of **101** (A) before cation exchange and after cation exchange with (B) ethidium bromide and (C) methylene blue.

further increase was observed. The changes in the absorption spectrum could be quantified using the measured extinction coefficient of methylene blue in CH_3CN, measured in 16.4 mM solution of TEAI in CH_3CN as (UV-vis (CH_3CN) λ_{max} / nm (ε_{max} /dm^3 mol^{-1} cm^{-1}): 291 (37,000) 655 (77,000)). The amount of methylene blue dye released from the first TEAI

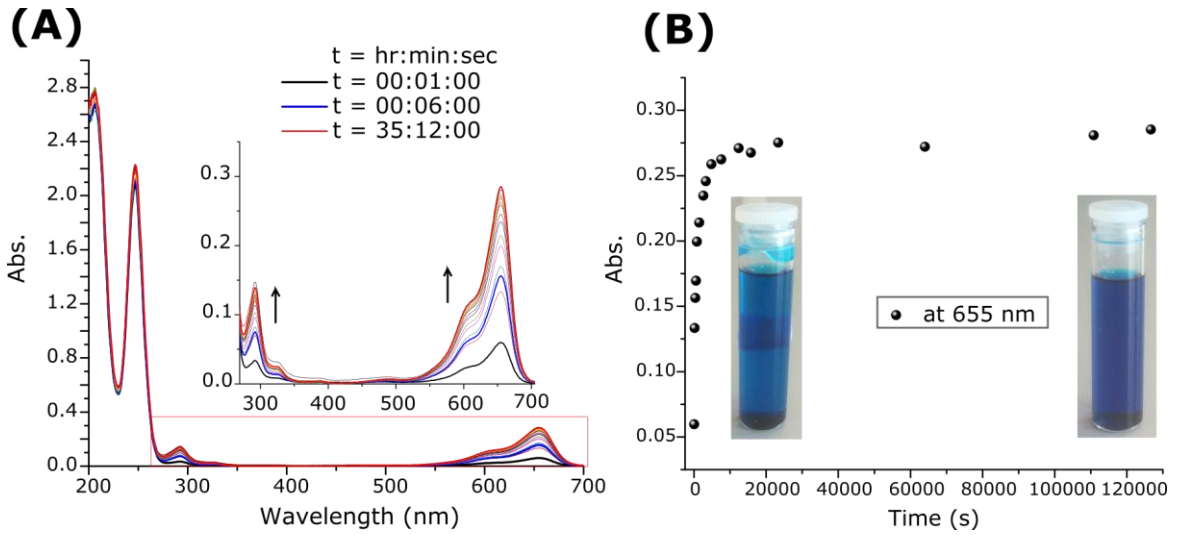

Figure 4.21 (A) Changes in UV-Vis spectrum of supernatent of **101** (6 mg) previously soaked in a concentrated solution of methylene blue in CH_3CN upon addition of TEAI in CH_3CN (c = 16.4 mM, 4 mL) solution at 21ºC. (Inset) magnification of the box-enclosed region. (B) Release profile monitoring the change in absorbance intenisty of the λ=655 nm band and photographs of the effect the relaeasing dye had on the colour and opaqueness of the supernatent.

soaking corresponded to 23% of the total cationic species required for charge balance within the framework. Further release of dye was observed when a fresh solution of TEAI (3 mL) was added to the same sample of **101** after removal of the original supernatant (Appendix C.22) and the release was at its maximum between 100 and 150 minutes after which no further substantial increase was observed. It was calculated from this that a further 8% of dye had been exchanged. A third replacement of the supernatant with fresh solution of TEAI in CH_3CN gave rise to a further release of 4% of dye (Appendix C.23). In each case, the blue color of the crystals remained evident following soaking, indicating that complete removal of the dye guest was not forthcoming under these conditions.

The same cation exchange was carried out with ethidium bromide solution in CH_3CN (Figure 4.22). Approximately 9% of the total cationic species, in the form of the ethidium cation, was released when TEAI solution was added. The samples were then digested in deuterated TFA; the ^1H resonance 2.91 ppm indicative of the $(CH_3)_2NH_2^+$ cation was not observed in the dye-soaked, TEAI-exchanged samples (Figure 4.23). The small amount of methylene blue and ethidium bromide still present in the samples accounted for the release of blue and red color, respectively, into solution upon digestion of the crystals in TFA-d_1. In particular, the residual methylene blue was evidenced by the diagnostic methyl resonance at 3.59 ppm which integrated to 0.4 protons per **84**, equating to <10% of the total cationic species. This also contributes to the explanation of why the total amount of methylene blue released by exchange with TEAI solution was observed to be less than the expected total.

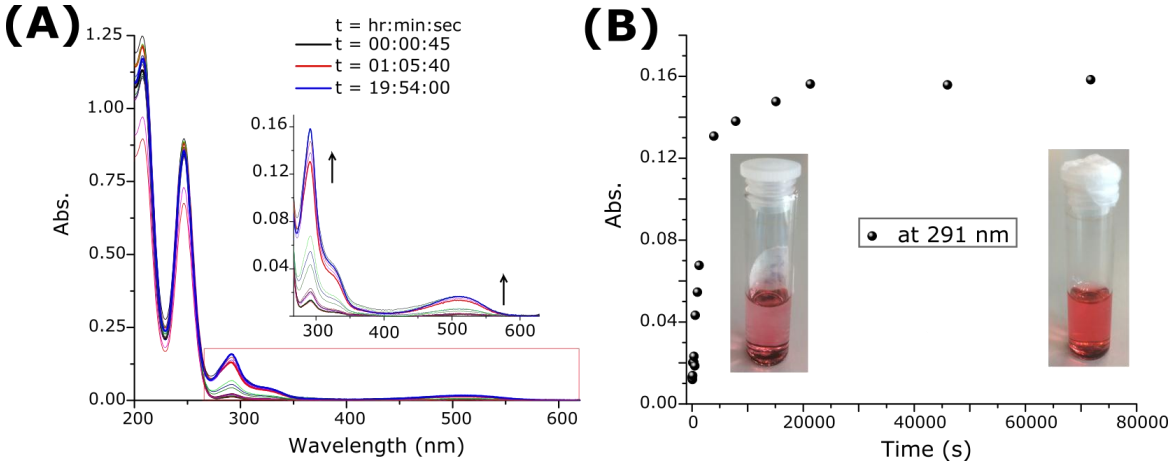

Figure 4.22 (A) Changes in UV-vis spectrum of **101** (5 mg) previously soaked in a concentrated solution of ethidium bromide in CH_3CN upon addition of tetraethylammonium iodide in CH_3CN (*c* = 6.4 mM, 2 mL) solution at 21ºC. (Inset) magnification of the box-enclosed region. (B) Release profile monitored at λ=291 nm and photographs of the effect the relaeasing dye had on the colour of the supernatent.

However, the most contributory factor to the total release of methylene blue accounting only for approximately *ca.* 35% of the amount expected, is most likely the less than complete exchange of the $(CH_3)_2NH_2^+$ cation. However, the remaining $(CH_3)_2NH_2^+$ was efficiently replaced by the TEA during the second cation exchange step. Integration of the ^{1}H NMR resonance indicative of TEA cation at 3.29 ppm and 1.38 ppm, see Figure 4.23, show the exchange with methylene blue and any original $(CH_3)_2NH_2^+$ was almost quantitative *i.e.* 6:4

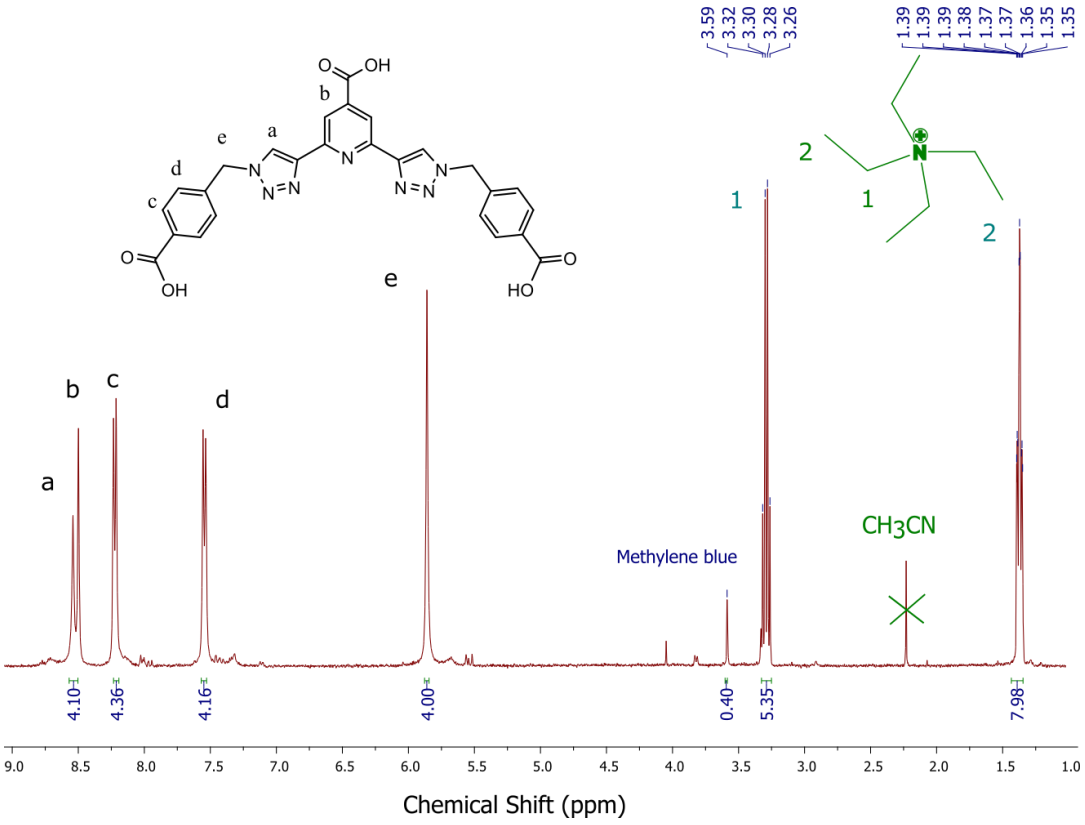

Figure 4.23 ^{1}H NMR (TFA-d_1) of **101** after methylene blue had been exchanged with TEA.

(**84**:TEA) ratio evidenced by peaks *e*,1 and 2 integrating in a 1: 1.33: 2 ratio (Figure 4.23).

The smaller volume of the TEA cation, and higher concentration of the stock solution used relative to methylene blue, most likely accounts for the more favorable uptake by **101**. For this same reason, methylene blue was less efficient compared to TEA in the replacement of the $(CH_3)_2NH_2^+$ cation initially, but more favorable than the substantially larger ethidium cation. Although complete exchange of the lattice cations in **101** with larger cations was not observed, the uptake of up to 35% of methylene blue, and complete exchange for TEA, is an encouraging observation for the use of **101** as a cation exchange material, and implies the retention of a considerable solvent-accessible volume. Having demonstrated the uptake ability of **101** for cationic guests, it was next investigated if the **btp** "antennae" embedded in the anionic framework could sensitise Ln(III) guests upon cationic exchange for the development of functional luminescent materials.

4.11 Spectroscopic monitoring of Ln(III) exchange and sensitisation studies.

As discussed in Section 1.10.2, the ability of MOFs to adsorb and recognise specific guests through various host–guest interactions within rationally designed, monodisperse pores has ensured that they continue to be the focus of much scientific attention.[176,205-206,208,222-225,228] The uptake of specific guests by MOFs in the development of luminescent materials[229-230] can occur in several ways, one of which is ion exchange.[226-227,317] Charge-balancing cations such as Ln(III) ions, namely Eu(III) and Tb(III) are ideal components in an anionic framework luminescent MOF capable of cation exchange where the host material is capable of the required sensitisation. It is well known that the **btp** motif is capable of sensitizing Ln(III) luminescent states[27,98,110,156] with some reports achieving photoluminescence quantum yields of 70% in CH_3CN solution.[103] The Eu(III) and Tb(III) radiative excited states are not heavily perturbed by ligand field effects, giving rise to line-like emission and pure colours of red and green, respectively. With this in mind, and encouraged by the ability of **101** to readily undergo cation exchange, two samples of **101** which had been previously exchanged with CH_3CN were separately treated with a CH_3CN solution of $Eu(CF_3SO_3)_3 \cdot 6H_2O$ and an equimolar CH_3CN solution of $Tb(CF_3SO_3)_3 \cdot 6H_2O$ (containing 0.16 eq. of Ln(III) *w.r.t.* **101**), respectively.

The results demonstrated that immediately, sensitisation of the Eu(III) and Tb(III) phosphorescence was evidenced by the characteristic red and green phosphorescence emitted from the respective samples, **101-Eu** and **101-Tb** under UV radiation at 365 nm

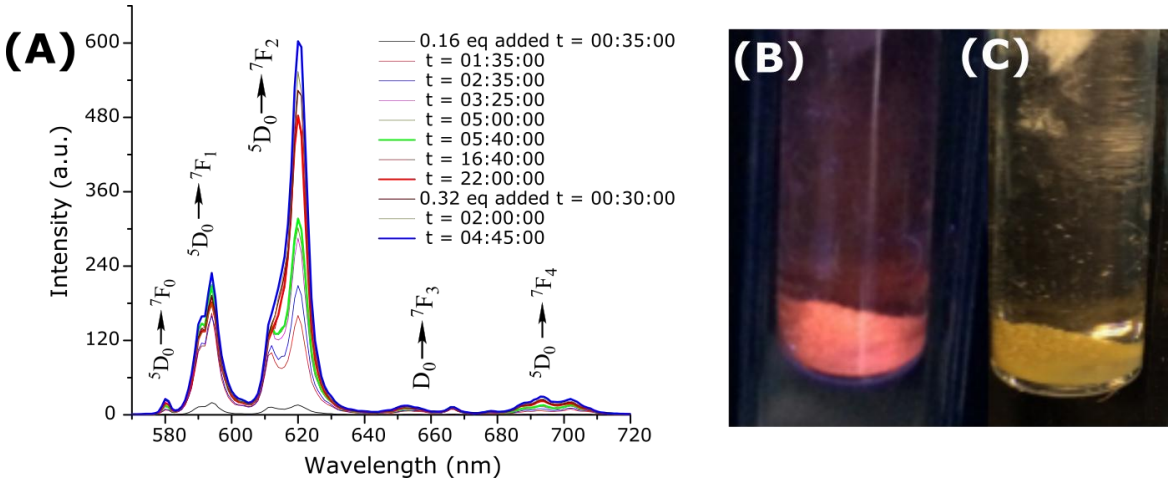

Figure 4.24 (A) Eu(III) centred phosphorescence observed increasing with time after compound **101** (11 mg, 3.49 µmol) was treated with $Eu(CF_3SO_3)_3 \cdot 6H_2O$ in CH_3CN solution (0.58 mM, 1 mL, 0.16 eq.) and. (B) Crystals of **101** under 365 nm UV radiation and (C) in daylight.

(Figure 4.24(B)/4.25, respectively). The phosphorescence changes were also monitored at specific time intervals. The line-like emission bands of the metal centred phosphorescence were observed under excitation at 365 nm, assigned to $^5D_0 \rightarrow {}^7F_J$: J = 0-4 transitions and to $^5D_4 \rightarrow {}^7F_J$: J = 6-2 transitions for Eu(III) and Tb(III), in samples **101-Eu** and **101-Tb** (Figure 4.24(A)/4.25, respectively). It should be noted that the absolute phosphorescence intensities could not be quantitatively determined as a function of time due to the unpredictable scattering and packing effects of the solid materials. Nonetheless, an unmistakable qualitative increase in overall phosphorescence intensity was observed over time. After no further increase in phosphorescence intensity was observed the solutions were

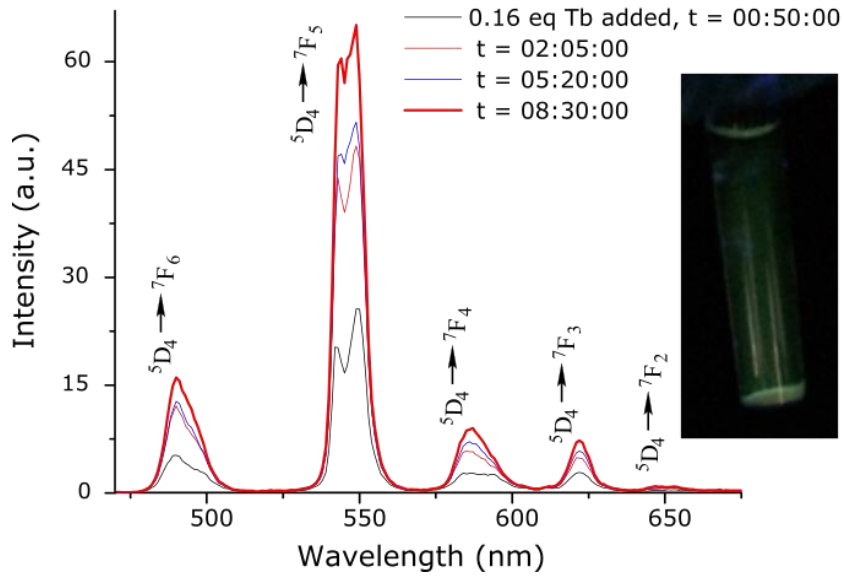

Figure 4.25 The Tb(III) centred phosphorescence was observed increasing with time after compound **101** (11 mg, 3.49 µmol) was treated with $Tb(CF_3SO_3)_3 \cdot 6H_2O$ in CH_3CN solution (0.58 mM, 1 mL, 0.16 eq.). (Inset) crystals of **101**-Tb under 365 nm UV radiation.

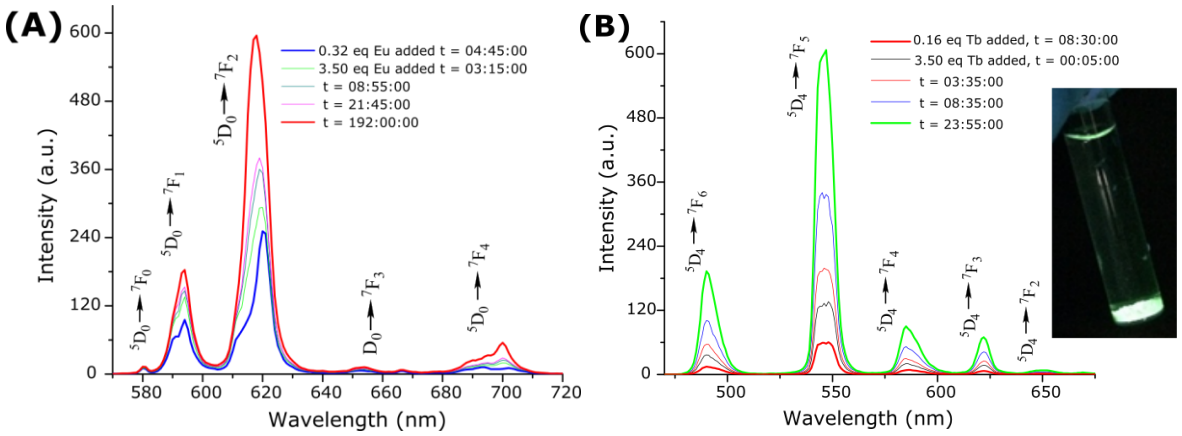

Figure 4.26 (A) A more concentrated solution of $Eu(CF_3SO_3)_3 \cdot 6H_2O$ in CH_3CN (12 mM, 1 mL, 3.5 eq.) displayed an increase in the Eu(III) centred phosphorescence increasing with time. (B) Increased Tb(III) centred emission observed after a more concentrated solution of $Tb(CF_3SO_3)_3 \cdot 6H_2O$ in CH_3CN (12 mM, 1 mL, 3.5 eq.) was added. The last spectra from previous graphs (Figure 4.20/4.21) have been included for reference. (Inset) Crystals of **101**-Tb under 365 nm UV radiation.

decanted and more concentrated solutions of $Eu(CF_3SO_3)_3 \cdot 6H_2O$ and $Tb(CF_3SO_3)_3 \cdot 6H_2O$ in CH_3CN (3.5 eq.) were then added to the respective samples **101-Eu** and **101-Tb**, respectively. This resulted in a further increase in the phosphorescence intensity for both samples (Figure 4.26). Higher emission intensities were recorded the longer the time interval between measurements became.

The excitation spectra were recorded holding the emission wavelength at 618 nm and 550 nm for **101-Eu** and **101-Tb**, respectively, displaying a band with peak maximum occurring at $\lambda = 336$ nm for both (Figure 4.27). This band maximum is indicative of the n→π* transition in the absorption spectrum of the **btp** core, hence, this would suggest that the **btp** is responsible for the sensitisation of the Eu(III) and Tb(III) radiative excited states, as expected. The fluorescence emission was measured for the two samples also, dominated

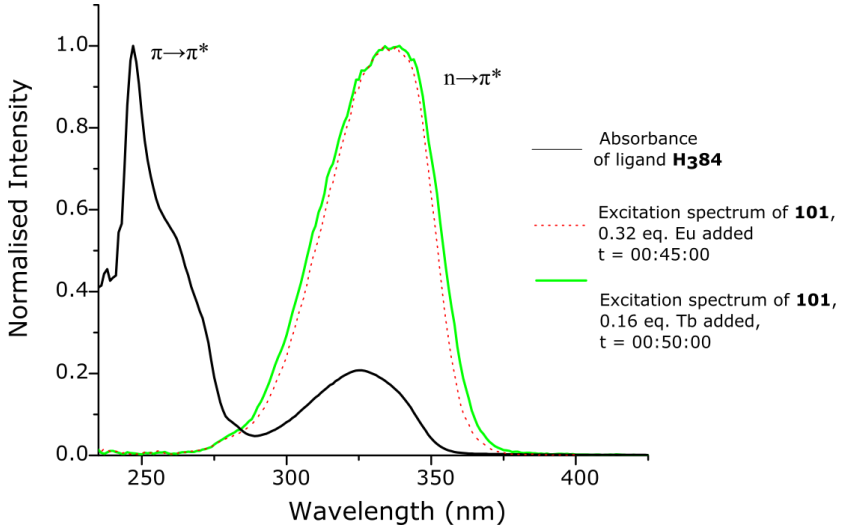

Figure 4.27 Absorption spectrum of **$H_3$84** in DMSO:CH_3CN (3:97) and excitation spectra of **101** holding emission wavelength at 618 nm and at 550 nm for **101-Eu** and **101-Tb**, respectively.

by broad scattering and also displaying Eu(III) centred bands at 590 nm and 618 nm corresponding to the $^5D_0 \rightarrow {}^7F_J$: J = 1,2 transitions, and Tb(III) centred bands at 545 nm, 585 nm and 622 nm corresponding to the $^5D_4 \rightarrow {}^7F_J$: J = 5-3 transitions, for the respective samples (Appendix C.24). It was also investigated if there was any leeching of ligand from the extended structure of **101** by measuring UV-vis absorption spectra of the supernatants of each sample (Appendix C.25). There was no indication of **btp** absorption bands observed. It was also concluded that the metal centred phosphorescence was produced exclusively by the crystals after it was confirmed there was no phosphorescence observed from the supernatants when crystals of **101-Eu** and **101-Tb** were not in the beam-path (Appendix C.25).

Radiative lifetime studies were carried out displaying biexponential radiative decay curves suggesting the presence of two Eu(III) environments and two Tb(III) environments in and **101-Tb**, respectively. The observed radiative lifetimes had average values of τ_1 = 0.48(01) ms and τ_2 = 1.91(10) ms for the Eu(III) species and of τ_1 = 0.92(01) ms and τ_2 = 4.45(14) ms for the Tb(III) species. A summary of the observed lifetimes is presented in Table 4.1. As time elapsed the radiative lifetimes of the two Eu(III) species and Tb(III) species inside **101-Eu** and **101-Tb**, respectively, remained constant, however, the abundance of the shorter lived species, τ_1, and the longer lived species, τ_2 gravitated towards a more even distribution as time elapsed becoming essentially identical after 20 hours.

The effect of adding Tb(III) to **101-Eu** and Eu(III) to **101-Tb** was investigated. Solutions of $Tb(CF_3SO_3)_3 \cdot 6H_2O$ and $Eu(CF_3SO_3)_3 \cdot 6H_2O$ in CH_3CN (12 mM, 1 mL, 3.5 eq.) were added to **101**-Eu and **101**-Tb, respectively. Signals indicative of new Tb(III) and Eu(III) phosphorescence were then observed in the respective samples. The Tb(III) $^5D_4 \rightarrow {}^7F_J$: J = 6, 5 transitions and the Eu(III) $^5D_0 \rightarrow {}^7F_J$: J = 1,2,4 transitions became steadily more intense with increasing time in **101-Eu** and **101-Tb** (Figure 4.28(A)/(B), respectively). The new $^5D_4 \rightarrow {}^7F_4$ Tb(III) transition in **101**-Eu appeared as a shoulder of the more intense $^5D_0 \rightarrow {}^7F_1$

Table 4.1 Observed radiative lifetimes of the two Eu(III) species (red) and Tb(III) species (green) present in **101**-Eu and **101**-Tb, respectively, at specific time intervals with associated abundances expressed as a percentage of the total.

Time measured (hr: min: s)	τ_1 (ms)	τ_2 (ms)	% τ_1	%τ_2
03:15:00	0.47	1.99	62	38
08:55:00	0.48	1.93	57	43
21:45:00	0.48	1.80	55	45
03:35:00	0.91	4.51	46	54
08:35:00	0.93	4.55	51	49
23:55:00	0.93	4.28	56	44

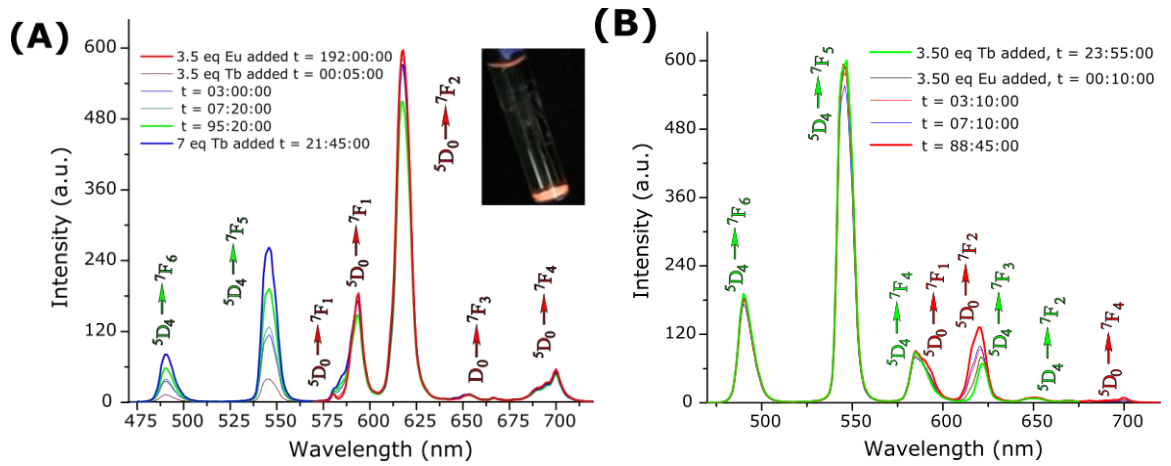

Figure 4.28 Sensitisation of the (A) Tb(III) centred and (B) Eu(III) centred phosphorescence transitions after addition of a solution of $Tb(CF_3SO_3)_3{\cdot}6H_2O$ and $Eu(CF_3SO_3)_3{\cdot}6H_2O$ in CH_3CN (12 mM, 1 mL, 3.5 eq.) to **101**-Eu and **101**-Tb, respectively. (Inset) Resultant orange emissive crystals of **101**-Eu under UV irradiation at 365 nm. The last spectra from previous graphs (Figure 4.22) have been included for reference.

Eu(III) transition while the original Eu(III) transition signals remained at approximately same intensity albeit with a slight decrease as the Tb(III) transitions grew more intense, see Figure 4.28(A). Sensitisation of the additional Eu(III) in **101-Tb** was not as pronounced, see Figure 4.28(B). Little changed with the overall colour of the crystals under UV irradiation at 365 nm was observed, except in the case of **101-Eu** when a slight yellowing of the initially red emission due to the additional Tb(III) sensitisation. Radiative lifetime studies were carried out at this point also; however, the radiative decay curves for the transitions centred at 550 nm, 589 nm, and 618 nm in both samples could not be fitted to a biexponential decay curve. More than two radiative lifetimes had been expected due to the additional Tb(III) and Eu(III) ions present in **101-Eu** and **101-Tb**, respectively.

The phosphorescence of both samples was shown to be rapidly quenched upon addition of TEAI in CH_3CN solution (Figure 4.29). This is as a result of the rapid displacement of

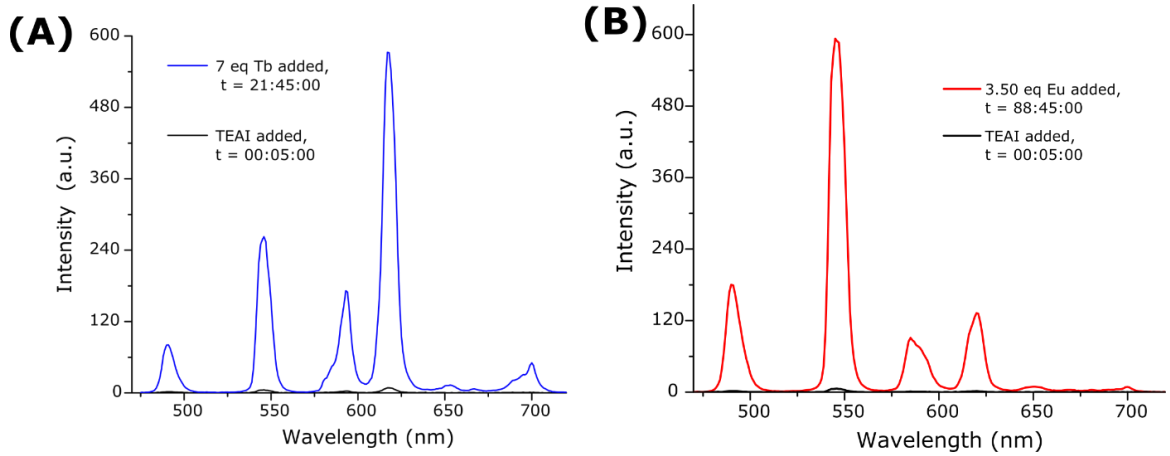

Figure 4.29 Rapid exchange of Ln(III) ions with TEA cations resulting in a dramatic intensity decrease in Ln(III) centred emission bands in (A) **101-Eu** and (B) **101-Tb**, respectively.

the cationic Eu(III) centres and replacement with TEA cations. Colourless crystals of $[Eu(H_2O)_9](CF_3SO_3)_3$ were formed upon slow evaporation of the supernatent after exchange with the TEAI solution in CH_3CN, the structure of which was confirmed using X-Ray diffraction analysis, the unit cell determination of which matched that of previous reports.[350] It is unclear whether this ion pair diffused from the channels of **101** into the supernatant due to the concentration gradient caused by the treatment with TEAI solution or whether the Eu(III) had been a charge balancing cation for the anionic **101** which recombined with $CF_3SO_3^-$ anions after its displacement by TEA cations. It was later attempted to exchange the TEA inside the channels with Eu(III) once more; however, the sensitisation of the Eu(III) by **101** was only seen to be minimal suggesting a higher affinity of the MOF for the TEA cations over the Eu(III) cations.

4.12 Conclusions and Future Work

Several crystalline coordination polymers derived from the semi-flexible tri-carboxylic acid **btp** ligand **$H_3$84** have been synthesised. The **btp** ligand, **$H_3$84**, adopts a three-dimensional hydrogen bonding network in the crystalline state through a combination of carboxylic acid dimer and *syn*-*anti*-**btp**:carboxylic acid hydrogen bonding synthons. The tri-sodium salt *poly*-**$Na_3$84** was characterised using single crystal X-ray diffraction analysis displaying a closely packed three dimensional coordination polymer network through the shared vertices of the two distinct Na^+ coordination polyhedra. A Cu(II)-derived coordination polymer **100** of the formula *poly*-$[Cu_3\mathbf{84}_2)]\cdot(DMF)_{3.3}$ was synthesised and characterised by single crystal and powder XRD analysis, and displayed a (4,4) net topology. Although a satisfactory phase purity was achieved, there were difficulties in optimising the synthetic conditions required to reproduce **100**, therefore sufficient quantities required or the investigation of permanent porosity could not be obtained. A three dimensional anionic framework coordination polymer, **101**, exhibiting a structure with the rare **crs** topology and formula $[Zn_7\mathbf{84}_6]\cdot((CH_3)_2NH_2)_4\cdot(H_2O)_{45}$ derived from ligand **$H_3$84** was synthesised in good yield with excellent bulk purity achieved. A second crystalline phase, *poly*-[Zn(**H84**)], which was present as a byproduct in initial attempts was successfully removed through synthetic optimisation. The extended structure of **101** was characterised using conventional methods: single crystal and powder X-ray diffraction analysis, gas adsorption studies together with TGA and elemental analysis. While a reduction in void volume was observed following the complete evacuation of **101**, efficient exchange was observed for guests from the solution phase, using cationic dye molecules as probes. Uptake and sensitisation of Eu(III) and

Tb(III) within the framework of **101** was also achieved. These observations demonstrate the potential of materials exhibiting poor structural resilience to complete evacuation such as **101** as nonetheless useful cation exchange matrices for the development of functional luminescent materials. Efforts are currently being made to appropriately tune the uptake of various luminescent guests by **101** in the pursuit of customisable white light emitting materials. Ln(III) luminescent MOF materials like **101** have been used in the detection of small molecules[256] and metal ions such as Fe(II)[258] through quenching of the metal-centred luminescence as described in Section 1.10.2. Having demonstrated that **101** can efficiently sensitise photoluminescent metal ions, the design of Ru(II) based MOFs derived from **101** could have promising applications for the photocatalyic production of hydrogen.[257,351] The redox active Ru(II) ion possesses photophysical properties that can be tuned by substituents on the sensitizing organic tecton,[99] such as the carbonyl moiety at the 4-pyridyl position of **H$_3$84**, as has been reported for **terpy** ligands.[73] It is with growing attention that MOF systems incorporating these properties[352] are being developed as water oxidation photocatalysts.[351,353]

In the chapters which have been discussed, efforts were focused on designing **btp** ligands with appended conjugated substituents at the 4-pyridyl position and study of the resulting functional metal based systems. In the next chapter, the variation of the *N1* triazolyl position of the unsubstituted **btp** motif using a choice of precursor aryl azide will be discussed in relation to the effect the aryl "arms" have on the self-templated synthesis of homocircuit [2]catenanes.

5 Study of the pre-organisation requirements for the formation of self-templated 2,6-bis(1,2,3-triazol-4-yl)pyridine [2]catenanes

5.1 Introduction

It is widely accepted that for effective formation of mechanically interlocked molecules it is a requirement for two or more molecular "threads" to assemble in close proximity before "clipping" the open forms together through covalent bond formation.[270,354] Templating the close proximity of the clipping sites requires careful molecular design such that functional groups are appropriately located spatially on the self-assembled components to allow intermolecular interaction in a controlled or pre-organised manner, thus facilitating the formation of systems such as knots,[261-264] rotaxanes[21,23,25,265-266] and catenanes.[21,261,267-270] In order to access these synthetically challenging and topologically non-trivial molecular species, a range of methodologies have been developed for templating the assembly of such systems. These include metal templation,[21-22,25,263-264,270] hydrogen bonding interactions,[266,272-276] donor acceptor interactions[277-278] and anion coordination.[279-280,355-356,23] Examples of self-templated formation of interlocked systems in which two equivalent molecules associate before interlocking mechanically have been less frequently reported. As was discussed in Section 1.11, crystal structure analysis of the homocircuit [2]catenanes **60-63**, suggested that the isophthaloyldiamide motifs self-templated in dimers through amide hydrogen bonding interactions.[266,272-273,275-276] Mechanisms for the self-templation of such systems were suggested by Leigh *et al.*,[275] however, confirmation of this self-templating dimerisation behaviour in the solid state for the unlocked precursors was not obtained. A range of **btp**-containing molecular precursors possessing potential for the formation of [2]catenanes will be synthesised in order to gain an insight into this interesting pathway towards self-templated mechanically interlocked molecules. Crystal structure analysis of the [2]catenanes formed herein along with analysis of supramolecular interactions between the precursors in solution will play a key role in understanding the intermolecular interactions which pre-organise the molecules into the conformations necessary to facilitate the efficient generation of these interlocked systems. As this is a process which is occurring in solution, solution state NMR studies will also be used to monitor the dynamic process involved in forming the interlocked systems.

5.2 Structural features of previous btp ligands in [2]catenane formation

As was discussed in section 1.6, Byrne *et al.* demonstrated the successful self-assembly of [2]catenanes **36a-c**,[156,160] Scheme 5.1. It was found that a combination of non-polar solvent and varying alkenyl chain length had a major impact on the efficiency of the [2]catenane

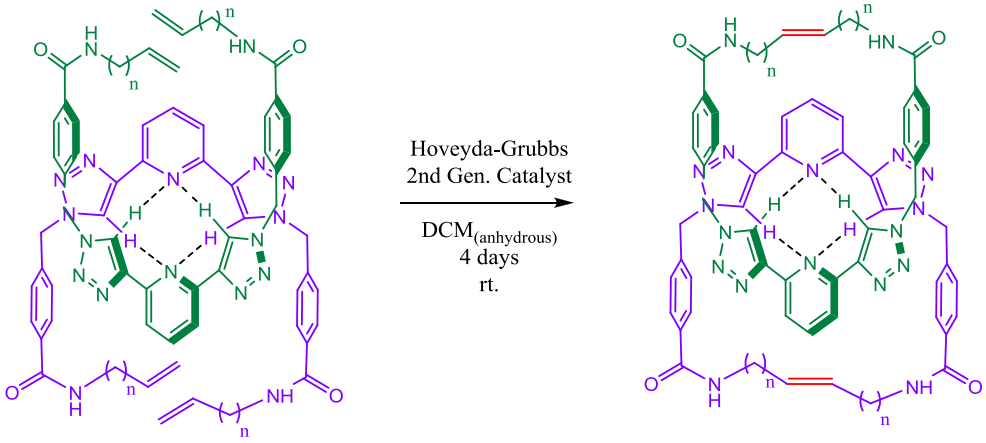

{102a-e}$_2$; n = 1 - 4, 9 **36a-c** ; n = 1 - 3

Scheme 5.1 Self-templated formation of [2]catenane **36a-c** through the hydrogen bonding dimerisation of olefin precursors **102a-c**. No [2]catenane formation was observed for n=4 and n=9.

formation. RCM of the olefin **102a** saw [2]catenane **36a** produced in 50% yield in anhydrous CH_2Cl_2. Precursors **102b** and **102c** possessing longer chains produced **36b** and **36c** (n=2 and n=3, respectively) in diminishing yields (35% and <1%, respectively). There was no catenane formation resulting from the same synthetic procedure involving olefin precursors **102d** and **102**e. When the RCM reactions were carried out in more polar solvents, such as CH_3OH, no observable quantity of catenane was formed. This suggested the importance of the non-classical hydrogen bonding interactions between the **btp** motifs for self-templating the desired interlocked structures. At the time, however, the significance of the amide hydrogen bonding interactions involving the 4'-(*N*-allylphenylcarboxamido)methylene (4'substituted "arm") substituents (Figure 5.1) in the pre-organisation of the self-templated

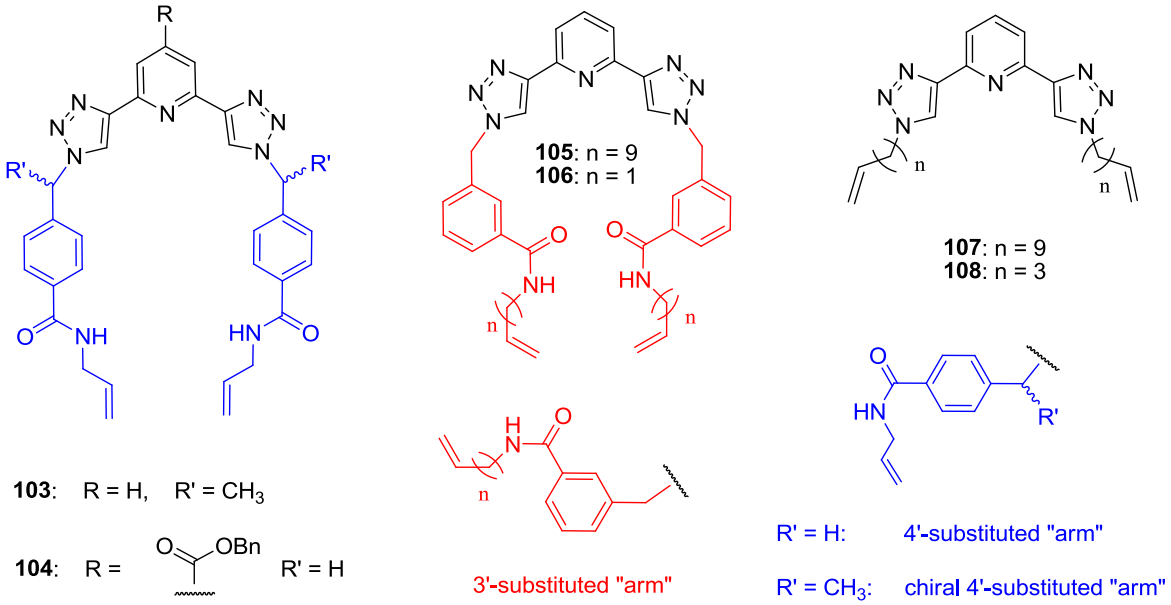

Figure 5.1 Olefin derivatised **btp** ligands for investigation of the structural requirements for successful [2]catenane formation.

synthesis of the homocircuit [2]catenanes remained elusive and is worthy of further investigation. It is one of the aims of this chapter to determine if the presence of the 4'-substituted "arm" is essential for efficient formation of analogous **36a** [2]catenanes. In the original report, solubility issues limited solution state analysis as the precursors were only soluble in polar DMSO.

In order to carry out this investigation, the synthesis of several **btp-**containing candidate molecules derivatised with 4'-substituted "arm" functionality and the attempts at forming mechanically interlocked [2]catenane systems will be presented. The effect of the introduction of other functional groups closer to the **btp** core on solubility in non-polar solvents and on efficient self-templated formation of [2]catenanes will be analysed. This will be in the form of placing chiral groups adjacent to the triazolyl *N1* position in the form of a 4'-(*N*-allylphenylcaboxamido)-(*R*/*S*)-1,1-ethylidene (chiral 4'-substituted "arm") substituent, in the case of **103R**/**S**, and also adding sterically bulky substituents at the 4-pyridyl position of the **btp** motif, **104**. Furthermore, **btp** ligands lacking the 4'-substituted "arm" functionality and replaced with the structurally isomeric 3'-(*N*-allylphenylcarboxamido)methylene (3'-substituted "arm") functionality, **105** and **106**, will be investigated, as control systems, for [2]catenane formation (Figure 5.1). The effect of this isomerism on the pre-organisation of the system required for catenation will be presented. Olefin derivatised **btp** ligands lacking any amide functionality, **107** and **108**, will also undergo similar investigation. A selection of the resulting **btp** systems will be investigated for their anion binding properties and selectivity. The data will be presented in the following sections and several hypotheses for their interpretation will be discussed separately in Section 5.13.

5.3 Synthesis and characterisation of chiral btp olefins 103R/S

Chirality is one of the fundamental properties found in nature. It is thus desirable to introduce chirality into a molecular structure so that 'optical activity' can be accessed. This arises from the ability of a pair of enantiomers to interact with polarised light resulting in an equal and opposite rotation of the polarisation direction.[357] Also, there are several advantageous biological properties chiral molecules possess, such as, a molecule's enantiomer's ability to discriminate between enantiomers of an analyte and also bind preferentially to particular chiral biological systems allowing them to be used as probes for substrates such as DNA.[358] Molecular chirality presents a decisive challenge in host-guest recognition and other asymmetric catalysis such that attention has been turned towards 3D scaffolds like chiral interlocked systems in designing efficient enantioselective receptors.[359] Furthermore,

molecular chirality can be transferred to supramolecular systems through endowing the coordination environments of metal centres, for example, with the chiral information inherent to the chelating motif.[357] Propagation of the chiral information through supramolecular interactions in the formation of materials, such as gels,[309,326] is also a highly topical area of research. More relevantly, there have been several reports of mechanically interlocked catenanes possessing an inherent chirality arising from the chirality of the precursors[359-360] but also from achiral precursors[273,361-363] wherein the chirality arises as a result of the mechanical bond, such was the case with self-templated homocircuit [2]catenanes discussed in Section 1.11.[266,272,274-275] To the best of my knowledge, there are no reports of chiral self-templated homocircuit [2]catenanes from starting materials possessing a classical chiral element such as a chiral centre.[359]

With this in mind, chiral **btp** ligands **103R**/**S** derivatised at the *N1* triazolyl position with chiral 4'-substituted "arm" moieties were synthesised according to Scheme 5.2. The methyl ester chiral **btp** ligand **109R**/**S** was synthesised in a two step one-pot *diazo-transfer–deprotection–'click'* reaction from alkyne **43** and the chiral amine.[156] In the first step, the relevant azide was formed *in situ* from (*R*/*S*)-methyl 4-(1-aminoethyl)benzoate through the

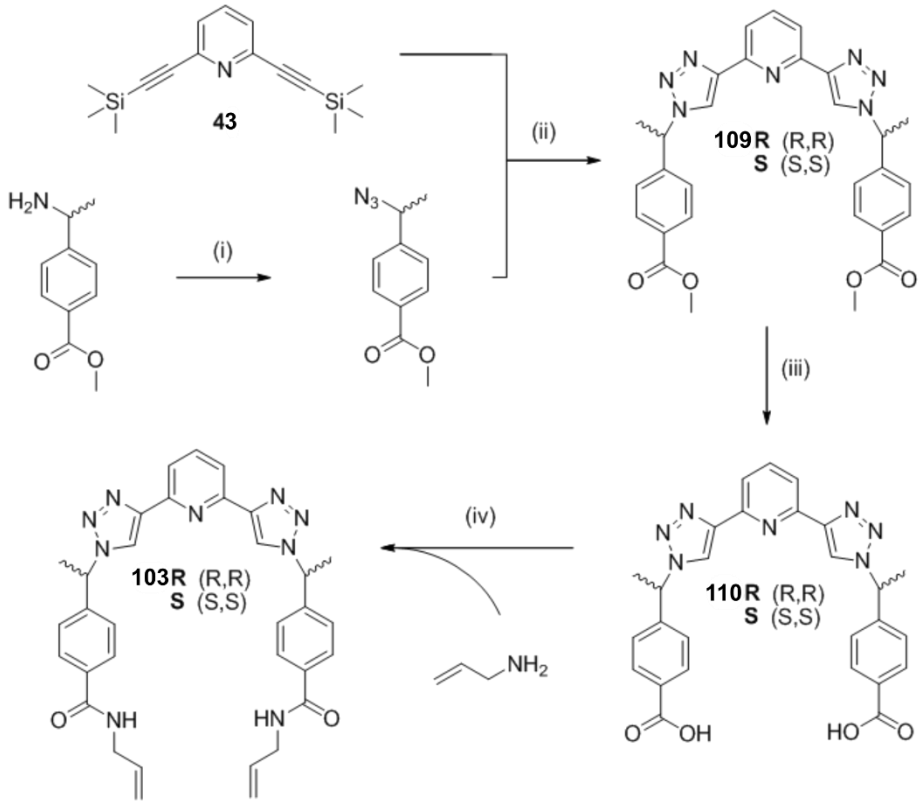

Scheme 5.2 Synthesis of chiral **btp** ligands **103R**/**S**. (i) $CuSO_4 \cdot 5H_2O$, $ImSO_2N_3 \cdot H_2SO_4$ and K_2CO_3 in CH_3OH, rt, 15 h; (ii) Sodium ascorbate, K_2CO_3, DMF/ tBuOH/ H_2O (5:5:3), rt, 18 h; (iii) $NaOH_{(aq)}$, MeOH, rt, 17 hrs (iv) 1) Et_3N, DMAP, CH_2Cl_2/ DMF (4:1), 0°C, 30 mins 2) EDCI·HCl, 0°C, 30 mins, rt, 66 hrs.

Cu(II) catalysed diazo transfer reaction in the presence of transfer reagent, $ImSO_2N_3 \cdot H_2SO_4$ and K_2CO_3. The progress of the reaction could easily be monitored through colour change. Initially, the reaction mixture was cyan in colour and upon successful formation of the azide after 15 hours the suspension turned lilac (Figure 1.33, Section 1.9.1).[156] The second step consisted of the addition of sodium ascorbate and K_2CO_3 after which the mixture was degassed to give a suspension which was a dull yellow colour in appearance. A solution of **43** in DMF was then added and allowed to stir at room temperature for 18 hours giving rise to an orange suspension upon completion of CuAAC. The reaction mixture was washed with aqueous EDTA/NH_4OH solution, in order to scavenge Cu(II) ions, and then extracted into EtOAc. After the solvent was removed under reduced pressure, the methyl ester **btp** ligands **109R**/**S** were purified by automatic flash chromatography (gradient DCM: CH_3OH (98:2) and obtained in high purity as confirmed by elemental analysis and in excellent yield of 76-81%. The carboxylic acid ligands **110R**/**S** were successfully prepared by ester hydrolysis of **109R**/**S** by stirring with aqueous NaOH in CH_3OH solution in 73-82% yield. **Btp** olefin precursors **103R**/**S** were synthesised from **110R**/**S** by amide coupling reaction with allylamines. The amide coupling was carried out by EDCI·HCl activation in the presence of Et_3N and DMAP. **Btp** olefins **103R**/**S** were obtained as white powders in 38-48% yield after automatic flash chromatography (gradient DCM:CH_3OH (95:5). All ligands were fully characterised by ^1H and ^{13}C NMR, HRMS, IR and CHN.

^1H NMR spectroscopy confirmed successful synthesis of the desired **btp** olefins; the spectra of each enantiomer were identical as expected, therefore, the proton resonances will be discussed in terms of **103R** only (Figure 5.2). The singlet at 8.22 ppm in $CDCl_3$, with an integration of 2, was assigned to the triazolyl CH resonance by HSQC and HMBC. The doublet at 8.14 ppm corresponded to the 3- and 5-pyridyl protons while the triplet at 7.96 ppm corresponded to the 4-pyridyl proton integrating to 1. The aryl proton resonances on the benzene rings can be found further upfield at 7.49 ppm and 6.92 ppm. The broadened singlet at 6.80 ppm was assigned as the amide proton by selective TOCSY. The doublet of doublets of doublets from 6.03 ppm, with an integration of 2, and the pair of doublets between 5.39 ppm and 5.24 ppm, integrating to 4, were assigned to the internal and terminal olefin protons, respectively. Between these resonances appeared a quartet at 5.59 ppm, corresponding to the methine proton of the chiral centre. The methylene protons of the aliphatic chain adjacent to the amide and olefin appeared further upfield at 4.15 ppm. Finally, the doublet at 1.63 ppm integrating to 6 protons was characteristic of the methyl substituent at the chiral centre. The ^{13}C NMR spectrum, HSQC and HMBC allowed assignment of the

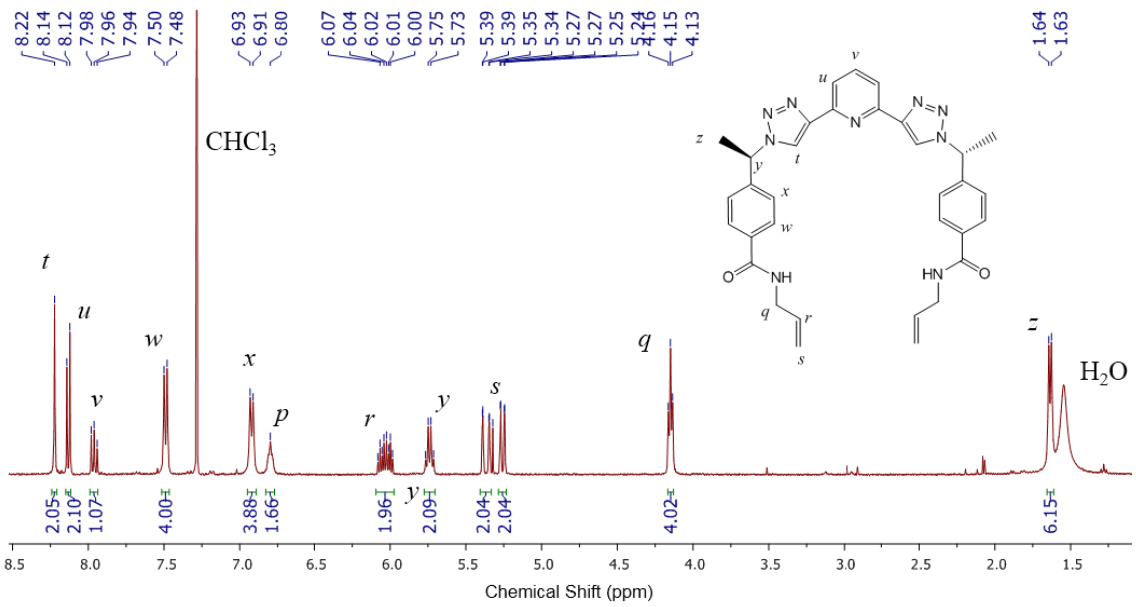

Figure 5.2 ^{1}H NMR spectrum of chiral **btp** olefin **103R** (400 MHz, $CDCl_3$) with resonances labelled.

carbonyl and quaternary carbons. ESI$^+$ mass spectrometry analysis displayed a characteristic peak at m/z = 588.2853, which agreed with the *m/z* calculated for $[M+H]^+$. Elemental analysis confirms bulk purity from expected atomic abundances of C = 65.52, H = 5.53, N= 20.62, for the monohydrate of **103R**.

5.3.1 Investigation into self-templating of 103R/S in solution by ^{1}H NMR spectroscopy and mass spectrometry

It was observed that the chemical shift of certain proton resonances of the chiral **btp** olefins **103R**/**S** was rather sensitive to the choice of solvent. High polarity solvents such as DMSO-d_6 gave sharp resonance signals, see Figure 5.4(A), whereas in less polar solvents, such as $CDCl_3$, signs of self-templating dimerisation (shown for **103R** only below) were manifested as broadening of certain signals and significant changes in chemical shifts; these changes were concentration-dependent. At low concentration the ^{1}H NMR spectrum of **103R** in $CDCl_3$ containing low quantities of H_2O displayed certain peaks which were broadened, in particular the triazolyl peak *t*. (Figure 5.3). This indicated several hydrogen bonding interactions at play in the self-assembly. Upon increasing the concentration of the solution of **103R** to 30 mM, while keeping the H_2O content in the $CDCl_3$ constant, a significant change in chemical shift of certain proton resonances was observed. The triazolyl proton resonance *t* became sharper and underwent an upfield shift from 8.44 ppm to 8.30 ppm. It remained somewhat broadened compared to the less effected resonances upon increasing concentration, which was suggestive of it partaking in hydrogen bonding interactions. The

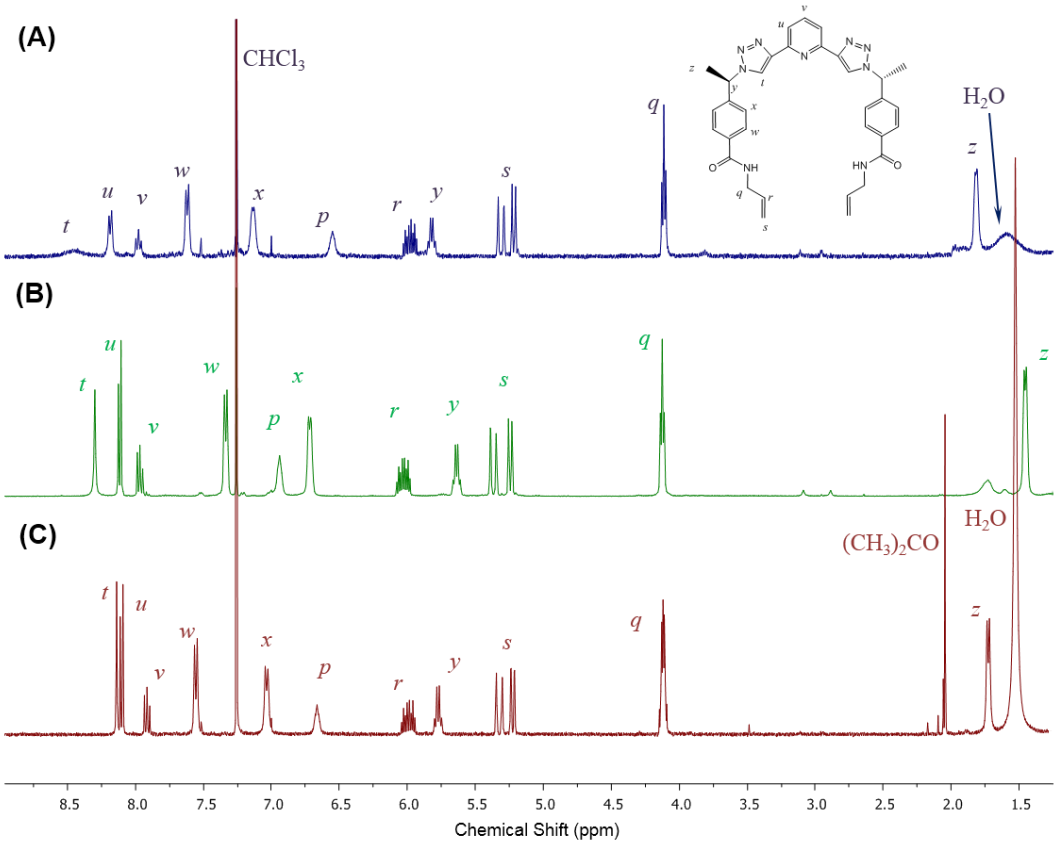

Figure 5.3 The dramatic changes in chemical shift of **btp** triazolyl (*t*), aryl (*w* and *x*) and amide (*p*) proton resonance signals upon increasing concentration of **103R** from (A) 1mM to (B) 30 mM in anhydrous $CDCl_3$ and (C) subsequently upon increasing the H_2O concentration to 75 mM in the same solution (400MHz, $CDCl_3$).

aryl protons *w* and *x*, underwent a significant shift upfield from 7.62 ppm and 7.14 ppm to 7.34 ppm and 6.71 ppm, respectively. This indicated a significant change in the chemical environment upon increasing concentration. Finally, the amide proton resonance *p*, became deshielded from 6.55 ppm to 6.94 ppm, an observation which coincided with a greater abundance of molecules being involved in hydrogen bonding at 30 mM than at 1 mM. The methine proton *y* and methyl proton *z* adjacent to it were also shifted upfield from 5.83 ppm and 1.82 ppm to 5.64 ppm and 1.46 ppm, respectively. Upon increasing the H_2O content of this solution of **103R** in $CDCl_3$ the broadened triazolyl resonance decreased in chemical shift with a concomitant sharpening of the resonance indicating the break-up of these intermolecular hydrogen bonding interactions by the more polar solvent content. The proton resonance signals associated with the aryl 'arms' *w* and *x*, became deshielded from 7.33 ppm and 6.72 ppm to 7.57 ppm and 7.04 ppm, respectively. The amide proton became more shielded as it changed chemical shift from 6.94 ppm to 6.66 ppm. And finally, the methine proton *y* and methyl proton *z* adjacent to it were shifted downfield to 5.78 ppm and 1.63 ppm,

respectively. The above experiment corroborated the rationale that dimerisation was occurring through non-classical hydrogen bonding of *anti-anti* oriented **btp** motifs,[102,156,160] the effect of which on the triazolyl proton resonance's chemical shift was clear at high concentration. The variability in the aryl and amide proton resonance shifts also supported the argument that the chiral 4'-substituted "arms" were pre-organising in a manner which was resulting in a significant change in the moiety's chemical environment through amide hydrogen bonding interactions. We will discover in section 5.10.1 that this was in contrast to the invariance in the chemical environment of the protons of the 3'-substituted "arms" for **105**. This change in chemical environment of the aryl 'arms' was also a feature in the RCM of chiral **btp** olefins **103R**/**S** using similar anhydrous solvent conditions and concentration ranges as the above.

5.4 RCM of chiral btp olefins 103R/S

Encouraged by Byrne *et al.*'s successful and high yielding synthesis of [2]catenane **36a** from **btp** olefin **102a**, RCM was carried out with **103R**/**S** under the same conditions. It was envisaged that like **102a**, which possessed 4'-substituted "arms", chiral **btp** olefins **103R**/**S** would also achieve the pre-organisation necessary for self-templated [2]catenanes to be efficiently synthesised. A solution containing **103R**/**S** and Hoveyda–Grubbs 2nd generation catalyst (50 mol %) in anhydrous CH_2Cl_2 was stirred under argon at room temperature in darkness for 7 days according to modified procedure for forming mechanically interlocked structures reported by Byrne *et al.*[102] The reaction mixture was concentrated before purifying by flash chromatography (gradient DCM: CH_3OH (95:5)) yielding a beige powder. In both enantiomers' cases, resonances indicative of [2]catenane formation were observed by ^{1}H NMR (Figure 5.4) For succinctness, only the data for **111R** will be discussed herein (see Appendix A.25 for **111S**). ^{1}H NMR analysis (400 MHz, DMSO-d_6) showed that the resonances related to the terminal olefin in **103R** (*s*) disappeared in the spectrum of the [2]catenane product **111R** and an apparent singlet resonance appeared at 6.13 ppm due to the remaining olefin protons (*r*); these signals were indicative of successful RCM. Other proton shifts, were more dramatic: the triazolyl *CH* resonance (*t*) was shielded to 7.89 ppm in the spectrum of **111R**, suggesting it occupied quite a different chemical environment to the triazolyl proton in the starting material which appeared at 8.78 ppm. The amide NH proton resonance (*p*, assigned by NH COSY) was also shifted upfield. The proton resonances assigned to the aryl rings were heavily shielded; the signals moving from 7.86 and 7.43 ppm for **103R** to 7.26 and 6.32 ppm for **111R** (*w* and *x*, respectively). This was indicative of

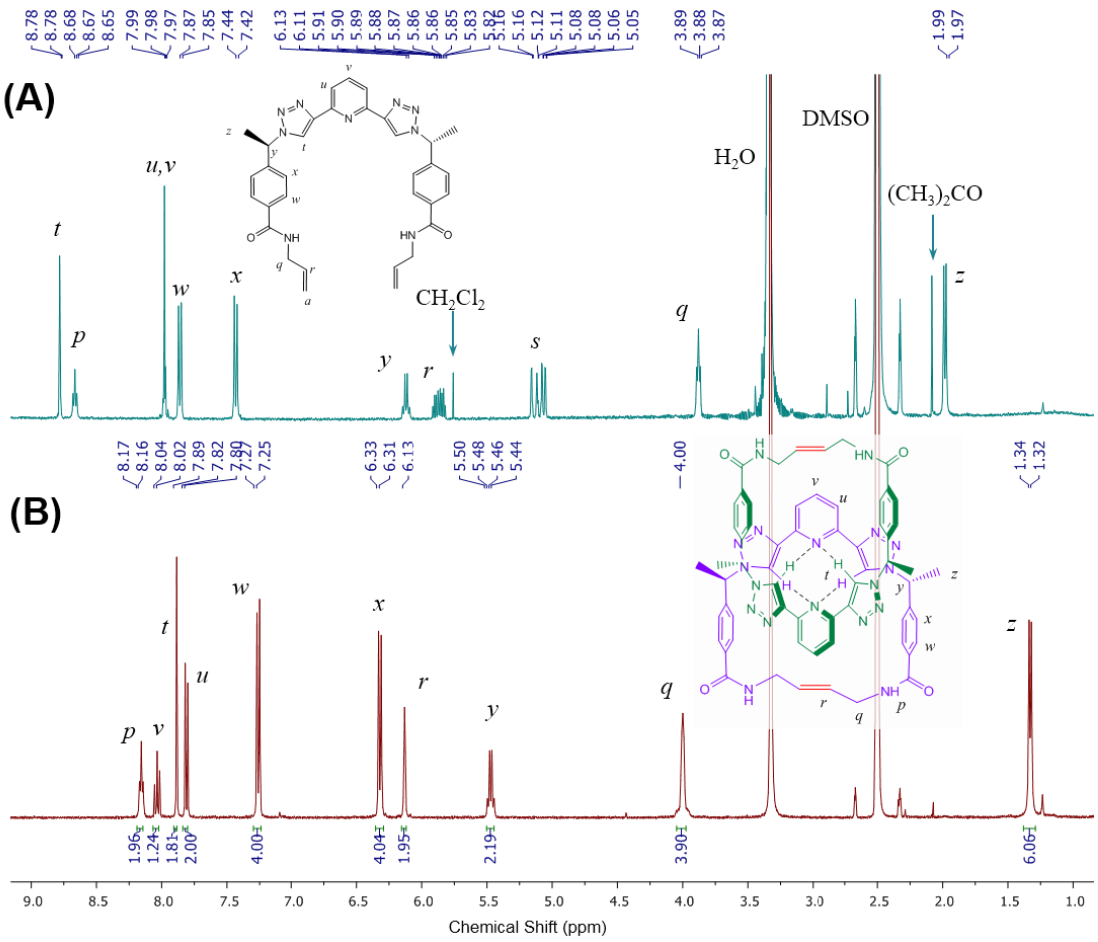

Figure 5.4 ^{1}H NMR spectra of chiral **btp** precursor **103R** (A) and chiral **btp** [2]catenane **111R** (B) (400 MHz, DMSO-d_6) with resonances labelled.

a freely-rotating catenane structure, where the protons of one ring were able to reside in close proximity to the aromatic rings of the other macrocycle.[276] In a similar fashion the chiral methine resonance (*y*) was shifted upfield to 5.47 ppm. An upfield shift was also observed for methyl protons from 1.98 ppm to 1.31 ppm. The ^{13}C NMR (150 MHz, DMSO-d_6) resonances were also assigned with the aid of HSQC and HMBC experiments (Appendix A.24, A.25). Weak through-space interactions between the aryl rings and the **btp** motif were observed using ROESY NMR spectroscopy (Appendix A.26). This was consistent with formation of an interlocked species. There was a stronger through-space interaction between aryl protons *w* and pyridyl protons *u* compared with that seen for aryl protons labelled *x* and the latter. Aryl protons *w* also interacted more strongly than aryl protons *x* with pyridyl proton *v* indicating a closer proximity of that end of the aryl aromatic rings with the **btp** motif.

The ^{1}H NMR of [2]catenane **111R**/**S** in $CDCl_3$ displayed pronounced broadening of particular proton resonances (Figure 5.5). The broadened nature of triazolyl (*t*), aryl (*x*),

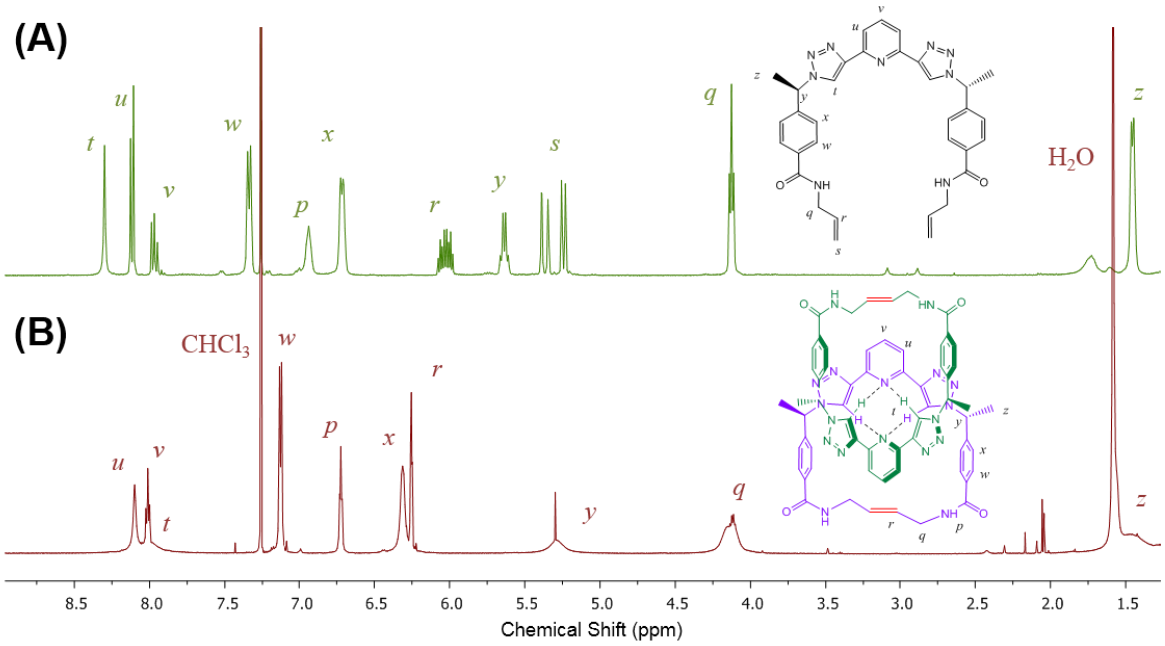

Figure 5.5 The ^{1}H NMR spectra of chiral **btp** precursor **103R** (A) and chiral **btp** [2]catenane **111R** (B) (400 MHz, $CDCl_3$) with resonances labelled.

methine (*y*) and methyl (*z*) proton resonances, and to a lesser extent the pyridyl resonances (*u* and *v*), indicated some fluxional process arising as a result of the movement of the component macrocycles relative to each other.[276] It is interesting to note that the broadened signals all corresponded to protons in the local vicinity of the [2]catenane's **btp** motifs. This was not the case in DMSO-d_6 where all resonances appeared to be well resolved and sharp; the reason for this being that in the more polar solvent, the transition state dipole of the fluxional process was better stabilised so the ring rotation had a lower activation barrier. The formation of the interlocked species was further confirmed by the appearance of characteristic peaks upon HRMS analysis. The MALDI^{+} spectra showed peaks at *m/z* = 1141.4824 and *m/z* = 1141.4813 corresponding to the $[M+H]^{+}$ species for **111R** and **111S**, respectively. As will be discussed in Section 5.7, formation of [2]catenane from epimerised **btp** olefin precursor **103** gave rise to a ^{1}H NMR spectrum which was difficult to interpret due to the mixture of diastereoisomers.

Formation of the interlocked system was also confirmed by single crystal X-ray diffraction analysis. All crystal structure refinement details are provided in Appendix E, Table E.4. Blade-like single crystals were obtained by slow evaporation of a solution consisting of CH_3CN:CH_2Cl_2 (9:1) and an epimerised mixture of the [2]catenane (the cause of the epimerisation will be discussed in Section 5.6 and 5.7).The data was solved and refined in the triclinic $P\bar{1}$ space group with one crystallographically distinct molecule in the asymmetric unit (Figure 5.6). Initially, the data was solved in *P*1 but after refinement it was

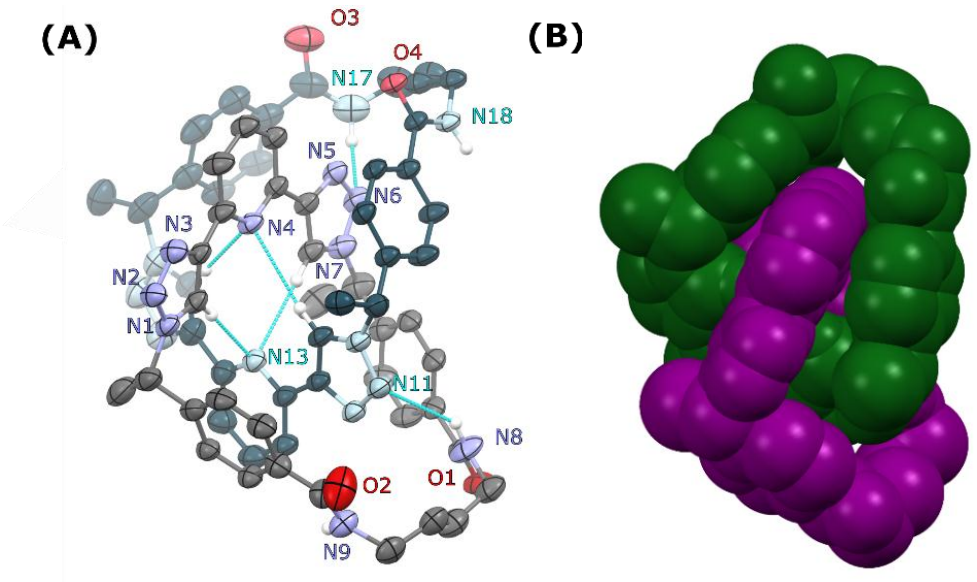

Figure 5.6 (A) Perspective view of the molecular structure of [2]catenane **111**. Thermal ellipsoids displayed at 30% probability and disordered contributor omitted for clarity. (B) Spacefill representation of crystal structure.

obvious that the compound was a mixture of diastereoisomers as evidenced by the methyl groups at the chiral centre being disordered. $P\bar{1}$ was used to retain data:parameter ratio and keep *Z'*=1 in order to avoid correlations on the atomic displacement parameters (ADPs) of the *pseudo*-equivalent atoms, accepting that no information could be extracted about the relative or absolute stereochemistry in either case. The molecular structure shows that the formation of the mechanical bond does not give rise to topological chirality due to the symmetric nature of the component macrocycles ensuring there is no directionality in their rings after RCM[359] unlike other systems[266,272,274-275] discussed in Section 1.11. There exists a number of intramolecular hydrogen bonding interactions as seen in the solid state structure of **36a**. There is a pair of non-classical hydrogen bonding interactions per interlocked macrocycle between **btp** motifs, directed to the pyridyl nitrogen atom acceptor of one constituent molecule from each triazolyl *CH* donors of the other interlocked consitutent macrocycle *i.e.* each pair of triazole donors binds to the pyridine acceptor of the other catenane 'thread'. The geometry of this hydrogen bonding moiety is *pseudo*-octahedral with the pyridyl nitrogen atoms of opposite macrocycles occupying the polyhedron apices and the triazolyl hydrogen atoms occupying the equatorial positions with hydrogen bonding distances ($|C_{triaz}–N_{pyr}|$) of ~3.5 Å and angles ∠ (*C-H···N*) of ~170 ° (see Table 4.1). The *pseudo*-octahedral polyhedron of the **btp-btp** hydrogen bonding moiety arises as a result of the planar **btp** motifs oriented essentially orthogonally to each other (the angle between the mean planes of the **btp** motifs is 97.5°). Significant π–π stacking is observed as the two aryl rings of both of the constituent

Table 5.1 Distances and angles associated with the *pseudo*-octahedron comprised by the non-classical **btp-btp** hydrogen bonding interactions.

D*···*A	**$\|C_{triaz}$–$N_{pyr}\|$ (Å)**	**∠(*C*-*H*···*N*) (°)**
C32···N4	3.42534(11)	172.8
C40···N4	3.65662(10)	170.7
C9···N13	3.40207(11)	169.0
C1···N13	3.51905(10)	172.6

macrocycles overlap with the pyridine-triazole unit of the **btp** motifs of the opposite constituent macrocycles. Thus, the four of these stacking interactions have perpendicular plane to plane centroid distances of between 3.4 Å-3.8 Å and angles between mean plane normals of between 11.9°-23.2°. This stacking behaviour seen in the solid state structure is consistent with the weak through-space interactions between the aryl rings and the **btp** motif observed using ROESY NMR spectroscopy, discussed earlier. As discussed above in relation to the ROESY experiment, the stronger through-space interaction between aryl protons *w* and pyridyl protons *u* compared with that seen between and aryl protons *x* and the latter, coincide with solid state structure demonstrating the closer proximity of that end of the aryl aromatic rings with the **btp** motif.

There is another pair of intramolecular hydrogen bonding interactions between one triazolyl nitrogen atom acceptor per [2]catenane constituent molecule and the amide nitrogen atom hydrogen bond donor on its interlocked equivalent. One of the hydrogen bonding interactions is between the cisoid amide *N17* donor and the medial triazolyl nitrogen atom *N6* of the other macrocycle. Here the distance |*N*-*H*···*N*| is 3.13592(10) Å and the angle ∠ (*N*-*H*···*N*) is 131.3°. The second hydrogen bonding interaction is between the transoid amide *N8* donor of the other macrocycle and the medial triazolyl *N11* acceptor of its equivalent constituent interlocked molecule. Here the distance |*N*-*H*···*N*| is 3.39956(10) Å and the angle ∠ (*N*-*H*···*N*) is 144.0°. There are also intermolecular hydrogen bonding interactions involving the amides. One of the cisoid amides is involved in a pair of hydrogen bonding interactions, firstly a hydrogen bond donor interaction between its *NH* and the *O1* oxygen of one of the transoid amides of a neighbouring molecule. The distance |*N*-*H*···*O*| in this case is 2.87843(7) Å with angle ∠ (*N*-*H*···*O*) of 149.3°. Simultaneously, the same amide is involved in a hydrogen bonding acceptor interaction between its oxygen *O4* and the *NH* of one of the transoid amides on another neighbouring molecule. The distance |*N*-*H*···*O*| is 2.88095(9) Å with angle ∠ (*N*-*H*···*O*) of 156.8°.

As expected, there are structural similarities between the solid state structure of **111** and **36a**[102] (Figure 1.29 in Section 1.6) but some geometrical variations also. The molecular structure of **111** was less tightly packed than its **36a** analogue as the π–π stacking distances measured *ca.* 3.4–3.8 Å and *ca.* 3.2–3.7 Å, respectively. Also the amide-triazole hydrogen bonding interactions measured *ca.* 3.4–3.6 Å and *ca.* 3.0–3.1 Å for **111** and **36a**, respectively, but the **btp**-**btp** hydrogen bonding interactions measuring *ca.* 3.4–3.7 Å for both, suggesting that this core interaction is unaffected by the structural changes to the system in the incorporation of the chiral centres.

[2]Catenanes **111R**/**S** were obtained in similar yields (42%/43% for **111R**/**S**, respectively) as the yield reported for [2]catenane **36a** (50%) indicating the chiral groups do not affect the efficiency of the [2]catenane formation. And as in the case of the synthesis of [2]catenane **36a** wherein some free macrocycle was formed, so too was the observation in synthesising **111R**/**S**. Macrocycle **112R**/**S** was separated, after concentrating the crude reaction mixture under reduced pressure, by flash chromatography (gradient DCM: CH_3OH (97:3)). In the case of both enantiomers, resonances indicative of macrocycle formation were observed by ^{1}H NMR (Figure 5.7). ^{1}H NMR analysis (600 MHz, DMSO-d_6) showed that the resonances related to the terminal olefin in **103S** disappeared in the spectrum of the product **112S** and an apparent triplet resonance appeared at 5.52 ppm due to the remaining olefin protons (*r*). The ^{1}H NMR of the enantiomer **112S** was identical (Appendix A.28). The low isolated yield

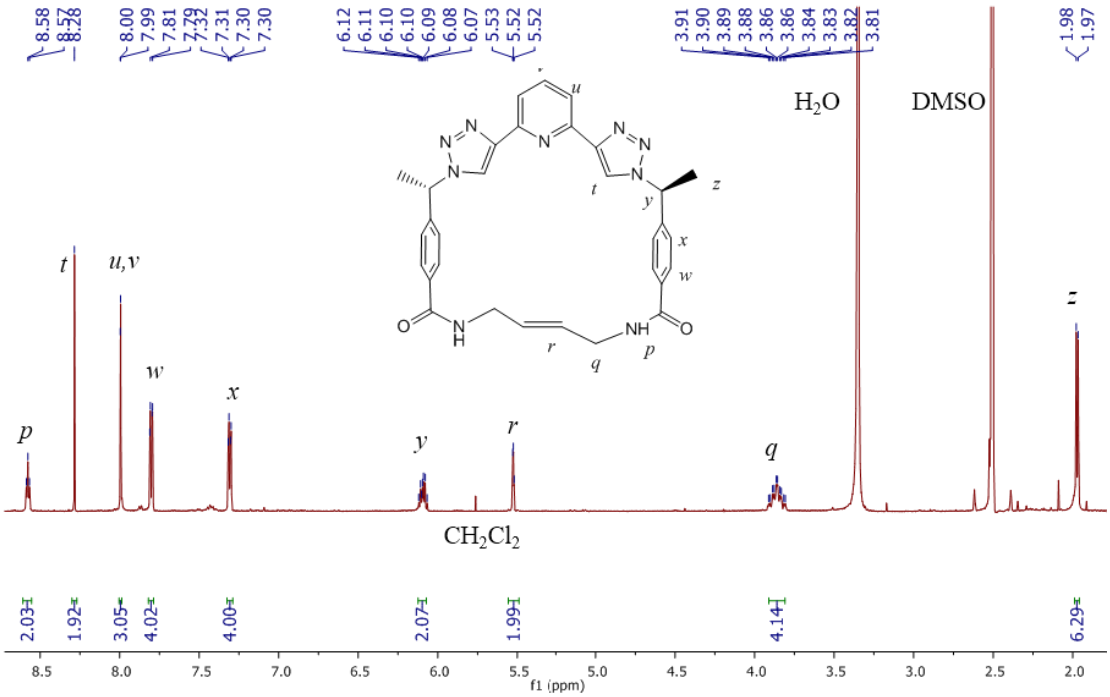

Figure 5.7 The ^{1}H NMR spectra of chiral **btp** macrocycle **112S** (600 MHz, DMSO-d_6) with resonances labelled.

of both enantiomers (8% and 14% for **112R** and **112S**, respectively) was evidence that the [2]catenane formation is favoured, once again demonstrating the suitability of the chiral 4'-substituted "arm" motif for pre-organising the formation of the interlocked system from the chiral **btp** olefin precursors.

It can be concluded that modification of the **btp** motif at the triazolyl *N1* position with a chiral centre in the incorporation of chiral 4'-substituted "arm" substituents does not have a detrimental effect on the synthesis of self-templated [2]catenane as yields for the formation of novel chiral [2]catenanes **111R**/**S** compared closely with that of **36a**.

5.5 ^{1}H NMR threading experiment

Having established that the chiral olefin precursor **103R**/**S** possesses the structural requirements which facilitates the necessary pre-organisation for efficient catenation to occur through hydrogen bonding interactions, it was next investigated if the self-templating dimerisation of the two **btp** precursors could be monitored in solution on the NMR timescale. However, it was necessary to be able to distinguish between two different components in the synthesis of the homocircuit [2]catenane **111R**/**S** in order to observe the point at which self-templation and catenation were occurring; the reason for this being, naturally, because two separate molecules of **btp** ligand **103R**/**S** are indistinguishable from the bulk. The two different components chosen were in the form of equimolar quantities of **btp** ligand **103S** and macrocycle **112S**. It was envisaged that a threading of the open form **btp** ligand **103S** through the ring of the macrocycle **112S** in a *pseudo*-rotaxane manner would result in proton resonance signals resembling those of the [2]catenane **111S**.

A $CDCl_3$ solution of **103S** (1.07 mM, 1 mL) and a $CDCl_3$ solution of **112S** (1.07mM, 1 mL) were analysed separately by ^{1}H NMR and the same broadening of certain proton resonances *i.e.* the triazolyl (*t*) aryl (*x*) and NH (*p*) was observed (Figure 5.8). However, the majority of the signals remained relative sharp. The two solutions were then mixed in an NMR tube and the resulting mixture was stirred in darkness over the course of the experiment. After initial mixing, all of the relatively sharp proton resonances visible in the ^{1}H NMR spectra of the isolated **103S** and **112S** became broadened. As remarked before, this broadening of the signals was indicative of a dynamic fluxional process involving the relative rotation of the self-assembly components.[276] There was no change in the broadened spectrum of the mixture after 120 hours. Little information could be gained from the spectrum at room temperature, however, upon carrying out the ^{1}H NMR experiment at −20 °C the resulting spectrum closely resembled that of the [2]catenane particularly in relation to the proximity of the chemical

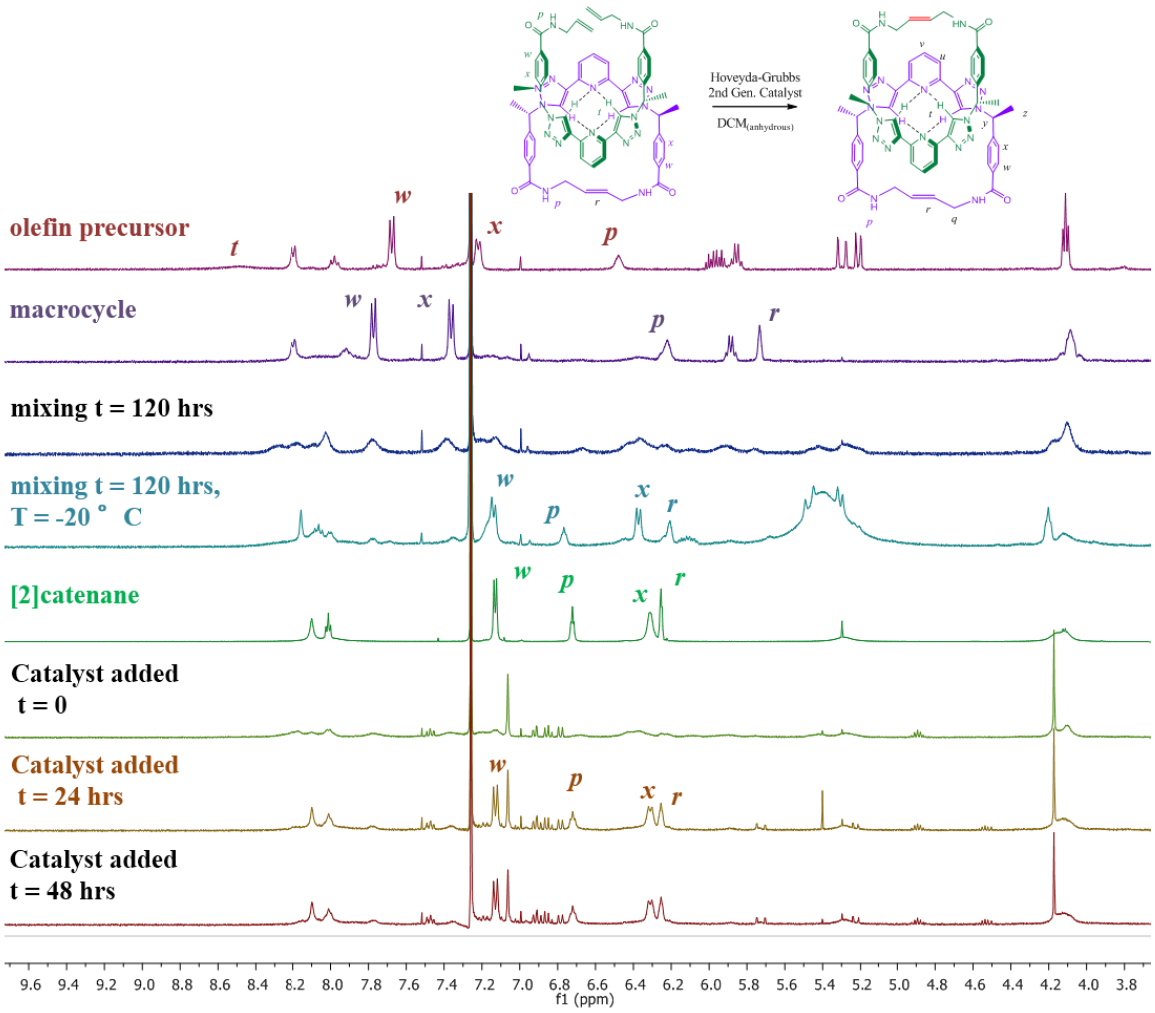

Figure 5.8 ^{1}H NMR spectra of the dimerisation of ligand **103S** with macrocycle **112S**. Initial broadening of the proton resonance signals followed by a change in signal chemical shifts indicated threading of **103S** through macrocycle **112S** *i.e.* pseudo-rotaxane formation. Addition of RCM catalyst demonstrated a ^{1}H spectrum which closely resembled that of the [2]catenane.

shifts of the now deshielded olefin proton signal *r*, around 6.2 ppm, and amide proton *p* around 6.7 ppm and of the now shielded aryl signals, *w* and *x*, at 7.3 ppm and 6.3 ppm, respectively. This was strong evidence for the threading of the open form **103S** through the cavity of the macrocycle **112S**. To this was added Hoveyda-Grubbs 2nd generation catalyst (0.5 eq.) in $CDCl_3$. Shortly after adding the catalyst the proton resonances regained their broadened appearance at room temperature, however, after 24 hours a clear resemblance with the spectrum of the [2]catenane was observed. The newly formed olefin proton's signal, *r*, appeared at 6.25 ppm, exactly coincident with the corresponding peak of the [2]catenane **111S**, while the same observation was made for the amide proton's resonance and the aryl proton's signals, *w* and *x*, at 6.73 ppm, 7.14 ppm and 6.31 ppm, respectively. There is little change to the ^{1}H NMR spectrum after 48 hours of adding the Hoveyda–Grubbs 2nd generation catalyst. This is spectroscopic evidence for the formation of a *pseudo*-rotaxane

between **btp** olefin **103S** and macrocycle **112S** prior to the formation of [2]catenane **111S**.

The same experiment was carried out in DMSO-d_6 solvent as it was envisaged that self-templating dimerisation would not be observed in a more polar solvent. Upon mixing of **btp** olefin **103S** and macrocycle **112S** there was no observed chemical shift changes and no broadening of signals initially and after 120 hours of stirring at room temperature (Figure 5.9) The spectrum after 120 hours of mixing **103S** and **112S** did not resemble that of the [2]catenane which can be rationalised by the more polar DMSO solvent molecules out-competing or breaking up any possible hydrogen bonding interactions necessary for threading to occur. It can be concluded that anhydrous non-polar solvents such as CH_2Cl_2

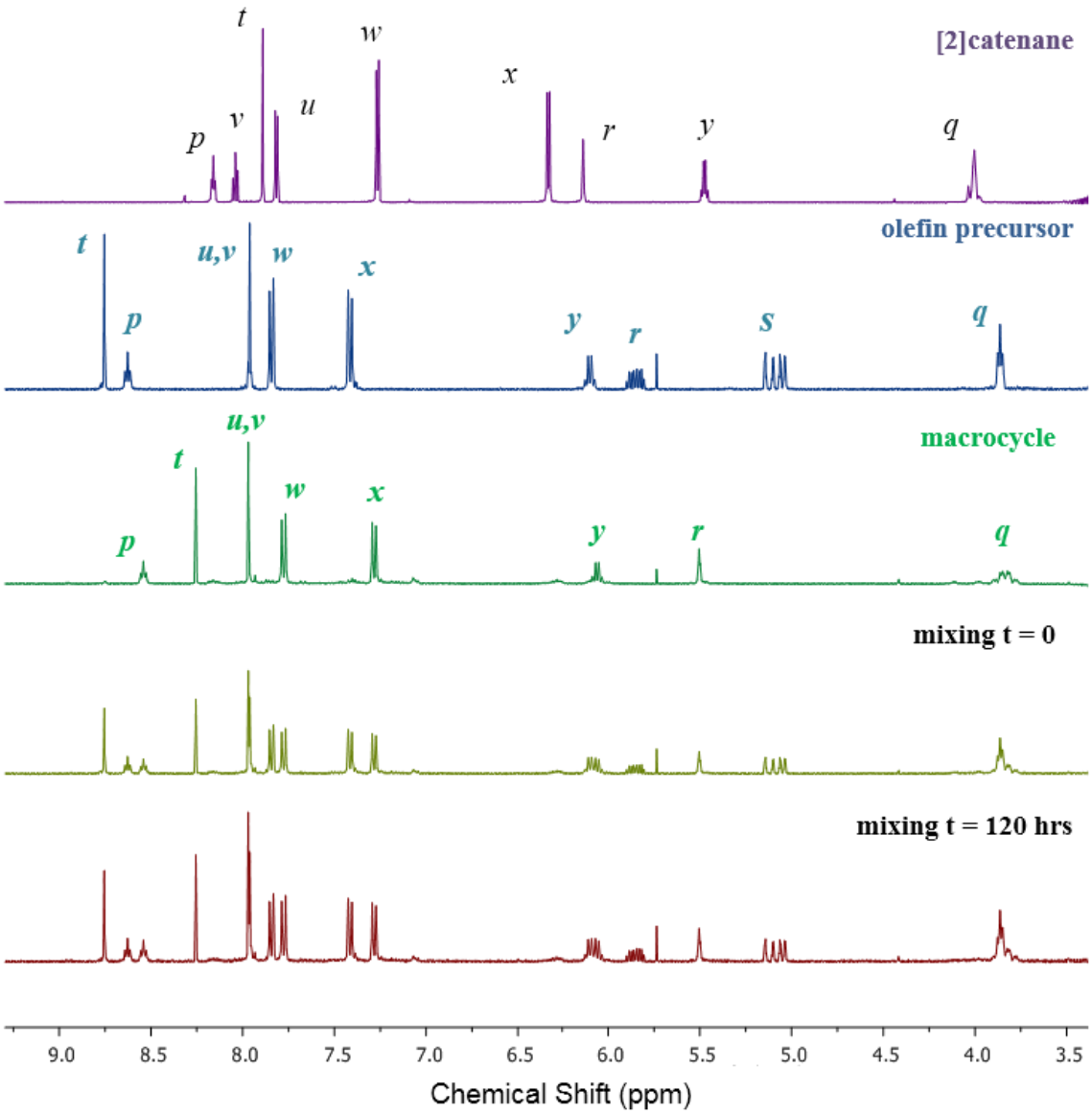

Figure 5.9 ^{1}H NMR (400 MHz, DMSO-d_6) spectra of the attempted dimerisation of ligand **103S** with macrocycle **112S**. No broadening of the proton resonances and no change in chemical shifts indicated that the threading of **103S** through macrocycle **112S** did not occur.

and $CHCl_3$ are more appropriate for the self-templating dimerisation process as they do not compete with **btp** hydrogen bonding interactions.

The threading of **btp** olefin **103S** through macrocycle **112S** is an important finding in understanding the process which leads to self-templated [2]catenane formation as it allowed the reaction to be monitored closely in solution using ^{1}H NMR spectroscopy and the *pseudo*-rotaxane reaction intermediate to be characterised prior to mechanically interlocking the system. This also may show potential for the synthesis of heterocircuit **btp** [2]catenanes as different components used in the RCM reaction nevertheless gave rise to [2]catenane formation. Having achieved and monitored the formation of self-templated chiral [2]catenanes **111R**/**S** from chiral **btp** ligands it was necessary to investigate their optical activity and spectroscopic properties.

5.6 Chiroptical spectroscopic characterisation of btp ligands 103R/S, 109R/S, 110R/S and [2]catenanes 111R/S

Optically active enantiomeric pairs interact with electromagnetic radiation in equal but opposite extents by absorbing the left or right handed polarisations of it as it passes through the sample in solution. As a result of these differing interactions with light, there exist 'chiroptical' spectroscopic techniques which allow further characterisation of such chiral systems and assemblies. Circular dichroism (CD) can be considered a chiral analogue to UV-vis absorbance in that it refers to the differential absorption of left- or right-handed polarised light by optically active compounds, resulting in radiation with elliptical polarisation,[364-365] consequently, enantiomers will give CD signals of equal magnitude and opposite signs. CD reflects structural properties of the system's electronic ground state. Introduction of chiral centres in close proximity to the **btp** chromophores is expected to exhibit more pronounced optical activity as demonstrated by Byrne *et al.*[103,156] This will allow us to monitor the retention of stereochemistry in the **btp** precursor ligands and in the resulting chiral [2]catenane systems **111R**/**S**.

UV-vis absorption spectra of ligands **103R**/**S** and **109R**/**S** in CH_3CN and **110R**/**S** in CH_3CN:CH_3OH (24:1) were recorded. All of these compounds had very similar molar extinction coefficients for bands centred at 301 nm (assigned to **btp** n→π* transitions) as well as a band with a maximum at 236 nm (assigned to the π→π* transitions in the aromatic rings). As expected the UV-vis absorption spectra for both enantiomers were identical. The enantiomers gave CD spectra of opposite sign with **103S**, **109S** and **110S** displaying positive peaks centred at 301 and 236 nm, while **103R**, **109R** and **110R** have negative signals of

equal intensity magnitude at the same wavelengths. Particularly in the cases of **109R/S**, this is consistent with mechanistic studies of the diazo-transfer reaction which showed successful retention of stereochemistry in conversion of the chiral amine to the corresponding azide.[366] These bands corresponded closely to the main absorbance bands (Figure 5.10). The molar extinction coefficients were similar in magnitude: (λ_{max} / nm (ε_{max} /dm^3 mol^{-1} cm^{-1}): 236 *(*43,000), 301 (8,800) for **103R/S**, 236 *(*43,000), 301 (8,700) for **109R/S** and 236 *(*46,000), 301 (9,100) for **110R/S** and the ellipticity was of similar magnitude across the three enantiomeric pairs. The enantiomers were present in equal abundances due to the equal and opposite extent to which the left- and right-handed polarised light was absorbed.

The [2]catenanes **111R/S** were also studied photophysically. There was a bathochromic effect observed for the band centred at 301 nm assigned to the assigned to **btp** n→π* transition of olefin precursor **103R/S** red-shifting to 306 nm for **111R/S** upon catenane formation, see Figure 5.11(A). There was also a hypsochromic effect on the band centred at 236 nm assigned to the π→π* transitions in the aromatic rings, blue-shifting to 231 nm for **111R/S**. The molar extinction coefficient also increased (λ_{max} / nm (ε_{max} /dm^3 mol^{-1} cm^{-1}): 231 (65,000), 306 (14,000) as a result of the increased number of chromophores in the [2]catenane relative to the precursor olefin. There was a dramatic effect on the bands of the CD spectra of the [2]catenanes **111R/S**, see Figure 5.11(B). The CD spectra of both **111R/S** displayed the Cotton effect in both of the bands at 231 nm and 306 nm, that is the bands were split such that the band components cross zero at the absorption maximum and exhibit

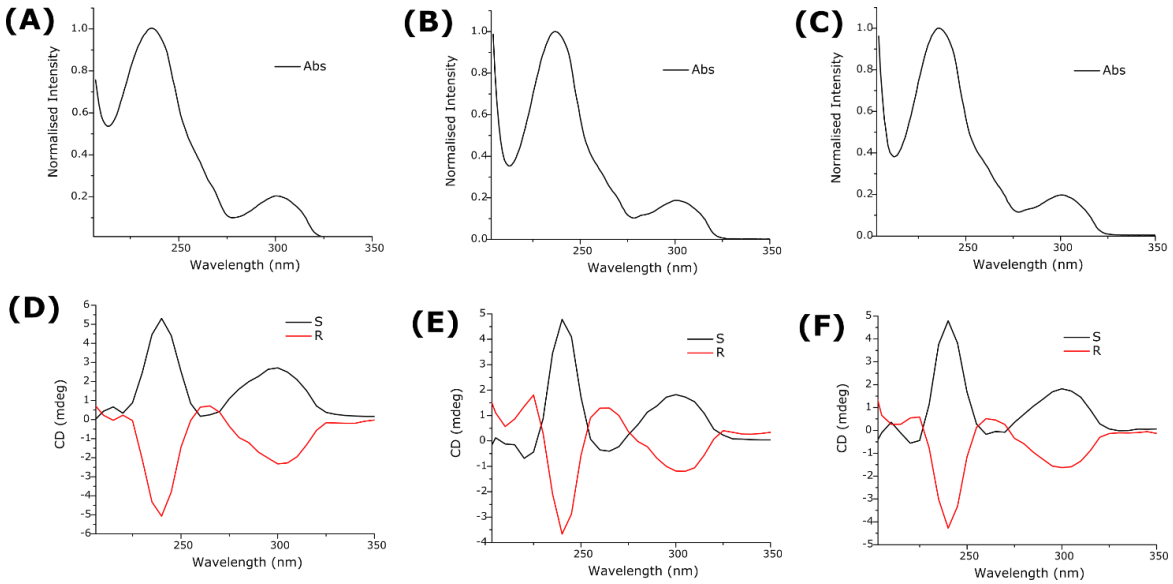

Figure 5.10 Photophysical spectra of ligands **103R/S**, **109R/S** measured in CH_3CN and **110R/S** measured in CH_3CN:CH_3OH (24:1) at room temperature (c = 1 × 10^{-5} M): UV-Vis absorption spectrum of (A) **103R/S**, (B) **109R/S** and (C) **110R/S**; CD spectra of ligands (D) **103R/S**, (E) **109R/S** and (F) **110R/S**.

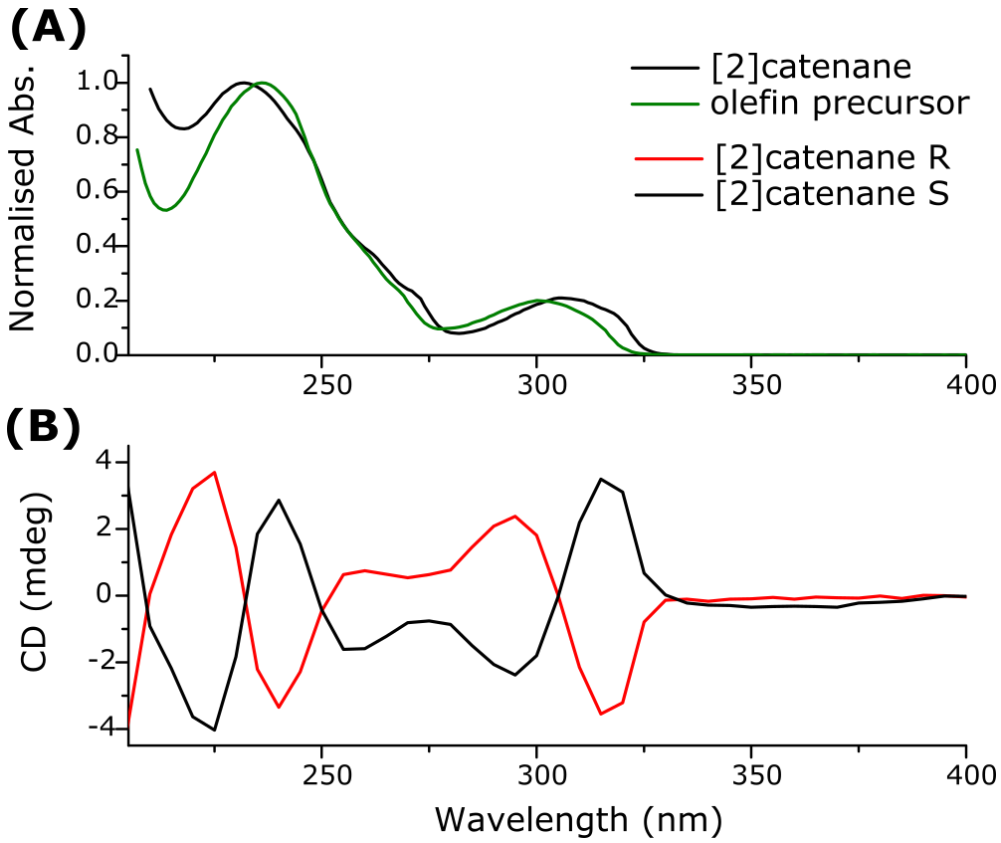

Figure 5.11 Photophysical spectra of ligands olefin precursor **103R/S** and [2]catenane **111R/S** measured in CH_3CN at room temperature ($c = 1\times10^{-5}$ M): (A) UV-vis absorption spectra comparison of **103R/S** and **111R/S;** (B) CD spectra of **111R/S**.

signals of opposite signs either side of zero.[364-365] Such changes arose as a result of exciton coupling between the chromophores of similar energy in close proximity, brought together by the self-templated [2]catenane formation. The spectrum of the **111S** enantiomer showed a large positive exciton couplet with a Davydov splitting of *ca.* 20 nm, arising from splitting of the 306 nm-centred **btp** n→π* transition. A shoulder at 257 nm to this signal was observed in the CD spectra of both **111R/S** which may also have arisen due to exciton coupling. The Cotton effect was also observed in the 231 nm centred π→π* transition. In this case, an exciton couplet with a Davydov splitting of *ca.* 15 nm, was observed also arising due to the close proximity of the aromatic rings as a result of [2]catenane formation. These studies confirmed that the **btp** ligands, **103R**, **109R** and **110R**, not only retained their optical activity, but also that the ligand precursors endowed the resulting self-templated [2]catenane **111R/S** with their inherent chirality. The chiral information transferred by the *R*- and *S*- enantiomers of the chiral **btp** olefin precursors **103R/S** was manifested in the equal and opposite manners by which the [2]catenanes **111R/S** interacted with circularly polarised electromagnetic radiation. It can be concluded that the self-templated synthesis of [2]catenanes from **103R/S** gave rise to **111R/S** which were enantiomers of each other.

As was briefly mentioned in Section 5.4 in relation to the single crystal X-ray diffraction analysis of the solid state [2]catenane, initial attempts at forming enantiopure [2]catenanes crystals were not successful due to the use of precursors which had undergone epimerisation. This was realised through the monitoring of the CD spectra of **btp** ligands **103S**, **109S** and **110S** (Figure 5.12). There was a sharp decrease in the intensity of CD signals relating to the **btp** n→π* transition at 301 nm and the π→π* transition at 236 nm for acid **110S** and olefin **103S**, see Figure 5.12(A). It was expected that all ligands **103S**, **109S** and **110S**, possessing the same chiral **btp** chromophore, and similar molar extinction coefficients, would display CD signals of comparable intensity when each was analysed at equal concentration (c=1×10^{-5} M). Hewlins *et al.* reported that drug enantiomers can undergo racemisation through benzylic proton abstraction at physiological pH,[367] therefore it was investigated if the epimerisation was occurring during the hydrolysis of **109S**. **109S** was stirred at 100 °C in CH_3OH:$NaOH_{(aq)}$ (1:1) for 24 hours, according to initial reaction conditions, and separately at 48 hours. Once again a sharp decrease in the intensity of the signals in the CD spectrum of **110S** was observed after 24 hours hydrolysis indicating epimerisation. After 48 hours of hydrolysis under the same conditions **110S** had racemised as evidenced by the lack of signal in the CD spectrum. Therefore, it was concluded that the hydrolysis conditions were too harsh; using excess of $NaOH_{(aq)}$ and high temperature was resulting in deprotonation of the methine proton and scrambling of the stereogenic centres through proton exchange, and therefore, a loss in the retention of stereochemistry. The synthesis was revised using stoichiometric amounts of $NaOH_{(aq)}$ in CH_3OH at room temperature for 17 hours. This resulted in a CD spectrum of **110S** which displayed band intensities which were

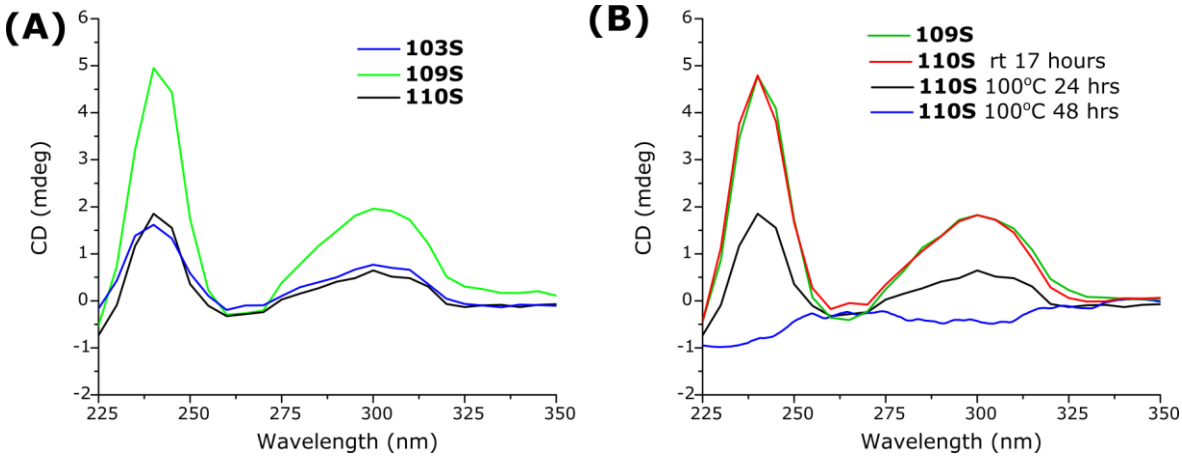

Figure 5.12 (A) CD spectra of ligands **103S**, **109S** measured in CH_3CN and **110S** measured in CH_3CN:CH_3OH (24:1) at room temperature (c = 1×10^{-5} M) after initial hydrolysis of ester **109S** to acid **110S**: (B) CD spectra of **109S** in CH_3CN and **110S** measured in CH_3CN:CH_3OH (24:1) at room temperature (c = 1×10^{-5} M) after varying conditions for hydrolysis of ester **109S**.

equal to those of the ester **109S** precursor, see Figure 5.12(B). As we saw in Section 5.4, this revised hydrolysis of the ester resulted in enantiopure precursors which lead to the synthesis of [2]catenanes **111R**/**S** as evidenced by the clean, one component ^{1}H NMR, see Figure 5.4(B). As we will now discuss in the following section, the presence of any diastereoisomers of the olefin precursor **103S** could be detected by ^{1}H NMR upon [2]catenane formation.

5.7 Epimerisation of chiral centre

As was discussed in the previous section, **110S** underwent epimerisation under harsh hydrolysis conditions of **109S** *via* abstraction of the methine proton. This was evidenced by CD spectroscopy but signs were also observed in the ^{1}H NMR spectra of **103S** in $CDCl_3$ (Figure 5.13). The resonances *y* and *z* associated with the chiral centre corresponding to the methine proton and methyl protons respectively were comprised of overlapping multiplets indicative of at least two different chemical environments which would arise due to a mixture of enantiomers **103R**/**S** and diastereoisomer **103**(*R*,*S*). **Btp** olefin **103S** no longer possessed exclusively (*S*,*S*) character, hence the (*R*,*S*) diastereoisomer was observed in non-polar solution. However, in DMSO-d_6 the ^{1}H NMR spectrum of epimerised **103S** appeared exactly as enantiopure **103R**/**S**, see Figure 5.4(A). This was indicative of a molecular conformation arising on account of the role of the hydrogen bonding interactions which were allowed to exist in non-polar solvent but were broken up in more competitive polar solvents. It was expected that this conformation was brought about by the dimerisation of the **btp**-**btp** motif and pre-organisation of the chiral 4'-substituted "arms" which resulted in the methine and methyl protons oriented diastereotopically in differing chemical environments. This was

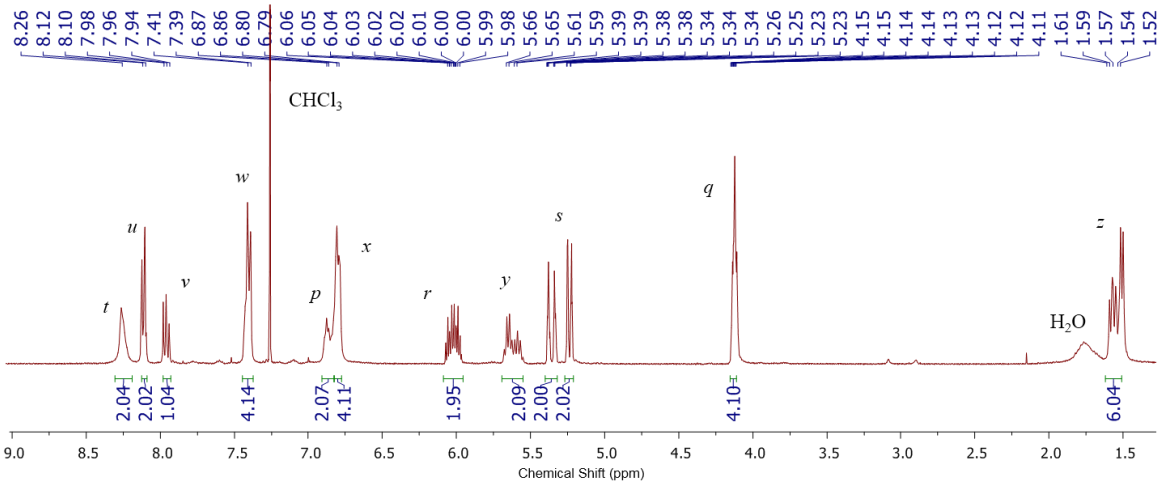

Figure 5.13 ^{1}H NMR spectra of epimerised chiral **btp** precursor **103S** (400 MHz, $CDCl_3$) with resonances labelled.

evidenced by the disordered methyl groups in the crystal structure of the epimer [2]catenane **111**, see Appendix E.14).

The effect of epimerisation on the ^{1}H spectrum of **103S** is more pronounced in the ^{1}H NMR spectrum of epimer [2]catenane **111** (Figure 5.14). When RCM was carried out on the epimerised olefin, consisting of a mixture of **103R**/**S** and **103**(*R*,*S*), mixed interlocked systems were formed upon [2]catenane formation. The mixture consisted of a potential number of components such as enantiomers **111R**/**S**, and their diastereoisomers **111**(*R*,*R*)(*S*,*S*), **111**(*R*,*R*)(*R*,*S*), **111**(*R*,*R*)(*S*,*R*), **111**(*S*,*S*)(*R*,*S*) and **111**(*S*,*S*)(*S*,*R*). The different orientations of the methyl groups of diastereoisomers **111**(*R*,*R*)(*R*,*S*) and **111**(*R*,*R*)(*S*,*R*), for example, when closely packed in their respective [2]catenane systems transferred notably different chemical environments to their protons resulting in groups of overlapping multiplet resonances. In particular, resonances associated with the **btp** motif and adjacent chiral centres were widely dispersed whereas resonances such as *w*, *r*, *q* and to a lesser extent *x*, were concentrated in narrower chemical shift ranges. This was evidence that the "self"-

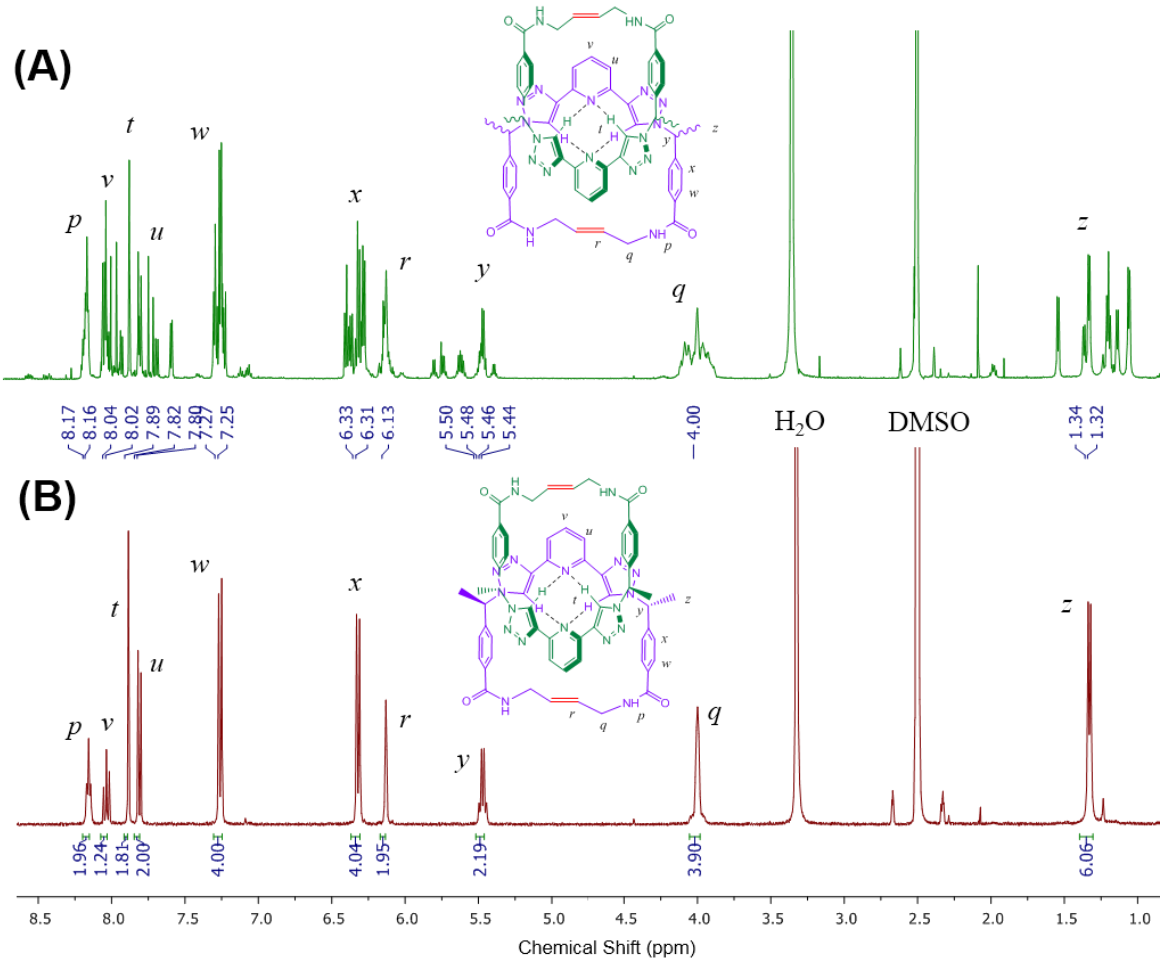

Figure 5.14 ^{1}H NMR spectra of epimer [2]catenane **111** (A) (600 MHz, DMSO-d_6) and chiral **btp** [2]catenane **111R** (B) (400 MHz, DMSO-d_6) with resonances labelled.

templated [2]catenane formation was not affected by the presence of the chiral centre as enantiomers and diastereoisomers alike templated the formation of mixed mechanically interlocked systems under the same reaction conditions used to obtain homocircuit [2]catenanes **111R**/**S** containing exclusively *R*- and *S*- chiral centres, respectively. It can also be concluded that the revised and milder hydrolysis conditions used to synthesise chiral **btp** acid **110R**/**S** successfully retained the stereochemistry of the chiral **btp** methyl ester as any evidence of epimerisation would have been observed by ^{1}H NMR spectroscopy upon [2]catenane formation. As already discussed in Section 5.4, a crystal structure was obtained from recrystallisation of the epimer [2]catenane **111**. These blade-like single crystals grew readily in a range of solvent mixtures with optimal conditions achieved through slow evaporation of a solution consisting of CH_3CN:CH_2Cl_2 (9:1). Despite this facile recrystallisation of the epimer, exhaustive efforts into attempts in obtaining an enantiopure crystal structure of [2]catenanes **111R**/**S**, using a range of solvent mixtures and recrystallisation methods, were unsuccessful. However, a second crystal structure arising from an epimerised mixture was obtained, this time for **btp** acid **110**.

Large colourless block-like single crystals were grown by slow evaporation of an EtOAc solution. It should be noted at this point that the structure was disordered to a large extent as a result of the epimerisation giving rise to weakly diffracting data with increasing angle 2θ despite the large size of the single crystals grown. As a result, the current partial solution is presented with some caution and represents a preliminary connectivity only, therefore geometrical parameters will not be included. The data for ligand **110** were solved and refined in the monoclinic *C*2/*c* space group. This space group was chosen because it was the most appropriate to describe the poor data obtained (as it makes certain assumptions about the nature and symmetry relationships of the diastereomers that may not prove true if better data could be obtained). There are four crystallographically distinct molecules in the asymmetric unit and it just so happens that the **btp**-**btp** dimerisation can be observed existing in the solid state as a result of the net dipole moment minimisation effect upon crystallisation as well as other packing factors such as conjugation,[107,331-332] see Figure 5.15(A). Both **btp** molecules adopt the *anti*-*anti* conformation necessary for the **btp**-**btp** dimers to aggregate and the benzoic acid arms adopt a skewed *trans*-like conformation relative to each other. Packing is facilitated along the *c*-axis direction through two pairs of $R_2^2(8)$ cyclic carboxylic acid dimers per molecule.[339] The resulting one dimensional hydrogen bonding network can be described in terms of a zig-zag chain since the 'handedness' alternates along the chain at each **110** molecule, see Figure 5.15(B). This results in a ‘figure of 8’ arrangement when viewed down the chain axis

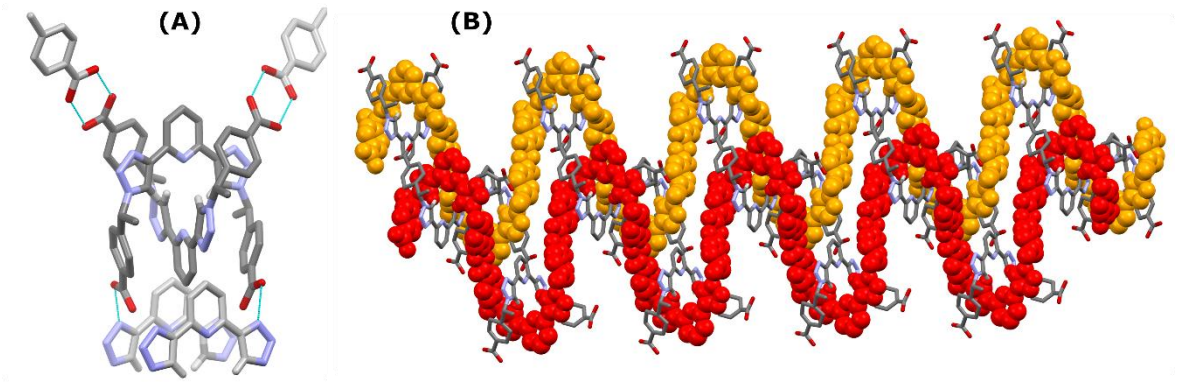

Figure 5.15 Crystal structure of epimerised acid **110**. (A) Fragment representation of the **btp**-**btp** dimer in the solid state also showing polymeric carboxylic acid and triazole-carboxylic acid hydrogen bonding interactions. The disordered contributor and hydrogen atoms are omitted for clarity. (B) Adjacent one dimensional carboxylic acid hydrogen bonding networks extending along the *c* axis, viewed along the *a* axis.

(Appendix E.15). The other **btp** molecule involved in the dimer facilitates the connection of adjacent zig-zag chains along the *a*-axis through triazole-carboxylic acid hydrogen bonding interactions, which are themselves directed along the *b* axis. Each of the carboxylic acid 'arms' per molecule is involved in one hydrogen bonding interaction with the proximal triazolyl nitrogen atom of its two symmetry related **btp** molecules either side of it.

There are striking similarities between chiral **btp** ligand **110R**/**S** with tricarboxylic acid **btp** ligand **H$_3$84** which showed the dual ability of templating the synthesis of both functional metallo-supramolecular gel soft materials and more rigid luminescent cation-exchange MOF materials. Efforts are underway to investigate the ability of chiral **btp** ligand **110R**/**S** to template the synthesis of analogous materials and explore the mechanical and optical properties of the resulting systems. Having concluded that the introduction of a chiral centre in the form of chiral 4'-substituted "arms' does not affect the efficiency of self-templated homocircuit [2]catenane synthesis, it was next investigated what effect functionalisation of the **btp** motif with sterically bulky groups would have on said synthesis' efficiency.

5.8 Synthesis and characterisation of btp olefin 104 functionalised at the 4-pyridyl position

It was proposed in Section 2.3 that modification of **btp** ligands with orthogonal carbonyl functionality would be beneficial for controlling the design of new ligands for various self-assembly processes. It was for this reason that **btp** ligand **86** was synthesised according to Scheme 2.5 in Section 2.3. It was envisaged that subjecting ligand **86** to amide coupling with allylamine, producing a **btp** olefin with the desired 4'-substituted "arm" substituent for self-templated [2]catenane formation, would allow the role a sterically bulky benzyl ester

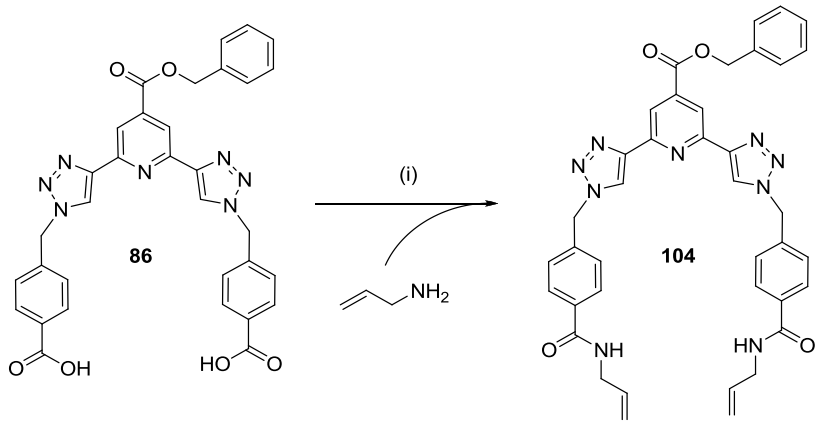

Scheme 5.3 Synthesis of ligands **104**. (i) 1) allylamine, Et_3N, DMAP, CH_2Cl_2/ DMF (4:1), 0°C, 30 mins, 2) EDCI·HCl, 0°C, 30 mins, rt, 66 hrs.

functionality would play to be ascertained, in terms of the efficiency of the synthesis of the interlocked system. For example, it was postulated that the benzyl aromatic ring could hinder the approach and pre-organisation of the 4'-substituted "arm" upon dimerisation, through blocking off the triazole nitrogen atom hydrogen bonding acceptor sites. And finally, the introduction of an electron-withdrawing substituent conjugated to the **btp** motif and its effect on **btp**-**btp** dimerisation in non-polar solvents would be explored. With this in mind, **btp** olefin **104** was synthesised from **86** according to Scheme 5.3. The amide coupling was carried out by EDCI·HCl activation in the presence of Et_3N and DMAP. **Btp** olefin **104** was obtained as a white solid after purification by automatic flash chromatography (gradient CH_2Cl_2: CH_3OH (95:5)) in a poor yield of 18%. ^{1}H NMR spectroscopy confirmed successful synthesis of **104** (Figure 5.16). The singlet at 8.81 ppm in DMSO-d_6, with an integration of 2, corresponded to be the triazolyl *CH r*esonance by HSQC and HMBC. The triplet at 8.67 corresponded to the amide proton and the pyridyl singlet appears at 8.38 ppm. The doublets at 7.87 ppm and at 7.74 ppm corresponded to the aryl proton resonances amongst which can be found overlapping resonances belonging to the 3,5- and 4-benzyl protons of the ester moiety. The 2,6-benzyl protons of the same aromatic ring were found at 7.54 ppm appearing as a doublet. The doublet of doublets of triplets at 5.87 ppm, with an integration of 2, and the pair of doublets of doublets of doublets at 5.15 ppm and 5.08 ppm, integrating to 4, were determined to be the internal and terminal olefin protons, respectively. Between these olefin resonances appeared two singlets at 5.78 ppm and 5.46 ppm, corresponding to the methylene protons adjacent to the triazolyl *N1* atoms and the benzyl ester, respectively. Finally, the apparent triplet of triplets appearing at 3.88 ppm integrating to 4 protons was indicative of the methylene protons adjacent to the olefin moieties. The ^{13}C NMR spectrum, HSQC and HMBC allowed assignment of the carbonyl and quaternary carbons. MALDI$^+$ mass

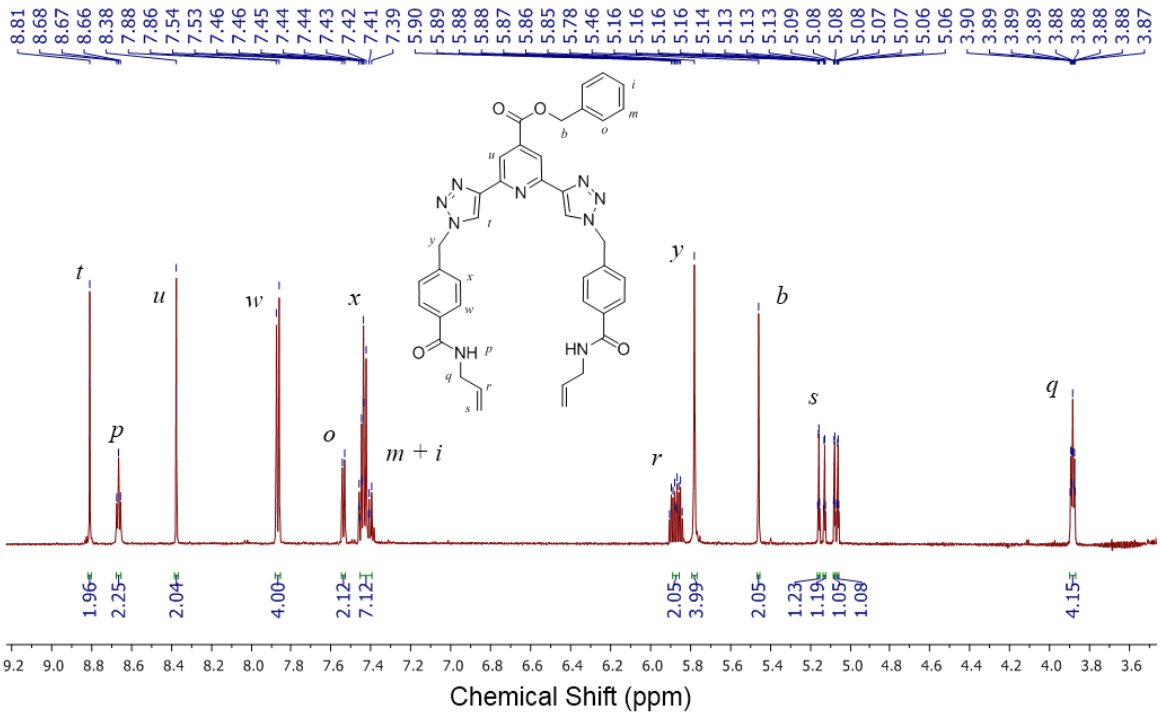

Figure 5.16 ^{1}H NMR spectrum of chiral **btp** olefin **104** (600 MHz, DMSO-d_6) with resonances labelled.

spectrometry analysis displayed a characteristic peak at *m/z* = 716.2741, which agreed with the *m/z* calculated for $[M+Na]^+$. Having confirmed synthesis of **btp** olefin **104** and encouraged by the success of chiral **btp** olefin precursors **103R/S** in formation of self-templated [2]catenanes, investigation of the effect of the **btp**-conjugated benzyl ester substituent on [2]catenane formation was carried out by Hoveyda-Grubbs catalysed RCM.

5.9 RCM of btp olefin 104 functionalised at the 4-pyridyl position

A solution containing **104** and Hoveyda–Grubbs 2nd generation catalyst (50 mol %) in anhydrous CH_2Cl_2 was stirred under argon at room temperature in darkness for 7 days according to the same synthetic procedure as before for [2]catenanes **111R/S** in Section 5.4. Trituration with CH_3CN achieved isolation of pure [2]catenane **113**. Peaks indicative of [2]catenane **113** formation were observed by ^{1}H NMR (Figure 5.17) sharing closely similar chemical shift trends as was seen for [2]catenane **111R/S** and **36a**, particularly in relation to shielded aryl resonances *w* and *x*. However, despite dissolving **113** in DMSO-d_6, certain peaks in the ^{1}H NMR spectrum remained broadened which was not the case for ^{1}H NMR spectra of **111R/S**. The broadened features of the ^{1}H NMR spectrum of **113** in DMSO-d_6 resembled those of **111R/S** in non-polar $CDCl_3$ which was indicative of a dynamic process involving the relative movement of the constituent macrocycles to each other. This suggests that the increased steric bulk of the benzyl ester substituent was contributing to a system

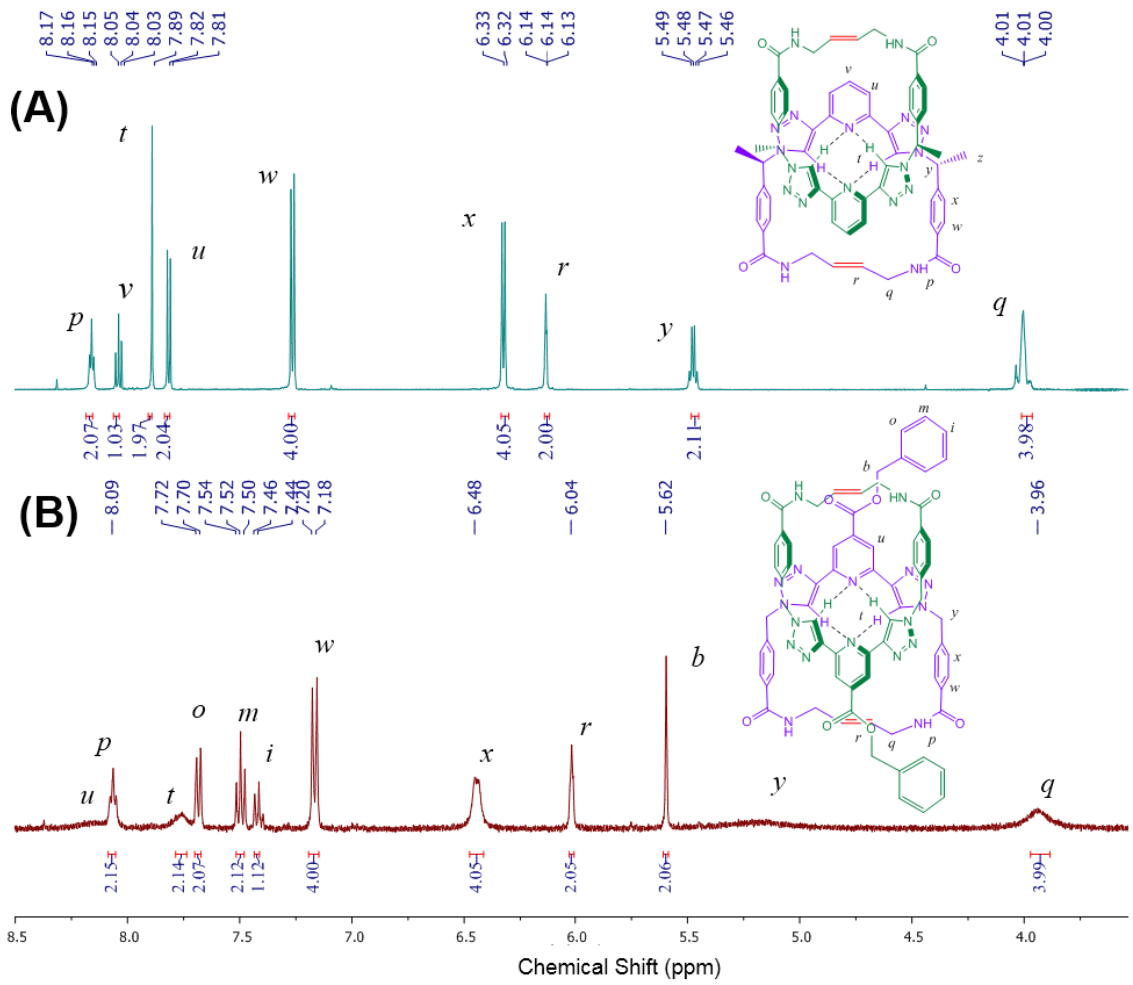

Figure 5.17 ^{1}H NMR (400 MHz, DMSO-d_6) comparison between (A) [2]catenanes **111R** and **113** (B) demonstrating the significant broadening of certain proton resonances of the more sterically bulky system of **113**. Such observations are indicative of a slower dynamic process in the case of **113** relative to **111R**.

which possessed less rotational freedom, the dynamic nature of which was slow on the NMR timescale. It was envisaged that the forces responsible for constraining the freedom of the system could be broken up by increasing the temperature of the DMSO-d_6 solution and a sharpening of proton resonance signals could be obtained. It could be observed that at high temperature, such as 80 °C, all signals were indeed sharpened (Figure 5.18). In particular, the proton resonance signals which saw the most pronounced sharpening effect were pyridyl proton *u*, triazolyl protons *t*, aryl protons *x*, and the two methylene protons *y* and *q*, adjacent to the aryl 'arm' moiety. The benzyl methylene proton signal remained sharp throughout. At room temperature the majority of these peaks had all but disappeared entirely as a result of the dynamic process. It was expected that the *NH* proton signal would see similar broadening behaviour as a result of its significant role in intramolecular hydrogen bonding in the [2]catenane. However, this proton resonance signal remained well resolved. Over the course

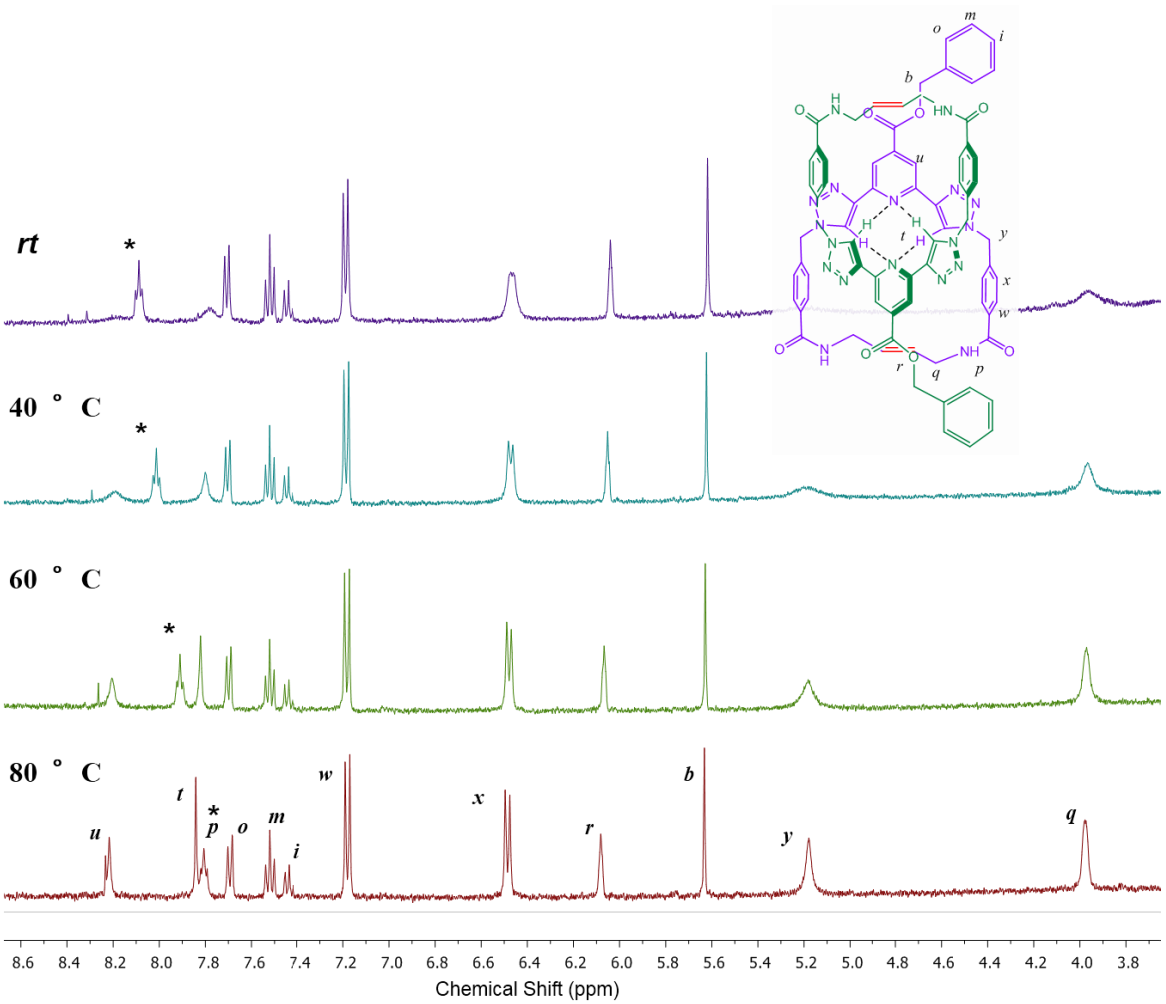

Figure 5.18 ^{1}H NMR (400 MHz, DMSO-d_6) spectra demonstrating the effect of changing temperature on proton peak resonance chemical shift and sharpness of **113**.

of the experiment, as the temperature was increased the chemical shift could be seen to change from 8.1 ppm at room temperature to 7.8 ppm at 80 °C.

The formation of the interlocked species was further confirmed by the appearance of characteristic peaks upon HRMS analysis. The MALDI^{+} spectra showed a peak at *m/z* = 1353.4913 corresponding to the [M+Na]$^{+}$ species. And as in the case of the synthesis of [2]catenane **36a** and **111R/S** wherein some free macrocycle was formed, so too was the observation in synthesising **113**. Macrocycle **114** was observed by ^{1}H NMR spectroscopy but could not be purified fully, as the filtrate obtained, following repeated trituration from CH_3CN, contained residual amounts of **113**. The MALDI^{+} spectra showed a peak at *m/z* = 688.2397 corresponding to the [M+Na]$^{+}$ species.

It can be concluded that self-templated [2]catenane formation can also be achieved with **btp** motifs functionalised at the 4-pyridyl position. It was envisaged that modification of the **btp** unit with a conjugated benzyl ester at the 4-pyridyl position may affect the self-templating dimerisation of olefins **104** and thus the yield of the [2]catenane formation either

through steric hindrance or as a result of the electron-withdrawing effect of the carbonyl groups situated *para* to the pyridyl nitrogen atom, thus, altering the **btp**-**btp** hydrogen bonding ability. However, the yield of 40 % was comparable to those recorded for [2]catenanes **111R**/**S** which were obtained in similar yields (42%/43% for **111R**/**S**, respectively) and the yield reported for [2]catenane **36a** (50%). This would indicate that the substitution at the 4-pyridyl position of the **btp** motif does not affect the efficiency of [2]catenane formation. This result presents numerous possibilities for the synthesis of a library of self-templated [2]catenanes through modification of the **btp** motif at the 4-pyridyl position and adjacent to the triazolyl *N1* position. All self-templated [2]catenanes synthesised up to this point possessed the 4'-substituted "arm" structural feature. In order to carry out a thorough analysis of whether this structural motif is essential for efficient [2]catenane formation, **btp** olefins lacking this motif were synthesised and investigated for their self-assembly behavior and ability to form analogous mechanically interlocked systems.

5.10 Synthesis and characterisation of olefin-derivatised btp ligands 105 and 106

As Byrne *et al.* demonstrated with **36a-c**, [2]catenanes were formed with olefin precursors **102a-c**, possessing the 4'-substituted "arm". And as we have seen in Section 5.4 and 5.9 for [2]catenanes **111R**/**S** and **113**, which were formed with olefin precursors featuring the chiral 4'-substituted "arm" and achiral 4'-substituted "arm" motifs, respectively. The effect of using structural isomers **105** and **106** as the olefin precursors was investigated in order to ascertain if the 3'-substituted "arm" shared the structural significance of the 4'-substituted "arm" moiety for pre-organising the formation of self-templated [2]catenanes. Olefin derivatised **btp** ligands **105** and **106** were synthesised according to Scheme 5.4, by undergraduate student, Billy McCarthy, as part of a final year project. Starting from **70**, Sonogashira coupling yielded **43** which was then subject to a one-pot deprotection/'click' reaction after the relevant azide intermediate was produced *in situ* by stirring the bromide with NaN_3 in DMF/ H_2O (4:1) mixture at room temperature for an hour. Once $CuSO_4{\cdot}5H_2O$, sodium ascorbate and K_2CO_3 were added the reaction was degassed under argon. A DMF solution of **43** was then added and the reaction was allowed to stir at room temperature for 18 hours. The reaction mixture was washed with aqueous EDTA/NH_4OH solution, in order to scavenge copper ions, and then extracted into EtOAc. After the solvent was removed under reduced pressure, the methyl ester **btp** ligand **115** was triturated with cold CH_3OH and obtained in high purity with excellent yield of 86%. The carboxylic acid ligand **116** was then

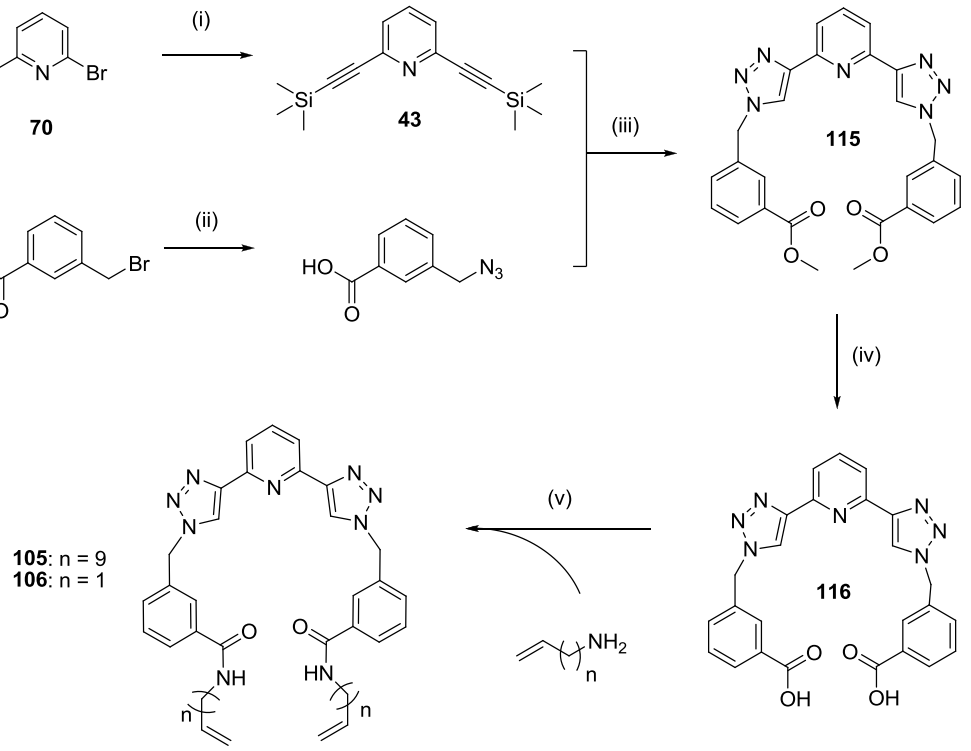

Scheme 5.4. Synthesis of ligands **105** and **106**. (i) CuI, $(PPh_3)_2PdCl_2$, THF/ Et_3N (1:1), trimethylsilylacetylene, 0 °C→rt; (ii) NaN_3, rt, 1h, DMF/ H_2O (4:1); (iii) $CuSO_4{\cdot}5H_2O$, sodium ascorbate, K_2CO_3, DMF/ H_2O (4:1), rt, 18 h; (iii) KOH, EtOH/ H_2O 85°C, 18 hrs (4:1) (v) 1) alkenylamine, HOBt, Et_3N, DMAP, CH_2Cl_2/ DMF (4:1), 0°C, 30 mins 2) EDCI·HCl, 0°C, 30 mins, rt, 66 hrs.

successfully prepared by ester hydrolysis of **115** by refluxing in aqueous KOH solution in 87% yield. **Btp** olefin precursors **105** and **106** were synthesised from **116** by amide coupling with 11-amino-1-undecene and allylamine, respectively. The amide coupling was carried out by EDCI·HCl activation using HOBt as initiator in the presence of Et_3N and DMAP. **Btp** olefin **105** was obtained as a white solid in 43% yield after trituration with cold CH_3OH. In a similar fashion, **btp** olefin **106** was obtained in 61% yield. All ligands were fully characterised.

^{1}H NMR spectroscopy confirmed successful synthesis of the desired **btp** olefins, Figure 5.18(A). In the case of **105**, the broadened singlet at 8.08 ppm in $CDCl_3$, with an integration of 2, can be assigned to the triazolyl CH resonance by HSQC, HMBC and selective TOCSY. The doublet at 8.06 ppm corresponds to the 3- and 5-pyridyl protons while the triplet at 7.85 ppm corresponds to the 4-pyridyl proton integrating to 1. The aryl proton resonances on the benzene rings can be found further upfield at between 7.85 and 7.40 ppm. The broadened singlet at 6.34 ppm was assigned as the amide proton by selective TOCSY. The multiplet from 5.90 ppm, with an integration of 2, and the pair of doublets around 5.23 ppm, integrating to 4, were determined to be the internal and terminal olefin protons, respectively,

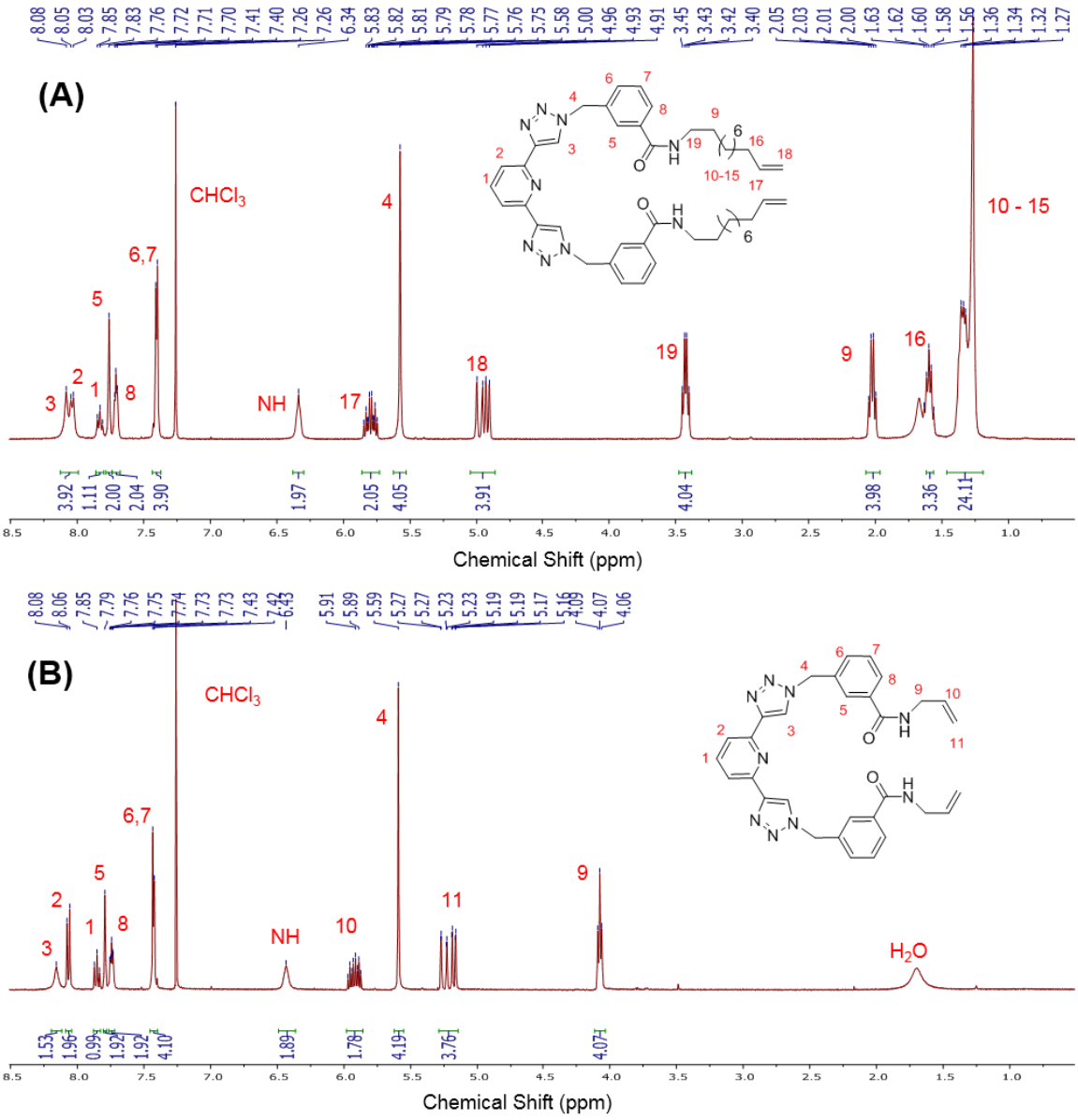

Figure 5.18 ^{1}H NMR spectra (400 MHz, $CDCl_3$) of **btp** olefins **105** (A) and **106** (B) with resonances labelled.

by selective TOCSY. Between these peaks appeared a singlet at 5.59 ppm, corresponding to the protons of the methylene linker between the triazole and aryl rings. The methylene protons of the aliphatic chain adjacent to the amide and olefin appeared further upfield at 3.45 and 2.0 ppm, respectively, being deshielded relative to their adjacent aliphatic methylene protons which appeared between 1.62 ppmm and 1.27 ppm. The ^{13}C NMR spectrum, HSQC, HMBC and various selective TOCSY experiments allowed assignment of the carbonyl and quaternary carbon. ESI$^-$ mass spectrometry analysis displayed a characteristic peak at m/z = 782.4886, which agrees with the *m/z* calculated for $[M-H]^-$. Elemental analysis also gave atomic abundances confirming bulk purity for **105**.

In a similar manner, the ^{1}H NMR confirmed synthesis and purity of **106**, see Figure

5.18(B), ESI^+ mass spectrometry analysis displayed a characteristic peak at *m/z* = 582.2342, which agreed with the *m/z* calculated for $[M+Na]^+$. Elemental analysis confirmed bulk purity for **106**.

Recrystallisation of **106** by slow evaporation of a solution of methanol produced blade-like colourless single crystals. The data were solved in the monoclinic system with $P2_1$ space group and refined as an inversion twin with Flack parameter = 0.0(3) and Hooft = -0.1(2). There was one molecule of **106** and one crystallographically resolved CH_3OH solvent molecule in the asymmetric unit. As seen for other **btp** systems, the *anti-anti* conformation is obtained in the solid state.[104-110] The two triazolyl and one pyridyl units are essentially coplanar. This planar conformation of **btp** facilitates the π-π stacking interactions between molecules along the *a* axis. Adjacent **btp** motifs associate in a parallel fashion, with a mean interplanar distance of ca. 4.6 Å. The packing is also dominated by several hydrogen bonding interactions. Each **btp** ligand is involved in a pair of intermolecular hydrogen bonding interactions linking it to two other **btp** molecules through amide moieties with the distance $|O^{\cdots}N|$ of 2.896(7) Å. There is a hydrogen bond observed between one amide oxygen and the CH_3OH solvent molecule of crystallisation with a distance $|O^{\cdots}O|$ of 2.782(6) Å. A combination of the above alongside packing factors, could explain the lack of a **btp**-**btp** dimer[156,160] observed in the solid state. Furthermore, this could be accounted for by the fact that the solvent from which the compound crystallised is highly polar and thus out-competes the **btp**-**btp** dimerising hydrogen bonding interactions as evidenced by the proximity of the CH_3OH molecule to the **btp** motif. This observation was further investigated in solution through ^1H NMR spectroscopy by varying the degree of hydration of the anhydrous $CDCl_3$ solvent, discussed next.

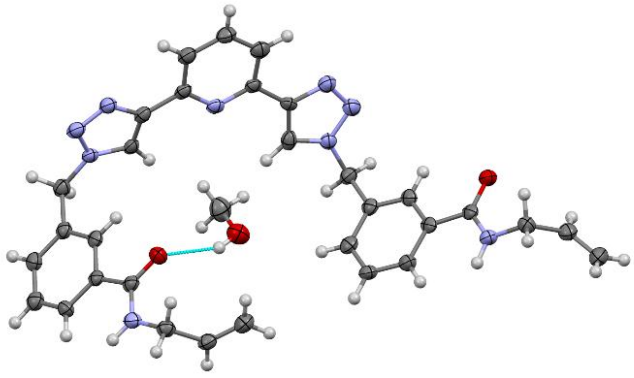

Figure 5.19 The asymmetric unit of **btp** olefin **106** with one CH_3OH molecule of crystallisation. Thermal ellipsoids displayed at 50% probability.

5.10.1 Investigation into self-templating of 105 and 106 in solution by ^{1}H NMR spectroscopy and mass spectrometry

The dependence of concentration on the formation of the hydrogen bond templated dimer of **105** was investigated by ^{1}H NMR titration, Figure 5.20. A sample of known concentration of **105** in anhydrous $CDCl_3$ was diluted and minimal upfield shifts of the triazolyl proton resonance can be observed form the ^{1}H NMR spectra. Similar minimal shifts can be observed for the pyridyl proton resonances and amide NH signal. This titration shows that the interactions between **btp** ligands were not very sensitive to concentration in the range between 10 mM and 0.1 mM.

In contrast, it was observed that the chemical shifts of certain proton resonances of the **btp** ligands were rather sensitive to solvent polarity properties. High polarity solvents such as DMSO-d_6 gave sharp resonance signals (see Appendix A.33) In less polar solvents, such as

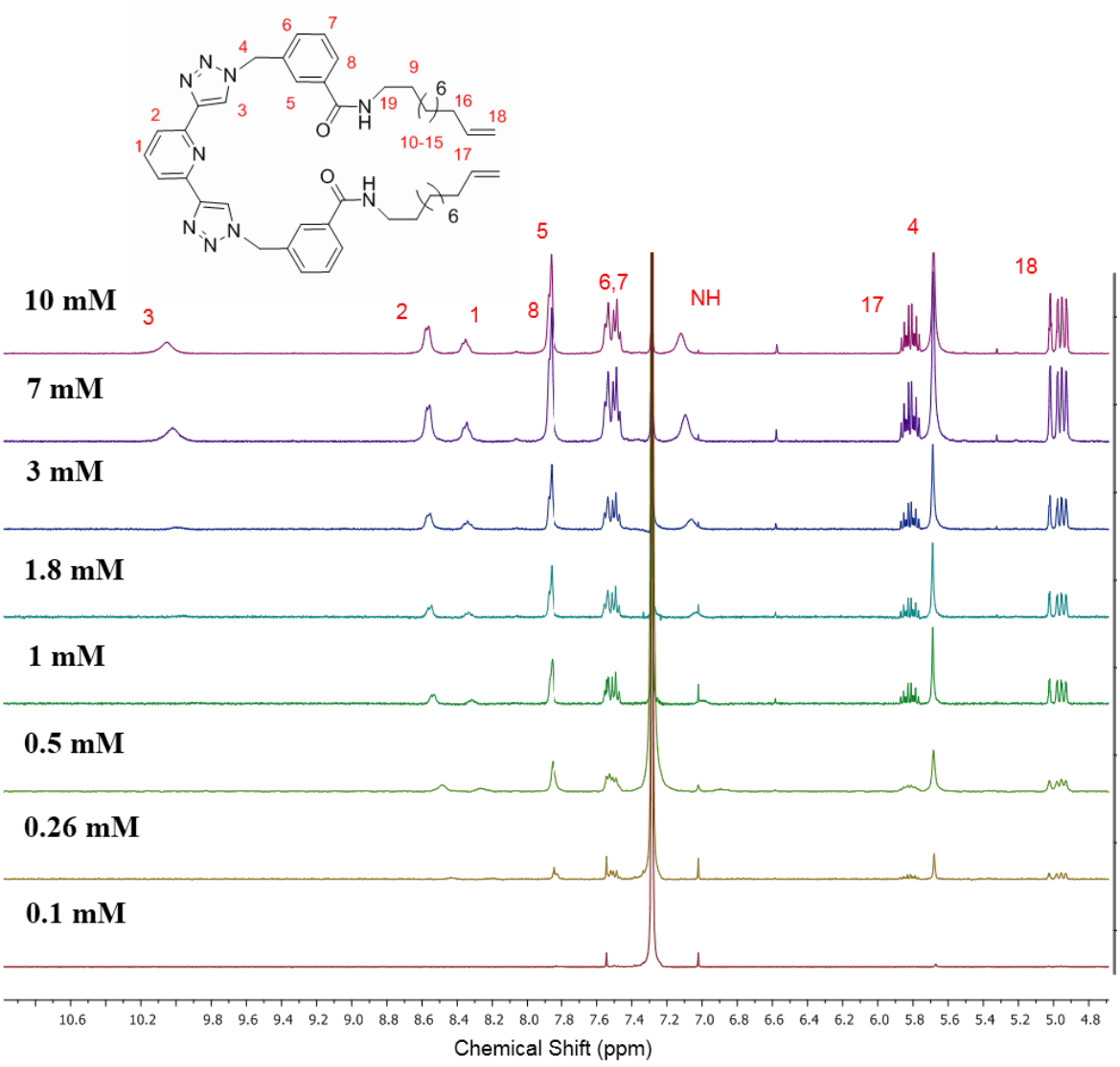

Figure 5.20 ^{1}H NMR dilution studies of **105** (400MHz, $CDCl_3$).

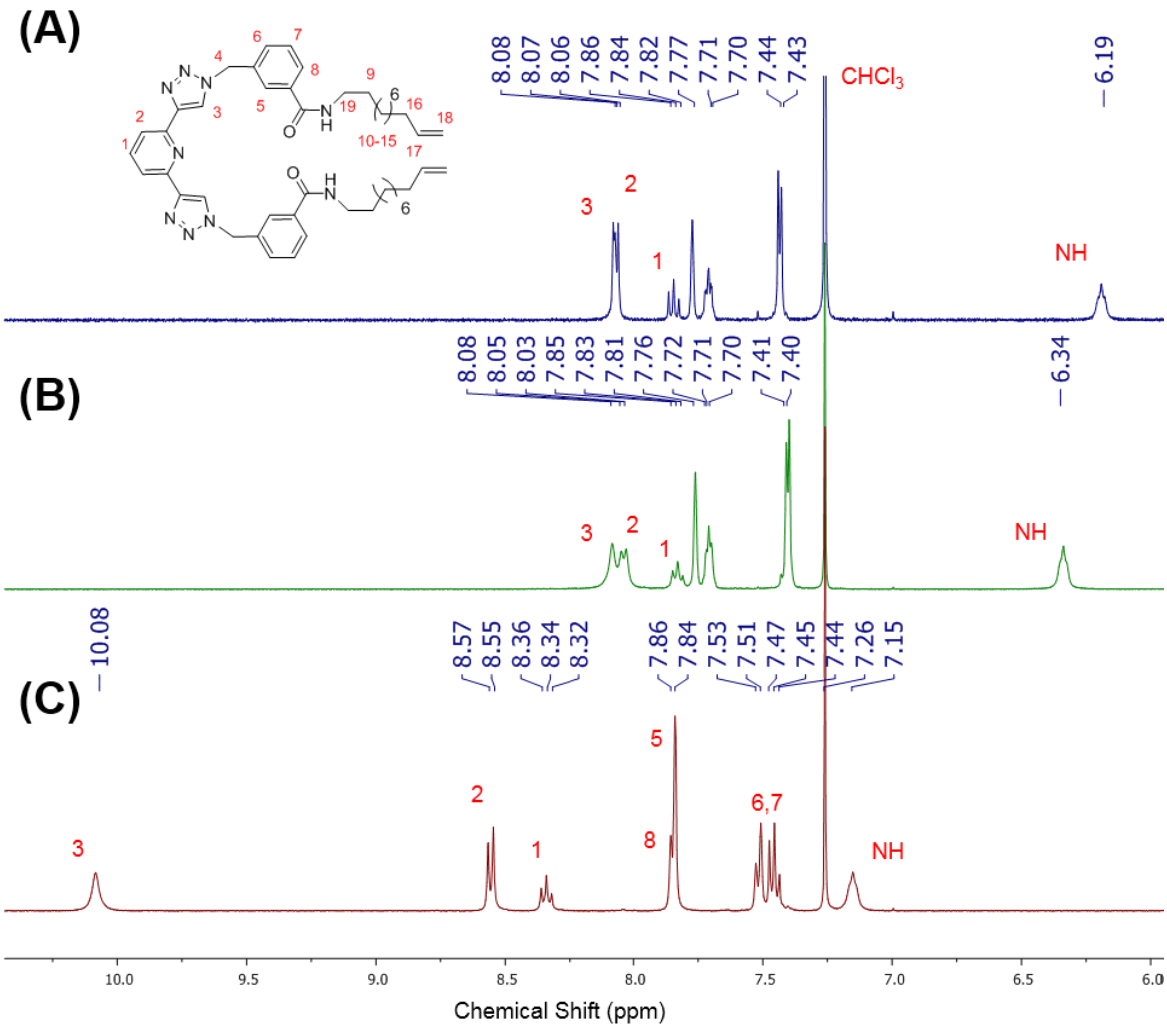

Figure 5.21. The significant changes in chemical shift of **btp** proton 1-3 and amide *NH* resonances in a 20 mM solution of **106** containing (A) 80 mM H_2O, (B) 40 mM H_2O and (C) anhydrous $CDCl_3$ (400 MHz).

$CDCl_3$, a broadening of certain signals can be observed alongside significantly changing chemical shifts, Figure 5.21. Upon varying the H_2O content of $CDCl_3$ the broadened and deshielded triazolyl *CH* changed chemical shift from 10.08 ppm to 8.07 ppm with a concomitant sharpening of the signal. The proton resonance signals associated with the **btp** motif *i.e.* the triazolyl, and two pyridyl protons (labelled 3 and 1,2, respectively) underwent the biggest changes. Not surprisingly, the amide NH signal was shifted upfield from 7.15 ppm to 6.19 ppm upon increasing the H_2O content of the $CDCl_3$ solution of **105**.

The same behaviour was seen for **106** with broadened deshielded proton resonances in non-polar solvents and sharp signals in more polar solvent like DMSO-d_6. (Appendix A.33) Also, ESI^+ mass spectrometry was able to observe, not only the monomer peak at *m/z*=582.2342, *i.e.* [**106**+Na]$^+$, but also a peak at *m/z* = 1141.4774, corresponding to the dimer, [**106**$_2$+Na]$^+$. Encouraged by these results indicating **btp** dimer formation for both **105**

and **106** it was next attempted to synthesise mechanically interlocked [2]catenanes by Hoveyda-Grubbs catalysed RCM.

5.10.2 RCM of btp olefins 105 and 106

Initially, RCM was carried out for both **105** and **106** using Hoveyda–Grubbs 2nd generation catalyst (40 mol %) in anhydrous CH_2Cl_2 under argon at room temperature in darkness for 4 days according to the procedure for forming mechanically interlocked structures reported by Byrne *et al.*[102] Resonances indicative of [2]catenane formation were not observed by ^{1}H NMR. Furthermore, mass spectrometry did not show any sign of [2]catenanes for either **105** or **106**. Instead, macrocycles **117** and **118** were obtained from ligands **105** or **106**, respectively, confirmed by ESI^+ and $MALDI^+$ mass spectrometry, respectively, showing characteristic peaks at *m/z* = 778.4509 and 532.2236 for $[M+H]^+$. ^{1}H NMR also confirmed successful RCM demonstrating the replacement of the terminal alkene signals at 5.77 ppm (m) and 4.93 ppm (pair of doublets) for **105** with an apparent singlet at 5.15 ppm, see Figure 5.22(A), and the corresponding resonances at 5.88ppm (multiplet) and 5.14 ppm (pair of doublets) for **106** with an apparent singlet at and 5.32 ppm, see Figure 5.22(B). Several other anhydrous solvent systems with varying equivalents of $CH_3NO_2/CH_2Cl_2/1,2\text{-}C_2H_4Cl_2$ were

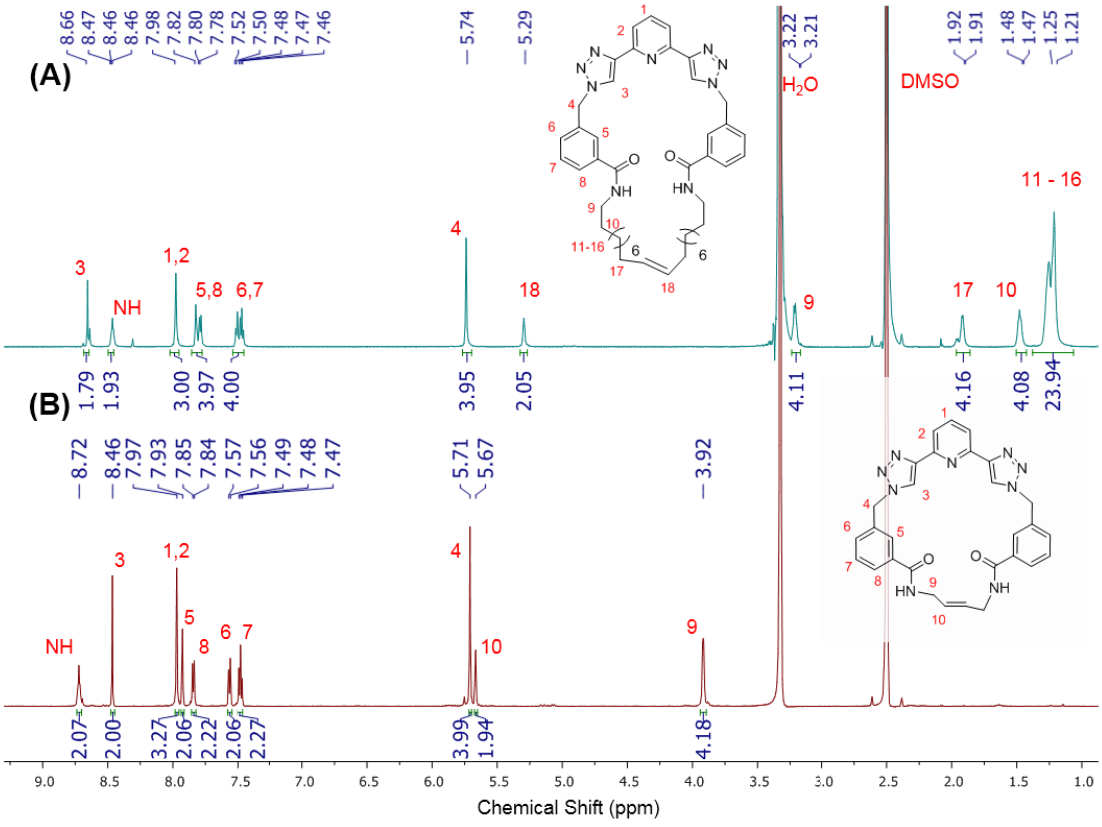

Figure 5.22 ^{1}H NMR spectra of **btp** macrocycles **117** (Top) (600MHz, DMSO-d_6) and **118** (Bottom) (400MHz, DMSO-d_6).

used to investigate if they were better suited for [2]catenane formation, however, these attempts also resulted in macrocycle formation. The best yields for macrocycle formation were obtained (58% and 49% for **117** and **118**, respectively) in a CH_3NO_2:CH_2Cl_2 (1:9) solvent system with 50 mol % of the Hoveyda-Grubbs 2nd generation catalyst, at 60°C for 24 hours under argon and in darkness.

Single crystals of **118** were grown by slow evaporation of an EtOAc: CH_3OH (1:1) solution. X-ray diffraction analysis allowed the structural model to be refined in the monoclinic system with $P2_1/n$ space group containing one molecule **118** and a quarter occupancy EtOAc solvent molecule in the asymmetric unit, Figure 5.23. The macrocycle adopts a chair-like conformation allowing the partial-occupancy EtOAc molecule to slot in the centre of the cavity as a supramolecular guest. The macrocycle *anti-anti* conformation is locked in place pre-organising the triazolyl protons for favourable electrostatic interactions with the somewhat polar guest molecule. There is a hydrogen bonding interaction between one triazolyl CH and the carbonyl oxygen of the EtOAc molecule (|D···A| is 3.629(3) Å, ∠ (*C-H*···*O*) is 161.9(2)°). There are also a pair of hydrophobic interactions between the acetyl CH_3 of EtOAc and the 2-aryl *CH* (|D···A| is 3.233(18) Å) and simultaneously with one of the *E*-configured olefin *CH*s (|D···A| 2.585(18) Å). The packing is dominated by a pair of hydrogen bonding interactions per molecule facilitated by the transoid orientation of the amide groups. The result is the linking together of each molecule to their two adjacent neighbours along the *a*-axis in an $R_2^2(16)$ motif (|(D···A| is 2.867(4) Å, ∠ (*N-H*···*O*) is 160.8(3)° and |D···A| is 2.855(4) Å, ∠ (*N-H*···*O*) is 161.7(3)°) (see Appendix E.10). The

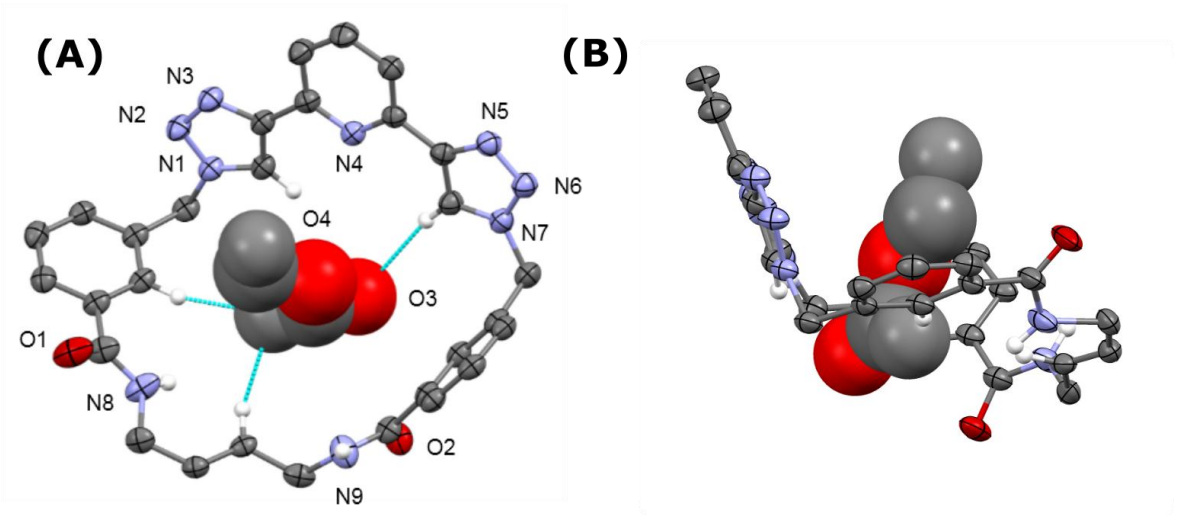

Figure 5.23 (A) Perspective view of the molecular structure of **118**·0.25EtOAc. (B) Chair conformation of macrocycle allows EtOAc molecule to occupy cavity as a guest. Thermal ellipsoids displayed at 50% probability for macrocycle **118** and spacefill representation used for EtOAc molecule for contrast.

above solid state properties, in particular, the pre-organised *anti-anti* geometry achieved through macrocyclisation, alongside previous reports of **btp**'s ability for anion recognition,[65,112,114] provide encouraging evidence for the guest binding potential of macrocycle **118**.This will be explored in Section 5.14.

It was concluded that **btp** olefins **105** and **106** possessing the 3'-substituted "arm" motif did not form [2]catenanes. In order to carry out a thorough analysis of the structural motif essential for efficient [2]catenane formation, **btp** olefins **107** and **108**, lacking any aryl amide functionality, were investigated in the same fashion as above. The lack of any other hydrogen bond donor/ acceptor moiety in the **btp** olefin structure would allow us to rule the possibility of competitive amide *NH* hydrogen bonding preventing **btp** dimerisation. If the same proton resonance signal broadening phenomenom seen in the ^{1}H NMR spectra of **105** and **106** is still observed in **btp** olefins **107** and **108**, lacking amide functionality, it would allow us to be better equipped to state that self-templating **btp** dimerisation is still occurring in solution but the 3'-substituted "arm" functionality lacks the structural significance of the 4'-substituted "arm" motif for [2]catenane synthesis.

5.11 Synthesis and characterisation of olefin-derivatised btp ligands 107 and 108

Btp ligands derivatised at the *N1* triazolyl position with long chain alkenyl groups were synthesised in a one-pot deprotection/'click' reaction from **43**, according to Scheme 5.5. The pentenyl or undecenyl azide intermediate was produced *in situ* by stirring the relevant bromide with NaN_3 in DMF/ H_2O (4:1) mixture at room temperature for an hour. CuI, DIPEA and K_2CO_3 were added and the reaction was then degassed under Argon. A DMF solution of **43** was then added and the reaction was allowed to stir at 100 °C under microwave radiation for 60 minutes. The reaction mixture was washed with aqueous EDTA/NH_4OH solution, in order to scavenge copper ions as before, and then extracted into EtOAc. The

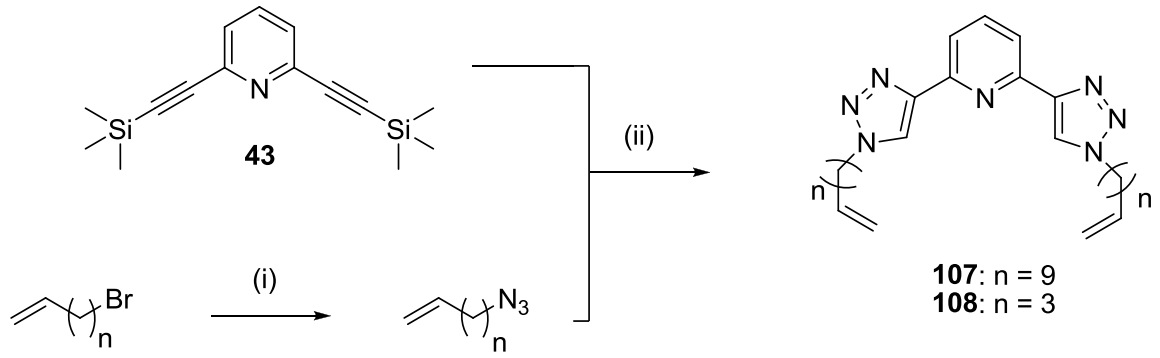

Scheme 5.5 Synthesis of ligands **107** and **108**. (i) NaN_3, rt, 1h, DMF–H_2O (4:1); (ii) CuI, K_2CO_3, DIPEA, 100 °C microwave irradiation, 60 mins.

undecenyl **btp** ligand **107** was purified by trituration with cold CH_3OH and was obtained in high purity with excellent yield of 85%. The pentenyl derivative **108** was isolated following flash chromatography of the crude oil residue yielding an off-white powder in 53% yield.

^{1}H NMR spectroscopy confirmed successful synthesis of the desired **btp** olefins (Figure 5.24). The ^{1}H NMR of **107** and **108** resemble each other with proton resonances associated with the **btp** motif, appearing between 8.15 ppm and 7.83 ppm, and the terminal olefin groups, appearing between 5.85 ppm and 4. 92 ppm, integrating appropriately. The aliphatic

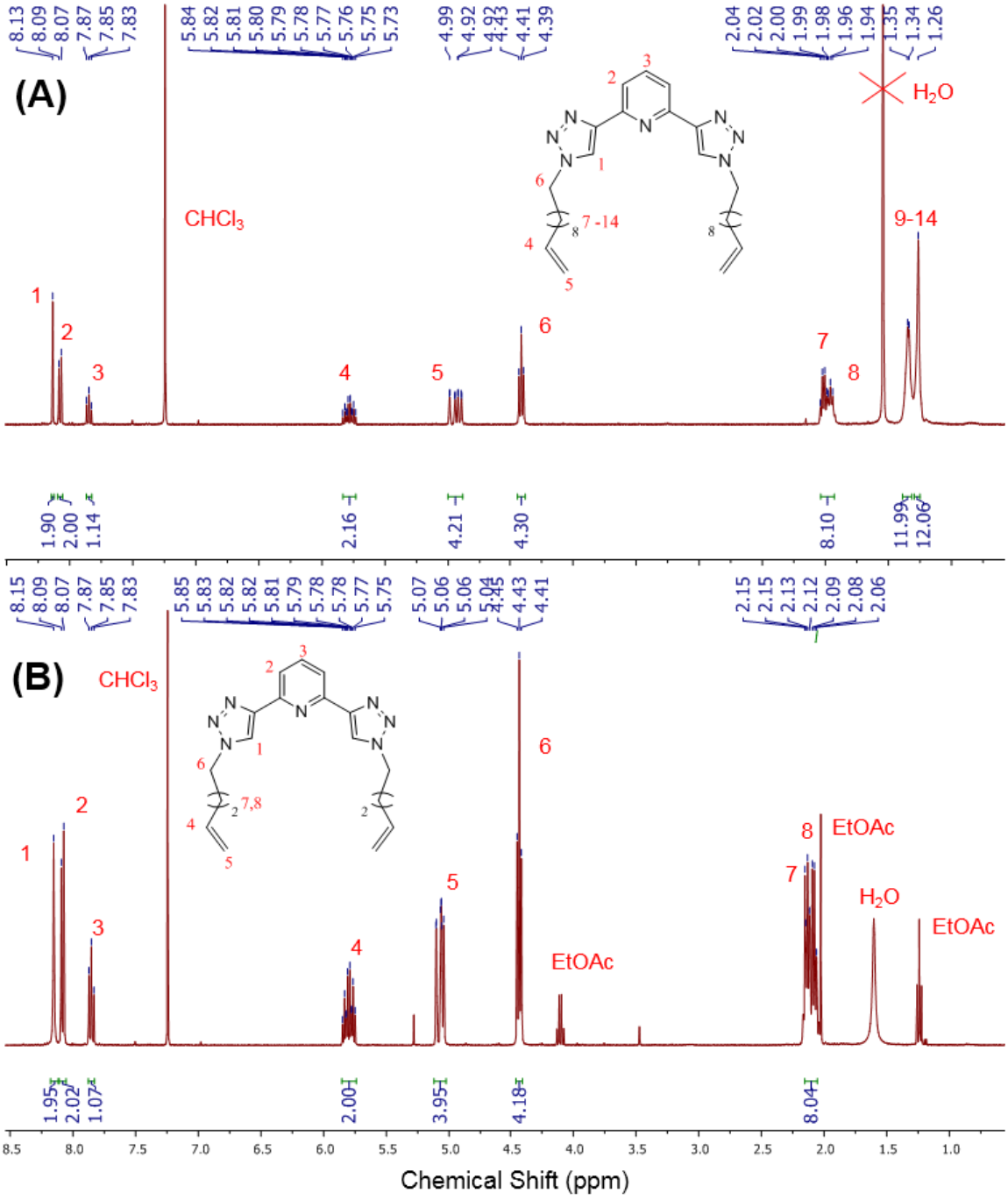

Figure 5.24 ^{1}H NMR spectra of **btp** olefins **107** (top) and **108** (bottom) (400 MHz, $CDCl_3$).

region contains all expected peaks between 2.04 ppm and 1.26 ppm for **107** and between 2.15 ppm and 2.06 ppm for **108**. Finally, elemental analysis confirmed the purity of the **btp** olefins.

5.12 Investigation into self-templating of 107 and 108 in solution by ^{1}H NMR spectroscopy and mass spectrometry

A similar experiment to that conducted in section 5.10.1 in order to investigate the dimerisation of **107** in non-polar $CDCl_3$ solution was carried out and the results are illustrated in Figure 5.25. The heavily deshielded nature of the triazolyl *CH* signal is immediately evident from the ^{1}H NMR spectrum of **107** in anhydrous $CDCl_3$ indicative of hydrogen bonding interactions. Upon dilution, from 10 mM to 0.6 mM, minimal upfield shifts of the triazolyl proton and pyridyl resonances were observed. Due to the low concentration, the triazolyl resonance was not visible, however, upon addition of increasing aliquots of polar solvent such as CH_3OH, the triazolyl resonance became visible once more at 9.75 ppm after addition of 10 µL of wet CH_3OH, increasing in sharpness, with a concomitant decrease in chemical shift to 9.15 ppm, once a total of 30 µL of wet CH_3OH was added. There was little concentration dependence of the self-templating interactions

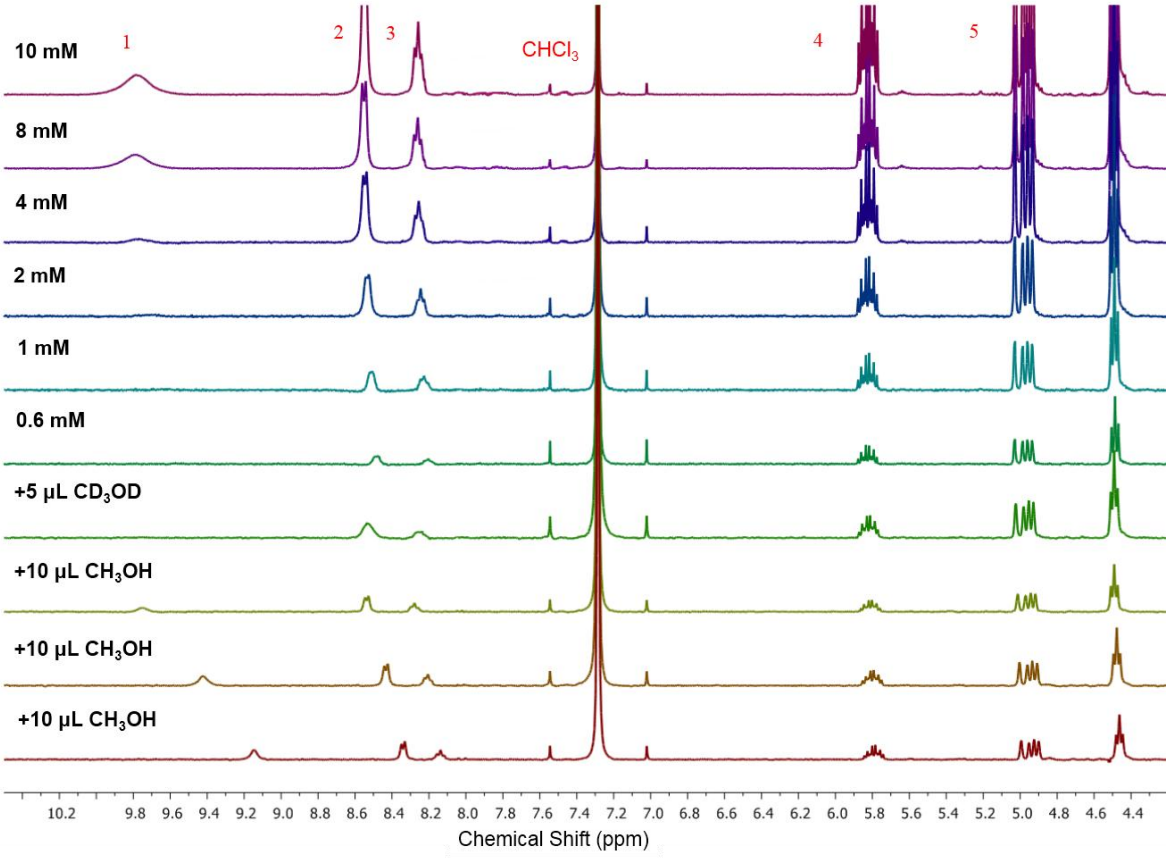

Figure 5.25 ^{1}H NMR dilution studies of **107** ((400 MHz, $CDCl_3$).

between **btp** ligands in the range between 10 mM and 0.1 mM. This titration mirrored that seen for the same dilution studies for **105**.

Btp olefin **108** showed similar results from ^{1}H NMR spectroscopy in non-polar solvent $CDCl_3$ of varying degree of hydration indicating the analogous dimer formation. Furthermore, ESI$^+$ mass spectrometry was able to observe, not only the monomer peak at *m/z*=350.2088 *i.e.* [**108**+H]$^+$, calculated for $C_{19}H_{24}N_7$ *i.e. m/z* = 350.2088 but also a peak at *m/z*=721.3973, corresponding to the dimer, [**108**$_2$+Na]$^+$calculated for $C_{38}H_{46}N_{14}Na$ *m/z*=721.3928. Encouraged by these observations indicating that **btp** olefins **107** and **108** dimerise under these conditions, it was still necessary to investigate if **107** and **108** possessed the structural features necessary to template the synthesis of [2]catenane which was carried out by RCM.

5.12.1 RCM of btp olefins 107 and 108

Initially, RCM was carried out for both **107** and **108** using Hoveyda–Grubbs 2nd generation catalyst (30 mol %) in anhydrous CH_2Cl_2 under argon at room temperature in darkness for 4 days according to procedure as before.[102] ^{1}H NMR resonances indicative of [2]catenane formation were not observed. Furthermore, mass spectrometry did not show any sign of [2]catenanes for either **107** and **108**. In the case of **107**, macrocycle formation was confirmed by ESI$^+$ mass spectrometry showing characteristic peak at *m/z* = 512.3478, calculated for [M+Na]$^+$ *i.e.* $C_{29}H_{43}N_7Na$ *m/z* = 512.3472. ^{1}H NMR also confirmed successful RCM demonstrating the replacement of the terminal alkene signals at 5.76 ppm (m) and 4.95 ppm (pair of doublets) for **105** with an apparent triplet at 5.36 ppm (Figure 5.26). Several other anhydrous solvent systems such as varying equivalents of a CH_3NO_2/CH_2Cl_2/1,2-$C_2H_4Cl_2$ were used to investigate if they were better suited for [2]catenane formation. However, these attempts also resulted in macrocycle formation. Reactions were also carried out at elevated temperature 60 °C, however, this did little to improve yields. The best yield for macrocycle **119** formation were obtained (48%) in anhydrous CH_2Cl_2 with 50 mol % of the Hoveyda-Grubbs 2nd generation catalyst, at room temperature for 10 days under argon and in darkness. There was also a substantial amount of **107** starting material recovered. Recrystallisation from slow evaporation of a CH_2Cl_2 solution of **119** yielded colourless needle-like crystals which were analysed by X-ray diffraction analysis.

The data were solved in the monoclinic system with $P2_1/c$ space group containing one molecule of **119** in the asymmetric unit (Figure 5.27). Macrocycle **119** adopts a chair-like conformation in the solid state similar to that seen in the solid state structure of **118** and the

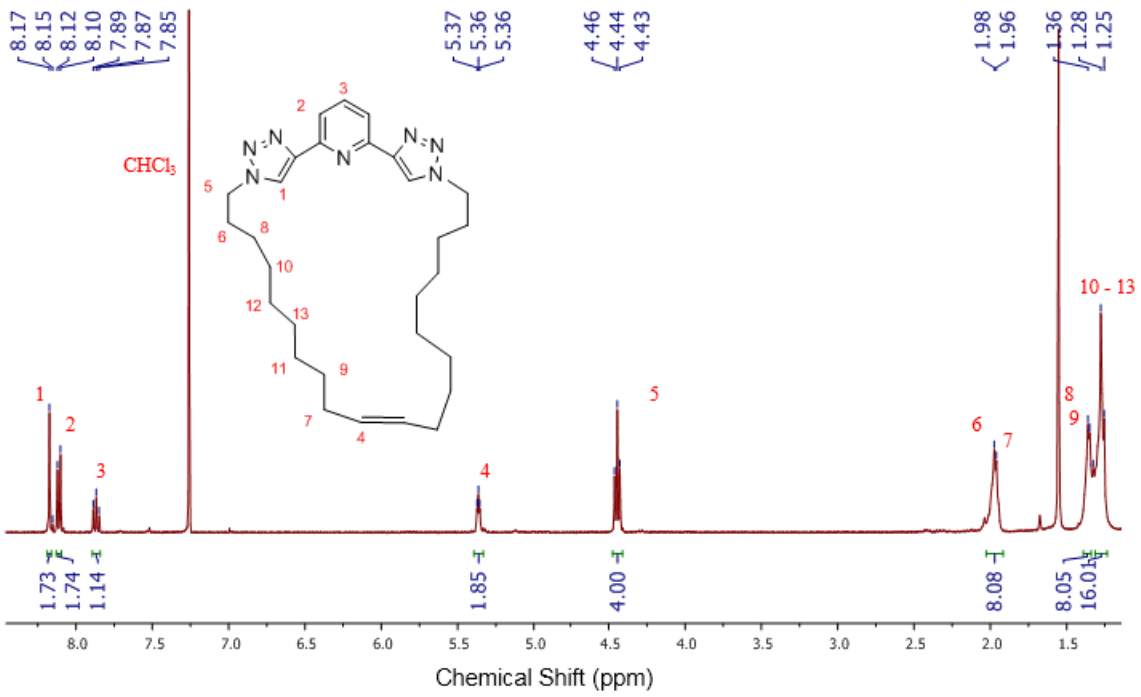

Figure 5.26 ^{1}H NMR spectrum of **btp** macrocycle **119** (400 MHz, $CDCl_3$).

anti-anti conformation of the **btp** motif is evident, alongside positional disorder in the twenty carbon chain of the newly formed internal alkene which is expected due to the flexible nature of the chain. There are no dimer interactions *via* **btp-btp** hydrogen bonding in the extended crystal structure of **119**. Crystal packing is dominated by hydrophobic interactions between the long carbon-carbon chains of adjacent molecule s but also other hydrogen bonding interactions. Each molecule has one triazole acting as a hydrogen bond donor/acceptor through its *CH* and medial nitrogen *N2*, respectively, linking to two of its adjacent

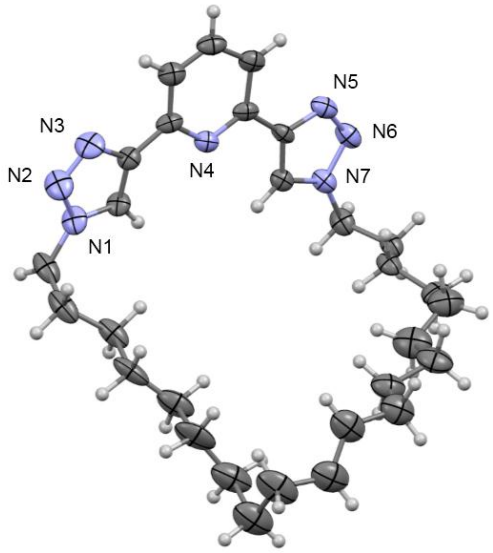

Figure 5.27. Perspective view of the molecular structure of **119**. Thermal ellipsoids displayed at 15% probability and disordered contributor omitted for clarity.

neighbouring molecules (|D···A| is 3.181(6) Å and ∠ (*C*-*H*···*N*) is 148.2(4)° for both as they are related by symmetry) (see Appendix E.11).

RCM attempts with **btp** olefin **108** in anhydrous CH_2Cl_2 at room temperature for 10 days did not produce substantial amounts of the analogous macrocyclic system **119** with mostly starting material being recovered. There was ESI^+ evidence of RCM for the mono-macrocycle with a peak corresponing to *m/z* = 322.2202, *i.e.* calculated for $[M+H]^+$ *i.e.* $C_{17}H_{20}N_7$ *m/z* = 322.1775. There was also ESI^+ evidence of a species with *m/z* = 643.3477, calculated for $[M+H]^+$ *i.e.* $C_{34}H_{39}N_{14}^+$ *m/z* = 643.3462, which is what would be expected for the [2]catenane. However, using these reaction conditions only olefin starting material **108** could be isolated and characterised. A range of other reaction conditions were attempted. The reaction was carried out using varying equivalents of Hoveyda–Grubbs 2nd generation catalyst (0.1 eq., 0.2 eq., 0.5 eq., 1 eq. and 2 eq.), and reaction temperatures –60°C, –10 °C and room temperature for 6 days. These attempts showed similar results indicating the chain length was perhaps too short to result in successful RCM. However, when a solution of **108** and Hoveyda–Grubbs 2nd generation catalyst (30 % mol) in degassed anhydrous CH_2Cl_2 was heated at 80 °C under microwave irradiation for two hours much of the starting material had been consumed, as observed by TLC. Following flash chromatography (gradient DCM: EtOAc 1:1) and trituration of the off-white residue using cold CH_3OH a white powder was obtained in poor yields. ESI^+ showed evidence of a species with *m/z* = 643.3477, calculated for $[M+H]^+$ *i.e.* $C_{34}H_{39}N_{14}^+$ *m/z* = 643.3462 indicating [2]catenane formation however, ^{1}H NMR spectroscopy closely resembled that of macrocycle **119** with sharp **btp** resonances in contrast with the broadened resonances of protons indicating [2]catenane formation as in the case of **36a**,[102] and **111** (Figure 5.5). Therefore a 2×2 macrocyclic structure was proposed for new macrocycle **120**, Figure 5.28. The ^{1}H NMR spectrum indicated successful RCM as a result of the replacement of the terminal alkene signals at 5.80 ppm (m) in the region of 5.10–5.07 ppm (pair of doublets) which were present in the ^{1}H NMR spectrum of **108** with an apparent triplet at 5.39 ppm for **120**. X-ray diffraction analysis was required to elucidate the structure to prove beyond doubt that the 2×2 macrocycle had been synthesised. Single needle-like crystals of **120** were grown from slow evaporation of a solution mixture of CH_3CN:CH_2Cl_2 (3:4). The data were solved in the monoclinic system with *C*2/*c* space group containing half a molecule of **120** in the asymmetric unit, Figure 5.29. Macrocycle **120** demonstrates the expected *anti-anti* conformation of the **btp** motifs with each of the heterocyclic rings per **btp** essentially co-planar and symmetry related **btp** unit mean planes tilted relative to each other by an angle of 36.5°. The packing shows hydrogen bonding

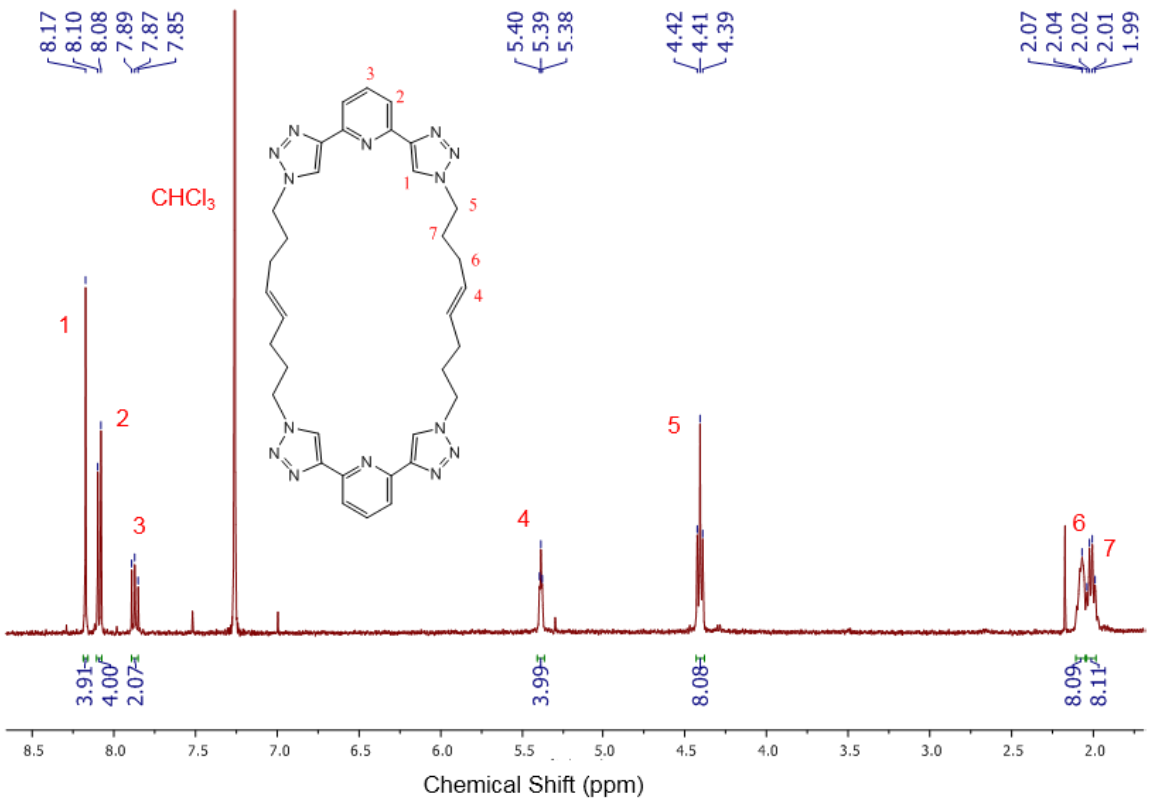

Figure 5.28 ^{1}H NMR spectrum of **btp** macrocycle **120** (400 MHz, $CDCl_3$).

interactions along the *c*-axis, hydrophobic interactions and π–π stacking interactions along the *a*-axis. Two of the four triazole units per molecule are involved in a hydrogen bonding interaction involving its *CH* donor connecting the proximal triazolyl nitrogens of the neighbouring molecules (Appendix E.12). The other two triazole units act as the corresponding hydrogen bond acceptors through the proximal triazolyl nitrogen atoms connecting the triazolyl *CH* of adjacent molecules (|D···A | is 3.352(14) Å, ∠ (*C*-*H*···*N*) is

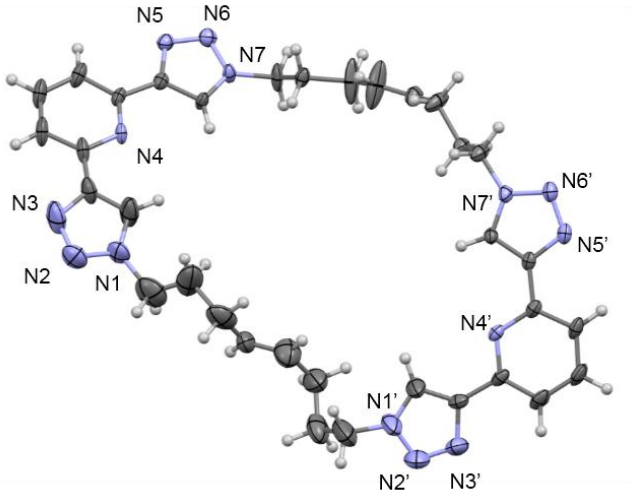

Figure 5.29 Perspective view of the molecular structure of **120**. Thermal ellipsoids displayed at 40% probability and disordered contributor omitted for clarity.

151.2(6)° for both pairs due to symmetry relation). Each molecule has a hydrogen donor and hydrogen bond acceptor interaction with the molecule packing above and simultaneously a hydrogen bond donor and hydrogen bond acceptor interaction with the molecule directly below. This allows molecules of **120** to sit above and below adjacent macrocyclic cavity grooves with the alkenyl chains of adjacent molecules aligned alongside. Also, due to the essentially planar conformation of **btp**, π-π stacking interactions between molecules are facilitated along the *a*-axis, (the perpendicular distance between the parallel mean planes comprised by the pyridine and triazole units is *ca.* 3.4 Å) (Appendix E.13).

It can be concluded that, while both **btp** olefins **107** and **108** lack the structural features necessary for [2]catenane synthesis, **btp 107** has olefin chain long enough to form macrocycles in reasonable yield whereas the shorter chain **108** can only do so in analogous fashion in trace amounts with most starting material remaining unreacted. By carrying out the synthesis under harsher conditions the 2×2 macrocycle **120** can be synthesised in poor yields.

5.13 Discussion

Having carried out a range of synthetic experiments in order to gain more of an insight into the deciding factor in achieving the necessary pre-organisation for efficient self-templated [2]catenane formation, the data will now be interpreted. It is clear that the for self-templated **btp** [2]catenane formation to be successful, it is necessary to incorporate of the 4'-substituted "arm" substituent into **btp** olefin precursors, as was the case for **102a**, in the synthesis of the original [2]catenane **36a**, and for **103R**/**S** and **104** in the synthesis of **111R**/**S** and **113**, respectively, which both the structurally isomeric 3'-substituted "arm" systems of **105** and **106** lacked, as did long chain **btp** olefins **107** and **108**.

One hypothesis for the significance of the 4'-substituted "arm" substituent is the hydrogen bonding pre-organisation which it achieves prior to "clipping" and formation of the mechanical bond by RCM. The crystal structure of [2]catenane **111** gives an insight into the nature of this hydrogen bond templated pre-organisation. The chiral 4'-substituted "arm" structural feature can be seen involved in an intricate network of intramolecular hydrogen bonding interactions. The amide-triazole hydrogen bonding interaction observed in the solid state could potentially be responsible for the intra-dimer interaction essential for "fixing" the chiral 4'-substituted "arms" in place in solution during self-templation, bringing both olefin groups of the same **btp** ligand into close proximity around the back of the **btp** motif of its dimerising partner molecule before RCM completes the mechanical interlocked system. The

difficulty with this hypothesis is the tightly packed conformation of [2]catenane **111** would still have these interactions in the crystalline phase once it had formed whether or not they played a role in the catenation. Two interlocked molecules which possess flexible linkages containing strong H-bond donors and acceptors are bound to have such interactions regardless of whether it was "pre-organised" or not. Nevertheless, the solid state characterisation of the [2]catenane may also provide a reason for why the 3'-substituted "arm" feature does not achieve [2]catenane formation as the isomerism does not allow the same "pre-organising" hydrogen bonding interactions between the amides and triazoles to take place. The crystal structure also allows a visualisation to be interpreted of the proposed solution state **btp–btp** dimerisation in non-polar solvent media.

The hypothesis for the pre-organisation achieved with the chiral 4'-substituted "arms" is supported by ^{1}H NMR spectroscopy in anhydrous $CDCl_3$ (Figure 5.3). Upon increasing the concentration of the solution of **103R** to from 1 mM to 30 mM, while keeping the H_2O content in the $CDCl_3$ constant, a significant change in chemical shift of proton resonance signals associated with the 4'-substituted "arms" was observed. The aryl protons *w* and *x*, underwent a significant shift upfield from 7.62 ppm and 7.14 ppm to 7.34 ppm and 6.71 ppm, respectively, indicative of a significant change in chemical environment of this moiety, in particular, upon increasing concentration relative to other moieties in the molecule which did not undergo as notable a change in their proton's chemical environment. A similar change in chemical shift for resonances associated with the 3'-substituted "arms" upon increasing concentration was not observed (Figure 5.20) as would be expected of the 3'-substituted "arm" if pre-organisation was resulting in a change in chemical environment of the moiety.

It is true to say that the broadening of signals observed in the ^{1}H NMR self-templating studies, particularly in the cases of 3'-substituted "arm" functionalised **105** and **107**, does not allow a differentiation to be made between potential hydrogen bond templated dimers and any other type of higher order oligomer or aggregate. The fact that the addition of hydrated solvent to anhydrous $CDCl_3$ results in a sharpening of initially broadened signals and significant deshielding of certain protons signals (Figure 5.21) would support that this behaviour is indicative of hydrogen bonding which is being broken up or out-competed by stronger hydrogen bonding species such as more polar solvents. It may also be possible that the hydrogen bonding interactions observed were not occurring through *anti-anti* oriented dimerising **btp** motifs and that the amide NHs were out-competing the desired **btp-btp** dimerising interactions. However, it is being hypothesised that the broadening associated

with the proton signals of the **btp** motifs, is as a result of the dimerisation occurring through non-classical hydrogen bonding of *anti-anti* oriented **btp** motifs.[102,156,160] This was supported by the heavily deshielded nature of the triazolyl *CH* signal from the ^{1}H NMR spectrum in anhydrous $CDCl_3$ of long chain olefin **105** and indicative of hydrogen bonding interactions exclusively involving the **btp** motif as no other hydrogen bond donor or acceptor moieties are present in the structure. In a similar way to the ^{1}H NMR self-templating study of **105**, it is postulated that in the ^{1}H NMR self-templating studies of **107**, the resonances associated with the **btp** motif became sharpened and underwent a decrease in chemical shift on account of the breaking up of the hydrogen bonding interaction between **btp-btp** dimers upon addition of polar and hydrated solvents to anhydrous $CDCl_3$. This observation allows the conclusion to be made that **btp-btp** assembly was occurring through the non-classical hydrogen bonding interactions *via* the *anti-anti* oriented dimerising **btp** motifs regardless of the structural motif comprising the olefin side "arms" appended at the triazolyl *N1* position, be they the long flexible carbon-carbon chains of **107**, or the 3'-substituted "arms" functionality of **105** and **106**. It was also possible to conclude that the same proton broadened resonances seen in section 5.10.1 for **105** and **106** were not a result of hydrogen bonding involving the amide functional groups out-competing the **btp**-**btp** dimerising interactions desirable for [2]catenane formation.

The crystal structure of 2×2 macrocycle **120** gives some insight into the ability of **btp** molecules to self-assemble into dimers in anhydrous CH_2Cl_2 and yet lack the pre-organisation requirements to form the [2]catenane. It is proposed that the large macrocycle is formed as a result of two molecules of **108** forming **btp**-**btp** dimers and undergoing RCM in a more random manner as a result of the flexible olefin "arms'". The olefin groups on each **btp** ligand **108** dimer react intermolecularly forming the 2×2 macrocycle or 'uncatenane' as opposed to intramolecularly to form the interlocked [2]catenane. The lack of directing groups on the flexible alkenyl "arms" of **btp** ligand **108** is the reason for this loss of pre-organisation and further demonstrates the necessary element of control the 4'-substituted "arm" functionality contributes to efficiently synthesising self-templated [2]catenanes **36a**, **113** and which the chiral 4'-substituted "arm" contributes in the synthesis of **111R/S**.

Finally the observations of the broadening of certain peaks in each of the [2]catenane systems synthesised herein will be interpreted as follows. One rationalisation for the contrast in ^{1}H NMR peak sharpness of **111R/S** in DMSO-d_6 and $CDCl_3$ (Figure 5.5) was the effective hydrogen bonding interactions occurring in the [2]catenane system. In the less polar $CDCl_3$

the ring rotation may be being slowed due to the restraining attractive forces resulting from a combination of non-classical **btp**-**btp** and amide-triazole hydrogen bonding interactions as they were not being out-competed in non-polar $CDCl_3$. However, it is possible that in DMSO-d_6, the hydrogen bonding interactions were being broken up and as such the restraining effect of the hydrogen bonding element was removed from the dynamic system allowing for a faster ring rotation process which appeared as a single chemical environment. A related hypothesis could provide an explanation as to why the resonances for **113** in the more polar DMSO-d_6 were broadened (Figure 5.17), in that the larger substituent at the 4-pyridyl position of the **btp** motif was also restraining the ring rotation process as an effect of its steric bulk. In DMSO-d_6, the resonances of **111R**/**S** were sharp as the absence of a bulky substituent allowed the fluxional process to proceed at a faster rate. It was shown that by increasing the temperature of the DMSO-d_6 solution a sharpening of proton resonances could be obtained. This can be rationalised by thermal energy overcoming the activation barrier to ring rotation. Also the peaks which were expected to be directly involved in the hydrogen bonding interactions or were closest to sites of hydrogen bonding saw the largest sharpening effect of the increase in temperature. In a similar fashion the observed shielding of the amide proton at higher temperature corroborates the rationale that the hydrogen bonding interactions were being broken up at higher temperature.

5.14 Anion recognition by [2]catenane and macrocycles

Recognition of an analyte, and the resultant signalling of such an event, represents an important application of discrete and supramolecular assemblies.[368] Systems possessing the ability to identify one or more molecular species out of a mixture have been explored for their potential use as molecular sensors, in particular for biological applications, where compounds of interest have small abundances relative to other components in a complex mixture.[369-370] Anions are such an analyte; certain anions have an adverse effect on the environment around us. Excessive use of phosphates and nitrates in fertilisers has lead to eutrophication in waterways.[355] Receptors employing electrostatic interactions are capable of binding anions in water. Despite being mostly electrostatic in nature, hydrogen bonding interactions are considered to possess insufficient strength to bind anions in aqueous conditions. These interactions can, however, offer a pre-organised directionality to appropriately complement distinct anion geometries in order to facilitate their binding in aprotic polar solvents. As we have discussed in Section 1.7, triazoles[157] and more specifically, **btp**[102,113,158-160] have shown the ability to act as anion receptors owing to their

hydrogen-bond-donor ability. The unique **btp**–**btp** hydrogen-bonding features and the presence of amide groups in macrocycles and [2]catenanes synthesised in this research project present potential for such anion recognition applications. In the Gunnlaugsson group, anion recognition is a focused area of research.[102,371] Byrne *et al.* demonstrated selective recognition of $H_2PO_4^-$ anions using **36a** through ^{1}H NMR titrations in DMSO-d_6.[102] Such use of catenanes as anion sensing hosts has been relatively unexplored whereas the anion-templated synthesis of interlocked structures has itself been elegantly demonstrated on numerous occasions.[355-356,23]

With this in mind, [2]catenanes **111R**/**S** were investigated for their anion binding ability in order to investigate what effect the introduction of the chiral groups had on anion recognition compared to the **36a**.[102] Similarly, macrocycles **112S** and **118** possessing an appropriate geometry and cavity for guest uptake, as seen from the crystal structure of the **118**·EtOAc adduct in Section 5.10.2, underwent a similar investigation. The ^{1}H NMR titrations were carried out by Anna Aletti in the Gunnlaugsson Group by addition of specific aliquots of TBA(H_2PO_4) in DMSO-d_6 to solutions of [2]catenanes **111R**/**S** and macrocycles **112S** and **118** in DMSO-d_6 and at the same concentration (c = 2 mM). Further investigation of these experiments is required so these preliminary results are presented in more of a qualitative rather than quantitative manner.

Unexpectedly, the titration for [2]catenanes **111R**/**S** with $H_2PO_4^-$ did not give rise to significant changes in the ^{1}H NMR spectrum, see Figure 5.30(A) compared with **36a**, see Figure 5.30(A). After adding 7.5 eq. of $H_2PO_4^-$, very minute downfield shifts and resonance

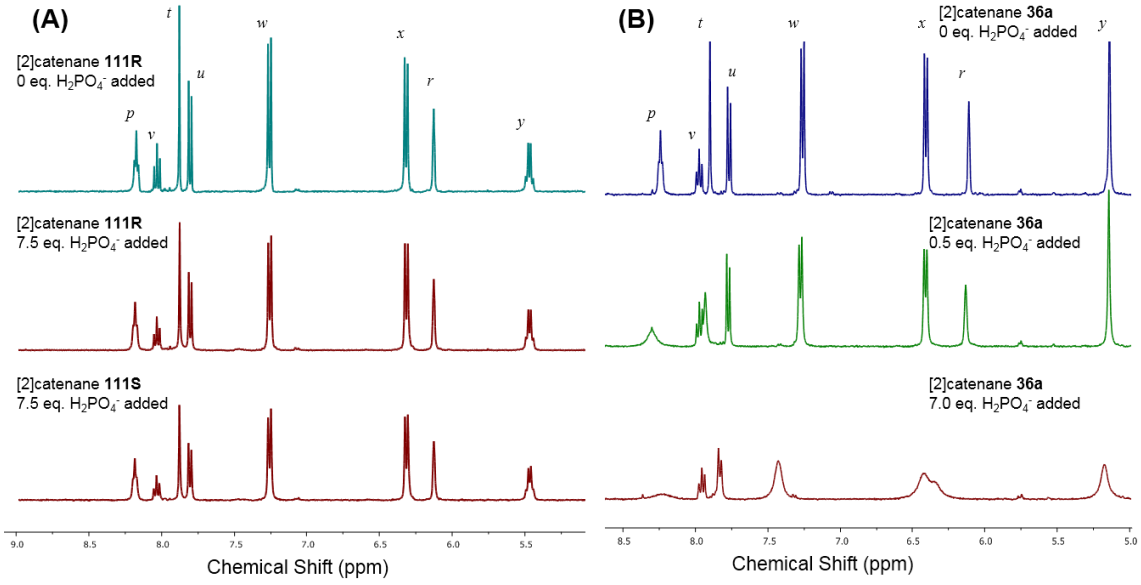

Figure 5.30 ^{1}H NMR titrations (400 MHz, DMSO-d_6) of TBA(H_2PO_4) with [2]catenanes (A) **111R/S** and (B) **36a**.

broadening can be observed for both the triazolyl and the amide hydrogen proton resonances of **111R/S** whereas the effect was more pronounced in the case of **36a**. This result indicates that interaction with the anion was not as strong for the chiral analogues. This suggests that the presence of the chiral groups restrained the system such that readily adopting a conformation for favourable binding of the $H_2PO_4^-$ anion was prevented for **111R/S**. In comparison, the extra degree of conformational freedom of **36a** in the absence of the chiral methyl groups could potentially allow for a more flexible system allowing a more facile rearrangement of the component macrocycles for anion recognition.

A similar trend was observed for macrocycle **112S** when the same titration was carried out with $H_2PO_4^-$, Figure 5.31(A) with noticeable differences observed compared to its achiral analogue **121**,[102] see Figure 5.31(B). As in the case of **111R/S**, after adding 7.5 eq. of $H_2PO_4^-$, very minute downfield shifts and resonance broadening were observed for the amide proton signal of **112S** whereas the effect was more pronounced in the case of **121** where both the triazolyl and amide proton signals underwent larger deshielding. This also suggests that the more restricted flexibility of the chiral macrocycle **112S** lessened the strength of the interaction with the $H_2PO_4^-$anion in contrast to the more flexible macrocycle **121**. Despite these apparently subtle changes observed upon addition of $H_2PO_4^-$ to **112S**, ESI^- HRMS experiment showed a characteristic signal at *m/z* 656.2128, assigned to the $[M+H_2PO_4]^-$ species (calculated *m/z* = 656.2140). However, this was obtained using a solution of $H_2PO_4^-$ and **112S** in CH_2Cl_2 and not DMSO-d_6 as in the ^{1}H NMR titration experiments. It must be

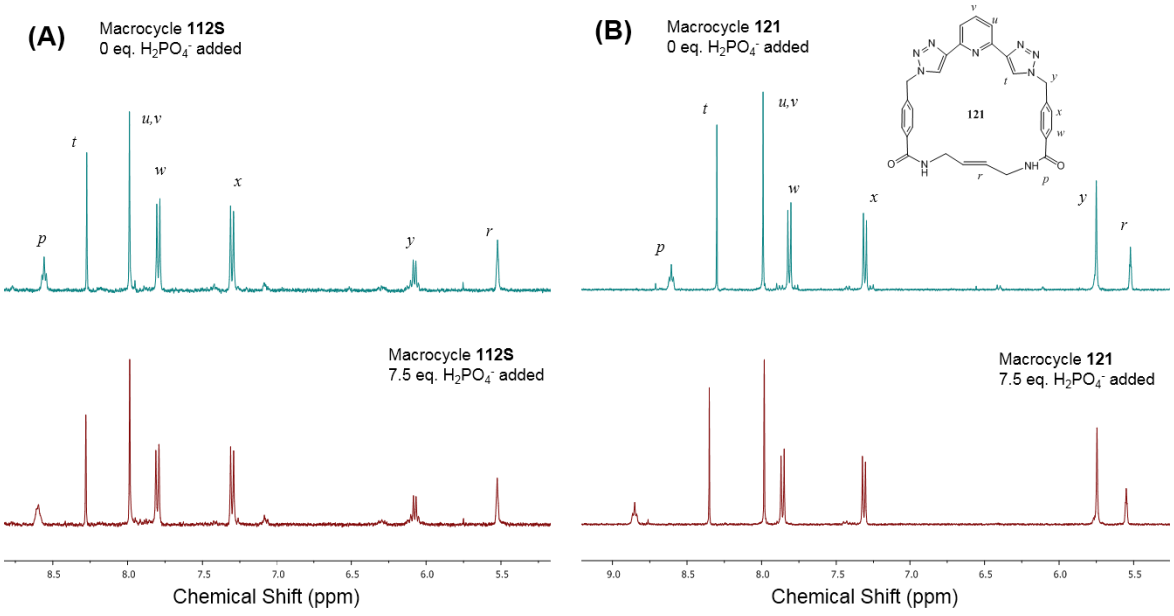

Figure 5.31 ^{1}H NMR titrations (400 MHz, DMSO-d_6) of TBA(H_2PO_4) with macrocycles (A) **112S** and (B) **121**.

noted that adducts detected by mass spectrometry exist in totally different physical environments to that in solution, however, the previous interaction in the CH_2Cl_2 can favour adduct formation and resilience in the ionised form.

Encouraged by the guest uptake potential of macrocycle **118** as evidenced by its crystal structure discussed in Section 5.10.2, this structural isomer of macrocycle **121** was also investigated for its anion recognition properties. It was clear from the first addition of 0.25 e.q. of $H_2PO_4^-$ anion to **118** in DMSO-d_6 that a bigger change in the chemical shifts was occurring (Figure 5.32) than for **112S** and **121** seen above. A broadening and splitting of the *NH* and triazolyl resonances were indicative of a hydrogen bonding interaction with the anion. These protons were also deshielded with their resonances appearing at higher chemical shifts upon addition of increasing equivalents of $H_2PO_4^-$. Aryl proton resonance (labelled 5) also became broadened with a concomitant increase in chemical shift. Proton resonance 10 associated with the olefin protons underwent deshielding also, eventually overlapping with methylene resonance 4 which too was somewhat deshielded.

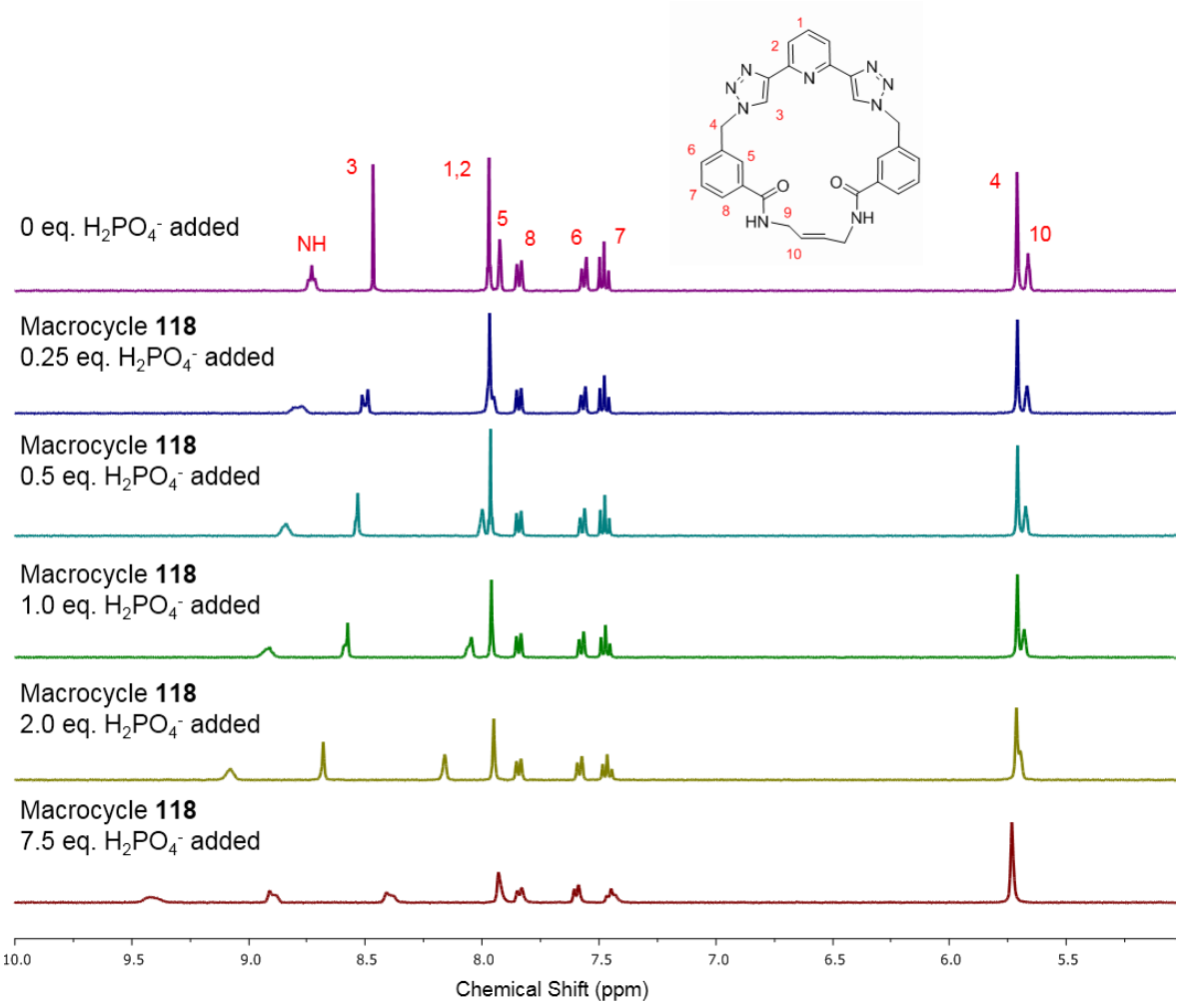

Figure 5.32 ^{1}H NMR titrations (400 MHz, DMSO-d_6) of TBA(H_2PO_4) with macrocycle **118**.

The same titrations as those carried out for **36a** and **121**,[102] were undertaken for **111R/S**, **112S** and **118** using TBACl solution in DMSO-d_6, however, such resonance changes upon titration with $H_2PO_4^-$ (slight as they are in the case of **111R/S** and **112S**) were not observed upon the addition of Cl^-, thus suggesting that **111R/S**, **112S** and **118** recognised $H_2PO_4^-$ preferentially (Appendix A.51-53). The more pronounced interaction of the isomeric macrocycle **118** with the $H_2PO_4^-$, compared to **112S** and **121** suggests that enhanced recognition is most likely due to the favorable pre-organisation of the anion-recognition site within **118**. This may be rationalised by the 3'-substituted nature of macrocycle **118** orienting the amide groups towards the *anti- anti* **btp** motif conformation, thus contracting the cavity in a manner which is preferential to the binding of the tetrahedral $H_2PO_4^-$ in comparison to the 4'-substituted nature of macrocycles **112S** and **121**. This is merely presented as one of many explanations of the observed data but as already mentioned from the outset, more work is required for substantiating these hypotheses.

5.15 Chiroptical probing of Ln(III)-directed formation of luminescent supramolecular gels

The photophysical characterisation of several of the chiral precursor ligands presented in this chapter, such as **103R/S**, **109R/S** and **110R/S**, has shown that these ligands exhibit chiroptical activity. There are striking similarities between these chiral **btp** ligands and the achiral analogues studied in Chapter 3 in their metal-templated self-assembly of novel luminescent molecules and materials. Efforts are underway to investigate the ability of chiral **btp** ligands **103R/S**, **109R/S** and **110R/S** to template the synthesis of analogous supramolecular systems and to study the transfer of their chiral information to the resulting systems.[309,326,357] In particular, **110R/S** has a notable resemblance to tricarboxylic acid **btp** ligand **H$_3$84** which showed the dual ability of templating the synthesis of both functional metallo-supramolecular gel soft materials and more rigid luminescent cation-exchange MOF materials. A brief summary of these promising preliminary studies into using chiral **btp** acids **110R/S** in the formation of chiroptically active Ln(III) luminescent gels will be presented in the following section.

In the closing stages of writing my PhD thesis I supervised work carried out by undergraduate student Mairéad O'Doherty as part of her final year research project. The preliminary results of the investigations into the formation of chiroptically active Ln(III) luminescent supramolecular gels derived from **btp** acids **110R/S** were promising and as such I was asked that the results of the work be included as a prologue to future studies.

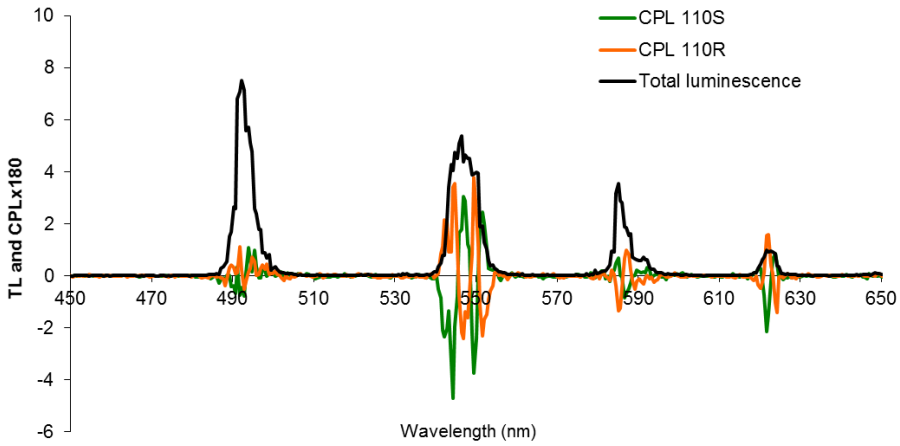

Figure 5.33 Circularly polarised luminescence spectra of both enantiomers **Tb(110R)$_3$** and **Tb(110S)$_3$** and total luminescence spectra of **Tb(110)$_3$** in CH_3CN.

The Eu(III) and Tb(III) complexes derived from **btp** acids **110R**/**S** were formed in the same way as those outlined in Section 3.3 and were partially characterised using ^{1}H NMR and photophysical spectroscopic techniques as well as HRMS. All complexes were obtained with the formula [Ln(**110R/S**)$_3$](CF$_3$SO$_3$)$_3$. As expected the **btp** ligands were seen to sensitise the Ln(III) radiative excited states and the resulting emission was probed by circularly polarised luminescence (CPL) spectroscopy, see Figure 5.33. In the case of the Tb(III) complex, the intensity of the radiative emission was very weak but the mirrored nature of the spectra of **Tb(110R)$_3$** and **Tb(110S)$_3$** were essentially enantiomeric.

In the same two-step one-pot procedure as outlined in Section 3.5, metallo-supramolecular gels were formed from the precursor Eu(III) and Tb(III) tris-complexes displaying the characteristic red and green emission under UV irradiation, see Figure 5.34. The gels were more translucent and homogenous in appearance than the corresponding systems formed

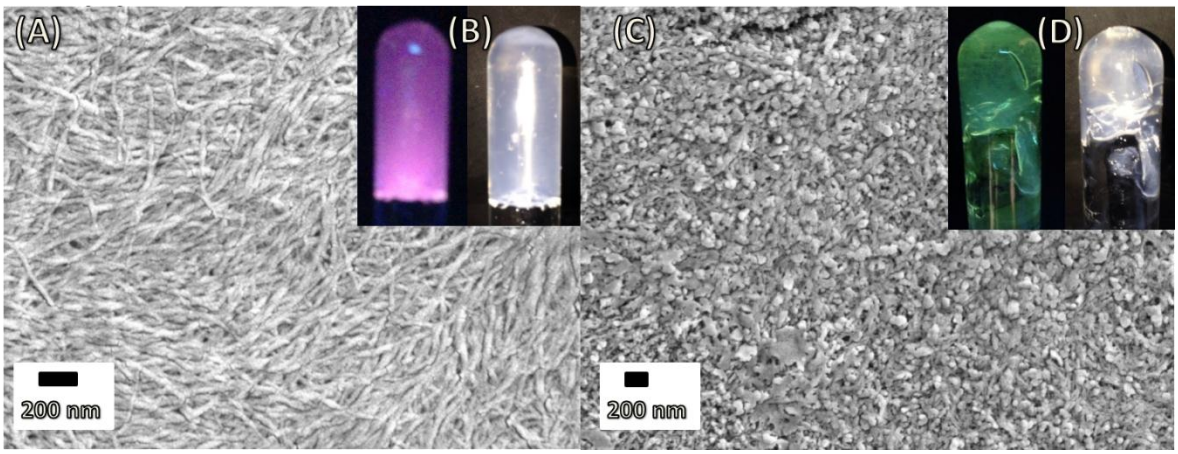

Figure 5.34 SEM images of dried out metallogels derived from (A) **Eu(110R)$_3$** and (C) **Tb(110R)$_3$** (scale bar 200 nm). Photographs of metallogels derived from (B) **Eu(110R)$_3$** and (D) **Tb(110R)$_3$** under UV irradiation and daylight.

from **H$_3$84** and this appearance of the gels could be compared with the metallogel systems derived from **dpa** amide derivative **52**, see Figure 1.35 in Section 1.10.1.[197] In a similar way, the morphology of the Eu(III) metallogel resembled the fibrous structures reported with **dpa** derivative **52**;[197] however, the morphology of the Tb(III) gel compared closely to the condensed structure of the **H$_3$84** derived metallogels presented in Figure 3.18 in Section 3.6.

The rheological behaviour was also investigated and the results demonstrated similar thixotropic properties to systems derived from **52** and **H$_3$84**, respectively. The Eu(III) metallogel was shown to be less robust and more subject to flow at moderate oscillation frequency than the corresponding Tb(III) metallogel, see Figure 5.35(A)/(B). This coincided with the lower observed yield strain of *ca.* 10% compared with that of the Tb(III) analogue which was *ca.* 30% strain, see Figure 5.35(C)/(D). However, the moduli values *G'* and *G''* were seen to recover quickly to their original magnitudes following consecutive application

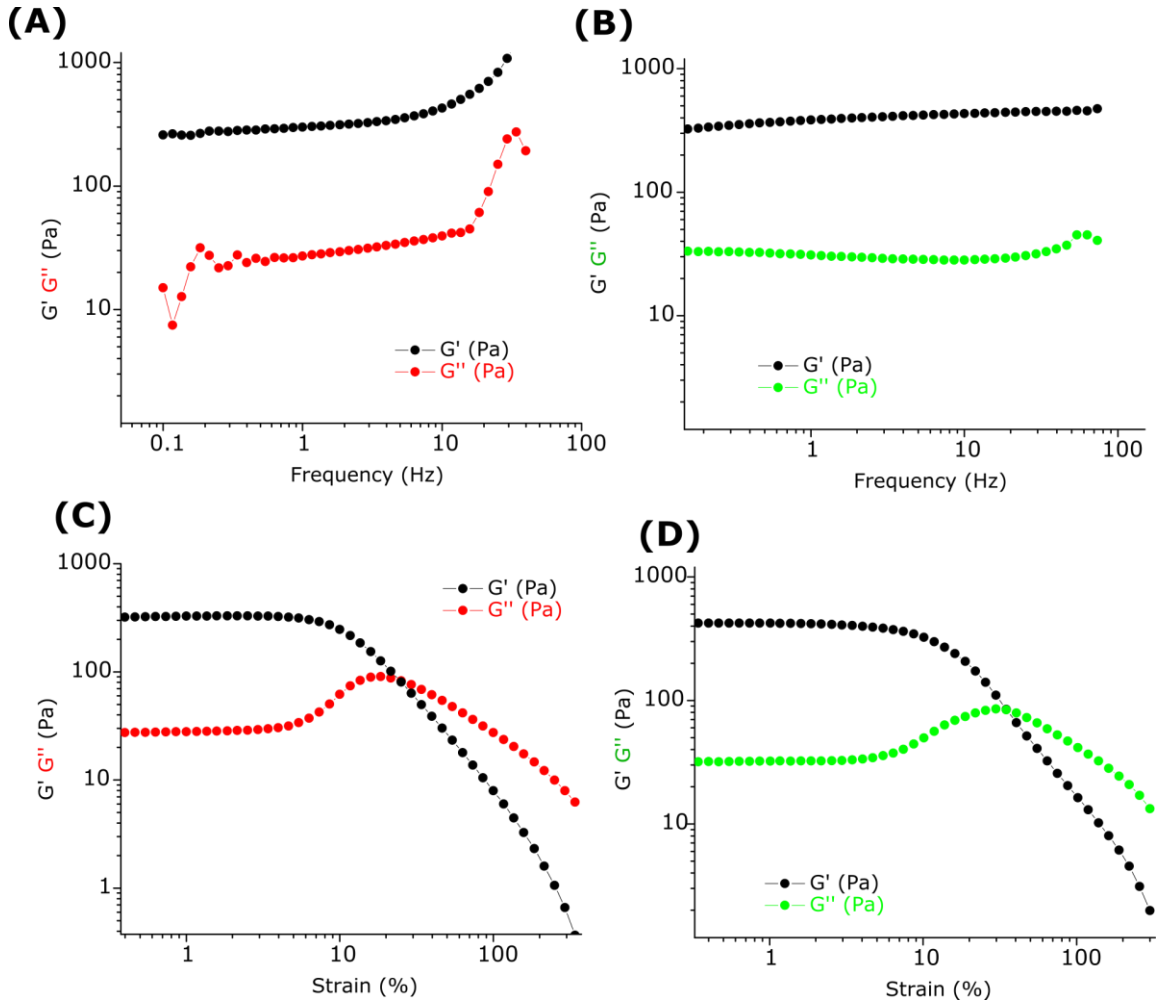

Figure 5.35 Oscillatory rheology frequency sweeps measurements of the storage modulus G′(■) and loss modulus G″(●) carried out at 1% strain amplitude for (A) the Eu(III) metallogel and (B) the Tb(III) metallogel. Oscillatory rheology strain dependence measurements of the storage modulus G′(■) and loss modulus G″(●) carried out at a f = 1 Hz for (C) the Eu(III) metallogel and (D) the Tb(III) metallogel.

of shear stress of alternating strain amplitudes of between 100% and 1% at f = 1 Hz, see Figure 5.36(A)/(B).

These are exciting preliminary results which may offer an insight into how the additional 4-pyridyl carboxylic acid in tri-carboxylic acid **btp** ligand **H$_3$84** effects the mechano-responsive properties of the healable systems compared to the di-carboxylic acid **110R/S**. It is also planned to investigate if the chiral information of enantiomers **110R/S** can be transferred to the resulting gel materials.[29,32-33] Further characterisation, exploration and reproduction of the results of the mechanical and optical observations of these stimuli-responsive gel systems are currently under investigation.

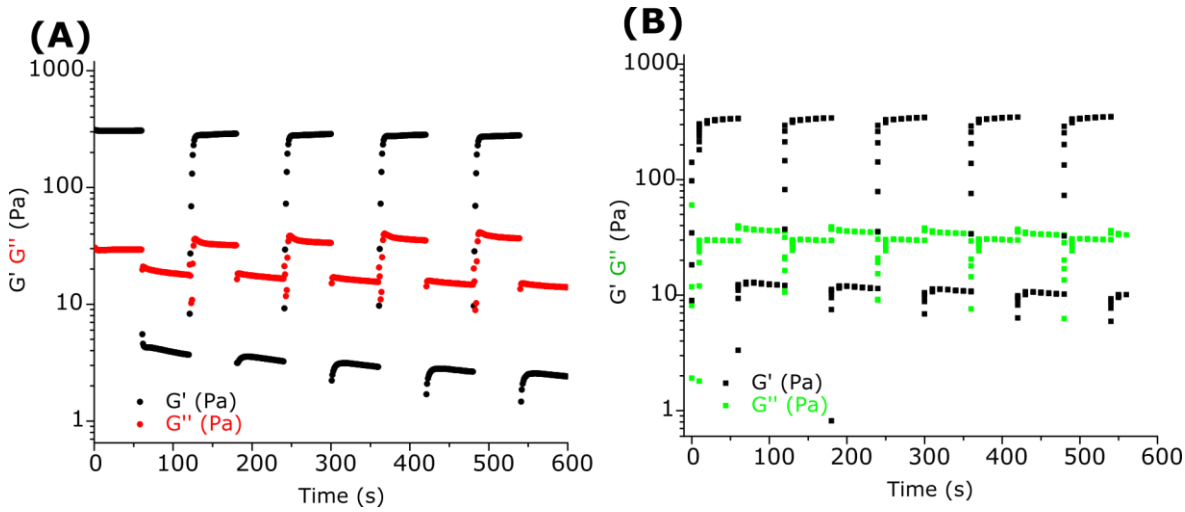

Figure 5.36 Oscillatory rheology time evolution recovery of the storage modulus G′(●) and loss modulus G″(●) for (A) the Eu(III) metallogel and (B) the Tb(III) metallogel with alternating strain amplitudes of 100% and 1% at f = 1 Hz.

5.16 Conclusions

It was the aim of this chapter to determine if the presence of the 4'-substituted "arm" substituent was essential for efficient formation of [2]catenanes analogous **btp** system **36a**. Several **btp**-olefin candidate molecules derivatised with 4'-substituted "arm" functionality in the form of placing chiral groups adjacent to the triazolyl *N1* position, **103R/S**, and also adding sterically bulky substituents at the 4-pyridyl position of the **btp** motif, **104**, were synthesised. Control **btp** ligands lacking the 4'-substituted "arm" functionality and replaced with the structurally isomeric 3'-substituted "arm" functionality, **105** and **106**, were synthesised and the effect of this isomerism on the pre-organisation of the system required for catenation was analysed. The successful synthesis of olefin derivatised **btp** ligands lacking any amide functionality, **107** and **108**, was also confirmed.

[2]Catenane formation was successful in the cases of both enantiomers of chiral olefins **103R**/**S** and the olefin **104** which was functionalised at the 4-pyridyl position. It can be concluded that modification of the **btp** motif at the triazolyl *N1* position with a chiral centre in the incorporation of chiral 4'-substituted "arm" substituents and separately at the 4-pyridyl position with a benzyl ester group does not have a detrimental effect on the synthesis of self-templated [2]catenane The threading of **btp** olefin **103S** though macrocycle **112S** and characterisation of the *pseudo*-rotaxane was an important finding in understanding the process which leads to self-templated [2]catenane formation.

It was concluded that the chiral information transferred by the *R*- and *S*-enantiomers of the chiral **btp** olefin precursors **103R/S** was manifested in the equal and opposite manners the [2]catenanes **111R**/**S** interacted with circularly polarised electromagnetic radiation. The self-templated synthesis of [2]catenanes from **103R/S** gave rise to **111R**/**S** which were enantiomers of each other as formation of the mechanical bond does not give rise to topological chirality due to the symmetric nature of the component macrocycles. To the best of our knowledge, the synthesis of **111R**/**S** represents the first instance of the formation of chiral self-templated homocircuit [2]catenanes from starting materials possessing a classical chiral element such as a chiral centre.[359]

Despite observing signs of possible dimerisation occurring through non-classical hydrogen bonding of *anti*-*anti* oriented **btp** motifs for all olefin derivatised **btp** ligands presented herein, it can be concluded that the deciding factor in achieving the necessary pre-organisation for efficient self-templated [2]catenane synthesis is the incorporation of the 4'-substituted "arm" substituent into **btp** olefin precursors, as was the case for **102a** in the synthesis of the original [2]catenane **36a**, and **103R/S** and **104** which both the structurally isomeric 3'-substituted "arm" systems of **105** and **106** lacked, as did long chain **btp** olefins **107** and **108**. These compounds, when treated identically formed macrocycles exclusively.

Anion binding titrations were carried out with **111R**/**S**, **112S** and **118** in the same way as had been previously reported by Byrne e*t al.* for **36a** and **121**,[102] with $H_2PO_4^-$ and Cl^- as analytes. As in the cases of **36a** and **121**, no change in the proton resonances of **111R**/**S**, **112S** and **118** were observed upon the addition of Cl^-. More subtle changes in the proton resonances of **111R**/**S** and **112S** were observed upon the addition of with $H_2PO_4^-$ than in the cases of **36a** and **121**. However, significant changes in the proton resonances of **118** were observed upon addition of $H_2PO_4^-$ suggesting that the 3'-substitution pattern on the aryl "arms" of the macrocycles brought about a more pronounced interaction with the tetrahedral anionic analyte relative to **36a** and **121**.[102]

5.17 Future work

The majority of the work involved in this chapter was concerned with ascertaining the ideal structural features necessary to incorporate into the **btp** olefin design in order to achieve ideal pre-organisation of the self-templating components for efficient homocircuit [2]catenane synthesis. In addition, a large part of the research was concerned with the effects various substitutions close to the **btp** core motif had on the synthesis efficiency. Now that a greater understanding of the formation of these intricate mechanically interlocked systems has been obtained, there remains a large scope for analysing their physical properties. In the first instance, the nature of the dynamic processes involving the relative motion of the constituent interlocked macrocycles to each other requires further exploration. Observation of the effects of external stimuli on the system, in particular, through the use of the dual ability of **btp** to interact with cations and anions opens potential for the study of these [2]catenanes in the development of molecular machines through stimuli-controlled motion.[372] This has become very topical recently as seen from the work celebrated by the 2016 Nobel Prize in Chemistry.[261,271,277,362,373-374]

The threading experiment of **103S** through macrocycle **112S** opens up avenues for the synthesis of mixed or heterocircuit systems. It would be particularly interesting to see whether threading olefin **103S** through macrocycles **117**, **118** or **119**, whose precursors could not achieve catenation, would result in heterocircuit [2]catenanes, or in the case of 2×2 macrocycle **120**, heterocircuit [3]catenanes, as presumably the second thread molecule needs only to possess the 4'-substituted "arm" for the desired hydrogen bonding pre-organisation.

This dual ability of **btp** could also be studied in the context of forming higher order supramolecular systems incorporating such [2]catenanes. The placement of functional groups such as the benzyl ester motif in **104** has shown compatibility with the self-templated formation of [2]catenanes and derivatisation of the resulting [2]catenane **113** with a carboxylic acid group through hydrolysis of the ester is the next logical step. A [2]catenane carboxylic acid, such as, **122** could then be incorporated in to a diverse variety of coordination polymer systems such as MOFs, gels *etc.* or more discrete systems with the acid acting as a 'handle' for attaching further functionality. It would be interesting to study the self-assembly behavior of these unique systems with various substrates in chemical applications,[375] such as host-guest recognition[355,376] or catalysis.[377] Similarly, it is envisaged that the derivatisation of the **btp** motif of the chiral ligand **110R**/**S** at the 4-pyridyl position, in a similar fashion to that demonstrated in Chapter 2, would promote promising gelator

properties in chiral **btp** tri-carboxylic acid ligands, such as **123R**/**S**, with Ln(III) ions. In the context of anion guest recognition, as has been shown by Byrne *et al.*, **36a** and **121**,[102] along with **111R**/**S**, **112S** and **118** synthesised in this research project, have shown the potential to bind anions with some selectivity. This project is in its early stages and more work must be done on ascertaining the global stability constants of this binding process.

122

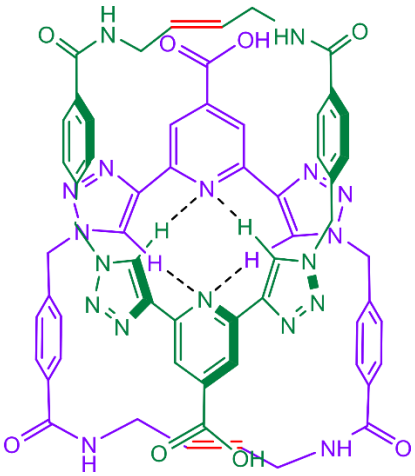

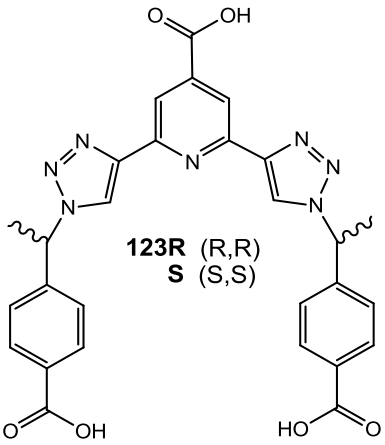

6 Synthesis and structural studies of the subtly unsymmetric 1,4-di(2-pyridyl)-1,2,3-triazole ligand and its transition metal complexes

6.1 Introduction

The design of appropriate and readily modifiable organic ligands to bind metal ions in the synthesis of diverse and novel structures has seen the progressive use of heteroaromatic chelators such as **btp** in constructing intricate coordination compounds for various functional endeavors.[54,60,89,104-110,150,286,378-380] As has been discussed in recent reports from the Gunnlaugsson Group[27,70,102-103,119,156,182] and in Chapters 3-5, the terdentate **btp** heteroaromatic ligand's coordination, photophysical and electrochemical behaviour with various *d*-metal ions,[113] and their formation of lanthanide bundles,[70,103,156] healable gels[182] and self-templated [2]catenanes[102] has been investigated. In the same way, there has been a significant interest in the incorporation of the bidentate **bpy** analogues, such as the **tp** motifs into coordination polymers, discrete polynuclear assemblies and mechanically interlocked systems.[42,48-53,281] The resulting intriguing architectures have found potential applications as materials in catalysis, separation, biomedical applications[45] *e.g.* drug delivery, sensors, in electronic and magnetic devices.[46]

Crowley *et al.* have employed the facile one-pot Cu(I)-catalysed azide-alkyne cycloaddition (CuAAC) method for the generation of 1,2,3-triazole ligands[42,50-51,53] including the reported the use of **tp** and **tp'** ligands in examining their coordination properties with Cu(II), Ag(I), Pd(II), Pt(II), gold(I), and Au(III) ions,[42,48-53] as was discussed in Section 1.4.2. In particular, the stability of "regular" binding (*reg*) **tp** ligands over "inverse" binding (*inv*) **tp'** (Scheme 6.1) was investigated.[54] It is the aim of this Chapter to investigate whether the typically active chelating functionality embedded in ligand **124** favours binding through the *reg*, *inv* (or both) binding pockets when the two metalation sites are simultaneously present in the ligand scaffold. The resulting selectivity observed in the metal binding will thus be explored with transition metals of varying kinetic lability ranging from Cu(I), Co(II), and Ag(I) to the more inert Pt(II). The complexes of the latter two metal ions have shown biological activity for the potential use as antibacterial and anti-cancer

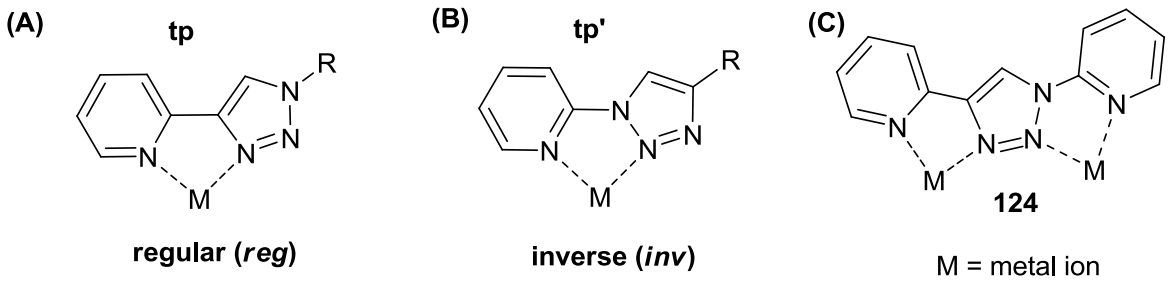

Scheme 6.1 The two metal ion (M) binding pockets (A) *reg* and (B) *inv* of the **tp** and **tp'** motifs, respectively. (C) The unsymmetric ligand **124** possessing both potential binding pockets.

agents.[381-382] Many heterocyclic metal complexes are biologically important, and although the 1,2,3-triazole motif is not known as a naturally occurring metal binding group it bears a physicochemical resemblance to the amide functional group arising as a result of its relative planarity, strong dipole moment and hydrogen bond donor and acceptor properties.[18-19] Ruiz *et al.* have reported discrete complexes of analogous compounds containing the 2-pyridyl-benzimidazole binding motif of Ru, Pt or Ir, which have shown promising activity as inhibitors of amyloid β-peptide[383-384] in the recent development of a potential treatment of Alzheimer disease.[385] Catalysis is another area in which these analogues have found application: Liu *et al*. reported a dinucleating system similar to **124**, which has been immobilized onto the surface of a graphene composite in its dinuclear Cu complex form as an Oxygen Reduction Reaction catalyst.[386] It will also be demonstrated that the binding selectivity was not affected by the coordinating ability of the counterion which ranged from PF_6^-, SbF_6^-, NO_3^- to Cl^-.

6.2 Synthesis and structural studies of 124

Despite the reaction being described as the 'cream of the crop' for 'click' chemistry,[11] certain substrates are known to display relatively poor efficiencies in the CuAAC reaction; *e.g.*, aryl azides such as 2-azidopyridine. The reason for this being that these azides exist in equilibrium between a closed form,[387-392] tetrazolo[1,5-a]pyridine **125** (Scheme 6.2) which is the main form at room temperature, particularly in polar solvent conditions, and its open form (2-azidopyridine) which is favourable at high temperatures and non-polar solvent conditions. There have been several reports dealing with the CuAAC methodology of 'clicking' 2-azidopyridines,[54,387-392] with both Zhang *et al.*[389] and Sangtrirutnugul *et al.*[390] presenting the synthesis, in particular, of **124** (Scheme 6.2) using 2-ethynylpyridine, **126**, albeit through a different synthetic approach to the one use in this research project.

Aryl azides have previously been prepared by diazotization of aryl amines and subsequent

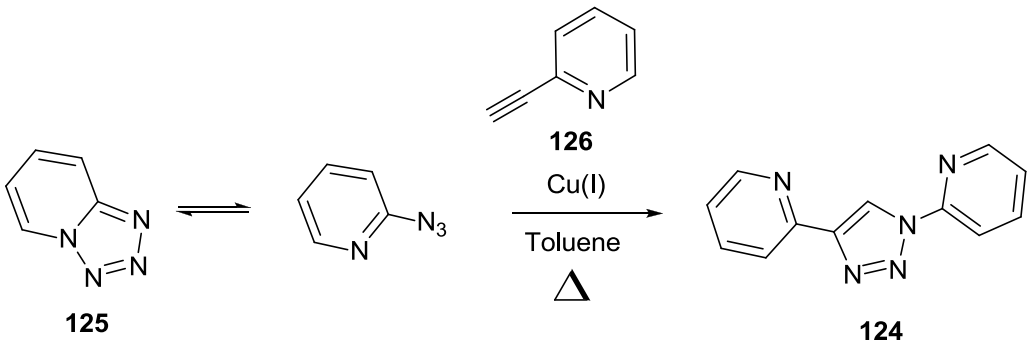

Scheme 6.2 Ring-tautomerisation of **125** and synthesis of **124**: $[Cu(CF_3SO_3)]_2 \cdot C_6H_6$, Toluene, 120°C.[390]

treatment with sodium azide, but this method is not compatible with some functional groups. Other methods include conversion of aryl amines to the corresponding azide using triflyl azide,[393] however, this reagent is not commercially available and must be freshly prepared.

The CuI/diamine catalysed variant of the Ullmann reaction was developed by Anderson *et al.* for the effective preparation of aryl azides from aryl halide starting materials.[51,165] It was using this last approach that **125** was synthesised from 2-bromopyridine using sodium azide. Upon completion of the reaction, the mixture was extracted with CH_2Cl_2. As was briefly discussed in Section 1.9.1, azide compounds, particularly low-weight organic azides, due to their potential explosive nature, are not recommended to be isolated with a rule of thumb being that special care should be taken when $(N_C + N_O)/N_N \leq 3$ where N_X is the number of a given atom X present in the molecule). Therefore, this compound was isolated on a small scale in order to gain more of an insight into the azide-tetrazole tautomerisation. The reaction CH_2Cl_2 solvent was removed under reduced pressure yielding an orange crystalline powder in 89% yield. HRMS (EI^+) confirmed the presence of the desired compound, found for $[M+H]^+$ m/z = 120.0438. However, there appeared to be two components visible in the ^1H NMR spectrum, see Figure 6.1(A), in which two sets of resonances with identical splitting

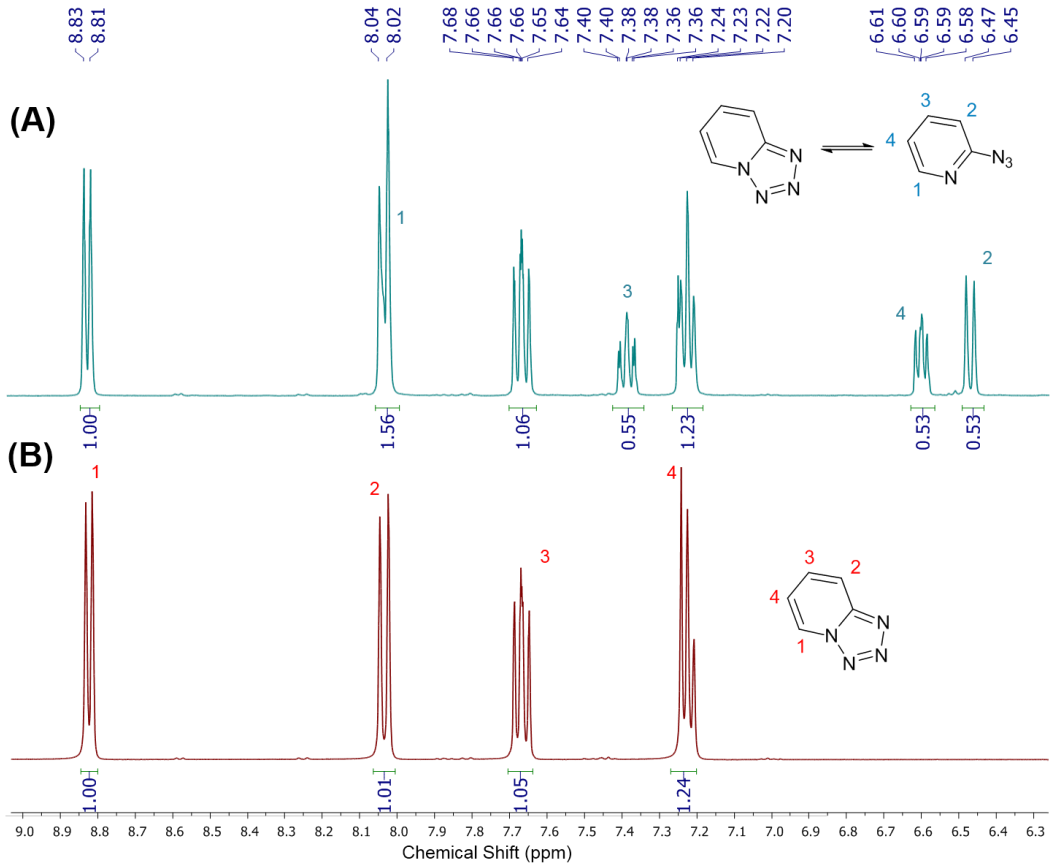

Figure 6.1 ^1H NMR (400 MHz, $CDCl_3$) comparison of **125** when isolated from (A) CH_2Cl_2 and from (B) CH_3OH

patterns integrating in a 2:1 ratio were observed. The resonances at at 8.02 ppm, 7.40 ppm, 6.59 ppm and 6.46 ppm each in a 1:1:1:1 relative abundance to eachother were at different chemical shifts to those of the 2-bromopyridine starting material. These resonances were removed upon dissolving the solid in CH_3OH. There was no observed precipitation. The ^1H NMR in $CDCl_3$ showed only the resonances at 8.82 ppm, 8.03 ppm, 7.66 ppm and 7.23 remaining, see Figure 6.1(B). Formation of the tetrazole was confirmed using X-ray diffraction analysis on single crystals formed from slow evaporation of the $CDCl_3$ solution, which were isostructural to those already reported (Figure 6.2).[390] The two component ^1H NMR spectrum may be rationalised by the existance of a solvent-dependent equilibirum between the open azide form and the closed tetrazole form of **125** as discussed earlier.[387-389] It is presumed that the CH_3OH solution forced the equilibrium to shift in favour of the closed ring-tautomer form. Its for this reason that non-polar solvents were used in the 'click'step.[54,387-392]

The TMS-protected ethynylpyridine, **46**, (Section 1.9.2) was synthesised by Sonogashira coupling.[99] Deprotection of **46** was carried out using TBAF (1 eq.), and **126** was isolated in 92% yield after purifying by flash chromatography. Ligand **124** was synthesised in an alternative fashion to that reported by Zhang *et al.*[389] and Sangtrirutnugul *et al.*[390] Tetrazole **125** was dissolved in anhydrous toluene (Scheme 6.2) and $[Cu(CH_3CN)_4]PF_6$ was added as the source of the Cu(I) catalyst along with TBTA as a Cu(I) stabilising ligand. This was degassed after the addition of **126**; the degassed reaction mixture was stirred at 90 ^oC for 48 hours under argon. The desired compound was purified by automatic flash chromatography producing a deep blue powder which was recrystallised from CH_3CN/H_2O (4:1) giving colourless crystals in 69% yield. The ^1H NMR (400 MHz, $CDCl_3$) showed characteristic

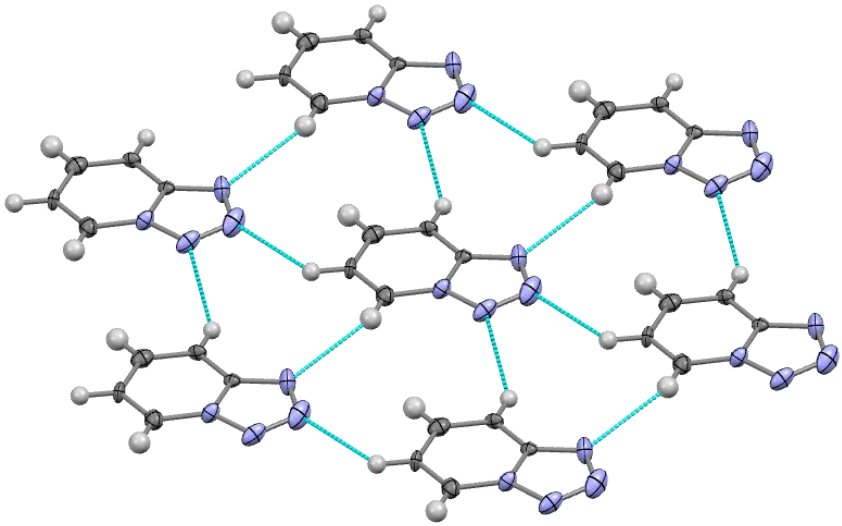

Figure 6.2 Crystal structure of **125**. Thermal ellipsoids displayed at 50% probability.

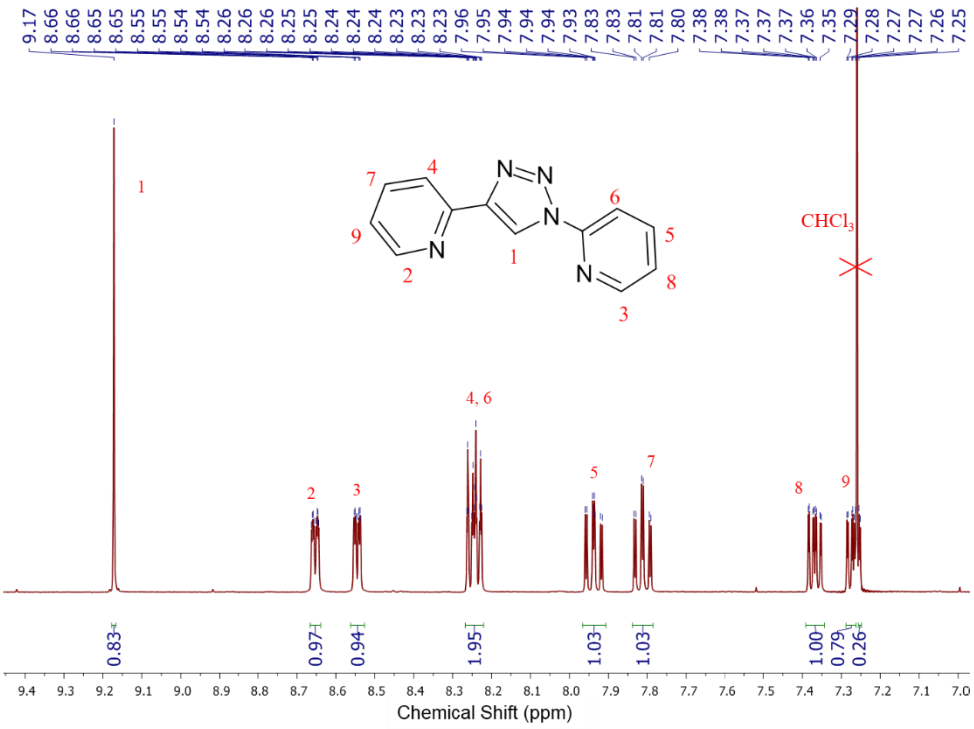

Figure 6.3 ^{1}H NMR (400 MHz, $CDCl_3$) of **124**.

splitting patterns of the nine protons of **124** (Figure 6.3) and demonstrated the subtly unsymmetric nature of the ligand.[389] The triazolyl singlet was found at 9.17 ppm and the two 6-pyridyl proton resonances for respective rings appeared as a pair of doublets of doublets of doublets at 8.65 ppm and 8.55 ppm. The two 3-pyridyl proton resonances overlapped with each other centred around 8.24 ppm and the two 4-pyridyl proton resonances appeared as a pair of doublets of doublets of doublets at 7.91 ppm and 7.84 ppm, respectfully. Finally, the two 5-pyridyl proton resonances could be found as a pair of doublets of doublets of doublets at 7.37 ppm and 7.27 ppm. Bulk purity was confirmed by elemental analysis.

The unbound ligand was also characterised in the solid state. This had not been reported to date. All crystal data, data collection, and structure refinement details are summarised in Appendix E, Table E.5. Needle-like transparent single crystals of **124** were obtained by diffusion of diethyl ether into a solution of CH_2Cl_2. The data were collected and solved by Dr. Salvador Blasco and the structure model was refined in the monoclinic system with $P2_1/n$ space group, see Figure 6.4(A), containing one molecule in the asymmetric unit. Disorder was detected over the triazole ring junction sites and thus overlapping carbon-nitrogen atoms were modelled at 50:50 occupancy and their ADPs restrained. The triazolyl and two pyridyl units are essentially coplanar; the planar conformation of **124** facilitates the π-π stacking interactions between molecules along the *b*-axis, (the perpendicular distance between the parallel mean planes of molecules is *ca.* 3.4 Å). The molecule packs in a herringbone

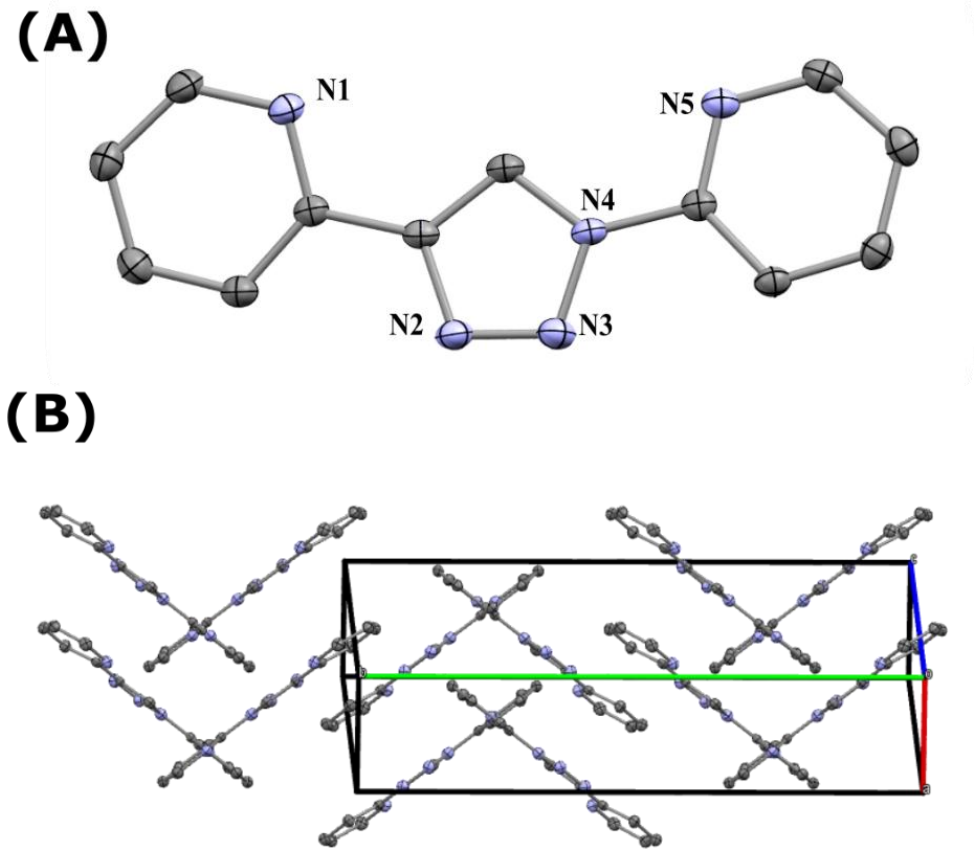

Figure 6.4 X-ray crystal structure of **124**. (A) Molecular structure displaying the *anti-anti* conformation and (B) the herringbone packing arrangement common in planar molecules, viewed "edge-on". Thermal ellipsoids at 50% probability and hydrogen atoms and disordered contributor omitted for clarity.

manner[394] common in planar aromatic molecules, see Figure 6.4(B). The angle between the mean planes of molecules of adjacent stacks is *ca.* 72.4°. As a result of this orientation, the triazolyl hydrogen atom is not involved in any intermolecular hydrogen bonding interactions. The observed molecular conformation in the solid state causes the chelating units to adopt an *anti–anti* arrangement as is often observed in these types of ligand systems.[104-107] The coordination chemistry of this ligand was then investigated with several *d*-metal ions. The

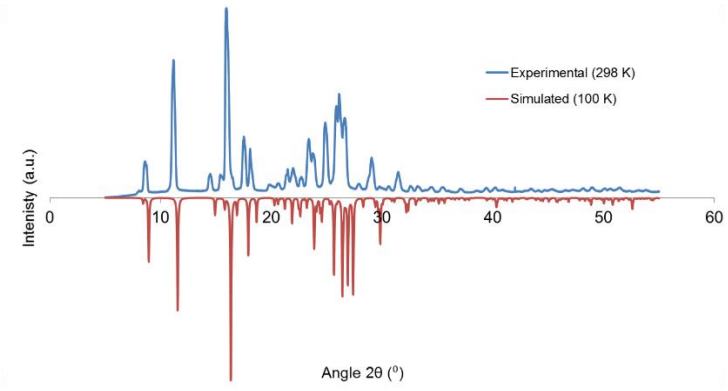

Figure 6.5 X-ray powder diffraction pattern for **124**

PXRD experimental data of the crystalline compounds to follow, unless otherwise specified, were compared with the simulated patterns from the single crystal data collections carried out at 100 K and were found to match satisfactorily confirming phase purity, (shown for **124** in Figure 6.5).

6.3 Synthesis and self-assembly studies of [Cu124$_2$]PF$_6$

There are several click-derived pyridyl triazole copper complexes already present in the literature,[41,395-397] therefore studying the coordination behaviour of **124** with Cu(I), for example, was a logical starting point. This was investigated by carrying out a ^{1}H NMR titration of **124** in CD_3CN at 2 mM by sequential addition of specific aliquots of a solution of $[Cu(CH_3CN)_4]PF_6$ in CD_3CN, see Figure 6.6(A). A deshielding and pronounced broadening of the proton resonances associated with the *reg* chelating site (1, 2, 4, 7 and 9) was observed demonstrating a binding selectivity for this pocket leaving only the signals associated with the unbound pyridine ring (3, 5, 6 and 8) unaffected. This is consistent with the DFT calculations reported by Crowley *et al*. which demonstrate that the *reg* binding of transition metals is energetically more favourable than the corresponding *inv* binding.[54] This has been rationalised by the preferred coordination through the more electron rich

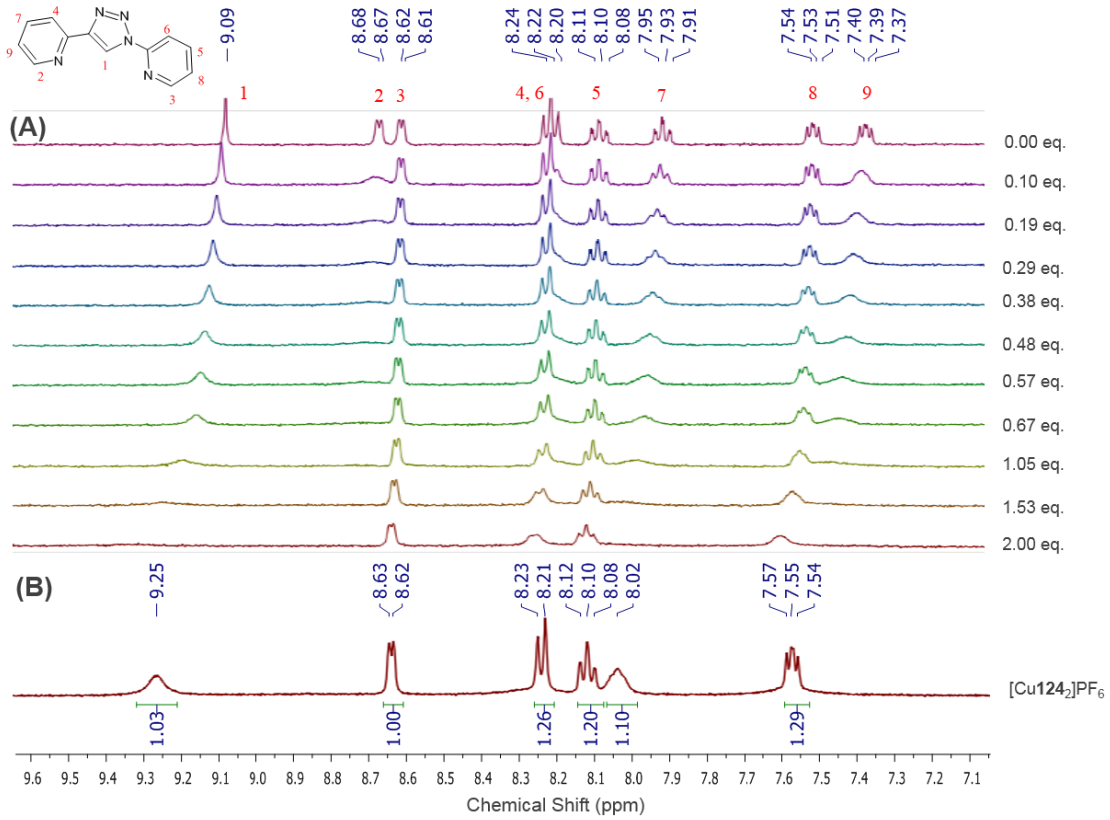

Figure 6.6 (A) ^{1}H NMR (400 MHz, CD_3CN) titration of **124** (c = 2 mM) with $[Cu(CH_3CN)_4]PF_6$ showing broadening of the proton resonances 1, 2, 4, 7 and 9. (B) ^{1}H NMR (400 MHz, CD_3CN) spectrum of complex [Cu**124**$_2$]PF$_6$.

proximal *N2* nitrogen atom of the 1,2,3-triazole unit. The medial *N3* nitrogen adjacent to two electron-withdrawing nitrogen atoms is affected by a more pronounced inductive effect and, hence, is a weaker sigma donor. This is in contrast to the proximal nitrogen atom *N2* which resides between a nitrogen atom and a less electron-withdrawing carbon atom. Cu(I) is known for lability, suggesting that ligand exchange is occurring on the NMR timescale (milliseconds) at room temperature, resulting in the broadening of the signals. Subsequent additions showed that the rest of the signals of **124** broadened only slightly. HRMS analysis displayed a peak at *m/z* = 509.0980 suggestive of a species with formula $[Cu\mathbf{124}_2]^+$ which was present even after 2.00 eq. of Cu(I) had been added in the titration experiment. Therefore, the optimised synthetic procedure for formation of the complex was then investigated.

$[Cu(CH_3CN)_4]PF_6$ was stirred with two molar equivalents of **124** in CH_3CN at room temperature for 60 minutes before diluting with diethyl ether, filtering the orange precipitate and drying under suction. The ^{1}H NMR of the Cu(I) complex formed, see Figure 6.6(B) correlated well with that of the ^{1}H NMR spectrum at 0.48 eq. addition of Cu(I) to **124** during the titration experiment. The broadening of the same resonances was observed which was further investigated through two-dimensional ^{1}H NMR spectroscopy showing that the sharp resonances associated with the non-chelating pyridine consisted of the one magnetically coupled ring system (Appendix A.43). This chelating preference through the *reg* binding pocket demonstrated by ^{1}H NMR analysis was also corroborated by single crystal X-ray diffraction analysis, confirming the $[Cu\mathbf{124}_2]PF_6$ formula.

6.4 Crystallographic Study of $[Cu\mathbf{124}_2]PF_6$

Orange single needle-like crystals were obtained *via* diethyl ether diffusion into a solution of $[Cu\mathbf{124}_2]PF_6$ in CH_3CN. The data were solved and the structure model was refined in the $P2_1/n$ space group with one molecule in the asymmetric unit (Figure 6.7). The two chelating **124** ligands adopt a *pseudo* tetrahedral geometry ($\tau_4 = 0.62$)[343] about the Cu(I) with the metal ion residing exclusively in the *reg* pocket which reflects the solution NMR studies. The *anti–anti* conformation of the ligand seen in the unbound ligand crystal structure changes to the *syn–anti* conformation to allow for the Cu(I) chelation. The free pyridine is locked in the *anti* geometry possibly due to the *N···N* lone pair repulsion and the ligands retain the essentially coplanar geometry in the complex. This compares closely to the optimised geometry of this complex using DFT calculations reported by Sangtrirutnugul *et al.*[395] There is a hydrogen bonding interaction between one CH_3CN molecule and the triazolyl proton, the donor-acceptor distance |D···A| is 3.312(6) Å, ∠ (*C-H···N*) is 139.0(3)°). The system

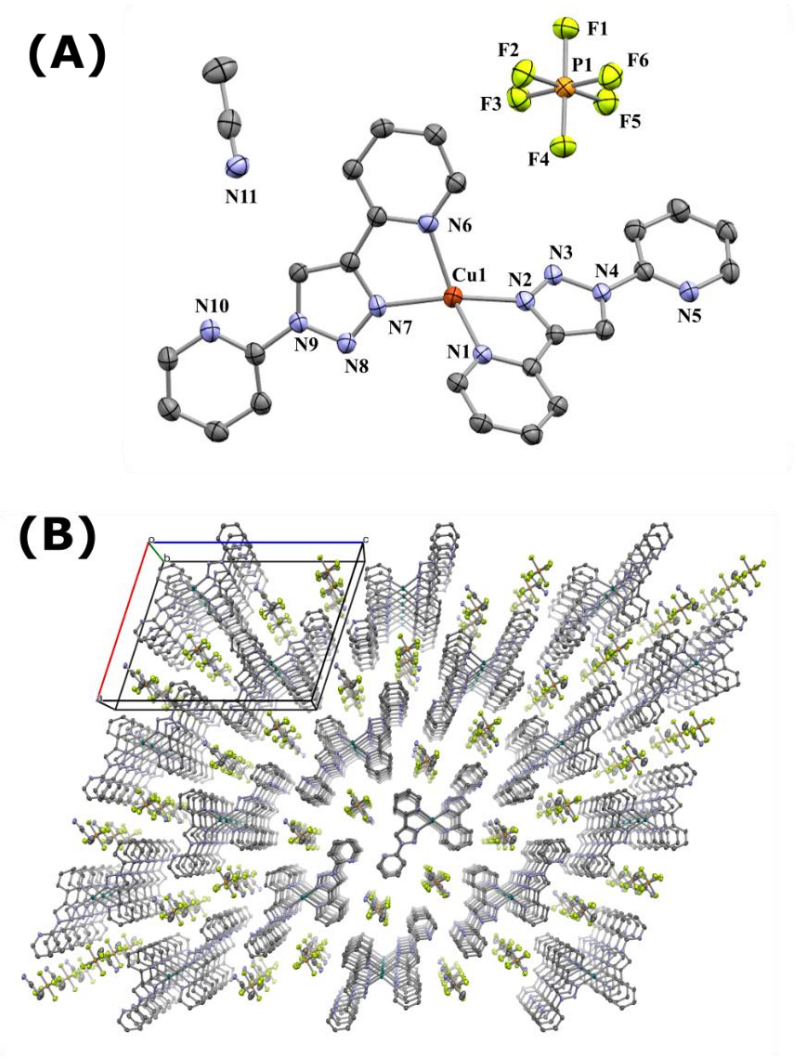

Figure 6.7 X-ray crystal structure of [Cu**124**$_2$]PF_6. Thermal ellipsoids at 50% probability and hydrogen atoms omitted.

also exhibits a *C-H···N* interaction between the acidic *CH* at the 6-position of the non-binding pyridyl ring and the *N3* nitrogen atom of the 1,2,3-triazole unit on the ligand of a neighbouring Cu(I) complex, also reported in similar systems.[54,347] The dihedral angle between the mean planes defined by the atoms comprising the two *reg* binding pockets of the **124** ligands about the Cu(I) metal centre is 68.38(13)° and the bite angles ∠ (*N-Cu-N*) are essentially the same at 81.74(15)° and 81.78(15)° for both Cu(I) binding **124** ligands. The corresponding |N_{pyr}-*Cu*| and |N_{triaz}-*Cu*| for the CH_3CN·**124** adduct portion of the complex are 2.062(4) Å and 2.037(4) Å, respectively. The corresponding bond lengths for the opposite **124** ligand are 2.053(4) Å and 2.045(4) Å, respectively. These dimensions differ from those calculated using DFT by Sangtrirutnugul *et al.*[395] reporting a longer |N_{pyr}-*Cu*| of 2.128 Å compared to a shorter |N_{triaz}-*Cu*| of 2.050 Å. Though this was calculated in the gas phase, the dimensions compare closely to those reported for the crystal structure of a similar

"click" triazole Cu(I) complex reported by Petitjean *et al.*[41] The overall crystal packing is largely dominated by Coulomb interactions between the Cu(I):**124** cation and the PF_6^- anion and also by π–π stacking interactions between adjacent discrete complexes parallel to the *b*-axis, see Figure 6.7(B). The phase purity was confirmed by elemental analysis and PXRD, see Figure 6.8. Another kinetically labile metal which has been studied for its coordination with multi-dentate Lewis basic ligands is silver, therefore it was investigated if the same *reg* binding preference would be observed in the complexation of Ag(I) with **124**.

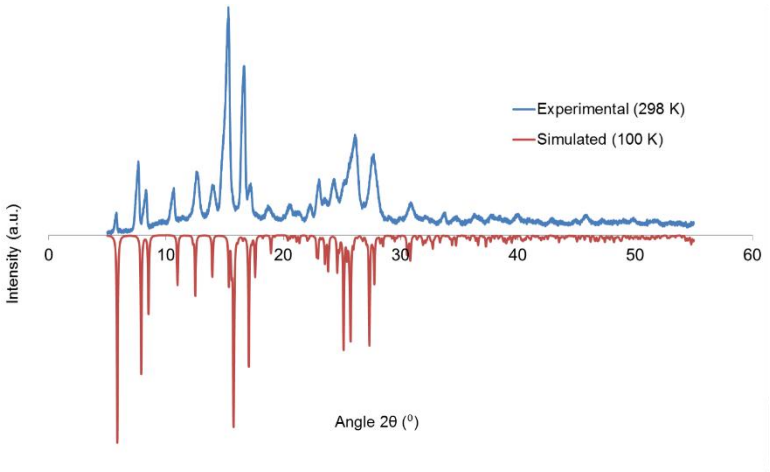

Figure 6.8 X-ray powder diffraction pattern for [Cu**124**$_2$]PF_6

6.5 Synthesis and structural studies of [Ag124$_2$]SbF_6

As was discussed in Section 1.5.3, the extensive use of Ag(I) ions in the construction of metallo-supramolecular architectures is evident from the literature[398-407] as the d^{10} electronic configuration of Ag(I) gives rise to diamagnetic and chemically labile complexes which can adopt a variety of coordination numbers ranging from 2 to 6.[126] Attractive metallophilic interactions have been exploited in the design of supramolecular systems alongside other non-coordinating intermolecular interactions.[399]

With this in mind, a synthetic procedure similar to that followed for [Cu**124**$_2$]PF_6 was carried out; a solution of $AgSbF_6$ in CH_3CN was added dropwise to solution of **124** in the same solvent in a 1:2 stoichiometric ratio and the mixture was kept in darkness for 24 hours. Crystallisation was carried out by slow evaporation of the solution resulting in the formation of large transparent single crystal blocks. The data were solved and the structure model for [Ag**124**$_2$]$_2$(SbF_6)$_2$, was refined in the $P2_1/n$ space group with half the molecule, *i.e.* [Ag**124**$_2$]SbF_6, present in the asymmetric unit. The other half is generated by symmetry and the Ag(I) centres are connected through an argentophilic interaction in the solid state (Figure 6.9). The Ag(I) centres are 3.0316(8) Å apart, considerably smaller than the sum of their

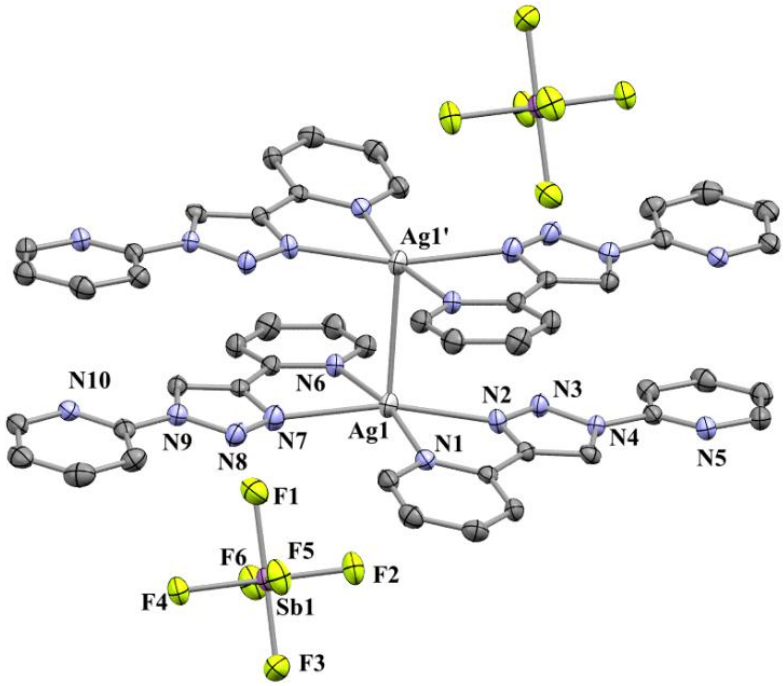

Figure 6.9 X-ray crystal structure of [Ag**124**$_2$]$_2$(SbF_6)$_2$. Thermal ellipsoids at 50% probability and hydrogen atoms omitted. Symmetry code used to generate equivalent atoms (1-x, 1-y, 1-z)

Van der Waals radii of 3.44 Å, indicative of a genuine interaction.[399] Two molecules of **124** coordinate in the usual manner through the *reg* binding pocket. The ligands are assembled around the Ag(I) ions in a head-to-tail manner. The triazoles adopt the same *trans* geometry about the Ag(I) centre, this being the most energetically favourable due to lone pair repulsion of the medial *N3* atom. The symmetry related Ag(I) ions both possess a distorted square planar geometry with the coordinating nitrogen atoms of **124**. One binding pocket with a bite angle of 71.96(12)° has an associated bond length |N_{pyr}-*Ag1*| of 2.348(4) Å and bond length |N_{triaz}-*Ag1*| of 2.333(4) Å; the other binding pocket with essentially the same bite angle of 71.92(13)° has a shorter |N_{pyr}-*Ag1*| bond length of 2.267(4) Å and longer bond length |N_{triaz}-*Ag1*| of 2.464(4) Å. There is a dihedral angle of *ca.* 9.5° (essentially planar) between the opposing *N-C-C-N-Ag1* chelation planes about each Ag(I) centre such that the *N-Ag1* bonds are tilted slightly in the opposite direction to the argentophilic interaction; the distance between *Ag1* and the mean plane comprised by the four nitrogen donors (*N1*, *N2*, *N6* and *N7*) is 0.184(2) Å. Each **124** molecule displays slight deviations from planarity with one possessing a dihedral angle between its two pyridyl rings of *ca.* 13.1° and the other possessing a smaller deviation with a dihedral angle of *ca.* 9.7°. The overall crystal packing is largely dominated by electrostatic interactions between the [Ag**124**$_2$]$_2^{2+}$ cation and the SbF_6^- anions. Also apparent in the extended crystal structure are π-π interactions between planar chelating units (the interplanar distance between mean planes of *N-C-C-N-Ag1*

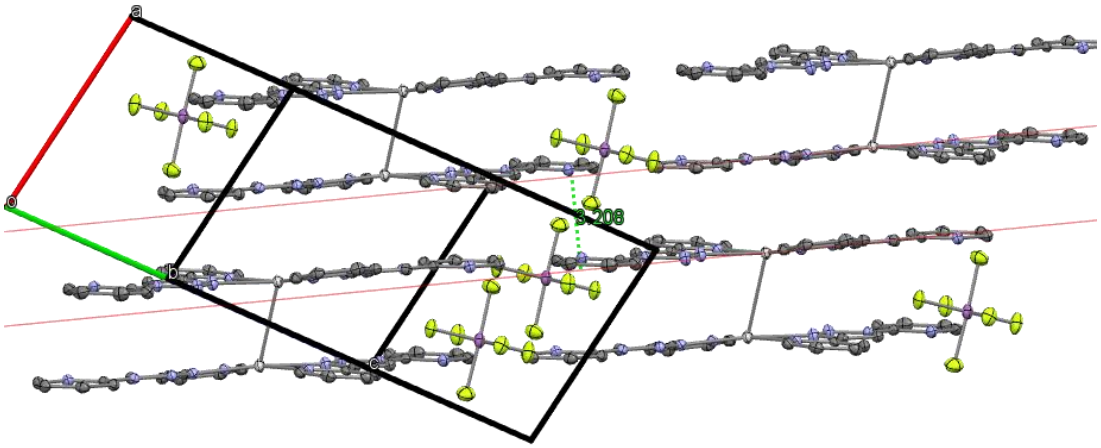

Figure 6.10 π-π stacking between complexes parallel to the *a*-axis resulting in a slip-stacked packing, viewed "edge-on" with the *boc*-plane.

chelating units is *ca.* 3.2 Å). This results in the formation of a one dimensional slip stack[51] of $[Ag\mathbf{124}_2]_2^{2+}$ cations parallel to the *a*-axis of the unit cell (Figure 6.10). The compound was also characterised by HRMS, ^{1}H NMR, FT-IR, PXRD (Figure 6.11) and elemental analysis. HRMS-ESI$^+$ gave no evidence of the $[Ag\mathbf{124}_2]_2^{2+}$ dimer which suggested that the argentophilic interaction was not retained in the solution state. HRMS-ESI$^+$ evidence of the $[Ag\mathbf{124}_2]^+$ cation indicated that discrete molecules of $[Ag\mathbf{124}_2]SbF_6$ existed in solution.

The ^{1}H NMR (400 MHz, CD_3CN) of $[Ag\mathbf{124}_2]SbF_6$ was similar in nature to that of its Cu(I) analogue, $[Cu\mathbf{124}_2]PF_6$, with broadening of the peaks associated with the *reg* binding pocket, see Figure 6.12(A). A ^{1}H NMR titration was carried out as before, see Figure 6.12(B). Sequential addition of specific aliquots of a solution of $AgSbF_6$ in CD_3CN to a solution of **124** in the same solvent (c = 2 x 10^{-3} M) demonstrated that after the first additions of Ag(I) the *reg* binding site resonances (1, 2, 4, 7 and 9) underwent a pronounced change in chemical shift with relatively small changes in the positions of the signals associated with the free

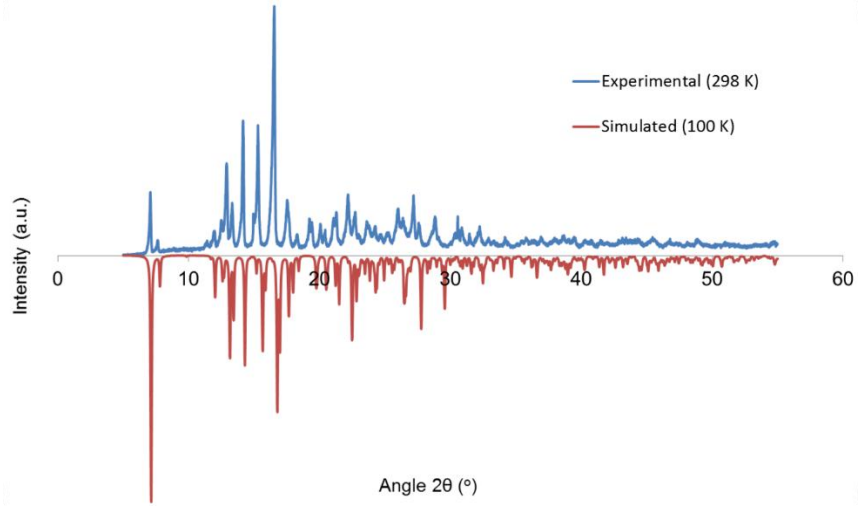

Figure 6.11 X-ray powder diffraction pattern for $[Ag\mathbf{124}_2]_2(SbF_6)_2$

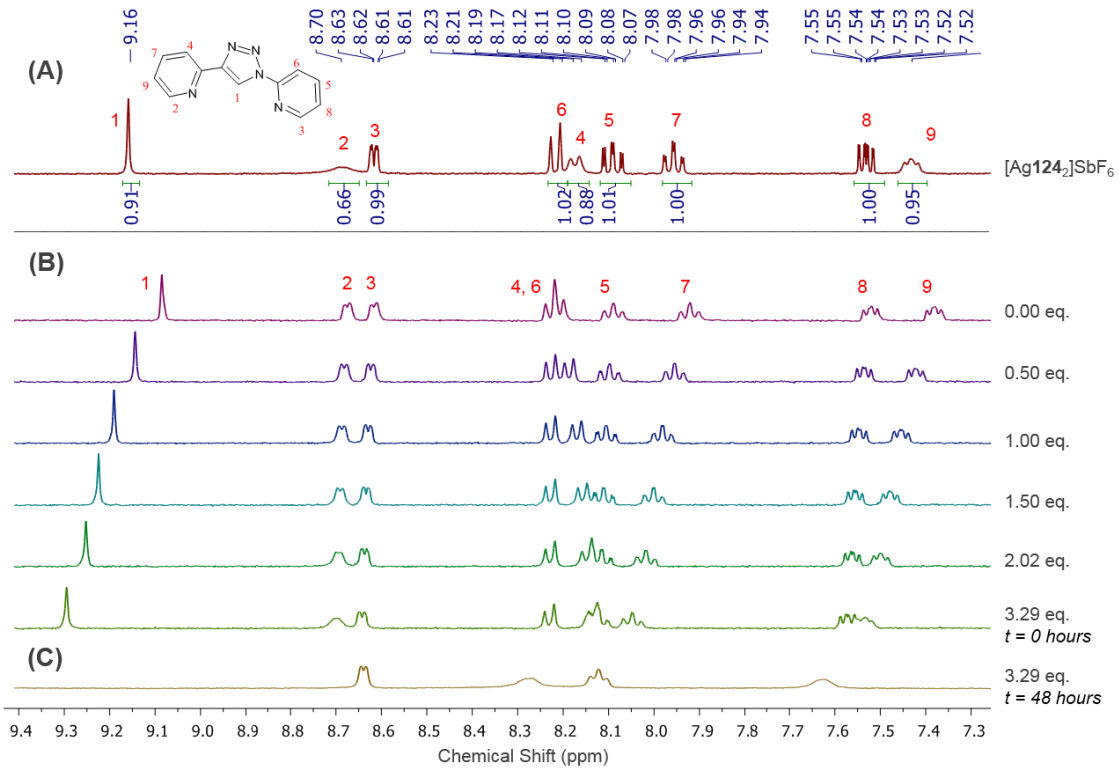

Figure 6.12 ^{1}H NMR (400 MHz, CD_3CN) of (A) complex [Ag**124**$_2$]SbF_6; (B) titration of **124** (c = 2 mM) with $AgSbF_6$ showing maximum chemical shift change in resonances 1, 2, 4, 7 and 9; (C) of aged titration solution after 48 hours at 3.29 eq. of $AgSbF_6$

pyridine ring (3, 5, 6 and 8). Broadening of the *reg* binding site proton signals was not observed initially. As a result of the sharper nature of these proton signals it was possible to trace the chemical shift change more readily than in the case of the titration with Cu(I). The triazolyl, 4-pyridyl and 5-pyridyl proton resonances (1, 7 and 9, respectively) were all deshielded due to the cationic presence of the Ag(I) ion, however, the 6-pyridyl proton (2) remained relatively unaffected. The 5-pyridyl proton (4) displayed a shift upfield, perhaps indicative of the increased shielding when the molecule adopted the *syn-anti* conformation required for cation chelation, thus, severing the intramolecular *C-H···N* interaction with the proximal triazolyl nitrogen *N3*, inferred from the solid state molecular structure of **124**, see Figure 6.4(A). After an excess of 3 eq. of $AgSbF_6$ had been added it was clear that there was no change in the continuous trend of the resonance shifts with each aliquot addition. The final spectrum at the end of the titration did not resemble that of the complex [Ag**124**$_2$]SbF_6. For instance the triazolyl resonance at 9.27 ppm was more deshielded than the corresponding signal in [Ag**124**$_2$]SbF_6 which was found at 9.16 ppm. The titration was carried out under the same conditions as the complexation reaction albeit at a lower concentration (c = 2 mM and 4.5 mM, respectively) and with an added excess of $AgSbF_6$. Therefore, the NMR solution mixture was allowed to stand in darkness for 48 hours

whereupon the ^{1}H NMR was re-examined. It shows that after allowing sufficient time to pass, the ^{1}H NMR spectrum of the solution upon aging, see Figure 6.12(C), displayed very broad peaks and resembled the ^{1}H NMR spectrum of the Cu(I):**124** titration after 2 eq. of Cu(I) was added, see Figure 6.6(A). The peaks corresponding to resonances 1, 2, 4, 7 and 9 were no longer visible and the excessive amount of $AgSbF_6$ added (3.29 molar eq. relative to **124**) began to cause the resonances for the other pyridyl ring to broaden also, suggesting an involvement of the *inv* binding pocket in the Ag(I) coordination. The important point to note is that the chemical shift of the proton resonances of [Ag**124**$_2$]SbF_6 compared closely to those of the titration of **124** at 0.5 eq. of Ag(I) and the broadening of the *reg* pocket proton resonances occurred after some time and not initially. This suggests that at 0.5 eq. of Ag(I) the resulting assembly was indeed [Ag**124**$_2$]SbF_6 in solution. It was then investigated whether other stoichiometric variations of Ag:**124** could be formed upon reacting higher molar eq. of $AgSbF_6$ with **124**. For example, a solution of $Ag(SbF_6)_2$ in CH_3CN was added dropwise to solution of **124** also in CH_3CN in a 1:1 stoichiometric ratio maintaining the same conditions as before. However, only crystal structures of the dimer [Ag**124**$_2$]$_2(SbF_6)_2$ were the result. Re-dissolving the crystals in CH_3CN and recrystallisation always resulted in the same crystalline phase being formed. It could be concluded that the dimer formation only occurred in the solid state and the monomer [Ag**124**$_2$]SbF_6 existed in solution.

6.6 Synthesis and structural study of [Co124$_2$(NO$_3$)$_2$]

Another labile *d*-metal used in the coordination chemistry study of ligand **124** was Co(II). The complexation was carried out in a similar manner as before, by dissolving cobalt(II) nitrate pentahydrate and **124** in a 1:2 stoichiometric ratio in CH_3CN which was allowed to stir at room temperature for 30 minutes. This resulted in a white suspension which was filtered and washed with CH_3CN. The white powder was recrystallised by diffusion of diethyl ether into its CH_3CN solution producing transparent rectangular crystals. The data were collected and solved and the structure model was refined in the $P2_1/n$ space group revealing the formation of discrete mononuclear complexes with molecular formula [Co**124**$_2$$(NO_3)_2$] possessing an octahedral geometry **(**Figure 6.13) with an inversion centre coincident with the Co(II) site such that the asymmetric unit is comprised of half of the molecule shown. Two **124** molecules coordinate equatorially around the Co(II) centre in the *syn-anti* ligand conformation through the *reg* binding pocket. The nitrate anions occupy the axial positions through the terminal monodentate binding mode. The ∠ (*N1-Co1-N2*) bite angles are 78.31(14)^o. The corresponding bond lengths |N_{pyr}-*Co1*| and |N_{triaz}-*Co1*| are

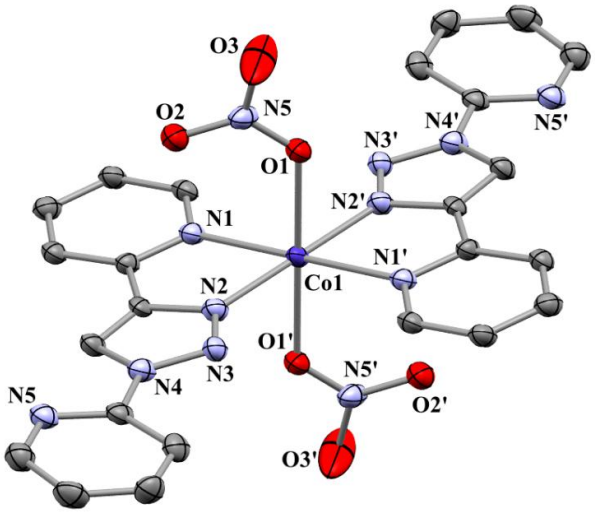

Figure 6.13 X-ray crystal structure of [Co**124**$_2$(NO$_3$)$_2$]. Thermal ellipsoids at 50% probability and H atoms omitted. Symmetry code used to generate equivalent atoms (1-x, -y, -z).

2.124(4) Å and 2.107(4) Å, respectively, and the bond lengths |O_{Nitrate}-*Co1*| are 2.088(3) Å. The coordinating **124** ligands, are related by inversion through the *Co1* centre such that the triazoles, for example, are *trans* to each other in a head-to-tail fashion similar to that previously described in the case of in the crystal structure of [Ag**124**$_2$]$_2$(SbF$_6$)$_2$. This sees that lone pair repulsion is avoided between the medial nitrogen atoms (*N3* and *N3'*) on opposite ligands but also such that *C-H*···*N* hydrogen bonding interactions are facilitated between the *CH*s at the 6-positions of both binding pyridyl rings and the medial nitrogen atoms (*N3* and *N3'*) of the triazole units on opposing **124** ligands[54,347] (|D···A| is 3.396(6) Å and ∠ (*C-H*···*N*) is 143.3(3)°) (Appendix E.16). The aromatic rings of the **124** ligands are essentially co-planar with a dihedral angle of *ca.* 9.3° between the mean planes comprised by the binding pyridyl ring system and the mean plane of the non-binding pyridyl motif. The

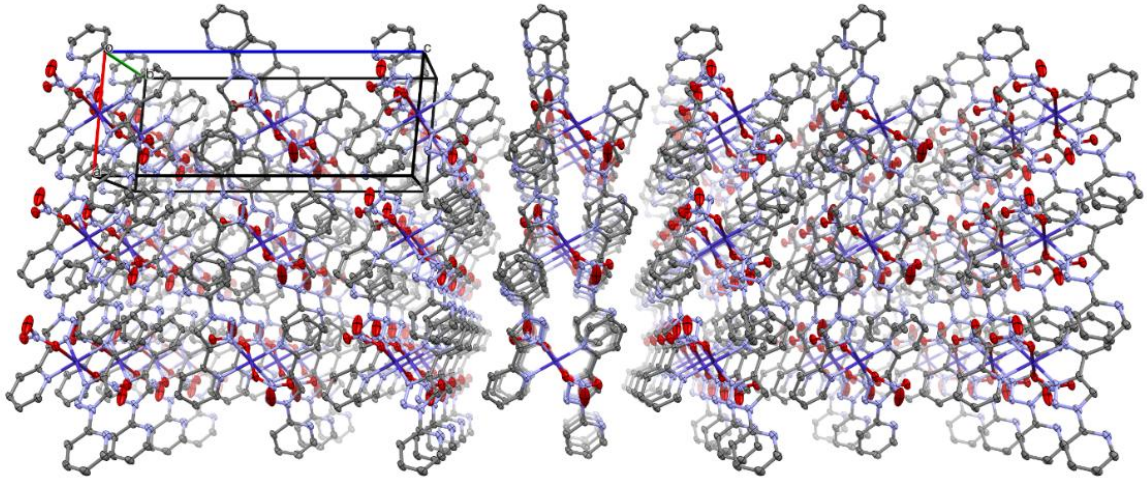

Figure 6.14 Crystal packing of [Co**124**$_2$(NO$_3$)$_2$] viewed parallel to the *b*-axis.

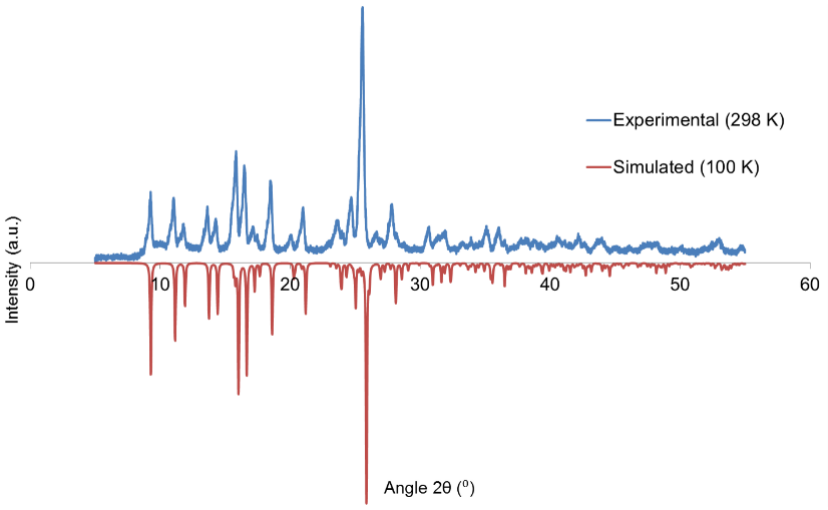

Figure 6.15 X-ray powder diffraction pattern for [Co**124**$_2$(NO$_3$)$_2$]$_2$

crystal packing is dominated by π-π interactions between pyridyl rings on adjacent molecules extending parallel to the *b*-axis (Figure 6.14). Phase purity was also confirmed by PXRD, see Figure 6.15.

6.7 Synthesis and crystallographic study of Pt(II) phases derived from 124

Less labile *d*-metals were also used in the study; the Pt(II) complex, [Pt**124**Cl$_2$], was prepared by stirring **124** with an equimolar mixture of [Pt(DMSO)$_2$Cl$_2$] in CH$_3$OH at 70 °C for 15 hours in darkness, giving a grey powder after filtration and washing with CH$_3$CN. A satisfactory CHN for this compound consistent to within ±0.5% of the calculated values could not be obtained, the best fit for which was obtained as calculated for the [Pt**124**Cl$_2$] phase *i.e.* C$_{12}$H$_9$N$_5$Cl$_2$Pt: C 29.46, H 1.85, N 14.32 and found for C 29.09, H 1.66, N 13.55. Recrystallisation by slow evaporation of a hot CH$_3$CN solution produced two different crystalline phases. The dominant phase consisted of transparent needles, with the molecular formula [Pt**124**Cl$_2$], while a trace quantity of transparent blocks of a second phase crystallised from the same batch, with the molecular formula [Pt**124**Cl$_2$]·CH$_3$CN. Each of the two phases were analysed by single crystal X-ray diffraction by Dr. Chris Hawes, both providing structure models in the monoclinic space group *P*2$_1$/*c*. The molecular structures of [Pt**124**Cl$_2$] and [Pt**124**Cl$_2$]·CH$_3$CN are shown in Figure 6.16. The molecular structure of [Pt**124**Cl$_2$] consists of a Pt(II) ion chelated by one bidentate **124** species, with the square planar coordination sphere completed by two *cis*-oriented chlorido ligands. As expected from a Pt(II) coordination sphere, the square planar geometry shows little deviation from the idealised geometry ($\tau_4 = 0.09$),[343] with a slightly condensed bite angle ∠ (*N1-Pt1-N2*) of

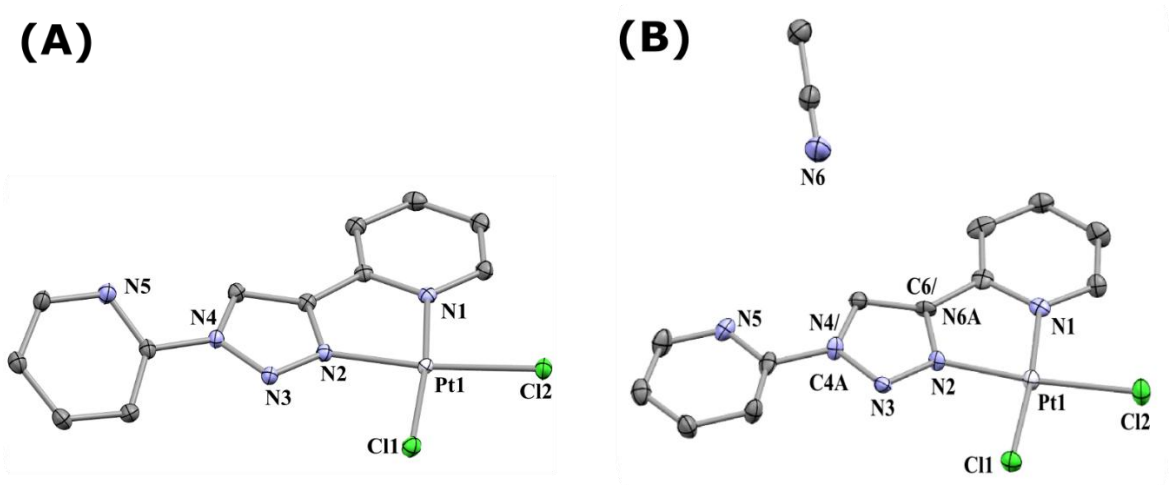

Figure 6.16 X-ray crystal structure of (A) [Pt**124**Cl_2] and (B) [Pt**124**Cl_2]·CH_3CN. Thermal ellipsoids at 50% probability and H atoms omitted.

80.01(8)°. As was the case in the previously encountered **124**-derived complexes, coordination unambiguously occurs within the *reg* binding pocket of **124** through proximal triazole *N2* nitrogen atom[52] and the ligand adopts the expected *syn-anti* conformation to facilitate metal binding through the *reg* pocket and minimise electron-electron repulsion from the non-coordinating triazole and pyridine nitrogen atoms, *N4* and *N5*, respectively. The |N_{pyr}-*Pt1*| and |N_{triaz}-*Pt1*| are 2.047(2) Å and 1.9864(17) Å, respectively. As expected, the *Pt1-Cl2* bond oriented *trans* to the triazole nitrogen atom is marginally longer than that *trans* to the pyridine nitrogen atom,[18,39] at distances of 2.2917(6) Å and 2.2891(6) Å, respectively.[408] The **124** molecule adopts a moderately twisted geometry, with the mean planes of each pyridine ring offset to one another by 33.68(8)°. This compares closely to the molecular structure of the Pd(II) analogue [Pd**124**Cl_2] which has recently been reported by Sangtrirutnugul *et al.*[390]

In comparison, the asymmetric unit of phase [Pt**124**Cl_2]·CH_3CN contains one complete [Pt**124**Cl_2] moiety and one CH_3CN molecule, see Figure 6.12(B). The square planar coordination geometry in [Pt**124**Cl_2]·CH_3CN is again comparatively regular (τ_4 = 0.09), and each of the *Pt1-Cl* and *Pt1-N* bond lengths are equivalent within error to those observed in the [Pt**124**Cl_2] phase. However, careful analysis of the anisotropic displacement parameters (ADPs) of carbon atom *C6* and nitrogen atom *N4* revealed a significant contribution of the *inv* binding isomer in which the positions of these atoms are reversed, see Figure 6.17(A). The best crystallographic model was obtained by assigning the ratio of *reg*:*inv* binding at 2:1 with *C6* and *N4* overlapped and constrained to equivalent *x*,*y*,*z* and ADP variables however this treatment necessarily introduces slight uncertainty into the exact ratio of the two isomers in the crystalline state. Additionally, residual electron density was detected

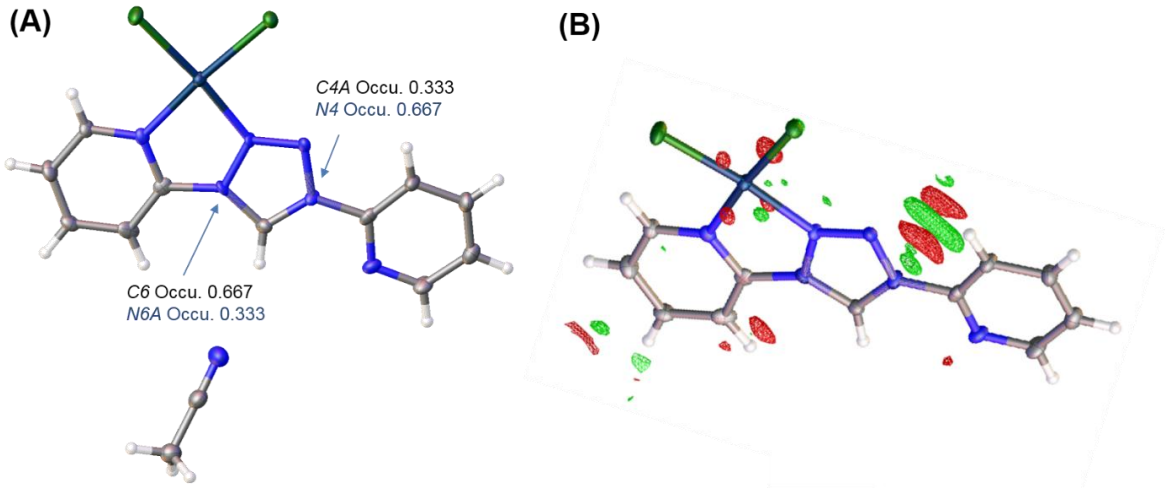

Figure 6.17 (A) X-Ray diffraction model of [Pt**124**Cl_2]·CH_3CN showing disordered nature of *N4/C4A* and *C6/N6A* due to the *reg* and *inv* binding isomerism. (B) Residual electron density map for compound [Pt**124**Cl_2]·CH_3CN with residual surfaces rendered at ±1.35 e·$Å^{-3}$. Positive regions of $F_o^2 - F_c^2$ shown in red. Negative regions shown in green.

within the second binding pocket of the molecule, possibly indicating a small contributor of additional disorder, see Figure 6.17(B), however no sensible electron density could be modelled at this position and the dominant *Pt1* site was modelled at full occupancy. The primary difference in molecular geometry between [Pt**124**Cl_2] and [Pt**124**Cl_2]·CH_3CN is the planarity of the **124** unit, which in the case of [Pt**124**Cl_2]·CH_3CN is effectively entirely coplanar, evidenced by the small pyridine-pyridine interplanar angle of 7.5(3)°, compared to the *ca.* 33° angle observed in [Pt**124**Cl_2].

The crystal packing of [Pt**124**Cl_2] displays one Pt(II) metal centre overlapping the *C4* of the triazole unit of an adjacent molecule, see Figure 6.18(A**)** such that the metal centres are slip-stacked in a herringbone fashion[394] parallel to the *a* axis of the unit cell, see Figure 6.18(B). The interplanar distance between the parallel mean planes comprised by the *N1-C5-C6-N2-Pt1* chelating unit is 3.3293(19) Å. The non-coordinating pyridine rings are aligned in slipped columns parallel to the *c*-axis, however no substantial overlap of the pyridine π systems is observed in this packing mode. The efficiency of the packing mode of [Pt**124**Cl_2] leads to an extended structure containing no void space or encapsulated solvent or guest molecules. The extended structure of [Pt**124**Cl_2]·CH_3CN consists of similar slip-stacked columns in which the main overlap occurs between the chelating domains of adjacent molecules, see Figure 6.18(A), defined by a small interplanar distance of *ca.* 3.4 Å between parallel mean planes comprised by the *N1-C5-C6-N2-Pt1* chelating unit and essentially zero interplanar angle of 0.07(18)°. Several additional *C-H···N* hydrogen bonding interactions are also present within the structure of [Pt**124**Cl_2]·CH_3CN which are not

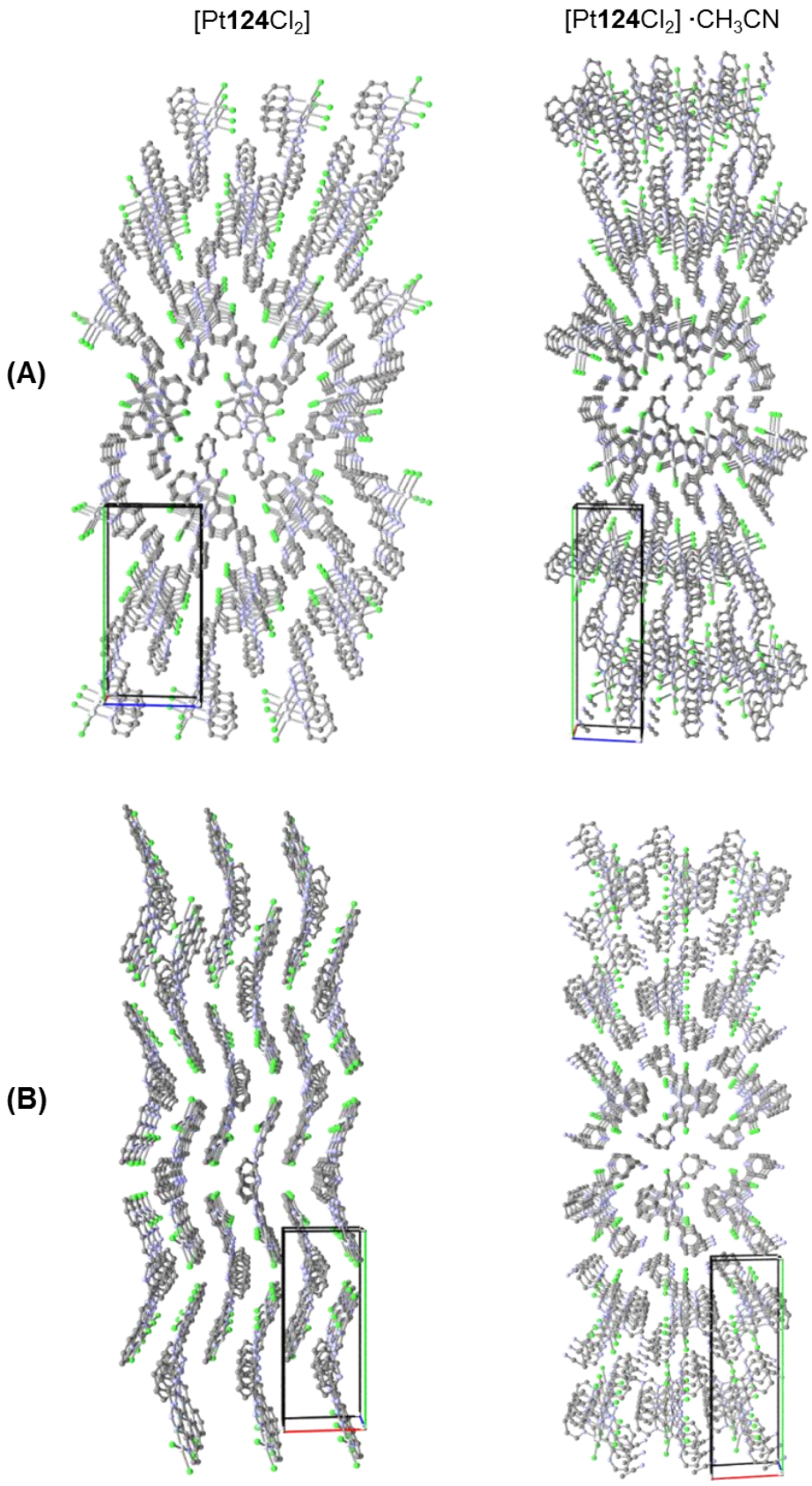

Figure 6.18 Packing diagrams of [Pt**124**Cl$_2$] and [Pt**124**Cl$_2$]·CH$_3$CN showing difference in the final crystal packing geometries viewed parallel to the (A) *a*-axis and (B) *c*-axis.

observed in the other phase of [Pt**124**Cl_2]: a *C-H···N* hydrogen bonding interaction originating from the triazole *C-H* group to the CH_3CN nitrogen atom (|D···A| is 3.333(12) Å, and ∠ (*C-H···N*) is 146.2(5)°), and a self-complementary dimeric hydrogen bonding interaction (|D···A| is 3.451(10) Å and ∠ (*C-H···N*) is 137.7(5)°) between the *C-H* group at the 6-position of the non-coordinating pyridyl ring and the pyridyl nitrogen atom on an adjacent complex[54] (Appendix E.17).

The origin of the disorder between the two coordinating domains in the structure of [Pt**124**Cl_2]·CH_3CN can be traced to several factors in the synthesis, and is most likely related to the well-known substitutionally inert nature of Pt(II)[409] coupled with the synthesis conditions. Analysis of the grey powder obtained from the original reaction of [Pt$(DMSO)_2Cl_2$] with **124** by PXRD, see Figure 6.19, showed the presence of only phase [Pt**124**Cl_2], with no additional peaks corresponding to additional solvated phases. Dissolution of this material in CH_3CN at room temperature and analysis by ^{1}H NMR spectroscopy revealed the presence of a single isomer, see Figure 6.20(B), consisting of *cis*-[Pt**124**Cl_2] with coordination occurring in the *reg* binding pocket. However, dissolving this material in DMSO-d_6 and analysis of the solution by ^{1}H NMR, see Figure 6.21(B) showed the presence of two isomers in approximately 2:1 ratio, in favour of the *reg* form. From these observations a solvent-dependent isomerisation process is proposed, converting the original *reg* isomer to a mixture of both isomers on heating in CH_3CN or by dissolution in DMSO, which is well known to facilitate ligand exchange for Pt(II) complexes.[410] This process would be expected to heavily favour the (thermodynamically preferred) *reg* binding mode but allow for traces of the kinetically stabilised *inv* binding mode. Furthermore, positional disorder between the *reg* and *inv* binding isomers would be expected to be favoured in the phase bearing a planar and therefore *pseudo*-symmetric **124**, limiting the disordered

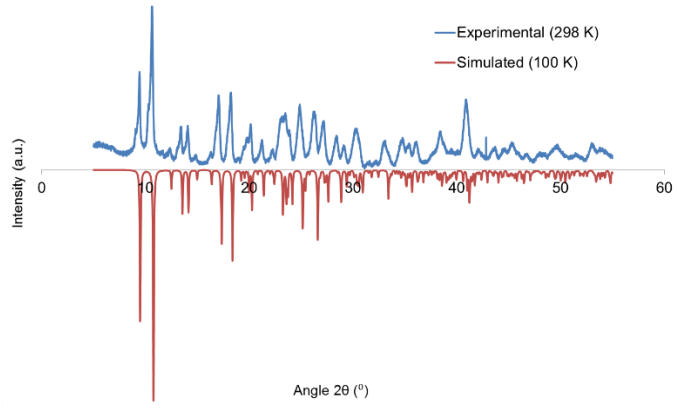

Figure 6.19 X-ray powder diffraction pattern for [Pt**124**Cl_2]

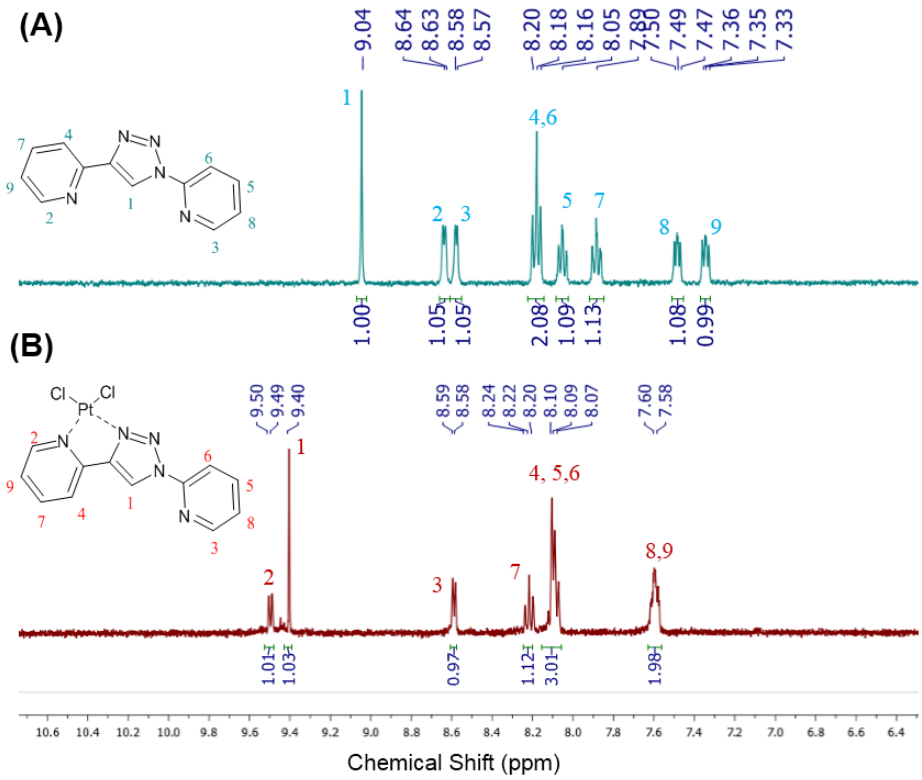

Figure 6.20 ^{1}H NMR (400 MHz, CD_3CN) comparison of (A) ligand **124** with (B) complex [Pt**124**Cl_2].

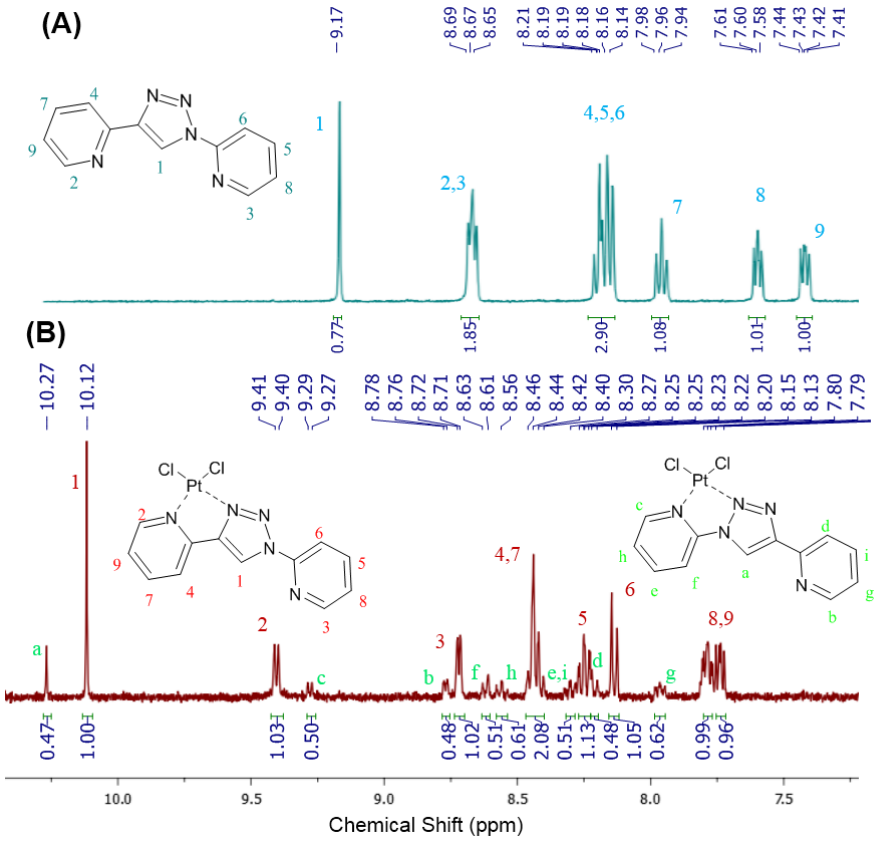

Figure 6.21 ^{1}H NMR (DMSO-d_6) comparison of the spectra of **124** ligand with a mixture of both *reg* and *inv* binding modes of the [Pt**124**Cl_2] complex.

components to selectively crystallise into phase [Pt**124**Cl_2]·CH_3CN rather than phase [Pt**124**Cl_2].

6.8 Photophysical studies of complexes in solution

The ligand **124** and its complexes [Cu**124**$_2$]PF_6, [Co**124**$_2$$(NO_3)_2$], [Ag**124**$_2$]$SbF_6$ and [Pt**124**Cl_2] were characterised spectroscopically in CH_3CN at 298 K. The UV-vis absorption and the luminescence spectra were recorded (Figure 6.22). The UV-vis absorption spectrum for **124** displayed two bands with maxima at 236 nm (ε_{max} = 17,400(450) dm^3 mol^{-1} cm^{-1}) and 287 nm (ε_{max} = 15,200(420) dm^3 mol^{-1} cm^{-1}) attributed to $\pi \rightarrow \pi^*$ transitions. The ground state spectra of the complexes in solution possessed similar features to those of the **124** ligand, namely ligand $\pi \rightarrow \pi^*$ transitions. Complexes [Cu**124**$_2$]PF_6, [Co**124**$_2$$(NO_3)_2$], [Ag**124**$_2$]$SbF_6$ and [Pt**124**Cl_2] possessed very weak *d*→*d* transitions at λ_{max} around 350 nm. Complex [Pt**124**Cl_2] displayed partially resolved bands which have been attributed to MLCT transitions in related Pt(II) complexes.[54,411] In any of the solutions of the complexes, there were no traces of *inv* isomers which are known to possess more pronounced red-shifted MLCT transitions compared with *reg* isomers.[54] Upon excitation at λ = 283 nm, **124** displayed very weak fluorescence emission with maximum at 350 nm. The complexes displayed similar weak ligand centred emission, the strongest and most red-shifted of which was exhibited by [Pt**124**Cl_2], with maximum at 424 nm.

This analysis was followed by titration studies in order to investigate the kinetic self-

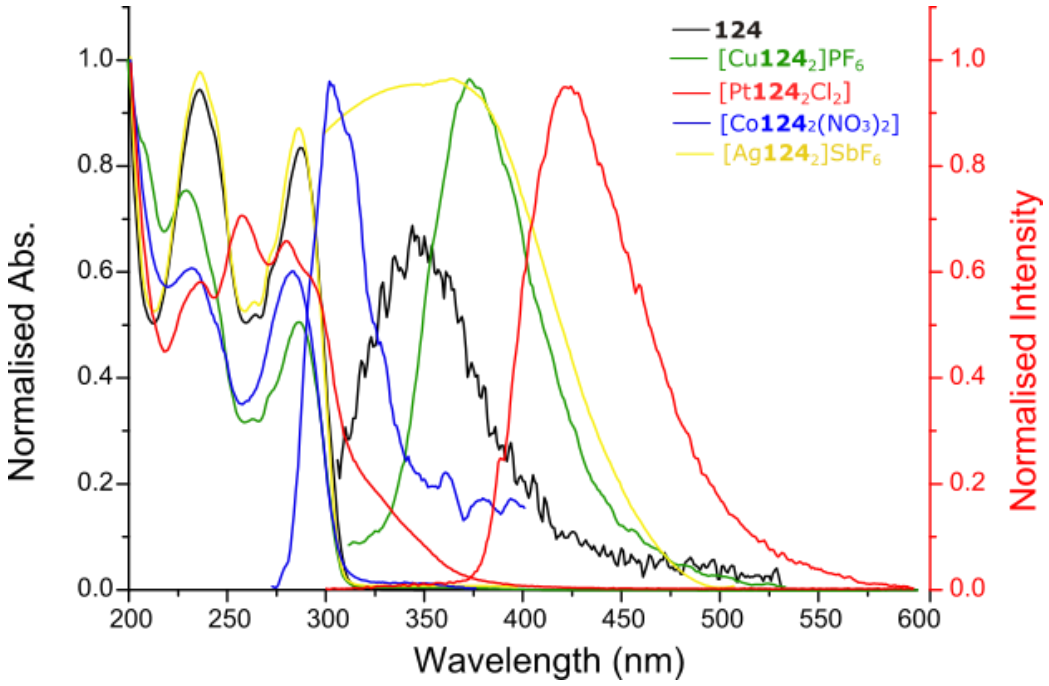

Figure 6.22 UV-vis absorption and fluorescence spectra of: (A) ligand **124** and corresponding complexes complex [Cu**124**$_2$]PF_6; [Ag**124**$_2$]SbF_6; [Co**124**$_2$$(NO_3)_2$]; and [Pt**124**$Cl_2$].

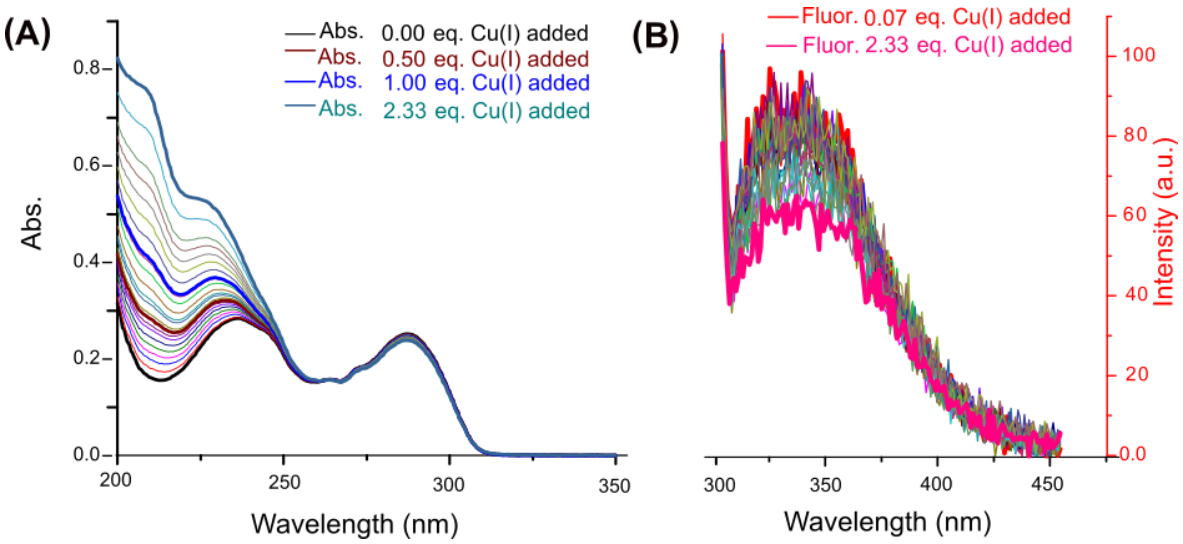

Figure 6.23 (A) UV-vis and (B) fluorescence titration of **124** with Cu(I) in CH_3CN (*c*=0.01 mM).

assembly of **124** with Cu(I) in solution. Here, specific aliquots of a stock solution of $[Cu(CH_3CN)_4]PF_6$ were added to a solution of **124** (c = 1 x 10^{-5} M) and the changes in the UV-vis absorption and the emission spectra were monitored, see Figure 6.23(A)/(B). Very small changes in ligand fluorescence were observed over the course of the titration. As Cu(I) was added to the **124** solution a hyperchromic effect was observed for the band with maximum at 236 nm relative to the band with maximum at 287 nm. At higher molar equivalents of Cu(I) the observed UV-vis absorption spectrum of the assembly was in good agreement with the UV-vis spectrum of [Cu**124**$_2$]PF_6, (Figure 6.22). This observation also correlated well with the results from the ^{1}H NMR titration in CD_3CN, the solution of which, when analysed by HRMS at Cu(I) concentrations in excess of 2 molar equivalents, confirmed the existence of [Cu**124**$_2$]PF_6, *i.e.* [Cu**124**$_2$]$^+$: $C_{24}H_{18}CuN_{10}^+$ *m/z* = 509.1006.

6.9 Discussion

As has been stated, the crystallographic analysis of [Cu**124**$_2$]PF_6, [Ag**124**$_2$]SbF_6, [Co**124**$_2$$(NO_3)_2$] and [Pt**124**$Cl_2$] showed preference for the *reg* binding mode involving the more electron rich proximal *N2*. In order to compare the R_1 *[I≥2σ(I)]* and U_{eq} values for each complex, the structures were modelled in both the *reg* and *inv* binding modes, summarised in Table 6.1. This test was carried out specifically to ensure that the small difference in electron density between carbon and nitrogen atoms was not suppressed by the contribution to F_c^2 of the nearby heavy atom, especially in the Pt(II) and Ag(I) cases. All cases showed an increase in the R_1 value for the *inv* model compared to the *reg* model. Thus there is less of an agreement between the crystallographic model of the *inv* isomer and the experimental X-ray diffraction data than the crystallographic model of the *reg* isomer with said data. In

Table 6.1 Comparison of R_1 and U_{eq} for *reg* and *inv* models of [Cu**124**$_2$]PF_6, [Ag**124**$_2$]SbF_6, [Co**124**$_2$$(NO_3)_2$], and [Pt**124**$Cl_2$].

[Cu**124**$_2$]PF_6	***reg***				***inv***			
R_1 ($I \geq 2\sigma$) / %	6.14				6.83			
U_{eq}	N_4	0.028	N_9	0.029	N_6	0.040	N_{18}	0.039
	C_6	0.029	C_{18}	0.028	C_4	0.019	C_9	0.020
[Ag**124**$_2$]SbF_6	***reg***				***inv***			
$_1$ ($I \geq 2\sigma$) / %	4.19				4.51			
U_{eq}	N_4	0.022	N_9	0.018	N_6	0.032	N_{18}	0.030
	C_6	0.020	C_{18}	0.018	C_4	0.012	C_9	0.009
[Co**124**$_2$$(NO_3)_2$]	***reg***				***inv***			
R_1 ($I \geq 2\sigma$) / %	6.95				7.41			
U_{eq}	N_4		0.023		N_6		0.038	
	C_6		0.023		C_4		0.011	
[Pt**124**$_2$$Cl_2$]	***reg***				***inv***			
R_1 ($I \geq 2\sigma$) / %	1.72				1.94			
U_{eq}	N_4		0.012		N_6		0.020	
	C_6		0.011		C_4		0.005	

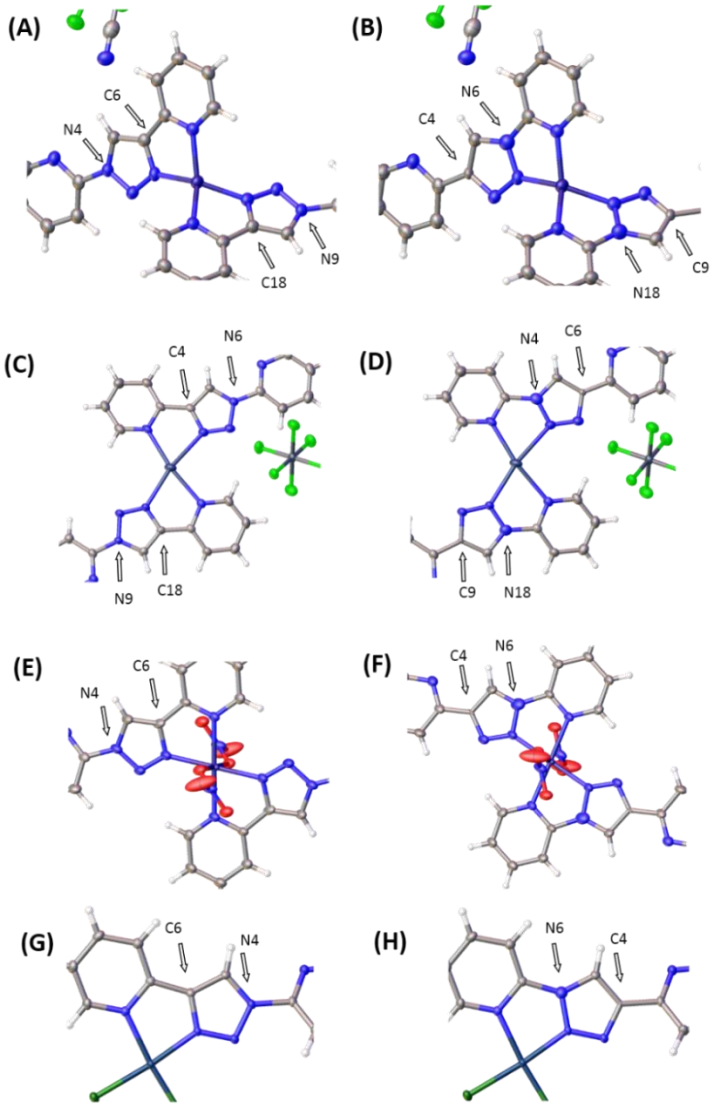

Figure 6.24 Complexes modelled with Cu(I), Ag(I), Co(II) and Pt(II) in the *reg* (A, C, E, G) and in the *inv* (B, D, F, H) binding pocket, respectively.

each case, the data is of a sufficient quality such that incorrect assignment of the carbon and nitrogen atom at the 1- and 4-position of the triazole moiety show a pronounced detrimental change in the relative U_{eq} values for the involved atoms which is depicted visually in Figure 6.24. This can be used to support the selectivity of the *reg* binding pocket for metal chelation. The ^{1}H NMR titration and photophysical studies corroborated this selectivity in solution.

6.10 Conclusion

The synthesis of the 'click' derived 1,4-di(2-pyridyl)-1,2,3-triazole (**124**) chelator from 2-azidopyridine and 2-ethynylpyridine using Cu(I) and TBTA by microwave assisted synthesis was demonstrated. The complexes of the subtly unsymmetric **124** ligand with Cu(I), Ag(I), Co(II), and Pt(II) were structurally characterised by conventional methods, (elemental analysis, HRMS, IR, ^{1}H NMR spectroscopy and TGA), and particularly, by using X-ray diffraction analysis. The molecular structures were confirmed by single crystal X-ray crystallography and the phase purity confirmed using PXRD analysis. The results of the studies showed formation of discrete molecules displaying preferential binding of metal cations through the pyridyl nitrogen *N1* and the proximal triazolyl nitrogen *N2 i.e.* the **tp** or 'regular' (*reg*) chelate moiety despite the presence of a second potential binding pocket *i.e.* the **tp'** chelate or 'inverse' (*inv*) moiety. This binding selectivity was corroborated through the study of the self-assembly of **124** with labile *d*-metal ions Cu(I) and Ag(I) using ^{1}H NMR titration in CD_3CN solution which showed a broadening of the proton resonances associated with that *reg* chelate pocket. The selectivity of the *reg* binding was also seen for the more kinetically inert Pt(II) complex [Pt**124**Cl_2] as one isomer was exclusively produced. A solvent-dependent isomerisation process, converting the original *reg* isomer of the Pt(II) complex to a mixture of both isomers, was observed upon heating in CH_3CN. This was evidenced by two crystalline phases; one consisting exclusively of *reg* isomer [Pt**124**Cl_2] and another disordered phase, [Pt**124**Cl_2]·CH_3CN, consisting of a mixture of *reg* and *inv* Pt(II) CH_3CN adducts. A similar isomerisation was observed by dissolution in DMSO-d_6. This work demonstrates the favoured binding of the subtly unsymmetric **124** ligand for metal cations, irrespective of their kinetic lability, through the *reg* binding pocket even when both *reg* and *inv* metalation sites are simultaneously present in the ligand scaffold.

6.11 Final Future Perspectives

This interesting concept of subtle unsymmetry in studying the coordination behaviour of suparamolecular systems could be further extended beyond *d*-metals and discrete complexes

and extended to *f*-metals and the formation of extended networks and higher order self-assembly systems. It would be interesting if this study were applied to ditopic ligand **98**, in the formation of coordination polymers. **Btp** ligands **127** and **128** can be synthesised in one

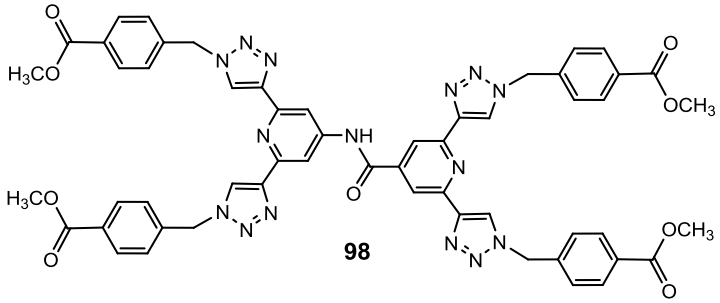

98

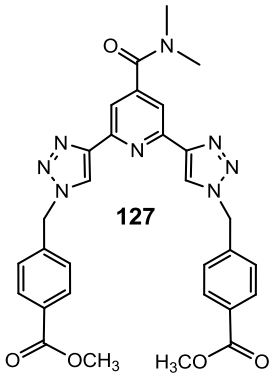

127

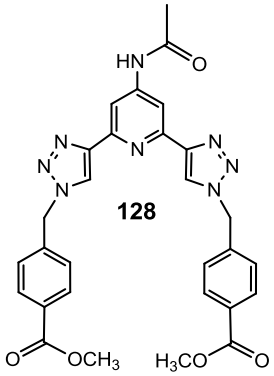

128

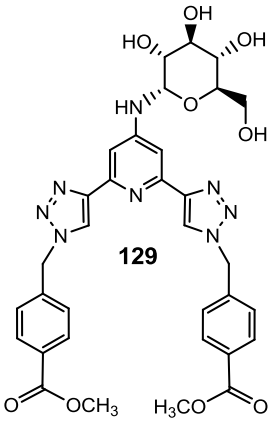

129

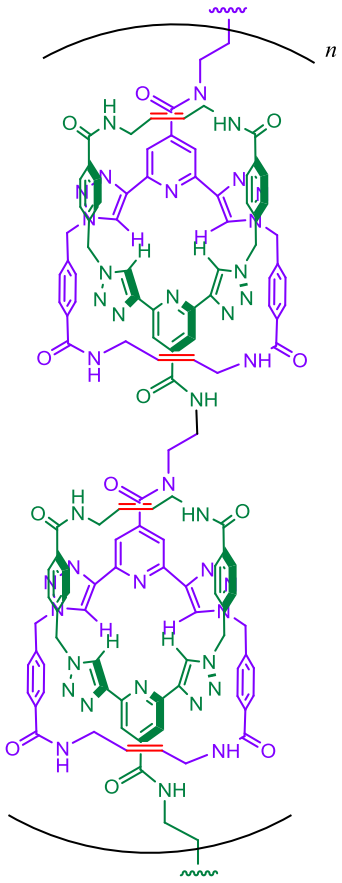

131

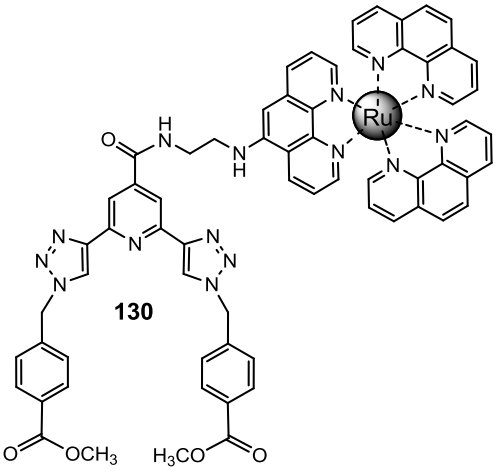

130

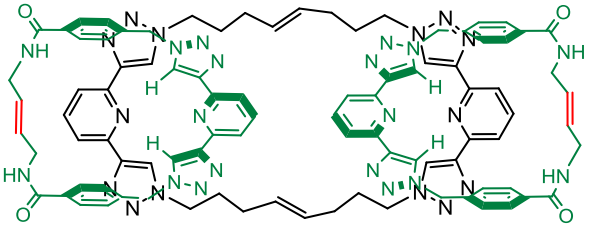

132

step from **87** and **95**, respectively, in order to compare the two subtly unsymmetric binding sites of the ditopic **98** such that a thorough study of the complex self-assembly process in the formation of extended networks and materials could be carried out.

Furthermore, throughout the entire work presented in this thesis, a number of avenues for development of novel **btp** systems have been opened up. As summarised in Section 2.7 following the successful appendage of further functionality at the 4-pyridyl position of the **btp** motif, it would be possible to incorporate carbohydrate groups (**129**) with a view to preparing luminescent Ln(III)-templated 'glycoclusters'. Such systems would be good candidates for reporting on biological analytes *via* changes in luminescence. In a similar fashion, the incorporation of bidentate chelators such as polypyridyl moieties (**130**) would allow for the formation of two distinctive supramolecular networks using a mixture of *d*- and *f*-metal ions ((Ru(II) and Ln(III), respectively)[139,286] which could then be used for DNA binding and cellular imaging. Evaluation of the biological applications in biological media such as in cancer cells would also be proposed.

As discussed in Section 5.16, following the demonstration that placement of the benzyl ester motif also gave rise to self-templated formation of [2]catenanes **113**, the next step would be the hydrogenation of **113** to the [2]catenane carboxylic acid (**122**). This could then be polymerised in to a diverse variety of [2]catenane-derived polymer systems (**131**) with the acid acting as a 'handle' for the polymerisation step *via* the reaction with a divergent nucleophile. In addition, it would also be interesting to use the macrocycles presented in Chapter 5, the precursors of which could not achieve catenation, in the formation of heterocircuit [2]catenanes, particularly in the case of the 2×2 macrocycle **120**. Encouraged by the success of the "threading" experiment conducted in Section 5.5, this heterocircuit [3]catenane (**132**), could be synthesised, as presumably the other "thread" molecules need only to possess the 4'-substituted "arm" feature for the desired hydrogen bonding pre-organisation.

6.12 Final Summary

The versatility of the 1,4-disubstitued-1,2,3-triazole motif, particularly in relation to the **tp** and **btp** binding systems, has been described in the context of its facile variability for applications in metal-coordination and the formation of supramolecular systems. In Chapter 1, the most relevant and recent advances from the literature involving the coordination chemistry of **tp** and **btp** was presented. The applications of these motifs, and

analogues thereof, in the formation of various functional systems such as metallo-supramolecular gels, MOFs and mechanically interlocked systems was discussed.

In Chapter 2, the modification of the **btp** core at the 4-pyridyl position was presented through introduction of carbonyl and amino moieties in the development of a number of new **btp** ligands (**83**, **H$_3$84**, **85**, **86**, **87**, **95**, **98** and **99**).

In Chapter 3, a number of Eu(III) and Tb(III) tris-complexes were formed from **btp** ligands **83**, **H$_3$84**, **85** and **99**, with **Eu83$_3$** being characterised extensively in solution and in the solid state. The self-assembly behaviour of **btp** ligands **83**, **85** and **99** with Eu(III) and Tb(III) in solution was explored and the resulting systems were found to be thermodynamically stable. The **btp** ligand **H$_3$84** was shown to function as a low molecular weight gelator giving rise to the formation of a hydrogel. The corresponding tris-complexes, **Eu(H$_3$84)$_3$** and **Tb(H$_3$84)$_3$**, gave rise to the formation of highly luminescent metallogels upon cross linking with Ln(III) ions. The combination of studying the photophysical properties of the Ln(III) metallogels alongside the rheological investigation allowed the origin of the interesting thixotropic properties of the materials to be correlated to the cross-linking Ln(III) ions. The materials were synthesised under a high degree of control and were shown to be healable upon shear-thinning.

In Chapter 4, several crystalline coordination polymers derived from the semi-flexible tri-carboxylic acid **btp** ligand **H$_3$84** were synthesised. The ligand and the tri-sodium salt *poly*-**Na$_3$84** were characterised using single crystal X-ray diffraction analysis displaying a three-dimensional hydrogen-bonding and coordination polymer network, respectively. A Cu(II)-derived coordination polymer **100** of the formula *poly*-[Cu$_3$**84**$_2$)]·(DMF)$_{3.3}$ was synthesised and characterised by single crystal and PXRD analysis, displaying a (4,4) net topology. The optimised synthesis of Zn(II)-derived coordination polymer **101**, of the formula [Zn$_7$**84**$_6$]·((CH$_3$)$_2$NH$_2$)$_4$·(H$_2$O)$_{45}$, produced a three dimensional anionic framework exhibiting the rare **crs** topology which was shown to have potential as a useful cation exchange matrix for the development of functional luminescent materials.

In Chapter 5, the presence of the 4'-substituted "arm" structural feature in **btp** olefins **103R/S** and **104** was determined to be essential for efficient formation of self-templated homocircuit [2]catenanes **111R/S** and **113**. This was found not to be the case with **btp** olefins **105** and **106**, possessing the 3'-substituted "arm", or olefin-derivatised **btp** ligands **107** and **108**, which lacked any amide functionality. It was concluded from this that the modification of the **btp** motif adjacent to the triazolyl *N1* position with a chiral centre in the incorporation of chiral 4'-substituted "arm" substituents did not have a detrimental effect on the synthesis

of self-templated [2]catenanes. Similarly, the variation of the 4-pyridyl position of the **btp** motif with a benzyl ester group also produced the [2]catenane. It was also concluded that the synthesis of enantiopure **111R/S** was the first instance of formation of chiral self-templated homocircuit [2]catenanes from starting materials possessing a chiral centre.

Finally in Chapter 6, the coordination chemistry studies of the subtly unsymmetric ligand **124** with *d*-metal ions of varying lability showed formation of discrete molecules displaying preferential binding of metal cations through the pyridyl nitrogen *N1* and the proximal triazolyl nitrogen *N2 i.e.* the 'regular' (*reg*) chelate moiety despite the presence of a second potential binding pocket *i.e.* 'inverse' (*inv*) moiety.

7 Experimental

7.1 General Experimental Details

7.1.1 Materials and Methods

All solvents and chemicals were purchased from commercial sources and used without further purification. All chemicals were purchased from Sigma-Aldrich, Ireland Ltd. or TCI Ltd. unless otherwise stated and used without further purification. Deuterated solvents used for NMR analysis ($CDCl_3$, CD_3OD, $(CD_3)_2SO$) were purchased from Apollo Scientific. All microwave reactions were carried out in 2–5 mL or 10–20 mL Biotage Microwave Vials in a Biotage Initiator Eight EXP microwave reactor.

The ^1H NMR spectra were recorded at 400 MHz using a Bruker Spectrospin DPX-400 instrument. The ^{13}C NMR spectra were recorded at 100 MHz using a Bruker Spectrospin DPX-400 instrument. NMR spectra were also recorded using a Bruker AV-600 instrument operating at 600.1 MHz for ^1H NMR and 150.9 MHz for ^{13}C NMR. Chemical shifts are reported in commercially available deuterated solvents; δ in ppm relative to $SiMe_4$ (= 0 ppm) referenced relative to the internal solvent signals: data were processed with MestReNova 6.0.2. Multiplicities are abbreviated as follows: singlet (s), doublet (d), triplet (t), multiplet (m) and broad singlet (br s): *J* in Hz. Unless otherwise stated, all NMR spectra were carried out at 293 K.

Mass-spectrometry was carried out using HPLC grade solvents. Electrospray mass spectra were determined on a Micromass LCT spectrometer and high resolution mass spectra were determined relative to a standard of leucine enkephaline. Maldi-Q-TOF mass spectra were carried out on a MALDI-Q-TOF-Premier (Waters Corporation, Micromass MS technologies, Manchester, UK) and high resolution mass spectrometry was performed using Glu-Fib with an internal reference peak of *m/z* 1570.6774.

Melting points were determined using an Electrothermal IA9000 digital melting point apparatus. Infrared spectra were recorded on a Perkin Elmer Spectrun One FT-IE spectrometer equipped with universal ATR sampling accessory.

Thermal gravimetric analysis was performed on Perkin Elmer Pyrus 1 TGA equipped with an ultra-micro balance with a sensitivity of 0.1 microgram. Unless otherwise stated, the temperature range is from 30-800 ^oC with a scan rate 5 ^oC/min.

Elemental analysis was carried out on Exter Analytical CE440 elemental analyser at the microanalysis laboratory, School of Chemistry and Chemical Biology, University College Dublin.

Gas adsorption isotherms were measured using a Quantachrome Autosorb IQ gas sorption analyser. Chemically pure (CP, N4.5) grade He, N_2, H_2 and CO_2 gases were used for the measurements.

7.1.2 X-ray Crystallography

Unless otherwise stated, X-ray data were collected on a Bruker APEX-II DUO diffractometer using microfocus Cu Kα (λ = 1.5405 Å) radiation. All data collections were carried out using standard ω and φ scans at 100K with temperature control provided by a Cobra cryostream. The data were reduced and multi-scan absorption corrections applied using SADABS[412] within the Bruker APEX3 software suite.[413] All datasets were solved with direct methods using SHELXS[414] and refined on F^2 by full-matrix least squares procedures with SHELXL-2014[415] within the OLEX-2 GUI.[416] All non-hydrogen atoms were freely refined with anisotropic displacement parameters, while hydrogen atoms were assigned to geometric positions and refined with a riding model with U_{iso} equivalent to 1.2 or 1.5 times the isotropic equivalent of the carrier atom. In some cases if data sets contained regions of diffuse electron density consistent with delocalized lattice solvent molecules, the diffuse electron density regions' scattering contribution to the measured structure factors was accounted for using SQUEEZE allowing for more representative refinement statistics for the framework atoms.[349]

Single crystal X-ray data for **H$_3$84** were collected at 100 K on a Rigaku AFC12 goniometer equipped with an enhanced sensitivity (HG) Saturn 724+ detector mounted at the window of an FR-E+ Superbright Mo-Kα rotating anode generator (λ = 0.71075 Å) with HF varimax optics.[417] Unit cell parameters were refined against all data and an empirical absorption correction applied in CrystalClear.[418] All structures were solved by direct methods using SHELXS-2013[414] and refined on F_o^2 by SHELXL-2013[414] using ShelXle.[419] Hydrogen atoms (except OH protons which were found from the difference map and then fixed with Uiso = 1.2 Ueq (O)) were positioned geometrically and refined using a riding model with d(CH) =0.95 Å, Uiso = 1.2 Ueq (C) for aromatic protons, d(CH) =0.99 Å, Uiso = 1.2 Ueq (C) for CH2. All non-hydrogen atoms were refined anisotropically.

Phase purity of crystalline materials was confirmed with X-ray powder diffraction patterns recorded with a Bruker D2 Phaser instrument using Cu Kα (λ = 1.5405 Å) radiation. Samples were finely ground and applied to a quartz sample holder. Data were measured at room temperature in the 2θ range 5-55° in 0.01° increments with concurrent rotation in φ of 1 RPM. Additional X-ray powder diffraction data for **101** was collected at 100K on a Bruker

Apex-II Duo instrument using Cu Kα radiation in the 2θ range 2-55°, and was converted to θ vs intensity data by integration of Debye rings obtained from the area detector data. Raw data were compared with the simulated patterns from the single crystal data collections carried out at 100 K.

7.1.3 Photophysical measurements

Unless otherwise stated, all measurements were performed at 298 K in CH_3OH (HPLC grade) and CH_3CN (spectroscopic grade, Aldrich) solutions. UV-vis absorption spectra were measured in 1 cm quartz cuvettes (Hellma) on a Varian Cary 50 spectrophotometer. Baseline correction was applied for all spectra. The wavelength range was set from 200 nm to 450 nm with a scan rate of 600 nm min^{-1}. Emission (fluorescence, phosphorescence and excitation) spectra and lifetimes were recorded on a Varian Cary Eclipse Fluorimeter equipped with a 1.0 cm path length quartz cell at room temperature. The temperature was kept constant throughout the measurements at 298 K by using a thermostated unit block. Fluorescence data were collected between 320 nm and 720 nm, while phosphorescence data were collected between 570 nm and 720 nm for Eu^{III} emission and between 565 nm and 575 nm for Tb(III) emission Phosphorescence lifetimes of the Eu($^5D_0$) excited states was measured in acetonitrile, methanol, water and deuterated water in time-resolved mode at 298 K. They are averages of four independent measurements, which were made by monitoring the emission decay at 618 nm, which corresponds to the maxima of the Eu(III) $^5D_0 \rightarrow {}^7F_2$ transition, enforcing a 0.1 ms delay. The data obtained was analysed using Origin 8.1®. CD spectra were measured in 1 cm quartz cuvettes on a Jassco J-810-150S spectrometer, which was under a constant flow of nitrogen. Baseline correction was applied for all spectra.

7.1.4 Spectrophotometric titrations and binding constants

The formation of the luminescent (M:L, where M = metal and L = **btp** based ligand) species was ascertained by both UV-visible and luminescence titrations of a solution of L (≈1 x 10^{-5} M) with $M(CF_3SO_3)_3 \cdot 6H_2O$ (M= Eu(III)) (0-4 equivalents). The data was fitted using the non-linear regression analysis program, ReactLab™ Equilibria.[1] It was only using the data obtained when the λ_{ex} = 325 nm that the model achieved a reliable fit for the several datasets using ReactLab. It is suggested that this was because the changes in absorptivity were minimal at this wavelength as opposed to at λ_{ex} = 350 nm where they are varying widely. Thus, the self-assembly is was probed *via* an electronic state which remained isoenergetic

across the entire range of added eq. of Eu(III). This allowed the accurate fitting of the self-assembly of **85** with Eu(III) after multiple failed attempts.

7.1.5 Microscopy and Rheological studies of the gels

To image the gel samples by scanning electron microscopy (SEM), they were deposited manually onto clean silicon samples with a thick silicon dioxide layer. The spatula and glass pipettes used for dosing and silicon pieces used as substrates were all cleaned thoroughly by sonication in HPLC grade acetone followed by HPLC grade propan-2-ol. All components were dried in two steps using a high pressure nitrogen gun and further dried under ambient conditions. The gels were manually drop cast on to the silicon at room temperature and dried during 5 days at ambient conditions. SEM was carried out using the Zeiss ULTRA Plus using either an SE2 or in-lens detector in the Advanced Microscopy Laboratory, CRANN, Trinity College Dublin. The samples prepared for the imaging using SEM did not have any additional conductive layer cover.

A rheometer with a 50 mm parallel plate geometry was used to measure the rheology of the gels. After placing the sample, the upper plate was lowered slowly giving a final gap of 0.5 mm in size. Measurements commenced once the normal force equilibrated after the data for several initial oscillatory strain sweeps were collected reproducibly. The samples were kept at a constant temperature of 20 °C. To avoid the evaporation of water or methanol during the measurements of the hydrogel and metallogel respectively a solvent trap was used refilling with solvent if required. A frequency of 1 Hz was used for the oscillatory strain sweep measurements while a constant strain amplitude of 0.1% was used in the frequency sweeps.

7.2 Synthetic Procedures

Synthetic procedures for compounds are presented in the order in which they appear in the text.

7.2.1 Synthesis of ligands discussed in Chapter 2

General procedure A for the synthesis of 83, 85 and 86.[113]

To a solution of methyl 4-(bromomethyl)benzoate or 4-(bromomethyl)benzoic acid (2 eq.) in 10 mL 4:1 DMF/water was added sodium azide (2 eq.) and the reaction mixture stirred for 1 hour, yielding the relevant azide compound which was not isolated due to the potential explosiveness of such compounds, and therefore used without further purification. After

formation of the relevant azide, $CuSO_4 \cdot 5H_2O$ (0.4 eq.) and sodium ascorbate (0.8 eq.) were added to the reaction mixture, followed by anhydrous K_2CO_3 (2 eq.). The solution was degassed, flushed with argon and stirred until the solution had turned yellow indicating formation of the desired Cu(I) catalytic species. To this solution was added the relevant pyridylacetylene (1 eq.) and stirred under inert conditions at room temperature for 60 hours. 1M EDTA/NH_4OH aqueous solution was added to the reaction mixture and stirred for 1 hour before isolating the product.

2,6-Bis(1-(4-(methylcarboxy)benzyl)-1,2,3-triazol-4-yl)-4-(methylcarboxy)pyridine (83)

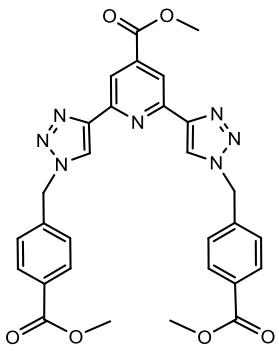

Ligand **83** was synthesised according to General Procedure A[113] from methyl 4-(bromomethyl) benzoate and methyl-2,6-(bis(trimethylsilyl)ethynyl)isonicotinate, **88**, (51 mg, 0.155 mmol). The EDTA/NH_4OH aqueous solution was extracted with EtOAc (25 mL *x* 3). The blue/green aqueous layer was separated, and the organic layer was washed with water (20 mL *x* 3) and brine (20 mL *x* 3), then dried over $MgSO_4$ and concentrated under reduced pressure. This was triturated with cold methanol to yield a beige flaky powder (75 mg, 0.132 mmol, 85%) The product decomposed over 186.2 ^oC. HRMS (*m/z*) (LD^+): Calculated for $C_{29}H_{26}O_6N_7$ *m/z* = 568.1945. Found for $[M+H]^+$ $C_{29}H_{26}O_6N_7$ *m/z* = 568.1968: calculated for $C_{29}H_{25}O_6N_7 \cdot 0.7CH_3OH$, C = 60.5, H = 4.7, N = 16.7. Found C = 60.8, H = 4.5 N = 16.4. ^1H NMR (600 MHz, $CDCl_3$): δ = 8.58 (2H, s, triazolyl) 8.10 (2H, s, pyridyl) 8.00 (4H, d, J = 7.6 Hz, 2,6-aryl) 7.31 (4H, d, J = 7.6 Hz, 3,5-aryl) 5.62 (4H, s, methylene) 3.97 (3H, s, methyl) 3.90 (6H, s, methyl). ^{13}C NMR (151 MHz, $CDCl_3$): δ = 166.3 (2C, methyl carbonyl), 165.1 (1C, methyl carbonyl), 150.6 (2C, 2,6-pyridyl), 147.8 (2C, 4-triazolyl), 139.7 (1C, 4-pyridyl), 139.2 (2C, 4-phenyl), 130.7 (2C, 1-phenyl), 130.4 (4C, 2,6-phenyl), 127.9 (4C, 3,5-phenyl), 122.9 (2C, 5-triazolyl), 119.0, (2C, 3,5-pyridyl), 53.9 (2C, methylene), 52.8 (1C, methyl), 52.3 (2C, methyl). UV-Vis (MeCN) λ_{max} / nm (ε_{max} /dm^3 mol^{-1} cm^{-1}): 236 (52,000), 327 (8,000). IR ν_{max} (cm^{-1}): 1716, 1572, 1435, 1277, 1108, 1043, 1016, 963, 844, 805, 770, 749, 731, 563, 538, 529.

2,6-Bis(1-(4-(carboxy)benzyl)-1,2,3-triazol-4-yl)-4-carboxypyridine ($H_3$84)

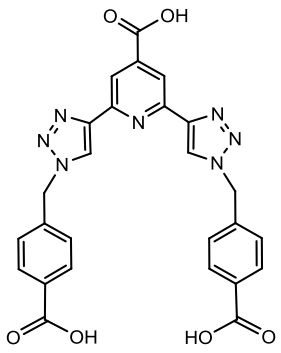

Ligand **83** (70 mg, 0.154 mmol) was stirred in aqueous MeOH and NaOH (3 eq.) solvent mixture (10 mL) at 110 °C for 24 hours. The MeOH was removed under reduced pressure and the remaining aqueous fraction was acidified to pH = 4. This was then extracted with EtOAc (10 mL *x* 2), washed with brine (5 mL *x* 2) and dried with $MgSO_4$. The solvent was removed under reduced pressure to yield a yellowish flaky powder (57 mg, 0.109 mmol, 71%). The product decomposed over 301 °C. HRMS (*m/z*) (ESI^+): Calculated for $C_{26}H_{19}O_6N_7Na$ *m/z* = 548.1289. Found for $[M+Na]^+$ $C_{26}H_{19}O_6N_7Na$ *m/z* = 548.1289: calculated for $C_{26}H_{19}O_6N_7 \cdot 0.4CH_3OH \cdot 0.67H_2O$, C = 57.6, H = 4.0, N = 17.8. Found C = 57.6, H = 3.6 N = 17.6. ^{1}H NMR (400 MHz, DMSO-d_6): δ = 13.11 (s, 3H, carboxylic), 8.82 (s, 2H, pyridyl), 8.37 (s, 2H, triazolyl), 7.96 (d, J = 8.2 Hz, 4H, 2,6-aryl), 7.45 (d, J = 8.2 Hz, 4H, 3,5-aryl$_l$), 5.82 (s, 4H, methylene). ^{13}C NMR (101 MHz, DMSO–d_6): δ = 167.4 (2C, carboxyl), 166.2 (1C, carboxyl), 151.4 (2C, 2,6-pyridyl), 147.3 (2C, 4-triazolyl), 141.1 (4C, 4-phenyl), 140.8 (1C, 4-pyridyl), 131.1 (2C, 1-phenyl), 130.3 (4C, 2,6-phenyl), 128.4 (4C, 3,5-phenyl), 124.8 (2C, 5-triazolyl), 117.8 (2C, 3,5-pyridyl), 53.2 (2C, methylene). IR υ_{max} (cm^{-1}): 3278, 2980, 2117, 1727, 1704, 1681, 1612, 1568, 1404, 1329, 1251, 1231, 1214, 1122, 1111, 1095, 1054, 1015, 947, 905, 845, 808, 773, 751, 729, 683.

2,6-Bis(1-(4-(methylcarboxy)benzyl)-1,2,3-triazol-4-yl)-4-(benzylcarboxy)pyridine (85)

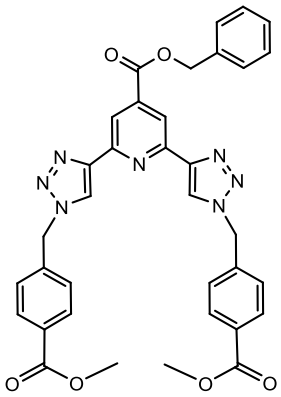

Ligand **85** was synthesised according to General Procedure A[113] from methyl 4-(bromomethyl) benzoate and benzyl 2,6-bis((trimethylsilyl)ethynyl)isonicotinate, **92**, (126 mg, 0.303 mmol). The EDTA/NH_4OH aqueous solution was extracted with EtOAc (20 mL*x*3). The blue/green aqueous layer was separated, and the organic layer was washed with water (10 mL *x* 3) and brine (10 mL*x*3), then dried over $MgSO_4$ and concentrated under reduced pressure. This was triturated with cold methanol to yield a white flaky powder (173 mg, 0.261 mmol, 84 %). m.p. 210–211 °C. HRMS (*m/z*) (ESI^+): Calculated for $C_{35}H_{29}O_6N_7Na$ *m/z* = 666.2062. Found for $[M+Na]^+$ $C_{35}H_{29}O_6N_7Na$ *m/z* = 666.2072: calculated for $C_{35}H_{29}O_6N_7 \cdot 0.5H_2O$, C = 64.4, H = 4.6, N=15.0. Found C = 64.6, H = 4.5, N = 15.0. ^{1}H NMR (600 MHz, $CDCl_3$) δ 8.65(s, 2H, pyridyl), 8.17(s, 2H, triazolyl) , 8.03 (d, J = 8.2 Hz, 4H, 2,6 -phenyl) , 7.47 (d, *J* = 7.2 Hz, 2H, *ortho* - benzyl), 7.40 (t, *J* = 7.4 Hz, 2H,

meta - benzyl), 7.36 (d, *J* = 7.2 Hz, 1H, *para* - benzyl), 7.35 (d, J = 8.2 Hz, 4H, 3,5 -phenyl) , 5.64 (s, 4H, triazole *N-1* methylene) , 5.43 (s, 2H, benzyl methylene) , 3.91 (s, 6H, methyl). ^{13}C NMR (151 MHz, $CDCl_3$): δ = 166.3 (2C, methyl carbonyl), 164.6 (1C, benzyl carbonyl), 150.6 (2C, 2,6-pyridyl), 147.8 (2C, 4-triazolyl), 139.9 (1C, 4-pyridyl), 139.2 (2C, 4-phenyl), 135.2 (1C, 1-benzyl), 130.7 (2C, 1-phenyl), 130.4 (4C, 2,6-phenyl), 128.7 (1C, 4-benzyl), 128.6 (2C, 3,5-benzyl), 128.6 (2C, 2,6-benzyl), 127.9 (4C, 3,5-phenyl), 122.8 (2C, 5-triazolyl), 119.1 (2C, 3,5-pyridyl), 67.7 (1C, triazole *N1* methylene), 53.9 (2C, benzyl methylene), 52.3, (2C, methyl). UV-Vis (CH_3CN) λ_{max} / nm (ε_{max} /dm^3 mol^{-1} cm^{-1}): 236 *(*68,000), 327 (10,500). IR ν_{max} (cm^{-1}): 3094, 2951, 1720, 1615, 1574, 1511, 1456, 1429, 1401, 1385, 1361, 1317, 1277, 1259, 1216, 1187, 1180, 1145, 1109, 1082, 1040, 1020, 966, 940, 901, 871, 830, 806, 78, 768, 745, 733, 726, 698, 685, 677, 665.

2,6-Bis(1-(4-(carboxy)benzyl)-1,2,3-triazol-4-yl)-4-(benzylcarboxy)pyridine (86)

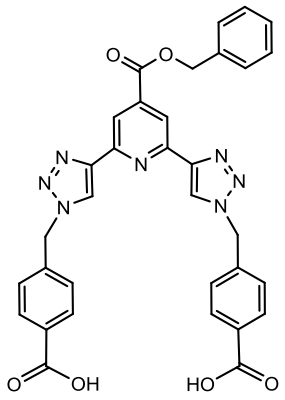

Ligand **86** was synthesised according to modified General Procedure A[113] from benzyl 2,6-diethynylisonicotinate, **93**, (72 mg, 0.278 mmol) and 4-(bromomethyl)benzoic acid (2 eq.) in the absence of K_2CO_3. The reaction mixture was diluted with 100 mL of distilled water and extracted with EtOAc (15 mL *x* 3). $HCl_{(aq)}$ solution (1M) was added until pH to 5 which aided phase separation due to partial solubility of **86** in water at pH ≥ 7. The organic layer was washed with brine (10 mL *x* 2), dried with $MgSO_4$ and the solvent was removed under reduced pressure. The crude brown powder was triturated with cold CH_3OH and filtered off and isolated as a white powder. (78 mg, 0.210 mmol, 75%). The product decomposed over 247 ºC. HRMS (*m/z*) (ESI$^-$) Calculated for [M-H]$^-$ *i.e.* $C_{33}H_{24}N_7O_6$, *m/z* = 614.1793. Found for *m/z* = 614.1803. ^{1}H NMR (600 MHz, DMSO-d_6): δ 8.81 (s, 2H, triazolyl), 8.38 (s, 2H, pyridyl), 7.95 (d, *J* = 8.1 Hz, 4H, 2,6-aryl), 7.53 (d, *J* = 7.3 Hz, 2H, *ortho*-benzyl), 7.44 (m *i.e.* apparent t, *J* = 7.3 Hz, 2H, *meta* - benzyl, apparent d, *J* = 8.1 Hz, 4H, 3,5-aryl), 7.39 (t, *J* = 7.3 Hz, 1H, *para* - benzyl), 5.81 (s, 4H, methylene), 5.46 (s, 2H, benzyl methylene). ^{13}C NMR (151 MHz, DMSO-d_6): δ = 166.9 (2C, carboxylic), 164.2 (1C, methoxy carbonyl), 151.1 (2C, 2,6-pyridyl), 146.7 (2C, 4-triazolyl), 140.5 (2C, 1-phenyl), 139.1 (1C, 4-pyridyl), 135.5 (2C, 4-phenyl), 130.7 (1C, 1-benzyl), 129.9 (4C, 2,6-phenyl), 128.7 (2C, 3,5-benzyl), 128.5 (1C, 4-benzyl), 128.4 (2C, 2,6-benzyl), 127.9 (4C, 3,5-phenyl), 124.5 (2C, 5-triazolyl), 117.1 (2C, 3,5-pyridyl), 67.3 (2C, triazole *N1* methylene), 52.8 (1C, benzyl methylene). IR υ_{max} (cm^{-1}): 3131, 2879, 2570, 2151, 1957,

1702, 1682, 1611, 1571, 1497, 1455, 1421, 1403, 1386, 1328, 1298, 1268, 1257, 1185, 1109, 1090, 1055, 1041, 1018, 945, 924, 870, 856, 843, 807, 770, 751, 734, 694.

2,6-Bis(1-(4-(methylcarboxy)benzyl)-1,2,3-triazol-4-yl)-4-(carboxy)pyridine (87)

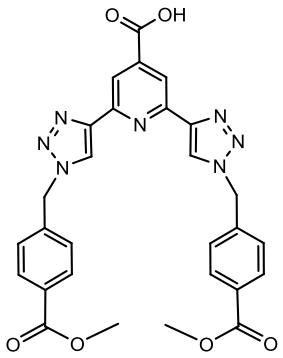

Ligand **85** (50 mg, 0.078 mmol) was suspended in EtOH (50 mL), sonicated and 10 wt % Pd/C (16.5 mg) was added. The reaction flask was put in a Parr Hydrogenator, evacuated and filled with H_2 gas (repeated *x* 2) and allowed to shake at 3 bar for 24 hours. The solution was filtered through celite which was washed with EtOH (50 mL *x* 2) and the solvent was removed under reduced pressure to yielding a white powder (40 mg, 0.076 mmol, 97 %). The product decomposed after exceeding 221ºC. HRMS (*m/z*) (ESI^-): Calculated for $C_{28}H_{22}O_6N_7$ *m/z* = 552.1637. Found for $[M-H]^-$ $C_{28}H_{22}O_6N_7$ *m/z* = 552.1641. ^1H NMR (400 MHz, DMSO-d_6): δ = 8.81 (s, 2H, triazolyl), 8.36 (s, 2H, pyridyl), 7.97 (d, *J* = 8.1 Hz, 4H, 2,6-aryl), 7.46 (d, *J* = 8.1 Hz, 4H, 3,5-aryl), 5.82 (s, 4H, methylene), 3.84 (s, 6H, methyl). ^{13}C NMR (101 MHz, DMSO-d_6): δ = 165.9 (2C, methoxy carbonyl), 165.9 (1C, carboxylic), 150.9 (2C, 2,6-pyridyl), 147.0 (2C, 5-triazolyl), 141.1 (2C, 4-phenyl), 129.8 (4C, 2,6-phenyl), 129.5 (2C, 1-phenyl), 128.2 (4C, 3,5-phenyl), 124.4 (2C, triazolyl), 118.1 (1C, 4-pyridyl), 117.5 (2C, pyridyl), 52.7 (2C, methylene), 52.3 (2C, methyl). IR υ_{max} (cm^{-1}) 3415. 3073, 2952, 2551, 2368, 2355, 2027, 1943, 1713, 1614, 1574, 1433, 1417, 1313, 1277, 1182, 1108, 1044, 1020, 961, 906, 839, 805, 775, 731, 680.

2,6-dichloroisonicotinic acid (66)

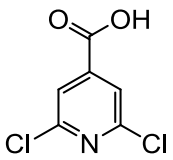

Compound **66** was synthesised according to modified literature procedure.[169] Citrazinic acid **65** (10 g, 64.5 mmol), benzyltriethylammonium chloride (16.2 g, 70.9 mmol) in 20 ml of $POCl_3$ were heated to 140ºC for 24 hours under a $CaCl_2$ drying tube. After being cooled to room temperature, the brown mixture was poured on ice (400 g) and stirred for 2 hours. The resulting brown solid was filtered off, washed with water and dissolved in EtOAc (400 mL). The organic phase was then washed with saturated NH_4Cl, dried over $MgSO_4$ and evaporated to dryness to afford the desired compound as a brown solid (11.59 g, 58.3 mmol, 90 %). m.p. 204 – 206 ºC. (lit. 205–207 ºC). ^1H and ^{13}C NMR were in accordance with those already reported.[169] HRMS (*m/z*) (ESI^-): Calculated for $C_6H_2NO_2Cl_2$ *m/z* = 198.9463. Found for $[M-H]^-$ $C_6H_2NO_2Cl_2$ *m/z* = 198.9457.^1H NMR (400 MHz, $CDCl_3$): δ = 7.83 (2H, s, pyridyl). IR ν_{max} (cm^{-1}): 3078, 2848,

2580, 1719, 1595, 1544, 1418, 1363, 1252, 1229, 1162, 1000, 925, 894, 814, 767, 714, 677, 559.

Methyl 2,6-dichloroisonicotinate (90)

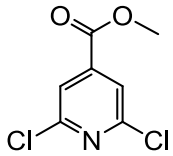

Compound **90** was synthesised according to a modified literature procedure[169] from **66** (500mg, 2.6 mmol) which was dissolved in dry CH_3OH (20 mL) and conc. H_2SO_4 (2 drops) was added. The solution was refluxed at 70 ^oC for 24 hours. The solvent was removed under reduced pressure and the residue was dissolved in EtOAc (10 mL) and washed with 1M citric acid (2 mL x 3), sat. $NaHCO_3$ solution (2 mL x 3), water (2 mL x 3) and brine (2 mL x 1). This was dried with $MgSO_4$ and the solvent was removed to give crude **90**. This was recrystallised from CH_3OH to afford clear needle-like crystals (200 mg, 0.97 mmol, 40%). HRMS (*m/z*) (EI^+): Calculated for $C_7H_5NO_2Cl_2$ *m/z* = 204.9697. Found for $[M]^+$ $C_7H_5NO_2Cl_2$; *m/z* = 204.9700. ^1H NMR (400MHz, $CDCl_3$): δ = 7.79 (2H, s, pyridyl), 3.96 (3H, s, methyl). IR ν_{max} (cm^{-1}): 3441, 3090, 2959, 1728, 1584, 1543, 1438, 1409, 1359, 1289, 1237, 1202, 1159, 1093, 974, 915, 895, 870, 813, 763, 736, 711, 624, 579.

Benzyl 2,6-dichloroisonicotinate (91)

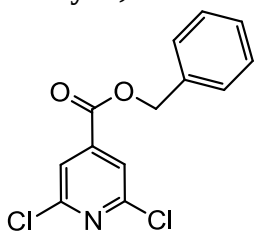

Compound **91** was synthesised according to literature procedure.[67] In this way, **66** (200mg, 1.042 mmol), $NaHCO_3$ (96 mg, 1.15 mmol) and benzyl bromide (124 µL, 1.042 mmol) were dissolved in anhydrous DMF (15 mL) and the resulting mixture was stirred at 70 °C for17 hours. The reaction mixture was diluted with H_2O (100 mL), and the resulting mixture was extracted with ethyl acetate, washed with aqueous $NaHCO_3$ (20 mL *x* 3), H_2O (20 mL *x* 1) and brine (20 mL *x* 1), dried with $MgSO_4$ and the solvent was evaporated under reduced pressure to afford a yellow semi-solid (252 mg, 0.896 mmol, 86 %). HRMS (*m/z*) (ESI^+): Calculated for $C_{13}H_{10}NO_2Cl_2$ *m/z* = 282.0083. Found for $[M+H]^+$ $C_{13}H_{10}NO_2Cl_2$ *m/z* = 282.0080. ^1H NMR (400 MHz, $CDCl_3$): δ = 7.80 (s, 2H, pyridyl), 7.42–7.37 (m, 5H, benzene), 5.37 (s, 2H, methylene). IR ν_{max} (cm^{-1}): 3036, 2626, 1726, 1652, 1597, 1566, 1550, 1498, 1457, 1443, 1395, 1381, 1356, 1337, 1317, 1280, 1243, 1214, 1157, 1102, 1092, 1081, 1030, 1003, 976, 943, 913, 896, 880, 857, 829, 815, 766, 748, 740, 723, 695, 681, 667, 664, 661.

General Procedure B for Sonogashira coupling of (trimethylsilyl)acetylene with halopyridines

2,6-dihalopyridine (8.44 mmol), bis(triphenylphosphine)palladium(II) dichloride (0.370 g; 0.53 mmol) and copper(I) iodide (0.201g; 1.06mmol) were stirred at 0 °C for 10 mins under argon, using a 1:1 TEA:THF solvent system prior to addition of (trimethylsilyl)acetylene (2.39 ml; 1.658 g; 16.89 mmol) was added by syringe and the solution was stirred at 70°C for 18 hours. The mixture was then concentrated under reduced pressure and subsequently dissolved in hexane and filtered through a plug of celite. The filtrate was concentrated under reduced pressure, yielding a fluffy brown solid.

Methyl-2,6-(bis(trimethylsilyl)ethynyl)isonicotinate (88)

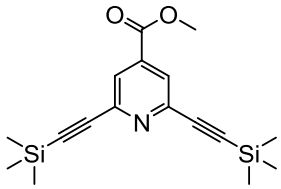

Compound **88** was synthesised according to general procedure B from **90** (180 mg, 0.874 mmol) scaled appropriately.[99] The crude solid was purified by flash chromatography (gradient Hexane/EtOAc (92/8) R_f = 0.6) yielding a yellow powder (205 mg, 0.622 mmol, 72 %). HRMS (*m/z*) (ESI^+): Calculated for $C_{17}H_{24}NO_2Si_2$ *m/z* = 330.1346. Found for $[M+H]^+$ $C_{17}H_{24}NO_2Si_2$ *m/z* = 330.1337. ^1H NMR (400MHz, $CDCl_3$): δ 7.89 (2H, s, pyridyl), 3.94 (3H, s, methyl), 0.24 (18H, s, silane methyl),. IR ν_{max} (cm^{-1}): 2956, 1725, 1558, 1436, 1395, 1329, 1245, 1185, 1119, 1106, 1071, 995, 975, 838, 757, 722, 695, 660, 636, 573.

Benzyl 2,6-bis((trimethylsilyl)ethynyl)isonicotinate (92)

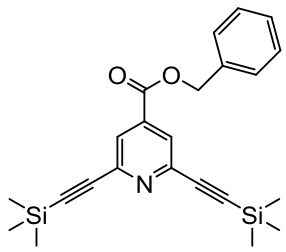

Compound **92** was synthesised according to general procedure B from **91** (478 mg, 1.695 mmol). The reaction mixture was concentrated under reduced pressure. This was then dissolved in hexane and filtered through celite. This yellow solution was purified by flash chromatography (gradient hexane/ EtOAc (98:2) yielding a yellow oil (343 mg, 0.848 mmol, 50 %). HRMS (*m/z*) (ESI^+): Calculated for $C_{23}H_{28}NO_2Si_2$ *m/z* = 406.1653. Found for $[M+H]^+$ $C_{23}H_{28}NO_2Si_2$ *m/z* = 406.1660. ^1H NMR (600 MHz, $CDCl_3$): δ 7.93 (s, 2H, pyridyl), 7.45-7.43 (m, 5H, benzene), 5.40 (s, 2H, methylene), 0.28 (s, 18H, silane methyl). IR ν_{max} (cm^{-1}): 3094, 2951, 1720, 1615, 1574, 1511, 1456, 1429, 1401, 1385, 1361, 1317, 1277, 1259, 1216, 1187, 1180, 1145, 1109, 1082, 1040, 1020, 966, 940, 901, 871, 830, 806, 78, 768, 745, 733, 726, 698, 685, 677, 665.

Benzyl 2,6-diethynylisonicotinate (93)

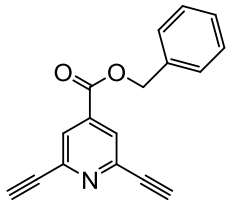

Compound **93** was synthesised according to modified literature procedure.[420-421] In this way, **92** (1.13 g, 3.37 mmol) was dissolved in anhydrous THF (25 mL), cooled to 0ºC and a solution of TBAF (1 eq.) in anhydrous THF (5 mL) was added dropwise. The mixture was then allowed to stir at rt for 1 hour. The mixture was concentrated under reduced pressure, dissolved in EtOAc (75 mL *x* 3), washed with H_2O (25 mL *x* 4), brine and dried with $MgSO_4$. The solvent was removed under reduced pressure to yield a reddish semi-solid (750 mg, 2.88 mmol, 85 %). HRMS (*m/z*) (EI^+): Calculated for $C_{17}H_{11}NO_2$ *m/z* = 261.0790. Found for $C_{17}H_{11}NO_2$, *m/z* =261.0779. ^{1}H NMR (400 MHz, $CDCl_3$): δ 7.98 (s, 2H, pyridyl), 7.54–7.31 (m, 5H, benzene), 5.39 (s, 2H, methylene), 3.22 (s, 2H, alkyne). IR υ_{max} (cm^{-1}): 3269, 2111, 1714, 1551, 1499, 1453, 1388, 1320, 1225, 1186, 1106, 975, 893, 766, 727, 693.

2,6-Bis(1-(4-(methylcarboxy)benzyl)-1,2,3-triazol-4-yl)-4-(amino)pyridine (95)

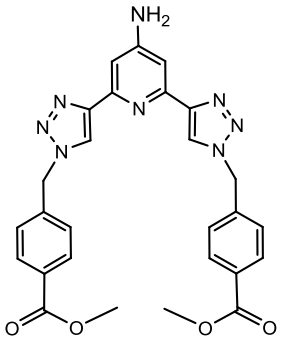

95 was synthesised according to General Procedure A from methyl 4-(bromomethyl)benzoate and **97** (636 mg, 2.22mmol). The EDTA/NH_4OH aqueous solution was extracted with EtOAc (25 mL *x* 3). The blue/green aqueous layer was separated, and the organic layer was washed with H_2O (20 mL *x* 3) and brine (20 mL *x* 3), then dried over $MgSO_4$ and concentrated under reduced pressure. A substantial amount of material precipitated during solvent extraction. This was filtered and washed with H_2O. This and the residue from the EtOAc evaporation were combined and triturated with cold methanol to yield a beige powder (650 mg, 1.21 mmol, 55%). m.p. 176 ºC decomp. HRMS (*m/z*) (ESI^+): Calculated for $C_{27}H_{25}O_4N_8$ *m/z* = 525.1999. Found for $[M+H]^+$ $C_{27}H_{25}O_4N_8$ *m/z* = 525.2004; calculated for $C_{27}H_{24}O_8N_4 \cdot 2CH_2Cl_2$, C = 50.21, H = 4.06, N=16.16. Found C = 50.30, H = 3.46, N = 16.01. ^{1}H NMR (600 MHz, DMSO-d_6) δ 8.52 (s, 2H, triazolyl), 7.98 (d, *J* = 8.3 Hz, 4H, 2,6-aryl) 7.45 (d, *J* = 8.3 Hz, 4H, 3,5-aryl), 7.21 (s, 2H, pyridyl), 6.34 (s, 2H, NH_2), 5.77 (s, 4H, methylene), 3.85 (s, 6H, methyl). ^{13}C NMR (151 MHz, DMSO-d_6) δ 166.3 (2C, carbonyl), 156.2 (1C, 4-pyridyl), 150.2 (2C, 2,6-pyridyl), 148.7 (2C, 4-triazolyl), 141.8 (2C, 1-aryl), 130.1 (4C, 2,6-aryl), 129.8 (2C, 4-aryl), 128.5 (4C, 3,5-aryl), 123.8 (2C, 5-triazolyl), 104.0 (2C, 3,5-pyridyl), 52.9 (2C, methylene), 52.7 (2C, methyl). UV-Vis (CH_3CN:DMSO (1:)) λ_{max} / nm (ε_{max} /dm^3 mol^{-1} cm^{-1}) 249 (33,000), 260 (21,000) 292 (1,900). IR ν_{max} (cm^{-1}): 3438, 3351, 3243, 3133, 3085, 2956, 2105, 1721, 1645, 1613, 1578, 1542, 1512, 1435, 1417, 1352,

1311, 1276, 1227, 1182, 1109, 1053, 1021, 976, 958, 925,861, 841, 803, 770, 743, 728, 697, 658.

2,6-Dibromopyridine-*N*-oxide (71)

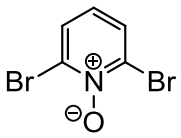

71 was synthesised according to literature procedure.[422] 2,6-dibromopyridine **70** (2 g, 8.44 mmol) was dissolved in TFA (15 mL) and H2O2 (2 mL) and heated at 100 °C for 19 hours. This was allowed to cool and H_2O (25 mL) was added until a precipitate was observed. This was filtered off yielding a beige powder (1.4 g, 5.65 mmol, 67%). HRMS (ES+): Calculated for $C_5H_3NOBr_2$ *m/z* = 250.8581. Found for $[M+H]^+$ $C_5H_4NOBr_2$ *m/z* = 251.8663. ^{1}H NMR (400MHz, $CDCl_3$, δ_H) 7.63 (2H, d, pyridyl) 6.91 (1H, t, pyridyl). IR ν_{max} (cm^{-1}): 3107, 3082, 3034, 2918, 2850, 2612, 2498, 2200, 2091, 1932, 1864, 1795, 1732, 1667, 1577, 1551, 1525, 1470, 1437, 1423, 1402, 1356, 1294, 1252, 1220, 1173, 1157, 1133, 1108, 1073, 1047, 978, 967, 902, 839, 765, 745, 699

2,6-Dibromo-4-nitropyridine-*N*-oxide (72)

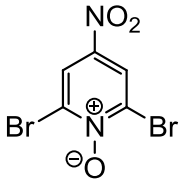

72 was synthesised according to literature procedure.[422] **71** (0.824g, 3.26mmol) was dissolved in fuming nitric acid (HNO_3:H_2SO_4, 3 mL:8 mL) and the mixture was heated at 80°C for 20 hours. This was allowed to cool to 0°C before adding cooled $NH_4OH_{(aq)}$ (0.5 M, 50 mL) slowly and while stirring. The precipitate formed was filtered yielding a yellow powder (0.75 g, 2.53 mmol, 78%). HRMS (ESI+): Calculated for $C_5H_2N_2O_3Br_2$ *m/z* = 295.8432. Found for $[M+H]^+$ $C_5H_3N_2O_3Br_2$ *m/z* = 295.8439 . ^{1}H NMR (400MHz, $CDCl_3$, δ_H) 8.52 (2H, s, pyridyl). IR ν_{max} (cm^{-1}): 3282, 3108, 3090, 2970, 2922, 2852, 2569, 2487, 2345, 2221, 1739, 1586, 1572, 1515, 1471, 1437, 1409, 1371, 1326, 1281, 1256, 1229, 1217, 1151, 912, 882, 830, 802, 767, 733, 708.

2,6-Dibromo-4-aminopyridine (96)

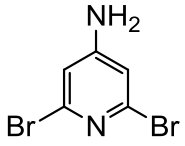

96 was synthesised according to literature procedure.[284] **72** (2 g, 6.3 mmol) was dissolved in AcOH (50 mL) and Fe powder (1.4 g, 26 mmol) was added. This was stirred at 100°C for 8 hours using an automated stirring apparatus in a conical flask and then cooled to rt while stirring continued for 8 hours. This was diluted with H_2O (100 mL) and extracted with EtOAc (50 mL x 3) and washed with K_2CO_3 (1M, 50 mL x 1) and brine solution (50 mL x 1). This was dried using $MgSO_4$ and the solvent was removed under reduced pressure yielding beige coloured powder (1.32 g,

5.24 mmol, 78%). HRMS (*m/z*) (ESI-): Calculated for $C_5H_4N_2Br_2$; *m/z* = 249.8663. Found for $[M-H]^-$ $C_5H_3N_2Br_2$ *m/z* = 248.8661. ^{1}H NMR (400MHz, $CDCl_3$, δ_H) 6.70 (2H, s, pyridyl) 4.37 (2H, s, NH_2). IR ν_{max} (cm^{-1}): 3466, 3302, 3185, 1716, 1624, 1579, 1528, 1435, 1410, 1277, 1153, 1107, 1072, 1023, 975, 936, 853, 830, 763, 729, 635, 601, 574, 560

Synthesis of 2,6-bis((trimethylsilyl)ethynyl))-4-aminopyridine (97)

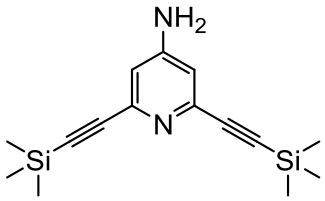

97 was synthesised according to General Procedure B from **96** (700 mg, 2.78 mmol).[99] The reaction mixture was concentrated under reduced pressure. This was then dissolved in hexane and filtered through celite. This yellow solution was purified by flash chromatography (gradient CH_2Cl_2/CH_3OH (96:4) yielding a yellow oil (634 mg, 2.22 mmol, 79%). HRMS (*m/z*) (ESI+): Calculated for $C_{15}H_{23}N_2Si_2$ *m/z* = 287.1400. Found for $[M+H]^+$ $C_{15}H_{23}N_2Si_2$; *m/z* = 287.1402. ^{1}H NMR (400MHz, $CDCl_3$, δ_H) 6.76 (2H, s, pyridyl) 5.28 (2H, s, NH_2) 0.19 (18H, s, silane methyl). IR ν_{max} (cm^{-1}): 3309, 3183, 3084, 2955, 2922, 2853, 1721, 1616, 1579, 1530, 1435, 1415, 1278, 1182, 1157, 1110, 1054, 1021, 973, 934, 840, 802, 761, 744, 725, 693.

Synthesis of ditopic btp 98

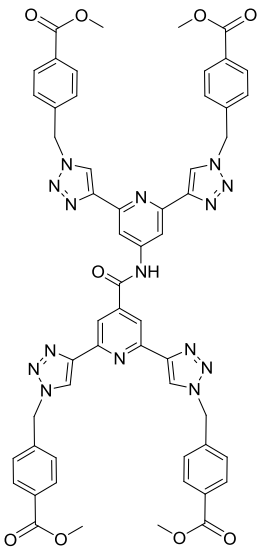

Btp acid **87** (85 mg, 0.16 mmol) was dissolved in $SOCl_2$ (7 mL) and two drops of DMF were added to the solution which was stirred while refluxing at 80°C for 3 hours. The $SOCl_2$ was distilled off and the residue was dissolved in anhydrous toluene (20 mL). Et_3N (200 µL) was added slowly followed by DMAP (2 mg, 0.016 mmol) and amino **btp** ligand **95** (85 mg, 0.16 mmol) This solution was degassed under Argon and refluxed at 130°C for 48 hours. The reaction mixture was concentrated under reduced pressure and treated with CH_2Cl_2 (50 mL) which was washed with H_2O (50 mL x 3). At this point, the resulting precipitate was filtered. The organic layer was dried with $MgSO_4$ and the CH_2Cl_2 was removed under reduced pressure yielding a crude brown solid. Both this and the filtered residue were adsorbed onto silica and purified by flash chromatography (gradient CH_2Cl_2:CH_3OH (93:7)) yielding a brown powder (75 mg, 0.072 mmol, 45 %). HRMS (*m/z*) (ESI^+): Calculated for $[M+H]^+$ *i.e.* $C_{53}H_{46}N_{15}O_7$ *m/z* = 1004.3705. Found for $[M+H]^+$ *m/z* = 1004.3721. ^{1}H NMR (400 MHz, DMSO-d_6) δ 11.24 (s, 1H, NH), 8.81 (s, 2H, triazole), 8.69 (s, 2H, triazole), 8.56 (s, 2H, pyridyl), 8.54 (s, 2H, pyridyl), 7.96 (d, *J* = 7.8 Hz, 4H, aryl), 7.45 (d, *J* = 8.3 Hz, 4H, aryl),

5.82 (s, 4H, CH_2), 5.79 (s, 4H, CH_2), 3.81 (s, 12H, CH_3). ^{13}C NMR (151 MHz, DMSO-d_6) δ 166.5 (4C, carbonyl), 165.4 (1C, carbonyl), 151.3 (2C, 2,6-pyridyl), 148.2 (2C, 4-triazolyl), 147.6 (2C, 4-triazolyl), 147.6 (2C, 2,6-pyridyl), 141.1 (4C, 4-aryl), 130.2 (8C, 2,6-aryl), 130.0 (4C, 1-aryl), 128.7 (8C, 3,5-aryl), 125.1 (2C, 5-triazolyl), 124.3 (2C, 5-triazolyl), 117.4 (2C, 3.5-pyridyl), 109.3 (2C, 3.5-pyridyl), 53.6 (4C, methylene), 52.7 (4C, methyl). UV-vis (CH_3CN) λ_{max} / nm (ε_{max} /dm^3 mol^{-1} cm^{-1}) 234 (15, 000) 313 (1,800). FT-IR (cm^{-1}), 3310, 3083, 2985, 2927, 1718, 1639, 1611, 1572, 1536, 1503, 1430 ,1381, 1345, 1280, 1222,1192, 1108 ,1092, 1040 ,1019, 993 ,917, 854, 810, 788, 768, 726, 687 ,664 ,626, 556.

2,6-Bis(hexadecyl)-1,2,3-triazol-4-yl)-4-(methylcarboxy)pyridine (99)

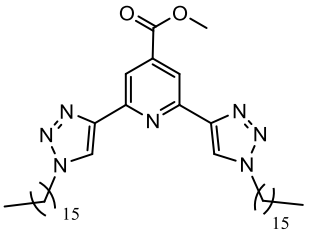

To a solution of hexadecylamine (108 mg, 0.45 mmol, 2 eq.) in CH_3OH (10 mL) was added the diazotransfer reagent imidazole-1-sulfonyl azide salt, $ImSO_2N_3 \cdot H_2SO_4$ (146 mg, 0.54 mmol, 2.4 eq.), K_2CO_3 (124 mg, 0.897 mmol, 4 eq.) and $CuSO_4 \cdot 5H_2O$ (22 mg, 0.09 mmol, 0.4 eq.) and the reaction mixture stirred for 1 hour, yielding the relevant azide after the suspension had turned form a blue to a purple colour. Sodium Ascorbate (40 mg, 0.20 mmol, 0.9 eq.) and additional K_2CO_3 (62 mg, 0.45 mmol, 2 eq.) were added with tBuOH:H_2O (3:2) (5 mL) to the reaction mixture. The solution was degassed, flushed with Argon and stirred until the solution had turned yellow indicating formation of the desired Cu(I) catalytic species. To this solution was added a solution of **88** (82 mg, 0.25 mmol, 1 eq.) in DMF (4 mL) and stirred under inert conditions at room temperature for 24 hours. 1 M EDTA/NH_4OH solution was added to the reaction mixture and stirred for 1 hour before isolating the product. The EDTA/NH_4OH aqueous solution was extracted with CH_2Cl_2 (25 mL *x* 3). The blue/green aqueous layer was separated, and the organic layer was washed with water (20 mL *x* 3) and brine (20 mL *x* 3), then dried over $MgSO_4$ and concentrated under reduced pressure. This was triturated with cold methanol to yield a white powder (104 mg, 0.14 mmol, 59 %) mp. 94.9–95.2 ^{o}C. HRMS (*m/z*) (ESI$^+$): Calculated for [M+Na]$^+$ *i.e.* $C_{43}H_{73}N_7NaO_2$ *m/z* = 742.5718. Found for [M+Na]$^+$ *m/z* = 742.5727; calculated. for $C_{43}H_{73}N_7O_2$: C 71.96, H 10.43, N 13.60. Found: C 71.72, H 10.22, N 13.62. ^{1}H NMR (400 MHz, $CDCl_3$) δ 8.65 (s, 2H, pyridyl), 8.30 (s, 2H, triazole), 4.44 (t, *J* = 7.2 Hz, 4H, methylene), 4.00 (s, 3H, methyl), 2.05 – 1.92 (m, 4H, methylene), 1.36 (d, *J* = 3.8 Hz, 8H, methylene), 1.27 (d, *J* = 18.5 Hz, 44H, methylene), 0.87 (t, *J* = 6.8 Hz, 6H, methyl). ^{13}C NMR (101 MHz, $CDCl_3$) δ 165.5 (1C, carbonyl), 151.2 (2C, 2,6-pyr), 147.5 (2C, 5-triaz), 139.8 (1C, 4-pyr), 122.7 (2C, 4-triaz), 119.0 (2C, 3,5-pyr), 52.9 (1C, methyl), 50.8 (2C,

methylene), 32.1 (2C, methylene), 30.5 (2C, methylene), 29.8 (12C, methylene), 29.7 (2C, methylene), 29.5 (4C, methylene), 29.2 (2C, methylene), 26.7 (2C, methylene), 22.8 (2C, methylene), 14.3 (1C, methyl). UV-vis (CH_3CN) λ_{max} / nm (ε_{max} /dm^3 mol^{-1} cm^{-1}) 239 (24, 000) 329 (8,000). IR ν_{max} (cm^{-1}): 2919, 2849, 1723, 1618, 1575, 1470, 1440, 1399, 1379, 1324, 1260, 1215, 1112, 1077, 1039, 967, 907, 834, 799, 771, 755, 719, 657.

7.2.2 Synthesis of complexes discussed in Chapter 3

General Procedure C for the preparation of Ln(III) Complexes

Btp ligand (0.07 mmol) and $Ln(CF_3SO_3)_3 \cdot 6H_2O$ (0.023 mmol) were dissolved in CH_3OH (5 mL) in a microwave tube. This underwent microwave irradiation at 70 ^oC for 20 minutes. On completion, the solution was filtered through a celite syringe and precipitated out of CH_3OH *via* ether diffusion followed by centrifugation to yield the white powder.

Eu83$_3$ complex

Eu83$_3$ was synthesised according to General Procedure C using **btp** ligand **83** (40 mg, 0.07 mmol) and $Eu(CF_3SO_3)_3 \cdot 6H_2O$ (16.3 mg, 0.023 mmol) to yield a white powder, (55 mg, 0.023 mmol, 99%). Crystals were obtained *via* ether diffusion into a CH_3CN solution of **Eu83$_3$**. The product decomposed over 145^oC. HRMS (*m/z*) (LD^+): Calculated for $C_{89}H_{75}N_{21}O_{24}F_6S_2Eu$ *m/z* = 2152.3852. Found for $[Eu\mathbf{83}_3\text{-}(CF_3SO_3^-)_2]^+$ *m/z* = 2152.3796; calculated for $C_{90}H_{75}N_{21}O_{27}F_9S_3Eu \cdot 3.5H_2O$, C = 45.7, H = 3.5, N=12.4. Found C = 45.1, H = 2.9, N = 12.1. ^1H NMR (400 MHz, CD_3OD): δ = 7.82 (d, *J* = 8.0 Hz, 4H, aryl), 7.69 (s, 2H, triazole), 7.23 (d, *J* = 8.0 Hz, 4H, aryl), 6.30 (d, *J* = 14.6 Hz, 2H, methylene), 5.52 (d, *J* = 14.6 Hz, 2H, methylene), 5.35 (s, 2H, pyridyl), 3.97 (s, 3H, methyl), 3.92 (s, 6H, methyl). ^{13}C NMR (101 MHz, CD_3OD): δ = 167.6 (2C, methyl carbonyl), 160.4 (2C, 5-triazolyl), 159.9 (1C, methyl carbonyl), 154.0 (1C, 4-pyridyl), 142.0 (2C, 1-phenyl), 135.8 (2C, 2,6-pyridyl), 131.8 (2C, 4-phenyl), 131.0 (4C, 2,6-phenyl), 129.4 (4C, 3,5-phenyl), 105.5 (2C, 5-triazolyl), 87.5 (2C, 3,5-pyridyl), 54.0 (2C, methylene), 52.9 (2C, methyl), 49.9 (1C, methyl). IR ν_{max} (cm^{-1}): 3104, 2957, 1719, 1615, 1587, 1549, 1437, 1276, 1254, 1223, 1183, 1155, 110, 1071, 1029, 965, 817, 772, 730. **Tb83$_3$** was synthesised in the same manner.

Eu(H$_3$84)$_3$ complex

Eu(H$_3$84)$_3$** was synthesised according to General Procedure C using **H$_3$84$_3$ (20 mg, 0.04 mmol) and $Eu(CF_3SO_3)_3 \cdot 6H_2O$ (9.4 mg, 0.013 mmol) to yield the white powder (29.3 mg, 0.013 mmol, 99 %). The product decomposed over 260 ^oC. HRMS (*m/z*) (ESI^+): Calculated for $C_{78}H_{57}N_{21}O_{18}Eu$ *m/z* = 1728.3403. Found for $[Eu\mathbf{(H_384)}_3]^{3+}$ *m/z* = 1728.3342. Also,

calculated for $C_{79}H_{57}N_{21}O_{21}EuF_3S$ *m/z* = 1877.2912. Found for $[Eu(\mathbf{H_384})_3\text{-}(CF_3SO_3^-)]^{2+}$ *m/z* = 1877.2968. ^{1}H NMR (400 MHz, CD_3OD): δ = 7.82 (br, 4H, aryl), 7.62 (br, 2H, triazolyl), 7.21 (br, 4H, aryl), 6.08 (br, 2H, methylene), 5.63 (br, 2H, methylene), 5.23 (br, 2H, pyridyl). IR υ_{max} (cm^{-1}): 3411, 1591, 1539, 1405, 1241, 1225, 1169, 1070, 1028, 907, 863, 817, 782, 737, 674. **Tb(H$_3$84)$_3$** was synthesised in the same manner.

Eu85$_3$ complex

Eu85$_3$ was synthesised according to General Procedure C using **85** (49 mg, 0.08 mmol) and $Eu(ClO_4)_3{\cdot}6H_2O$ (12 mg, 0.025 mmol) to yield the white powder (14 mg, 0.012 mmol, 48 %). HRMS (*m/z*) (LD^+): Calculated for $[\mathbf{Eu85_2}\text{-}(ClO_4)]^+$ *i.e.* $C_{70}H_{58}EuN_{14}O_{20}Cl_2$ *m/z* = 1637.2541. Found for $[\mathbf{Eu85_2}\text{-}(CF_3SO_3)]^+$ *m/z* = 1637.2582. IR υ_{max} (cm^{-1}) 3282, 2923, 2851, 1719, 1583, 1417, 1281, 1184, 1071, 1019, 934817, 771, 730, 700.

Eu99$_3$ complex

Eu99$_3$ was synthesised according to General Procedure C using **99** (20 mg, 0.04 mmol) and $Eu(CF_3SO_3)_3{\cdot}6H_2O$ (9.4 mg, 0.013 mmol) to yield the white powder (6 mg, 0.002 mmol, 56 %) after precipitating out of CH_3OH *via* toluene diffusion followed by centrifugation. mp. 160.1-160.5^{o}C HRMS (*m/z*) (LD^+): Calculated for $[\mathbf{Eu99_2}\text{-}(CF_3SO_3)]^+$ *i.e.* $C_{88}H_{146}F_6EuN_{14}O_{10}S_2$ *m/z* = 1889.9904. Found for $[\mathbf{Eu99_2}\text{-}(CF_3SO_3)]^+$ *m/z* = 1889.9867. IR υ_{max} (cm^{-1}) 3432, 2920, 2851, 1739, 1589, 1447, 1245, 1186, 1159, 1074, 1029, 815, 773, 721, 636, 573.

Synthesis of Tb99$_3$ complex

Tb99$_3$ was synthesised according to General Procedure C using **99** (7 mg, 0.01 mmol) and $Tb(CF_3SO_3)_3{\cdot}6H_2O$ (2.4 mg, 0.003 mmol) to yield the white powder (5 mg, 0.002 mmol, 68 %) after precipitating out of CH_3OH *via* toluene diffusion followed by centrifugation. The product decomposed over 155 ^{o}C HRMS (*m/z*) (ESI^+): Calculated for $[\mathbf{Tb99_2}\text{-}(CF_3SO_3^-)]^+$ *i.e.* $C_{88}H_{146}F_6TbN_{14}O_{10}S_2$ *m/z* = 1895.9946. Found for $[\mathbf{Tb99_2}\text{-}(CF_3SO_3)]^+$ *m/z* = 1895.9962. IR υ_{max} (cm^{-1}) 3438, 2918, 2850, 1735, 1576, 1468, 1448, 1378, 1251, 1224, 1154, 1074, 1029, 967, 906, 816, 772, 754, 720, 636, 572.

7.2.3 Preparation of supramolecular gels derived from H$_3$84

Preparation of ligand hydrogel

The hydrogel was prepared by dissolving the compound **H$_3$84** in a NaOH solution in H_2O (2 mL). This was slowly acidified with HCl solution to pH~6. At this point, a fluffy off-

white soft precipitate was formed which was allowed to settle for 5 minutes before decanting off the excess solvent and isolating the hydrogel.

Preparation of Ln(III) luminescent metallogels

The synthesis of the Eu(III) and Tb(III) luminescent gel was performed in a two step one pot reaction. Firstly, $Eu(CF_3SO_3)_3$ (1 eq.) and **$H_3$84** (3 eq.) were suspended in methanol to give a 1.55 mM solution relative to the Ln(III). The mixture was irradiated in the microwave for 60 minutes at 80 ºC giving rise to a clear colourless solution. Then, $Eu(C_2H_3O_2)_3$ salt (2.13 eq.) was added. Instantaneously a white soft precipitate could be observed as the acetate salt was dissolved. This mixture was irradiated again in the microwave for 30 minutes at 80ºC giving rise to the formation of a fluffy off-white soft precipitate, the luminescence of which far exceeded that of the mixture prior to addition of the acetate salt. This was centrifuged for 5 minutes at 3500 rpm and isolated in its gel form. The Tb(III) analogue was synthesised in the same manner.

7.2.4 Preparation of coordination polymer materials derived from $H_3$84 presented in Chapter 4

Synthesis of *poly*-$Na_3$84·$(H_2O)_2$

$H_3$84 (5 mg, 0.0097 mmol) was dissolved in $NaOH_{(aq)}$ (2 mL, 1 M) and allowed to stand and slowly evaporate for two weeks. Yellow single crystals were formed (trace amounts) which were analysed by X-ray diffraction. There were difficulties in optimizing the synthetic conditions required to reproduce *poly*-**$Na_3$84·$(H_2O)_2$**. Further characterisation could not be carried out as a result.

Synthesis of *poly*-[$Cu_3$84$_2$)]·$(DMF)_{3.3}$ (100).

To 1 mL of a 95:5 DMF:H_2O mixture were added **$H_3$84** (15 mg, 0.029 mmol, 1 eq.) and copper(II) nitrate hemipentahydrate (11 mg, 0.047 mmol, 1.6 eq.) and the mixture was sealed and heated at 100 °C for 2.5 hours. The resulting green crystals were isolated by filtration, washed with DMF, and dried under suction (23 mg, 0.016 mmol, 93%); mp 254−258 decomp. There were difficulties in optimizing the synthetic conditions required to reproduce **100**. calculated for [Cu_3**84**$_2$)]·12(H_2O) *i.e.* $C_{52}H_{56}N_{14}O_{24}Cu$; C = 42.73, H = 4.10, N = 14.49, found C = 43.02, H = 43.88, N = 13.51. IR υ_{max} (cm^{-1}) 3381, 3073, 2357, 2317, 2051, 1983, 1648, 1596, 1552, 1382, 1180, 1100, 1071, 1033, 1020, 855, 826, 810, 779, 735, 703, 694, 686, 682, 664, 655. Phase purity supported by X-ray powder diffraction.

Synthesis of *poly*-[$Zn_7$84**$_6$]·($C_2H_8N)_4$·($H_2O)_{45}$ (101)**.

To 1 mL of a 95:5 DMF:H_2O mixture were added **$H_3$84** (15 mg, 0.029 mmol, 1 eq.) and zinc(II) nitrate hexahydrate (11 mg, 0.036 mmol, 1.2 eq.) and the mixture was sealed and heated at 100 °C for 40 hours. The resulting faint yellow crystals were isolated by filtration, washed with DMF, and dried under suction: (13 mg, 0.021 mmol, 72%); mp 348−351°C (decomp.); found C = 42.73, H = 4.10, N = 14.49, calculated for [Zn_7**84**$_6$]·($C_2H_8N)_4$·($H_2O)_{45}$ *i.e* $C_{164}H_{218}N_{46}O_{81}Zn_7$ C = 42.97, H = 4.78, N = 14.06. IR υ_{max} (cm^{-1}) 2977 br, 2371, 2296, 2253, 2044, 1610, 1560, 1550, 1442, 1357, 1258, 1180, 1066, 1019, 907, 861, 851, 839, 817, 791, 773, 761, 738, 728, 717, 705, 694, 684, 672, 659. Phase purity supported by X-ray powder diffraction.

Synthesis of *poly*-[Zn(H84)].

Compound **2** formed as a side-product impurity in the synthesis of **1**. It was characterized by single crystal and powder X-ray diffraction analysis. There were difficulties in optimizing the synthetic conditions required to produce pure phase. Ensuring there was a slight excess of zinc(II) nitrate hexahydrate (1.2 eq. *w.r.t.* **$H_3$84**) gave rise to pure phase **101**.

7.2.5 Synthesis of compounds presented in Chapter 5

General Procedure D: Synthesis of chiral btp ligands 109R/S

To a stirring suspension of $ImSO_2N_3$·H_2SO_4 (1.5 g, 5.54 mmol), K_2CO_3 (1.27 g, 9.22 mmol), and $CuSO_4$·$5H_2O$ (230 mg, 0.92 mmol) in CH_3OH (100 mL) at room temperature (rt) was added the *R*/*S*-amine [(*R*/*S*)-methyl 4-(1-aminoethyl)benzoate] (750 mg, 4.2 mmol). Significant color change (blue to lilac) was observed after 15 h, at which point then 6 mL of an aqueous solution of sodium ascorbate (435mg, 2.2 mmol) and K_2CO_3 (635 mg, 4.6 mmol) was added along with tBuOH (10 mL), and the reaction mixture degassed with argon. A solution of **43** (500 mg, 1.85 mmol) in DMF (10 mL) was added by syringe, and the reaction mixture was stirred at room temperature for 18 h. Reaction mixture was diluted with H_2O (100 mL) followed by aqueous EDTA/NH_4OH (1:9, 50 mL) solution, and product was extracted into EtOAc (50 mL x 2). The organic layer was washed with H_2O (50 mL x2) followed by brine solution (50 mL x 1). The organic layer was dried using $MgSO_4$, filtered and the solvent was removed under reduced pressure. The oil residue was dissolved in a minimum amount of DCM and product was purified by flash chromatography (gradient DCM: CH_3OH (98:2)).

2,6-Bis(1-(4'-(methylcarboxyphenyl)-*R*-1,1-ethylidenyl)-1,2,3-triazol-4-yl)pyridine (109R)

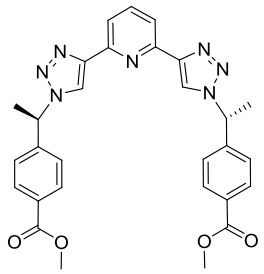

Ligand **109R** was synthesized according to the general procedure D from *R*-methyl 4-(1-aminoethyl)benzoate yielding an orange oil (810 mg, 1.5 mmol, 81 %). HRMS (*m/z*) (APCI$^+$): Calculated for $[M+H]^+$ *i.e.* $C_{29}H_{28}N_7O_4$ *m/z* = 538.2187. Found for $[M+H]^+$ *m/z* = 538.2191. calculated for $C_{29}H_{27}N_7O_4 \cdot 0.49CH_2Cl_2$, C = 61.16, H = 4.87, N = 16.93. Found C = 61.32, H = 5.06, N = 16.46. ^{1}H NMR (400 MHz, $CDCl_3$) δ 8.18 (s (br), 2H, triazole), 8.15 (d, *J* = 7.8 Hz, 2H, pyridyl), 7.99 (d, *J* = 8.2 Hz, 4H, aryl), 7.92 (t, *J* = 7.8 Hz, 1H, pyridyl), 7.31 (d, *J* = 8.1 Hz, 4H, aryl), 5.92 (q, *J* = 7.1 Hz, 2H, methine), 3.94, (s, 6H, methyl), 1.99 (d, *J* = 7.1 Hz, 6H, methyl). ^{13}C NMR (101 MHz, $CDCl_3$) δ 166. 4 (2C, carbonyl), 149.7 (2C, 2,6-pyridyl), 148.0 (1C, 4-pyridyl), 144.5 (2C, 4-aryl), 138.2 (2C, 4-triazolyl), 130.3 (2C, 1-aryl), 130.3 (4C, 2,6-aryl), 126.4 (4C, 3,5-aryl), 120.9 (2C, 5-triazolyl), 119.7 (3,5-pyridyl), 60.0 (2C, methine), 52.3, (2C, carbonylmethyl), 21.0 (2C, methyl). FT-IR (cm^{-1}) 2979, 2624, 2113, 1713, 1610, 1573, 1511, 1431, 1418, 1381, 1314, 1275, 1223, 1181, 1111 ,1037, 1018, 994, 951, 858, 812, 776, 745, 719, 636, 583, 571, 563. UV-Vis (CH_3CN) λ_{max} / nm (ε_{max} /dm^3 mol^{-1} cm^{-1}): 236 *(*43,000), 301 (8,700).

2,6-Bis(1-(4'-(methylcarboxyphenyl)-*S*-1,1-ethylidenyl)-1,2,3-triazol-4-yl)pyridine (109S)

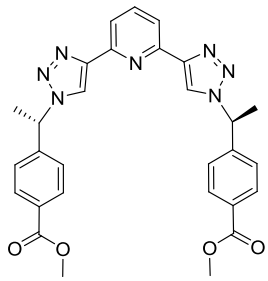

Ligand **109S** was synthesized according to the general procedure D from *S*-methyl 4-(1-aminoethyl)benzoate yielding an orange oil (755 mg, 1.4 mmol, 76 %). HRMS (*m/z*) (APCI$^+$): Calculated for $[M+H]^+$ *i.e.* $C_{29}H_{28}N_7O_4$ *m/z* = 538.2187. Found for $[M+H]^+$ *m/z* = 538.2197. calculated for $C_{29}H_{27}N_7O_4 \cdot H_2O \cdot 0.2NaCl$, C = 61.16, H = 5.13, N = 17.22. Found C = 60.88, H = 5.06, N = 18.24. ^{1}H NMR (400 MHz, $CDCl_3$) δ 8.12 (d, *J* = 7.8 Hz, 2H, pyridyl), 8.12 (s (br), 2H, triazole), 8.02 (d, *J* = 8.3 Hz, 4H, aryl), 7.88 (t, *J* = 7.9 Hz, 1H, pyridyl), 7.35 (d, *J* = 8.3 Hz, 4H, aryl), 5.93 (q, *J* = 7.1 Hz, 2H, methine), 3.92 (s, 6H, methyl), 2.04 (d, *J* = 7.1 Hz, 6H, CH_3). ^{13}C NMR (151 MHz, $CDCl_3$) δ 166.5 (2C, carbonyl), 146.0 (2C, 2,6-pyridyl), 143.8 (1C, 4-pyridyl), 143.8 (2C, 4-aryl),141.0 (2C, 4-triazolyl), 130.7 (2C, 1-aryl), 130.5 (4C, 2,6-aryl), 126.6 (4C, 3,5-aryl), 124.8 (2C, 5-triazolyl), 122.2 (3,5-pyridyl), 61.0 (2C, methine), 52.3 (2C, carbonylmethyl), 21.02 (2C, methyl). UV-Vis (CH_3CN) λ_{max} / nm (ε_{max} /dm^3 mol^{-1} cm^{-1}): 236 *(*43,000), 301

(8,700). FT-IR (cm^{-1}) 3127, 2991, 2952, 2850, 2251, 2112, 1937, 1717 ,1610, 1573, 1433, 1417, 1382, 1313, 1276, 1221 ,1184, 1110, 1035, 1018, 993, 964, 858, 833 ,813, 767 ,745, 719, 706, 663, 651, 593, 583, 570.

General Procedure E: Synthesis of chiral btp ligands 110R/S

To a solution of **110R/S** (363 mg, 0.676 mmol) in CH_3OH (20 mL) was added an aqueous solution of $NaOH_{(aq)}$ (1 M, 3 mL) and allowed to stir at rt. Reaction progress was monitored by TLC and after 17 hours was diluted with H_2O (150 mL) and extracted into EtOAc (30 mL x 3). The organic layer was washed with H_2O (50 mL x2) and dried using $MgSO_4$ before the solvent was removed under reduced pressure. This residue was triturated with CH_3OH, filtered and the solvent was removed under reduced pressure.

Synthesis of 2,6-Bis(1-(4'-(carboxyphenyl)-*R*-1,1-ethylidenyl)-1,2,3-triazol-4-yl)pyridine (110R)

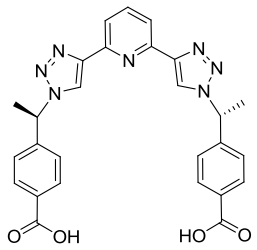

Ligand **110R** was synthesized according to the general procedure E from **109R** yielding a yellow powder (280 mg, 0.55 mmol, 82%). HRMS (*m/z*) (ESI^-): Calculated for $[M-H]^-$ *i.e.* $C_{27}H_{23}N_7O_4Na$ *m/z* = 532.1704. Found for $[M+Na]^+$ *m/z* = 532.1697. calculated for $C_{27}H_{23}N_7O_4 \cdot 0.16NaCl \cdot 0.76CH_3OH$, C = 61.38, H = 4.83, N = 18.05. Found C = 61.49, H = 4.49, N = 17.75. ^1H NMR (600 MHz, DMSO-d_6) δ 8.78 (s, 2H, pyridyl), 7.99 (app s, 3H, triazole and pyridyl), 7.95 (d, *J* = 7.6 Hz, 4H, 2,6-aryl), 7.45 (d, *J* = 7.6 Hz, 4H, 3,5-aryl), 6.15 (q, *J* = 6.8 Hz, 2H, methine), 1.99 (d, *J* = 6.8 Hz, 6H, methyl). ^{13}C NMR (151 MHz, DMSO-d_6) δ 167.4 (2C, carbonyl), 150.3 (2C, 4-triazolyl), 147.7 (2C, 2,6-pyridyl), 146.1 (2C, 1-aryl), 138.9 (1C, 4-pyridyl), 131.0 (2C, 4-aryl) , 130.3 (4C, 2,6-aryl), 127.0 (4C, 3,5-aryl), 123.0 (2C, 3,5-pyridyl), 119.0 (2C, 5-triazolyl), 59.7 (2C, methine), 21.4 (2C, methyl). UV-Vis (CH_3OH:CH_3CN (4:96)) λ_{max} / nm (ε_{max} /dm^3 mol^{-1} cm^{-1}): 236 *(*46,000), 301 (9,100). FT-IR (cm^{-1}), 2983, 2506, 2162, 1980, 1691, 1610, 1573, 1512, 1419, 1381,1315, 1223, 1180, 1111, 1091, 1038, 994, 859, 811, 776, 744, 718, 628, 606, 589, 576, 554.

Synthesis of 2,6-Bis(1-(4'-(carboxyphenyl)-*S*-1,1-ethylidenyl)-1,2,3-triazol-4-yl)pyridine (110S)

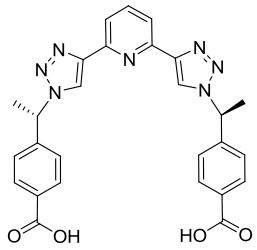

Ligand **110S** was synthesized according to the general procedure E from **109S** yielding a yellow powder (250 mg, 0.49 mmol, 73%). HRMS (*m/z*) (ESI$^-$): Calculated for [M-H]$^-$ *i.e.* $C_{27}H_{22}N_7O_4$ *m/z* = 508.1738. Found for [M-H]$^-$ *m/z* = 508.1747. calculated for $C_{27}H_{23}N_7O_4 \cdot 0.2NaCl \cdot 0.5CH_3OH$, C = 61.58, H = 4.70, N = 18.27. Found C = 61.68, H = 4.39, N = 18.0. ^{1}H NMR (400 MHz, DMSO-d_6) δ 8.78 (d, *J* = 1.9 Hz, 2H, triazol), 8.00 – 7.97 (t, *J* = 1.9 Hz, 3H, pyridyl), 7.98 (s, 2H, triazole), 7.94 (d, *J* = 8.1 Hz, 4H, 2,6-aryl), 7.45 (d, *J* = 8.1 Hz, 4H, 3,5-aryl), 6.15 (q, *J* = 7.0 Hz, 2H, methine), 1.99 (d, *J* = 7.0 Hz, 6H, methyl). ^{13}C NMR (151 MHz, DMSO-d_6) δ 167.6 (2C, carbonyl), 150.3 (2C, 4-triazolyl), 147.7 (2C, 2,6-pyridyl), 145.7 (2C, 1-aryl), 138.8 (1C, 4-pyridyl), 131.0 (2C, 4-aryl), 130.3 (4C, 2,6-aryl), 126.9 (4C, 3,5-aryl), 123.0 (2C, 3,5-pyridyl), 119.1 (2C, 5-triazolyl), 59.8 (2C, methine), 21.6 (2C, methyl). UV-Vis (CH_3OH:CH_3CN (4:96)) λ_{max} / nm (ε_{max} /dm^3 mol^{-1} cm^{-1}): 236 *(*46,000), 301 (9,100). FT-IR (cm-1), 2500, 1975, 1690, 1610, 1572, 1418, 1314, 1222, 1179, 1111, 1038, 1017, 994, 859, 811, 776, 743, 718, 627, 604, 590, 576, 555.

General Procedure F: Synthesis of chiral btp ligands 103R/S and btp ligand 104

A solution of the relevant **btp** acid (300 mg, 0.59 mmol), DMAP (75 mg, 0.62 mmol), allylamine (132 µL, 1.78 mmol), TEA (173 µL, 1.24 mmol) in anhydrous DCM:DMF (4:1, 150 mL) was degassed with Argon and cooled to 0 °C for 30 minutes. EDCI·HCl (353 mg, 1.78 mmol) was added and the reaction mixture was allowed to warm to rt and stirred 66 hours. The solvent was removed under reduced pressure and the oil residue was dissolved in a minimum amount of DCM and product was purified by flash chromatography (gradient DCM: CH_3OH (95:5)).

2,6-Bis(1-(4'-(*N*-allylphenylcaboxamido)-*R*-1,1-ethylidenyl)-1,2,3-triazol-4-yl)pyridine (103R)

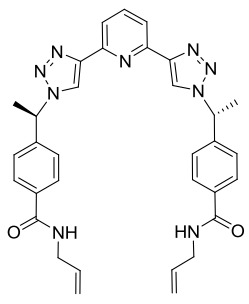

Ligand **103R** was synthesized according to the general procedure F from **110R** yielding a white powder (131 mg, 0.224 mmol, 38%). m.p. 110.1-113.9°C. HRMS (*m/z*) (MALDI$^+$): Calculated for [M+H]$^+$ *i.e.* $C_{33}H_{34}N_9O_2$ *m/z* = 588.2835. Found for [M+H]$^+$ *m/z* = 588.2853. calculated for $C_{33}H_{33}N_9O_2 \cdot 0.25CH_2Cl_2 \cdot 0.04CH_3OH$, C = 65.51, H = 5.56, N = 20.65. Found C = 65.52, H = 5.53, N = 20.62. ^{1}H NMR (400

MHz, $CDCl_3$) δ 8.22 (s, 2H, triazole), 8.13 (d, *J* = 7.8 Hz, 2H, pyridyl), 7.96 (t, *J* = 7.8 Hz, 1H, pyridyl), 7.49 (d, *J* = 8.1 Hz, 4H, 2,6-aryl), 6.92 (d, *J* = 7.8 Hz, 4H, 3,5-aryl), 6.80 (s, 2H, NH), 6.03 (ddd, *J* = 17.2, 10.2, 5.6 Hz, 2H, 2-olefin), 5.74 (q, *J* = 7.0 Hz, 2H, methine), 5.37 (dd, *J* = 17.2, 1.4 Hz, 2H, 1-olefin), 5.26 (dd, *J* = 10.2, 1.4 Hz, 2H, 1-olefin), 4.15 (t, *J* = 5.7 Hz, 4H, methylene), 1.63 (d, *J* = 7.0 Hz, 6H, methyl).^{13}C NMR (101 MHz, $CDCl_3$) δ 167.1 (2C, carbonyl), 149.8 (2C, 2,6-pyridyl), 148.4 (2C, 4-triazolyl), 141.9 (2C, 4-aryl), 138.5 (1C, 4-pyridyl), 135.2 (2C, 1-aryl), 134.1 (2C, 2-olefin), 127.7 (4C, 2,6-aryl), 126.1 (4C, 3,5-aryl), 120.6 (2C, 5-triazolyl), 119.4 (2C, 3,5-pyridyl), 116.9 (2C, 1-olefin), 59.6 (2C, methine), 42.6 (2C, methylene), 20.3 (2C, methyl). UV-Vis (CH_3CN) λ_{max} / nm (ε_{max} /dm^3 mol^{-1} cm^{-1}): 236 *(*43,000), 301 (8,800). FT-IR (cm-1), 3302, 3083, 2983, 1638, 1610, 1572, 1535, 1501, 1450, 1429, 1381, 1345, 1301, 1260, 1221, 1164, 1089, 1036, 1018, 993, 918, 854, 813, 788, 766, 719, 669, 615, 572.

2,6-Bis(1-(1-(4'-(*N*-allylphenylcaboxamido)-*S*-1,1-ethylidenyl)-1,2,3-triazol-4-yl)pyridine (103S)

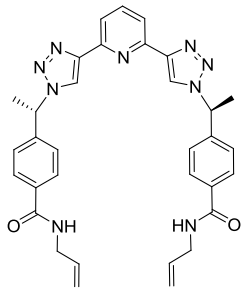

Ligand **103S** was synthesized according to the general procedure F from **110S** yielding a white powder (169 mg, 0.28 mmol, 48%). m.p. 110.3-114.1 °C. HRMS (*m/z*) (MALDI$^+$): Calculated for $[M+H]^+$ *i.e.* $C_{33}H_{34}N_9O_2$ *m/z* = 588.2835. Found for $[M+H]^+$ *m/z* = 588.2850. calculated for $C_{33}H_{33}N_9O_2 \cdot 0.22CH_2Cl_2 \cdot 0.16CH_3OH$, C = 65.55, H = 5.62, N = 20.61. Found C = 65.56, H = 5.59, N = 20.58. ^{1}H NMR (400 MHz, $CDCl_3$) δ 8.14 (s, 2H, triazole), 8.10 (d, *J* = 7.8 Hz, 2H, pyridyl), 7.92 (t, *J* = 7.8 Hz, 2H, pyridyl), 7.56 (d, *J* = 8.0 Hz, 4H, 2,6-aryl), 7.04 (d, *J* = 8.0 Hz, 4H, 3,5-aryl), 6.66 (s (br), 2H, NH), 5.99 (ddd, *J* = 7.2, 10.4, 6.4 Hz, 2H, 2-olefin), 5.77 (q, *J* = 5.7 Hz, 2H, methine), 5.32 (dd, *J* = 17.2, 1.4 Hz, 2H, 1-olefin), 5.22 (dd, *J* = 10.3, 1.4 Hz, 4H, 1-olefin) 4.12 (t, *J* = 5.7 Hz, 4H, methylene), 1.72 (d, *J* = 6.7 Hz, 6H, CH_{methyl}). ^{13}C NMR (101 MHz, $CDCl_3$) δ 167.1 (2C, carbonyl), 149.8 (2C, 2,6-pyridyl), 148.1 (2C, 4-triazolyl), 141.9 (2C, 4-aryl), 138.5 (1C, 4-pyridyl), 135.2 (2C, 1-aryl), 134.1 (2C, 2-olefin), 127.7 (4C, 2,6-aryl), 126.1 (4C, 3,5-aryl), 120.6 (2C, 5-triazolyl), 119.4 (2C, 3,5-pyridyl), 116.8 (2C, 1-olefin), 59.6 (2C, methine), 42.6 (2C, methylene), 20.3 (2C, methyl). UV-vis (CH_3CN) λ_{max} / nm (ε_{max} /dm^3 mol^{-1} cm^{-1}): 236 *(*43,000), 301 (8,800). FT-IR (cm^{-1}), 3302, 3081, 2985, 2937, 1638, 1611, 1572, 1535, 1501, 1450, 1429, 1381, 1345, 1301, 1260, 1221, 1166, 1090, 1036, 1018, 993, 919, 854, 813, 788, 766, 719, 676, 626, 583.

Synthesis of 2,6-Bis(1-(4-(*N*-allyl-phenylcarboxamido)methylene)-1,2,3-triazol-4-yl)-4-(benzylcarboxy)pyridine (104)

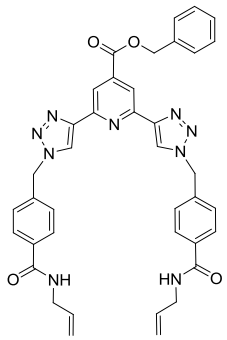

Ligand **104** was synthesized according to the general procedure F from **86** (166 mg, 0.27 mmol) yielding a white powder (34 mg, 0.049 mmol, 18%). HRMS (*m/z*) (MALDI$^+$): Calculated for $[M+Na]^+$ *i.e.* $C_{39}H_{58}N_9O_4Na$ *m/z* = 716.2710. Found for $[M+Na]^+$ *m/z* = 716.2741. ^{1}H NMR (600 MHz, DMSO-d_6) δ 8.81 (s, 2H, triazole), 8.67 (t, *J* = 5.6 Hz, 2 NH), 8.38 (s, 2H, pyridyl), 7.87 (d, *J* = 8.4 Hz, 4H, 2,6-aryl), 7.54 (d, *J* = 7.1 Hz, 2H, *o*-benzyl), 7.43 (m, 7H, 3,5-aryl and *m*-benzyl), 5.87 (ddt, *J* = 17.2, 10.3, 5.2 Hz, 2H, 2-olefin), 5.78 (s, 4H, methylene), 5.46 (s, 2H, methylene), 5.15 (ddd, *J* = 17.2, 3.5, 1.7 Hz, 2H,1-olefin), 5.07 (ddd, *J* = 10.3, 3.5, 1.7 Hz, 2H, 1-olefin), 3.88 (app tt, *J* = 5.6, 1.7 Hz, 4H, methylene). ^{13}C NMR (151 MHz, DMSO-d_6) δ 166.0 (2C, carbonyl), 164.6 (1C, carbonyl), 151.6 (2C, 2,6-pyridyl), 147.1 (5-triazolyl), 139.6 (1C, 4-pyridyl), 139.2 (2C, 1-aryl), 136.0 (2C, 2-olefin), 135.8 (1C, 1-phenyl), 134.8 (2C, 4-aryl), 129.1 (2C, 3,5-benzyl), 128.9 (1C, 4-benzyl), 128.9 (2C, 2,6-benzyl), 128.3 (4C, 2,6-aryl), 128.2 (4C, 3,5-aryl), 124.8 (2C, 4-triazolyl), 117.5 (2C, 3,5-pyridyl), 115.6 (2C, 1-olefin), 67.8 (1C, methylene), 53.2 (2C, methylene), 41.9 (2C, methylene). . UV-Vis (CH_3CN:$CHCl_3$ (4:1)) λ_{max} / nm (ε_{max} /dm^3 mol^{-1} cm^{-1}): 238 *(*54,000), 328 (9,500).

General Procedure G: Synthesis of chiral btp [2]catenanes 111R/S and macrocycles 112R/S and [2]catenane 113 and macrocycle 114.

A solution of the relevant olefin (169 mg, 0.288 mmol) in anhydrous DCM (40 mL) was degassed with argon. A solution of Hoveyda–Grubbs 2nd generation catalyst (90 mg, 0.144 mmol, 50 mol%) in anhydrous DCM (20 mL) was added under inert conditions and after further degassing, the solution was allowed to stir at rt in darkness for 7 days. The reaction mixture was concentrated under reduced pressure and purified by flash chromatography (gradient DCM: CH_3OH (95:5)).

Synthesis of [2]Catenane 111R

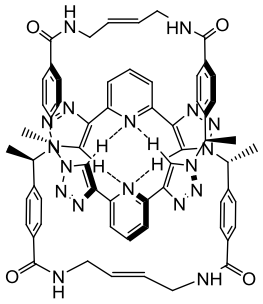

[2]catenane **111R** was synthesized according to the general procedure G from **103R.** The reaction mixture was concentrated under reduced pressure and purified by flash chromatography (gradient DCM: CH_3OH (95:5)) yielding a beige powder (67 mg, 0.061 mmol, 42%). m.p. 238°C decomp. HRMS (*m/z*) (MALDI$^+$): Calculated for $[M+Na]^+$ *i.e.* $C_{62}H_{58}N_{18}O_4Na$ *m/z* = 1141.4786. Found for $[M+Na]^+$ *m/z* = 1141.4824. calculated for $C_{33}H_{33}N_9O_2 \cdot 1.31CH_2Cl_2$, C = 61.81, H = 4.97, N = 20.49. Found C = 61.99, H = 5.00, N = 20.49. ^{1}H NMR (400 MHz, DMSO-*d*$_6$) δ 8.16 (t, *J* = 5.5 Hz, 2H, NH), 8.04 (t, *J* = 7.8 Hz, 1H, pyridyl), 7.89 (s, 2H, triazolyl), 7.81 (d, *J* = 7.8 Hz, 2H, pyridyl), 7.26 (d, *J* = 8.3 Hz, 4H, 2,6-aryl), 6.32 (d, *J* = 8.3 Hz, 4H, 3,5-aryl), 6.13 (s, 2H, olefin), 5.47 (q, *J* = 6.9 Hz, 2H, methine), 4.00 (s, 4H, methylene), 1.33 (d, *J* = 6.9 Hz, 6H, methyl). ^{13}C NMR (151 MHz, DMSO-*d*$_6$) δ 165.9 (2C, carbonyl), 149.3 (2C, 2,6-pyridyl), 147.6 (2C, 4-triazolyl), 142.5 (2C, 1-aryl), 138.5 (1C, 4-pyridyl), 134.3 (2C, 4-aryl), 128.7 (2C, olefin), 127.6 (4C, 2,6-aryl), 125.0 (4C, 3,5-aryl), 121.4 (2C, 5-triazolyl), 119.2 (2C, 3,5-pyridyl), 58.8 (2C, methine), 40.3 (2C, methylene), 20.3 (2C, methyl). UV-Vis (CH_3CN) λ_{max} / nm (ε_{max} /dm^{3}mol^{-1}cm^{-1}): 231 (65,000), 306 (14,000). FT-IR (cm^{-1}), 3366, 2922, 1646, 1610, 1572, 1532, 1504, 1434, 1296, 1261, 1220, 1087, 1036, 1019, 966, 854, 815, 767, 717, 582, 563.

Synthesis of [2]Catenane 111S

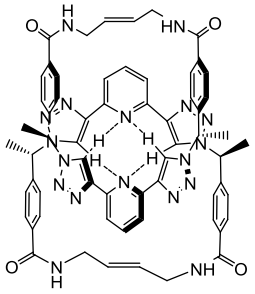

[2]catenane **111S** was synthesized according to the general procedure G from **103S.** The reaction mixture was concentrated under reduced pressure and purified by flash chromatography (gradient DCM: CH_3OH (95:5)) yielding a beige powder (69 mg, 0.062 mmol, 43%). m.p. 238°C decomp. HRMS (*m/z*) (MALDI$^+$): Calculated for $[M+Na]^+$ *i.e.* $C_{62}H_{58}N_{18}O_4Na$ *m/z* = 1141.4786. Found for $[M+Na]^+$ *m/z* = 1141.4813. calculated for $C_{33}H_{33}N_9O_2 \cdot 1.28CH_2Cl_2$, C = 61.90, H = 4.97, N = 20.54. Found C = 61.99, H = 4.64, N = 20.38. ^{1}H NMR (400 MHz, DMSO-*d*$_6$) δ 8.16 (t, *J* = 5.5 Hz, 2H, NH), 8.04 (t, *J* = 7.8 Hz, 1H, pyridyl), 7.89 (s, 2H, triazolyl), 7.81 (d, *J* = 7.8 Hz, 2H, pyridyl), 7.26 (d, *J* = 8.3 Hz, 4H, 2,6-aryl), 6.32 (d, *J* = 8.3 Hz, 4H, 3,5-aryl), 6.14 (s, 2H, olefin), 5.47 (q, *J* = 6.9 Hz, 2H, methine), 4.00 (s, 4H, methylene), 1.33 (d, *J* = 6.9 Hz, 6H, methyl). ^{13}C NMR (151 MHz, DMSO-*d*$_6$) δ 165.9 (2C, carbonyl), 149.3 (2C, 2,6-pyridyl), 147.6 (2C, 4-triazolyl), 142.5 (2C, 1-aryl), 138.5 (1C, 4-pyridyl), 134.3 (2C, 4-aryl), 128.7 (2C, olefin),

127.6 (4C, 2,6-aryl), 125.0 (4C, 3,5-aryl), 121.4 (2C, 5-triazolyl), 119.2 (2C, 3,5-pyridyl), 58.8 (2C, methine), 40.3 (2C, methylene), 20.3 (2C, methyl). UV-Vis (CH_3CN) λ_{max} / nm (ε_{max} /dm^3 mol^{-1} cm^{-1}): 231 *(*65,000), 306 (14,000). FT-IR (cm^{-1}), 3360, 3103, 2924, 1646, 1610, 1571, 1534, 1502, 1432, 1379, 1348, 1296, 1261, 1220, 1180, 1152, 1088, 1036, 1019, 969, 854, 815, 767, 746, 717, 650, 599, 569, 558.

Synthesis of Macrocycle 112R

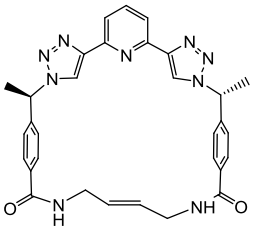

Macrocycle **112R** was synthesized according to the general procedure G from **103R.** The reaction mixture was concentrated under reduced pressure and purified by flash chromatography (gradient DCM: CH_3OH (95:5)) yielding a beige powder (12 mg, 0.022 mmol, 8%). HRMS (*m/z*) (MALDI$^+$): Calculated for $[M+H]^+$ *i.e.* $C_{31}H_{30}N_9O_2$ *m/z* = 560.2522. Found for $[M+H]^+$ *m/z* = 560.2548. ^{1}H NMR (400 MHz, DMSO-d_6) δ 8.54 (t, *J* = 5.7 Hz, 2 NH), 8.26 (s, 2H, triazole), 7.97 (s, 3H, pyridyl), 7.78 (d, *J* = 8.4 Hz, 4H, aryl), 7.28 (d, *J* = 8.4 Hz, 4H, aryl), 6.06 (q, *J* = 7.1 Hz, 2H, methine), 5.50 (app t, *J* = 2.4 Hz, 2H, olefin), 3.84 (ddd, *J* = 17, 15, 5.7 Hz, 4H), 1.95 (d, *J* = 7.0 Hz, 6H, methyl).^{13}C NMR (151 MHz, DMSO-d_6) δ 165.7 (2C, carbonyl), 150.3 (2C, 2,6-pyridyl), 148.3 (2C, 4-triazolyl), 144.1 (2C, 1-aryl), 134.8 (2C, 4-aryl), 128.3 (4C, 2,6-aryl), 128.3 (2C, olefin), 127.0 (4C, 3,5-aryl), 122.5 (2C, 5-triazolyl), 119.2 (2C, 3,5-pyridyl), 59.7 (2C, methine), 39.7 (2C, methylene, overlaps with solvent peak, assigned by HSQC), 20.8 (2C, methyl).

Synthesis of Macrocycle 112S

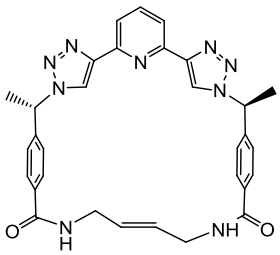

Macrocycle **112S** was synthesized according to the general procedure G from **103S.** The reaction mixture was concentrated under reduced pressure and purified by flash chromatography (gradient DCM: CH_3OH (95:5)) yielding a beige powder (22 mg, 0.039 mmol, 14%). HRMS (*m/z*) (MALDI$^+$): Calculated for $[M+H]^+$ *i.e.* $C_{31}H_{30}N_9O_2$ *m/z* = 560.2522. Found for $[M+H]^+$ *m/z* = 560.2553. ^{1}H NMR (600 MHz, DMSO-d_6) δ 8.56 (t, *J* = 5.8 Hz, 2H, NH), 8.28 (s, 2H, triazolyl), 7.99 (s, 3H, pyridyl), 7.80 (d, *J* = 8.4 Hz, 4H, aryl), 7.31 (d, *J* = 8.4 Hz, 4H, aryl), 6.08 (q, *J* = 7.0 Hz, 2H, methine), 5.53 (app t, *J* = 2.4 Hz, 2H, olefin), 3.86 (ddd, *J* = 19.9, 15.2, 5.7 Hz, 4H, methylene), 1.97 (d, *J* = 7.0 Hz, 6H, methyl). ^{13}C NMR (151 MHz, DMSO-d_6) δ 165.7 (2C, carbonyl), 150.3 (2C, 2,6-pyridyl), 148.3 (2C, 4-triazolyl), 144.1 (2C, 1-aryl), 134.8 (2C, 4-aryl), 128.3 (4C, 2,6-aryl), 128.3 (2C, olefin), 127.0 (4C, 3,5-aryl), 122.5 (2C, 5-triazolyl), 119.2 (2C, 3,5-pyridyl), 59.7 (2C, methine), 39.9 (2C, methylene, overlaps with solvent peak, assigned by

HSQC), 20.8 (2C, methyl). UV-Vis (CH_3CN:$CHCl_3$ (19:1)) λ_{max} / nm (ε_{max} /dm^3 mol^{-1} cm^{-1}): 232 *(*60,000), 302 (11,500).

Synthesis of [2]Catenane 113

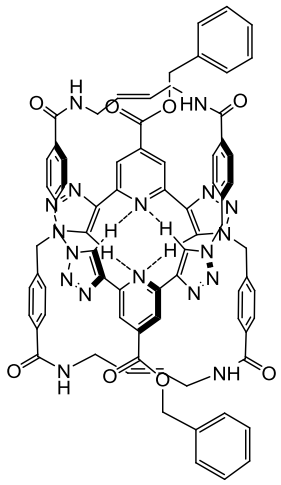

[2]catenane **113** was synthesized according to the general procedure G from **104** (10mg, 0.0144 mmol). The reaction mixture was concentrated under reduced pressure and purified by flash chromatography (gradient DCM: CH_3OH (98:2)) yielding a beige powder containing both [2]catenane **113** and macrocycle **114**. Trituration with CH_3CN yielded a white crystalline material (8 mg, 0.0058 mmol, 40 %). HRMS (*m/z*) (MALDI$^+$): Calculated for [M+Na]$^+$ *i.e.* $C_{74}H_{62}N_{18}O_8Na$ *m/z* = 1353.4896. Found for [M+Na]$^+$ *m/z* = 1353.4913. ^{1}H NMR (400 MHz, 80 °C, DMSO-*d*$_6$) δ 8.22 (s, 2H, pyridyl), 7.84 (s, 2H, triazole), 7.81 (t, *J* = 5.7 Hz, 2H, NH), 7.69 (d, *J* = 7.4 Hz, 2H, *o*-benzyl), 7.52 (t, *J* = 7.4 Hz, 2H, *m*-benzyl), 7.44 (t, *J* = 7.4 Hz, 1H, *p*-benzyl), 7.18 (d, *J* = 8.1 Hz, 4H, 2,6-aryl), 6.49 (d, *J* = 8.1 Hz, 4H, 3,5-aryl), 6.08 (s, 2H, olefin), 5.63 (s, 2H, benzyl-methylene), 5.18 (s, 4H, methylene), 3.98 (s, 4H, allyl-methylene). ^{13}C NMR (151 MHz, DMSO-*d*$_6$) δ 166.3 (1C, carbonyl), 165.0 (2C, carbonyl), 150.3 (2C, 2,6-pyridyl), 147.2 (2C, 4-triazolyl), 139.6 (1C, 4-pyridyl), 137.4, (1C, 1-benzyl), 136.2 (2C, 1-aryl), 134.7 (2C, 4-aryl), 129.2 (2C, 3,5-benzyl), 128.9 (2C, olefin), 128.8 (1C, 4-benzyl), 128.8 (2C, 2,6-benzyl), 127.4 (4C, 2,6-aryl), 126.9 (4C, 3,5-aryl), 67.9 (1C, methylene), 53.0 (2C, methylene), 40.1 (2C, methylene).

Synthesis of Macrocycle 114

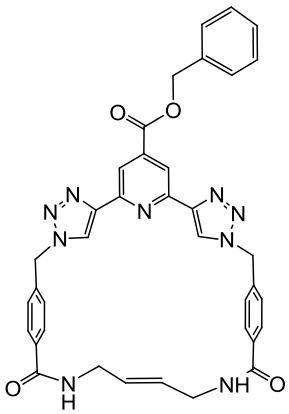

Macrocycle **114** was synthesized according to the general procedure G from **104**. The reaction mixture was concentrated under reduced pressure and purified by flash chromatography (gradient DCM: CH_3OH (98:2)) yielding a beige powder containing both [2]catenane **113** and macrocycle **114**. Recrystallisation from acetonitrile yielded a brown crystalline material, however, **114** could not be achieved in isolation. HRMS (*m/z*) (MALDI$^+$): Calculated for [M+Na]$^+$ *i.e.* $C_{37}H_{31}N_9O_4Na$ *m/z* = 688.2397. Found for [M+Na]$^+$ *m/z* = 688.2409.

2,6-Bis(1-(3-(methylcarboxy)benzyl)-1,2,3-triazol-4-yl)pyridine (115)

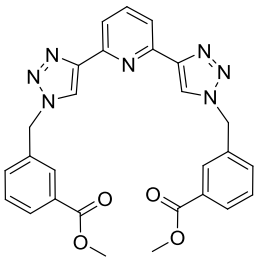

To a solution of methyl 3-(bromomethyl)benzoate (2.109 g; 9.21 mmol) in DMF: H_2O (4:1, 70 mL) was added NaN_3 (0.599 g; 9.21 mmol). This was stirred at room temperature (rt) for 60 minutes before adding **43** (1 g; 3.68 mmol), $CuSO_4 \cdot 5H_2O$ (0.368 g, 1.47 mmol) and sodium ascorbate (0.584 g; 2.95 mmol), followed by K_2CO_3 (1.018 g; 7.37 mmol). The reaction mixture was degassed under argon and stirred at rt for 18 hours. The reaction mixture was added to a solution of aqueous EDTA/NH_4OH (1:9, 50 mL) and was extracted with EtOAc (50 mL x 2) and the organic layer washed with H_2O (50 mL x 2) followed by brine (50 mL). The EtOAc layer was dried over $MgSO_4$ and concentrated under reduced pressure to yield a brown solid. The crude residue was triturated with cold CH_3OH, yielding a beige solid (1.613 g, 3.17 mmol, 86%). m.p.: 170.6-172.4°C; HRMS (*m/z*) (ESI^+): Calculated for $C_{27}H_{23}N_7O_4Na^+$ *m/z* = 532.1709 $[M+Na]^+$. Found *m/z* = 532.1698; δH (400MHz, $CDCl_3$, ppm): 8.11 (s, 2H, triazolyl CH), 8.09 (d, *J* = 7.8Hz, 2H, 3- and 5-pyridyl CH), 7.99-8.03 (m, 4H, phenyl CH), 7.88 (t, *J* = 7.8Hz, 1H, 4-pyridyl), 7.41-7.47 (m, 4H, phenyl CH), 5.60 (s, 4H, CH_2), 3.91 (s, 6H, CH_3); δC (151 MHz, $CDCl_3$, ppm): 166.3 (C=O), 149.6 (2C, 2,6-pyridyl), 148.5 (2C, 4-triazolyl), 138.0 (1C, 4-pyridyl CH), 134.9 (2C, 3-aryl), 132.5 (2C, 6-aryl CH), 131.1 (2C, 1-aryl), 130.0 (2C, 2-aryl), 129.3 (2C, 4-aryl), 129.1 (2C, 5-aryl), 122.2 (2C, 5-triazolyl), 119.6 (2C, 3,5-pyridyl), 53.9 (2C, methylene), 52.3 (2C, methyl); FT-IR (cm^{-1}): 3154, 2952, 1718 (C=O), 1608, 1574, 1430, 1364, 1304, 1261, 1200, 1156, 1102, 1083, 1044, 992, 977, 911, 821, 801, 755, 730, 673.

Synthesis of 2,6-Bis(1-(3-(carboxy)benzyl)-1,2,3-triazol-4-yl)pyridine (116)

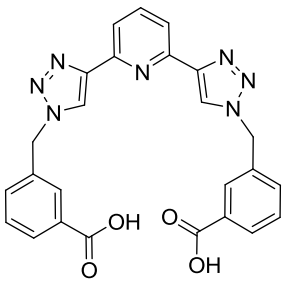

To a solution of **115** (1.5 g; 2.94 mmol) in EtOH (40 ml) was added an aqueous solution of KOH (0.413 g, 7.36 mmol) in H_2O (10 mL). The reaction mixture was refluxed at 85 °C for 17 hours. The reaction mixture was concentrated under reduced pressure and acidified to pH 1 with $HCl_{(aq)}$ (1 M). This was extracted with EtOAc (50 mL x 2) and the organic layer washed with H_2O (50 mL x 2) followed by brine solution (50 mL x 1). The EtOAc layer was dried over $MgSO_4$ and concentrated under reduced pressure to yield a beige solid (1.228 g; 2.55 mmol; 87%). m.p.: 286 °C (decomp.); HRMS (*m/z*) (ESI^-): Calculated for $C_{25}H_{18}N_7O_4^-$ *m/z* = 480.1420 $[M-H]^-$. Found *m/z* = 480.1415; δH (400MHz, DMSO-d_6, ppm): 13.12 (s, 2H, OH), 8.73 (s, 2H, triazolyl CH), 7.98 (m, 3H, 3, 4, 5-pyridyl CH), 7.90-7.93 (m, 4H, phenyl CH), 7.62 (d, *J* =

7.8 Hz, 2H, phenyl CH), 7.53 (t, *J* = 7.8Hz, 2H, phenyl CH), 5.79 (s, 4H, CH_2); δC (151 MHz, DMSO-d_6, ppm): 167.0 (C=O), 149.8 (2C, 2, 6-pyridyl), 147.4 (2C, 4-triazolyl), 138.4 (1C, 4-pyridyl), 136.6 (2C, 3-aryl), 132.4 (6-aryl), 131.3 (2C, 1-aryl), 129.3 (4-aryl), 129.1 (2C, 2-aryl), 128.7 (5-aryl), 123.8 (5-triazolyl), 118.6 (3, 5-pyridyl), 52.6 (CH_2); FT-IR (ATR, cm^{-1}): 3134, 2784, 2506, 1680 (C=O), 1609, 1575, 1534, 1271, 1235, 1189, 1082, 1040, 993, 811, 794, 746, 729, 681.

General Procedure G: Synthesis of btp ligands 105 and 106

Acid **116** (0.500 g, 1.04 mmol), HOBt (0.29 g, 2.18 mmol), DMAP (0.133 g; 1.09 mmol) TEA (0.304 ml, 2.18 mmol) and the appropriate alkyl amine (2.28 mmol) were dissolved in DCM: DMF (4:1, 70 mL) and stirred at 0°C for 30 mins. EDCI·HCl (0.597 g; 3.12 mmol) was added and the reaction mixture stirred for a further 30 mins at 0°C, under argon. The reaction mixture was then allowed to reach room temperature and stirred for 66 hours. The reaction mixture was diluted with DCM and washed with $HCl_{(aq)}$ (1 M), saturated $NaHCO_{3(aq)}$ and H_2O. The organic layer was washed with brine and dried over $MgSO_4$. The solution was then concentrated under reduced pressure to give a pale yellow solid.

2,6-Bis(1-(3-(*N*-undecenyl-phenylcarboxamide)methylene)-1,2,3-triazol-4-yl)pyridine (105)

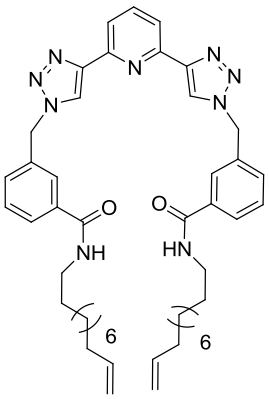

Ligand **105** was synthesised according to general procedure G from **116** and 11-amino-1-undecene. The crude product was triturated with cold methanol, yielding a white solid (0.350 g; 0.446 mmol; 43%). m.p. 198.4-201.1°C; HRMS (*m/z*) (ESI^-): Calculated for $C_{47}H_{60}N_9O_2^-$ *m/z* = 783.4948 $[M-H]^-$. Found *m/z* = 782.4886; calculated for $C_{47}H_{61}N_9O_2$, C = 72.00, H = 7.84, N = 16.08. Found, C = 71.81, H = 7.87, N = 15.88. δ_H (400MHz, $CDCl_3$, ppm): 10.08 (s, 2H, triazolyl CH), 8.56 (d, *J* = 8Hz, 2H, 3- and 5-pyridyl CH), 8.34 (t, *J* = 8Hz, 2H, 4-pyridyl CH), 7.85 (overlapping s and d, 4H, phenyl CH), 7.52 (d, *J* = 7.6Hz, 2H, phenyl CH), 7.45 (t, *J* = 7.9Hz 2H, phenyl CH), 7.15 (s, 2H, NH), 5.73–5.83 (m, 2H, alkene CH), 5.66 (s, 4H, CH_2), 4.90-4.99 (m, 4H, terminal alkene CH_2), 3.41 (q, *J* = 6.8Hz, 4H, CH_2), 2.00 (q, *J* = 6.8Hz, 4H, CH_2), 1.62 (qt, *J* = 7.6Hz, 4H, CH_2), 1.23-1.33 (m, 26H, CH_2); δ_C (151 MHz, $CDCl_3$, ppm): 166.9 (C=O), 149.4 (qt, 2- and 6-pyridyl), 148.0 (qt, triazolyl), 139.3 (alkene CH), 138.3 (4-pyridyl CH), 135.9 (qt, phenyl), 134.9 (qt, phenyl), 131.0 (phenyl CH), 129.4 (phenyl CH), 127.5 (phenyl CH), 127.0 (phenyl CH), 122.7 (3- and 5-pyridyl CH), 119.5 (triazolyl CH), 114.2 (terminal alkene CH_2), 54.1 (CH_2),

40.3 (CH_2), 33.9 (CH_2), 29.6 (CH_2), 29.5 (CH_2), 29.5 (CH_2), 29.4 (CH_2), 29.2 (CH_2), 29.0 (CH_2), 27.1 (CH_2); FT-IR (ATR, cm^{-1}): 3276, 3077, 2922, 2851, 1632 (C=O), 1605, 1581, 1536, 1421, 1316, 1206, 1194,1165, 1086, 1072, 1043, 992, 976, 908, 814, 800, 785, 739, 721, 707.

2,6-Bis(1-(3-(*N*-allyl-phenylcarboxamide)methylene)-1,2,3-triazol-4-yl)pyridine (106)

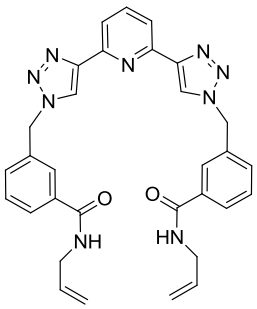

Ligand **106** was synthesised according to General Procedure G from **116** (0.500 g; 1.04 mmol), allylamine (0.171 ml; 0.130 g; 2.28 mmol). The crude product was triturated with cold methanol, yielding a white solid (0.355 g; 0.634 mmol; 61%). m.p.: 198.6-201.3°C; HRMS (*m/z*) (ESI$^+$): Calculated for $C_{31}H_{29}N_9O_2Na^+$ *m/z* = 582.2342 $[M+Na]^+$. Found *m/z* = 582.2318; CHN: Calculated for $C_{31}H_{29}N_9O_2$, C = 66.53, H = 5.22, N = 22.53. Found, C = 66.38, H = 5.12, N = 22.40.; δ_H (400MHz, DMSO-d_6, ppm): 8.70 (s (sh), 4H, triazolyl CH and NH), 7.98 (app t, 3H, 3-, 4- and 5-pyridyl CH), 7.87 (s, 2H, phenyl CH), 7.84 (d, *J* = 5Hz, 2H, phenyl CH), 7.84-7.52 (m, 4H, phenyl CH), 5.86 (m, 2H, alkene CH), 5.75 (s, 4H, CH_2), 5.15 (s, 2H, terminal alkene CH_2), 5.07 (s, 2H, terminal alkene CH_2), 3.88 (app t, 4H, allyl CH_2); δ_C (151 MHz, DMSO-d_6, ppm): 165.1 (C=O), 150.3 (2C, qt, 2,6-pyridyl), 147.9 (2C, qt, 4-triazolyl), 138.8 (1C, 4-pyridyl), 136.6 (qt, 3-aryl), 135.8 (2C, 2-olefin), 135.4 (2C, 1-aryl), 131.2 (2C, 6-aryl), 129.3 (2C, 5-aryl), 127.5 (2C, 4-aryl), 127.3 (2C, 2-aryl), 124.1 (2C, 5-triazolyl), 119.0 (2C, 3,5-pyridyl), 115.7 (2C, 1-olefin), 53.3 (2C, CH_2), 42.0 (2C, allyl CH_2).; FT-IR (ATR, cm^{-1}): 3262, 3072, 1637 (C=O), 1604, 1579, 1542, 1450, 1347, 1309, 1215, 1164, 1072, 1042, 992, 910, 800, 785, 705.

General Procedure H: Synthesis of macrocycles 117 and 118

Ligand **105**/**106** (0.089 mmol) and Hoveyda-Grubbs II catalyst (0.028 g; 0. 035 mmol) were added to a round bottom flask which was then degassed with argon. A CH_3NO_2:CH_2Cl_2 (1:9, 40 mL) solvent system was degassed by bubbling with argon and added to the reagents *via* cannula. The round bottom flask was covered in aluminium foil and the reaction mixture stirred under argon at 60°C for 24 hours in darkness. The reaction mixture was allowed to cool and then allowed to stir at rt for 3 days.

Synthesis of Macrocycle 117

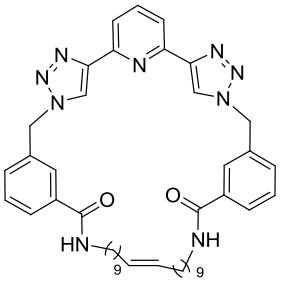

Macrocycle **117** was synthesised according to General Procedure H from ligand **105** ((0.053 g; 0.065 mmol). The reaction mixture was concentrated under reduced pressure and the crude product was purified by flash chromatography (gradient DCM/ CH_3OH). The pure product was obtained as a light brown solid (0.029 g; 0.038 mmol; 58%). m.p. 260.1-261.2°C. HRMS (*m/z*) (ESI^-): Calculated for $C_{45}H_{56}N_9O_2^-$ *m/z* = 754.4557 $[M-H]^-$. Found *m/z* = 754.4568. ^1H NMR (600 MHz, DMSO-d_6) δ 8.68 (s, 2H, triazolyl), 8.49 (t, *J* = 5.2 Hz, 2H, NH), 8.00 (app s, 3H, pyridyl), 7.85 (s, 2H, 2-aryl), 7.81 (d, *J* = 7.6 Hz, 2H, 4-aryl), 7.53 (d, *J* = 7.6 Hz, 2H, 6-aryl), 7.49 (t, *J* = 7.6 Hz, 2H, 5-aryl), 5.76 (s, 4H, methylene), 5.32 (s, 2H, olefin), 3.24 (d, *J* = 6.0 Hz, 4H, methylene), 1.94 (d, *J* = 4.7 Hz, 4H, methylene), 1.50 (d, *J* = 6.4 Hz, 4H, methylene), 1.26 (m, *J* = 24.3 Hz, 24H, methylene). ^{13}C NMR (151 MHz, DMSO-d_6) δ 166.1 (2C, carbonyl), 150.3 (2C, 2,6-pyridyl), 147.9 (2C, 5-triazolyl), 138.8 (1C, 4-pyridyl), 136.5 (2C, 1-aryl), 135.8 (2C, 3-aryl), 131.2 (2C, 6-aryl), 130.7 (2C, olefin), 129.3 (2C, 5-aryl), 127.5 (2C, 2-aryl), 127.3 (2C, 4-aryl), 124.1 (2C, 5-triazolyl), 119.0 (2C, 3,5-pyridyl), 53.4 (2C, methylene), 39.6 (2C, 9-methylene overlap with solvent peak assigned by HSQC) 32.1 (2C, 2-methylene), 29.5 (2C, 8-methylene), 29.3 - 26.9 (12C, alkyl chain methylenes). UV-Vis (CH_3CN:$CHCl_3$) (4:1)) λ_{max} / nm (ε_{max} /dm^3 mol^{-1} cm^{-1}): 231 (17,000), 301 (3,500).

Synthesis of Macrocycle 118

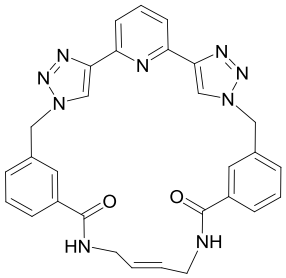

Macrocycle **118** was synthesised according to General Procedure H from ligand **106** (0.050 g; 0.089 mmol). The reaction mixture was diluted with DCM (100 mL) and H_2O (100 mL) was added. The resulting precipitate formed was isolated by vacuum filtration as a brown solid (0.023 g; 0.043 mmol; 49%). HRMS (*m/z*) ($MALDI^+$): Calculated for $C_{29}H_{26}N_9O_2^+$ *m/z* = 532.2209 $[M+H]^+$. Found *m/z* = 532.2236; calculated for $C_{29}H_{25}O_2N_9 \cdot 0.4CH_3OH \cdot 1.6CH_2Cl_2$, C = 54.68, H = 4.39, N=18.5. Found C = 54.81, H = 4.09, N = 18.26. δ_H (400MHz, DMSO-d_6, ppm): 8.72 (s, 2H, NH), 8.46 (s, 2H, triazolyl), 7.97 (app s, 3H, pyridyl), 7.93 (s, 2H, aryl), 7.84 (d, , *J* = 7.7Hz, 2H, aryl), 7.56 (d, *J* = 7.6Hz, 2H, aryl), 7.48 (t, *J* = 7.7Hz, 2H, aryl), 5.71 (s, 4H, CH_2), 5.67 (app s, 2H, olefin), 3.92 (app s, 4H, CH_2); δ_C (150MHz, DMSO-d_6, ppm): 166.0 (C=O), 150.3 (qt, 2,6-pyridyl), 148.1 (qt, triazolyl), 138.8 (pyridyl CH), 136.2 (qt, phenyl), 135.5 (alkene CH), 131.9 (phenyl CH), 129.5 (phenyl CH), 128.2 (phenyl CH), 127.7 (phenyl CH), 123.4 (triazolyl CH), 119.1

(pyridyl CH), 53.6 (CH_2), 40.8 (allyl CH_2). UV-Vis (CH_3CN:$CHCl_3$)(19:1)) λ_{max} / nm (ε_{max} /dm^3 mol^{-1} cm^{-1}): 232 (25,000), 301 (5,200). FT-IR (ATR, cm^{-1}): 3266, 1632 (C=O), 1609, 1584, 1541, 1484, 1461, 1428, 1342, 1303, 1217, 1199, 1147, 1084, 1046, 983, 809, 788, 737, 674.

General Procedure I: Synthesis of btp ligands 107 and 108.

A solution of NaN_3 (253 mg, 3.9 mmol) and the relevant bromo-olefin (850 µL, 3.9 mmol) was stirred in DMF:H_2O (4:1, 5 mL) at 40 °C for 60 minutes. Compound **43** (300 mg, 1.11 mmol) was dissolved in DMF (15 mL) and added along with K_2CO_3 (306 mg, 2.22 mmol) DIPEA (580 µL, 3.33 mmol) CuI (107 mg, 0.56 mmol). This was degassed with Argon and stirred at 100 °C for 60 mins under microwave irradiation. This was diluted with aqueous EDTA/NH_4OH (1:9, 50 mL) solution and extracted into EtOAc (50 mL x 2). The organic layer was washed with H_2O (50 mL x2) and then dried using $MgSO_4$, filtered and the solvent was removed under reduced pressure resulting in a crude oil residue.

2,6-Bis(1-(1-undecen-11-yl)-1,2,3-triazol-4-yl)pyridine 107

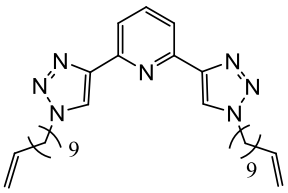

Ligand **107** was synthesized according to the general procedure I from **43** and 11-bromoundec-1-ene. The crude oil residue was purified repeated trituration with cold CH_3OH yielding a white powder which was collected by filtration (485 mg, 0.94 mmol, 85%). m.p. 95–99 °C; HRMS (*m/z*) (ESI^+): Calculated for $[M+Na]^+$ *i.e.* $C_{31}H_{47}N_7Na$ *m/z* = 540.3794. Found for $[M+Na]^+$ *m/z* = 540.3791; calculated for $C_{31}H_{47}N_7$, %C = 71.91, %H = 9.15, %N = 18.94. Found %C = 71.62, %H = 9.31, %N = 18.81. ^1H NMR (400 MHz, $CDCl_3$) δ 8.13 (s, 2H, triazole), 8.08 (d, *J* = 7.8 Hz, 2H, pyridyl), 7.85 (t, *J* = 7.8 Hz, 1H, pyridyl), 5.78 (ddt, *J* = 16.9, 10.1, 7.2 Hz, 2H, 2-olefin), 4.97 (dd, *J* = 16.9, 1.6 Hz, 2H, 1-olefin), 4.91 (dd, *J* = 10.1, 1.0 Hz, 2H, 1-olefin), 4.41 (t, *J* = 7.2 Hz, 4H, CH_2), 2.06–1.88 (m, 8H, CH_2), 1.34 (m, *J* = 5.0 Hz, 12H), 1.26 (s, 12H). ^{13}C NMR (151 MHz, $CDCl_3$) δ 150.1 (2C, 2,6-pyridyl), 148.4 (2C, 4-triazolyl), 139.1 (2C, 2-olefin), 137.7 (1C, 4-pyridyl), 121.8 (2C, 5-triazolyl), 119.3 (2C, 3,5-pyridyl), 114.2 (2C, 1-olefin), 50.6 (2C, methylene), 33.8 (2C, methylene), 30.4 (2C, methylene), 29.3 (2C, methylene), 29.3 (2C, methylene), 29.0 (2C, methylene), 29.0 (2C, methylene), 28.9 (2C, methylene), 26.5 (2C, methylene).

2,6-Bis(1-(1-penten-5-yl)-1,2,3-triazol-4-yl)pyridine 108

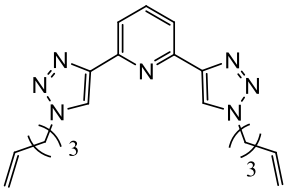

Ligand **108** was synthesized according to the general procedure I from **43** and 5-btomopent-1-ene. The crude oil residue was purified by flash chromatography (gradient DCM: EtOAc (60:40)) yielding an off-white powder (220 mg, 0.59 mmol, 53%). m.p. 61–65 °C; HRMS (*m/z*) (ESI$^+$): Calculated for $[M+Na]^+$ *i.e.* $C_{19}H_{23}N_7Na$ *m/z* = 372.1913. Found for $[M+Na]^+$ *m/z* = 372.1923; calculated for $C_{19}H_{23}N_7$, C = 65.31, H = 6.63, N=28.05. Found C = 65.35, H = 6.65, N = 27.79. ^{1}H NMR (400 MHz, $CDCl_3$) δ 8.15 (s, 2H, triazole), 8.08 (d, *J* = 7.8 Hz, 2H, pyridyl), 7.85 (t, *J* = 7.8 Hz, 1H, pyridyl), 5.80 (ddt, *J* = 16.8, 10.2, 6.3 Hz, 2H, 2-olefin), 5.10 (dd, *J* = 14.1, 1.3 Hz, 2H, 1-olefin), 5.07 (dd, *J* = 7.4 Hz, 1.3 Hz, 2H, 1-olefin), 4.43 (t, *J* = 6.9 Hz, 4H, CH_2), 2.21 – 2.05 (m, 8H, CH_2). ^{13}C NMR (101 MHz, $CDCl_3$) δ 150.0 (2C, 2,6-pyridyl), 148.3 (2C, 4-triazolyl), 137.9 (1C, 4-pyridyl), 136.5 (2-olefin), 122.0 (5-triazolyl), 119.4 (2C, 3,5-pyridyl), 116.4 (2C, 1-olefin), 49.8 (2C, methylene), 30.4 (2C, methylene), 29.3 (2C, methylene). UV-vis (CH_3CN:CH_2Cl_2 (9:1)) λ_{max} / nm (ε_{max} /dm^3 mol^{-1} cm^{-1}): 238 (26,000), 301 (9,500). FT-IR (cm^{-1}), 3105, 3082, 2929, 1688, 1642, 1608, 1573, 1455, 1425, 1374, 1341, 1309, 1255, 1230, 1198, 1148, 1085, 1044, 992, 973, 917, 851, ,818 787, ,744 ,678 663, 648, 626, 581.

Synthesis of Macrocycles 119

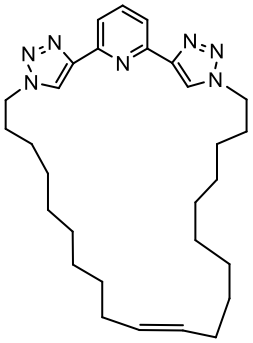

Btp ligand **107** (33 mg, 0.064 mmol) was dissolved in anhydrous DCM (40 mL) was degassed with Argon. A solution of Hoveyda–Grubbs 2nd generation catalyst (12 mg, 0.019 mmol, 30 mol%) in anhydrous DCM (20 mL) was added under inert conditions and after further degassing, the solution was allowed to stir at rt in darkness for 10 days. The reaction mixture was concentrated under reduced pressure and purified by flash chromatography (gradient DCM: EtOAc (95:5)) yielding a white powder (15 mg, 0.03 mmol, 48%). m.p. 193.3-195.4°C. HRMS (*m/z*) (ESI$^+$): Calculated for $[M+Na]^+$ *i.e.* $C_{29}H_{43}N_7Na$ *m/z* = 512.3472. Found for $[M+Na]^+$ *m/z* = 512.3478. ^{1}H NMR (400 MHz, $CDCl_3$) δ 8.17 (s, 2H, triazole), 8.11 (d, *J* = 7.8 Hz, 2H, pyridyl), 7.87 (t, *J* = 7.8 Hz, 1H, pyridyl), 5.36 (t, *J* = 3.6 Hz, 2H, olefin), 4.44 (t, *J* = 7.0 Hz, 4H, CH_2), 1.98 - 1.96 (m, 6H, CH_2), 1.41 – 1.32 (m, 8H, CH_2), 1.27 - 1.25 (m, 16H, CH_2). ^{13}C NMR (101 MHz, $CDCl_3$) δ 150.2 (2C, 2,6-pyridyl), 148.5 (2C, 4-triazolyl), 138.0 (1C, 4-pyridyl), 130.5 (2C, olefin), 122.2 (2C, 5-triazolyl), 119.4 (2C, 3,5-pyridyl), 50.9 (2C, methylene), 32.6 (2C, methylene),

30.4 (2C, methylene), 29.4 (2C, methylene), 29.3 (2C, methylene), 29.2 (2C, methylene), 29.1 (2C, methylene), 28.8 (2C, methylene), 26.6 (2C, methylene).

Synthesis of Macrocycle 120

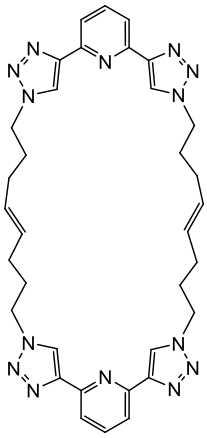

Btp ligand **108** (30 mg, 0.086 mmol), Hoveyda–Grubbs 2nd generation catalyst (15 mg, 0.024 mmol, 30 mol%) were dissolved in anhydrous DCM (5 mL) and degassed with Argon. The resulting solution was heated under microwave irradiation for two hours at 80 °C. The resulting suspension was filtered and the filtrate was concentrated under reduced pressure and purified by flash chromatography (gradient DCM: EtOAc 1:1) yielding an off-white powder. After trituration with cold CH_3OH a white powder was obtained (5 mg, 0.008 mmol, 9 %). HRMS (*m/z*) (ESI^+): Calculated for $[M+H]^+$ *i.e.* $C_{34}H_{39}N_{14}^+$ *m/z* = 643.3462. Found for $[M+H]^+$ *m/z* = 643.3477. ^1H NMR (400 MHz, $CDCl_3$) δ 8.17 (s, 4H, triazole), 8.09 (d, *J* = 7.8 Hz, 4H, pyridyl), 7.87 (t, *J* = 7.8 Hz, 2H, pyridyl), 5.38 (m, 4H, olefin), 4.41 (t, *J* = 6.7 Hz, 8H, CH_2), 2.07 (m, 8H, CH_2), 2.01 (m, 8H, CH_2). ^{13}C NMR (101 MHz, $CDCl_3$) δ 150.2 (4C, 2,6-pyridyl), 148.5 (4C, 4-triazolyl), 138.0 (2C, 3-pyridyl), 129.9 (4C, olefin), 122.1 (4C, 5-triazolyl), 119.5 (4C, 3,5-pyridyl), 50.2 (4C, methylene), 30.0 (4C, methylene), 29.6 (4C, methylene). UV-Vis (CH_3CN) λ_{max} / nm (ε_{max} /dm^3 mol^{-1} cm^{-1}): 238 (23,000), 301 (7,500).

Synthesis of 1,4-(dipyridin-2-yl)-1,2,3-triazole (124)

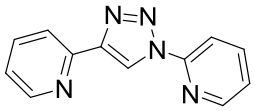

Compoud **124** was synthesised according to a modified literature procedure.[23] The modification is as follows: 2-ethynylpyridine, **126**, (0.8 mL, 8 mmol), tetrakis(acetonitrile)copper(I) hexafluorophosphate, (300 mg, 0.8 mmol) TBTA, (212 mg, 0.4 mmol) was suspended in Toluene (50 mL) which had been previously degassed. Tetrazole, **125**, (480 mg, 4 mmol) was then added and once the mixture was degassed again it was allowed to stir under Argon at 90ºC for 48 hours. The toluene was removed under reduced pressure and the compound was purified by column chromatography using DCM and acetone as eluent (gradient increase of acetone from 0 to 8%) yielding a blue crystalline powder. This was recrystallised from CH_3CN/H_2O (4:1) yielding colourless transparent needles (610 mg, 2.74 mmol, 69%). mp. 199 – 200° C. HRMS (*m/z*) (ESI^+): Calculated for $C_{12}H_9N_5Na$ *m/z* = 246.0750. Found for $[M+Na]^+$ *m/z* = 246.0759; calculated. for $C_{12}H_5N_9$: C = 64.56, H = 4.06, N = 31.37. Found: C = 64.47, H = 4.01, N = 31.12. ^1H NMR (400 MHz, $CDCl_3$) δ 9.17 (s, 1H, triazole), 8.65 (ddd, *J* = 4.8, 1.7, 0.9 Hz, 1H, 6-pyridyl), 8.55 (ddd, *J* = 4.9, 1.6, 0.8 Hz, 1H, 6'-pyridyl),

8.26-8.23 (m, 2H, 3,3'-pyridyl), 7.94 (ddd, *J* = 8.2, 7.5, 1.8 Hz, 1H, 4'-pyridyl), 7.81 (ddd, *J* = 8.0, 7.6, 1.6 Hz, 1H, 4-pyridyl), 7.37 (ddd, *J* = 7.5, 4.9, 0.8 Hz, 1H, 5'-pyridyl), 7.27 (ddd, *J* = 7.6, 4.8, 0.9 Hz, 1H, 5-pyridyl).^{13}C NMR (151 MHz, $CDCl_3$) δ 149.9 (qt), 149.4 (CH_{Pyr}), 149.3 (qt), 149.0 (CH_{Pyr}), 148.4 (qt), 139.2 (CH_{pyr}), 137.3 (CH_{pyr}), 123.8 (CH_{pyr}), 123.3 (CH_{pyr}), 120.8 (CH_{pyr}), 119.8 (CH_{triaz}), 114.0 (CH_{pyr}). IR υ_{max} (cm^{-1}) 3176, 3061, 1591, 1576, 1551, 1478, 1460, 1426, 1402, 1310, 1276, 1260, 1235, 1190, 1151, 1093, 1044, 1020, 994, 973, 885, 828, 793, 777, 731, 706, 669, 661, 653, 639, 631, 621, 609, 601, 594, 588, 579, 571. UV-vis (CH_3CN) λ_{max} / nm (ε_{max} /dm^3 mol^{-1} cm^{-1}) 236 (17,400) 287 (15,200).

Synthesis of tetrazolo[1,5-a]pyridine (125)

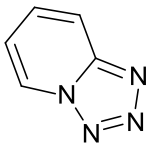

Compound **125** was synthesised according to modified literature procedure.[16] 2-bromopyridine (300mg, 1.9 mmol), Sodium Azide (136 mg, 2.1 mmol), CuI (65 mg, 0.342 mmol), *N,N'*-dimethylethylenediamine (50 mg, 0.57 mmol), and Sodium Ascorbate (188 mg, 0.950 mmol) were suspended in EtOH/ H_2O (7:3, 20 mL), degassed, filled with Argon and refluxed at 120°C for 2 hours. The mixture was diluted with water (20 mL) and extracted with DCM, washed with water (20 mL x 2), brine (20 mL x 2) and dried with $MgSO_4$. The solvent was removed under reduced pressure to yield an orange crystalline powder (202 mg, 1.691 mmol, 89%). Great care was exercised in this endeavour due to the explosive nature of low molecular weight azides.[52] Characterisation were consistent with literature. HRMS (*m/z*) (EI^+): Calculated for $C_5H_5N_4$ *m/z* = 120.0436. Found for $[M+H]^+$ *m/z* = 120.0438. ^{1}H NMR (400 MHz, $CDCl_3$) δ 8.82 (d, *J* = 7.0 Hz, 1H), 8.03 (d, *J* = 9.0 Hz, 1H), 7.67 (dd, *J* = 9.0 Hz, *J* = 8.0 Hz, 1H), 7.23 (dd, *J* = 8.0 Hz, *J* = 7.0 Hz, 1H). IR υ_{max} (cm^{-1}) 3081, 2981, 1684, 1630, 1612, 1490, 1431, 1365, 1325, 1277, 1234, 1158, 1138, 1092, 1052, 1014, 988, 916, 844, 798, 766, 740, 699.

Synthesis of 2-ethynylpyridine (126)

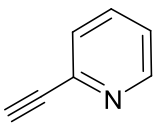

Compound **126** was synthesised by treating 2-((trimethylsilyl)ethynyl)pyridine, **127**, (3.35 g, 19.2 mmol) with TBAF (6.05 g, 19.2 mmol) in dry THF (50 mL) of according to literature procedure.[53] The mixture was cooled to 0°C upon dropwise addition of a concentrated solution of TBAF in the same solvent. The mixture was then allowed to stir at rt for 2.5 hours. The mixture was concentrated under reduced pressure, dissolved in DCM (30 mL), washed with water (25 mL x 4), brine and dried with $MgSO_4$. The solvent was removed under reduced pressure to yield a dark brown oil (1.811 g, 0.0176 mmol, 92%) Characterisation were consistent with literature. HRMS (*m/z*) (EI^+): Calculated for C_7H_5N *m/z* = 103.0422. Found for [M] *m/z* =

103.04232. ^{1}H NMR (400 MHz, $CDCl_3$) δ 8.60 (d, *J* = 7.7 Hz, 1H), 7.67 (t, *J* = 7.7 Hz, 1H), 7.49 (d, *J* = 7.7 Hz, 1H), 7.28 (d, *J* = 7.7 Hz, 2H), 3.16 (s, 1H). IR υ_{max} (cm^{-1}) 3291, 3053, 2478, 2108, 1678, 1614, 1582, 1561, 1461, 1427, 1285, 1244, 1213, 1182, 1150, 1091, 1045, 1015, 990, 843, 807, 777, 739.

Synthesis of 2-((trimethylsilyl)ethynyl)pyridine (46)

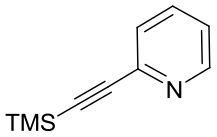

Compound **46** was synthesised according to literature procedure from 2-bromopyridine (2.16 mL, 22.6 mmol).[29] Upon completion as determined by TLC, the solvent was removed under reduced pressure. The black crude residue was then dissolved in hexane and filtered through celite. This yellow solution was purified by column chromatography in hexane increasing to 98:2 hexane:EtOAc mixture to yield a colourless oil (3.62 g, 20.68 mmol, 91.5%). Characterisation were consistent with literature. HRMS (*m/z*) (ESI^+): Calculated for $C_{10}H_{14}NSi$ *m/z* = 176.0890. Found for $[M+H]^+$ *m/z* = 176.0891. ^{1}H NMR (400 MHz, $CDCl_3$) δ 8.55 (d, *J* = 7.8 Hz, 1H), 7.61 (td, *J* = 7.7, 1.8 Hz, 1H), 7.43 (d, *J* = 7.8 Hz, 1H), 7.20 (ddd, *J* = 7.6, 4.9, 1.1 Hz, 1H), 0.24 (s, 9H).

Synthesis of [Cu124$_2$]PF$_6$

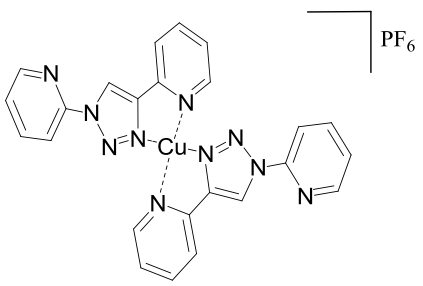

$[Cu(CH_3CN)_4]PF_6$ (50 mg, 0.134 mmol) and **124** (60 mg, 0.269 mmol) were dissolved in CH_3CN (10 mL) and stirred at rt for 60 minutes. Recrystallisation was carried by diffusing diethyl ether into the CH_3CN solution and the orange crystals were isolated by filtration. (40 mg, 0.079 mmol, 59 %). mp. 228° C (decomp.) HRMS (*m/z*) (LD^+): Calculated for [Cu**124**$_2$]$^+$ *i.e.* $C_{24}H_{18}CuN_{10}^+$ *m/z* = 509.1006. Found for [Cu**124**$_2$]$^+$ *m/z* = 509.0980; calculated. for $C_{24}H_{18}N_{10}F_6PCu$: C = 44.01, H = 2.77, N = 21.39. Found: C = 43.64, H = 2.62, N = 20.95. ^{1}H NMR (400 MHz, CD_3CN) δ 9.25 (s (br), 1H), 8.62 (d, *J* = 4.1 Hz, 1H), 8.22 (d, J = 8.1 Hz, 1H), 8.10 (t, *J* = 7.3 Hz, 1H), 8.02 (s (br), 1H), 7.58 – 7.52 (dd, *J* = *4.1* Hz, 8.1 Hz, 1H). ^{1}H NMR (400 MHz, CD_3CN) δ 9.25 (s (br), 1H), 8.62 (d, *J* = 4.1 Hz, 1H), 8.22 (d, *J* = 8.1 Hz, 1H), 8.10 (t, *J* = 7.3 Hz, 1H), 8.02 (s (br), 1H), 7.58 – 7.52 (dd, *J* = 4.1 Hz, 8.1 Hz, 1H). IR υ_{max} (cm^{-1}) 3156, 1608, 1570, 1485, 1467, 1454, 1444, 1361, 1322, 1261, 1163, 1072, 1017, 837, 816, 779, 738, 636, 574, 557, 541, 528.

Synthesis of [Co124$_2$(NO$_3$)$_2$]

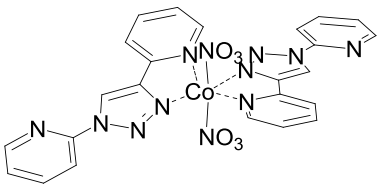

Cobalt(II) nitrate pentahydrate (21 mg, 0.09mmol) and **124** (40 mg, 1.8 mmol) were suspended in CH_3CN (20 mL) and allowed to stir at rt for 30 mins. The reaction mix had turned into a cloudy suspension and the product was filtered and washed with CH_3CN (10 mL x 2) to afford a white crystalline powder (21 mg, 0.033 mmol, 74%). Recrystallisation by diffusion of diethyl ether into a CH_3CN solution afforded transparent crystals. mp. 258 °C (decomp.). HRMS (*m/z*) (ESI$^+$): Calculated for [Co**124**$_2$(NO$_3$)]$^+$ *i.e.* $C_{24}H_{18}CoN_{11}O_3$ *i.e. m/z* = 567.0959. Found for *m/z* = 567.0926; calculated. for $C_{24}H_{18}N_{12}O_6Co$: C = 45.80, H = 2.88, N = 26.70. Found: C = 45.66, H = 2.76, N = 26.56. IR υ_{max} (cm^{-1}) IR υ_{max} (cm^{-1}) 3164, 3066, 1612, 1599, 1576, 1473, 1453, 1431, 1299, 1269, 1239, 1216, 1151, 1103, 1063, 1024, 995, 905, 822, 797, 777, 737, 704, 643, 619, 580, 561, 550, 543, 527, 518, 511, 508.

Synthesis of [Ag124$_2$] SbF$_6$

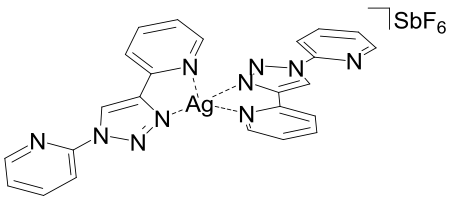

$AgSbF_6$ (9 mg, 0.027 mmol) and **124** (12 mg, 0.054 mmol) were dissolved separately in CH_3CN (4 mL each) and the solution of **124** was added dropwise to the solution of $AgSbF_6$, capped and left in darkness for 24 hours. Diffusion of diethyl ether into the CH_3CN solution followed by slow evaporation afforded transparent rod-like single crystals which were isolated by filtration (23 mg, 0.043 mmol, 79%). mp. 239 °C-240 °C. HRMS (*m/z*) (ESI$^+$): Calculated for $C_{24}H_{18}N_{10}Ag$ *m/z* = 553.0767. Found for [Ag**124**$_2$]$^+$ *m/z* = 553.0777; calculated. for $C_{48}H_{36}N_{20}F_{12}Sb_2Ag_2$: C = 36.48 H = 2.30, N = 17.73. Found: C = 36.55, H = 2.15, N = 17.54. ^{1}H NMR (400 MHz, CD_3CN) δ 9.16 (s, 1H), 8.70 (s (br), 1H), 8.62 (dd, *J* = 4.8, 0.9 Hz, 1H), 8.22 (d, *J* = 8.2 Hz, 1H), 8.18 (d (br), *J* = 7.8 Hz, 1H), 8.09 (td, *J* = 8.2, 0.9 Hz, 1H), 7.96 (td, *J* = 7.8, 1.7 Hz, 1H), 7.53 (ddd, *J* = 8.2, 4.8, 0.9 Hz, 1H), 7.42 (ddd (br), *J* = 7.8 Hz, 1H). IR υ_{max} (cm^{-1}) 3158, 1737, 1617, 1597, 1574, 1560, 1479, 1469, 1453, 1403, 1362, 1288, 1257, 1234, 1202, 1164, 1153, 1053, 1035, 1016, 993, 946, 926, 909, 892, 872, 850, 820, 779, 744, 734, 722, 705, 684, 661, 648, 629, 609, 591, 589, 587, 585, 583, 579, 577, 575, 571, 553, 549, 539, 535, 531.

Synthesis of [Pt124Cl$_2$]

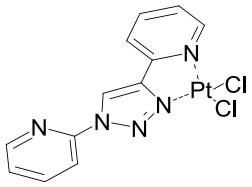

[PtCl$_2$(DMSO)$_2$] (30 mg, 0.072 mmol) and **124** (16 mg, 0.072 mmol) were suspended in CH_3OH (30 mL) and stirred at reflux at 70^{o}C for 15 hours in darkness. The mixture was allowed to cool to rt and stirring continued for a further 4 hours. The precipitate was recovered by filtration and washed with CH_3OH (15 mL x 2) and diethyl ether (15 mL x 2) to afford an off-white powder. Recrystallisation from slow evaporation of a CH_3CN solution afforded two crystalline phase types, needles which contained just the molecule [Pt**124**Cl$_2$] in the asymmetric unit and blocks which contained the [Pt**124**Cl$_2$]·CH_3CN adduct in the asymmetric unit. Powder X-ray diffraction showed the grey powder contained the phase [Pt**124**Cl$_2$] exclusively. (28 mg, 0.029 mmol, 39.8 %). mp. 315° C (decomp.) HRMS (*m/z*) (ESI$^+$): Calculated for [Pt**124**Cl]$^+$ *i.e.* $C_{12}H_9N_5ClPt$ *m/z* = 453.0188. Found for [Pt**124**Cl]$^+$ *m/z* = 453.0194. HRMS (*m/z*) (LD$^+$): Calculated for [[Pt**124**Cl]·CH_3CN]$^+$ *i.e.* $C_{14}H_{12}N_6ClPt$ *m/z* = 494.0460. Found for [[Pt**124**Cl]·CH_3CN]$^+$ *m/z* = 494.0470; calculated for $C_{12}H_9N_5Cl_2Pt$: C = 29.46, = H 1.85, N= 14.32. Found: C = 29.09, H = 1.66, N = 13.55. ^{1}H NMR (400 MHz, DMSO-d$_6$) δ 10.07 (s, 1H), 9.36 (d, J = 5.6 Hz, 1H), 8.68 (d, J = 3.9 Hz, 1H), 8.39 (m, 7.6 Hz, 2H), 8.25 – 8.17 (m, 1H), 8.10 (d, J = 8.2 Hz, 1H), 7.79 – 7.66 (m, 2H). IR υ_{max} (cm^{-1}) 3153, 3053, 2962, 2917, 1625, 1615, 1596, 1584, 1572, 1457, 1448, 1407, 1361, 1287, 1259, 1220, 1146, 1075, 1018, 995, 889, 796, 776, 741, 700, 693, 650, 616, 565, 535, 524, 511, 502.

8 References

1. Lehn, J.-M., *Science* **2002**, *295*, 2400-2403.
2. Matsumoto, K.; Yuan, J., *Metal ions in biological systems*. Marcel Dekker Inc.: New York, 2003; Vol. 40.
3. Faulkner, S.; Pope, S. J. A.; Burton-Pye, B. P., *Appl. Spectrosc. Rev.* **2005**, *40*, 1-31.
4. Zhang, J.; Su, C.-Y., *Coord. Chem. Rev.* **2013**, *257*, 1373-1408.
5. Tam, A. Y.-Y.; Yam, V. W.-W., *Chem. Soc. Rev.* **2013**, *42*, 1540-1567.
6. Piepenbrock, M.-O. M.; Lloyd, G. O.; Clarke, N.; Steed, J. W., *Chem. Rev.* **2009**, *110*, 1960-2004.
7. Gunnlaugsson, T.; Stomeo, F., *Org. Biomol. Chem.* **2007**, *5*, 1999-2009.
8. Perry Iv, J. J.; Perman, J. A.; Zaworotko, M. J., *Chem. Soc. Rev.* **2009**, *38*, 1400-1417.
9. Huisgen, R., 1,3-Dipolar cycloadditions - Introduction, survey, mechanism. In *1,3-Dipolar Cycloaddition Chemistry*, Padwa, A., Ed. Wiley: New York, 1984; pp 1-176.
10. Rostovtsev, V. V.; Green, L. G.; Fokin, V. V.; Sharpless, K. B., *Angew. Chem. Int. Ed.* **2002**, *41*, 2596-2599.
11. Wu, P.; Feldman, A. K.; Nugent, A. K.; Hawker, C. J.; Scheel, A.; Voit, B.; Pyun, J.; Fréchet, J. M. J.; Sharpless, K. B.; Fokin, V. V., *Angew. Chem. Int. Ed.* **2004**, *43*, 3928-3932.
12. Kolb, H. C.; Finn, M. G.; Sharpless, K. B., *Angew. Chem. Int. Ed.* **2001**, *40*, 2004-2021.
13. Finn, M. G.; Fokin, V. V., *Chem. Soc. Rev.* **2010**, *39*, 1231-1232.
14. Rideout, D. C.; Breslow, R., *J. Am. Chem. Soc.* **1980**, *102*, 7816-7817.
15. Fahmi Himo, T. L., Robert Hilgraf, Vsevolod V. Rostovtsev, Louis Noodleman, K. Barry Sharpless, and Valery V. Fokin, *J. Am. Chem. Soc.* **2005**, *127*, 214.
16. Schulze, B.; Schubert, U. S., *Chem. Soc. Rev.* **2014**, *43*, 2522-2571.
17. Worrell, B. T.; Malik, J. A.; Fokin, V. V., *Science* **2013**, *340*, 457-460.
18. Horne, W. S.; Yadav, M. K.; Stout, C. D.; Ghadiri, M. R., *J. Am. Chem. Soc.* **2004**, *126*, 15366-15367.
19. Kolb, H. C.; Sharpless, K. B., *Drug Discov. Today* **2003**, *8*, 1128-1137.
20. Johnson, J. A.; Finn, M. G.; Koberstein, J. T.; Turro, N. J., *Macromol. Rapid Commun.* **2008**, *29*, 1052-1072.
21. Hanni, K. D.; Leigh, D. A., *Chem. Soc. Rev.* **2010**, *39*, 1240-1251.
22. Goldup, S. M.; Leigh, D. A.; Long, T.; McGonigal, P. R.; Symes, M. D.; Wu, J., *J. Am. Chem. Soc.* **2009**, *131*, 15924-15929.
23. Lahlali, H.; Jobe, K.; Watkinson, M.; Goldup, S. M., *Angew. Chem. Int. Ed.* **2011**, *50*, 4151-4155.
24. Bordoli, R. J.; Goldup, S. M., *J. Am. Chem. Soc.* **2014**, *136*, 4817-4820.
25. Winn, J.; Pinczewska, A.; Goldup, S. M., *J. Am.Chem. Soc.* **2013**, *135*, 13318-13321.
26. Struthers, H.; Mindt, T. L.; Schibli, R., *Dalton Trans.* **2010**, *39*, 675-696.
27. Byrne, J. P.; Kitchen, J. A.; Gunnlaugsson, T., *Chem. Soc. Rev.* **2014**, *43*, 5302-5325.
28. Crowley, J. D., McMorran, D. A., "Click-Triazole": Coordination Chemistry: Exploiting 1,4-Disubstituted-1,2,3-Triazoles as Ligands. In *Click Triazoles*, Košmrlj, J., Ed. Springer: New York, 2012; Vol. 28, pp 31-83.
29. Mindt, T. L.; Struthers, H.; Brans, L.; Anguelov, T.; Schweinsberg, C.; Maes, V.; Tourwé, D.; Schibli, R., *J. Am. Chem. Soc.* **2006**, *128*, 15096-15097.
30. Constable, E. C.; Steel, P. J., *Coord. Chem. Rev.* **1989**, *93*, 205-23.
31. Balzani, V.; Juris, A.; Venturi, M.; Campagna, S.; Serroni, S., *Chem. Rev.* **1996**, *96*, 759-834.
32. Fletcher, N. C., *J. Chem. Soc., Perkin Trans. 1* **2002**, 1831-1842.
33. Blau, F., *Ber. Dtsch. Chem. Ges.* **1888**, *27*, 1077.
34. Keefe, M. H.; Benkstein, K. D.; Hupp, J. T., *Coord. Chem. Rev.* **2000**, *205*, 201-228.

35. Beer, P. D.; Cadman, J., *Coord. Chem. Rev.* **2000**, *205*, 131-155.
36. Juris, A., Balzani, V., Barigelletti, F., Campagna, S., Belser, P., van Zelewsky, A. , *Coord. Chem. Rev.* **1988**, *84*, 85.
37. Balzani, V.; Ceroni, P.; Juris, A.; Venturi, M.; Campagna, S.; Puntoriero, F.; Serroni, S., *Coord. Chem. Rev.* **2001**, *219*, 545-572.
38. Newkome, George R.; Patri, Anil K.; Holder, E.; Schubert, Ulrich S., *Eur. J. Org. Chem.* **2004**, *2004*, 235-254.
39. Kaes, C.; Katz, A.; Hosseini, M. W., *Chem. Rev.* **2000**, *100*, 3553-3590.
40. Hommes, P.; Reissig, H.-U., *Beilstein J. Org. Chem.* **2016**, *12*, 1170-1177.
41. Fleischel, O.; Wu, N.; Petitjean, A., *Chem. Commun.* **2010**, *46*, 8454-8456.
42. Crowley, J. D.; Bandeen, P. H.; Hanton, L. R., *Polyhedron* **2010**, *29*, 70-83.
43. Meudtner, R. M.; Ostermeier, M.; Goddard, R.; Limberg, C.; Hecht, S., *Chem. Eur. J.* **2007**, *13*, 9834-9840.
44. Goddard-Borger, E. D.; Stick, R. V., *Org. Lett.* **2007**, *9*, 3797-3800.
45. Dong, R.; Zhou, Y.; Huang, X.; Zhu, X.; Lu, Y.; Shen, J., *Adv. Mater.* **2015**, *27*, 498-526.
46. Du, L.-Y.; Wang, H.; Liu, G.; Xie, D.; Guo, F.-S.; Hou, L.; Wang, Y.-Y., *Dalton Trans.* **2015**, *44*, 1110-1119.
47. Ballesteros-Garrido, R.; Abarca, B.; Ballesteros, R.; Ramirez de Arellano, C.; Leroux, F. R.; Colobert, F.; Garcia-Espana, E., *New J. Chem.* **2009**, *33*, 2102-2106.
48. Kilpin, K. J.; Gavey, E. L.; McAdam, C. J.; Anderson, C. B.; Lind, S. J.; Keep, C. C.; Gordon, K. C.; Crowley, J. D., *Inorg. Chem.* **2011**, *50*, 6334-6346.
49. Kilpin, K. J.; Paul, U. S. D.; Lee, A.-L.; Crowley, J. D., *Chem. Commun.* **2011**, *47*, 328-330.
50. Gower, M. L.; Crowley, J. D., *Dalton Trans.* **2010**, *39*, 2371-2378.
51. Crowley, J. D.; Bandeen, P. H., *Dalton Trans.* **2010**, *39*, 612-623.
52. Kilpin, K. J.; Crowley, J. D., *Polyhedron* **2010**, *29*, 3111-3117.
53. Crowley, J. D.; Gavey, E. L., *Dalton Trans.* **2010**, *39*, 4035-4037.
54. Lo, W. K. C.; Huff, G. S.; Cubanski, J. R.; Kennedy, A. D. W.; McAdam, C. J.; McMorran, D. A.; Gordon, K. C.; Crowley, J. D., *Inorg. Chem.* **2015**, *54*, 1572-1587.
55. McCarney, E. P.; Hawes, C. S.; Blasco, S.; Gunnlaugsson, T., *Dalton Trans.* **2016**, *45*, 10209-10221.
56. Bunzli, J.-C. G.; Piguet, C., *Chem. Soc. Rev.* **2005**, *34*, 1048-1077.
57. Gassner, A.-L.; Duhot, C. l.; G. Bünzli, J.-C.; Chauvin, A.-S., *Inorg. Chem.* **2008**, *47*, 7802-7812.
58. Chauvin, A. S.; Gumy, F.; Imbert, D.; Bünzli, J. C. G., *Spectrosc. Lett.* **2004**, *37*, 517-532.
59. Chauvin, A. S.; Gumy, F.; Imbert, D.; Bünzli, J. C. G., *Spectrosc. Lett.* **2007**, *40*, 193-193.
60. Leonard, J. P.; Jensen, P.; McCabe, T.; O'Brien, J. E.; Peacock, R. D.; Kruger, P. E.; Gunnlaugsson, T., *J. Am. Chem. Soc.* **2007**, *129*, 10986-10987.
61. Kotova, O.; Kitchen, J. A.; Lincheneau, C.; Peacock, R. D.; Gunnlaugsson, T., *Chem. Eur. J.* **2013**, *19*, 16181-16186.
62. Lincheneau, C.; Leonard, J. P.; McCabe, T.; Gunnlaugsson, T., *Chem. Commun.* **2011**, *47*, 7119-7121.
63. Lincheneau, C.; Destribats, C.; Barry, D. E.; Kitchen, J. A.; Peacock, R. D.; Gunnlaugsson, T., *Dalton Trans.* **2011**, *40*, 12056-12059.
64. Bradberry, S. J.; Savyasachi, A. J.; Martinez-Calvo, M.; Gunnlaugsson, T., *Coord. Chem. Rev.* **2014**, *273–274*, 226-241.

65. Kotova, O.; Blasco, S.; Twamley, B.; O'Brien, J.; Peacock, R. D.; Kitchen, J. A.; Martinez-Calvo, M.; Gunnlaugsson, T., *Chem. Sci.* **2015**, *6*, 457-471.
66. Galanti, A.; Kotova, O.; Blasco, S.; Johnson, C. J.; Peacock, R. D.; Mills, S.; Boland, J. J.; Albrecht, M.; Gunnlaugsson, T., *Chem. Eur. J.* **2016**, *22*, 9709-9723.
67. Stomeo, F.; Lincheneau, C.; Leonard, J. P.; O'Brien, J. E.; Peacock, R. D.; McCoy, C. P.; Gunnlaugsson, T., *J. Am. Chem. Soc.* **2009**, *131*, 9636-9637.
68. Barry, D. E.; Kitchen, J. A.; Albrecht, M.; Faulkner, S.; Gunnlaugsson, T., *Langmuir* **2013**, *29*, 11506-11515.
69. Lincheneau, C.; Jean-Denis, B.; Gunnlaugsson, T., *Chem. Commun.* **2014**, *50*, 2857-2860.
70. Bradberry, S. J.; Byrne, J. P.; McCoy, C. P.; Gunnlaugsson, T., *Chem. Commun.* **2015**.
71. Barry, D. E.; Caffrey, D. F.; Gunnlaugsson, T., *Chem. Soc. Rev.* **2016**.
72. Kotova, O.; Comby, S.; Lincheneau, C.; Gunnlaugsson, T., *Chem. Sci.* **2017**.
73. Sauvage, J. P.; Collin, J. P.; Chambron, J. C.; Guillerez, S.; Coudret, C.; Balzani, V.; Barigelletti, F.; De Cola, L.; Flamigni, L., *Chem. Rev.* **1994**, *94*, 993-19.
74. Cargill Thompson, A. M. W., *Coord. Chem. Rev.* **1997**, *160*, 1-52.
75. Constable, E. C., *Adv. Inorg. Chem.* **1986**, *30*, 69-121.
76. Wang, P.; Li, Z.; Lv, G.-C.; Zhou, H.-P.; Hou, C.; Sun, W.-Y.; Tian, Y.-P., *Inorg. Chem. Commun.* **2012**, *18*, 87-91.
77. Andres, P. R.; Schubert, U. S., *Adv. Mater.* **2004**, *16*, 1043-1068.
78. Cummings, S. D., *Coord. Chem. Rev.* **2009**, *253*, 1495-1516.
79. Banerjee, S.; Kitchen, J. A.; Bright, S. A.; O'Brien, J. E.; Williams, D. C.; Kelly, J. M.; Gunnlaugsson, T., *Chem. Commun.* **2013**, *49*, 8522-8524.
80. Terech, P.; Yan, M.; Marechal, M.; Royal, G.; Galvez, J.; Velu, S. K. P., *Phys. Chem. Chem. Phys.* **2013**, *15*, 7338-7344.
81. Bazzicalupi, C.; Bianchi, A.; Biver, T.; Giorgi, C.; Santarelli, S.; Savastano, M., *Inorg. Chem.* **2014**.
82. Han, F. S.; Higuchi, M.; Ikeda, T.; Negishi, Y.; Tsukuda, T.; Kurth, D. G., *J. Mater. Chem.* **2008**, *18*, 4555-4560.
83. Gou, L.; Wu, Q.-R.; Hu, H.-M.; Qin, T.; Xue, G.-L.; Yang, M.-L.; Tang, Z.-X., *Inorg. Chim. Acta* **2008**, *361*, 1922-1928.
84. Lashgari, K. K., M.; Norrestam, R.; Norrby, T., *Acta Crystallogr. Sect. C* **1999**, *55*, 64-67.
85. Ziessel, R.; Grosshenny, V.; Hissler, M.; Stroh, C., *Inorg. Chem.* **2004**, *43*, 4262-4271.
86. Kotova, O.; Daly, R.; dos Santos, C. M. G.; Boese, M.; Kruger, P. E.; Boland, J. J.; Gunnlaugsson, T., *Angew. Chem. Int. Ed.* **2012**, *51*, 7208-7212.
87. Kotova, O.; Daly, R.; dos Santos, C. M. G.; Kruger, P. E.; Boland, J. J.; Gunnlaugsson, T., *Inorg. Chem.* **2015**, *54*, 7735-7741.
88. Daly, R.; Kotova, O.; Boese, M.; Gunnlaugsson, T.; Boland, J. J., *ACS Nano* **2013**, *7*, 4838-4845.
89. Kitchen, J. A.; Boyle, E. M.; Gunnlaugsson, T., *Inorg. Chim. Acta* **2012**, *381*, 236-242.
90. Hernandez-Gil, J.; Ferrer, S.; Castineiras, A.; Lloret, F., *Inorg. Chem.* **2012**, *51*, 9809-19.
91. Hannon, M. J.; Green, P. S.; Fisher, D. M.; Derrick, P. J.; Beck, J. L.; Watt, S. J.; Ralph, S. F.; Sheil, M. M.; Barker, P. R.; Alcock, N. W.; Price, R. J.; Sanders, K. J.; Pither, R.; Davis, J.; Rodger, A., *Chem. - Eur. J.* **2006**, *12*, 8000-8013.
92. Morgan, G. T.; Burstall, F. H., *J. Chem. Soc.* **1932**, 20-30.

93. Badger, G. M.; Sasse, W. H. F., *J. Chem. Soc* **1956**, 616-620.
94. Burstall, F. H., *J. Chem. Soc* **1938**, 1662-1672.
95. Jameson, D. L.; Guise, L. E., *Tetrahedron Lett.* **1991**, *32*, 1999-2002.
96. Chandrasekhar, N., Chandrasekar, R., , *Dalton Trans.* **2010**, *39*, 9872.
97. Schuster, E. M., Botoshansky, M., Gandelman, M., *Dalton Trans.* **2011**, *40*, 8764.
98. Li, Y.; Huffman, J. C.; Flood, A. H., *Chem. Commun.* **2007**, 2692-2694.
99. Ostermeier, M.; Berlin, M.-A.; Meudtner, R. M.; Demeshko, S.; Meyer, F.; Limberg, C.; Hecht, S., *Chem. Eur. J.* **2010**, *16*, 10202-10213.
100. Chan, T. R.; Hilgraf, R.; Sharpless, K. B.; Fokin, V. V., *Org. Lett.* **2004**, *6*, 2853-2855.
101. Meudtner, R. M.; Hecht, S., *Angew. Chem., Int. Ed.* **2008**, *47*, 4926-4930.
102. Byrne, J. P.; Blasco, S.; Aletti, A. B.; Hessman, G.; Gunnlaugsson, T., *Angew. Chem. Int. Ed.* **2016**, *55*, 8938-8943.
103. Byrne, J. P.; Kitchen, J. A.; O'Brien, J. E.; Peacock, R. D.; Gunnlaugsson, T., *Inorg. Chem.* **2015**, *54*, 1426-1439.
104. Schweinfurth, D.; Hardcastle, K. I.; Bunz, U. H. F., *Chem. Commun.* **2008**, 2203-2205.
105. Meudtner, R. M.; Ostermeier, M.; Goddard, R.; Limberg, C.; Hecht, S., *Chem. Eur. J.* **2007**, *13*, 9834-9840.
106. McMorran, D. A., *Inorg. Chem.* **2008**, *47*, 592-601.
107. Fitchett, C. M.; Richardson, C.; Steel, P. J., *Org. Biomol. Chem.* **2005**, *3*, 498-502.
108. El Malah, T.; Ciesielski, A.; Piot, L.; Troyanov, S. I.; Mueller, U.; Weidner, S.; Samori, P.; Hecht, S., *Nanoscale* **2012**, *4*, 467-472.
109. Zornik, D.; Meudtner, R. M.; El Malah, T.; Thiele, C. M.; Hecht, S., *Chem. Eur. J.* **2011**, *17*, 1473-1484.
110. Chandrasekhar, N.; Chandrasekar, R., *J. Org. Chem.* **2010**, *75*, 4852-4855.
111. Hanan, G. S.; Lehn, J.-M.; Kyritsakas, N.; Fischer, J., *J. Chem. Soc., Chem. Commun.* **1995**, 765-766.
112. Meudtner, R. M.; Hecht, S., *Macromol. Rapid Commun.* **2008**, *29*, 347-351.
113. Byrne, J. P.; Kitchen, J. A.; Kotova, O.; Leigh, V.; Bell, A. P.; Boland, J. J.; Albrecht, M.; Gunnlaugsson, T., *Dalton Trans.* **2013**, *43*, 196-209.
114. Midya, G. C.; Paladhi, S.; Bhowmik, S.; Saha, S.; Dash, J., *Org. Biomol. Chem.* **2013**, *11*, 3057-3063.
115. Schulze, B.; Friebe, C.; Hoeppener, S.; Pavlov, G. M.; Hager, M. D.; Winter, A.; Schubert, U. S., *Polym. Prepr. (Am. Chem. Soc., Div. Polym. Chem.)* **2011**, *52*, 917-918.
116. Li, Y.; Zhao, L.; Tam, A. Y.-Y.; Wong, K. M.-C.; Wu, L.; Yam, V. W.-W., *Chem. - Eur. J.* **2013**, *19*, 14496-14505.
117. Lang, C.; Pahnke, K.; Kiefer, C.; Goldmann, A. S.; Roesky, P. W.; Barner-Kowollik, C., *Polym. Chem.* **2013**, *4*, 5456-5462.
118. Younes, A. H.; Clark, R. J.; Zhu, L., *Supramol. Chem.* **2012**, *24*, 696-706.
119. Byrne, J. P. *Novel btp [2,6-bis(1,2,3-triazol-4-yl)pyridine] systems: a versatile motif for the formation of supramolecular self-assembly structures*. Ph.D. Thesis, University of Dublin, Trinity College, Dublin, 2015.
120. Danielraj, P.; Varghese, B.; Sankararaman, S., *Acta Crystallogr., Sect. C: Cryst. Struct. Commun.* **2010**, *66*, m366-m370.
121. Gałęzowska, J.; Boratyński, P. J.; Kowalczyk, R.; Lipke, K.; Czapor-Irzabek, H., *Polyhedron* **2017**, *121*, 1-8.
122. Boratyński, P. J.; Kowalczyk, R., *J. Org. Chem.* **2016**, *81*, 8029-8034.
123. Kraft, J.; Schmollinger, D.; Maudrich, J.; Ziegler, T., *Synthesis* **2015**, *47*, 199-208.

124. Addison, A. W.; Rao, T. N.; Reedijk, J.; Van Rijn, J.; Verschoor, G. C., *J. Chem. Soc., Dalton Trans.* **1984**, 1349-56.
125. Yuan, J.; Fang, X.; Zhang, L.; Hong, G.; Lin, Y.; Zheng, Q.; Xu, Y.; Ruan, Y.; Weng, W.; Xia, H.; Chen, G., *J. Mater. Chem.* **2012**, *22*, 11515-11522.
126. Steel, P. J.; Fitchett, C. M., *Coord. Chem. Rev.* **2008**, *252*, 990-1006.
127. Naziruddin, A. R.; Lee, C.-S.; Lin, W.-J.; Sun, B.-J.; Chao, K.-H.; Chang, A. H. H.; Hwang, W.-S., *Dalton Trans.* **2016**, *45*, 5848-5859.
128. Schulze, B.; Winter, A.; Friebe, C.; Birckner, E.; Schubert, U. S., *ACS Macro Lett.* **2017**, *6*, 181-184.
129. Prokop, A.; Czaplewska, J. A.; Clausen, M.; König, M.; Wild, A.; Thorwirth, R.; Schulze, B.; Babiuch, K.; Pretzel, D.; Schubert, U. S.; Gottschaldt, M., *Eur. J. Inorg. Chem.* **2016**, *2016*, 3480-3488.
130. Lowe, G.; Droz, A. S.; Vilaivan, T.; Weaver, G. W.; Park, J. J.; Pratt, J. M.; Tweedale, L.; Kelland, L. R., *J. Med. Chem.* **1999**, *42*, 3167-3174.
131. Chan, A. K.-W.; Wu, D.; Wong, K. M.-C.; Yam, V. W.-W., *Inorg. Chem.* **2016**, *55*, 3685-3691.
132. Zhang, C.; Shen, X.; Sakai, R.; Gottschaldt, M.; Schubert, U. S.; Hirohara, S.; Tanihara, M.; Yano, S.; Obata, M.; Xiao, N.; Satoh, T.; Kakuchi, T., *J. Polym. Sci., Part A: Polym. Chem.* **2011**, *49*, 746-753.
133. Chen, Y.; Xiao, N.; Satoh, T.; Kakuchi, T., *Polym. Chem.* **2014**, *5*, 4993-5001.
134. Schulze, B.; Friebe, C.; Hoeppener, S.; Pavlov, G. M.; Winter, A.; Hager, M. D.; Schubert, U. S., *Macromol. Rapid Commun.* **2012**, *33*, 597-602.
135. Bünzli, J.-C. G.; Chauvin, A.-S.; Vandevyver, C. D. B.; Bo, S.; Comby, S., *Ann. N.Y. Acad. Sci.* **2008**, *1130*, 97-105.
136. Bünzli, J.-C. G., *Chem. Rev.* **2010**, *110*, 2729-2755.
137. Eliseeva, S. V.; Bunzli, J.-C. G., *Chem. Soc. Rev.* **2010**, *39*, 189-227.
138. Lincheneau, C.; Stomeo, F.; Comby, S.; Gunnlaugsson, T., *Aust. J. Chem.* **2011**, *64*, 1315-1326.
139. Nonat, A. M.; Quinn, S. J.; Gunnlaugsson, T., *Inorg. Chem.* **2009**, *48*, 4646-4648.
140. dos Santos, C. M. G.; Harte, A. J.; Quinn, S. J.; Gunnlaugsson, T., *Coord. Chem. Rev.* **2008**, *252*, 2512-2527.
141. Leonard, J. P.; Nolan, C. B.; Stomeo, F.; Gunnlaugsson, T., *Top. Curr. Chem.* **2007**, *281*, 1-43.
142. Kruger, P. E.; Gunnlaugsson, T., *Dalton Trans.* **2011**, *40*, 12003-12004.
143. Andreiadis, E. S.; Imbert, D.; Pecaut, J.; Demadrille, R.; Mazzanti, M., *Dalton Trans.* **2012**, *41*, 1268-1277.
144. Le Borgne, T.; Benech, J.-M.; Floquet, S.; Bernardinelli, G.; Aliprandini, C.; Bettens, P.; Piguet, C., *Dalton Trans.* **2003**, 3856-3868.
145. Hua, K. N. T.; Xu, J.; Quiroz, E. E.; Lopez, S.; Ingram, A. J.; Johnson, V. A.; Tisch, A. R.; de Bettencourt-Dias, A.; Straus, D. A.; Muller, G., *Inorg. Chem.* **2012**, *51*, 647-660.
146. Frost, G. H.; Hart, F. A.; Heath, C.; Hursthouse, M. B., *J. Chem. Soc., Chem. Commun.* **1969**, 1421-1422.
147. Panak, P. J.; Geist, A., *Chem. Rev.* **2013**, *113*, 1199-1236.
148. Wagner, C.; Mossini, E.; Macerata, E.; Mariani, M.; Arduini, A.; Casnati, A.; Geist, A.; Panak, P. J., *Inorg. Chem.* **2017**, *56*, 2135-2144.
149. Macerata, E.; Mossini, E.; Scaravaggi, S.; Mariani, M.; Mele, A.; Panzeri, W.; Boubals, N.; Berthon, L.; Charbonnel, M.-C.; Sansone, F.; Arduini, A.; Casnati, A., *J. Am. Chem. Soc.* **2016**.
150. Kiefer, C.; Wagner, A. T.; Beele, B. B.; Geist, A.; Panak, P. J.; Roesky, P. W., *Inorg. Chem.* **2015**, *54*, 7301-7308.

151. Schulze, B.; Escudero, D.; Friebe, C.; Siebert, R.; Görls, H.; Köhn, U.; Altuntas, E.; Baumgaertel, A.; Hager, M. D.; Winter, A.; Dietzek, B.; Popp, J.; González, L.; Schubert, U. S., *Chem. Eur. J.* **2011**, *17*, 5494-5498.
152. Brown, D. G.; Schauer, P. A.; Borau-Garcia, J.; Fancy, B. R.; Berlinguette, C. P., *J. Am. Chem. Soc.* **2013**, *135*, 1692-1695.
153. Iwasaki, H.; Yamada, Y.; Ishikawa, R.; Koga, Y.; Matsubara, K., *Eur. J. Org. Chem.* **2016**, *2016*, 1651-1654.
154. Iwasaki, H.; Teshima, Y.; Yamada, Y.; Ishikawa, R.; Koga, Y.; Matsubara, K., *Dalton Trans.* **2016**, *45*, 5713-5719.
155. Jang, C. G.; Kim, U.; Kim, Y. H.; Kim, J. S.; Kim, H. J.; Lee, N. H.; Jung, J. Y.; Chae, M. Y.; Heo, D. H. *Iridium complex as blue or green electroluminescent dopant for organic optoelectronic device*. KR2015081658A, 2015.
156. Byrne, J. P.; Martínez-Calvo, M.; Peacock, R. D.; Gunnlaugsson, T., *Chem. Eur. J.* **2016**, *22*, 486-490.
157. Hua, Y.; Flood, A. H., *Chem. Soc. Rev.* **2010**, *39*, 1262-1271.
158. Li, Y.; Pink, M.; Karty, J. A.; Flood, A. H., *J. Am. Chem. Soc.* **2008**, *130*, 17293-17295.
159. Duan, Q.; Xia, W.; Lin, C.; Pan, Y.; Wang, L., *Tetrahedron Lett.* **2015**, *56*, 4002-4006.
160. Bosmani, A.; Pujari, S. A.; Besnard, C.; Guenee, L.; Poblador-Bahamonde, A. I.; Lacour, J., *Chem. - Eur. J.* **2017**, *23*, 8678-8684.
161. Thomas, J.; Jana, S.; Liekens, S.; Dehaen, W., *Chem. Commun.* **2016**, *52*, 9236-9239.
162. Wang, S.; Shen, D. L.; Lafont, D.; Vercoutter-Edouart, A.-S.; Mortuaire, M.; Shi, Y.; Maniti, O.; Girard-Egrot, A.; Lefebvre, T.; Pinto, B. M.; Vocadlo, D.; Vidal, S., *MedChemComm* **2014**, *5*, 1172-1178.
163. Fletcher, J. T.; Bumgarner, B. J.; Engels, N. D.; Skoglund, D. A., *Organomet.* **2008**, *27*, 5430-5433.
164. Fletcher, J. T.; Walz, S. E.; Keeney, M. E., *Tetrahedron Lett.* **2008**, *49*, 7030-7032.
165. Andersen, J.; Madsen, U.; Björkling, F.; Liang, X., *Synlett* **2005**, *2005*, 2209-2213.
166. Smith, N. M.; Greaves, M. J.; Jewell, R.; Perry, M. W. D.; Stocks, M. J.; Stonehouse, J. P., *Synlett* **2009**, *2009*, 1391-1394.
167. Potter, G. T.; Jayson, G. C.; Miller, G. J.; Gardiner, J. M., *The J. Org. Chem.* **2016**, *81*, 3443-3446.
168. Goddard-Borger, E. D.; Stick, R. V., *Org. Lett.* **2011**, *13*, 2514-2514.
169. Klein, C.; Baranoff, E.; Grätzel, M.; Nazeeruddin, M. K., *Tetrahedron Lett.* **2011**, *52*, 584-587.
170. Byrne, J. P.; Kitchen, J. A.; Kotova, O.; Leigh, V.; Bell, A. P.; Boland, J. J.; Albrecht, M.; Gunnlaugsson, T., *Dalton Trans.* **2013**.
171. Yang, L.; Tan, X.; Wang, Z.; Zhang, X., *Chem. Rev.* **2015**, *115*, 7196-7239.
172. Estroff, L. A.; Hamilton, A. D., *Chem. Rev.* **2004**, *104*, 1201-1218.
173. McKee, J. R.; Appel, E. A.; Seitsonen, J.; Kontturi, E.; Scherman, O. A.; Ikkala, O., *Adv. Funct. Mater.* **2014**, *24*, 2706-2713.
174. Dobrawa, R.; Würthner, F., *J. Polym. Sci., Part A: Polym. Chem.* **2005**, *43*, 4981-4995.
175. Zhang, Z.; Zaworotko, M. J., *Chem. Soc. Rev.* **2014**, *43*, 5444-5455.
176. James, S. L., *Chem. Soc. Rev.* **2003**, *32*, 276-288.
177. Flory, P. J., *Faraday Discuss. Chem. Soc.* **1974**, *57*, 7-18.
178. Gunnlaugsson, T.; Pandurangan, K.; Kitchen, J. A.; Blasco, S.; Paradisi, F., *Chem. Commun.* **2014**.

179. Weng, W.; Beck, J. B.; Jamieson, A. M.; Rowan, S. J., *J. Am. Chem. Soc.* **2006**, *128*, 11663-11672.
180. Wang, Q.; Mynar, J. L.; Yoshida, M.; Lee, E.; Lee, M.; Okuro, K.; Kinbara, K.; Aida, T., *Nature* **2010**, *463*, 339-343.
181. Buerkle, L. E.; Rowan, S. J., *Chem. Soc. Rev.* **2012**, *41*, 6089-6102.
182. McCarney, E. P.; Byrne, J. P.; Twamley, B.; Martinez-Calvo, M.; Ryan, G.; Mobius, M. E.; Gunnlaugsson, T., *Chem. Commun.* **2015**, *51*, 14123-14126.
183. Barnes, H. A., *A Handbook of Elementary Rheology*. The University of Wales: Aberystwyth, 2000.
184. Dawn, A.; Kumari, H., *Chem. Eur. J.* **2017**, Advance Article; DOI: 10.1002/chem.201703374.
185. Fiore, G. L.; Rowan, S. J.; Weder, C., *Chem. Soc. Rev.* **2013**, *42*, 7278-7288.
186. Harada, A.; Takashima, Y.; Nakahata, M., *Acc. Chem. Res.* **2014**, *47*, 2128-2140.
187. Qi, Z.; Schalley, C. A., *Acc. Chem. Res.* **2014**, *47*, 2222-2233.
188. Burattini, S.; Greenland, B. W.; Chappell, D.; Colquhoun, H. M.; Hayes, W., *Chem. Soc. Rev.* **2010**, *39*, 1973-1985.
189. Sambri, L.; Cucinotta, F.; Paoli, G. D.; Stagni, S.; Cola, L. D., *New J. Chem.* **2010**, *34*, 2093-2096.
190. Burnworth, M.; Tang, L.; Kumpfer, J. R.; Duncan, A. J.; Beyer, F. L.; Fiore, G. L.; Rowan, S. J.; Weder, C., *Nature* **2011**, *472*, 334-7.
191. Yerushalmi, R.; Scherz, A.; van der Boom, M. E.; Kraatz, H.-B., *J. Mater. Chem.* **2005**, *15*, 4480-4487.
192. Tam, A. Y.-Y.; Wong, K. M.-C.; Wang, G.; Yam, V. W.-W., *Chem. Commun.* **2007**, 2028-2030.
193. Yang, B.; Zhang, H.; Peng, H.; Xu, Y.; Wu, B.; Weng, W.; Li, L., *Polym. Chem.* **2014**, *5*, 1945-1953.
194. Yuan, J.; Zhang, H.; Hong, G.; Chen, Y.; Chen, G.; Xu, Y.; Weng, W., *J. Mater. Chem. B* **2013**, *1*, 4809-4818.
195. Beck, J. B.; Rowan, S. J., *J. Am. Chem. Soc.* **2003**, *125*, 13922-13923.
196. Balkenende, D. W. R.; Coulibaly, S.; Balog, S.; Simon, Y. C.; Fiore, G. L.; Weder, C., *J. Am. Chem. Soc.* **2014**, *136*, 10493-10498.
197. Martinez-Calvo, M.; Kotova, O.; Mobius, M. E.; Bell, A. P.; McCabe, T.; Boland, J. J.; Gunnlaugsson, T., *J. Am. Chem. Soc.* **2015**, *137*, 1983-1992.
198. Moulton, B.; Zaworotko, M. J., *Chem. Rev.* **2001**, *101*, 1629-1658.
199. O'Keeffe, M.; Yaghi, O. M., *Chem. Rev.* **2012**, *112*, 675-702.
200. Li, M.; Li, D.; O'Keeffe, M.; Yaghi, O. M., *Chem. Rev.* **2014**, *114*, 1343-1370.
201. Furukawa, H.; Cordova, K. E.; O'Keeffe, M.; Yaghi, O. M., *Science* **2013**, *341*.
202. Lee, J. Y.; Farha, O. K.; Roberts, J.; Scheidt, K. A.; Nguyen, S. B. T.; Hupp, J. T., *Chem. Soc. Rev.* **2009**, *38*, 1450-1459.
203. Moon, H. R.; Lim, D.-W.; Suh, M. P., *Chem. Soc. Rev.* **2013**, *42*, 1807-1824.
204. Gao, X.; Liu, M.; Lan, J.; Liang, L.; Zhang, X.; Sun, J., *Cryst. Growth Des.* **2017**, *17*, 51-57.
205. Wang, J.; Sun, W.; Chang, S.; Liu, H.; Zhang, G.; Wang, Y.; Liu, Z., *RSC Adv.* **2015**, *5*, 48574-48579.
206. Wang, Y.-Q.; Tan, Q.-H.; Liu, H.-T.; Sun, W.; Liu, Z.-L., *RSC Adv.* **2015**, *5*, 86614-86619.
207. Kreno, L. E.; Leong, K.; Farha, O. K.; Allendorf, M.; Van Duyne, R. P.; Hupp, J. T., *Chem. Rev.* **2012**, *112*, 1105-1125.
208. Cui, X.; Chen, K.; Xing, H.; Yang, Q.; Krishna, R.; Bao, Z.; Wu, H.; Zhou, W.; Dong, X.; Han, Y.; Li, B.; Ren, Q.; Zaworotko, M. J.; Chen, B., *Science* **2016**, *353*, 141-144.

209. Chen, C.-X.; Liu, Q.-K.; Ma, J.-P.; Dong, Y.-B., *J. Mater. Chem.* **2012**, *22*, 9027-9033.
210. Chaemchuen, S.; Kabir, N. A.; Zhou, K.; Verpoort, F., *Chem. Soc. Rev.* **2013**, *42*, 9304-9332.
211. Eddaoudi, M.; Kim, J.; Rosi, N.; Vodak, D.; Wachter, J.; O'Keeffe, M.; Yaghi, O. M., *Science* **2002**, *295*, 469-472.
212. Moellmer, J.; Lange, M.; Moeller, A.; Patzschke, C.; Stein, K.; Laessig, D.; Lincke, J.; Glaeser, R.; Krautscheid, H.; Staudt, R., *J. Mater. Chem.* **2012**, *22*, 10274-10286.
213. Thallapally, P. K.; Tian, J.; Kishan, M. R.; Fernandez, C. A.; Dalgarno, S. J.; McGrail, P. B.; Warren, J. E.; Atwood, J. L., *J. Am. Chem. Soc.* **2008**, *130*, 16842-16843.
214. Reichenbach, C.; Kalies, G.; Lincke, J.; Lässig, D.; Krautscheid, H.; Moellmer, J.; Thommes, M., *Microporous Mesoporous Mater.* **2011**, *142*, 592-600.
215. Lincke, J.; Lässig, D.; Kobalz, M.; Bergmann, J.; Handke, M.; Möllmer, J.; Lange, M.; Roth, C.; Möller, A.; Staudt, R.; Krautscheid, H., *Inorg. Chem.* **2012**, *51*, 7579-7586.
216. Nugent, P. S.; Belmabkhout, Y.; Burd, S. D.; Cairns, A.; Luebke, R.; Forrest, K. A.; Pham, T. T.; Ma, S.; Space, B.; Wojtas, Ł.; Eddaoudi, M.; Zaworotko, M. J., *Nature* **2013**, *495*, 80–84
217. Hawes, C. S. *1,2-Diazoles: Versatile Tectons for Metallosupramolecular Assemblies*. Ph.D. Thesis, University of Canterbury, New Zealand, 2012.
218. Ockwig, N. W.; Delgado-Friedrichs, O.; O'Keeffe, M.; Yaghi, O. M., *Acc. Chem. Res.* **2005**, *38*, 176-182.
219. Delgado Friedrichs, O.; O'Keeffe, M.; Yaghi, O. M., *Acta Crystallogr., Sect. A* **2003**, *59*, 515-525.
220. O'Keeffe, M.; Peskov, M. A.; Ramsden, S. J.; Yaghi, O. M., *Acc. Chem. Res.* **2008**, *41*, 1782-1789.
221. Batten, S. R. N., S. M.; Turner, D. R., *Coordination Polymers: Design, Analysis and Application*. RSC Publishing: Cambridge: 2009.
222. Hawes, C. S.; Byrne, K.; Schmitt, W.; Gunnlaugsson, T., *Inorg. Chem.* **2016**, *55*, 11570-11582.
223. Xiao, Y.; Wang, S.-H.; Zheng, F.-K.; Wu, M.-F.; Xu, J.; Liu, Z.-F.; Chen, J.; Li, R.; Guo, G.-C., *CrystEngComm* **2016**, *18*, 721-727.
224. Huang, W.; Pan, F.; Liu, Y.; Huang, S.; Li, Y.; Yong, J.; Li, Y.; Kirillov, A. M.; Wu, D., *Inorg. Chem.* **2017**, *56*, 6362-6370.
225. Karmakar, A.; Samanta, P.; Desai, A. V.; Ghosh, S. K., *Acc. Chem. Res.* **2017**.
226. Fritzsche, J. C.; Grzywa, M.; Denysenko, D.; Bon, V.; Senkovska, I.; Kaskel, S.; Volkmer, D., *Dalton Trans.* **2017**, *46*, 6745-6755
227. Khatua, S.; Kumar Bar, A.; Konar, S., *Chem. Eur. J.* **2016**, *22*, 16277-16285.
228. Schneemann, A.; Bon, V.; Schwedler, I.; Senkovska, I.; Kaskel, S.; Fischer, R. A., *Chem. Soc. Rev.* **2014**, *43*, 6062-6096.
229. Cui, Y.; Yue, Y.; Qian, G.; Chen, B., *Chem. Rev.* **2012**, *112*, 1126-1162.
230. Wu, H.; Ying, L.; Yang, W.; Cao, Y., *Chem. Soc. Rev.* **2009**, *38*, 3391-3400.
231. Johnson, J. A.; Finn, M. G.; Koberstein, J. T.; Turro, N. J., *Macromol. Rapid Commun.* **2008**, *29*, 1052-1072.
232. Zhang, C.; Shen, X.; Sakai, R.; Gottschaldt, M.; Schubert, U. S.; Hirohara, S.; Tanihara, M.; Yano, S.; Obata, M.; Xiao, N.; Satoh, T.; Kakuchi, T., *J. Polym. Sci., Part A: Polym. Chem.* **2011**, *49*, 746-753.
233. Munuera, L.; O'Reilly, R. K., *Dalton Trans.* **2010**, *39*, 388-391.
234. Xiao, N.; Chen, Y.; Shen, X.; Zhang, C.; Yano, S.; Gottschaldt, M.; Schubert, U. S.; Kakuchi, T.; Satoh, T., *Polym. J.* **2013**, *45*, 216-225.

235. Shi, W.; Zhang, J.; Cheng, P. *Metal organic framework material with acid and base stability and its preparation method and application*. CN105924460A, 2016.
236. Zou, J.-Y.; Shi, W.; Zhang, J.-Y.; He, Y.-F.; Gao, H.-L.; Cui, J.-Z.; Cheng, P., *CrystEngComm* **2014**, *16*, 7133-7140.
237. Zhao, J.-P.; Zhao, R.; Song, W.-C.; Yang, Q.; Liu, F.-C.; Bu, X.-H., *Cryst. Growth Des.* **2013**, *13*, 437-439.
238. Tian, D.; Liu, S.-J.; Chang, Z.; Zhang, Y.-H.; Zhao, J.-P.; Bu, X.-H., *CrystEngComm* **2013**, *15*, 9344-9347.
239. Wang, X.-J.; Li, P.-Z.; Liu, L.; Zhang, Q.; Borah, P.; Wong, J. D.; Chan, X. X.; Rakesh, G.; Li, Y.; Zhao, Y., *Chem. Commun.* **2012**, *48*, 10286-10288.
240. Ruan, C.-Z.; Wen, R.; Liang, M.-X.; Kong, X.-J.; Ren, Y.-P.; Long, L.-S.; Huang, R.-B.; Zheng, L.-S., *Inorg. Chem.* **2012**, *51*, 7587-7591.
241. Jiang, Z.-Q.; Jiang, G.-Y.; Wang, F.; Zhao, Z.; Zhang, J., *Chem. Commun.* **2012**, *48*, 3653-3655.
242. Gao, W.-Y.; Yan, W.; Cai, R.; Williams, K.; Salas, A.; Wojtas, L.; Shi, X.; Ma, S., *Chem. Commun.* **2012**, *48*, 8898-900.
243. Gao, W.-Y.; Yan, W.; Cai, R.; Williams, K.; Salas, A.; Wojtas, L.; Shi, X.; Ma, S., *Chem. Commun. (Cambridge, U. K.)* **2012**, *48*, 8898-8900.
244. Rybak, J.-C.; Tegel, M.; Johrendt, D.; Mueller-Buschbaum, K., *Z. Kristallogr. - Cryst. Mater.* **2010**, *225*, 187-194.
245. Zou, J.-Y.; Gao, H.-L.; Shi, W.; Cui, J.-Z.; Cheng, P., *CrystEngComm* **2013**, *15*, 2682-2687.
246. Seth, S.; Savitha, G.; Moorthy, J. N., *Inorg. Chem.* **2015**, *54*, 6829-6835.
247. Zhang, Z.; Xiang, S.; Chen, Y.-S.; Ma, S.; Lee, Y.; Phely-Bobin, T.; Chen, B., *Inorg. Chem.* **2010**, *49*, 8444-8448.
248. Devic, T.; David, O.; Valls, M.; Marrot, J.; Couty, F.; Ferey, G., *J. Am. Chem. Soc.* **2007**, *129*, 12614-12615.
249. Yan, Y.; Suyetin, M.; Bichoutskaia, E.; Blake, A. J.; Allan, D. R.; Barnett, S. A.; Schroeder, M., *Chem. Sci.* **2013**, *4*, 1731-1736.
250. Wang, X.-J.; Li, P.-Z.; Chen, Y.; Zhang, Q.; Zhang, H.; Chan, X. X.; Ganguly, R.; Li, Y.; Jiang, J.; Zhao, Y., *Sci. Rep.* **2013**, *3*, 1149, 5 pp.
251. Handke, M.; Weber, H.; Lange, M.; Möllmer, J.; Lincke, J.; Gläser, R.; Staudt, R.; Krautscheid, H., *Inorg. Chem.* **2014**, *53*, 7599-7607.
252. Naik, A. D.; Dîrtu, M. M.; Railliet, A. P.; Marchand-Brynaert, J.; Garcia, Y., *Polymers* **2011**, *3*, 1750.
253. Kobalz, M.; Lincke, J.; Kobalz, K.; Erhart, O.; Bergmann, J.; Laessig, D.; Lange, M.; Moellmer, J.; Glaeser, R.; Staudt, R.; Krautscheid, H., *Inorg. Chem.* **2016**, *55*, 3030-3039.
254. Li, J.-R.; Sculley, J.; Zhou, H.-C., *Chem. Rev.* **2012**, *112*, 869-932.
255. Bulut, A.; Zorlu, Y.; Kirpi, E.; Çetinkaya, A.; Wörle, M.; Beckmann, J.; Yücesan, G., *Cryst. Growth Des.* **2015**, *15*, 5665-5669.
256. Wu, Z.-L.; Dong, J.; Ni, W.-Y.; Zhang, B.-W.; Cui, J.-Z.; Zhao, B., *Inorg. Chem.* **2015**, *54*, 5266-5272.
257. Toyao, T.; Saito, M.; Dohshi, S.; Mochizuki, K.; Iwata, M.; Higashimura, H.; Horiuchi, Y.; Matsuoka, M., *Chem. Commun.* **2014**, *50*, 6779-6781.
258. Zheng, M.; Tan, H.; Xie, Z.; Zhang, L.; Jing, X.; Sun, Z., *ACS Appl. Mater. Interfaces* **2013**, *5*, 1078-1083.
259. Paul, A.; Ribeiro, A. P. C.; Karmakar, A.; Guedes da Silva, M. F. C.; Pombeiro, A. J. L., *Dalton Trans.* **2016**, *45*, 12779-12789.
260. Wang, W.; Xiao, Z.; Lin, H.; Wang, R.; Zhang, L.; Sun, D., *RSC Adv.* **2016**, *6*, 16575-16580.

261. Forgan, R. S.; Sauvage, J.-P.; Stoddart, J. F., *Chem. Rev.* **2011**, *111*, 5434-5464.
262. Marcos, V.; Stephens, A. J.; Jaramillo-Garcia, J.; Nussbaumer, A. L.; Woltering, S. L.; Valero, A.; Lemonnier, J.-F.; Vitorica-Yrezabal, I. J.; Leigh, D. A., *Science* **2016**, *352*, 1555-1559.
263. Zhang, G.; Gil-Ramírez, G.; Markevicius, A.; Browne, C.; Vitorica-Yrezabal, I. J.; Leigh, D. A., *J. Am. Chem. Soc.* **2015**, *137*, 10437-10442.
264. Ayme, J.-F.; Gil-Ramírez, G.; Leigh, D. A.; Lemonnier, J.-F.; Markevicius, A.; Muryn, C. A.; Zhang, G., *J. Am. Chem. Soc.* **2014**, *136*, 13142-13145.
265. Jiménez, M. C.; Dietrich-Buchecker, C.; Sauvage, J.-P., *Angew. Chem. Int. Ed.* **2000**, *39*, 3284-3287.
266. Jäger, R.; Vögtle, F., *Angew. Chem. Int. Ed.* **1997**, *36*, 930-944.
267. Cesario, M.; Dietrich-Buchecker, C. O.; Guilhem, J.; Pascard, C.; Sauvage, J. P., *J. Chem. Soc., Chem. Commun.* **1985**, 244-247.
268. Fujita, M., *Acc. Chem. Res.* **1999**, *32*, 53-61.
269. Weck, M.; Mohr, B.; Sauvage, J.-P.; Grubbs, R. H., *J. Org. Chem.* **1999**, *64*, 5463-5471.
270. Lewis, J. E. M.; Beer, P. D.; Loeb, S. J.; Goldup, S. M., *Chem. Soc. Rev.* **2017**.
271. Dietrich-Buchecker, C. O.; Sauvage, J. P.; Kintzinger, J. P., *Tetrahedron Lett.* **1983**, *24*, 5095-8.
272. Hunter, C. A., *J. Am. Chem. Soc.* **1992**, *114*, 5303-5311.
273. Adams, H.; Carver, F. J.; Hunter, C. A., *J. Chem. Soc., Chem. Commun.* **1995**, 809-810.
274. Ottens-Hildebrandt, S.; Nieger, M.; Rissanen, K.; Rouvinen, J.; Meier, S.; Harder, G.; Vogtle, F., *J. Chem. Soc., Chem. Commun.* **1995**, 777-778.
275. Johnston, A. G.; Leigh, D. A.; Pritchard, R. J.; Deegan, M. D., *Angew. Chem. Int. Ed.* **1995**, *34*, 1209-1212.
276. Marrs, C. N.; Evans, N. H., *Org.Biomol. Chem.* **2015**, *13*, 11021-11025.
277. Ashton, P. R.; Goodnow, T. T.; Kaifer, A. E.; Reddington, M. V.; Slawin, A. M. Z.; Spencer, N.; Stoddart, J. F.; Vicent, C.; Williams, D. J., *Angew. Chem. Int. Ed.* **1989**, *28*, 1396-1399.
278. Hamilton, D. G.; Davies, J. E.; Prodi, L.; Sanders, J. K. M., *Chem. Eur. J.* **1998**, *4*, 608-620.
279. Sambrook, M. R.; Beer, P. D.; Wisner, J. A.; Paul, R. L.; Cowley, A. R., *J. Am. Chem. Soc.* **2004**, *126*, 15364-15365.
280. Huang, B.; Santos, S. M.; Felix, V.; Beer, P. D., *Chem. Commun.* **2008**, 4610-4612.
281. Lewis, J. E. M.; Bordoli, R. J.; Denis, M.; Fletcher, C. J.; Galli, M.; Neal, E. A.; Rochette, E. M.; Goldup, S. M., *Chem. Sci.* **2016**, *7*, 3154-3161.
282. Kirketerp, M. S., *Photophysical properties of pi-conjugated molecular ions in the gas phase*. PhD Thesis, Aarhus University: 2011.
283. Amb, C. M.; Rasmussen, S. C., *J. Org. Chem.* **2006**, *71*, 4696-4699.
284. Hay, D. A.; Adam, F. M.; Bish, G.; Calo, F.; Dixon, R.; Fray, M. J.; Hitchin, J.; Jones, P.; Paradowski, M.; Parsons, G. C.; Proctor, K. J. W.; Pryde, D. C.; Smith, N. N.; Tran, T.-D., *Tetrahedron Lett.* **2011**, *52*, 5728-5732.
285. Johnson, C. J.; Morgan, G. G.; Albrecht, M., *J. Mater. Chem. C* **2015**, *3*, 7883-7889
286. Nonat, A. M.; Allain, C. m.; Faulkner, S.; Gunnlaugsson, T., *Inorg. Chem.* **2010**, *49*, 8449-8456.
287. Bunzli, J.-C. G.; Eliseeva, S. V., *Chem. Sci.* **2013**, *4*, 1939-1949.
288. de Bettencourt-Dias, A., *Dalton Trans.* **2007**, 2229-2241.
289. Feng, J.; Zhang, H., *Chem. Soc. Rev.* **2013**, *42*, 387-410.
290. Desreux, J. F.; Reilley, C. N., *J. Am. Chem. Soc.* **1976**, *98*, 2105-2109.

291. Parker, D., *Coord. Chem. Rev.* **2000**, *205*, 109-130.
292. Indapurkar, A.; Henriksen, B.; Tolman, J.; Fletcher, J., *J. Pharm. Sci.* **2013**, *102*, 2589-2598.
293. Kelkar, S. S.; Xue, L.; Turner, S. R.; Reineke, T. M., *Biomacromolecules* **2014**.
294. Thibon, A.; Pierre, V. C., *Anal. Bioanal. Chem* **2009**, *394*, 107-120.
295. Bobba, G.; Bretonniere, Y.; Frias, J.-C.; Parker, D., *Org. Biomol. Chem.* **2003**, *1*, 1870-1872.
296. Eliseeva, S. V.; Bunzli, J.-C. G., *Chem. Soc. Rev.* **2010**, *39*, 189-227.
297. Werts, M. H. V.; Jukes, R. T. F.; Verhoeven, J. W., *Phys. Chem. Chem. Phys.* **2002**, *4*, 1542-1548.
298. Supkowski, R. M.; Horrocks Jr, W. D., *Inorg. Chim. Acta* **2002**, *340*, 44-48.
299. J.C.G. Bunzli, G. R. C., *Lanthanide Probes in Life, Chemical and Earth Sciences, Theory and Practice*. 1 ed.; Elsevier Science: Amsterdam, 1989.
300. Beeby, A.; M. Clarkson, I.; S. Dickins, R.; Faulkner, S.; Parker, D.; Royle, L.; S. de Sousa, A.; A. Gareth Williams, J.; Woods, M., *J. Chem. Soc., Perkin Trans. 2* **1999**, 493-504.
301. Shavaleev, N. M.; Eliseeva, S. V.; Scopelliti, R.; Bunzli, J.-C. G., *Inorg. Chem.* **2014**, *53*, 5171-5178.
302. Gampp, H.; Maeder, M.; Meyer, C. J.; Zuberbühler, A. D., *Talanta* **1985**, *32*, 95-101.
303. JPlus Consulting Pty Ltd. http://jplusconsulting.com/products/reactlab-equilibria/.
304. Di Pietro, S.; Imbert, D.; Mazzanti, M., *Chem. Commun.* **2014**, *50*, 10323-10326.
305. Amabilino, D. B.; Smith, D. K.; Steed, J. W., *Chem. Soc. Rev.* **2017**, *46*, 2404-2420.
306. van Esch, J. H., *Langmuir* **2009**, *25*, 8392-8394.
307. Di Lorenzo, M. L.; Cocca, M.; Gentile, G.; Avella, M.; Gutierrez, D.; Della Pirriera, M.; Kennedy, M.; Ahmed, H.; Doran, J., *J. Colloid Interface Sci.* **2013**, *398*, 95-102.
308. Aida, T.; Meijer, E. W.; Stupp, S. I., *Science* **2012**, *335*, 813-817.
309. Smith, D. K., *Chem. Soc. Rev.* **2009**, *38*, 684-694.
310. Dehn, S.; Tong, K. W. K.; Clady, R. G. C.; Owen, D. M.; Gaus, K.; Schmidt, T. W.; Braet, F.; Thordarson, P., *New J. Chem.* **2011**, *35*, 1466-1471.
311. Poolman, J. M.; Boekhoven, J.; Besselink, A.; Olive, A. G. L.; van Esch, J. H.; Eelkema, R., *Nat. Protoc.* **2014**, *9*, 977-988.
312. D'Andrade, B. W.; Forrest, S. R., *Adv. Mater.* **2004**, *16*, 1585-1595.
313. Aparna, M.; Pankaj, K.; Kamalasanan, M. N.; Subhas, C., *Semicond. Sci. Technol.* **2006**, *21*, R35.
314. Stan, C. S.; Horlescu, P.; Popa, M.; Coroaba, A.; Ursu, E. L., *New J. Chem.* **2016**.
315. Abbel, R.; Grenier, C.; Pouderoijen, M. J.; Stouwdam, J. W.; Leclère, P. E. L. G.; Sijbesma, R. P.; Meijer, E. W.; Schenning, A. P. H. J., *J. Am. Chem. Soc.* **2009**, *131*, 833-843.
316. Tang, J. F.; Li, G. N.; Yang, C.; Gou, J.; Luo, D. H.; He, H., *CrystEngComm* **2015**.
317. Ma, M.-L.; Qin, J.-H.; Ji, C.; Xu, H.; Wang, R.; Li, B.-J.; Zang, S.-Q.; Hou, H.-W.; Batten, S. R., *J. Mater. Chem. C* **2014**, *2*, 1085-1093.
318. Rong, J.; Zhang, W.; Bai, J., *CrystEngComm* **2016**, *18*, 7728-7736.
319. Wang, H.; Ji, X.; Li, Z.; Zhu, C. N.; Yang, X.; Li, T.; Wu, Z. L.; Huang, F., *Mater. Chem. Front.* **2017**, *1*, 167-171.
320. Maiwald, M. M.; Wagner, A. T.; Kratsch, J.; Skerencak-Frech, A.; Trumm, M.; Geist, A.; Roesky, P. W.; Panak, P. J., *Dalton Trans.* **2017**, *46*, 9981-9994.
321. Leoncini, A.; Huskens, J.; Verboom, W., *Chem. Soc. Rev.* **2017**, *46*, 7229-7273.
322. Kaltsoyannis, N., *Inorg. Chem.* **2013**, *52*, 3407-3413.
323. Fryer-Kanssen, I.; Austin, J.; Kerridge, A., *Inorg. Chem.* **2016**, *55*, 10034-10042.

324. Macerata, E.; Mossini, E.; Scaravaggi, S.; Mariani, M.; Mele, A.; Panzeri, W.; Boubals, N.; Berthon, L.; Charbonnel, M.-C.; Sansone, F.; Arduini, A.; Casnati, A., *J. Am. Chem. Soc.* **2016**, *138*, 7232-7235.
325. Wilson, A. K.; van Mourik, T.; Dunning, T. H., *J. Mol. Struct. Thechem* **1996**, *388*, 339-349.
326. Duan, P.; Cao, H.; Zhang, L.; Liu, M., *Soft Matter* **2014**, *10*, 5428-5448.
327. Kitchen, J. A.; Barry, D. E.; Mercs, L.; Albrecht, M.; Peacock, R. D.; Gunnlaugsson, T., *Angew. Chem. Int. Ed.* **2012**, *51*, 704-708.
328. Lohe, M. R.; Rose, M.; Kaskel, S., *Chem. Commun.* **2009**, 6056-6058.
329. Lu, W.; Wei, Z.; Gu, Z.-Y.; Liu, T.-F.; Park, J.; Park, J.; Tian, J.; Zhang, M.; Zhang, Q.; Gentle Iii, T.; Bosch, M.; Zhou, H.-C., *Chem. Soc. Rev.* **2014**, *43*, 5561-5593.
330. Lin, Z.-J.; Lu, J.; Hong, M.; Cao, R., *Chem. Soc. Rev.* **2014**, *43*, 5867-5895.
331. Giacovazzo, C., Monaco, H. L., Viterbo, D., Scordari, F., Gilli, G., Zanotti, G., Catti, M., *Fundamentals of Crystallography*. International Union of Crystallography, Oxford University Press Inc.: New York, 1992.
332. Whitesell, J. K.; Davis, R. E.; Saunders, L. L.; Wilson, R. J.; Feagins, J. P., *J. Am. Chem. Soc.* **1991**, *113*, 3267-3270.
333. Liu, T.-F.; Lu, J.; Tian, C.; Cao, M.; Lin, Z.; Cao, R., *Inorg. Chem.* **2011**, *50*, 2264-2271.
334. Hong, M.; Zhao, Y.; Su, W.; Cao, R.; Fujita, M.; Zhou, Z.; Chan, A. S. C., *Angew. Chem., Int. Ed.* **2000**, *39*, 2468-2470.
335. Xu, B.; Lin, X.; He, Z.; Lin, Z.; Cao, R., *Chem. Commun.* **2011**, *47*, 3766-3768.
336. Hawes, C. S.; Knowles, G. P.; Chaffee, A. L.; Turner, D. R.; Batten, S. R., *Cryst. Growth Des.* **2015**, *15*, 3417-3425.
337. Li, J.-R.; Kuppler, R. J.; Zhou, H.-C., *Chem. Soc. Rev.* **2009**, *38*, 1477-1504.
338. Murray, L. J.; Dinca, M.; Long, J. R., *Chem. Soc. Rev.* **2009**, *38*, 1294-1314.
339. Etter, M. C., *Acc. Chem. Res.* **1990**, *23*, 120-6.
340. *GAVROG*, *Systre* 1.2.0; 2004.
341. Delgado-Friedrichs, O.; O'Keeffe, M., *Acta Crystallogr., Sect. A, Found Crystallogr.* **2003**, *A59*, 351-360.
342. Burrows, A. D.; Cassar, K.; Friend, R. M. W.; Mahon, M. F.; Rigby, S. P.; Warren, J. E., *CrystEngComm* **2005**, *7*, 548-550.
343. Yang, L.; Powell, D. R.; Houser, R. P., *Dalton Trans.* **2007**, 955-964.
344. Marques, L. F.; Marinho, M. V.; Correa, C. C.; Speziali, N. L.; Diniz, R.; Machado, F. C., *Inorg. Chim. Acta* **2011**, *368*, 242-246.
345. Bußkamp, H.; Deacon, G. B.; Hilder, M.; Junk, P. C.; Kynast, U. H.; Lee, W. W.; Turner, D. R., *CrystEngComm* **2007**, *9*, 394-411.
346. Groom, C. R.; Bruno, I. J.; Lightfoot, M. P.; Ward, S. C., *Acta Crystallographica Section B* **2016**, *72*, 171-179.
347. Wang, K.-W.; Chen, J.-L.; Cheng, Y.-M.; Chung, M.-W.; Hsieh, C.-C.; Lee, G.-H.; Chou, P.-T.; Chen, K.; Chi, Y., *Inorg. Chem.* **2010**, *49*, 1372-1383.
348. Pavia, D. L., Lampman, G. M., Kriz, G.S., *Introduction to Spectroscopy*. 3rd ed.; Thomson: Bellingham, Washington, 2001.
349. Spek, A. L., *Acta Crystallogr., Sect. C: Struct. Chem.* **2015**, *71*, 9-18.
350. Chatterjee, A., *Pak. J. Sci. Ind. Res.* **1986**, *29*, 255-8.
351. Wang, S.; Wang, X., *Small* **2015**, *11*, 3097-3112.
352. Constable, E. C.; Devereux, M.; Dunphy, E. L.; Housecroft, C. E.; Rudd, J. A.; Zampese, J. A., *Dalton Trans.* **2011**, *40*, 5505-5515.
353. Meyer, K.; Ranocchiari, M.; van Bokhoven, J. A., *Energy Environ Sci.* **2015**, *8*, 1923-1937.

354. Coskun, A.; Banaszak, M.; Astumian, R. D.; Stoddart, J. F.; Grzybowski, B. A., *Chem. Soc. Rev.* **2012**, *41*, 19-30.
355. Evans, N. H.; Beer, P. D., *Angew. Chem. Int. Ed.* **2014**, *53*, 11716-11754.
356. Caballero, A.; Zapata, F.; Beer, P. D., *Coord. Chem. Rev.* **2013**, *257*, 2434-2455.
357. Crassous, J., *Chem. Soc. Rev.* **2009**, *38*, 830-845.
358. Satyanarayana, S.; Dabrowiak, J. C.; Chaires, J. B., *Biochemistry* **1993**, *32*, 2573-2584.
359. Evans, N. H., *Chem. Eur. J.* **2017**, Advance Article, DOI: 10.1002/chem.201704149.
360. Ashton, P. R.; Iriepa, I.; Reddington, M. V.; Spencer, N.; Slawin, A. M. Z.; Stoddart, J. F.; Williams, D. J., *Tetrahedron Lett.* **1994**, *35*, 4835-8.
361. Li, S.-H.; Zhang, H.-Y.; Xu, X.; Liu, Y., *Nat. commun.* **2015**, *6*, 7590.
362. Ashton, P. R.; Reder, A. S.; Spencer, N.; Stoddart, J. F., *J. Am. Chem. Soc.* **1993**, *115*, 5286-5287.
363. McArdle, C. P.; Van, S.; Jennings, M. C.; Puddephatt, R. J., *J. Am. Chem. Soc.* **2002**, *124*, 3959-3965.
364. Pescitelli, G.; Di Bari, L.; Berova, N., *Chem. Soc. Rev.* **2014**, *43*, 5211-5233.
365. Berova, N.; Di Bari, L.; Pescitelli, G., *Chem. Soc. Rev.* **2007**, *36*, 914-931.
366. Pandiakumar, A. K.; Sarma, S. P.; Samuelson, A. G., *Tetrahedron Lett.* **2014**, *55*, 2917-2920.
367. Pepper, C.; Smith, H. J.; Barrell, K. J.; Nicholls, P. J.; Hewlins, M. J. E., *Chirality* **1994**, *6*, 400-404.
368. Collins, B. E.; Anslyn, E. V., *Chem. Eur. J.* **2007**, *13*, 4700-4708.
369. Veale, E. B.; Frimannsson, D. O.; Lawler, M.; Gunnlaugsson, T., *Org. Lett.* **2009**, *11*, 4040-4043.
370. Magri, D. C.; Brown, G. J.; McClean, G. D.; de Silva, A. P., *J. Am. Chem. Soc.* **2006**, *128*, 4950-4951.
371. Pandurangan, K.; Kitchen, J. A.; Blasco, S.; Boyle, E. M.; Fitzpatrick, B.; Feeney, M.; Kruger, P. E.; Gunnlaugsson, T., *Angew. Chem. Int. Ed.* **2015**, *54*, 4566-4570.
372. Erbas-Cakmak, S.; Leigh, D. A.; McTernan, C. T.; Nussbaumer, A. L., *Chem. Rev.* **2015**, *115*, 10081-10206.
373. Kistemaker, J. C. M.; Štacko, P.; Visser, J.; Feringa, B. L., *Nat. Chem.* **2015**, *7*, 890-896.
374. https://www.nobelprize.org/nobel_prizes/chemistry/laureates/2016/.
375. van Dongen, S. F. M.; Cantekin, S.; Elemans, J. A. A. W.; Rowan, A. E.; Nolte, R. J. M., *Chem. Soc. Rev.* **2014**, *43*, 99-122.
376. Langton, M. J.; Beer, P. D., *Acc. Chem. Res.* **2014**, *47*, 1935-1949.
377. Leigh, D. A.; Marcos, V.; Wilson, M. R., *ACS Catal.* **2014**, *4*, 4490-4497.
378. Pandurangan, K.; Kitchen, J. A.; McCabe, T.; Gunnlaugsson, T., *CrystEngComm* **2013**, *15*, 1421-1431.
379. Mirica, L. M.; Ottenwaelder, X.; Stack, T. D. P., *Chem. Rev.* **2004**, *104*, 1013-1046.
380. Kusukawa, T.; Fujita, M., *J. Am. Chem. Soc.* **2002**, *124*, 13576-13582.
381. Johnstone, T. C.; Suntharalingam, K.; Lippard, S. J., *Chem. Rev.* **2016**, *116*, 3436-3486.
382. Mukhopadhyay, S.; Gupta, R. K.; Paitandi, R. P.; Rana, N. K.; Sharma, G.; Koch, B.; Rana, L. K.; Hundal, M. S.; Pandey, D. S., *Organomet.* **2015**.
383. Rezai-Zadeh, K.; Shytle, R. D.; Bai, Y.; Tian, J.; Hou, H.; Mori, T.; Zeng, J.; Obregon, D.; Town, T.; Tan, J., *J. Cell. Mol. Med.* **2009**, *13*, 574-588.
384. Collin, F.; Sasaki, I.; Eury, H.; Faller, P.; Hureau, C., *Chem. Commun.* **2013**, *49*, 2130-2132.

385. Yellol, G. S.; Yellol, J. G.; Kenche, V. B.; Liu, X. M.; Barnham, K. J.; Donaire, A.; Janiak, C.; Ruiz, J., *Inorg. Chem.* **2014**, *54*, 470-475.
386. Xi, Y.-T.; Wei, P.-J.; Wang, R.-C.; Liu, J.-G., *Chem. Commun.* **2015**, *51*, 7455-7458.
387. Zhang, Q.; Wang, X.; Cheng, C.; Zhu, R.; Liu, N.; Hu, Y., *Org. Biomol. Chem.* **2012**, *10*, 2847-2854.
388. Chattopadhyay, B.; Vera, C. I. R.; Chuprakov, S.; Gevorgyan, V., *Org. Lett.* **2010**, *12*, 2166-2169.
389. Sun, R.; Wang, H.; Hu, J.; Zhao, J.; Zhang, H., *Org. Biomol. Chem.* **2014**, *12*, 5954-5963.
390. Jindabot, S.; Teerachanan, K.; Thongkam, P.; Kiatisevi, S.; Khamnaen, T.; Phiriyawirut, P.; Charoenchaidet, S.; Sooksimuang, T.; Kongsaeree, P.; Sangtrirutnugul, P., *J. Organomet. Chem.* **2014**, *750*, 35-40.
391. Bertrand, H. C.; Clede, S.; Guillot, R.; Lambert, F.; Policar, C., *Inorg. Chem.* **2014**, *53*, 6204-23.
392. Stengel, I.; Mishra, A.; Pootrakulchote, N.; Moon, S.-J.; Zakeeruddin, S. M.; Gratzel, M.; Bauerle, P., *J. Mater. Chem.* **2011**, *21*, 3726-3734.
393. Liu, Q.; Tor, Y., *Org. Lett.* **2003**, *5*, 2571-2572.
394. Desiraju, G. R.; Gavezzotti, A., *Acta Crystallogr. Sect. B* **1989**, *45*, 473-482.
395. Thongkam, P.; Jindabot, S.; Prabpai, S.; Kongsaeree, P.; Wititsuwannakul, T.; Surawatanawong, P.; Sangtrirutnugul, P., *RSC Adv.* **2015**, *5*, 55847-55855.
396. Bai, S.-Q.; Jiang, L.; Young, D. J.; Hor, T. S. A., *Aust. J. Chem.* **2016**, *69*, 372-378.
397. Bai, S.-Q.; Kai, D.; Ke, K. L.; Lin, M.; Jiang, L.; Jiang, Y.; Young, D. J.; Loh, X. J.; Li, X.; Hor, T. S. A., *ChemPlusChem* **2015**, *80*, 1235-1240.
398. Che, C.-M.; Tse, M.-C.; Chan, M. C. W.; Cheung, K.-K.; Phillips, D. L.; Leung, K.-H., *J. Am. Chem. Soc.* **2000**, *122*, 2464-2468.
399. Koskinen, L.; Jaaskelainen, S.; Oresmaa, L.; Haukka, M., *CrystEngComm* **2012**, *14*, 3509-3514.
400. Serpe, A.; Artizzu, F.; Marchiò, L.; Mercuri, M. L.; Pilia, L.; Deplano, P., *Cryst. Growth Des.* **2011**, *11*, 1278-1286.
401. Chu, Q.; Swenson, D. C.; MacGillivray, L. R., *Angew. Chem., Int. Ed.* **2005**, *44*, 3569-3572.
402. Khlobystov, A. N.; Blake, A. J.; Champness, N. R.; Lemenovskii, D. A.; Majouga, A. G.; Zyk, N. V.; Schroder, M., *Coord. Chem. Rev.* **2001**, *222*, 155-192.
403. Hollis, C. A.; Batten, S. R.; Sumby, C. J., *Cryst. Growth Des.* **2013**, *13*, 2350-2361.
404. Zhao, L.; Zhao, X.-L.; Mak, T. C. W., *Chem. - Eur. J.* **2007**, *13*, 5927-5936.
405. Burgess, J.; Steel, P. J., *Coord. Chem. Rev.* **2011**, *255*, 2094-2103.
406. Kelemu, S. W.; Steel, P. J., *Eur. J. Inorg. Chem.* **2014**, *2014*, 434-436.
407. Ovsyannikov, A.; Lang, M. N.; Ferlay, S.; Solovieva, S. E.; Antipin, I. S.; Konovalov, A. I.; Kyritsakas, N.; Hosseini, M. W., *Dalton Trans.* **2013**, *42*, 116-126.
408. Appleton, T. G.; Clark, H. C.; Manzer, L. E., *Coord. Chem. Rev.* **1973**, *10*, 335-422.
409. Sherman, S. E.; Lippard, S. J., *Chem. Rev.* **1987**, *87*, 1153-1181.
410. Hall, M. D.; Telma, K. A.; Chang, K.-E.; Lee, T. D.; Madigan, J. P.; Lloyd, J. R.; Goldlust, I. S.; Hoeschele, J. D.; Gottesman, M. M., *Cancer Res.* **2014**, *74*, 3913-3922.
411. Adams, C. J.; Fey, N.; Parfitt, M.; Pope, S. J. A.; Weinstein, J. A., *Dalton Trans.* **2007**, 4446-4456.
412. *SADABS*, Bruker-AXS Inc.: Madison, WI, 2001.
413. *Bruker APEX3*, Bruker-AXS Inc.: Madison, WI, 2015.
414. Sheldrick, G. M., *Acta Crystallogr., Sect. A: Found. Crystallogr.* **2008**, *64*, 112-122.
415. Sheldrick, G. M., *Acta Crystallogr., Sect. C: Struct. Chem.* **2015**, *71*, 3-8.

416. Dolomanov, O. V.; Bourhis, L. J.; Gildea, R. J.; Howard, J. A. K.; Puschmann, H., *J. Appl. Crystallogr.* **2009**, *42*, 339-341.
417. Coles, S. J.; Gale, P. A., *Chemical Science* **2012**, *3*, 683-689.
418. *CrystalClear-SM Expert 3.1*, Rigaku: 2012.
419. Huebschle, C. B.; Sheldrick, G. M.; Dittrich, B., *J. Appl. Crystallogr.* **2011**, *44*, 1281-1284.
420. Cai, C.; Vasella, A., *Helv. Chim. Acta* **1995**, *78*, 732-757.
421. Bauer, S.; Ochoa-Puentes, C.; Sun, Q.; Bause, M.; Bernhardt, G.; König, B.; Buschauer, A., *ChemMedChem* **2013**, *8*, 1773-1778.
422. Nettekoven, M.; Jenny, C., *Org. Process Res. Dev.* **2002**, *7*, 38-43.

9 Appendices

9.1 Appendix A (NMR)

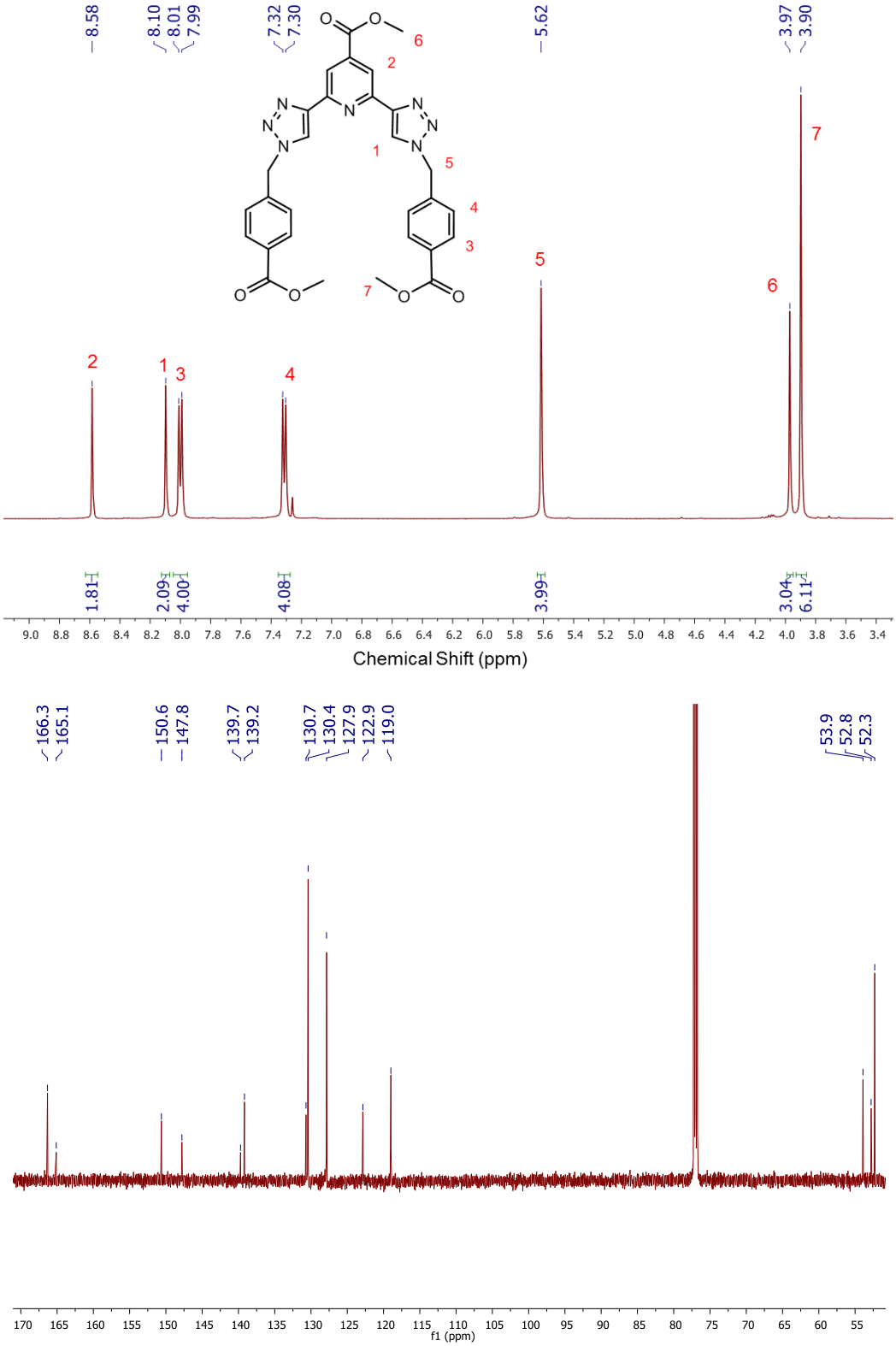

Figure A.1 (Top) ^{1}H NMR (600 MHz, $CDCl_3$) and (Bottom) ^{13}C NMR (151 MHz, DMSO-d_6) spectra of **btp** ligand **83**.

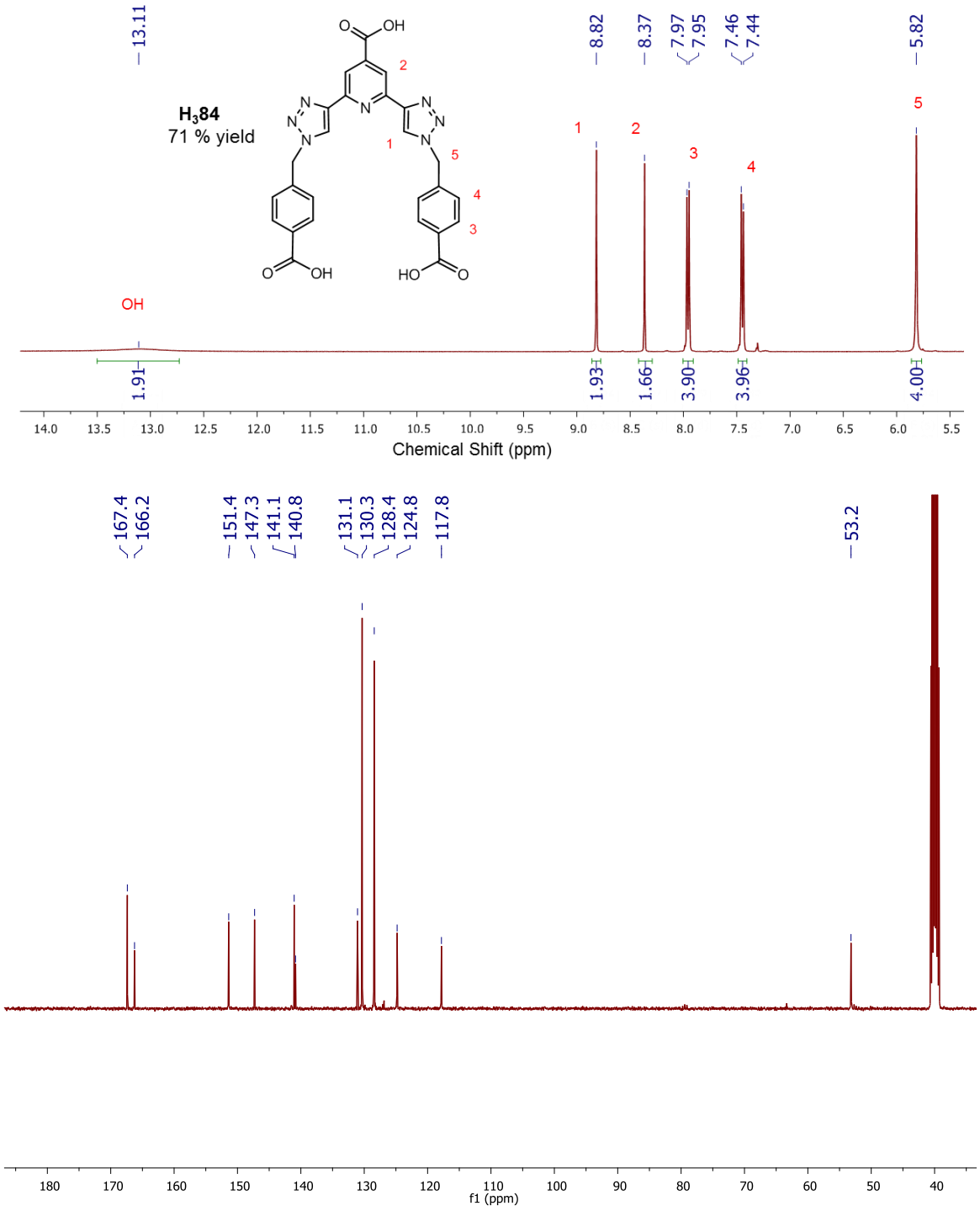

Figure A.2 (Top) ^{1}H NMR (400 MHz, DMSO-d_6) and (Bottom) ^{13}C NMR (101 MHz, DMSO-d_6) spectra of **btp** ligand **H$_3$84**.

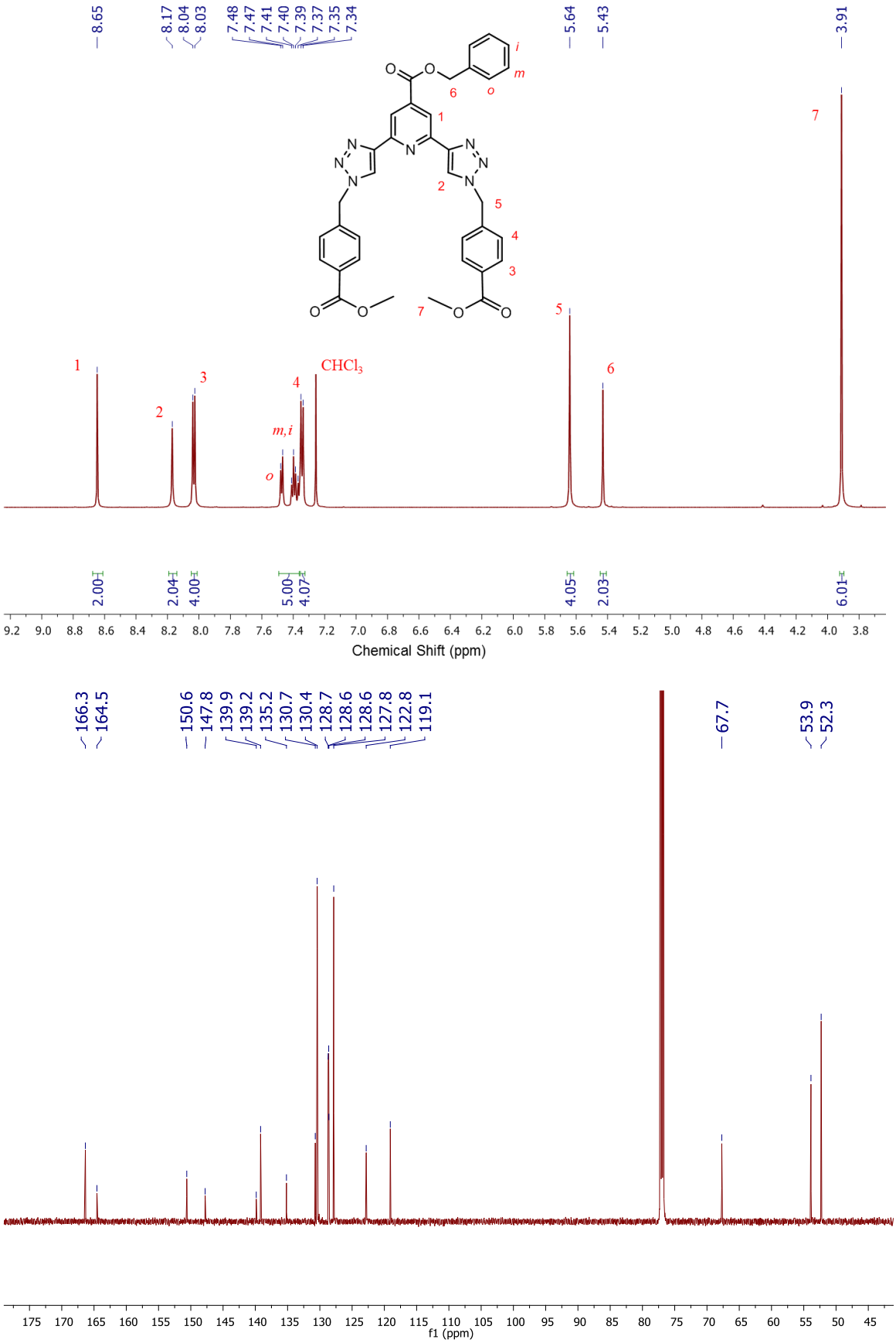

Figure A.3 (Top) ^{1}H NMR (600 MHz, $CDCl_3$) and (Bottom) ^{13}C NMR (151 MHz, DMSO-d_6) spectra of **btp** ligand **85**

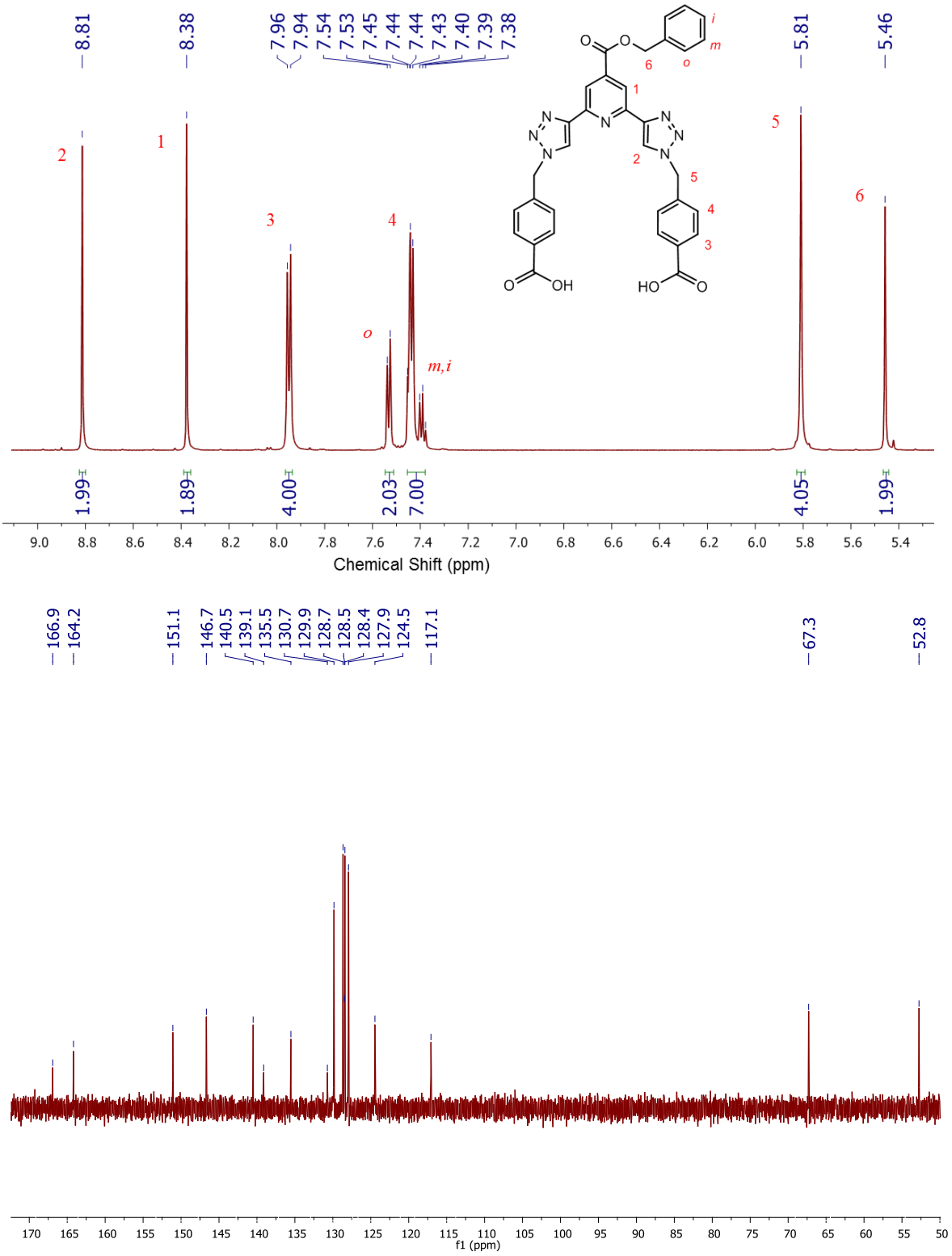

Figure A.4 (Top) ^{1}H NMR (600 MHz, DMSO-d_6) and (Bottom) ^{13}C NMR (101 MHz, DMSO-d_6) spectra of **btp** ligand **86**

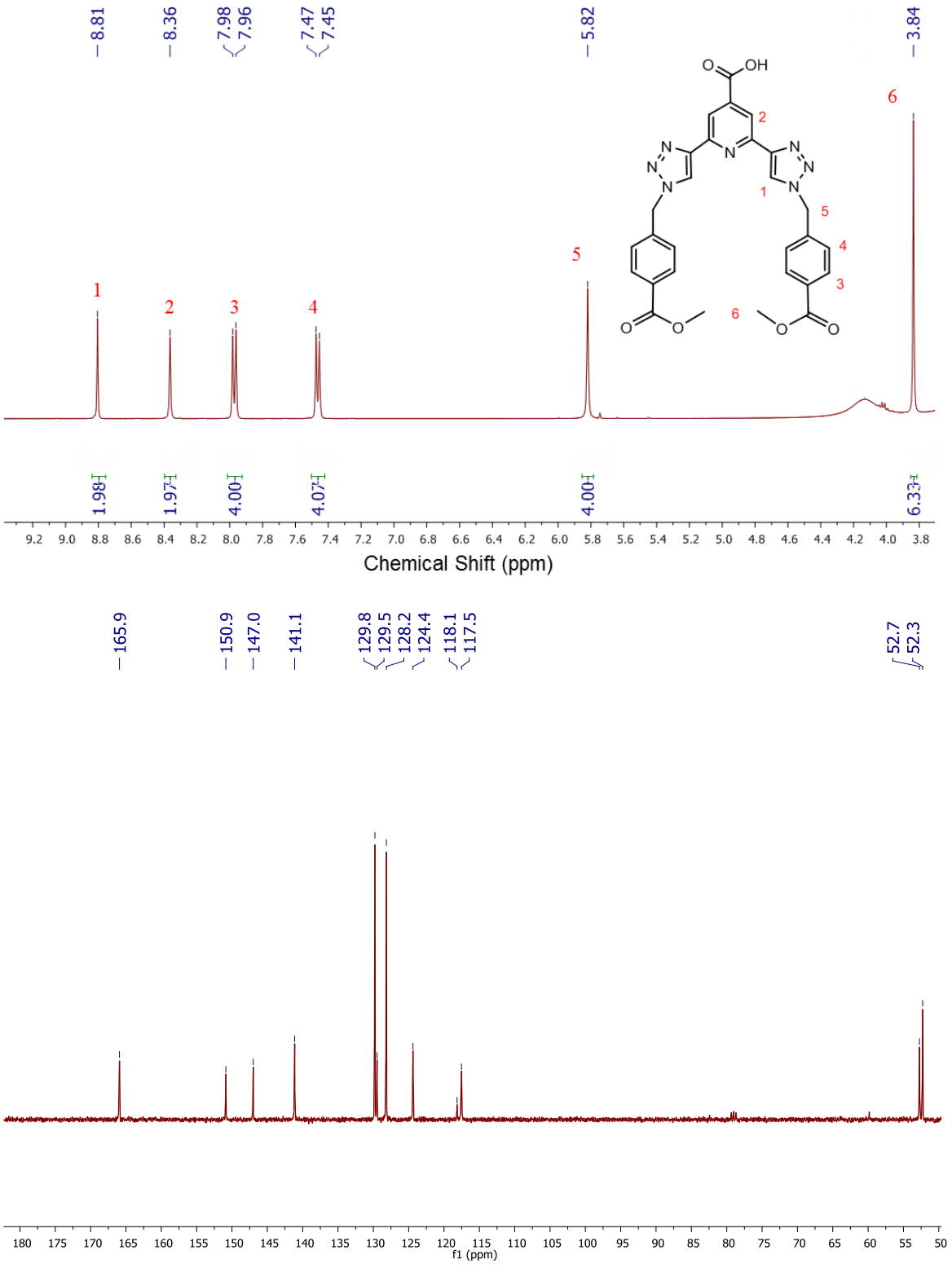

Figure A.5 (Top) ^{1}H NMR (400 MHz, DMSO-d_6) and (Bottom) ^{13}C NMR (101 MHz, DMSO-d_6) spectra of **btp** ligand **87**

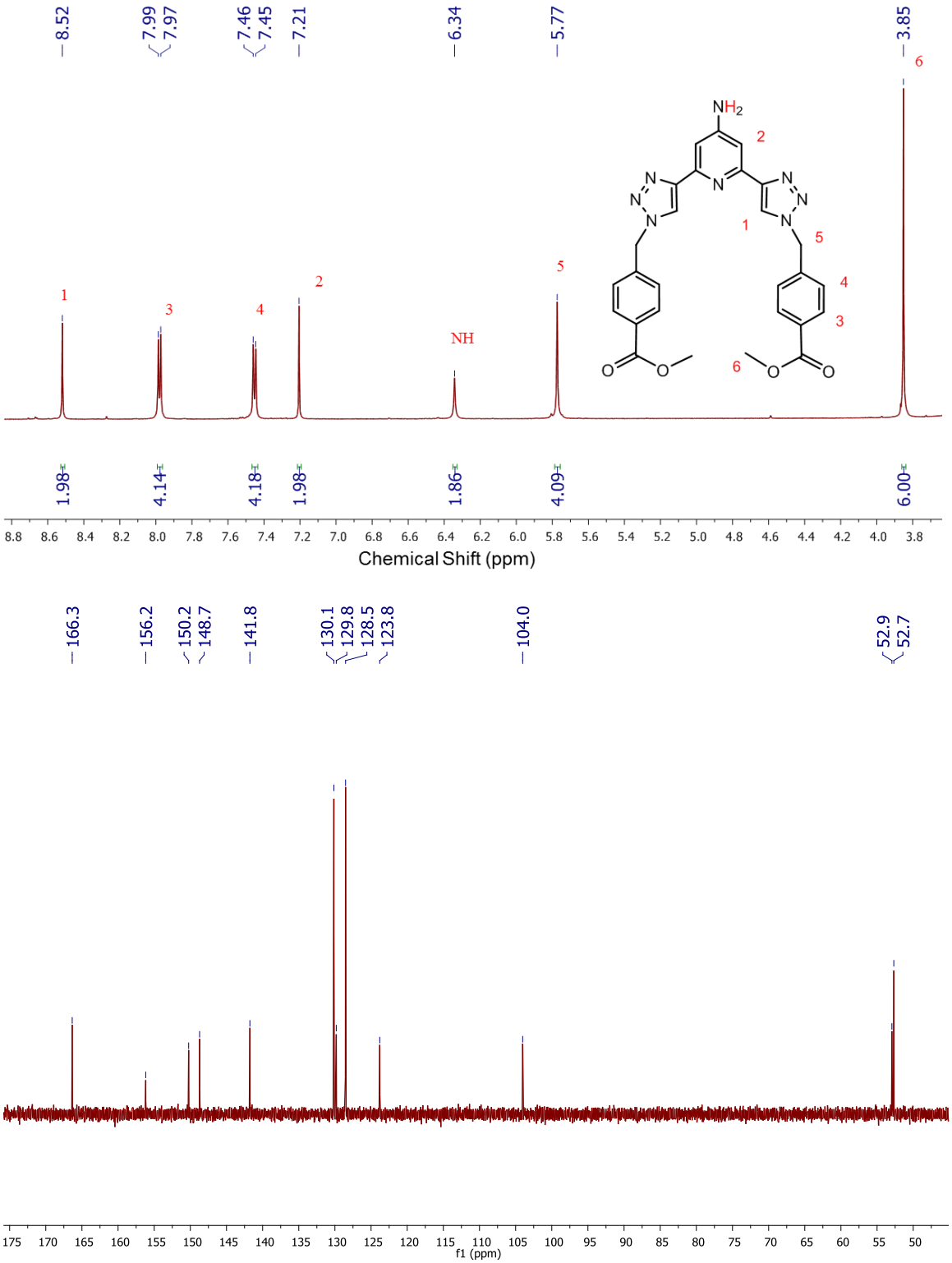

Figure A.6 (Top) ^{1}H NMR (600 MHz, DMSO-d_6) and (Bottom) ^{13}C NMR (151 MHz, DMSO-d_6) spectra of **btp** ligand **95**

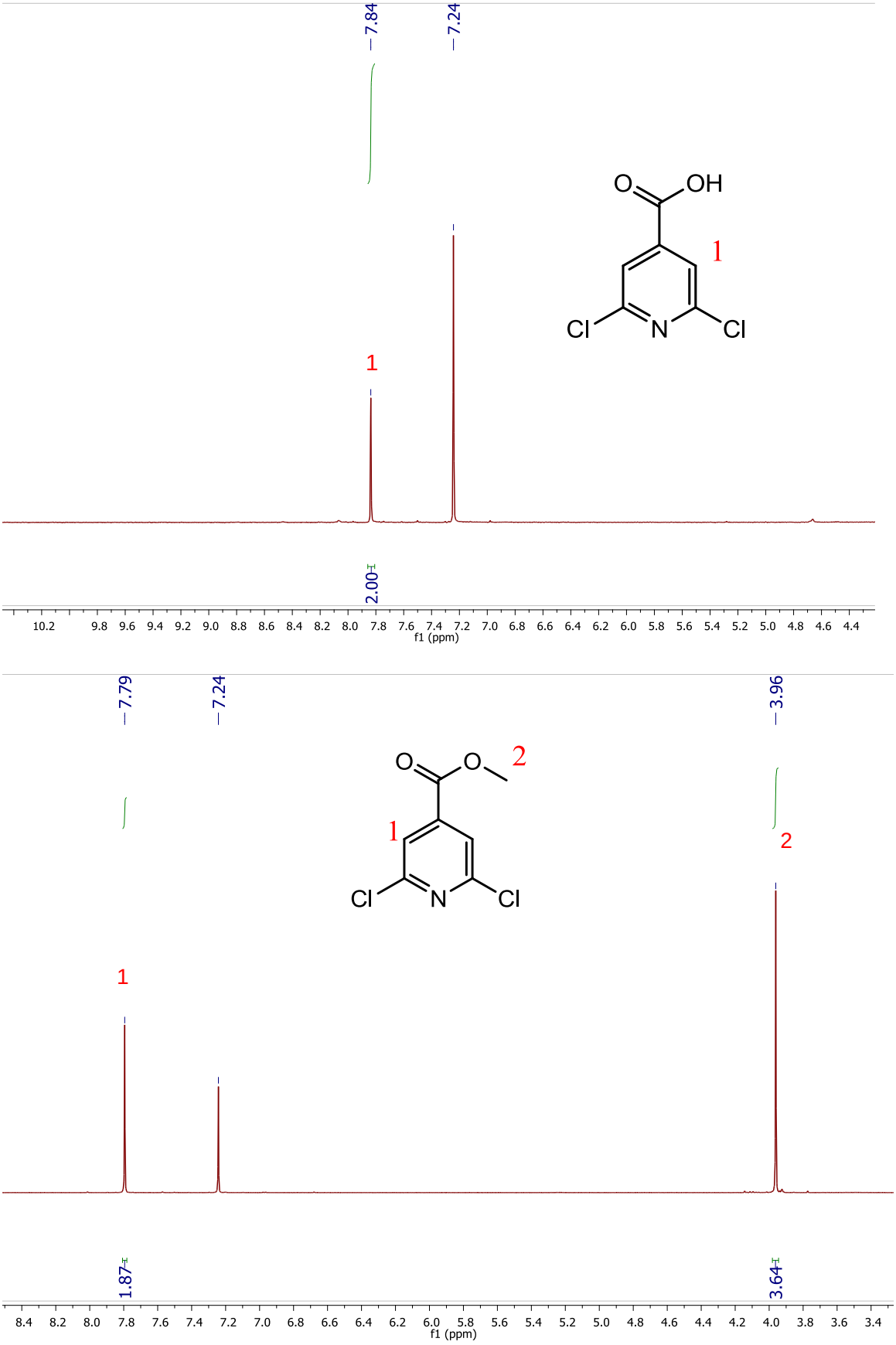

Figure A.7 ^{1}H NMR (400 MHz, $CDCl_3$) spectra of (Top) **66** and (Bottom) **90**

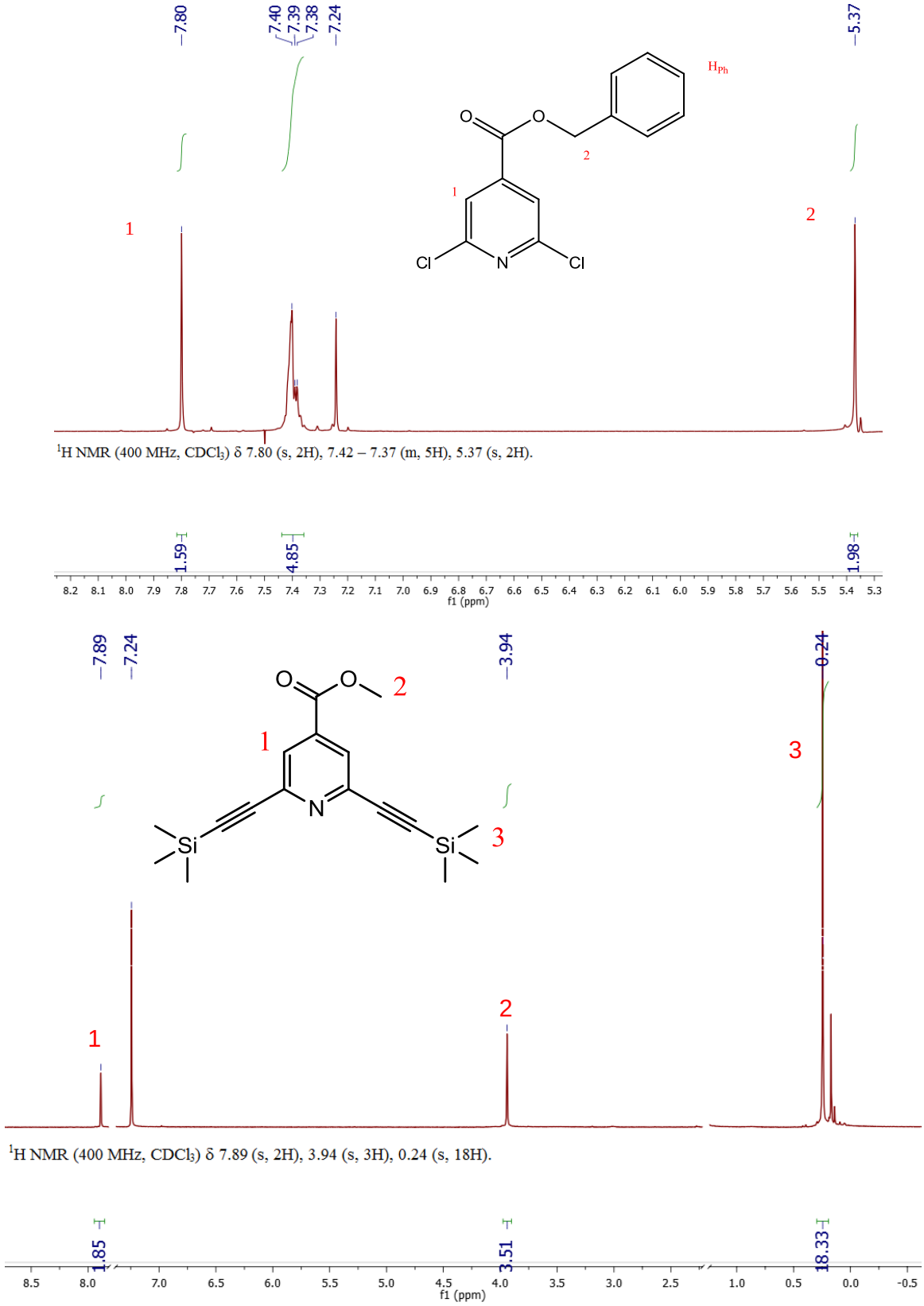

^{1}H NMR (400 MHz, $CDCl_3$) δ 7.80 (s, 2H), 7.42 – 7.37 (m, 5H), 5.37 (s, 2H).

^{1}H NMR (400 MHz, $CDCl_3$) δ 7.89 (s, 2H), 3.94 (s, 3H), 0.24 (s, 18H).

Figure A.7 ^{1}H NMR (400 MHz, $CDCl_3$) spectra of (Top) **90** and (Bottom) **88**

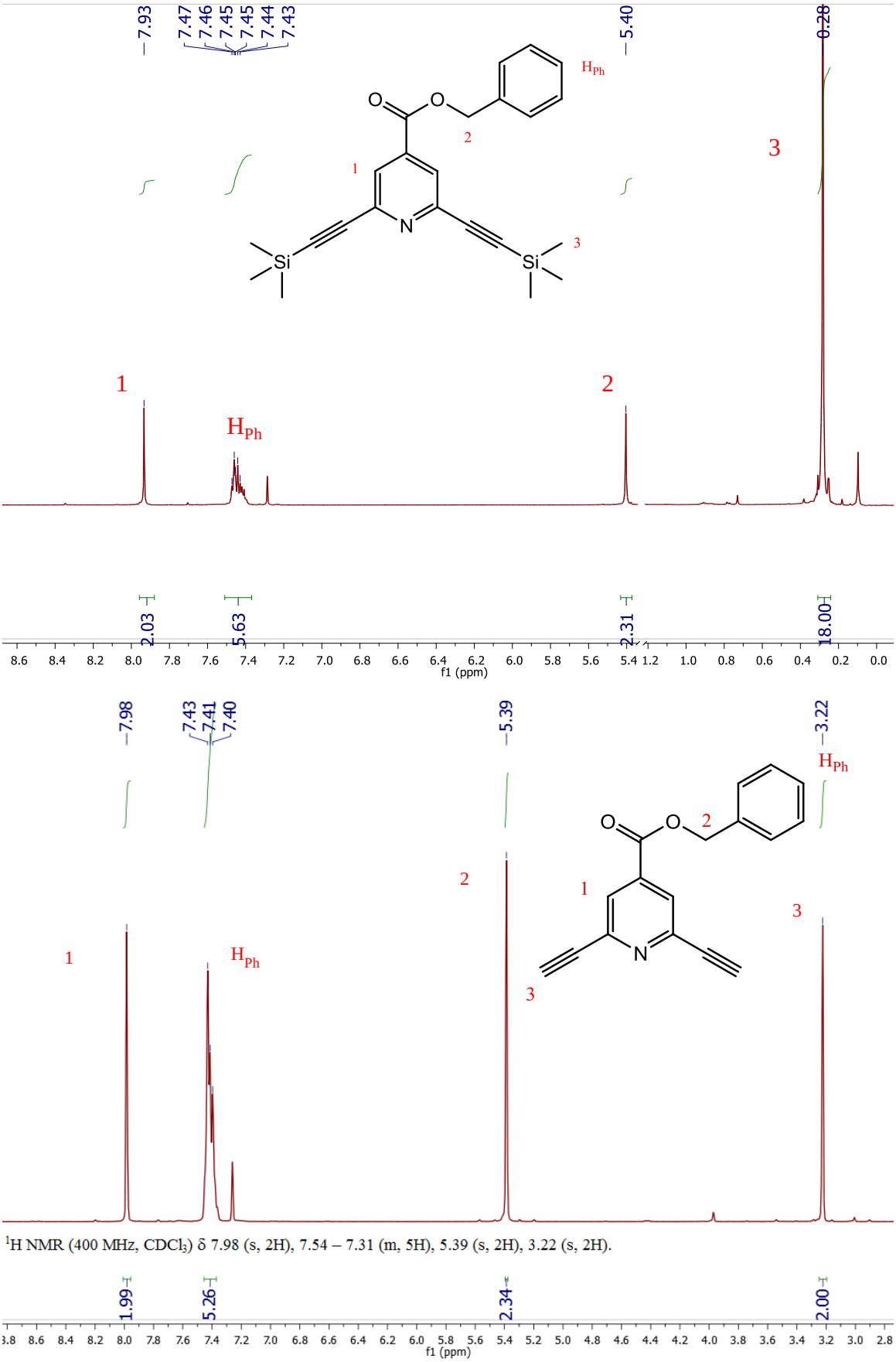

Figure A.8 ^{1}H NMR (400 MHz, $CDCl_3$) spectra of (Top) **92** and (Bottom) **93**

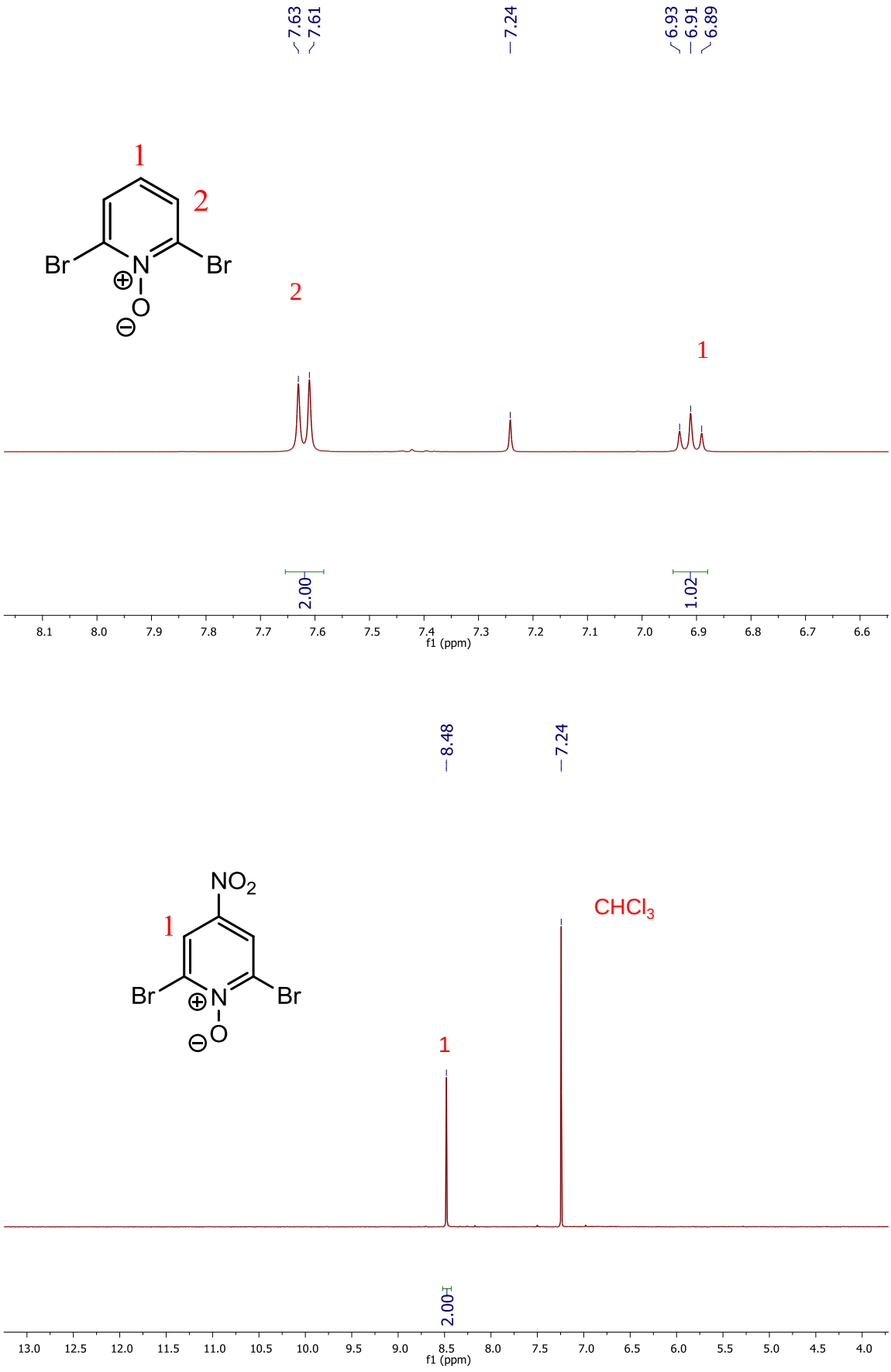

Figure A.9 ^{1}H NMR (400 MHz, $CDCl_3$) spectra of (Top) **71** and (Bottom) **72**

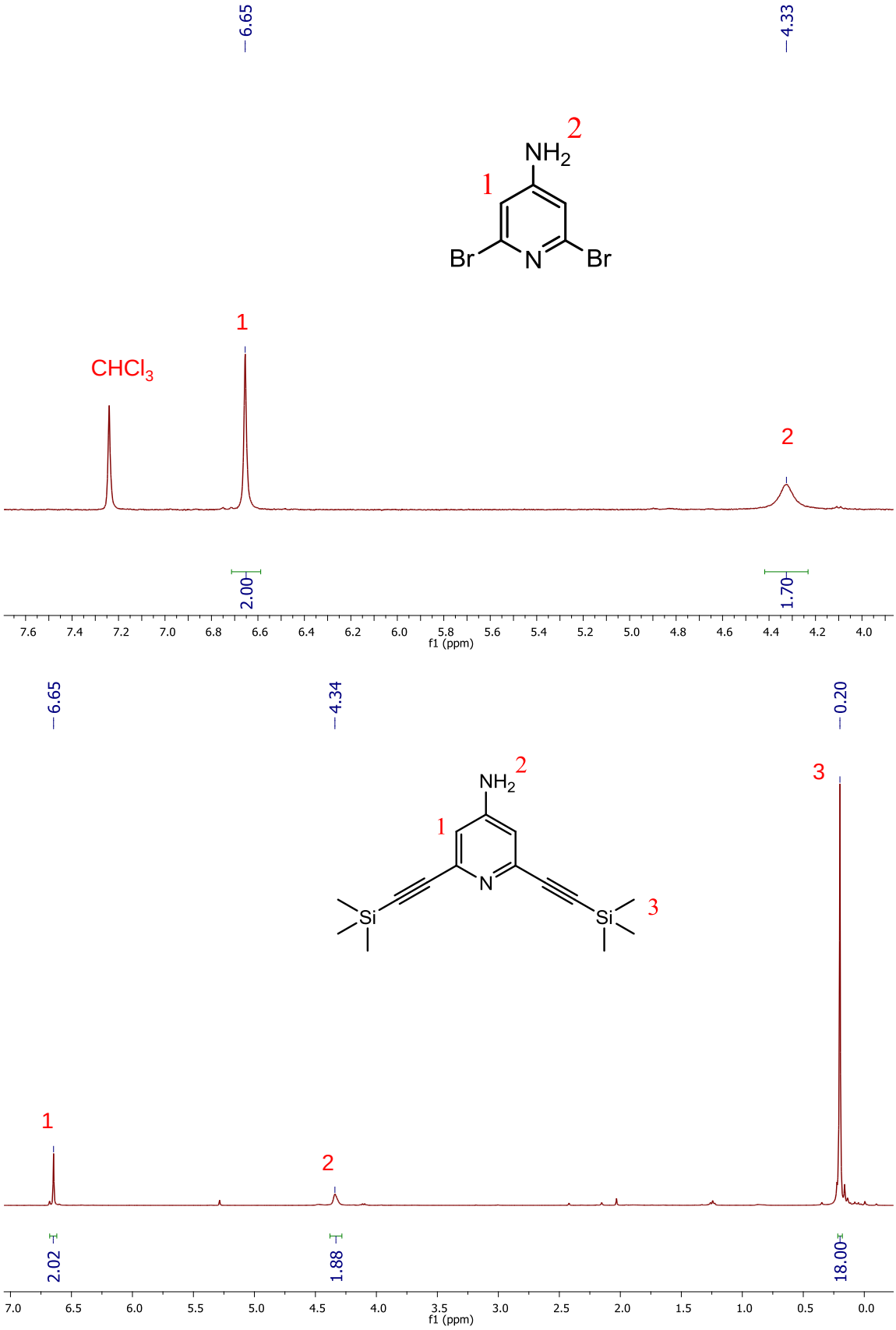

Figure A.9 ^{1}H NMR (400 MHz, $CDCl_3$) spectra of (Top) **96** and (Bottom) **97**

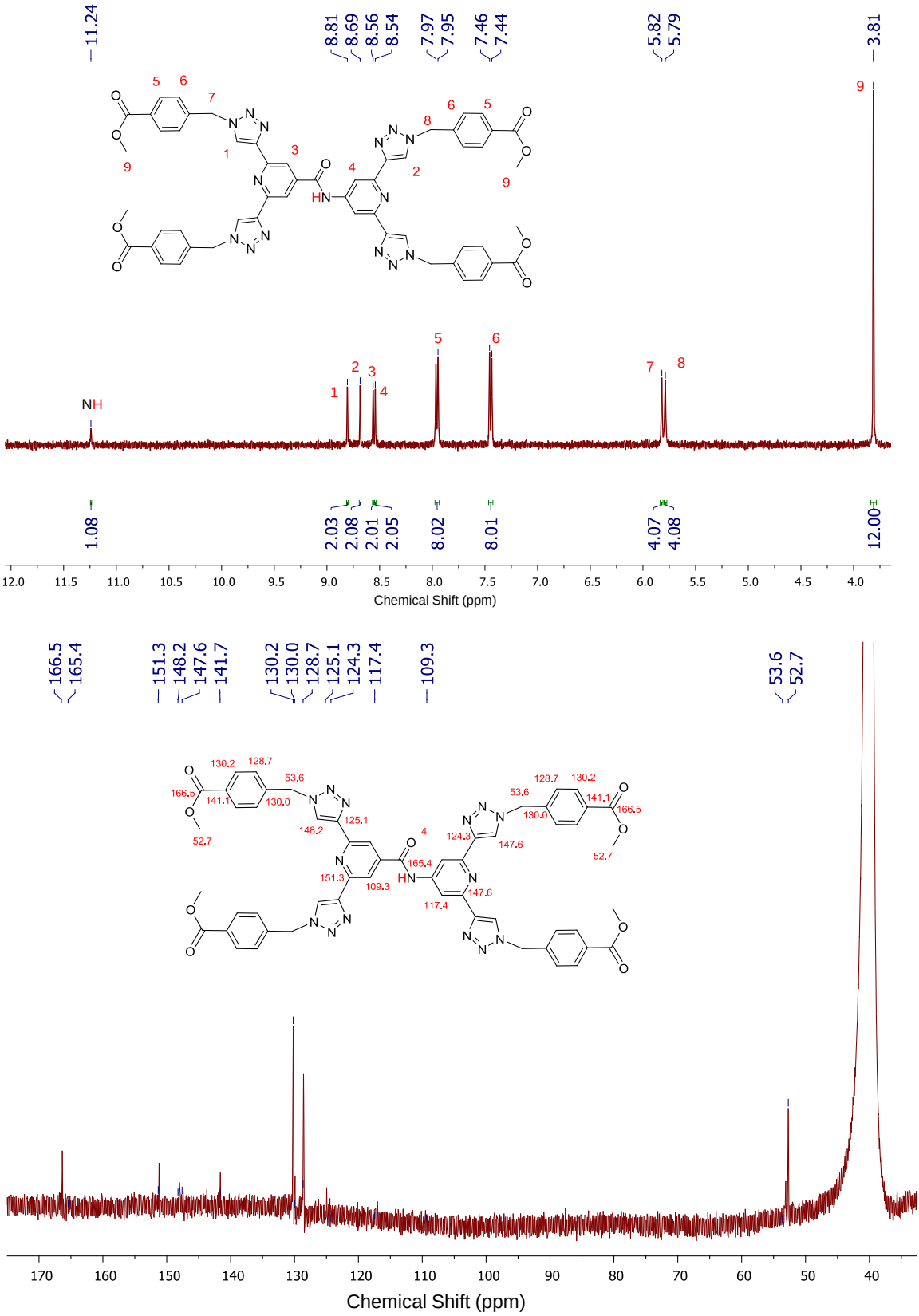

Figure A.10 (Top) ^{1}H NMR (400 MHz, DMSO-d_6) and (Bottom) ^{13}C NMR (101 MHz, DMSO-d_6) spectra of **btp** ligand **98**

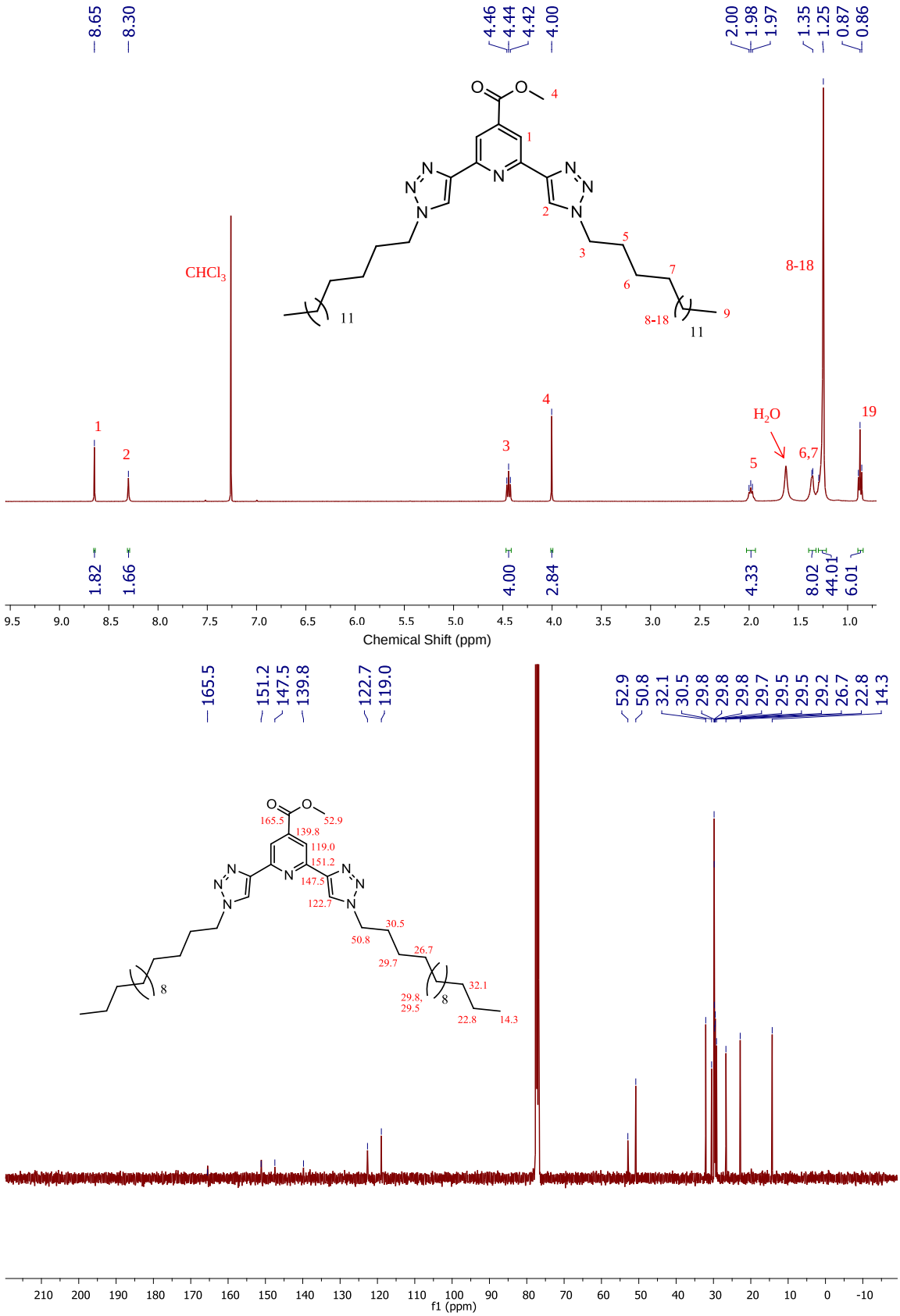

Figure A.11 (Top) ^{1}H NMR (400 MHz, $CDCl_3$) and (Bottom) ^{13}C NMR (101 MHz, $CDCl_3$) spectra of **btp** ligand **99**

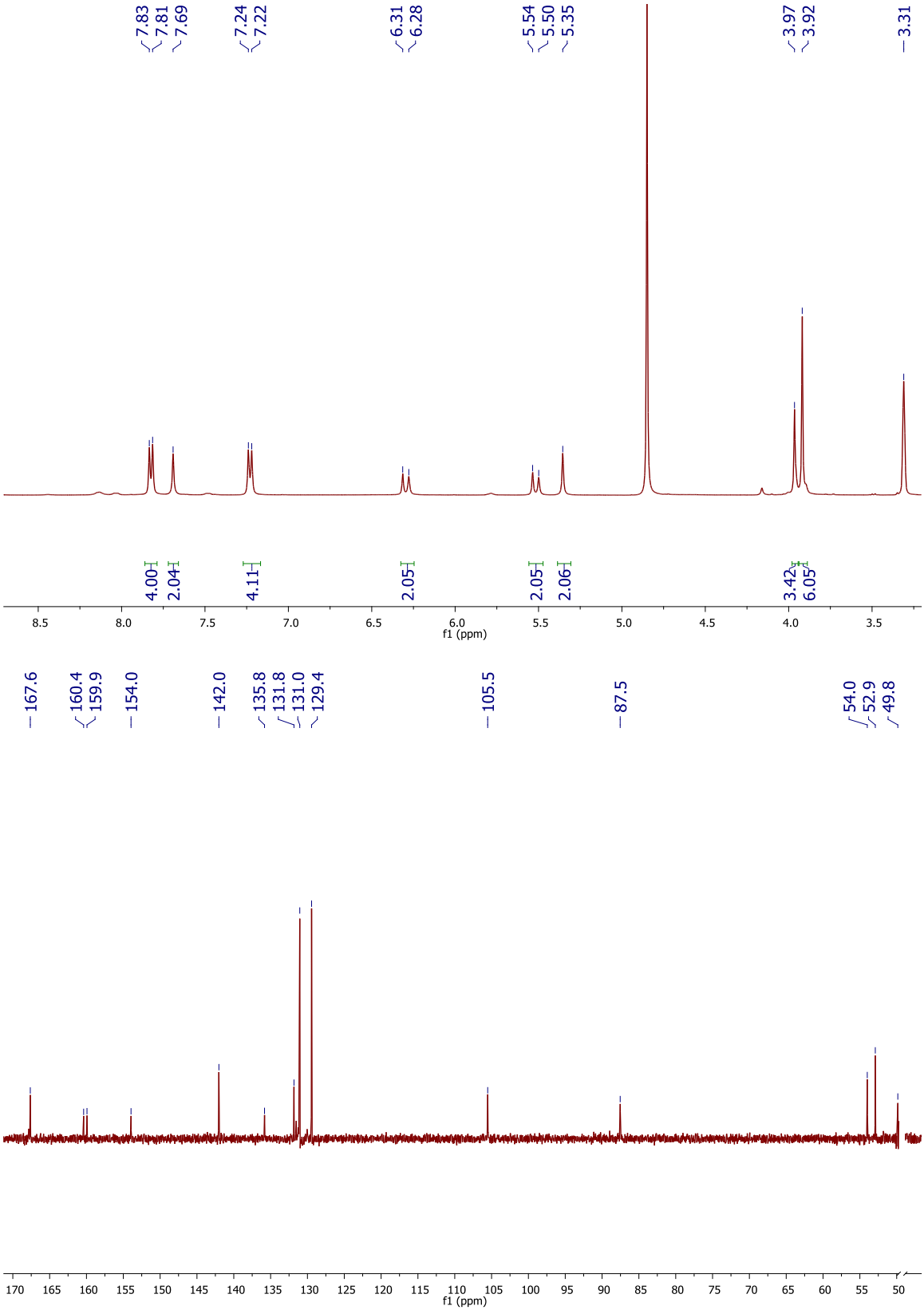

Figure A.12 (Top) ^{1}H NMR of **Eu83$_3$** (400 MHz, CD_3OD), (Bottom) ^{13}C NMR of **Eu83$_3$** (101 MHz, CD_3OD).

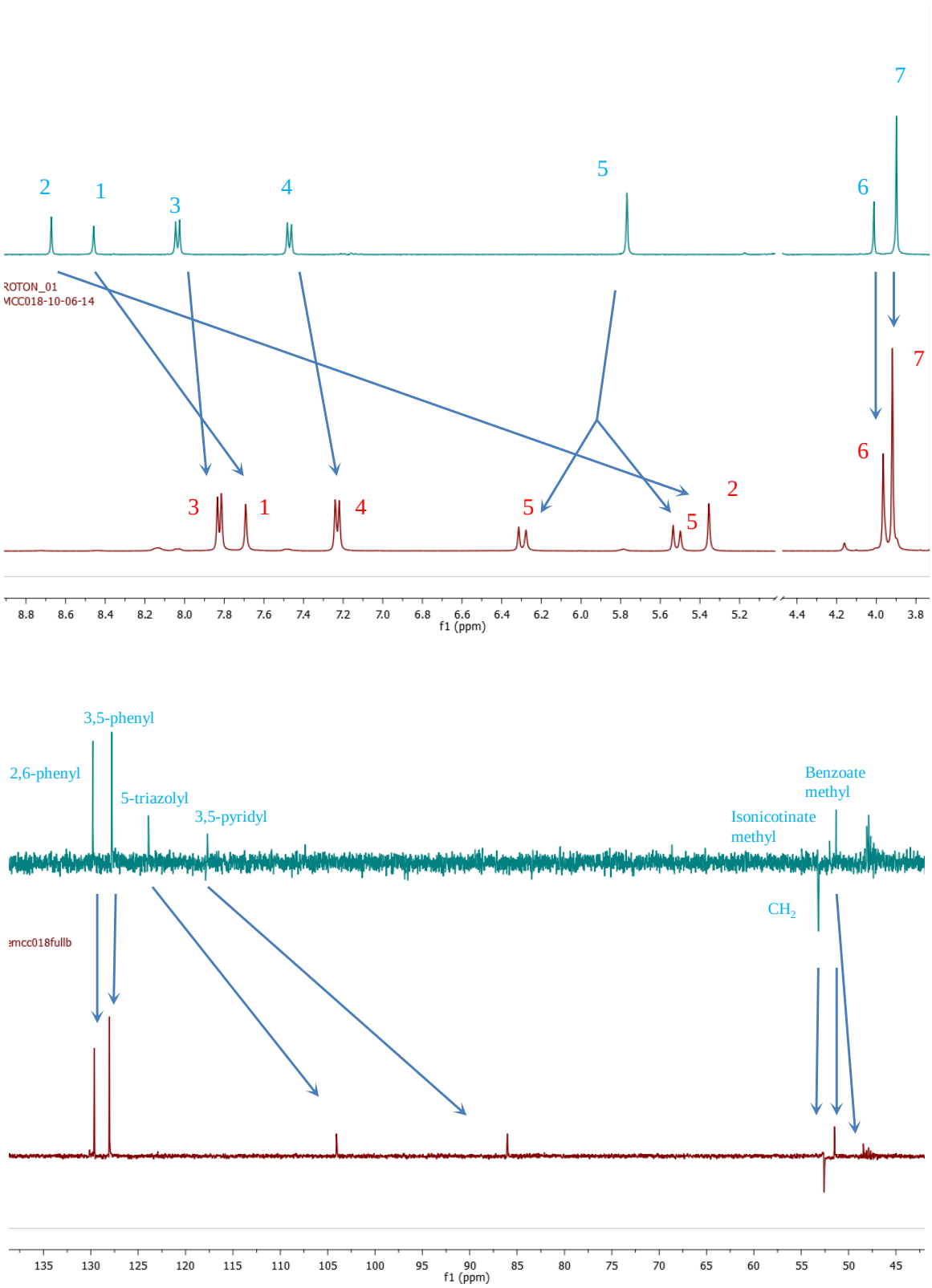

Figure A.13 (Top) ^{1}H NMR comparison of peak shift of **83** (blue) and **Eu83$_3$** (red) (400 MHz, CD_3OD), (Bottom) ^{13}C NMR comparison of peak shift of **83** (blue) and Eu**1**$_3$ (red) (101 MHz, CD_3OD).

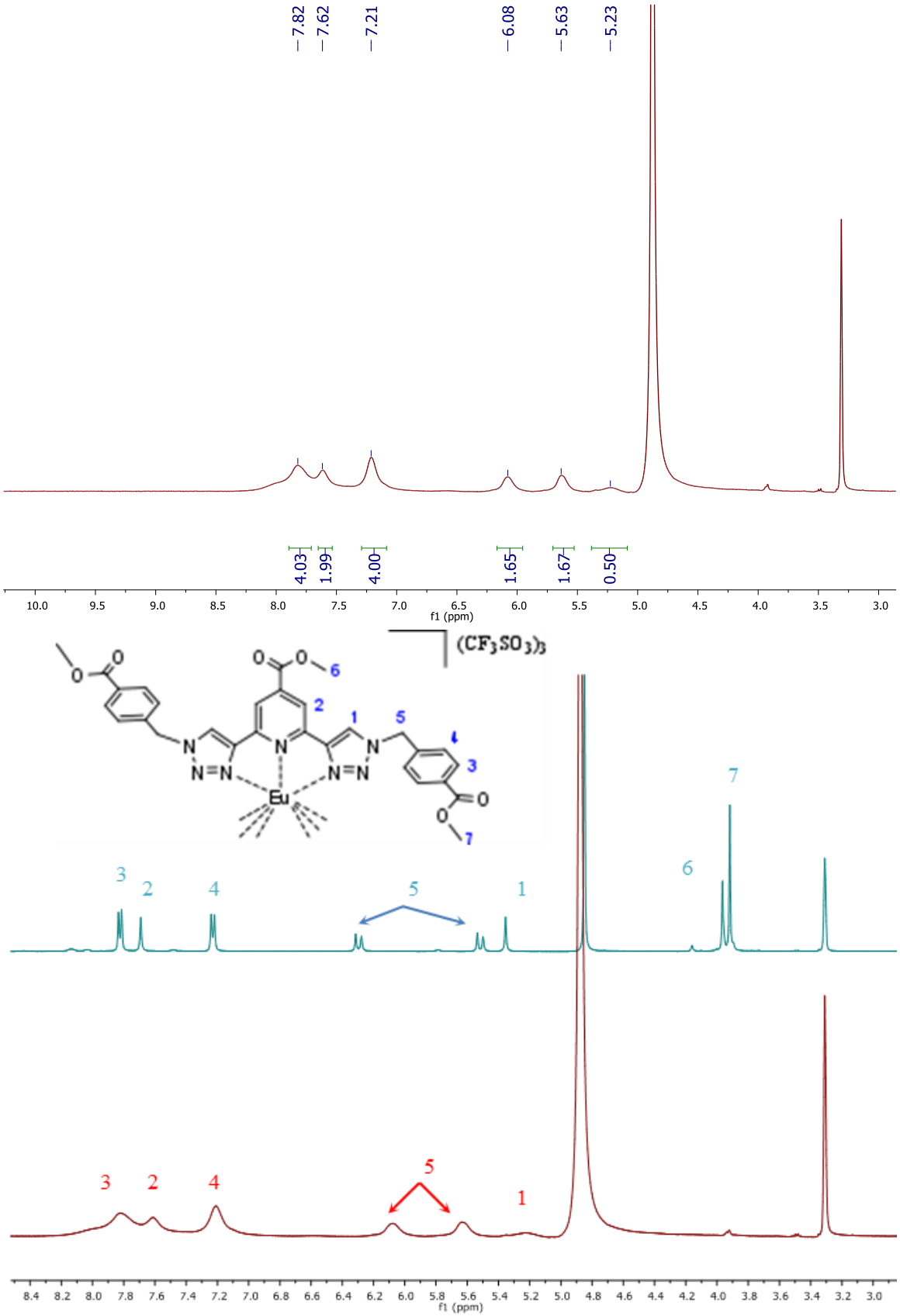

Figure A.14 (Top) ^{1}H NMR of **Eu(H$_3$84)$_3$** (400 MHz, CD_3OD), (Bottom) ^{1}H NMR comparison of peak shift of **Eu83$_3$** (blue) and **Eu(H$_3$84)$_3$** (red) (400 MHz, CD_3OD).

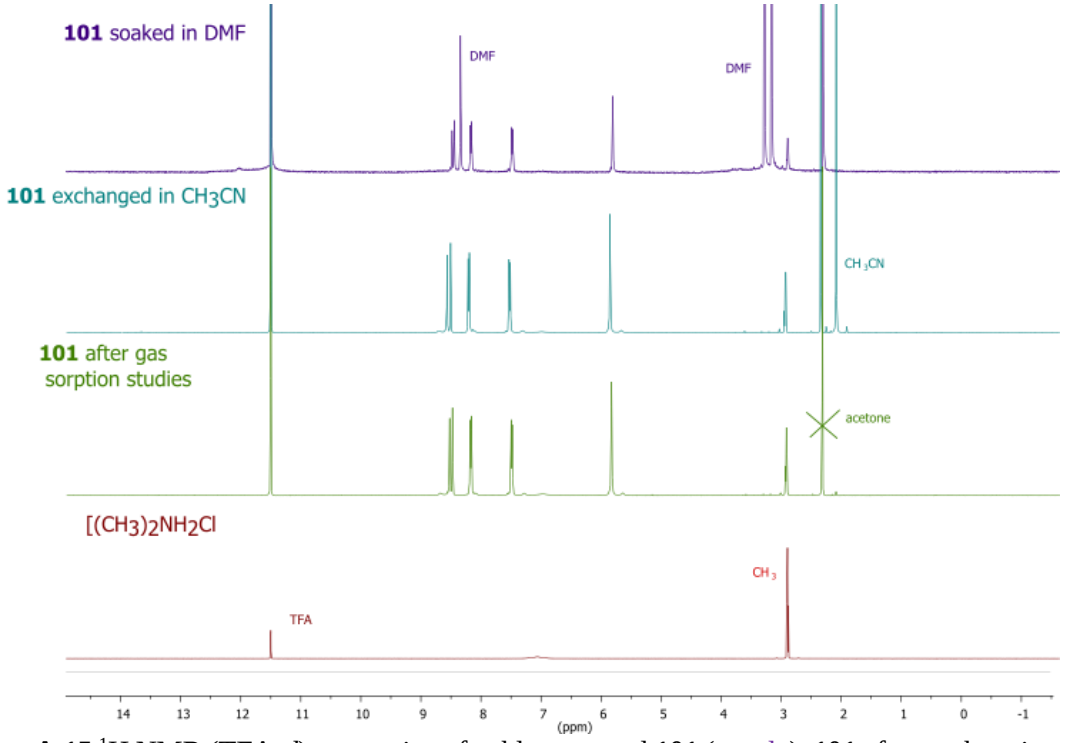

Figure A.15 ^{1}H NMR (TFA-*d*) comparison freshly prepared **101** (purple), **101** after exchanging with CH_3CN (cyan) and **101** after gas sorption studies (green). ^{1}H resonance at 2.98 ppm is indicative of the dimethyl ammonium charge balancing counter-ion which correspond closely to that in the ^{1}H NMR spectrum of $(CH_3)_2NH_2Cl$ (red).

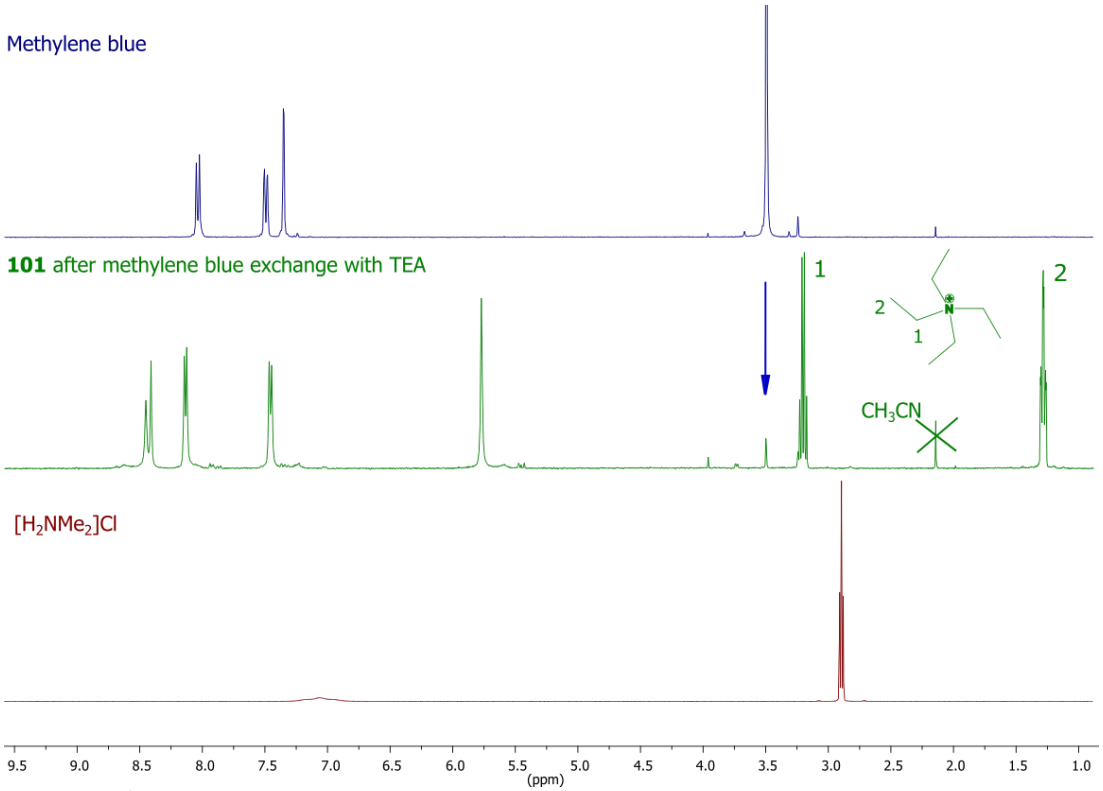

Figure A.16 ^{1}H NMR (TFA-d_1) comparison between methylene blue (blue), digestion of **101** after methylene blue has been exchanged with TEAI solution (green) and H_2NMe_2Cl (red). A resonance at 3.59 ppm indicative of a small amount of methylene blue was present after cation exchange with 16.4 mM solution of TEAI in CH_3CN. The uptake of TEA cation was evidenced by the resonances at 3.29 ppm and 1.38 ppm.

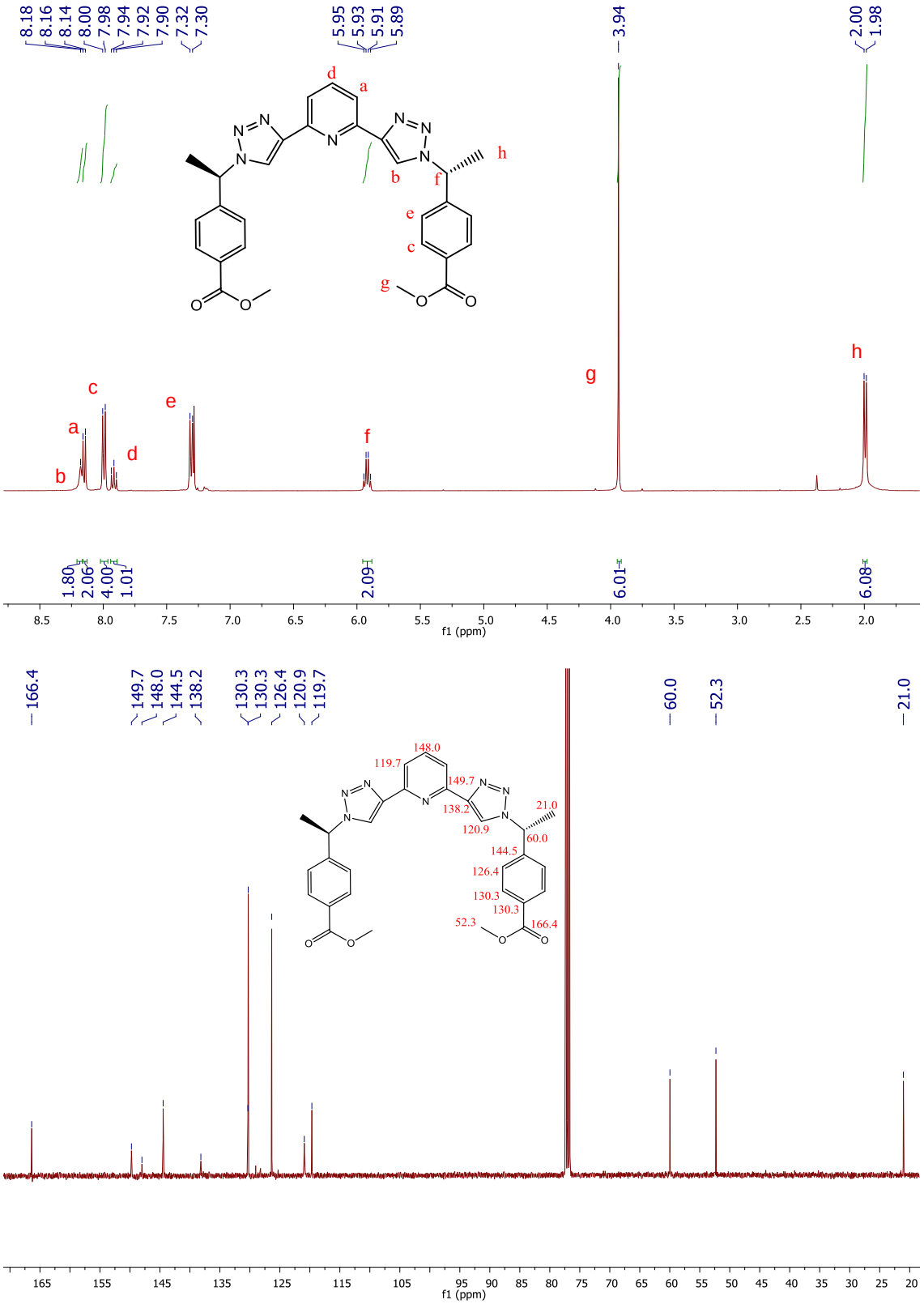

Figure A.17 (Top) ^{1}H NMR (400 MHz, DMSO-d_6) and (Bottom) ^{13}C NMR (101 MHz, DMSO-d_6) spectra of **btp** ligand **109R**

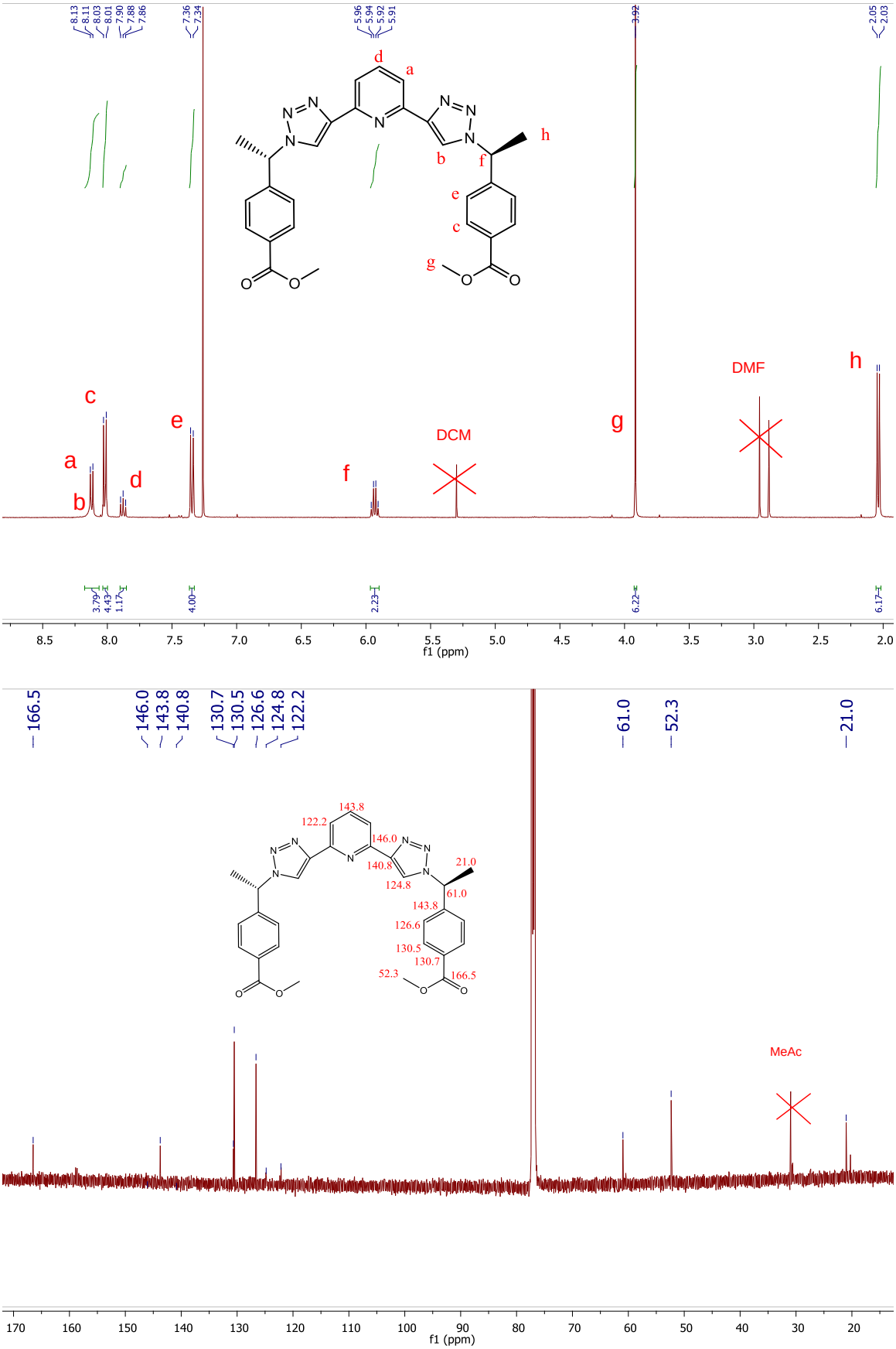

Figure A.18 (Top) ^{1}H NMR (400 MHz, DMSO-d_6) and (Bottom) ^{13}C NMR (101 MHz, DMSO-d_6) spectra of **btp** ligand **109S**

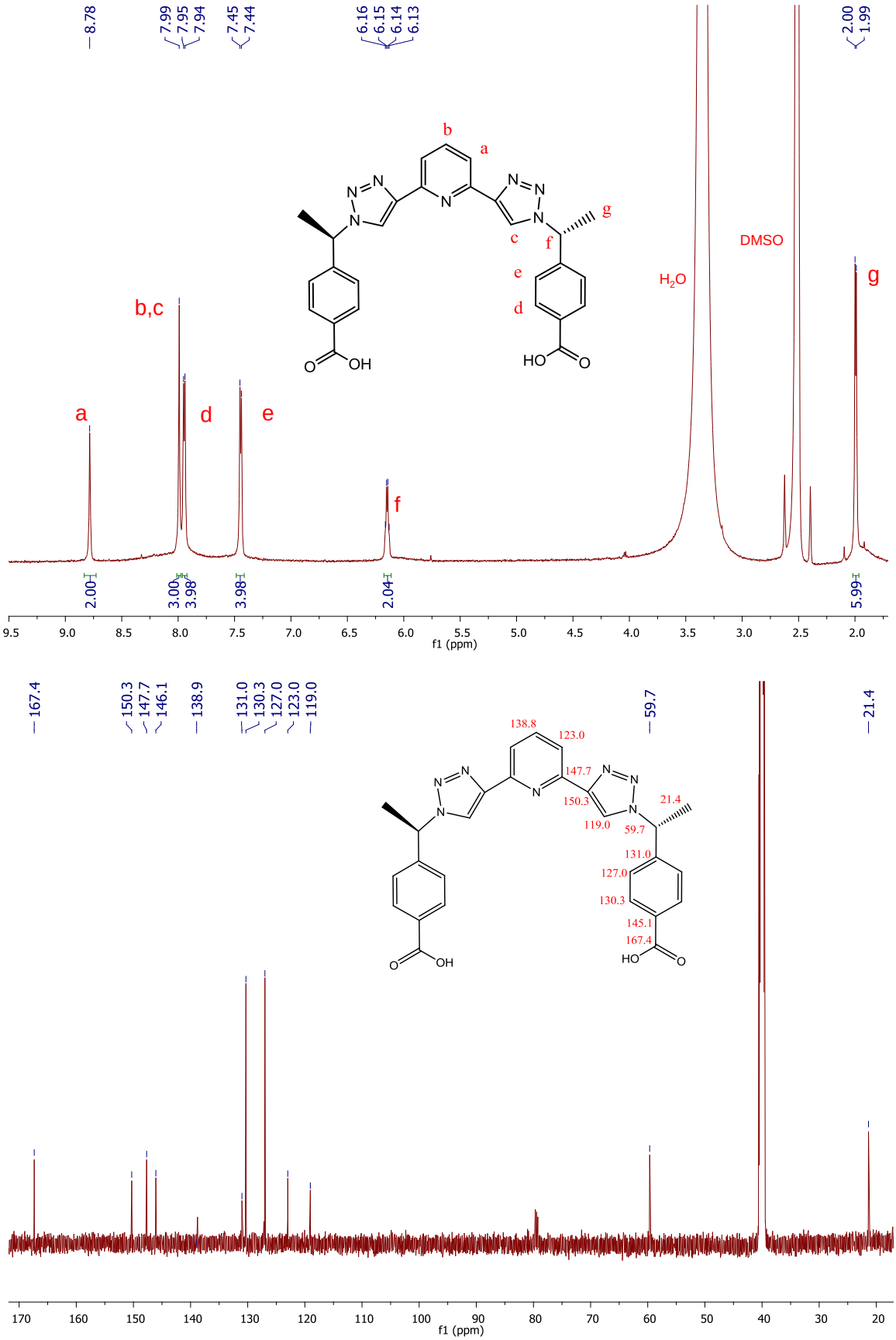

Figure A.19 (Top) ^{1}H NMR (600 MHz, DMSO-d_6) and (Bottom) ^{13}C NMR (151 MHz, DMSO-d_6) spectra of **btp** ligand **110R**

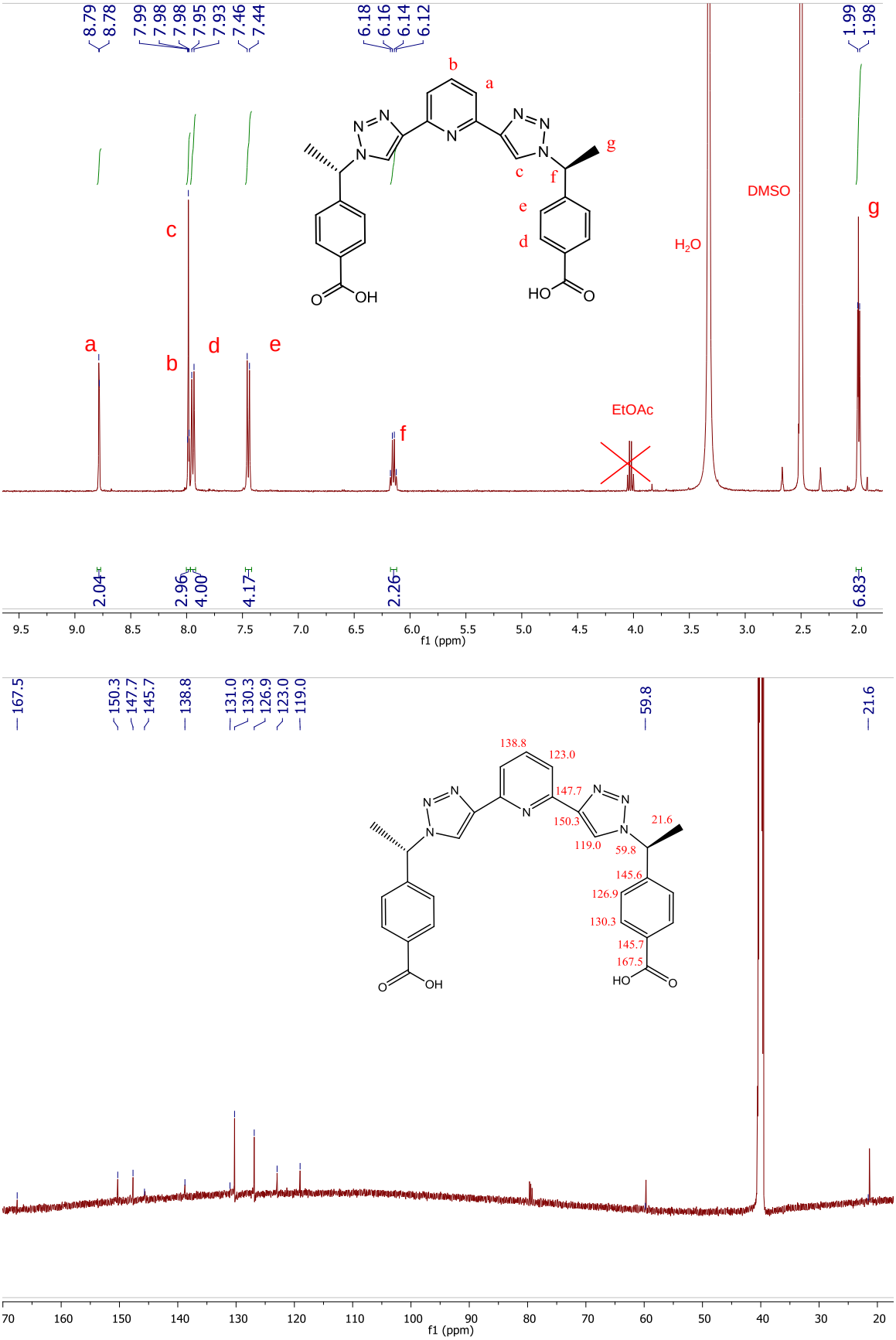

Figure A.20 (Top) ^{1}H NMR (600 MHz, DMSO-d_6) and (Bottom) ^{13}C NMR (151 MHz, DMSO-d_6) spectra of **btp** ligand **110S**

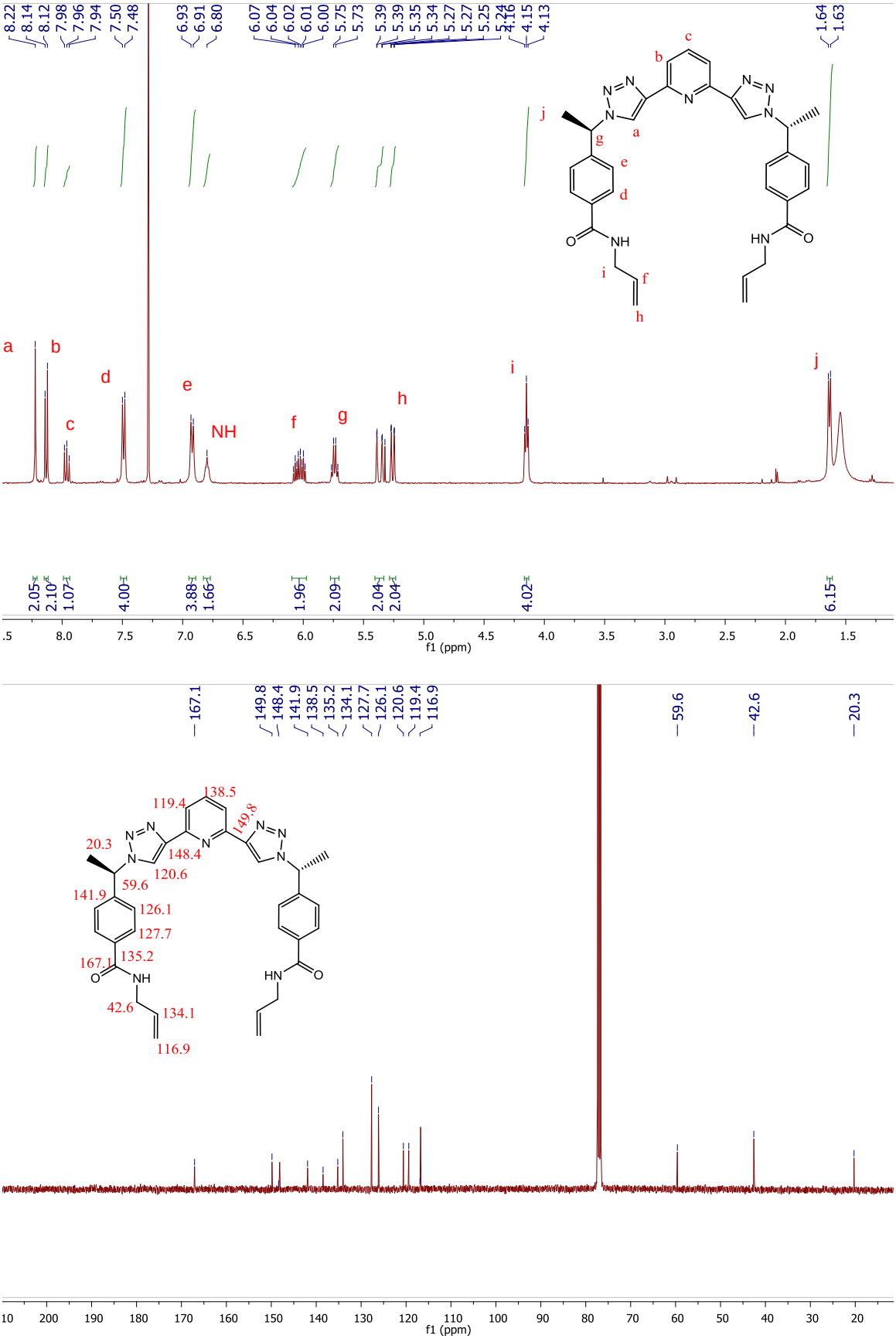

Figure A.21 (Top) ^{1}H NMR (400 MHz, $CDCl_3$) and (Bottom) ^{13}C NMR (101 MHz, $CDCl_3$) spectra of **btp** ligand **103R**

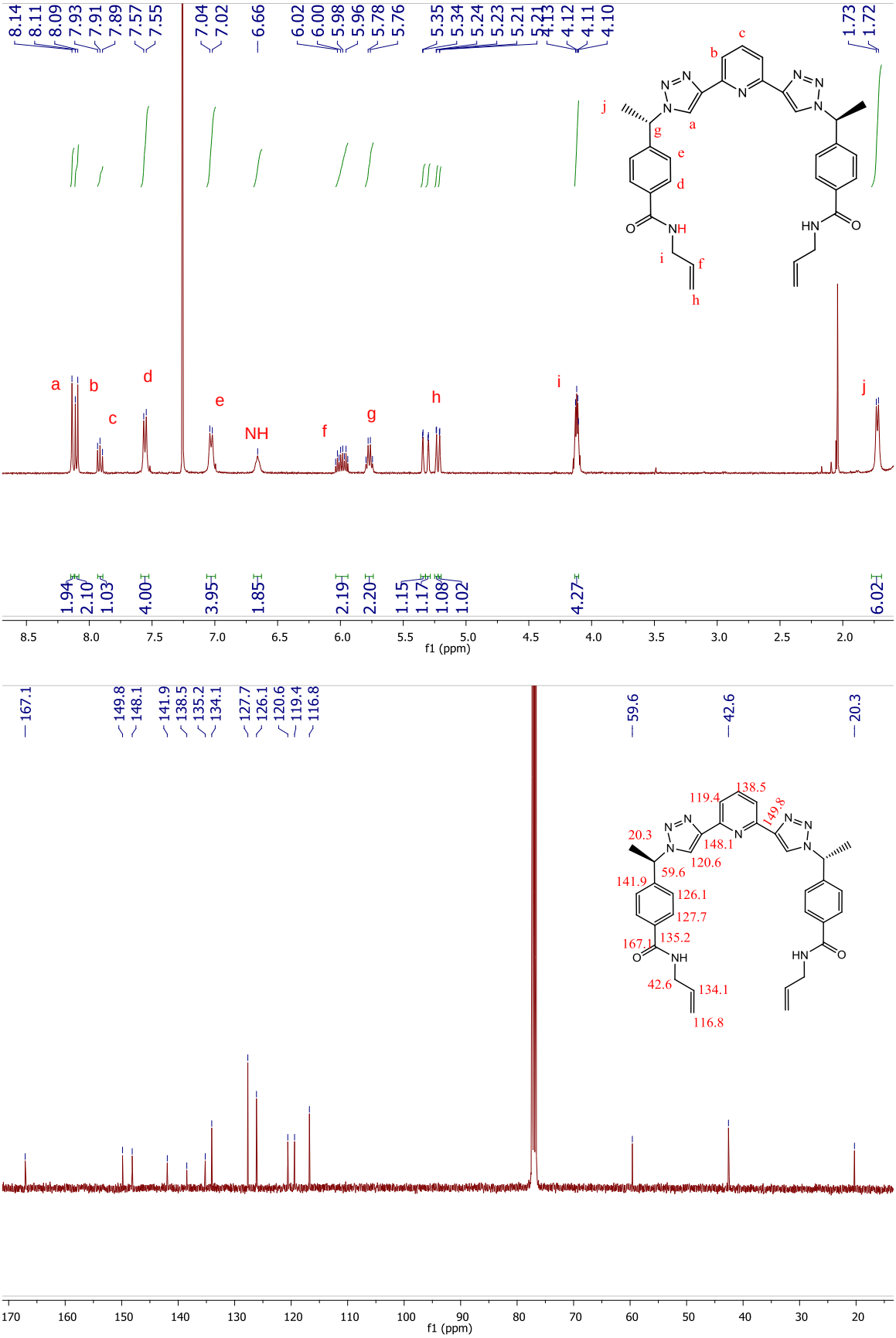

Figure A.22 (Top) ^{1}H NMR (400 MHz, $CDCl_3$) and (Bottom) ^{13}C NMR (101 MHz, $CDCl_3$) spectra of **btp** ligand **103S**

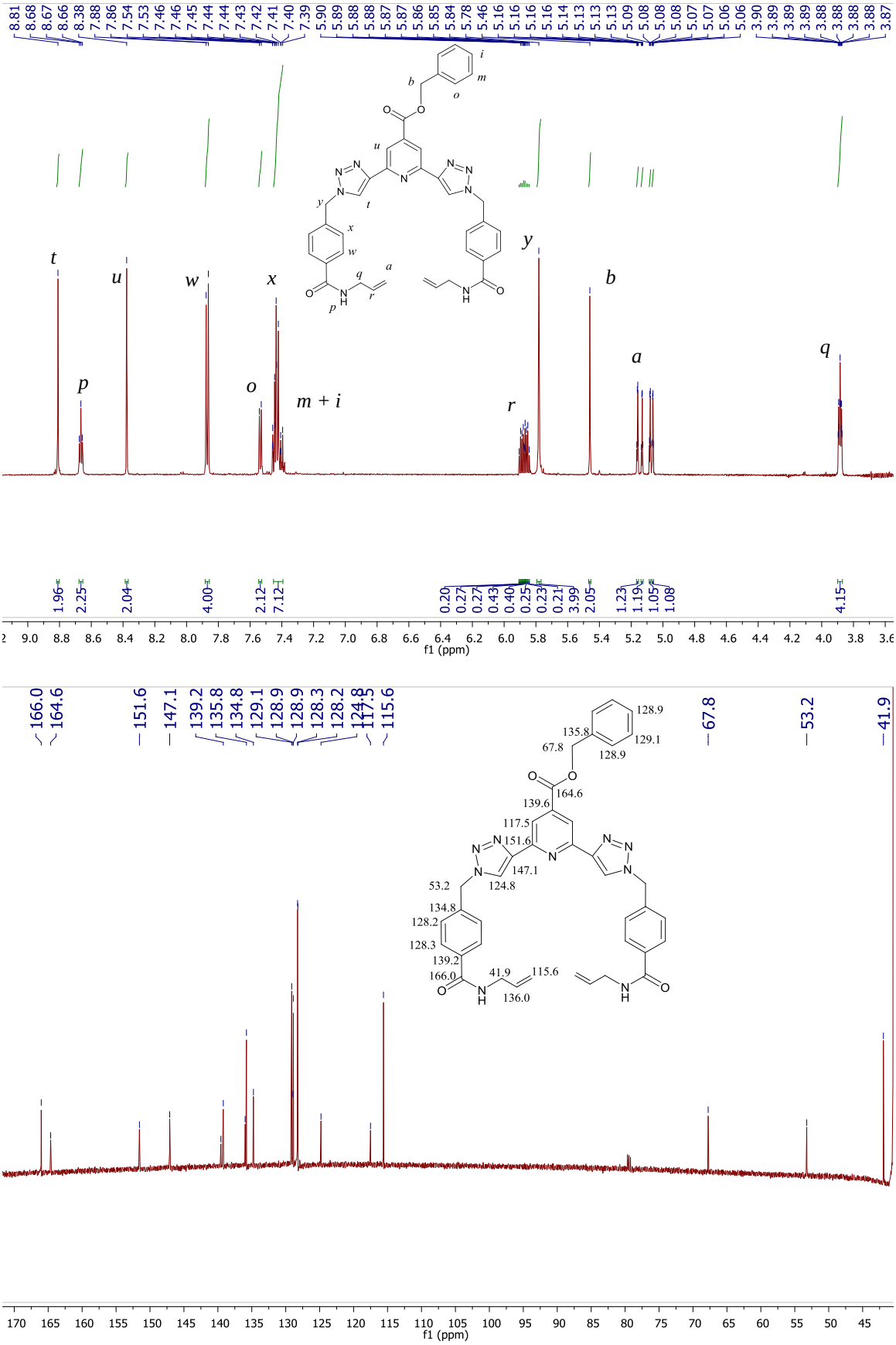

Figure A.23 (Top) ^{1}H NMR (600 MHz, DMSO-d_6) and (Bottom) ^{13}C NMR (151 MHz, DMSO-d_6) spectra of **btp** ligand **104**

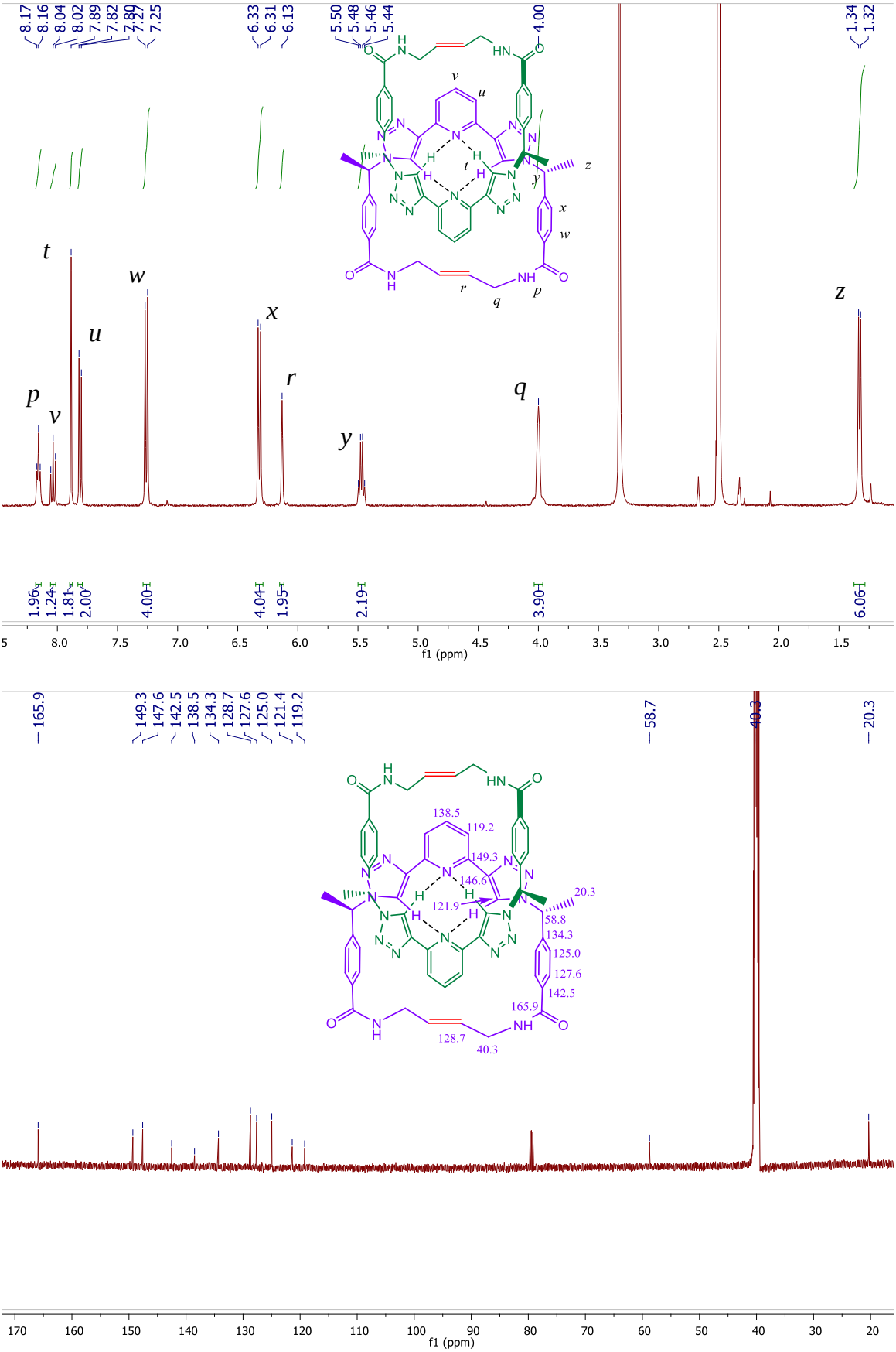

Figure A.24 (Top) ^{1}H NMR (400 MHz, DMSO-d_6) and (Bottom) ^{13}C NMR (101 MHz, DMSO-d_6) spectra of **btp 111R**

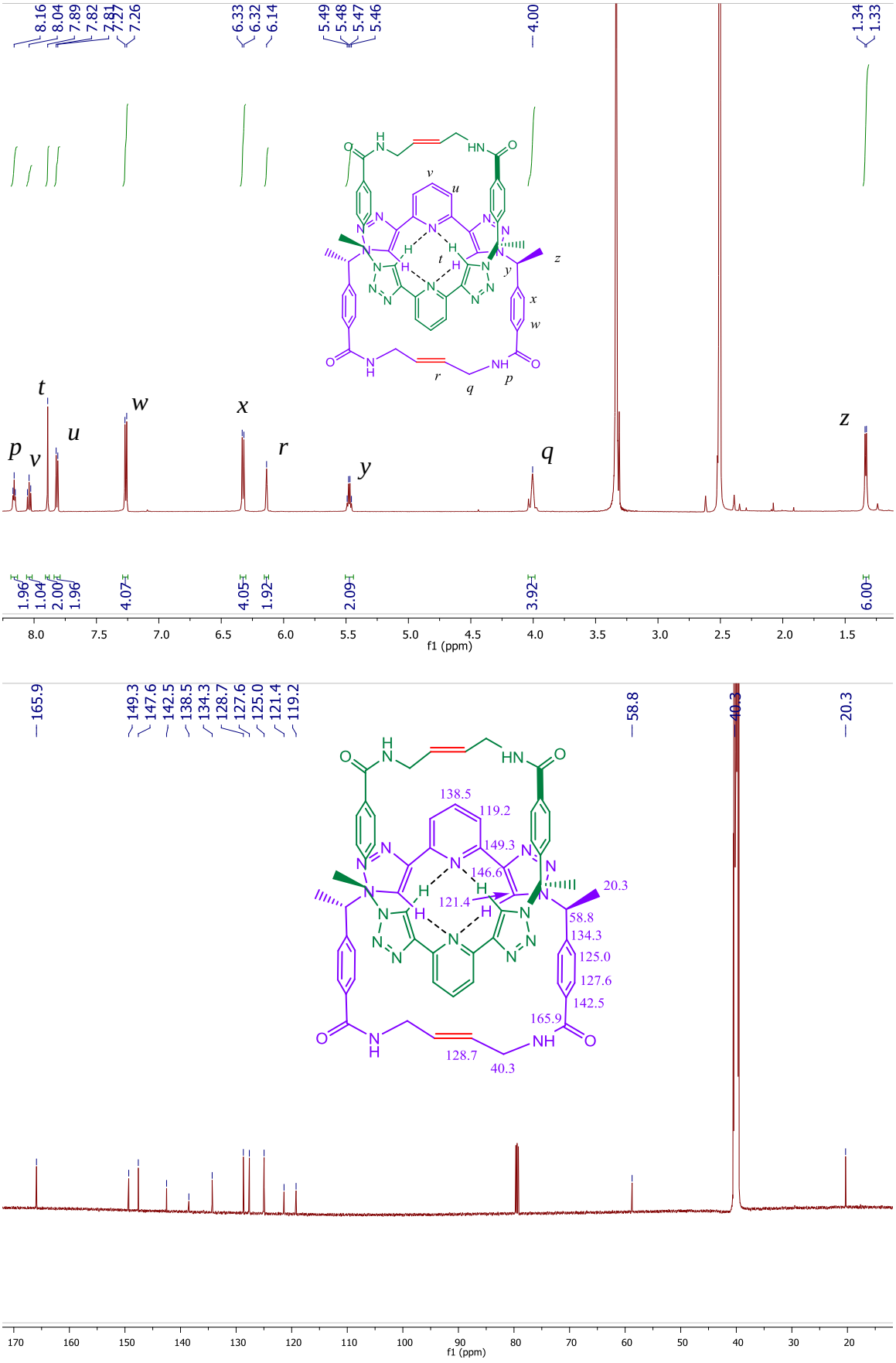

Figure A.25 (Top) ^{1}H NMR (400 MHz, DMSO-d_6) and (Bottom) ^{13}C NMR (101 MHz, DMSO-d_6) spectra of **btp 111S**

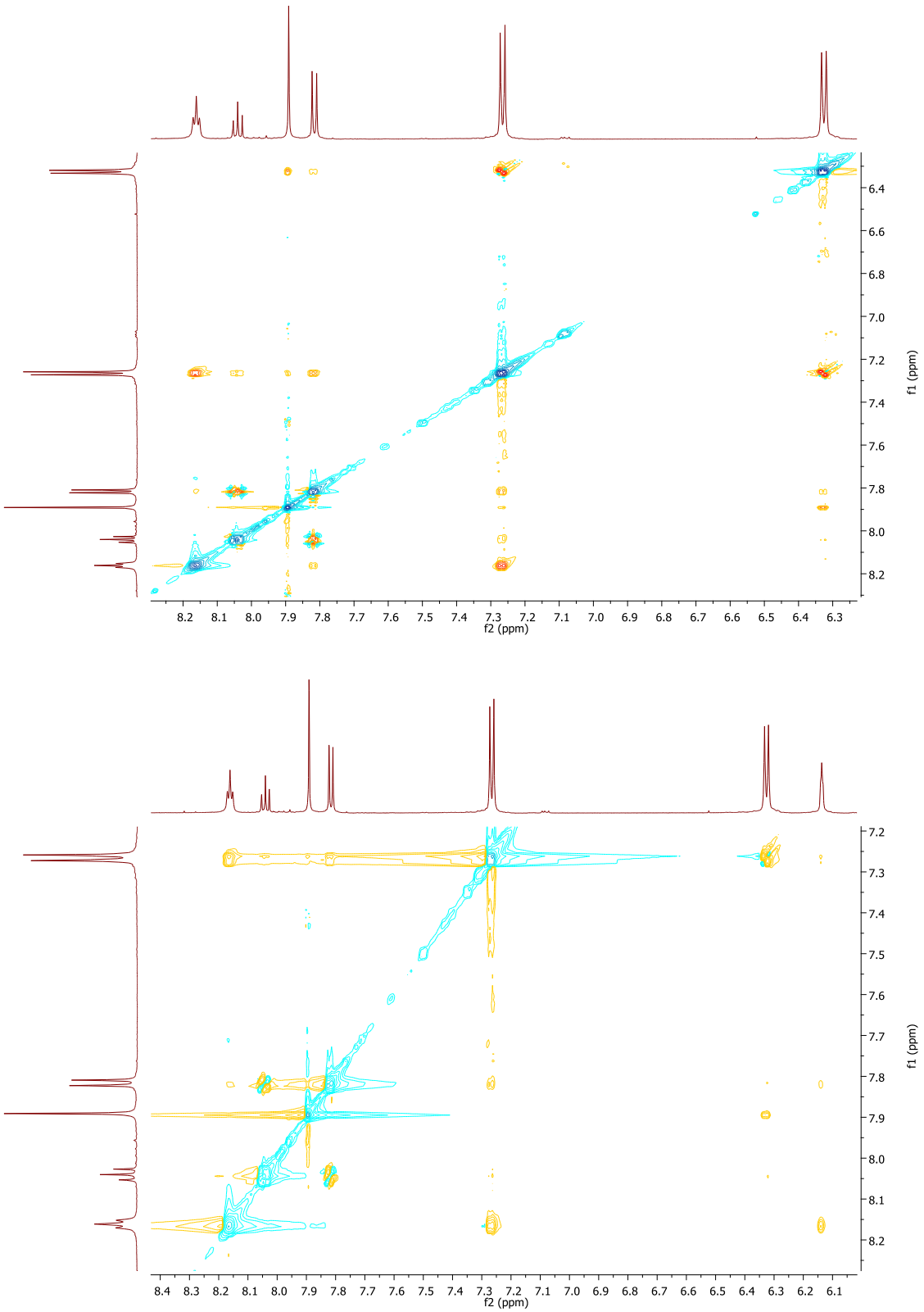

Figure A.26 ROESY NMR spectra **111R** (top) and **111S** (bottom) (101 MHz, DMSO-d_6)

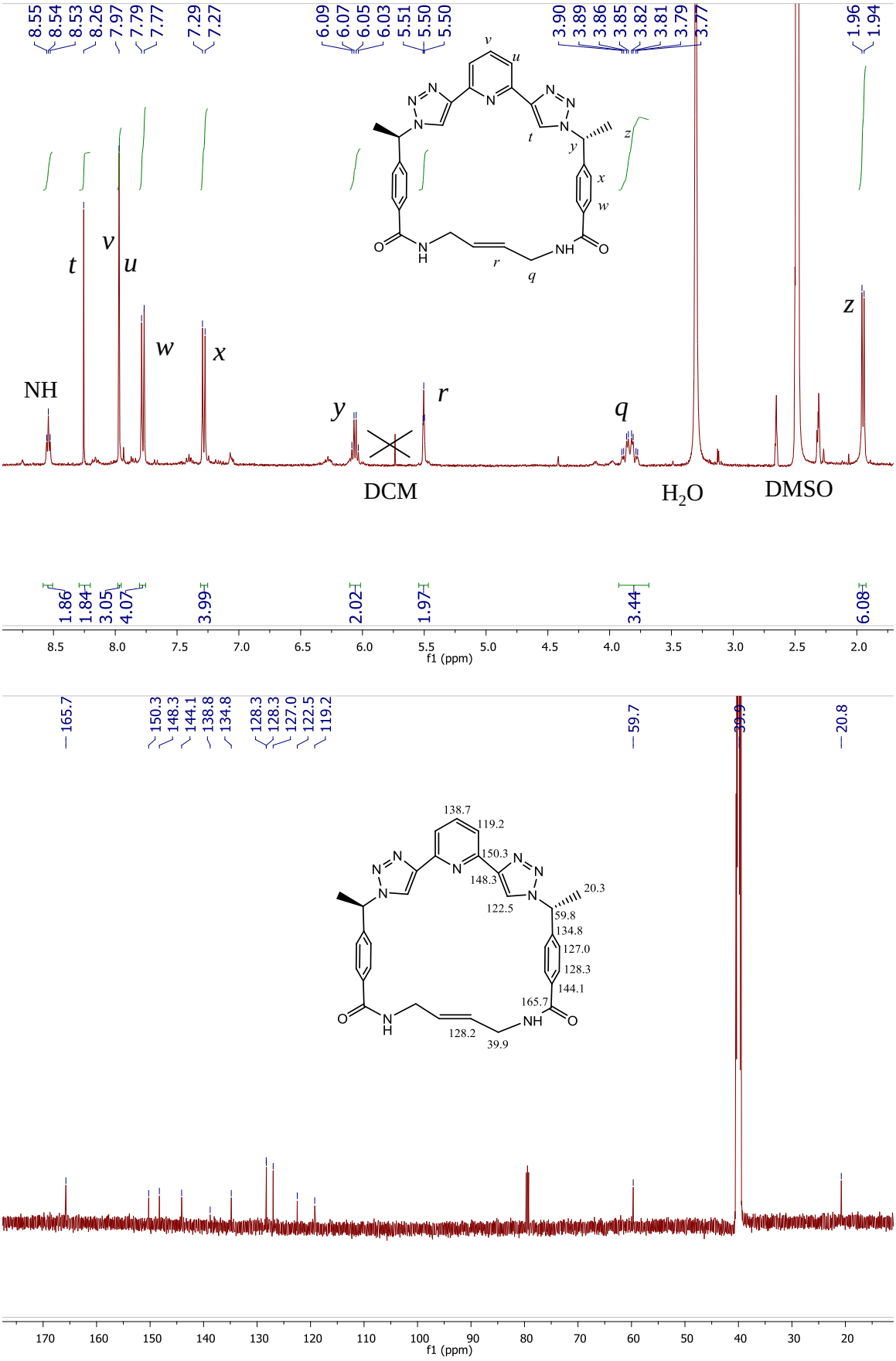

Figure A.27 (Top) ^{1}H NMR (400 MHz, DMSO-d_6) and (Bottom) ^{13}C NMR (101 MHz, DMSO-d_6) spectra of **btp 112R**

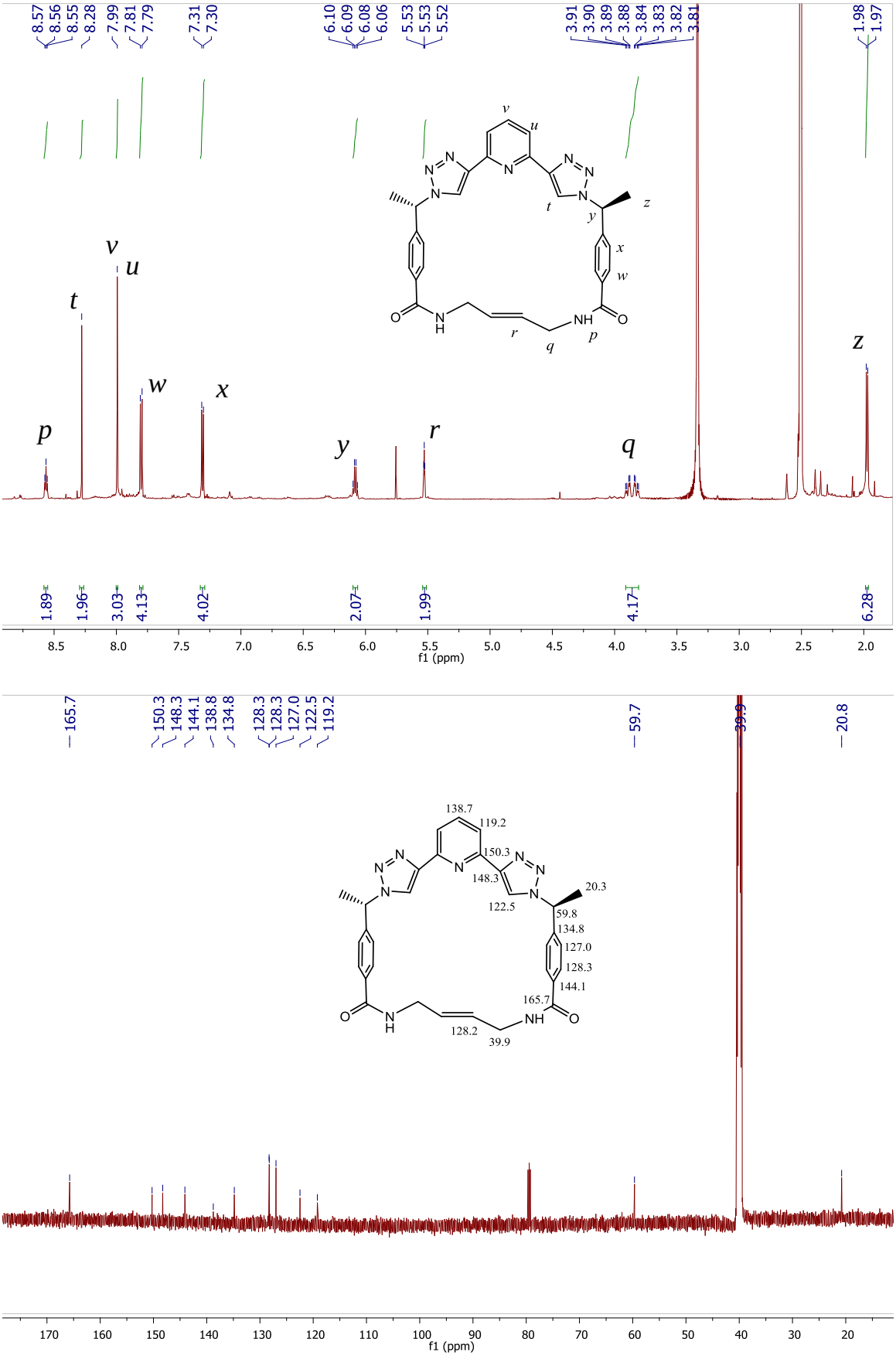

Figure A.28 (Top) ^{1}H NMR (600 MHz, DMSO-d_6) and (Bottom) ^{13}C NMR (151 MHz, DMSO-d_6) spectra of **btp 112S**

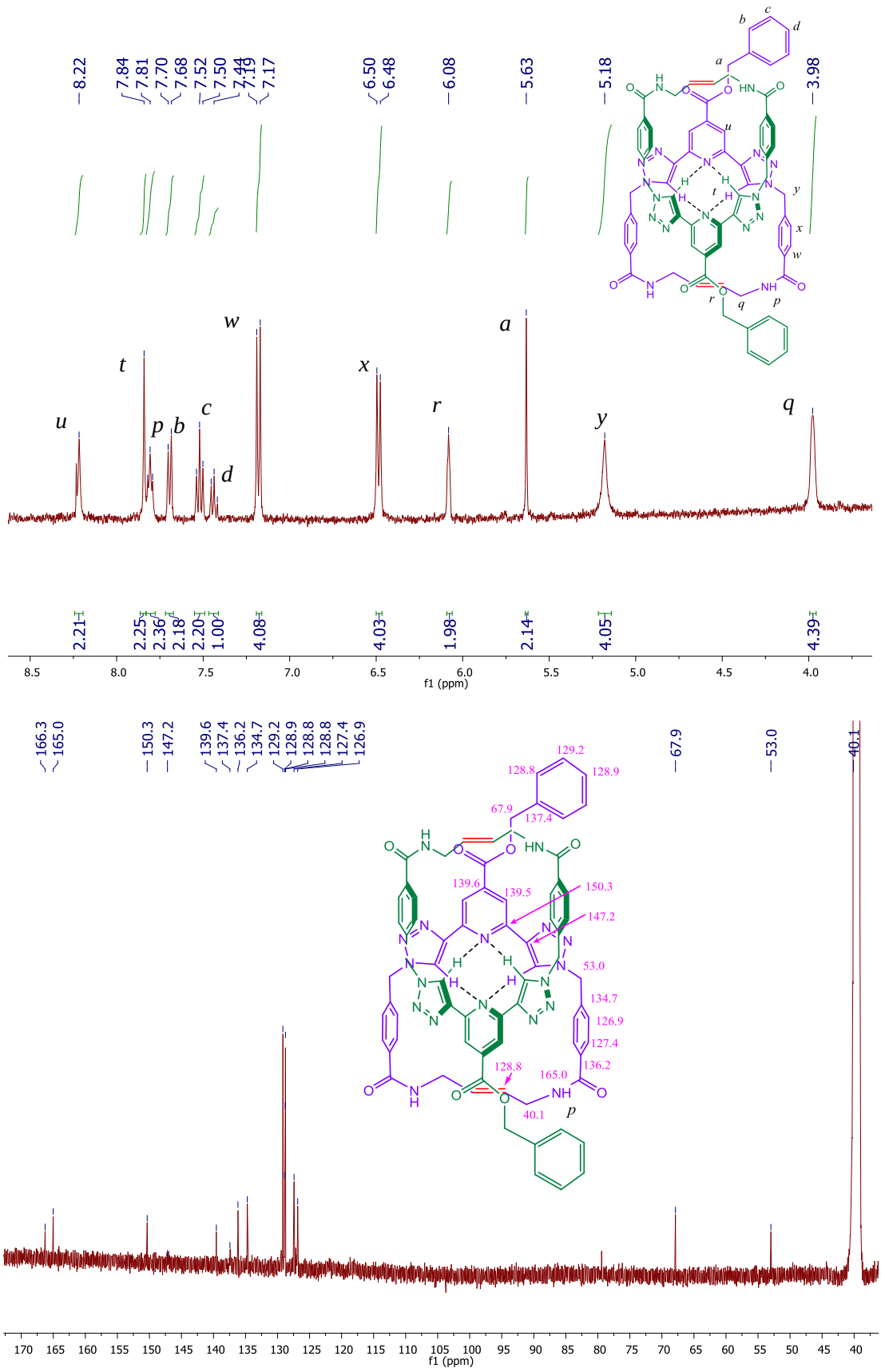

Figure A.29 (Top) ^{1}H NMR (400 MHz, $CDCl_3$) and (Bottom) ^{13}C NMR (151 MHz, DMSO-d_6) spectra of **btp 113**

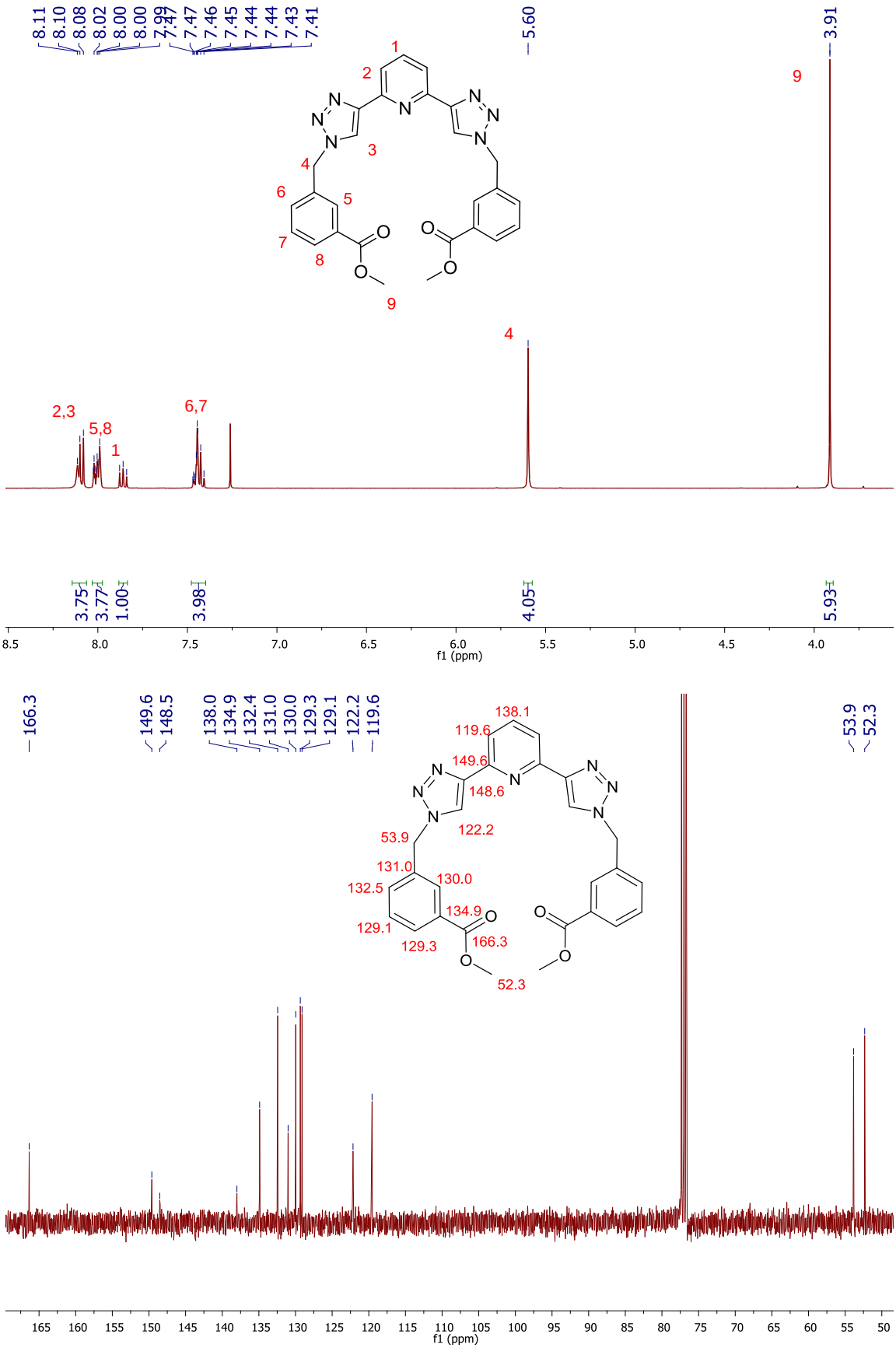

Figure A.30 (Top) ^{1}H NMR (400 MHz, $CDCl_3$) and (Bottom) ^{13}C NMR (151 MHz, $CDCl_3$) spectra of **btp** ligand **115**

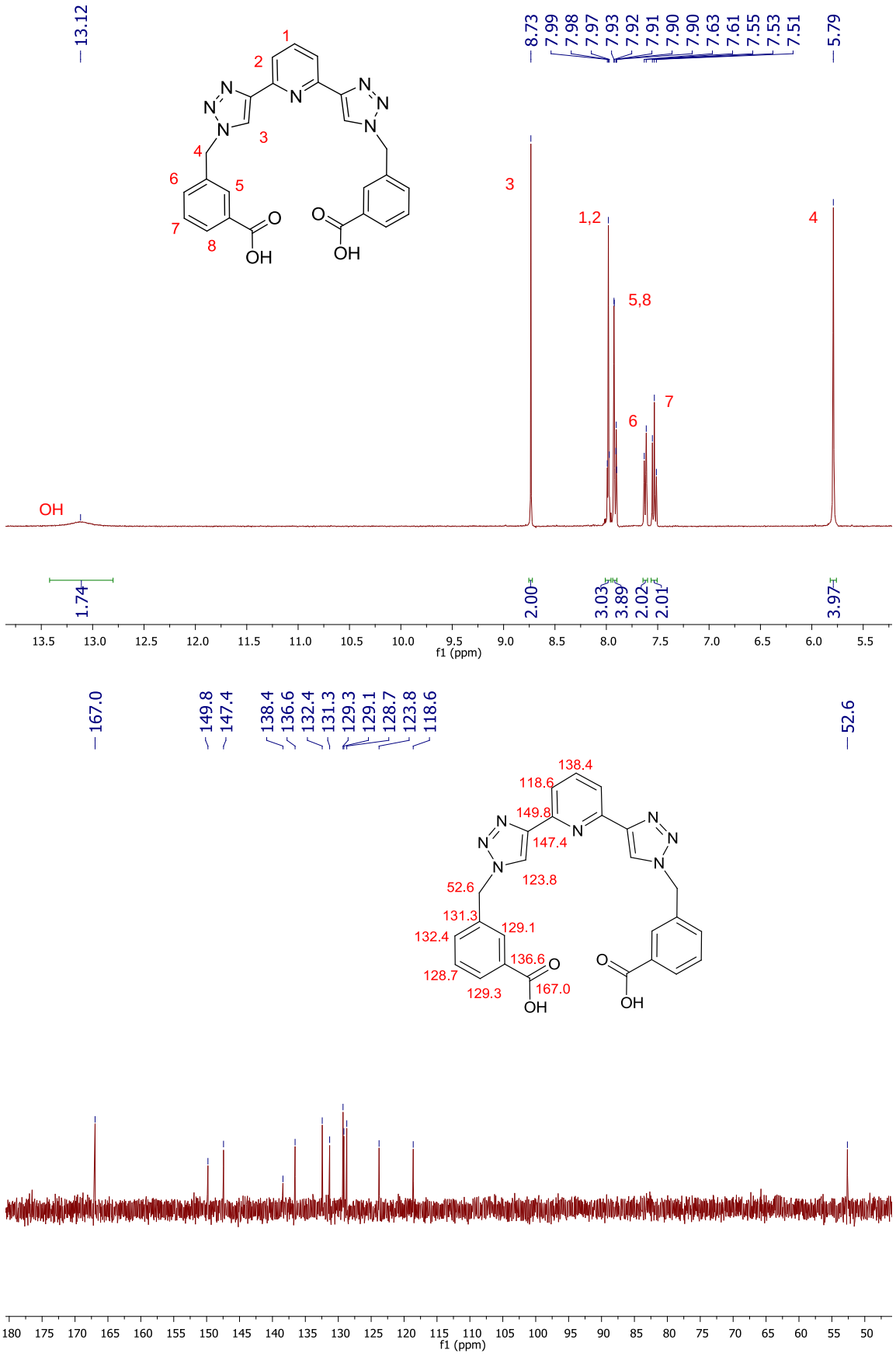

Figure A.31 (Top) ^{1}H NMR (400 MHz, DMSO-d_6) and (Bottom) ^{13}C NMR (151 MHz, DMSO-d_6) spectra of **btp** ligand **116**

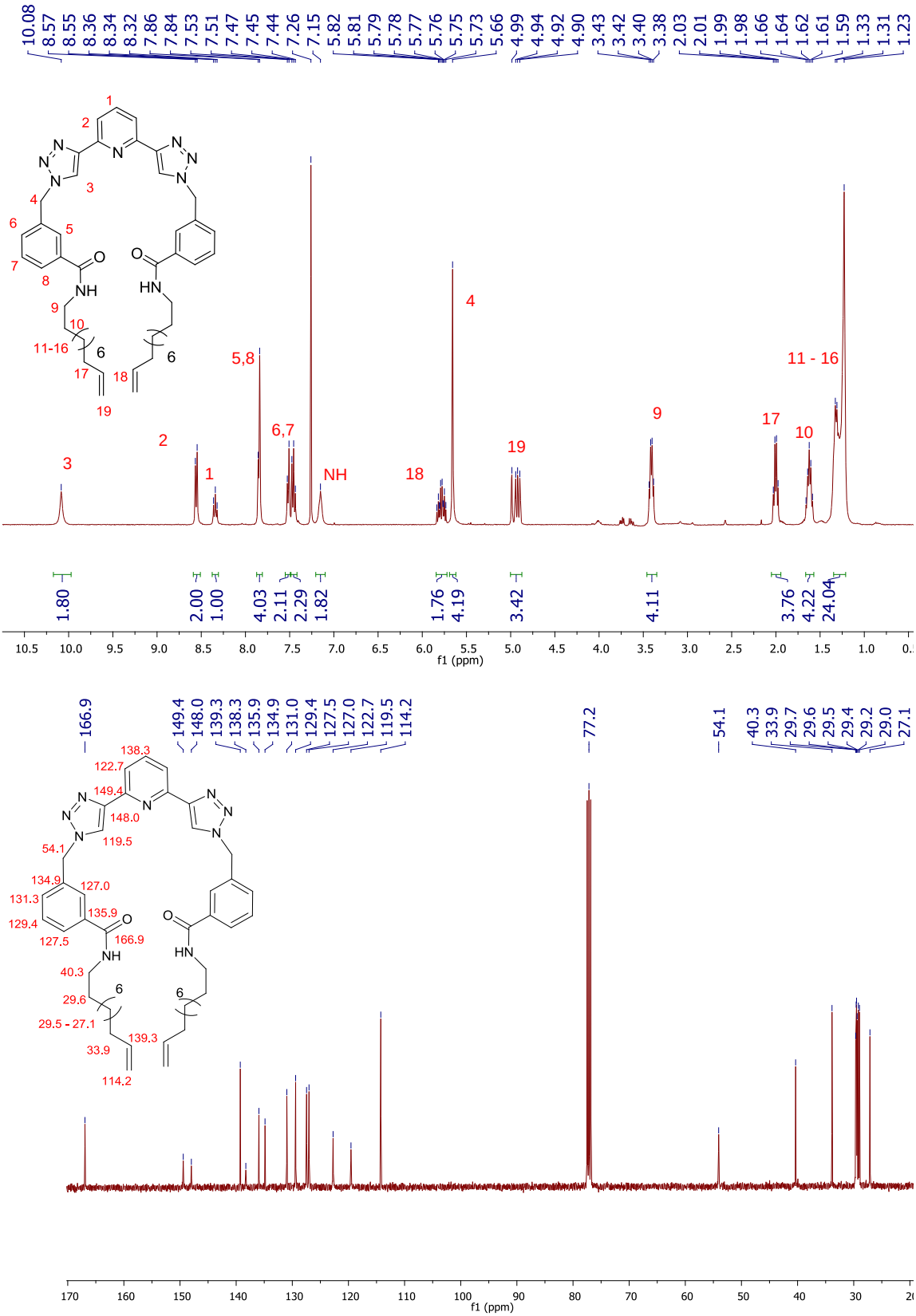

Figure A.32 (Top) ^{1}H NMR (400 MHz, $CDCl_3$) and (Bottom) ^{13}C NMR (151 MHz, $CDCl_3$) spectra of **btp** ligand **105**

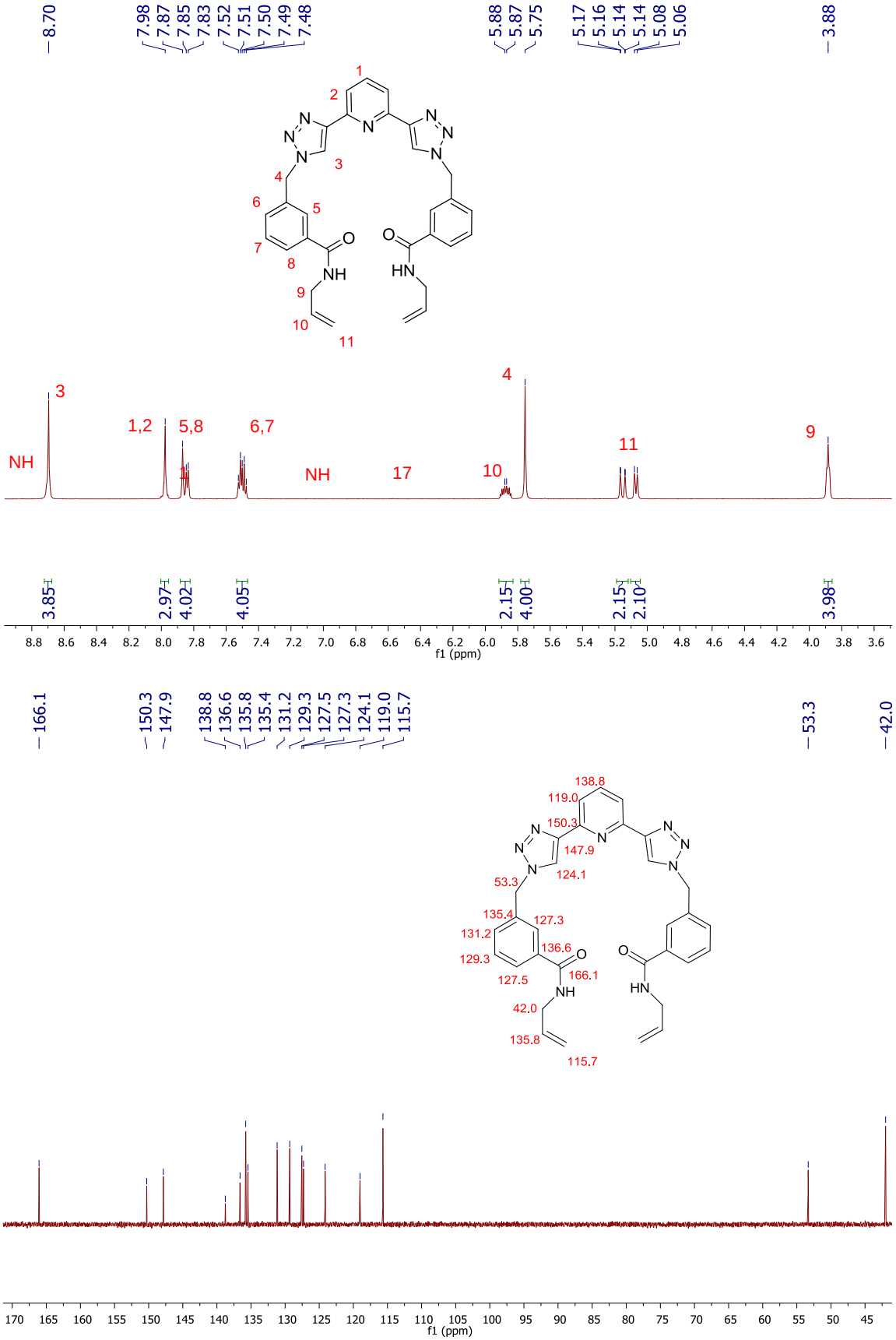

Figure A.33 (Top) ^{1}H NMR (400 MHz, DMSO-d_6) and (Bottom) ^{13}C NMR (151 MHz, DMSO-d_6) spectra of **btp** ligand **106**

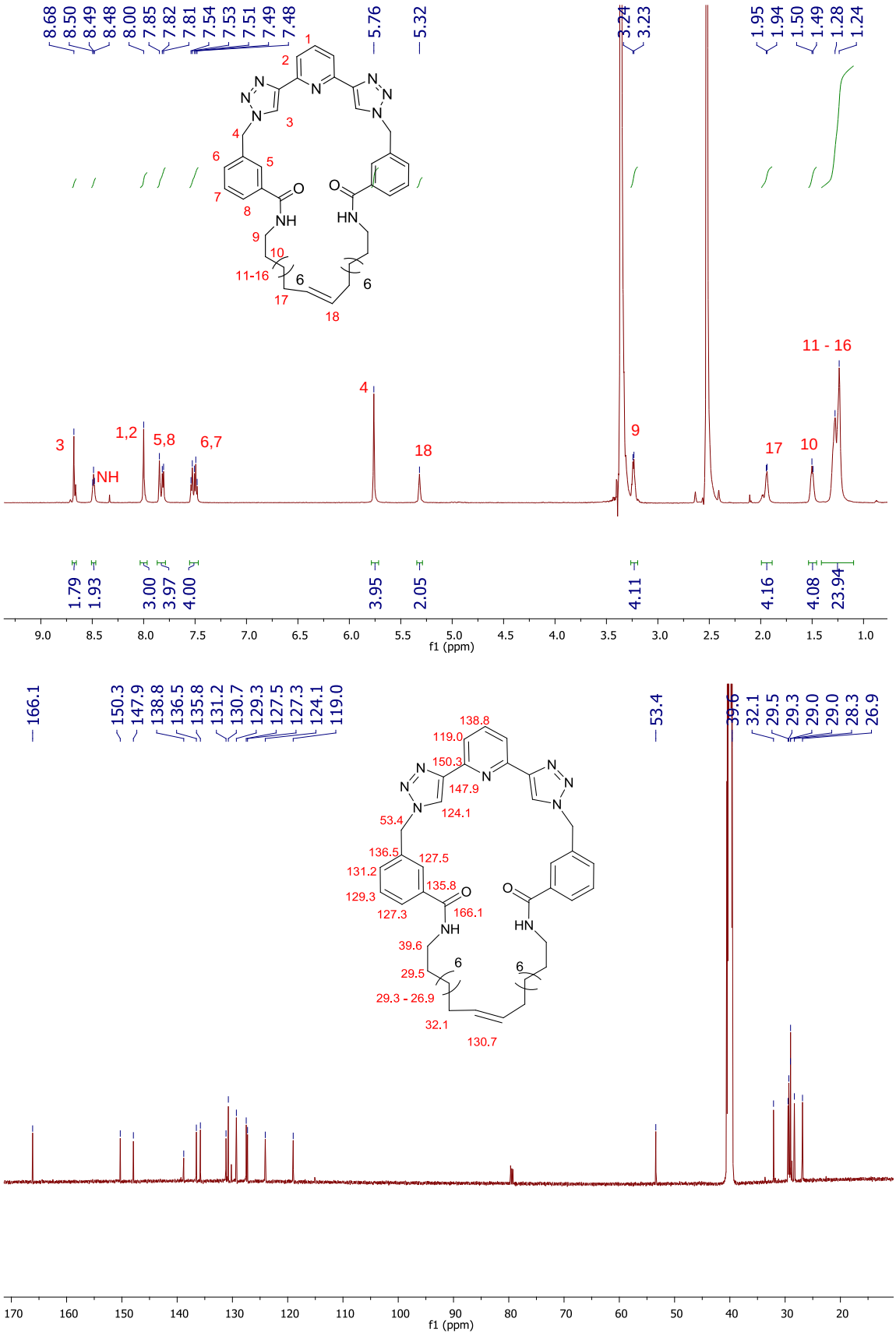

Figure A.33 (Top) ^{1}H NMR (400 MHz, DMSO-d_6) and (Bottom) ^{13}C NMR (101 MHz, DMSO-d_6) spectra of **btp 117**

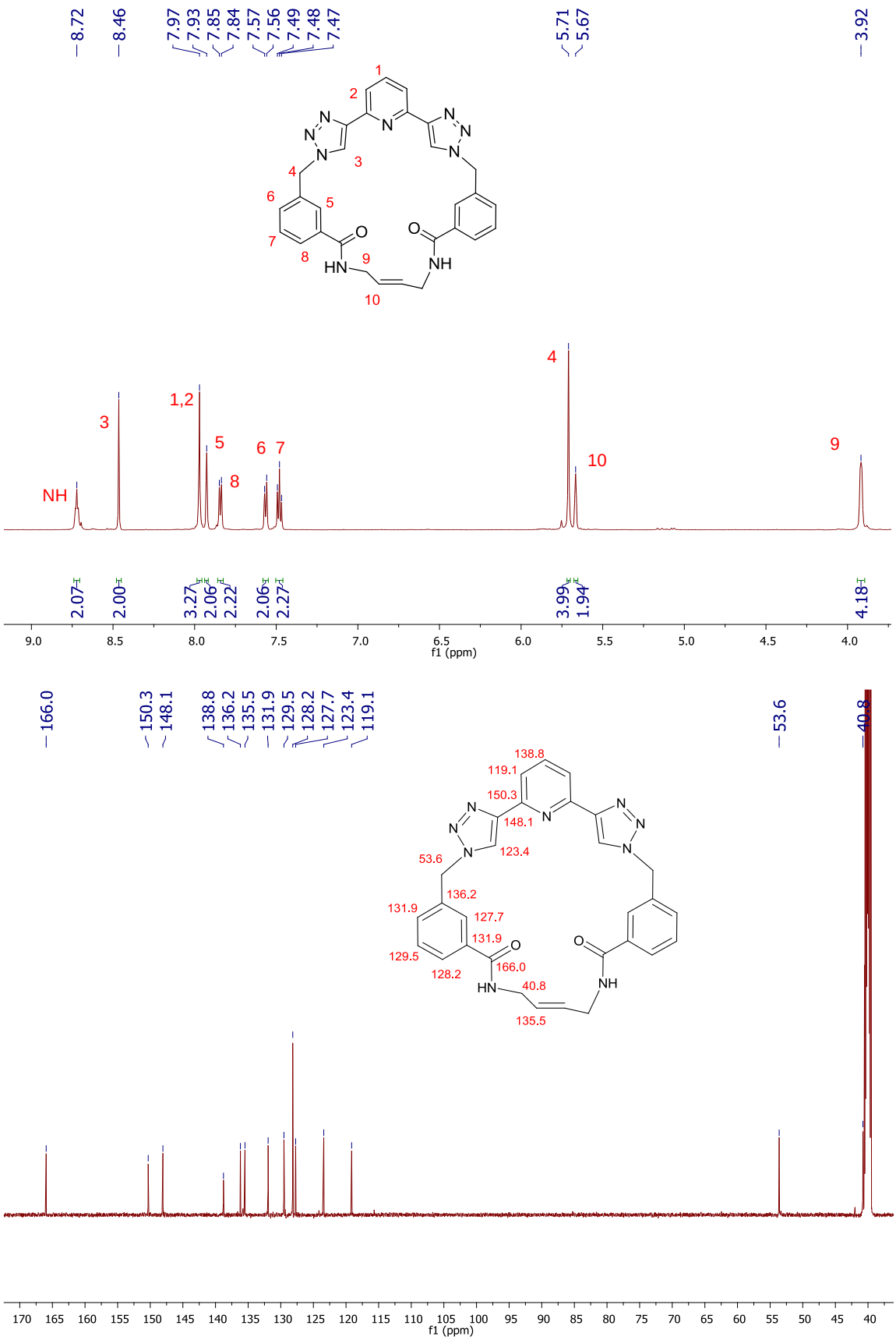

Figure A.34 (Top) ^{1}H NMR (400 MHz, DMSO-d_6) and (Bottom) ^{13}C NMR (151 MHz, DMSO-d_6) spectra of **btp** ligand **118**

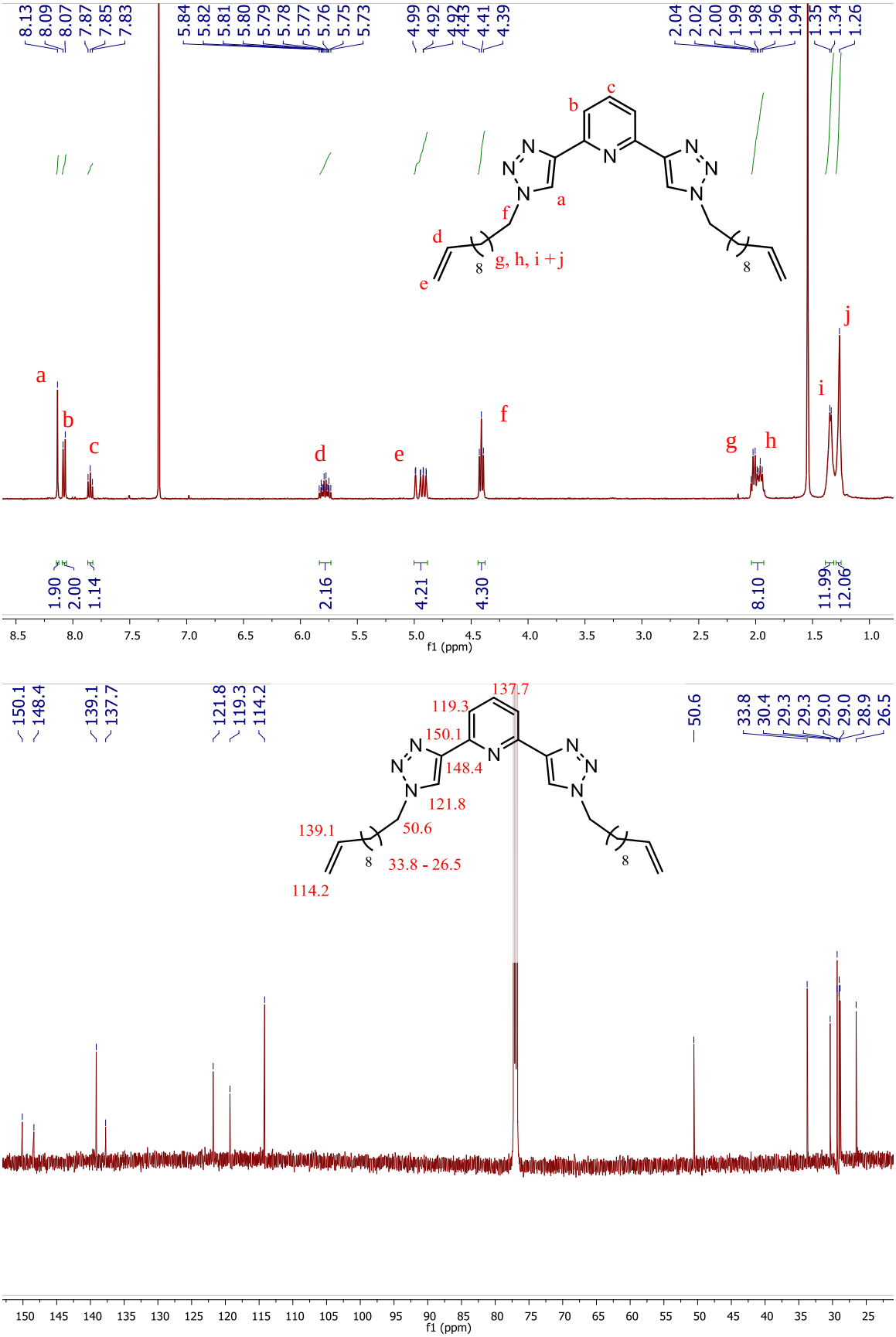

Figure A.35 (Top) ^{1}H NMR (400 MHz, $CDCl_3$) and (Bottom) ^{13}C NMR (151 MHz, $CDCl_3$) spectra of **btp** ligand **107**

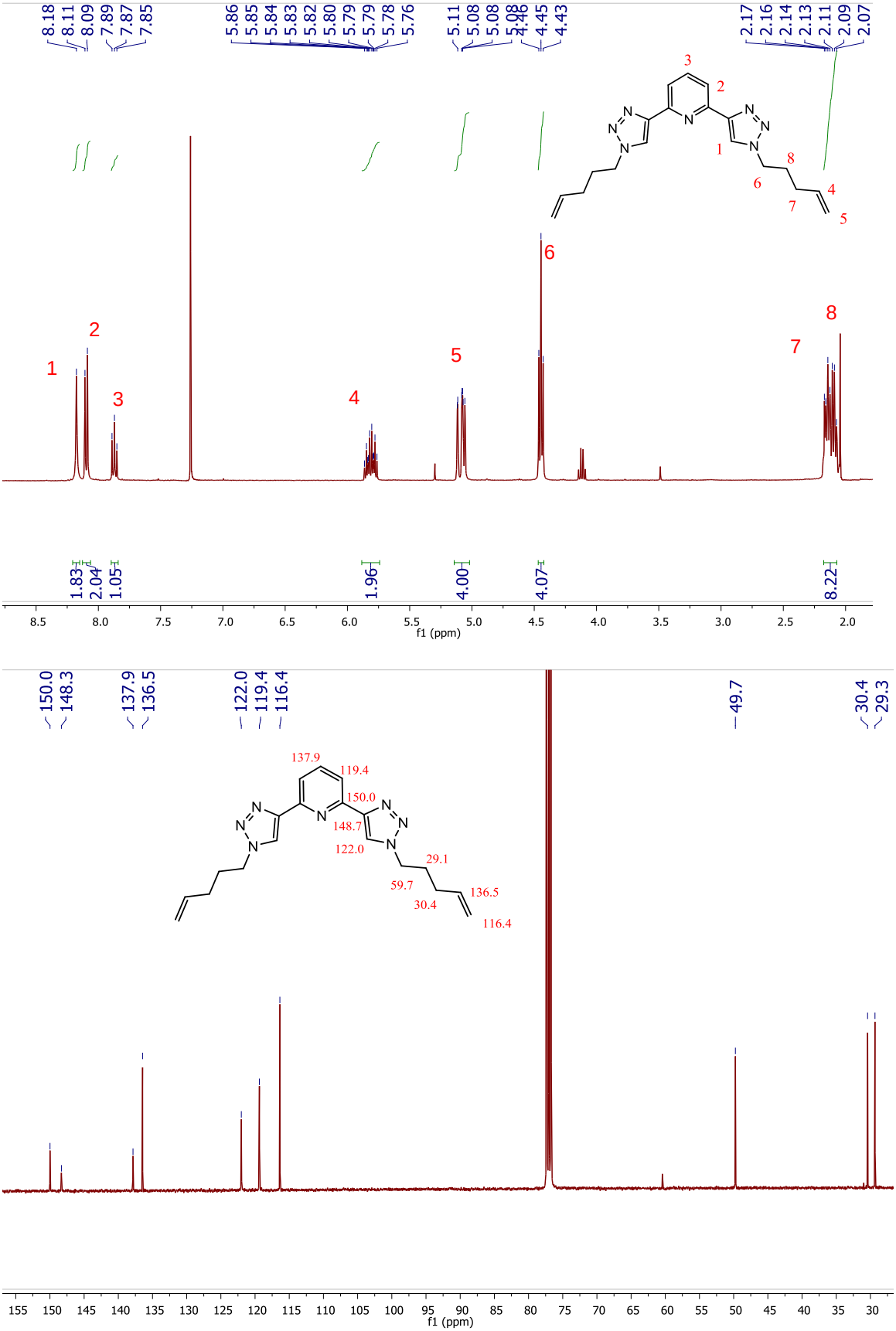

Figure A.36 (Top) ^{1}H NMR (400 MHz, $CDCl_3$) and (Bottom) ^{13}C NMR (101 MHz, $CDCl_3$) spectra of **btp** ligand **108**

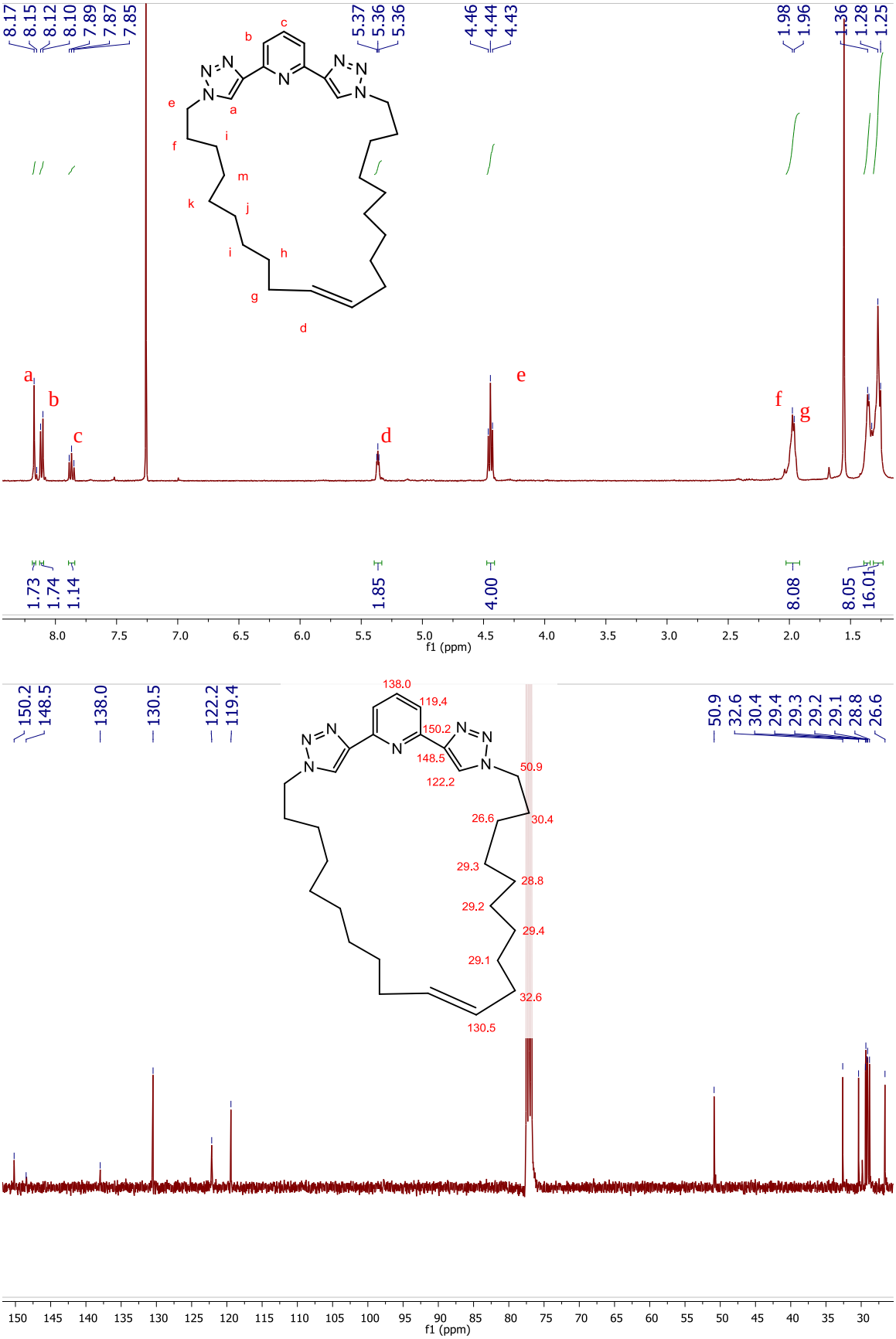

Figure A.37 (Top) ^{1}H NMR (400 MHz, $CDCl_3$) and (Bottom) ^{13}C NMR (101 MHz, $CDCl_3$) spectra of **btp** ligand **119**

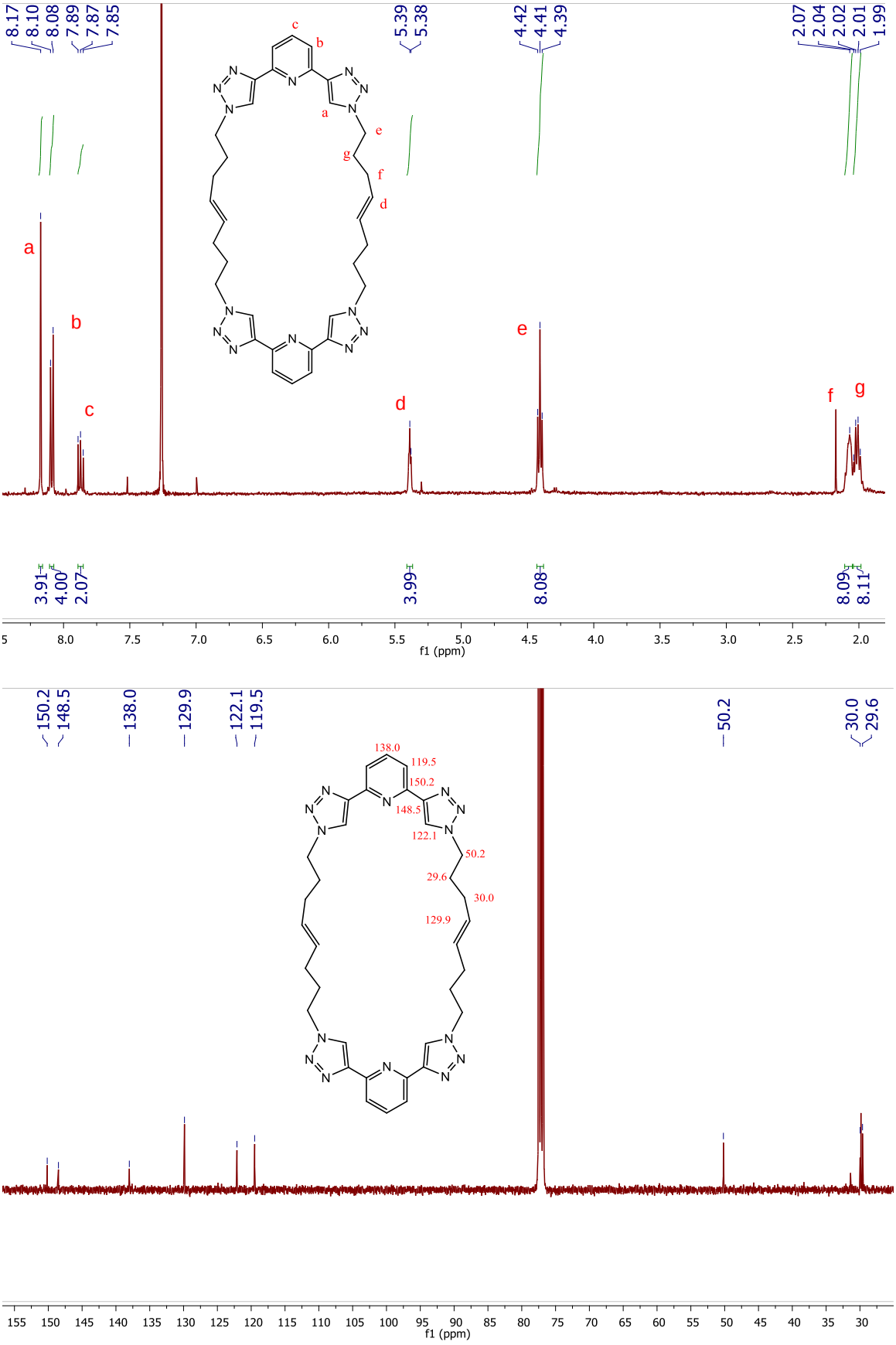

Figure A.38 (Top) ^{1}H NMR (400 MHz, $CDCl_3$) and (Bottom) ^{13}C NMR (101 MHz, $CDCl_3$) spectra of **btp** ligand **120**

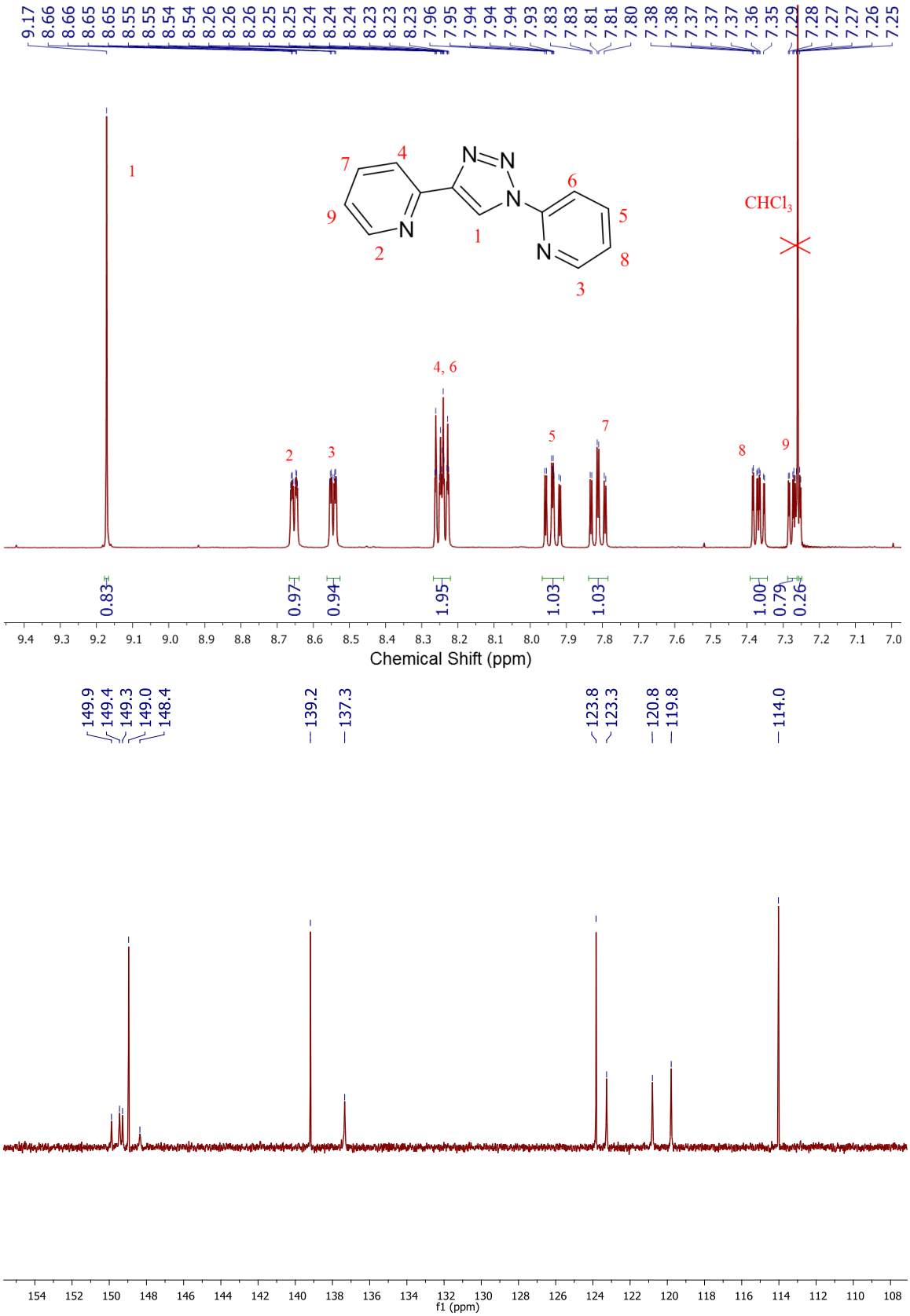

Figure A.39 (Top) ^{1}H NMR (600 MHz, $CDCl_3$) and (Bottom) ^{13}C NMR (151 MHz, $CDCl_3$) spectra of **btp** ligand **124**

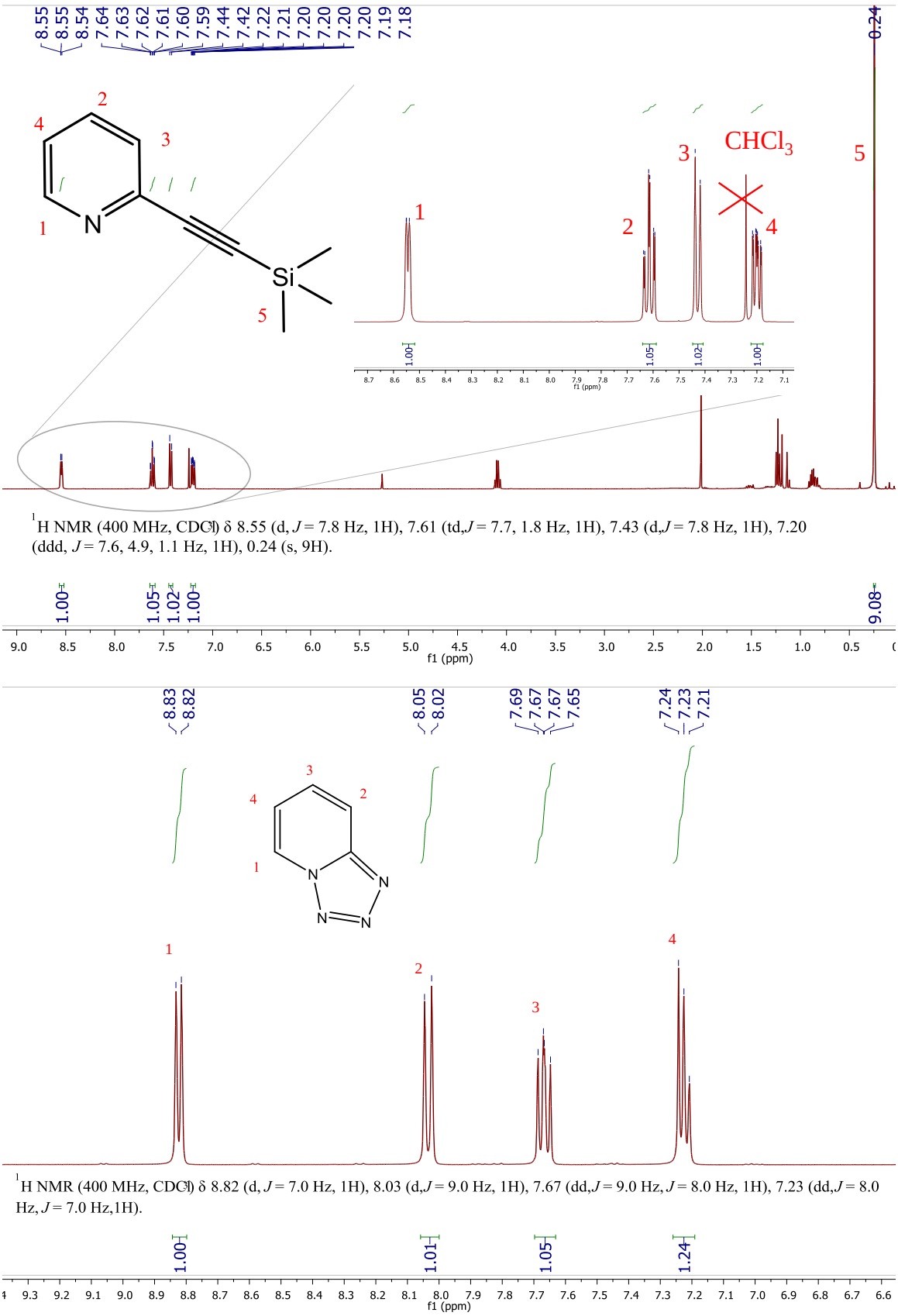

^{1}H NMR (400 MHz, $CDCl_3$) δ 8.55 (d, J = 7.8 Hz, 1H), 7.61 (td, J = 7.7, 1.8 Hz, 1H), 7.43 (d, J = 7.8 Hz, 1H), 7.20 (ddd, J = 7.6, 4.9, 1.1 Hz, 1H), 0.24 (s, 9H).

^{1}H NMR (400 MHz, $CDCl_3$) δ 8.82 (d, J = 7.0 Hz, 1H), 8.03 (d, J = 9.0 Hz, 1H), 7.67 (dd, J = 9.0 Hz, J = 8.0 Hz, 1H), 7.23 (dd, J = 8.0 Hz, J = 7.0 Hz, 1H).

Figure A.40 ^{1}H NMR (400 MHz, $CDCl_3$) spectra of (Top) **46** and (Bottom) **125**

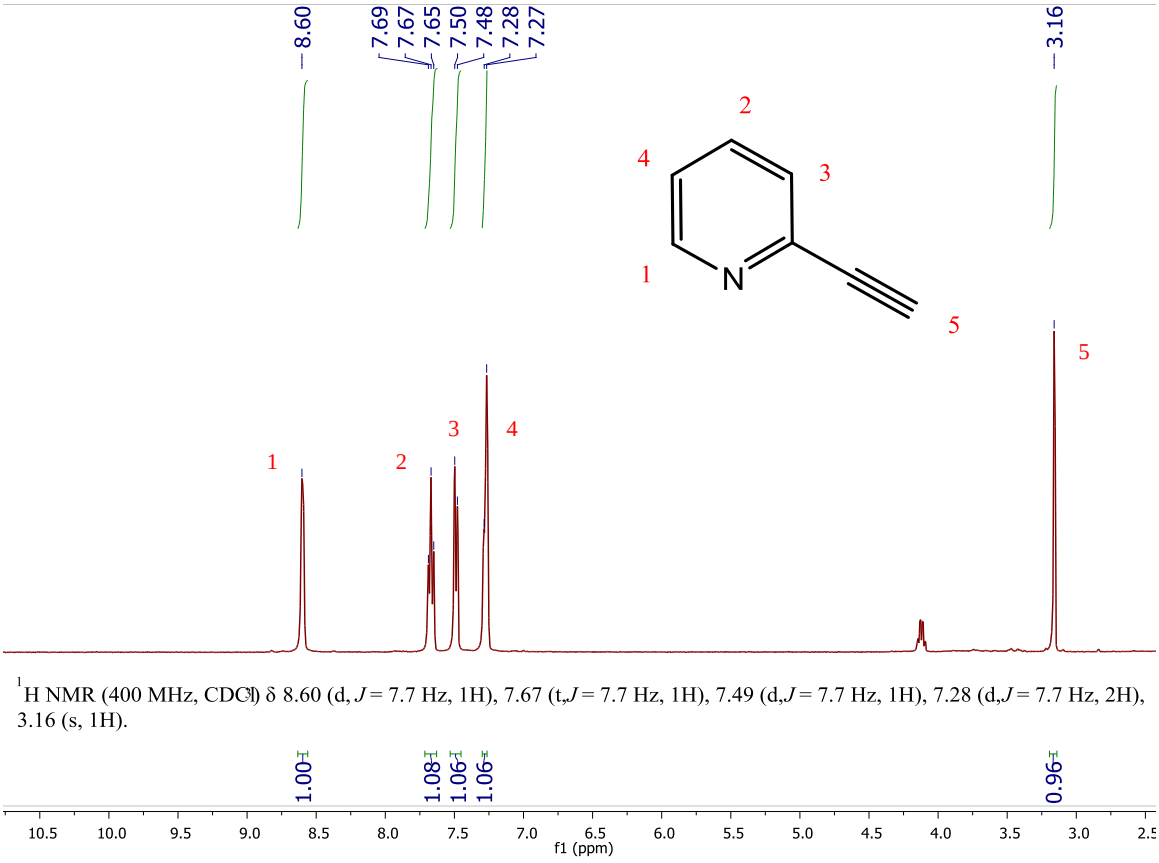

^{1}H NMR (400 MHz, CDCl$_3$) δ 8.60 (d, J = 7.7 Hz, 1H), 7.67 (t, J = 7.7 Hz, 1H), 7.49 (d, J = 7.7 Hz, 1H), 7.28 (d, J = 7.7 Hz, 2H), 3.16 (s, 1H).

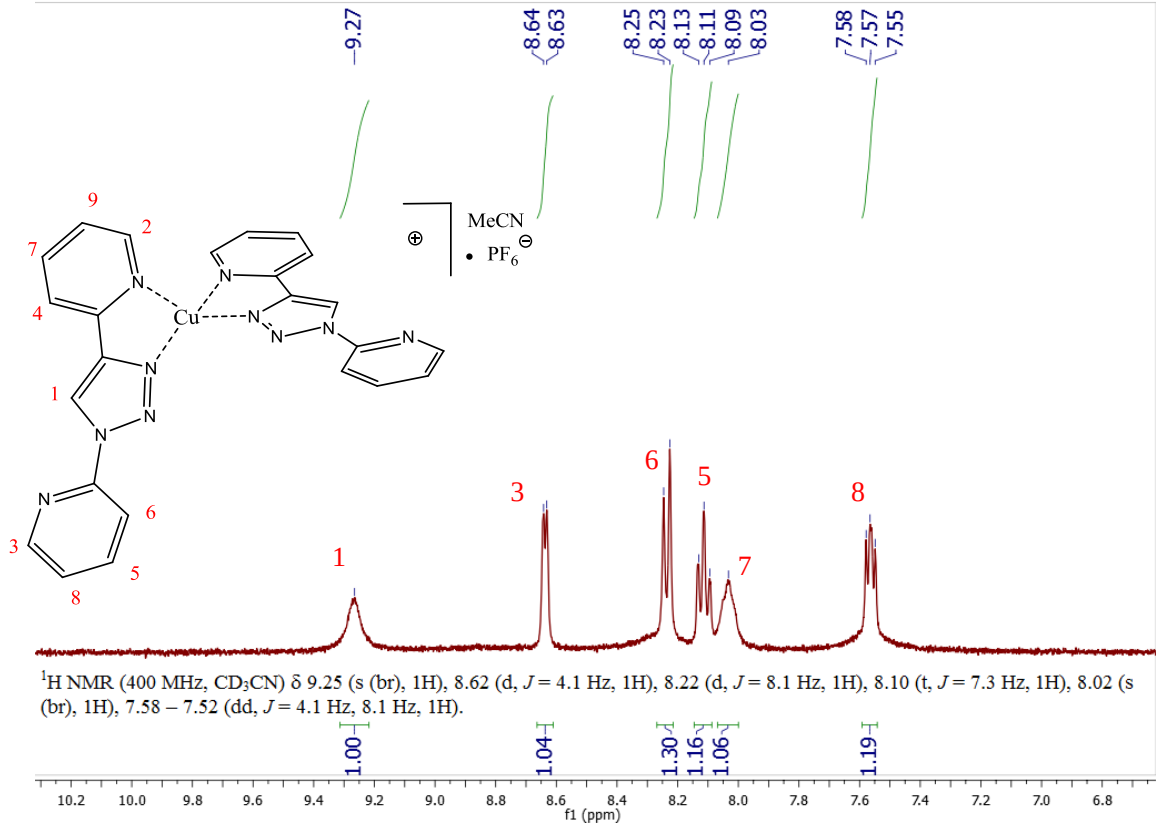

^{1}H NMR (400 MHz, CD$_3$CN) δ 9.25 (s (br), 1H), 8.62 (d, J = 4.1 Hz, 1H), 8.22 (d, J = 8.1 Hz, 1H), 8.10 (t, J = 7.3 Hz, 1H), 8.02 (s (br), 1H), 7.58 – 7.52 (dd, J = 4.1 Hz, 8.1 Hz, 1H).

Figure A.41 ^{1}H NMR (400 MHz, $CDCl_3$) spectra of (Top) **126** and (Bottom) [Cu**124**$_2$]PF_6 (400 MHz, CD_3CN).

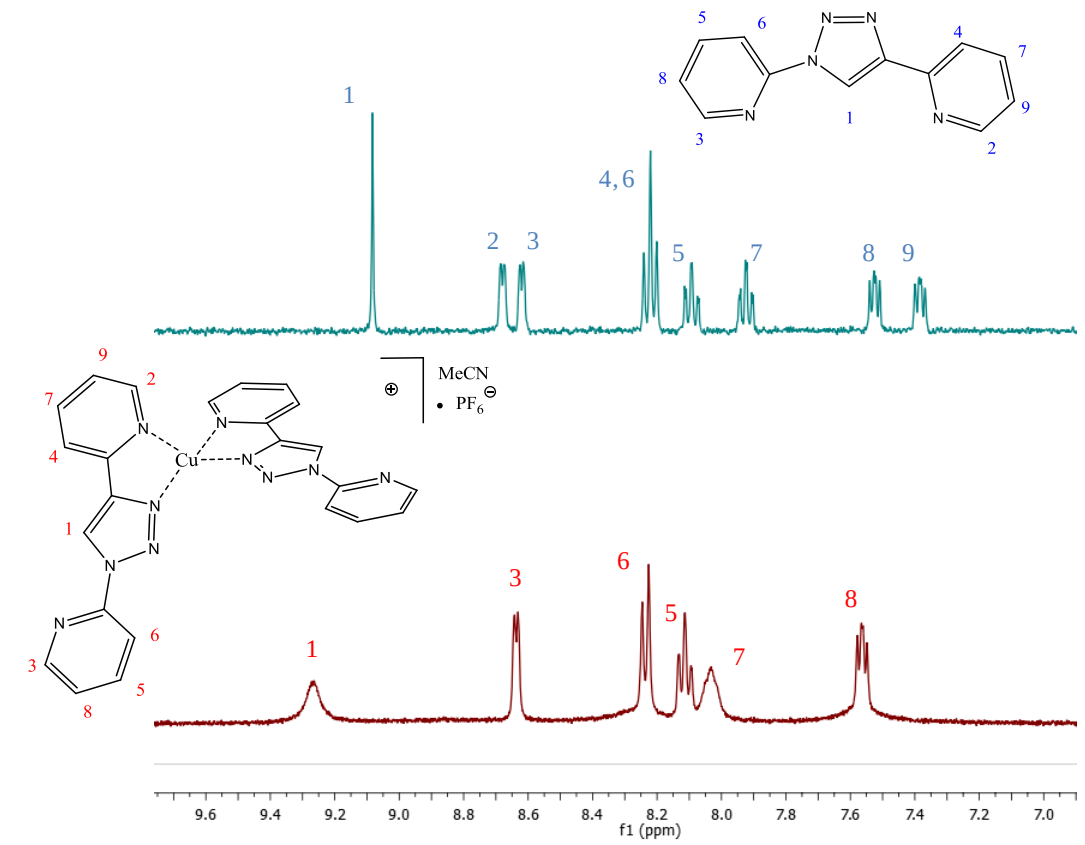

Figure A.42 ^{1}H NMR (400 MHz, CD_3CN) comparison of **124** (blue) and [Cu**124**$_2$]PF_6 (red) showing the broadening of the peaks associated with the *reg* chelate pocket.

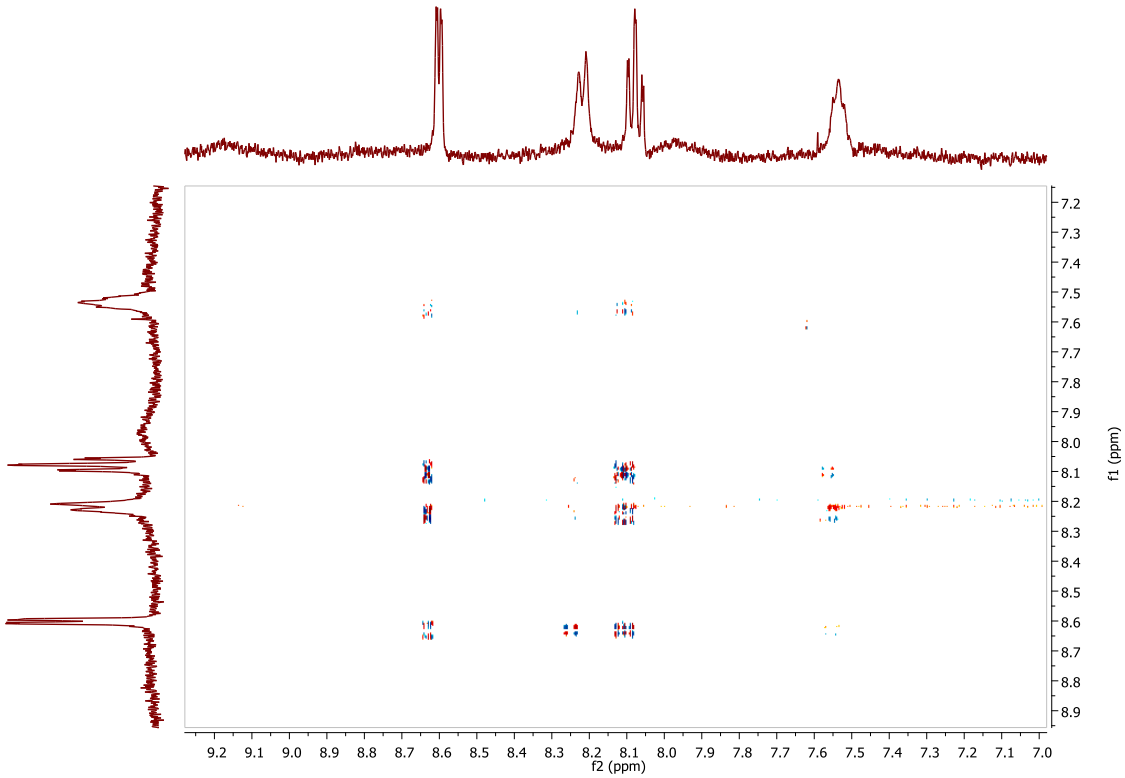

Figure A.43 ^{1}H NMR (400 MHz, CD_3CN) HH COSY of [Cu**124**$_2$]PF_6 showing that the sharp peaks associated with the non-chelating pyridine consisted of the one magnetically coupled ring system.

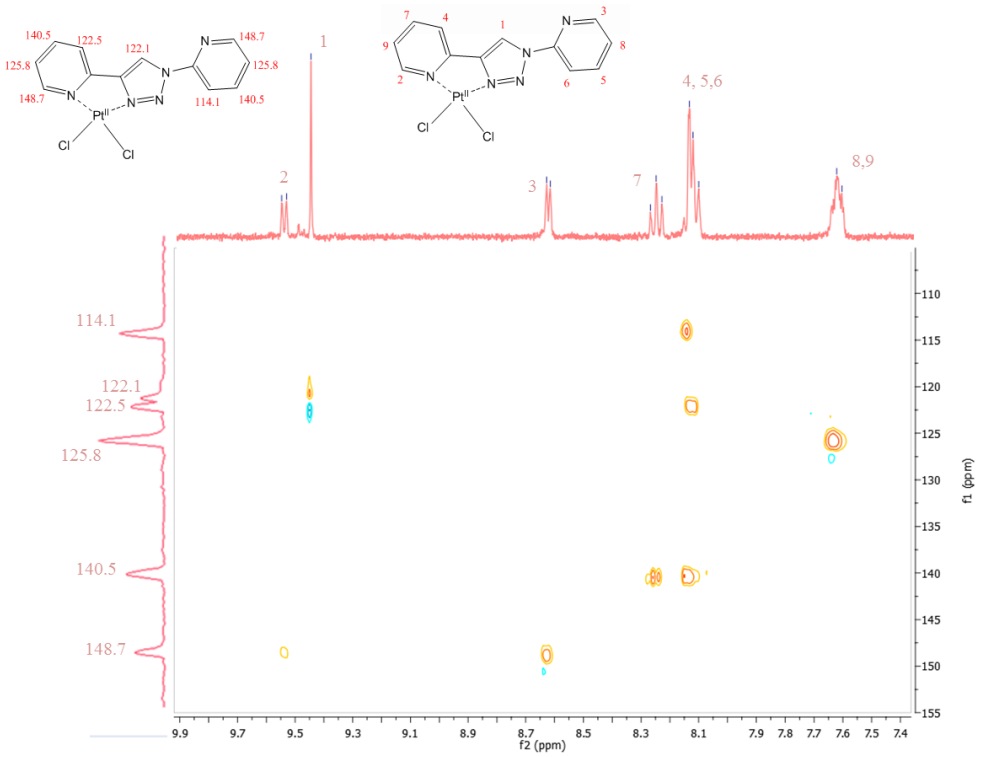

Figure A.44 HSQC in CD_3CN of one component phase of [Pt**124**Cl_2]

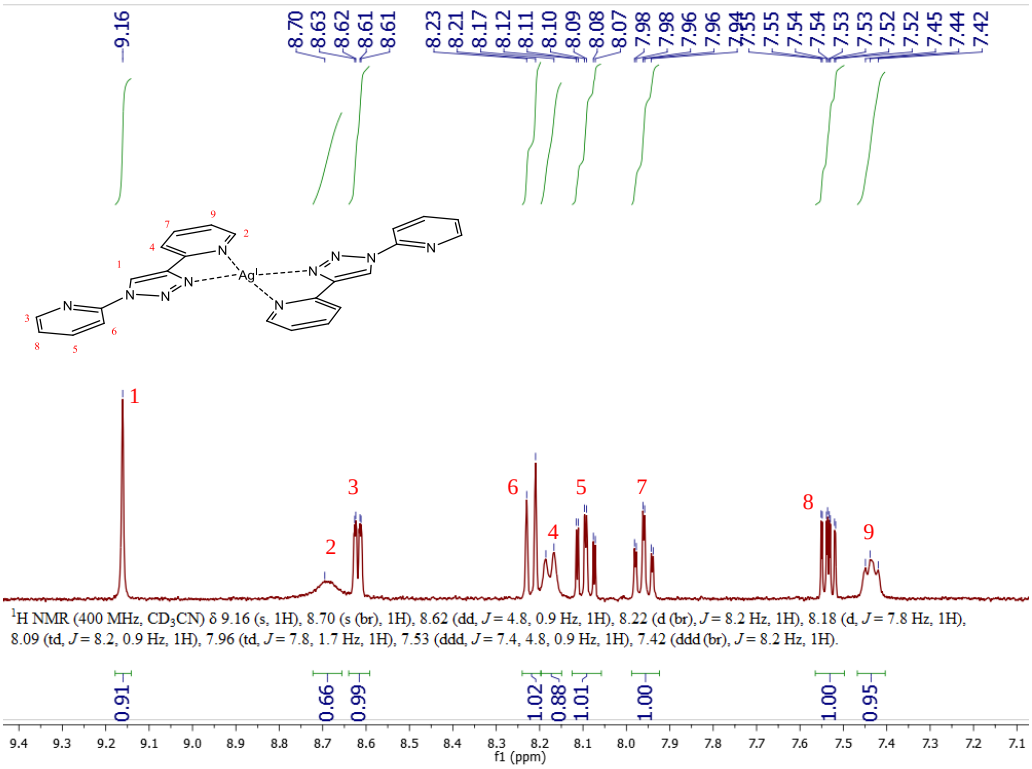

^{1}H NMR (400 MHz, CD_3CN) δ 9.16 (s, 1H), 8.70 (s (br), 1H), 8.62 (dd, *J* = 4.8, 0.9 Hz, 1H), 8.22 (d (br), *J* = 8.2 Hz, 1H), 8.18 (d, *J* = 7.8 Hz, 1H), 8.09 (td, *J* = 8.2, 0.9 Hz, 1H), 7.96 (td, *J* = 7.8, 1.7 Hz, 1H), 7.53 (ddd, *J* = 7.4, 4.8, 0.9 Hz, 1H), 7.42 (ddd (br), *J* = 8.2 Hz, 1H).

Figure A.45 ^{1}H NMR (400 MHz, CD_3CN) spectrum of [Ag**124**$_2$]SbF_6.

^{1}H NMR titrations (400 MHz, DMSO-d_6) of [2]catenanes 36a and 111R/S and macrocycles 106, 112S and 121 with TBA(H_2PO_4) and TBACl

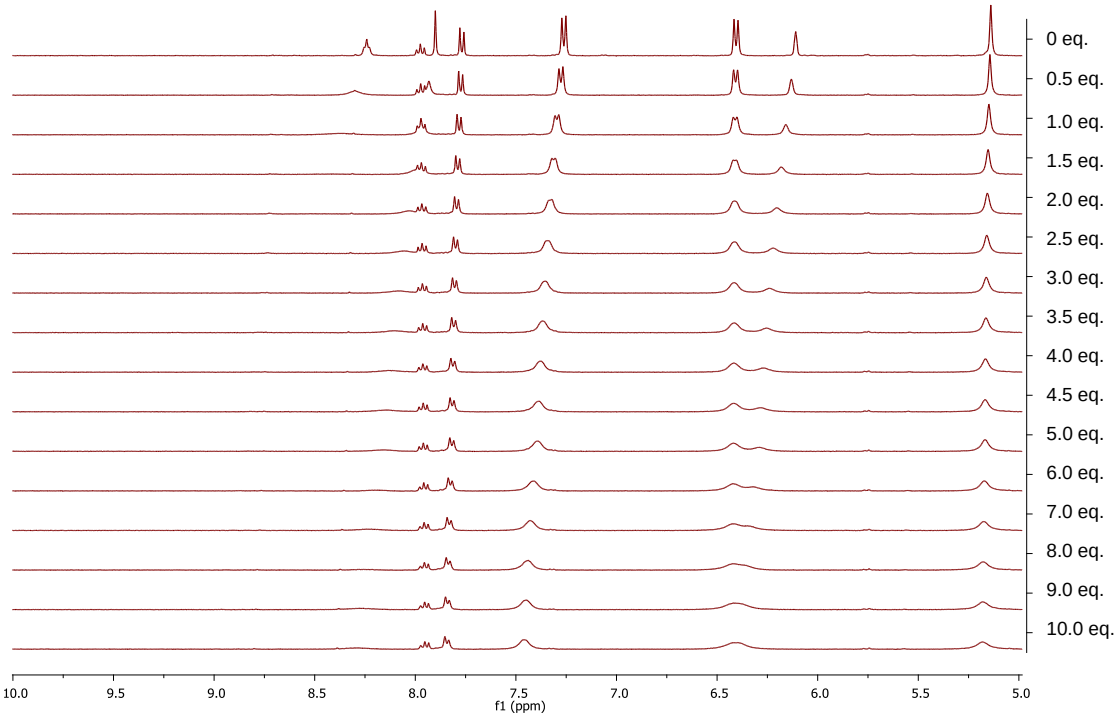

Figure A.46 ^{1}H NMR titrations (400 MHz, DMSO-d_6) of [2]catenanes **36a** with TBA(H_2PO_4)

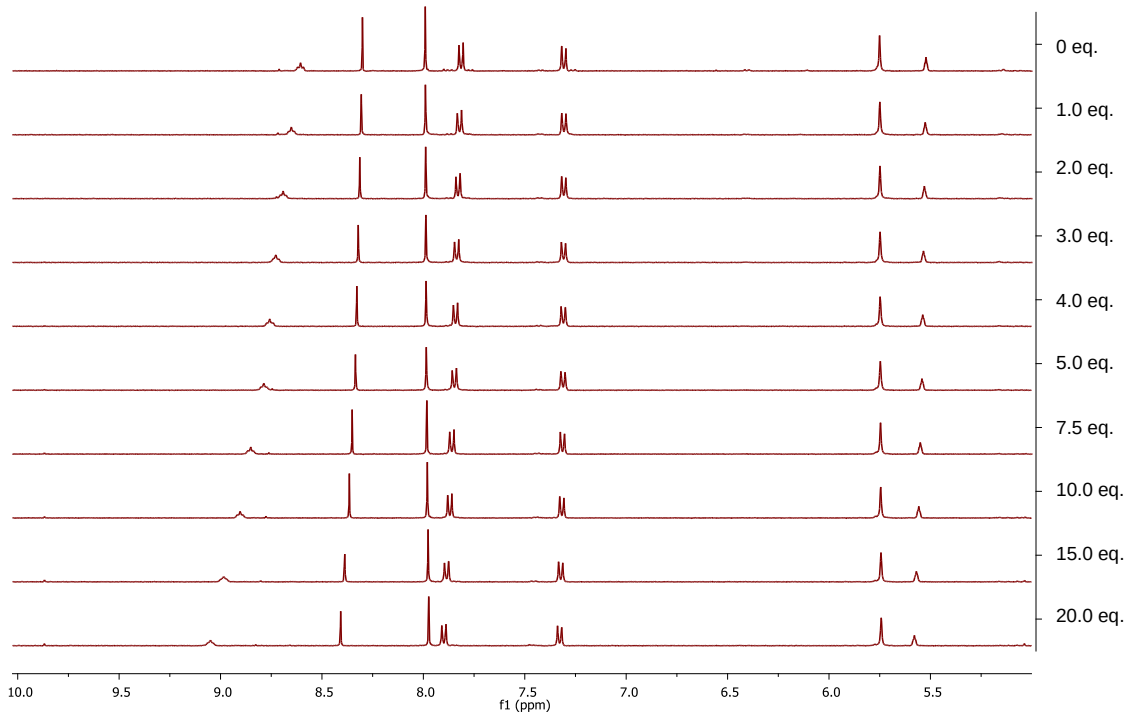

Figure A.47 ^{1}H NMR titrations (400 MHz, DMSO-d_6) of macrocycle **121** with TBA(H_2PO_4)

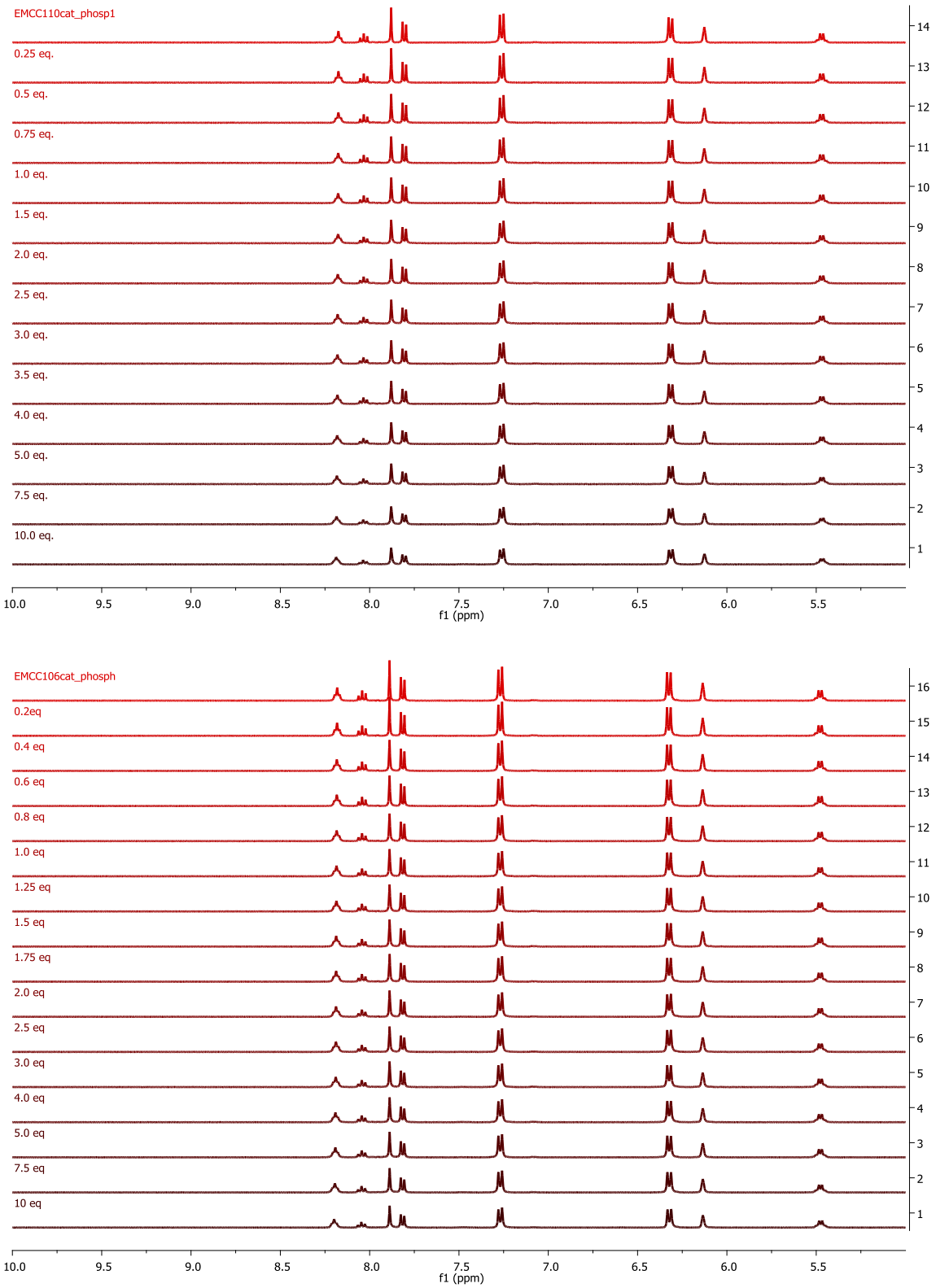

Figure A.48 ^{1}H NMR titrations (400 MHz, DMSO-d_6) of [2]catenanes **111R** (top) and **111S** (bottom) with TBA(H_2PO_4)

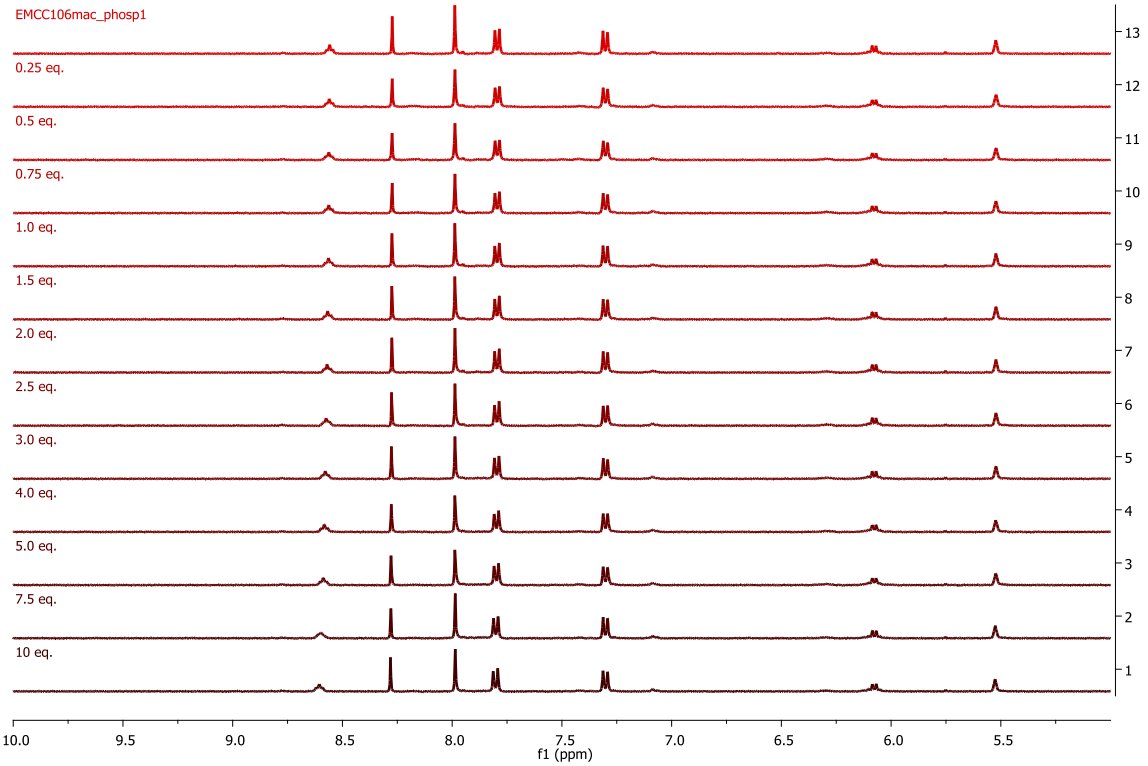

Figure A.49 ^{1}H NMR titrations (400 MHz, DMSO-d_6) of macrocycle **112S** with TBA(H_2PO_4)

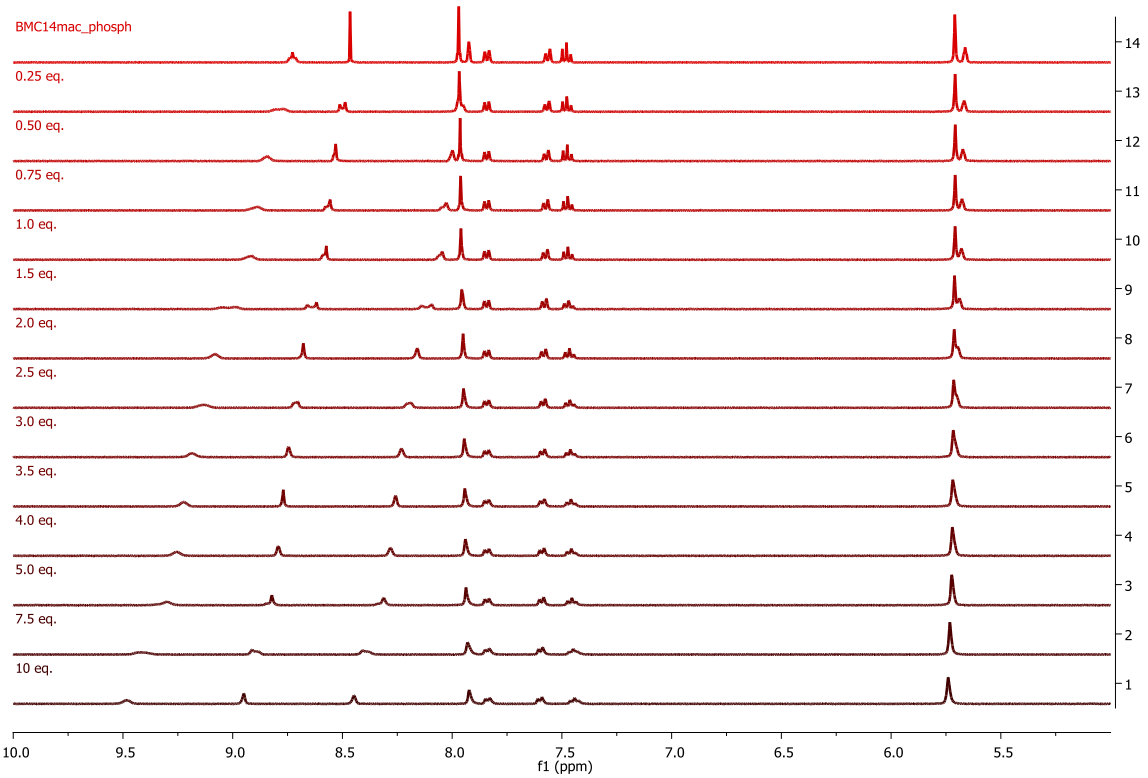

Figure A.50 ^{1}H NMR titrations (400 MHz, DMSO-d_6) of macrocycle 1**18** with TBA(H_2PO_4)

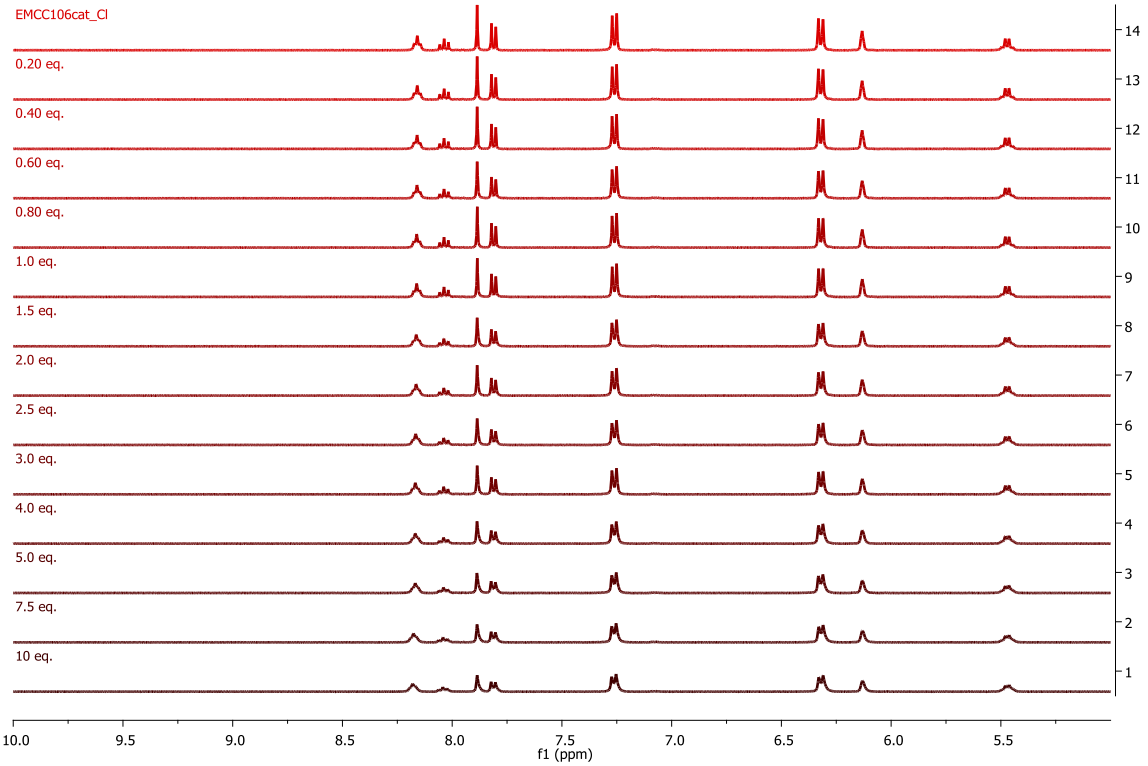

Figure A.51 ^{1}H NMR titrations (400 MHz, DMSO-d_6) of [2]catenanes **111S** with TBACl

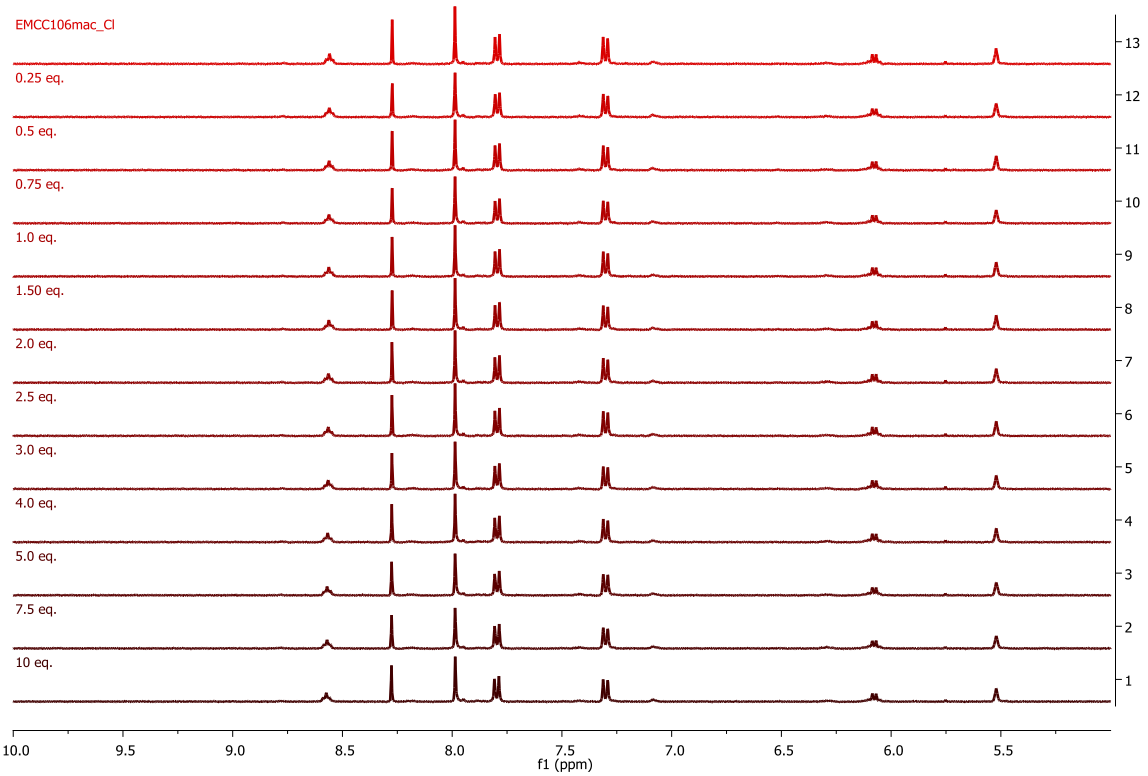

Figure A.52 ^{1}H NMR titrations (400 MHz, DMSO-d_6) of macrocycle **112S** with TBACl

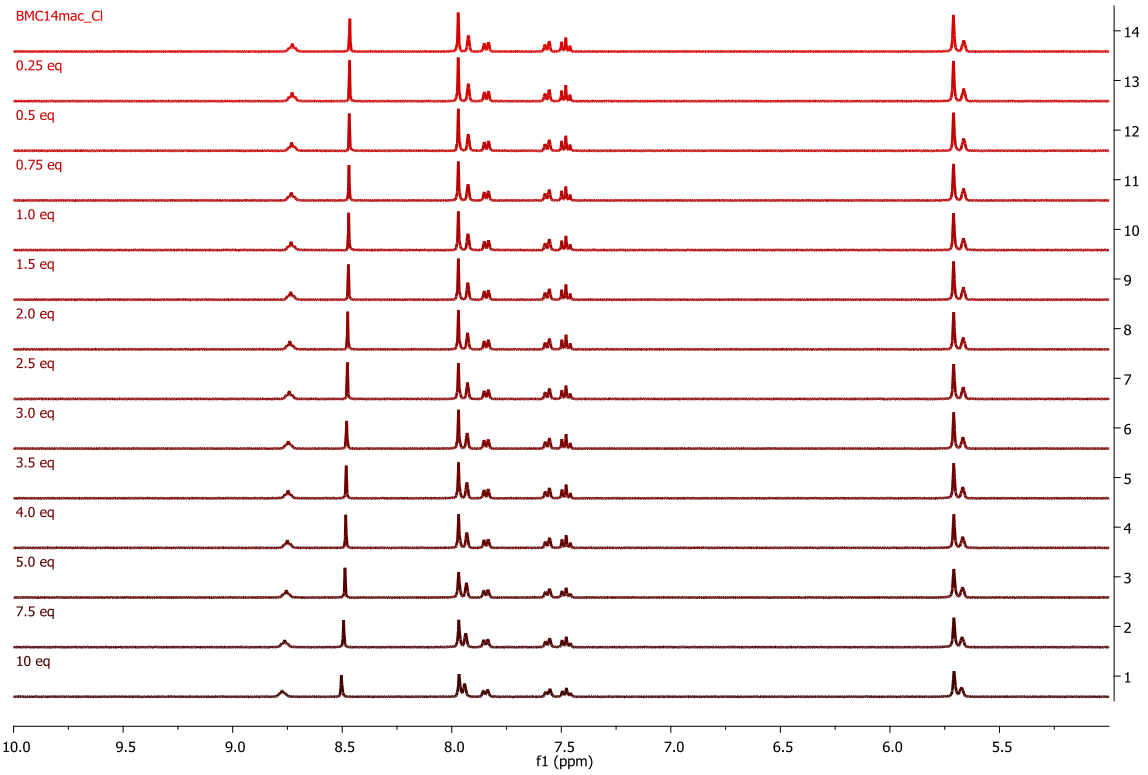

Figure A.53 ^{1}H NMR titrations (400 MHz, DMSO-d_6) of macrocycle **118** with TBACl

9.2 Appendix B (Mass Spectrometry)

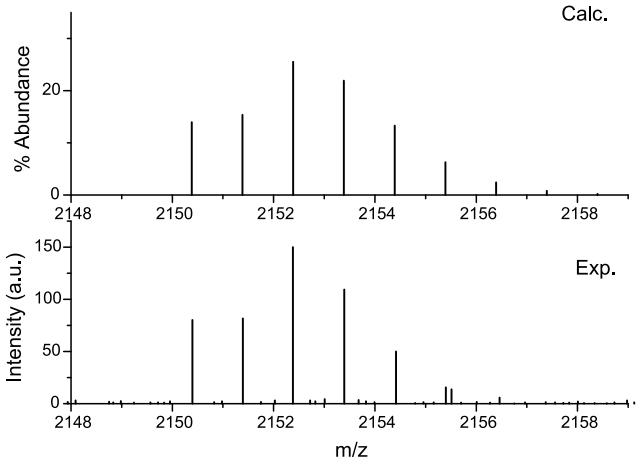

Figure B.1 HRMS (*m/z*) (LD$^+$) of Eu**83**$_3$; Calculated for $C_{89}H_{75}N_{21}O_{24}F_6S_2Eu$ *m/z* = 2152.3852. Found for [Eu**83**$_3$-$CF_3SO_3^-$]$^+$ *m/z* = 2152.3796

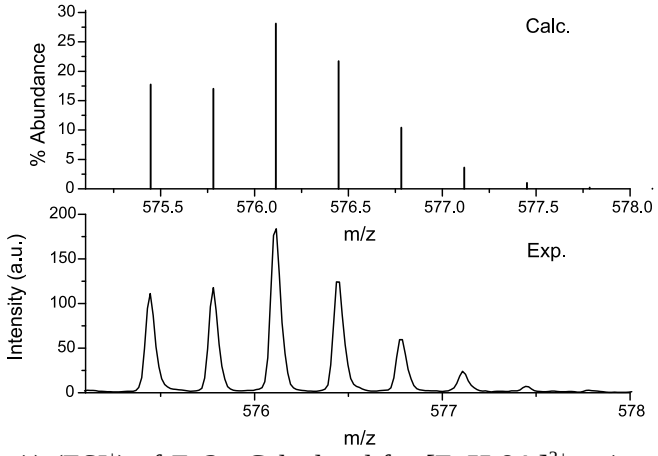

Figure B.2 HRMS (*m/z*) (ESI$^+$) of Eu**2**$_3$: Calculated for [Eu**H$_3$84**$_3$]$^{3+}$; *m/z* = 576.1134 where *z*=3. Found for [Eu**H$_3$84**$_3$]$^{3+}$; *m/z* = 576.1114.

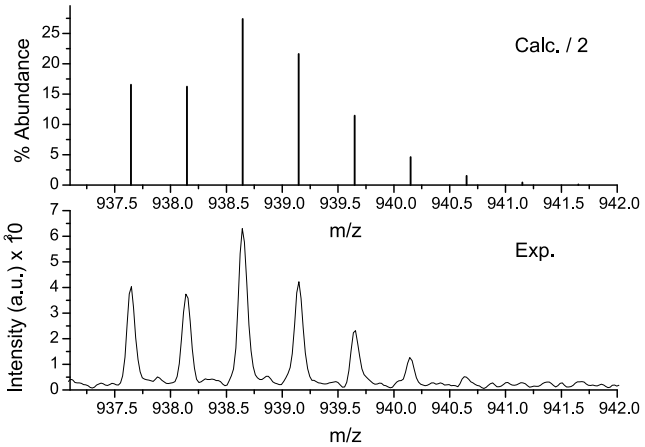

Figure B.3 HRMS (*m/z*) (ESI$^+$) of Eu**2**$_3$: Also, calculated for [Eu**H$_3$84**$_3$-$CF_3SO_3^-$]$^{2+}$; 938.6456 (above) *i.e. m/z* = 1877.2912. Found for [Eu**H$_3$84**$_3$-$CF_3SO_3^-$]$^{2+}$; 938.6484 i.e. *m/z* = 1877.2968.

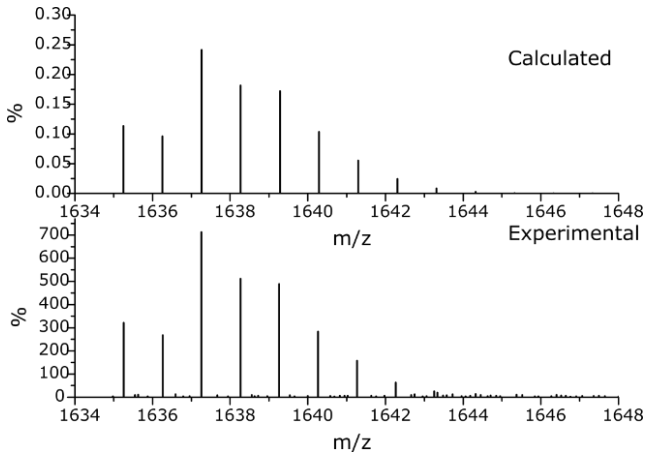

Figure B.4 HRMS (*m/z*) (ESI$^+$) of **Eu85$_2$**: Calculated for [**Eu85$_2$**-ClO_4^-]$^+$ *i.e.* $C_{70}H_{58}F_6EuN_{14}O_{20}Cl_2$ *m/z* = 1637.2541. Found for *m/z* = 1637.2582.

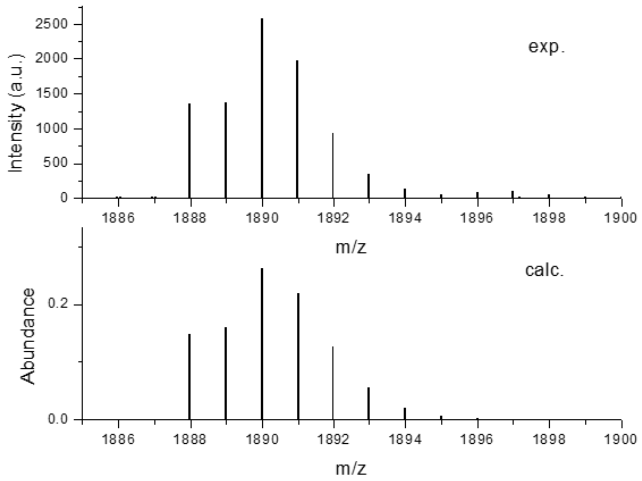

Figure B.5 HRMS (*m/z*) (LD$^+$) of **Eu99$_2$**: Calculated for [**Eu99$_2$**-$CF_3SO_3^-$]$^+$ *i.e.* $C_{88}H_{146}F_6EuN_{14}O_{10}S_2$ *m/z* = 1889.9904. Found for *m/z* = 1889.9867.

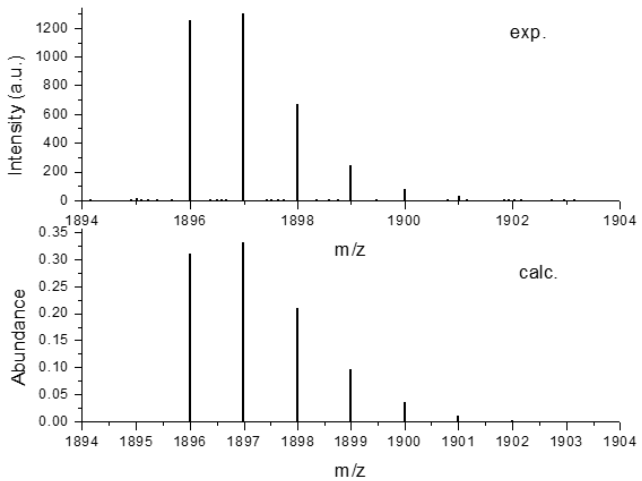

Figure B.6 HRMS (*m/z*) (ESI$^+$) of **Tb99$_2$**: Calculated for [**Tb99$_2$**-$CF_3SO_3^-$]$^+$ *i.e.* $C_{88}H_{146}F_6TbN_{14}O_{10}S_2$ *m/z* = 1895.9946. Found for *m/z* = 1895.9962.

9.3 Appendix C (Spectroscopy)

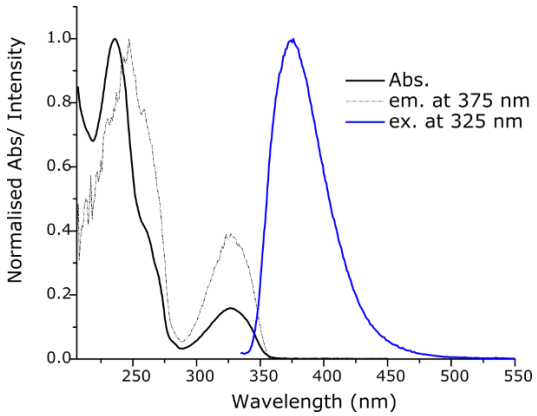

Figure C.1 Photophysical characterisation of **btp 83** in CH_3CN

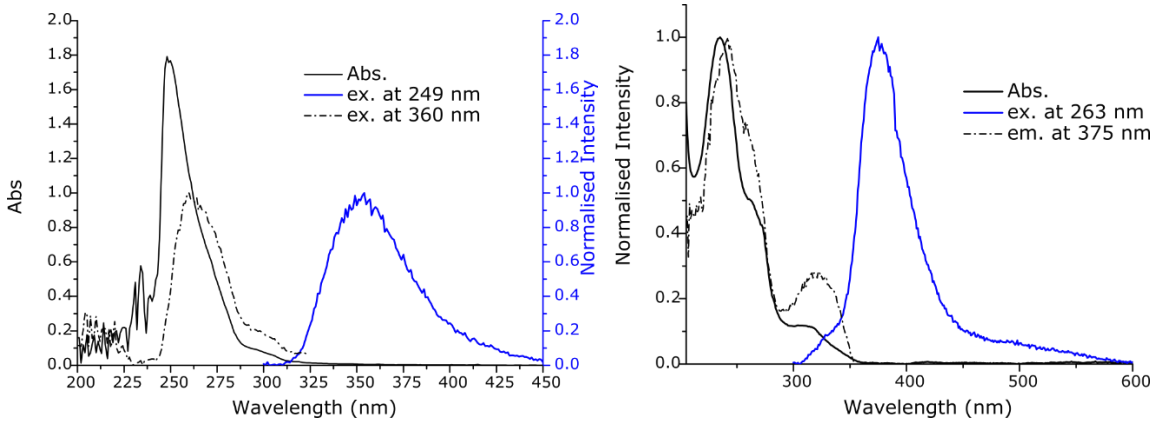

Figure C.2 Photophysical characterisation of amino **btp 95** in CH_3CN:DMSO (1:1) and ditopic **btp 98** in CH_3CN.

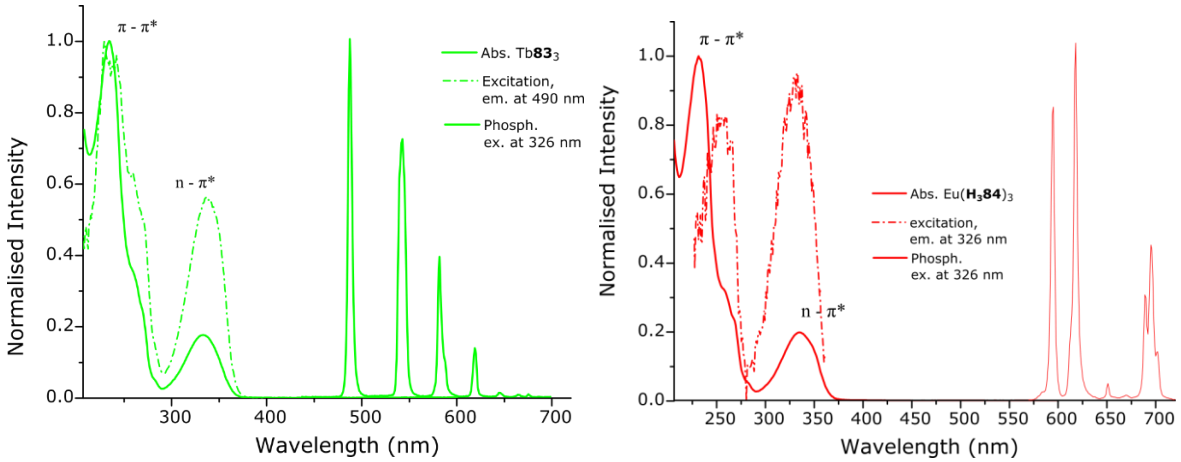

Figure C.3 Photophysical characterisation of Tb**83**$_3$ (Left) and Eu**84**$_3$ (Right) in CH_3CN

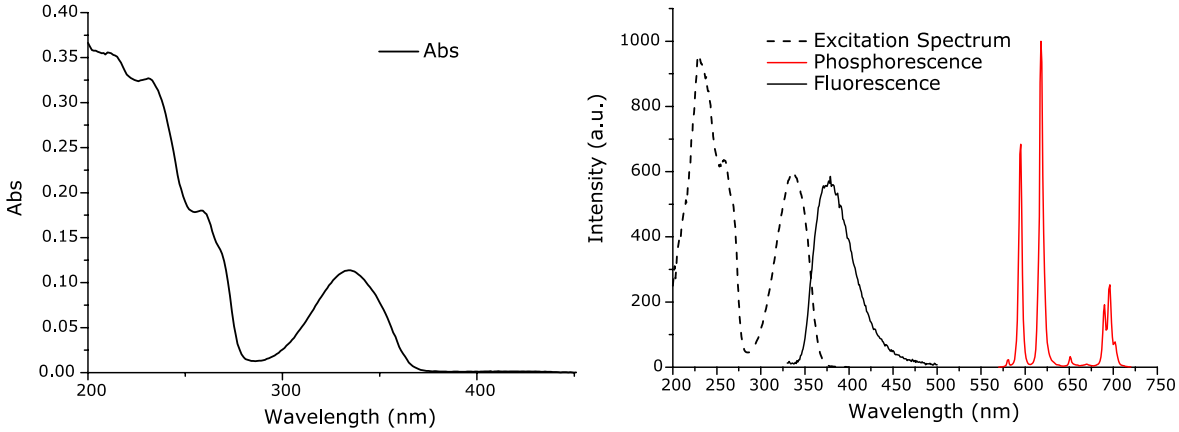

Figure C.4 (Left) UV-vis spectrum of **Eu99$_3$** in CH_2Cl_2:CH_3CN (1:9) solution at 21 °C. (right) Luminescence and excitation spectra of **Eu99$_3$**. (λ_{ex} = 325 nm).

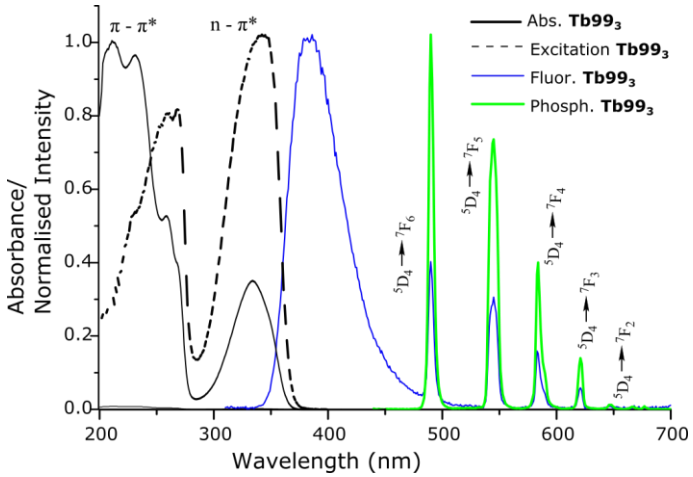

Figure C.5 UV-vis absorbance, excitation and Ln(III) phosphorescence spectra of **99** and **Tb99$_3$** in CH_2Cl_2:CH_3CN (1:9) solution. (*c* = 0.2 mM)

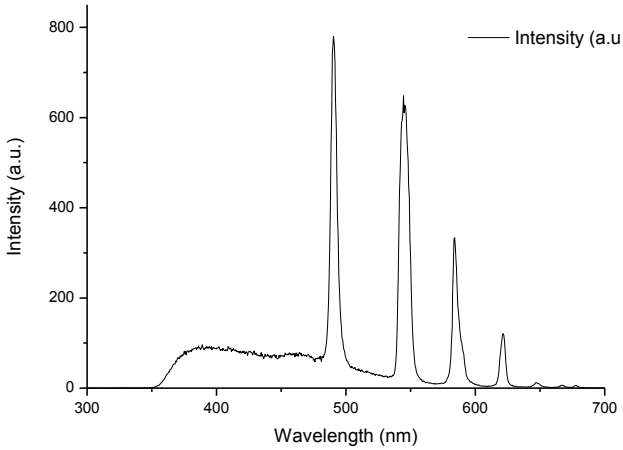

Figure C.6 Fluorescence spectrum of **Tb84$_3$** showing trailing braod emission band extending into Tb(III) luminescence range.

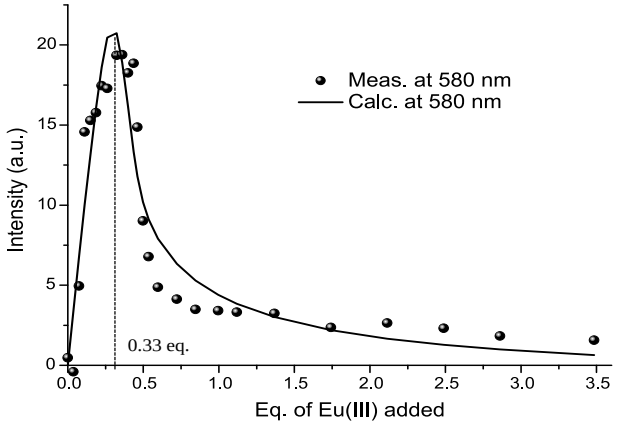

Figure C.7 Experimental binding isotherm for the Eu(III) centred emission titration of **83** (c=1x10^{-5}M) upon addition of Eu(CF_3SO_3)$_3$ 0–4 eq. in CH_3CN solution at 21 ºC at 580 nm ($^5D_0$ – $^7F_0$) and its corresponding fit.

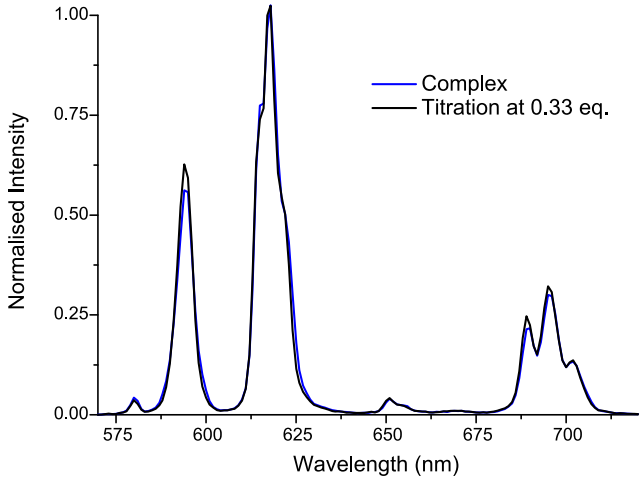

Figure C.8 Luminescence Spectra of **83** upon addition of 0.33 eq. of Eu(III) (c=1x10^{-5} M, acetonitrile, 21 ºC)) and of Eu**83**$_3$

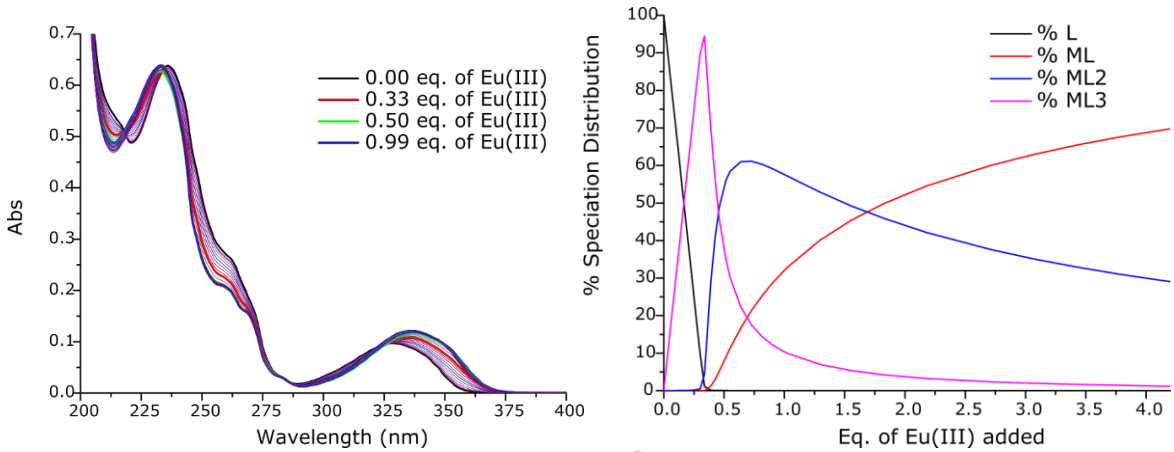

Figure C.9 (Left) UV-Vis Titration of **85** (c = 1x10^{-5} M) upon addition of Eu(CF_3SO_3)$_3$ 0–4 eq. in CH_3CN solution at 20.9 ºC. (Right) Speciation Distribution Diagram of **85** with Eu(III) calculated from UV-vis titration.

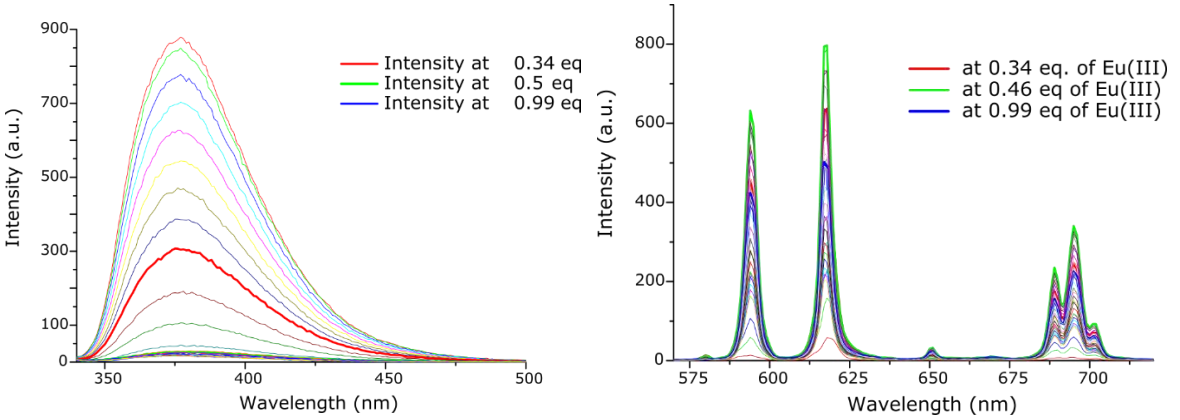

Figure C.10 Changes in (Left) ligand and (Right) Eu(III) centred luminescence spectra of **85** upon addition of $Eu(CF_3SO_3)_3$ from 0–4 eq. recorded in CH_3CN (c = 1x10^{-5} M)

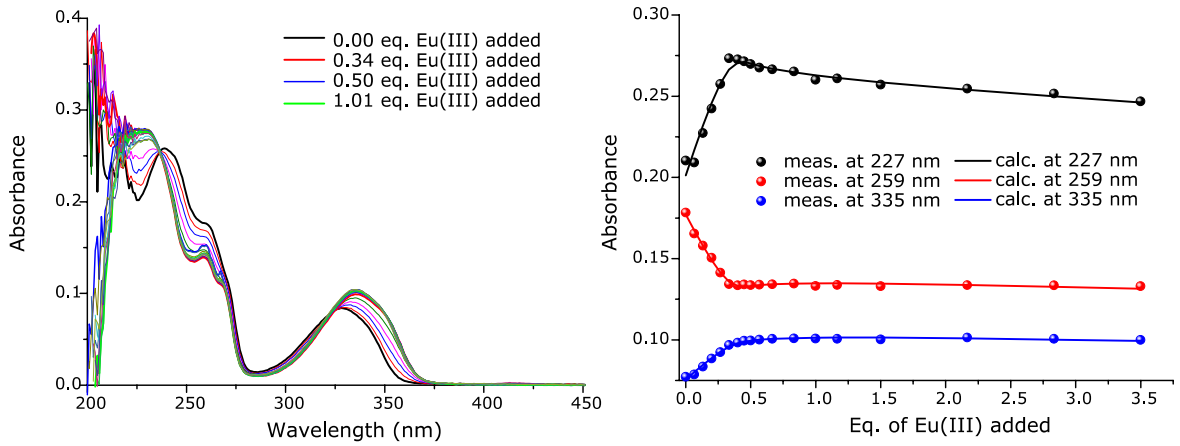

Figure C.11 (left) UV-Vis Titration of **99** (c=1x10^{-5}M) upon addition of $Eu(CF_3SO_3)_3$ 0→3 eq. in CH_2Cl_2:CH_3CN (1:9) solution at 21 ºC. (right) Experimental binding isotherm at band wavelegnths. (λ_{ex} = 325 nm).

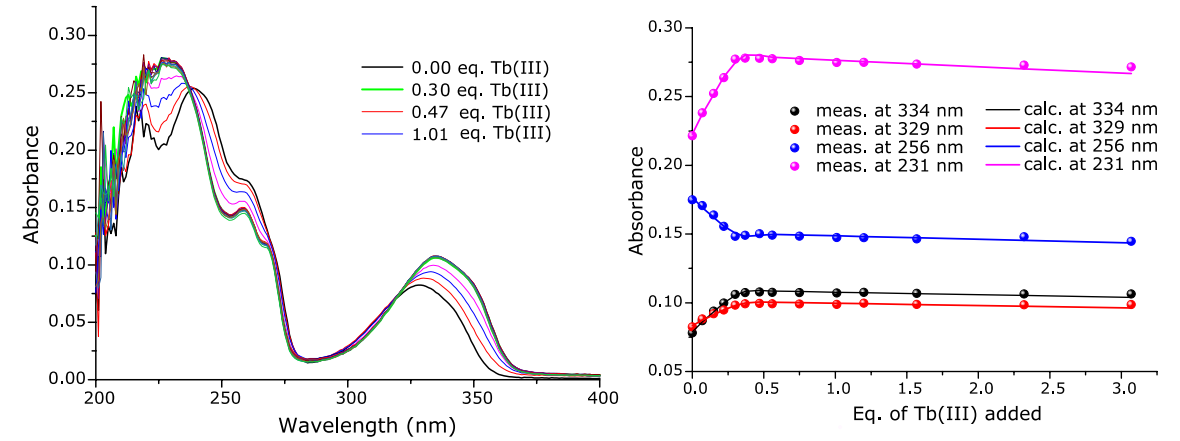

Figure C.12 UV-*Vis* Titration of **99** (c=1x10^{-5}M) upon addition of $Tb(CF_3SO_3)_3$ 0→3 eq. in CH_2Cl_2:CH_3CN (1:9) solution at 21 ºC. (right) Experimental binding isotherm at band wavelengths. (λ_{ex} = 325 nm).

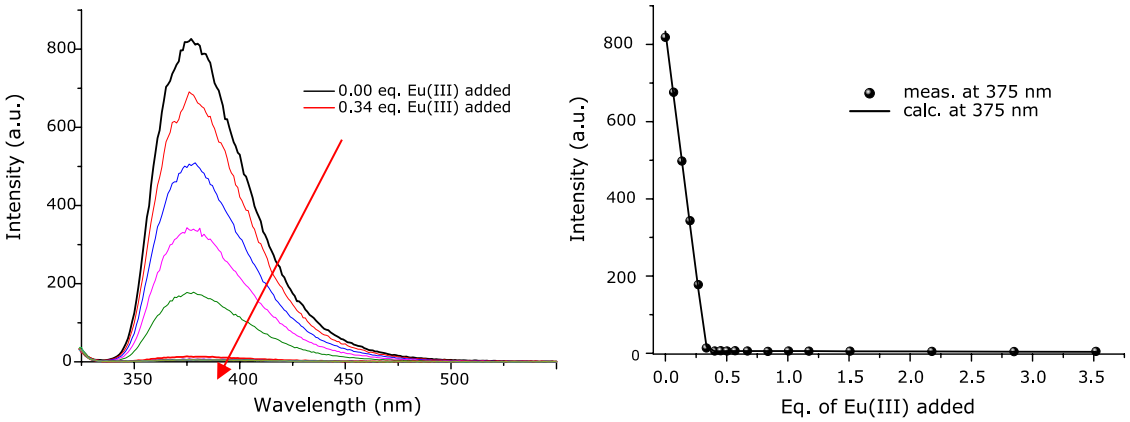

Figure C.13 (left) Fluorescence Titration of **99** (c=1x10^{-5}M) upon addition of Eu(CF_3SO_3)$_3$ 0–3 eq. in CH_2Cl_2:CH_3CN (1:9) solution at 21 ^{o}C. (right) Experimental binding isotherm at 375 nm. (λ_{ex} = 325 nm).

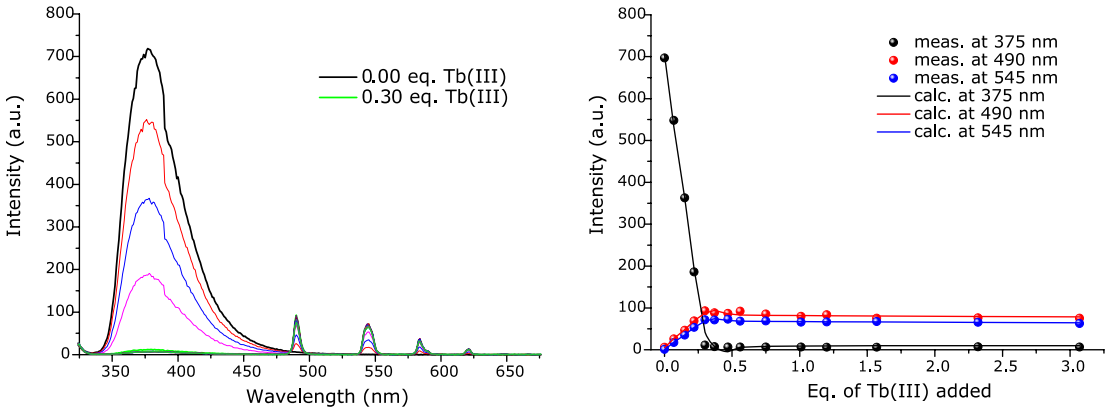

Figure C.14 (left) Fluorescence Titration of **99** (c=1x10^{-5}M) upon addition of Tb(CF_3SO_3)$_3$ 0–3 eq. in CH_2Cl_2:CH_3CN (1:9) solution at 21 ^{o}C. (right) Experimental binding isotherm at 375 nm. (λ_{ex} = 325 nm).

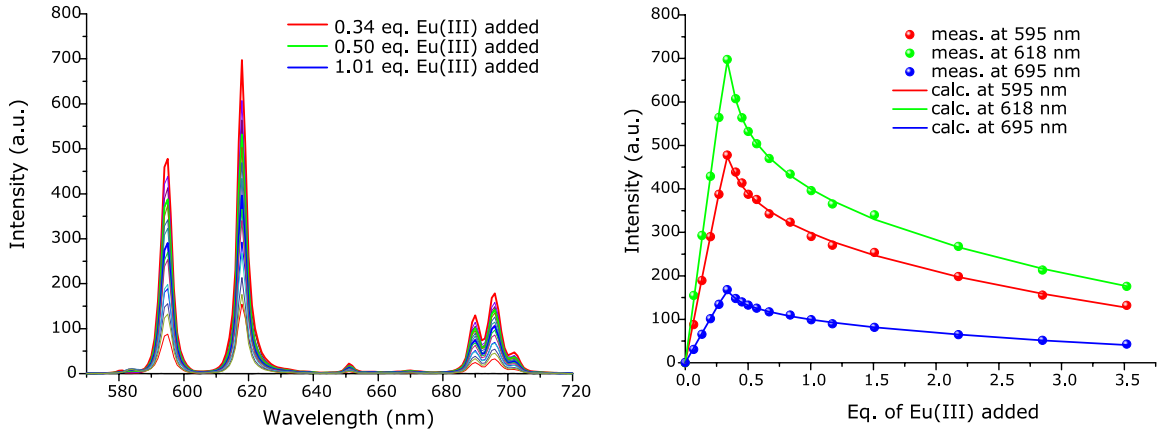

Figure C.15 (left) Changes in Eu(III) centred luminescence spectra upon titration of **99** in CH_2Cl_2:CH_3CN (1:9) (c = 1x10^{-5} M) against 0→3 eq. of Eu(CF_3SO_3)$_3$ recorded at 21 ^{o}C. (right) Experimental binding isotherms at band wavelengths. (λ_{ex} = 325 nm).

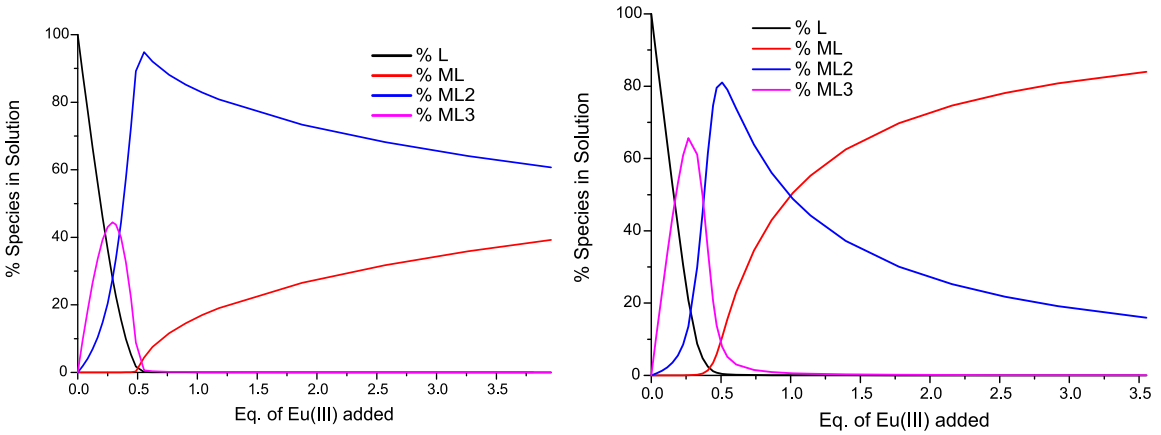

Figure C.16 Speciation Distribution of **83** from Fluorescence titration (left) Phosphorescence Titration (right)

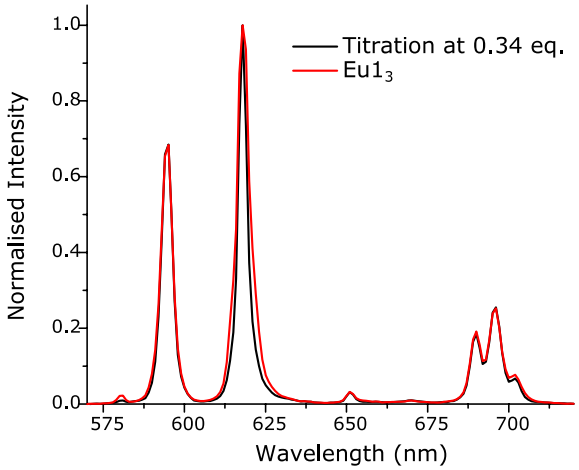

Figure C.17 Luminescence Spectra of titration of **99** with Eu(III) (c=1x10^{-5}M, CH_2Cl_2:CH_3CN (1:9) solution, 21 ^{o}C)) and **Eu99$_3$**

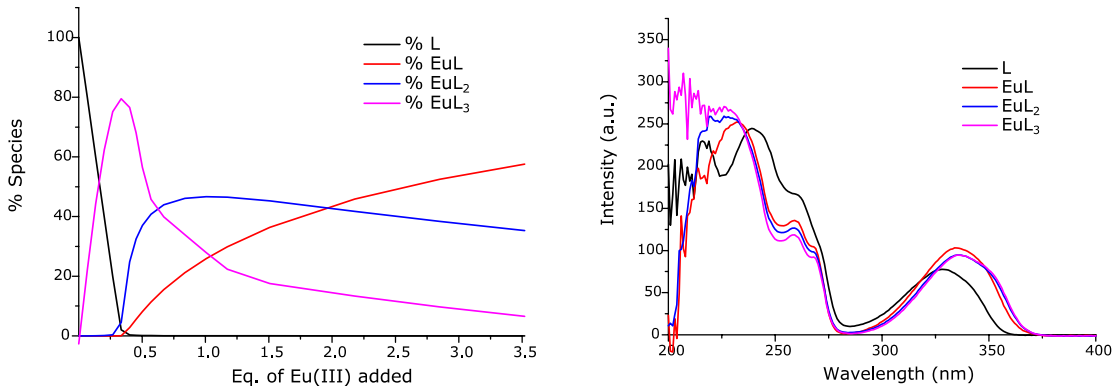

Figure C.18 (left) Speciation Distribution Diagram calculated using ReactLab from UV-Vis absorption spectral changes of **99** in CH_2Cl_2:CH_3CN (1:9) (c = 1x10^{-5} M) upon addition of Eu(CF_3SO_3)$_3$ recorded at 21 ^{o}C. (right) Calculated UV-Vis spectra of various Eu(III) equilibrium species.

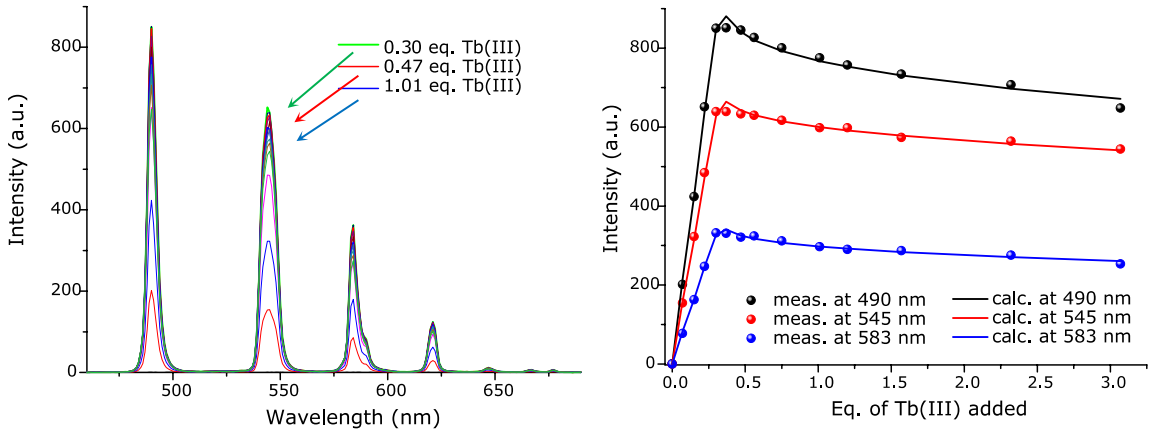

Figure C.19 (left) Changes in Tb(III) centred luminescence spectra upon titration of **99** in CH_2Cl_2:CH_3CN (1:9) (c=1x10^{-5} M) against 0 → 3 eq. of $Tb(CF_3SO_3)_3$ recorded at 21 °C. (right) Experimental binding isotherms at band wavelengths. (λ_{ex} = 325 nm).

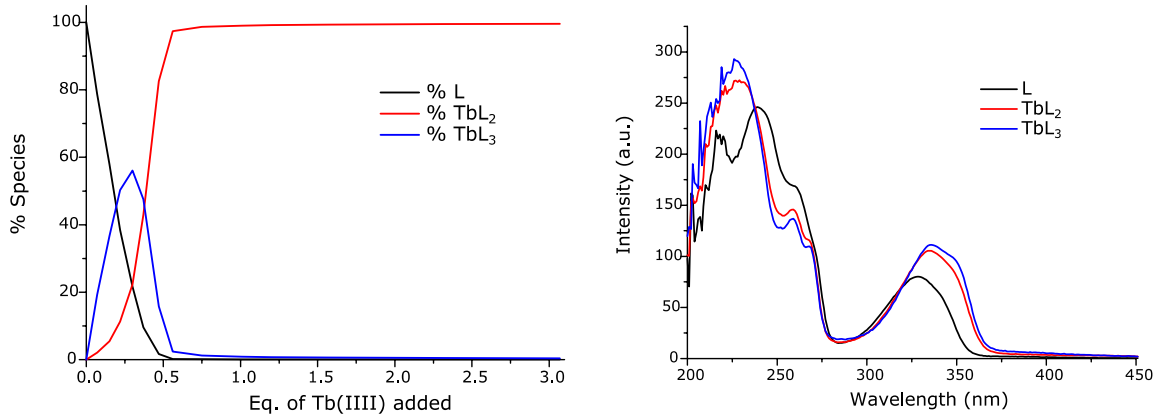

Figure C.20 (left) Speciation Distribution Diagram calculated using ReactLab from UV-Vis absorption spectral changes of **99** in CH_2Cl_2:CH_3CN (1:9) (c = 1x10^{-5} M) upon addition of $Tb(CF_3SO_3)_3$ recorded at 21 °C. (right) Calculated UV-Vis spectra of various Tb(III) equilibrium species.

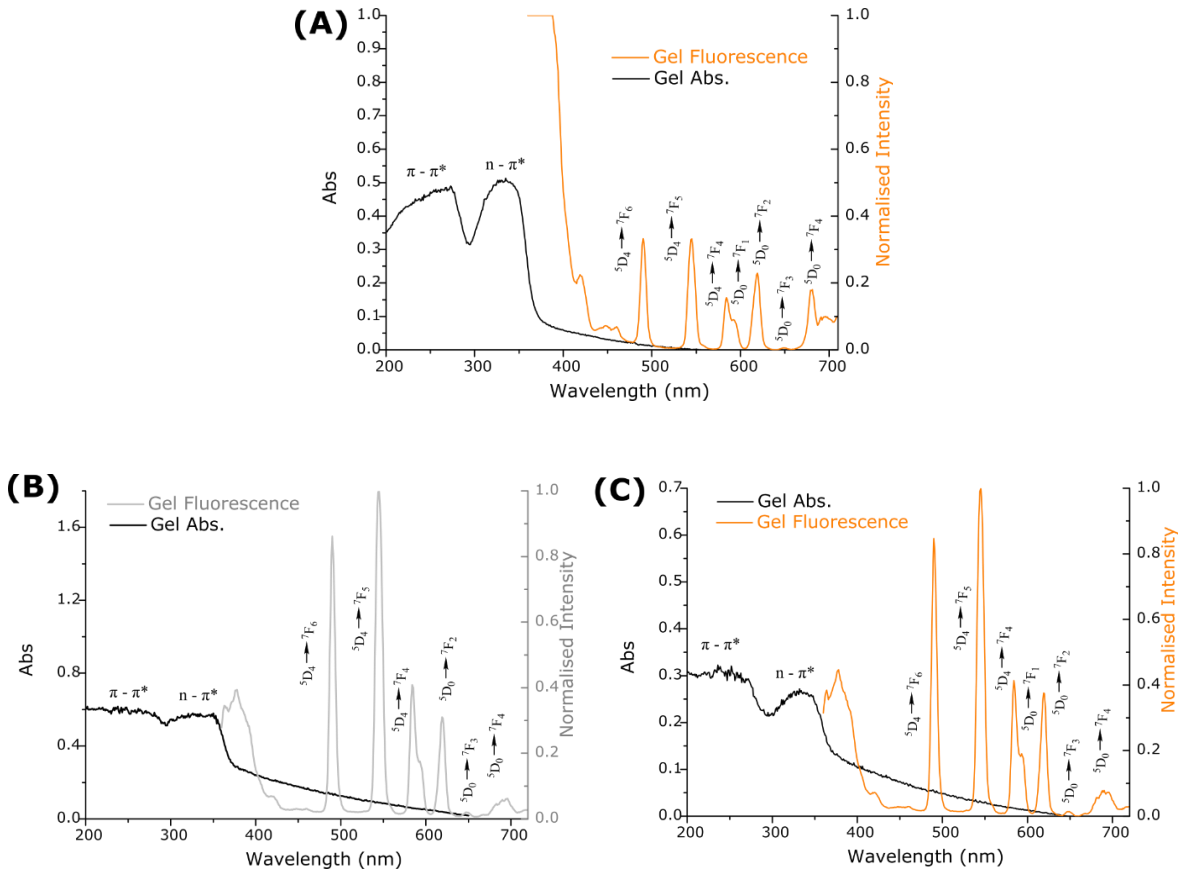

Figure C.21 UV-vis absorption and fluorescence emission spectra (λ_{ex}=326 nm) for mixed Eu(III)/Tb(III) metallogel: (A) *poly*-[**Ln_3($Eu84_3$)**] where **Ln**=**Eu**:**Tb** (1:1); (B) *poly*-[**Ln_3($Eu84_3$)**] where **Ln**=**Eu**:**Tb** (1:4); (C) *poly*-[**Ln_3($Eu84_3$)**] where **Ln**=**Eu**:**Tb** (1:2).

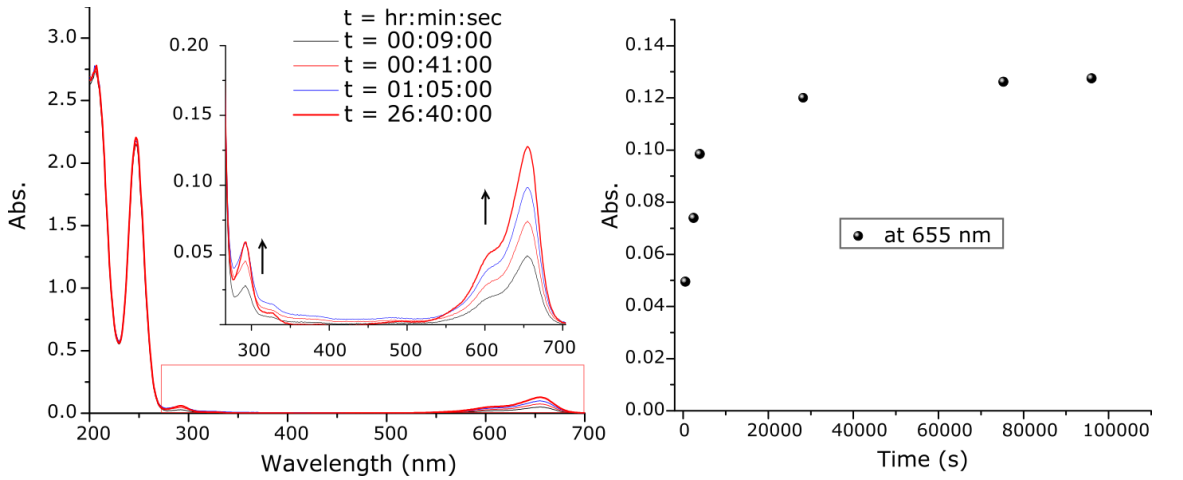

Figure C.22 Changes in UV-Vis spectrum of supernatent of **101** (6 mg) after second addition of tetraethylammonium iodide in CH_3CN (*c* = 16.4 mM, 3 mL) solution at 21°C following plateauing of methylene blue release.

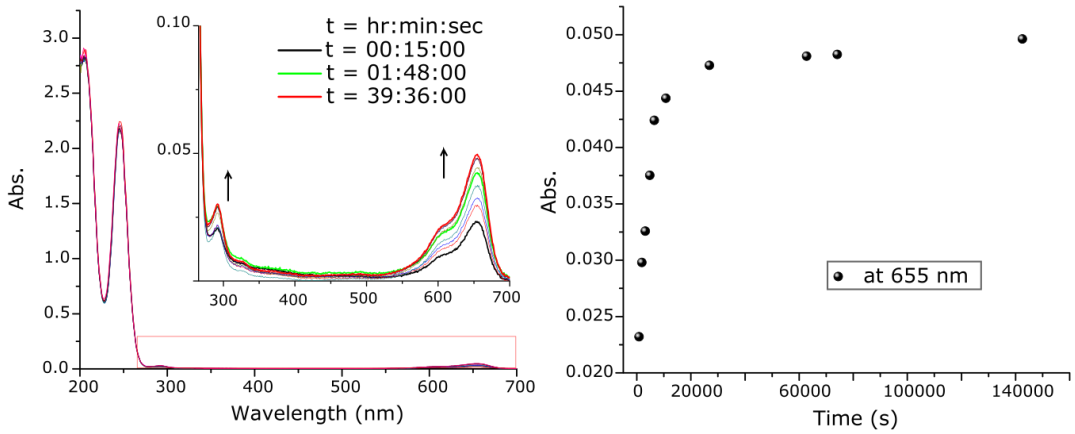

Figure C.23 Changes in UV-Vis spectrum of supernatent **101** (6 mg) after third addition of tetraethylammonium iodide in CH_3CN (c = 17.4 mM, 4 mL) solution at 21°C following plateauing of methylene blue release.

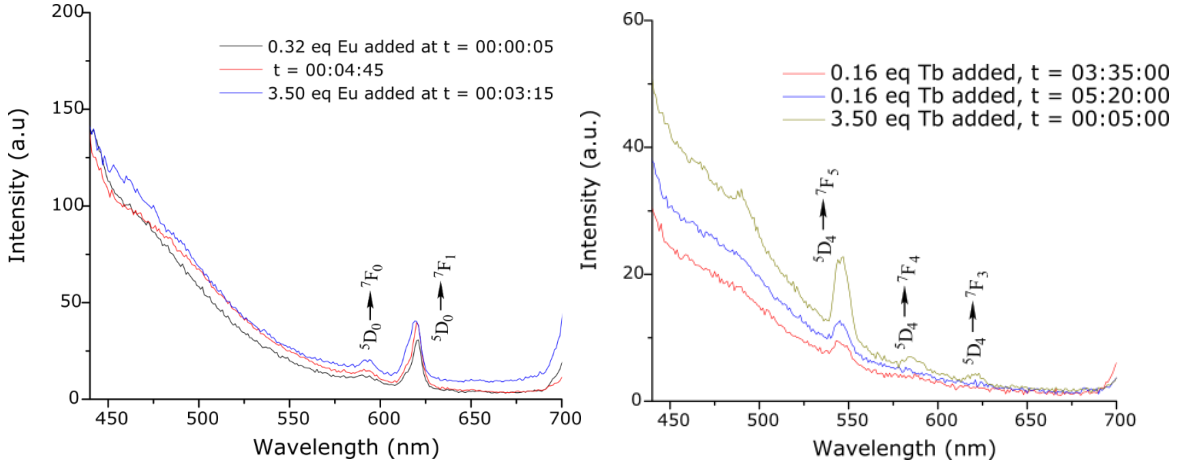

Figure C.24 Fluorescence spectrum of (Left) **101-Eu** showing dominant scattering and Eu(III) centred emission and (Right) **101-Tb** showing fluorescence band and Tb(III) centered emission.

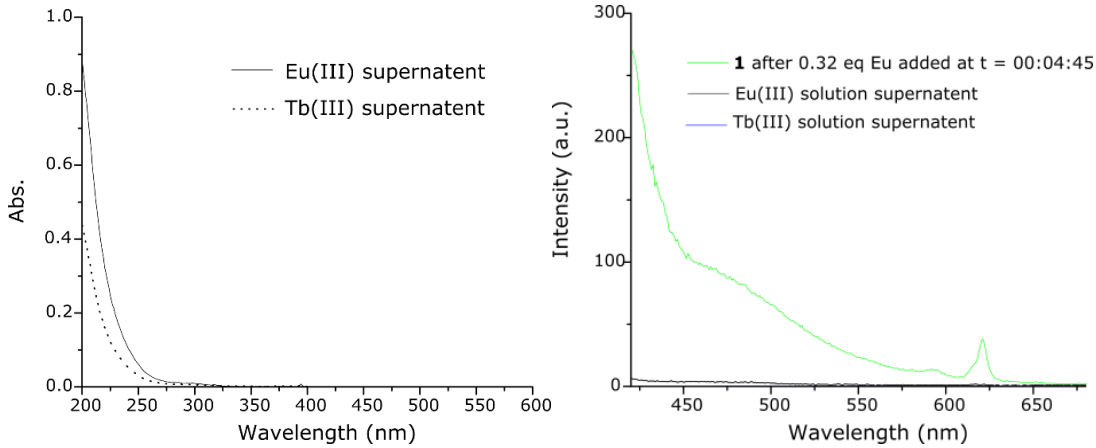

Figure C.25 (Left) UV-Vis spectrum of supernatent solutions of **101-Eu** and **101-Tb** when the crystals are not in the beam-path displaying no signs of ligand leeching during exchange. (Right) Fluorescence spectrum excited at 365 nm of the same supernatants when crystals of **101-Eu** and **101-Tb** are not in the beam-path showing no evidence of metal centred phosphorescence compared with the corresponding spectrum when crystals of **101-Eu** are in the beam-path.

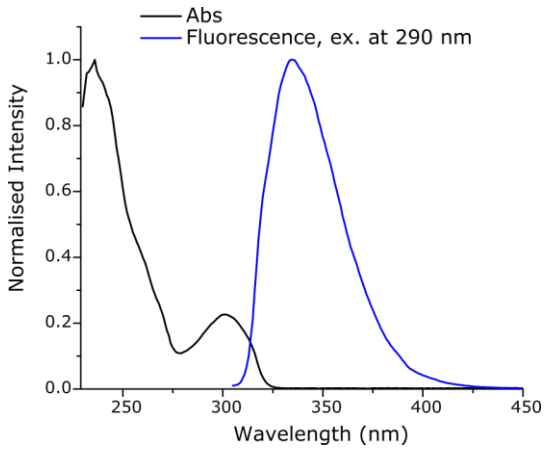

Figure C.26 Photophysical spectrum of **btp** olefin **105** measured in $CH_3CN:CHCl_3$ (4:1) at room temperature. (c = 1 x 10^{-5} M)

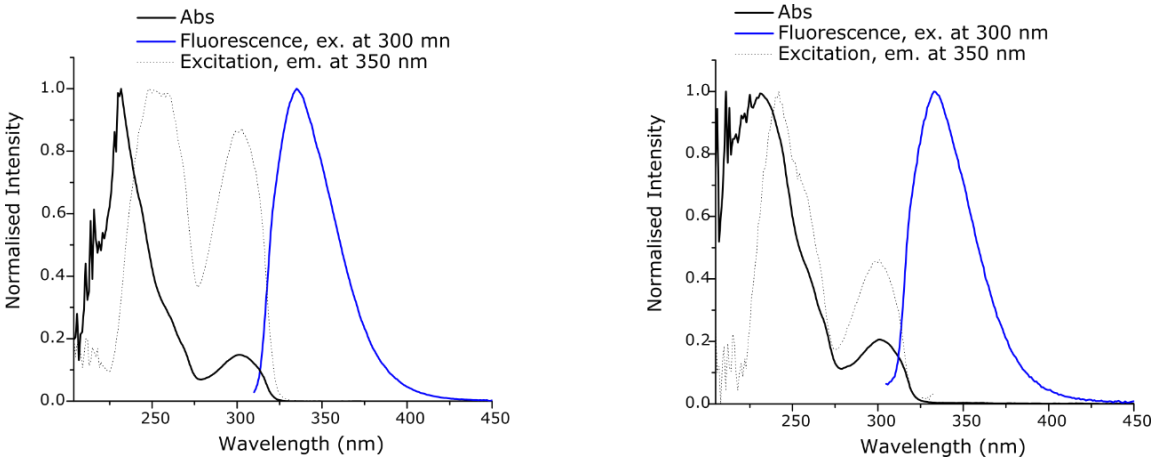

Figure C.27 Photophysical spectra of the of **btp** macrocycles **117** (left) and **118** (right) measured in $CH_3CN:CHCl_3$ (4:1)/(19:1) at room temperature. (c = 1 x 10^{-5} M)

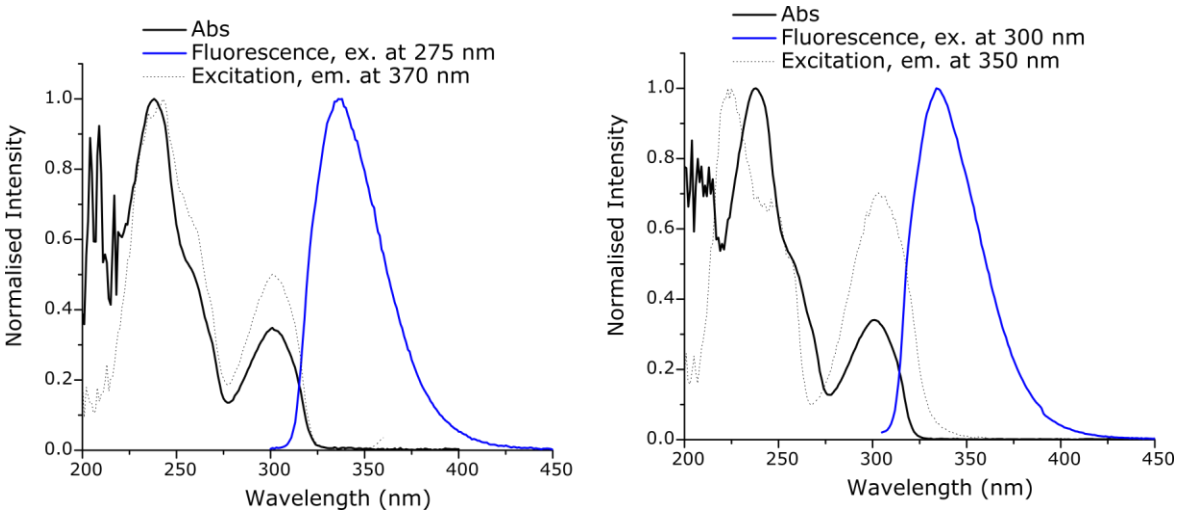

Figure C.28 Photophysical spectra of the of **btp** olefins **107** (left) and **108** (right) measured in $CH_3CN:CH_2Cl_2$ (9:1) at room temperature. (c = 1 x 10^{-5} M)

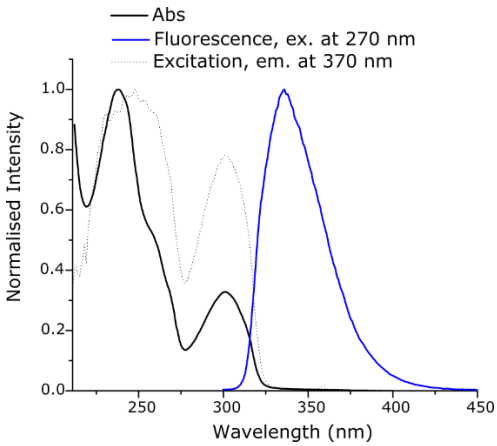

Figure C.29 Photophysical spectra of the of **btp** macrocycles **119** (left) and **120** (right) measured in CH_3CN at room temperature. (c = 1 x 10^{-5} M)

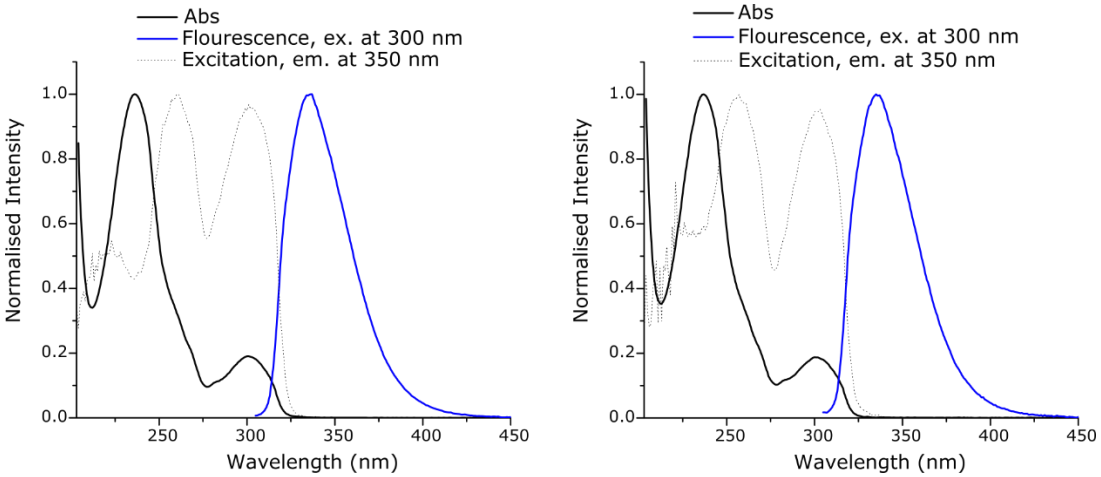

Figure C.30 Photophysical spectra of the of chiral **btp** ligands **109R** (left) and **109S** (right) measured in CH_3CN at room temperature. (c = 1 x 10^{-5} M)

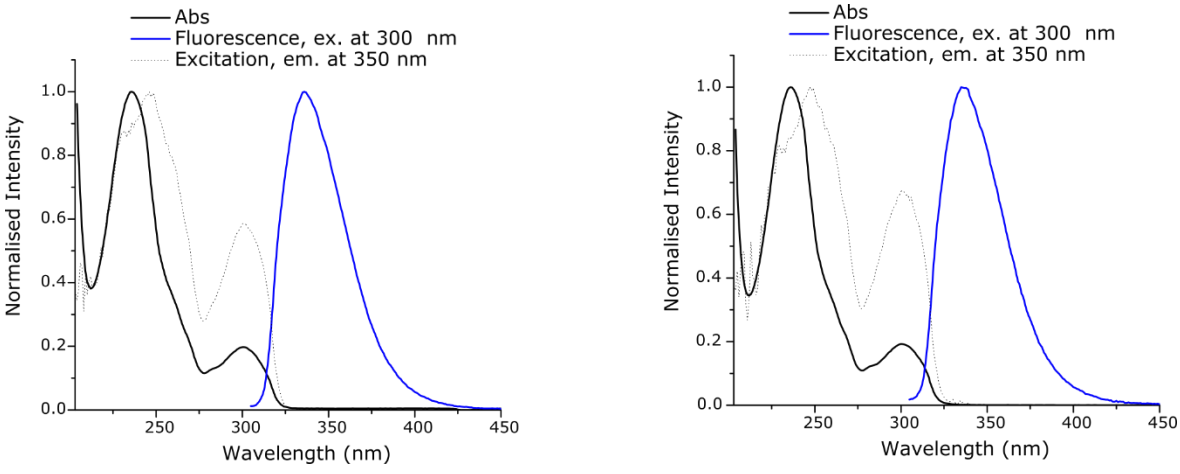

Figure C.31 Photophysical spectra of the of chiral **btp** ligands **110R** (left) and **110S** (right) measured in CH_3CN:CH_3OH (96:4) at room temperature. (c = 1 x 10^{-5} M)

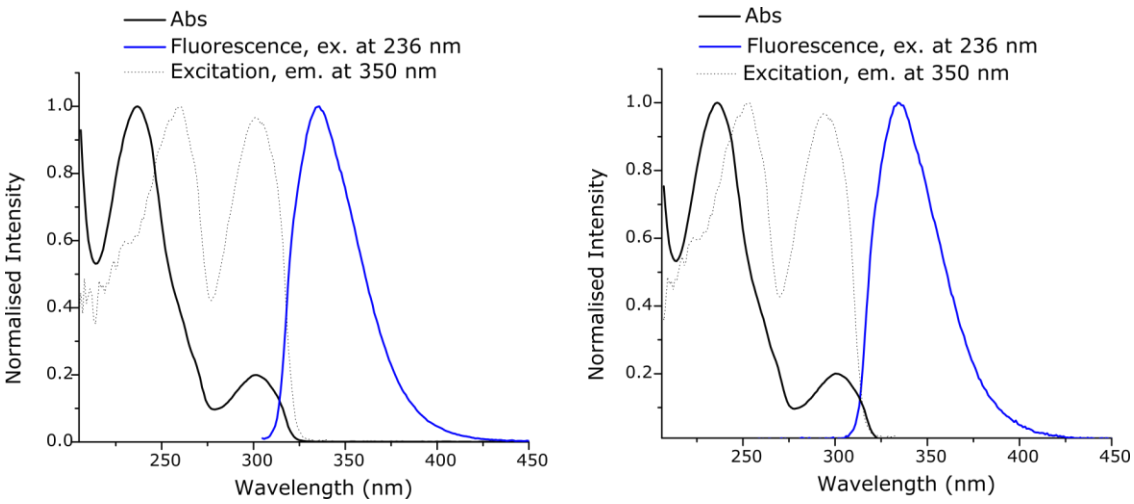

Figure C.32 Photophysical spectra of the of chiral **btp** ligands **103R** (left) and **103S** (right) measured in CH_3CN at room temperature. (c = 1 x 10^{-5} M)

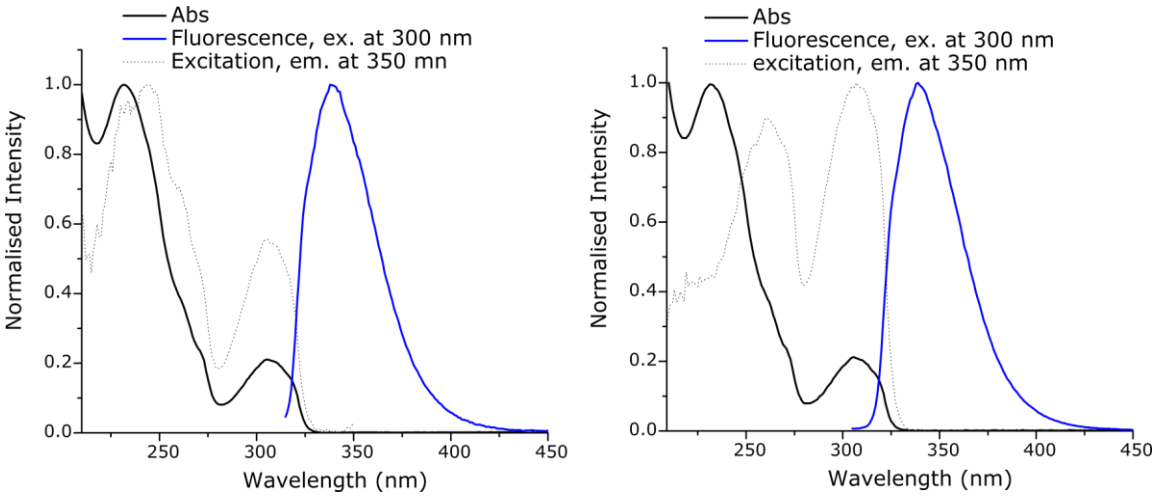

Figure C.33 Photophysical spectra of the of chiral **btp** [2]catenanes **111R** (left) and **111S** (right) measured in CH_3CN at room temperature. (c = 1 x 10^{-5} M)

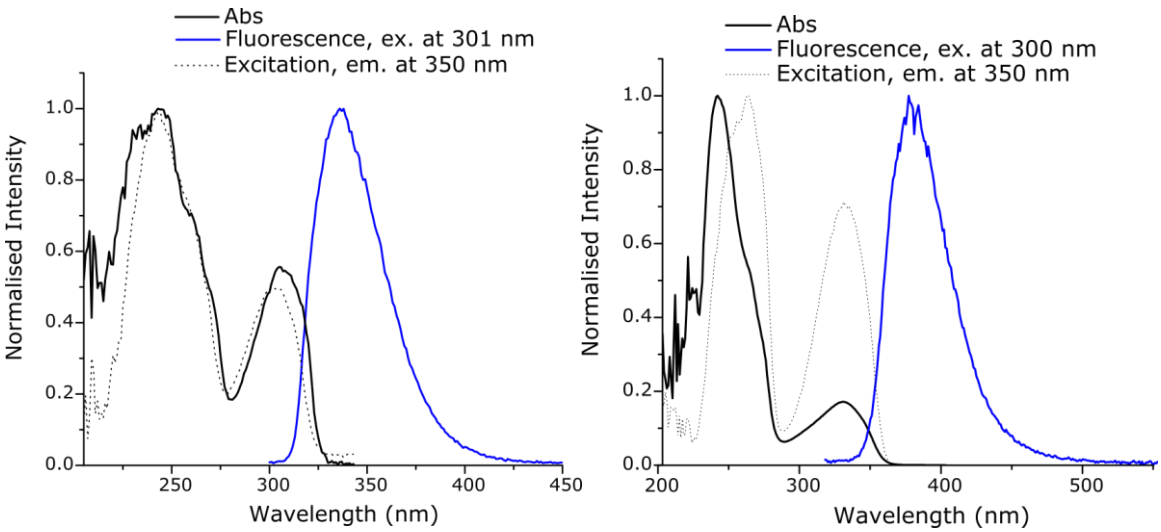

Figure C.34 Photophysical spectra of the of chiral **btp** macrocycle **112S** (left) and olefin **104** (right) measured in CH_3CN:$CHCl_3$ (19:1)/(4:1) (c = 1 x 10^{-5} M) at room temperature.

9.4 Appendix D (Thermogravimetric Analysis)

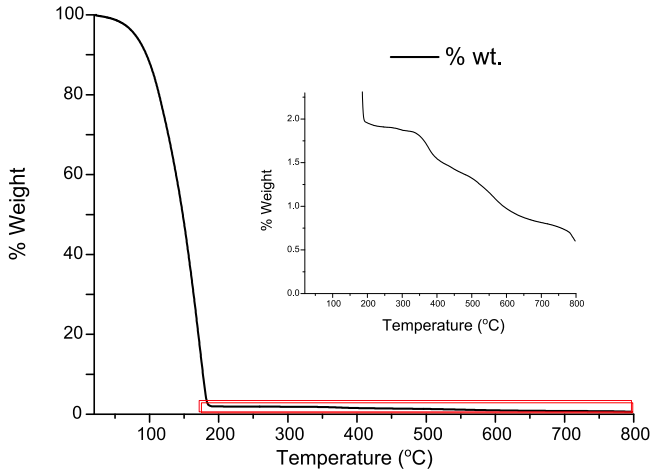

Figure D.1 Thermogravimetric Analysis of hydrogel formed from **$H_3$84** with 1.9(4) wt. %.

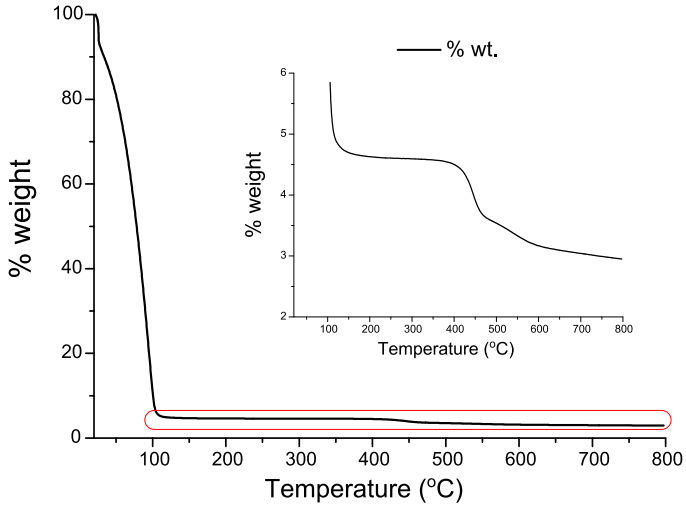

Figure D.2 Thermogravimetric Analysis of metallogel of *poly*-**[Eu$_3$(Eu84$_3$)]** with 4.8(8) wt. %.

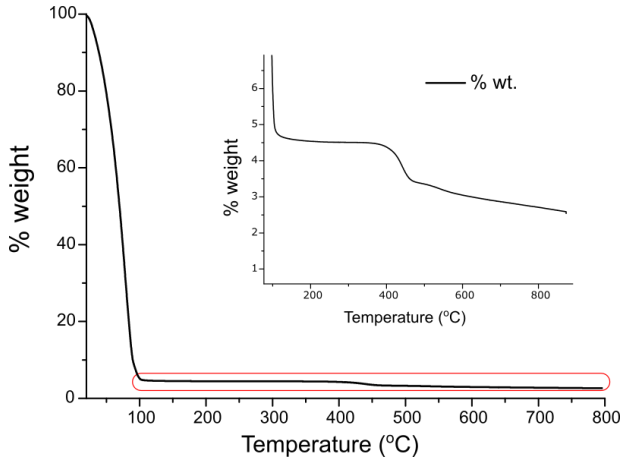

Figure D.3 Thermogravimetric Analysis of metallogel of *poly*-**[Tb$_3$(Tb84$_3$)]** with 4.5(5) wt. %.

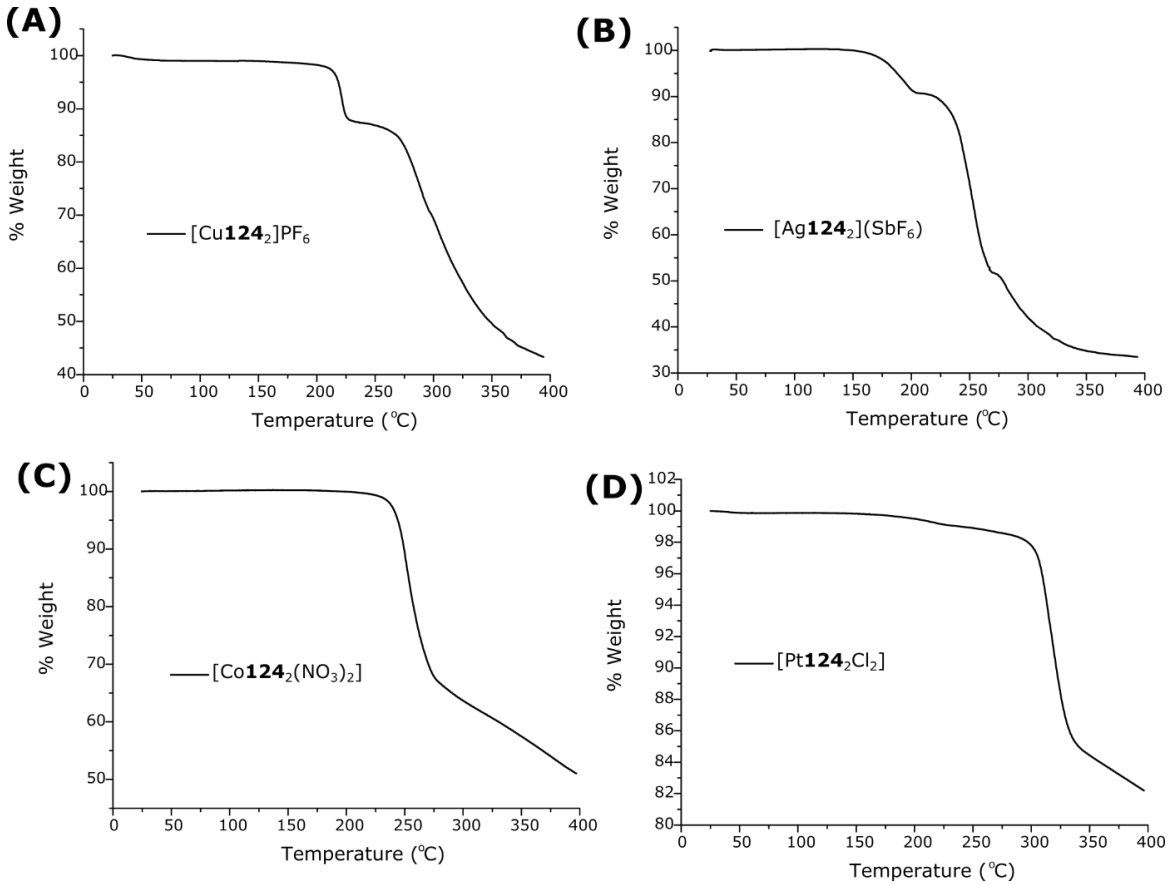

Figure D.4 Thermogravimetric Analysis for compound (A) [Cu**124**$_2$]PF_6; (B) [Ag**124**$_2$](SbF_6); (C) [Co**124**$_2$(NO_3)$_2$] and (D) [Pt**124**Cl_2].

9.5 Appendix E (Crystallography)

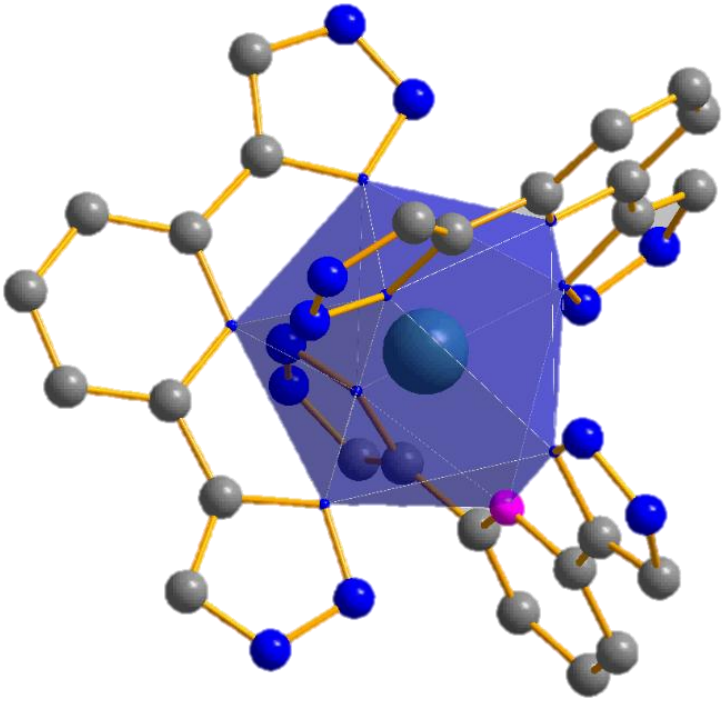

Figure E.1 Coordination polyhedron of Eu**83**$_3$ inner sphere showing distorted triaugmented trigonal prism geometry

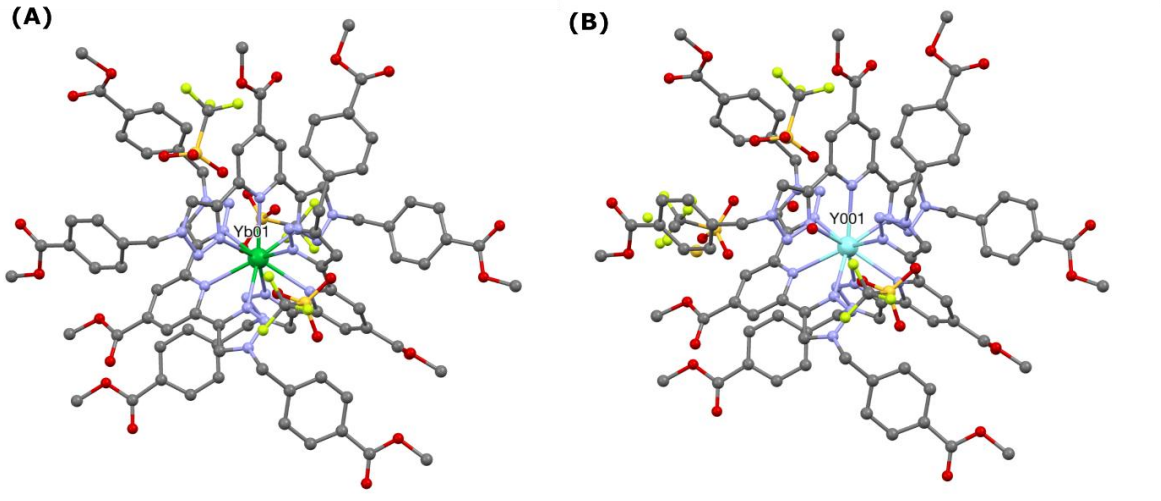

Figure E.2 Crystal structures of (A) **Yb83$_3$** and (B) **Y83$_3$** showing isostructural nature compared wiith **Eu83$_3$**.

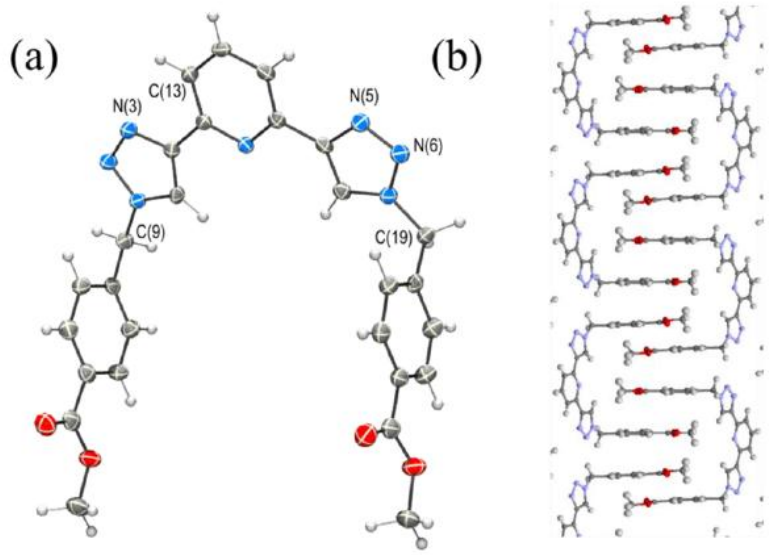

Figure E.3 (A) Molecular structure of unsubstituted **btp** ligand **17**. (B) The interdigitated packing structure viewed parallel to the *b*-axis. Thermal ellipsoids displayed at 50% probability and disordered contributor omitted for clarity

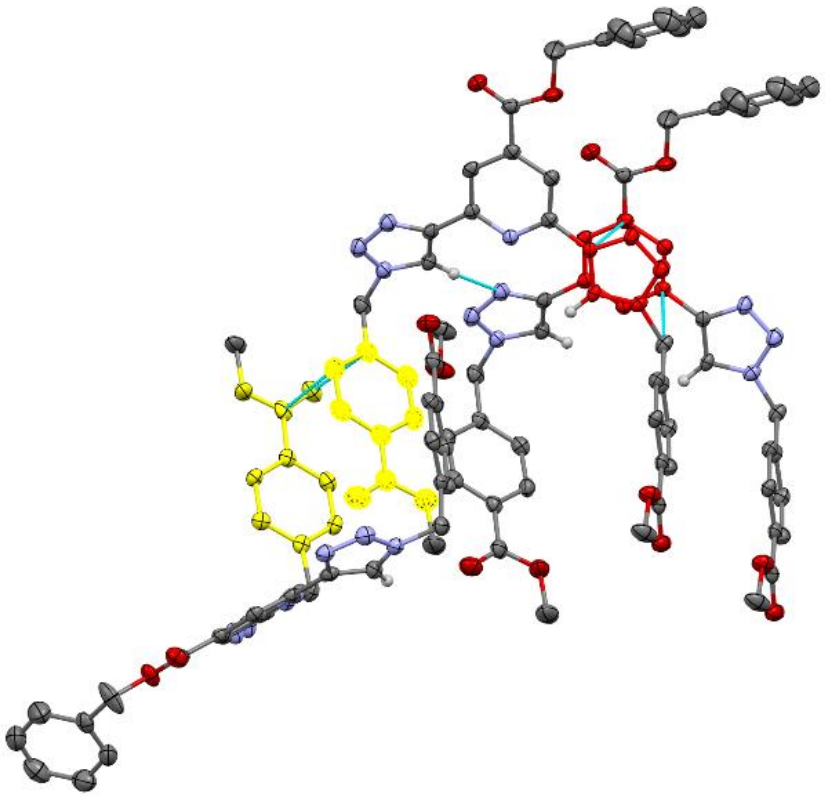

Figure E.4 π–π stacking interactions between adjacent **btp** motifs (red) and aryl "arms" (yellow) of **85** and intermolecular triazole-triazole hydrogen bonding interactions.

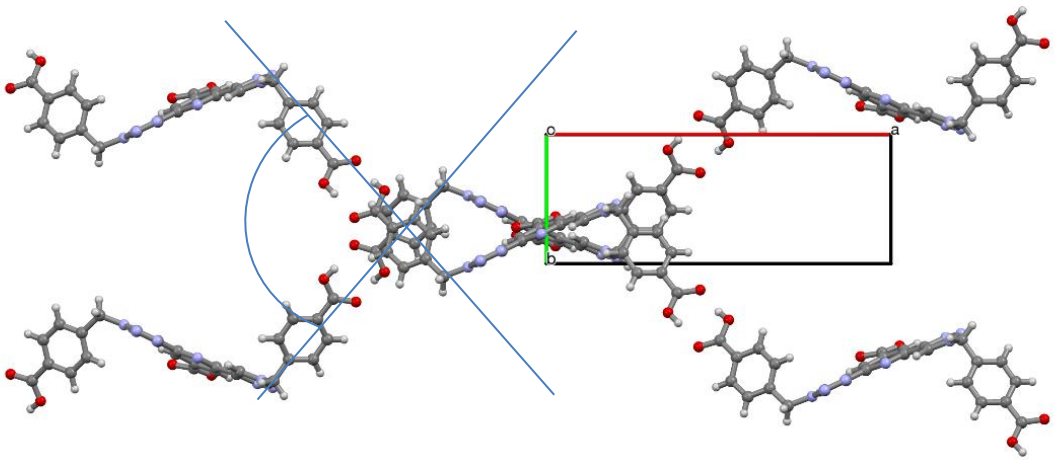

Figure E.5 Twist between AB layers in one of the interpenetrated 3-dimensional hydrogen bonded nets of the crystal structure of **H$_3$84** giving rise to the **cds** topology.

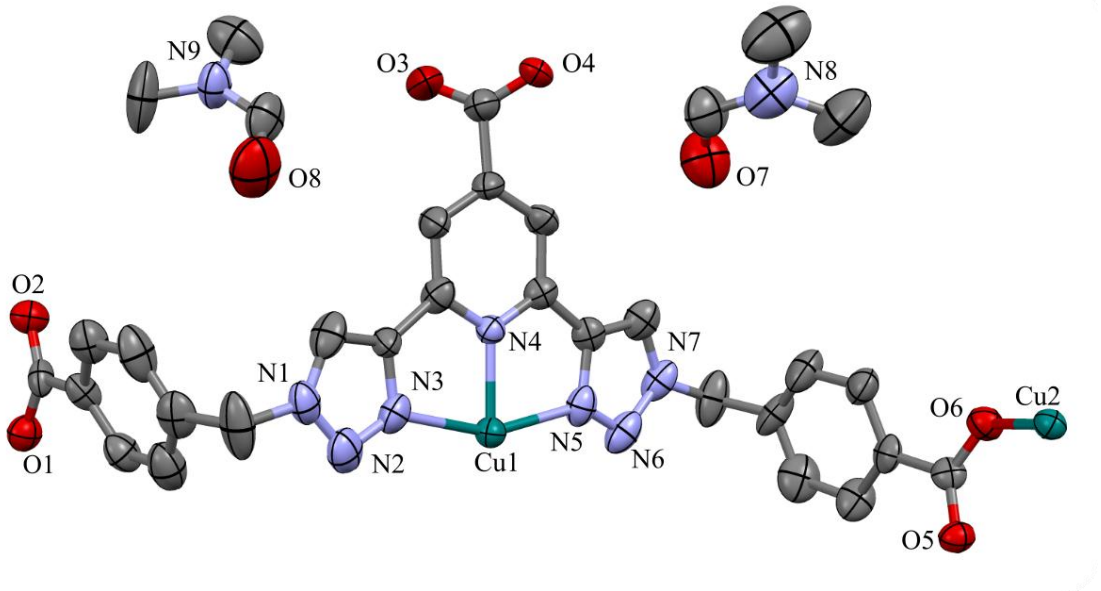

Figure E.6 X-ray crystal structure asymmetric unit of Cu(II) coordination polymer **100** including the partial occupancy lattice DMF solvent molecules. Thermal ellipsoids at 50% probability and hydrogen atoms omitted.

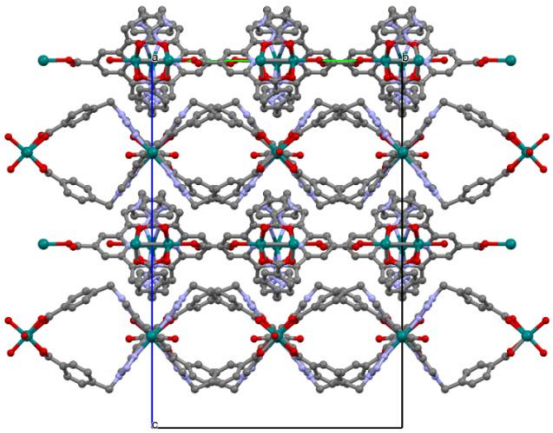

Figure E.7 Packing diagram of Cu(II) coordination polymer **100** viewed down the *b*-axis displaying the thickness of the (4,4) net.

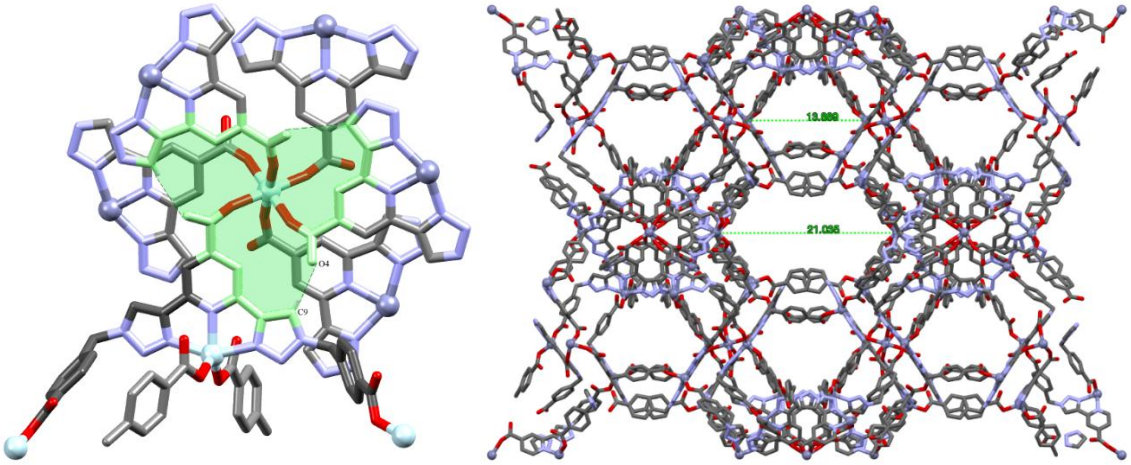

Figure E.8 (Left) Hydrogen bonding $R_3^3(24)$ motif mean plane between non-binding carboxylate oxygen atom O4 and triazolyl C9-H on adjacent **btp** moieties.(Right) Porous windows of compound **101** of alternating sizes of irregular hexagon viewed along the [1,1,0] vector. Maximum interatomic edge-to-edge displacements are displayed for comparison.

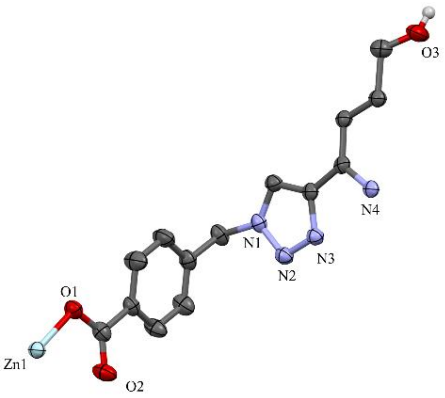

Figure E.9 Asymmetric unit of *poly*-[Zn(**H84**)]. Thermal ellipsoids at 50% probability and H atoms omitted

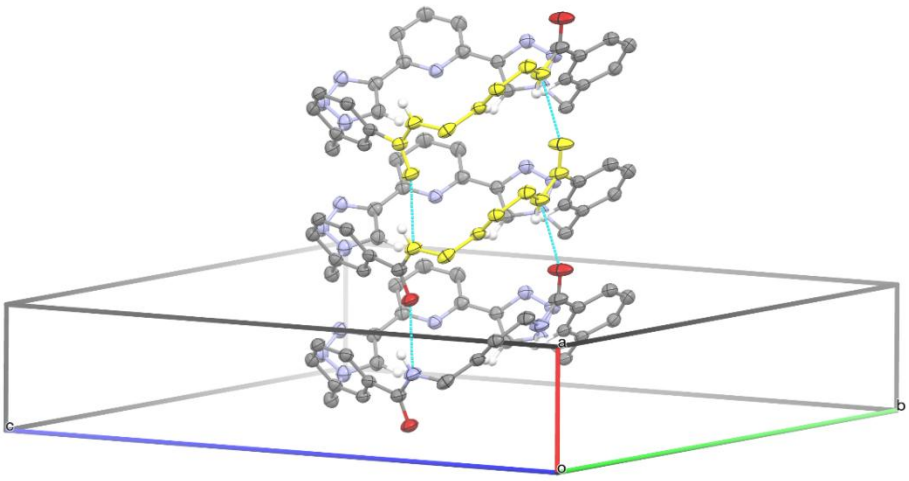

Figure E.10 The $R_2^2(16)$ hydrogen bonding motif linking adjacent molecules of **118** along the *a*-axis.

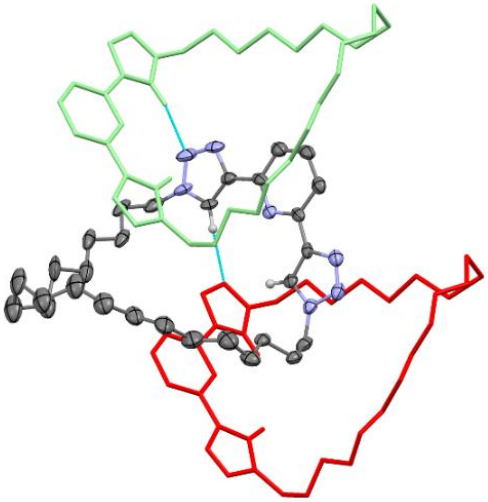

Figure E.11 Intermolecular hydrogen bonding interaction linking adjacent molecules of **119** with one donor and one acceptor from the same triazolyl unit.

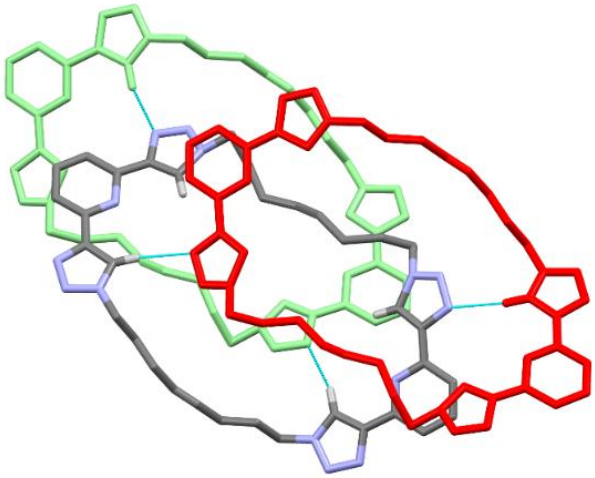

Figure E.12 Intermolecular hydrogen bonding interactions between proximal triazolyl nitrogens and triazolyl *CH*s connecting molecules of **120** with the neighbours situated above and below.

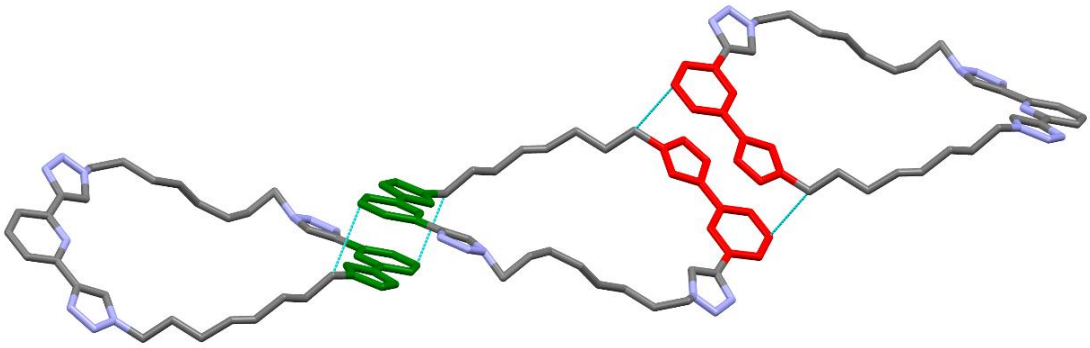

Figure E.13 π – π stacking interactions along the *a*- axis between **btp** motifs of macrocycle **120**.

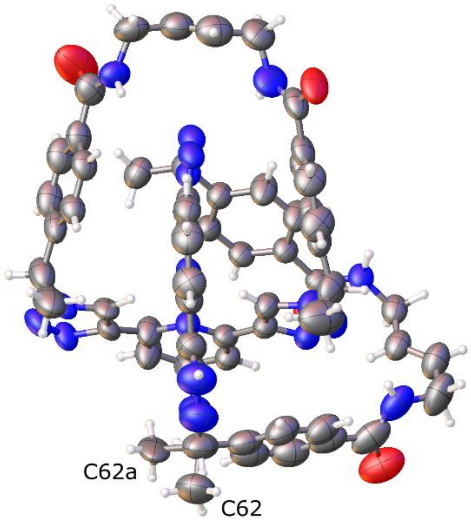

Figure E.14 Disordered contribution of chiral centre in [2]catenane **111** due to the epimerisation of **btp** precursor in *P*1.

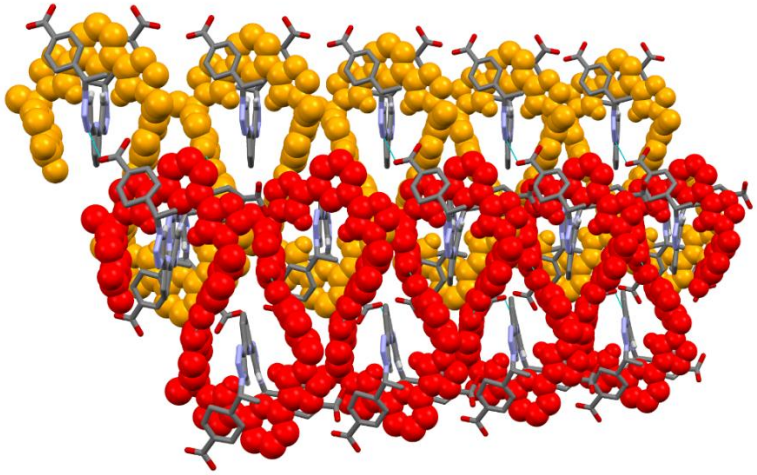

Figure E.15 Perspective view of adjacent one dimensional carboxylic acid hydrogen bonding networks in the crystal structure of **110** extending along the *c* axis in a zig-zag chain.

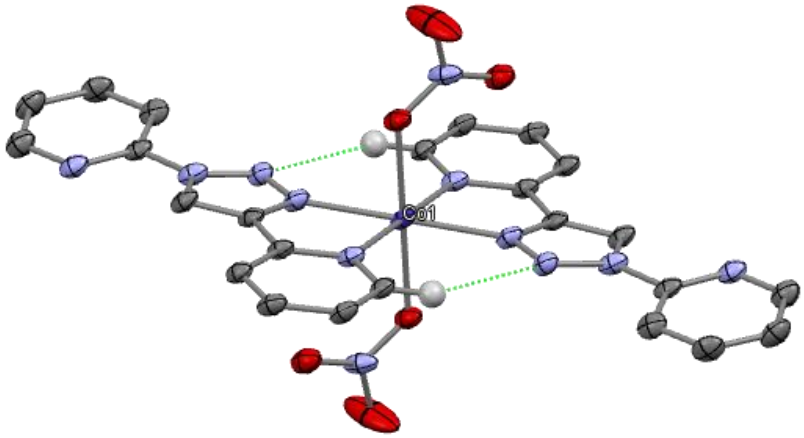

Figure E.16 Intramolecular *C*-*H*···*N* interactions in [Co**124**$_2$(NO_3)$_2$].

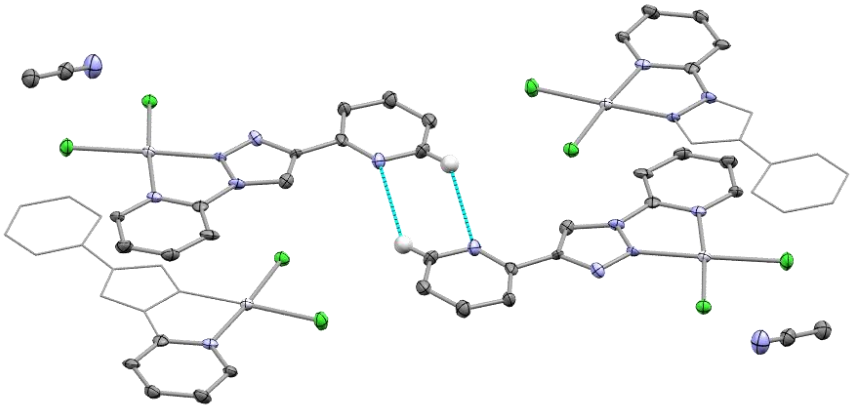

Figure E.17 Dimeric *C-H···N* interaction between two molecules of crystalline phase [Pt**124**Cl_2]·CH_3CN.

9.5.1 Powder XRD

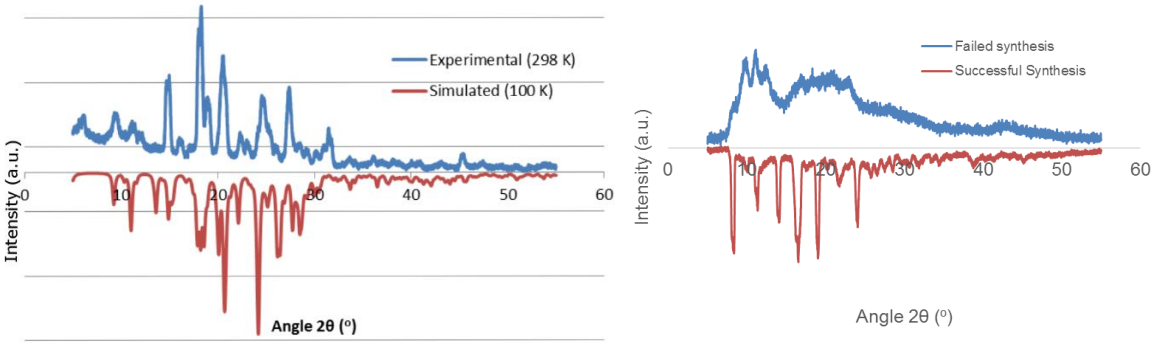

Figure E.18 X-ray powder diffraction pattern for (left) **H$_3$84** and for (right) unsuccessful synthesis of **100**.

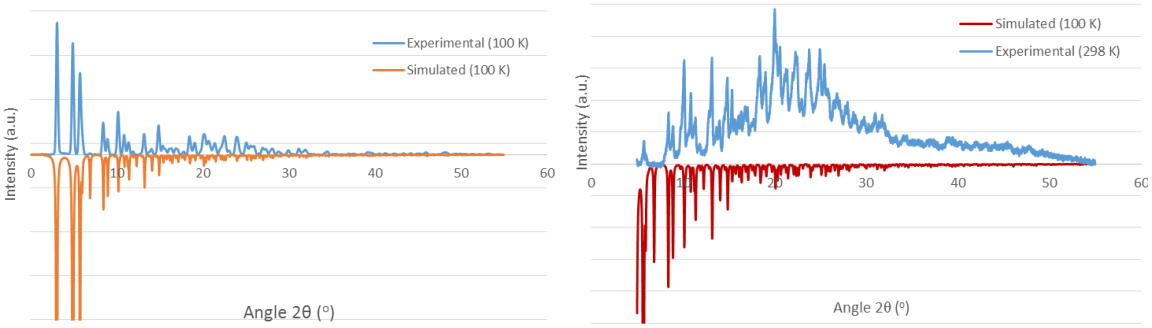

Figure E.19 X-ray powder diffraction patterns for as-synthesized **101** carried out experimentally at (left) 100 K and (right) 298 K on a on a Bruker Apex-II Duo instrument and a Bruker D2 Phaser instrument, respectively**.**

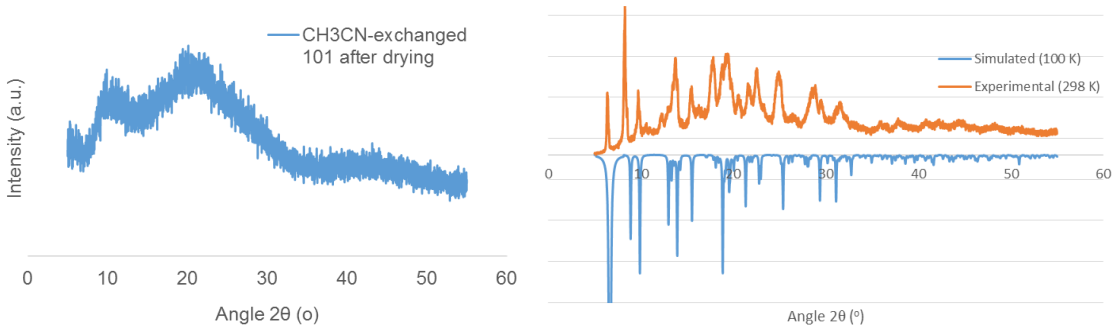

Figure E.20 X-ray powder diffraction pattern for (left) CH_3CN-exchanged **101** after drying and for (right) phase *poly*-[Zn(**H84**)].

9.5.2 Crystallographic Refinement details

Table E.1 Crystallographic refinement details for **85** and **99** from Chapter 2

Compound	**85**	**99**
Empirical formula	$C_{35}H_{29}N_7O_6$	$C_{43}H_{73}N_7O_2$
Formula weight/gmol^{-1}	643.65	720.08
Temperature/K	100(2)	100(2)
Crystal system	Monoclinic	Monoclinic
Space group	$P2_1$	$P2_1/c$
a/Å	15.1835(10)	7.6710(4)
b/Å	5.5085(4)	62.454(4)
c/Å	18.5555(13)	9.2328(5)
α/°	90	90
β/°	102.307(2)	104.752(3)
γ/°	90	90
Volume/Å^3	1516.29(18)	4277.5(4)
Z	2	4
ρ_{calc}/g cm^{-3}	1.410	1.118
μ/mm^{-1}	0.099	0.536
F(000)	672.0	1584.0
Radiation source	Mo Kα	Cu Kα
2θ range/°	3.156 to 50.716	5.66 to 136.656
Reflns. collected	5505	26264
Independent reflns.	5424 [R_{int} = 0.0236, R_{sigma} = 0.0740]	7744 [R_{int} = 0.0438, R_{sigma} = 0.0549]
Reflns. Obs. *[I≥2σ (I)]*		
Data/restraints/parameters	5424/115/471	7744/0/472
GOOF on F^2	0.984	1.111
R indices [*I≥2σ (I)*]	R_1 = 0.0501, wR_2 = 0.0926	R_1 = 0.0644, wR_2 = 0.1678
R indices [all data]	R_1 = 0.0934, wR_2 = 0.1083	R_1 = 0.0779, wR_2 = 0.1765
Largest diff. peak/hole / e Å^{-3}	0.20/-0.19	0.23/-0.26
Flack parameter	0.3(1)	-

Table E.2 Crystallographic refinement details for isostructural *tris*-complexes derived from **83** from Chapter 3.

.

Compound	**Eu83$_3$**	Y**83**$_3$	**Yb83$_3$**
Formula weight	2393.71	2274.83	886.68
Temperature/K	100.0(2)	100.0(2)	100.0(2)
Crystal system	Triclinic	Triclinic	Triclinic
Space group	$P\bar{1}$	$P\bar{1}$	$P\bar{1}$
a/Å	15.6080(9)	15.5438(7)	15.5296(5)
b/Å	15.7058(9)	15.6711(7)	15.6709(5)
c/Å	22.7440(13)	21.8931(10)	21.9687(7)
α/°	88.9700(10)	75.7480(10)	76.2840(10)
β/°	80.5030(10)	87.8710(10)	88.0520(10)
γ/°	77.2110(10)	77.7710(10)	77.3990(10)
Volume/Å^3	5361.5(5)	5050.9(4)	5067.9(3)
Z	2	2	2
ρ_{calc}/ gcm^{-3}	1.483	1.496	1.743
μ/mm^{-1}	0.743	0.744	3.032
F(000)	2438.0	2332.0	2610.0
Radiation	Mo*Kα*	MoKα	MoKα (λ = 0.71073)
2θ range/°	2.66 to 52.044	1.92 to 51.00	1.908 to 52.822
Reflns collected	118699	115427	57379
Independent reflns	21057 [R_{int} = 0.0519, R_{sigma} = 0.0393]	18808 [R_{int} = 0.0849, R_{sigma} = 0.0639]	20766 [R_{int} = 0.0537, R_{sigma} = 0.0747]
Data/restraints/parameters	21057/78/1462	18808/111/1447	20766/0/1393
GOOF on F^2	1.064	1.037	1.023
R indeces [$I \geq 2\sigma(I)$]	R_1 = 0.0637, wR_2 = 0.1697	R_1 = 0.0647, wR_2 = 0.1546	R_1 = 0.0516, wR_2 = 0.1173
R indeces [all data]	R_1 = 0.0828, wR_2 = 0.1855	R_1 = 0.1037, wR_2 = 0.1740	R_1 = 0.0779, wR_2 = 0.1290
Largest diff. peak/hole / e Å^{-3}	2.68/-1.14	1.90/-0.88	2.69/-1.62

Table E.3 Crystallographic refinement details for **$H_3$84** and coordination polymers from Chapter 4.

Compound	**$H_3$84**	*poly*-[**$Na_3$84**·$(H_2O)_2$]	**100**	*poly*-**Zn(H84)**	**101**
Empirical formula	$C_{26}H_{19}N_7O_6$	$C_{26}H_{20}N_7Na_3O_8$	$[Cu_3\mathbf{84}_2]\cdot(DMF)_{3.3}$	$C_{26}H_{17}N_7O_6Zn$	$[Zn_7\mathbf{84}_6]\cdot(C_2H_8N)_4\cdot(H_2O)_{45}$
Formula weight/gmol^{-1}	525.48	627.46	1476.75	588.83	3592.33
Temperature/K	100(2)	100(2)	120(2)	100(2)	100(2)
Crystal system	Monoclinic	Monoclinic	Tetragonal	Monoclinic	Cubic
Space group	$P2_1/c$	$C2/c$	$I4_1cd$	$C2/c$	$Fd\bar{3}$
a/Å	20.486(4)	27.8377(11)	20.977(19)	21.9888(15)	51.459(2)
b/Å	7.1760(14)	9.6099(4)	20.977(19)	17.8548(13)	51.459(2)
c/Å	17.144(3)	10.4222(4)	30.79(3)	10.4152(7)	51.459(2)
α/°	90	90	90	90	90
β/°	111.00(3)	102.7868(15)	90	115.420(5)	90
γ/°	90	90	90	90	90
Volume/Å^3	2352.9(9)	2718.98(19)	13549(28)	3693.2(5)	136266(13)
Z	4	4	8	4	96
ρ_{calc}/g cm^{-3}	1.483	1.533	1.448	1.059	0.701
μ/mm^{-1}	0.109	1.385	1.011	1.264	0.897
F(000)	1088.0	1288.0	6056.0	1200.0	29184.0
Radiation source	Mo Kα	Cu Kα	Mo Kα	Cu Kα	Cu Kα
2θ range/°	4.76 to 49.99	6.512 to 136.694	2.35 to 52.74	6.66 to 136.59	4.86 to 137.36
Reflns. collected	22769	25903	45256	5913	96596
Independent reflns.	4142 [R_{int} = 0.0949, R_{sigma} = 0.0751]	2502 [R_{int} = 0.0333, R_{sigma} = 0.0144]	6932 [R_{int} = 0.1160, R_{sigma} = 0.0741]	3383 [R_{int} = 0.0669, R_{sigma} = 0.0732]	10479 [R_{int} = 0.1232, R_{sigma} = 0.0561]
Reflns. Obs. *[I≥2σ (I)]*	2915		3715	2506	5097
Data/restraints/parameters	4142/0/352	2502/0/209	6932/13/459	3383/0/187	10479/0/363
GOOF on F^2	1.130	1.074	1.015	1.006	1.005
R indices [*I≥2σ (I)*]	R_1 = 0.0741, wR_2 = 0.1393	R_1 = 0.0318, wR_2 = 0.0901	R_1 = 0.0629, wR_2 = 0.1479	R_1 = 0.0529, wR_2 = 0.1369	R_1 = 0.1087, wR_2 = 0.2949
R indices [all data]	R_1 = 0.1136, wR_2 = 0.1548	R_1 = 0.0336, wR_2 = 0.0919	R_1 = 0.1392, wR_2 = 0.1853	R_1 = 0.0720, wR_2 = 0.1470	R_1 = 0.1435, wR_2 = 0.3343
Largest diff. peak/hole / e Å^{-3}	0.25/-0.30	0.31/-0.20	0.62/-0.28	0.48/-0.44	0.56/-0.74

Table E.4 Crystallographic refinement details for compounds from Chapter 5.

Compound	**111**	**110**	**106**	**118·(EtOAc)$_{0.25}$**	**119**	**120**
Empirical formula	$C_{31}H_{29}N_9O_2$	$C_{27}H_{23}N_7O_4$	$C_{32}H_{33}N_9O_3$	$C_{30}H_{27}N_9O_{2.5}$	$C_{29}H_{43}N_7$	$C_{34}H_{38}N_{14}$
Temperature/K	100(2)	100(2)	100(2)	100(2)	100(2)	100(2)
Crystal system	Triclinic	Monoclinic	Monoclinic	Monoclinic	Monoclinic	Monoclinic
Space group	$P\bar{1}$	$C2/c$	$P2_1$	$P2_1/n$	$P2_1/c$	$C2/c$
a/Å	12.8677(5)	55.622(3)	4.5953(3)	4.8236(2)	17.559(2)	24.878(4)
b/Å	12.9157(4)	19.1919(9)	22.3253(11)	23.2321(13)	16.2368(18)	12.691(2)
c/Å	20.0012(6)	20.6749(8)	14.0938(9)	25.2997(15)	10.1778(12)	10.7991(19)
α/°	77.618(2)	90	90	90	90	90
β/°	87.237(2)	105.555(4)	92.820(3)	90.640(4)	101.744(7)	104.388(3)
γ/°	81.157(2)	90	90	90	90	90
Volume/Å^3	3207.79(19)	21262.0(18)	1444.15(15)	2835.0(3)	2841.0(6)	3302.6(10)
Z	4	32	2	4	4	4
ρ_{calc}/g cm^{-3}	1.159	1.401	1.361	1.313	1.145	1.127
μ/mm^{-1}	0.620	0.990	0.743	0.929	0.542	0.092
F(000)	1176.0	9280.0	624.0	1160.0	1064.0	1160.0
Radiation source	Cu Kα	Cu Kα	Cu Kα	Cu Kα	Cu Kα	Mo Kα
2θ range/°	4.524 to 137.324	4.89 to 136	6.278 to 101.136	6.988 to 137.206	7.488 to 136.762	3.38 to 50.778
Reflns. collected	56420	170325	6613	29265	14372	15994
Independent reflns.	11736 [R_{int} = 0.0848, R_{sigma} = 0.0499]	19354 [R_{int} = 0.1693, R_{sigma} = 0.0992]	2938 [R_{int} = 0.0385, R_{sigma} = 0.0473]	5192 [R_{int} = 0.0836, R_{sigma} = 0.0655]	5003 [R_{int} = 0.0540, R_{sigma} = 0.0724]	3031 [R_{int} = 0.0385, R_{sigma} = 0.0358]
Data/restraints/parameters	11736/0/816	19354/26/563	2938/1/399	5192/0/417	5003/238/505	3031/30/223
GOOF on F^2	1.043	3.238	1.072	1.741	1.012	1.923
R indices [$I \geq 2\sigma(I)$]	R_1 = 0.0886, wR_2 = 0.2625	R_1 = 0.3629, wR_2 = 0.6628	R_1 = 0.0443, wR_2 = 0.1140	R_1 = 0.0925, wR_2 = 0.2520	R_1 = 0.0868, wR_2 = 0.2420	R_1 = 0.1896, wR_2 = 0.4871
R indices [all data]	R_1 = 0.1201, wR_2 = 0.3033	R_1 = 0.4776, wR_2 = 0.7109	R_1 = 0.0483, wR_2 = 0.1167	R_1 = 0.1076, wR_2 = 0.2610	R_1 = 0.1926, wR_2 = 0.3214	R_1 = 0.2593, wR_2 = 0.5328
Largest diff. peak/hole / e Å^{-3}	0.67/-0.31	2.42/-0.70	0.17/-0.20	1.32/-0.29	0.17/-0.17	0.83/-0.4
Flack Parameter	-	-	0.0(3)	-	-	-

Table E.5 Crystallographic refinement details for **124** and metal compounds from Chapter 6.

Compound	**124**	[Cu**124**$_2$]·CH_3CN	[Pt**124**Cl_2]	[Pt**124**Cl_2]·CH_3CN	[Co**124**$_2$$(NO_3)_2$]	[Ag**124**$_2$]$_2$$(SbF_6)_2$
Empirical formula	$C_{12}H_9N_5$	$C_{26}H_{21}CuF_6N_{11}P$	$C_{14}H_{12}Cl_2N_6Pt$	$C_{12}H_9Cl_2N_5Pt$	$C_{24}H_{18}CoN_{12}O_6$	$C_{48}H_{36}Ag_2F_{12}N_{20}Sb_2$
Formula weight	223.24	837.64	530.29	489.23	629.43	1580.21
Temperature/K	100(2)	100(2)	100(2)	100(2)	100(2)	100(2)
Crystal system	Monoclinic	Monoclinic	Monoclinic	Monoclinic	Monoclinic	Monoclinic
Space group	$P2_1/n$	$P2_1/n$	$P2_1/c$	$P2_1/c$	$P2_1/c$	$P2_1/n$
a/Å	4.4318(2)	16.8836(12)	8.5058(4)	7.8483(4)	7.454(2)	7.9055(7)
b/Å	20.9733(8)	8.0136(6)	24.9233(12)	18.6289(10)	8.717(3)	14.7905(14)
c/Å	11.2920(4)	21.7775(14)	7.7725(4)	9.3808(5)	19.132(5)	22.650(2)
α/°	90	90	90	90	90	90
β/°	96.678(2)	107.411(5)	105.421(2)	102.9220(10)	95.314(6)	92.542(2)
γ/°	90	90	90	90	90	90
Volume/Å^3	1042.46(7)	2811.5(3)	1588.39(14)	1336.79(12)	1237.8(6)	2645.8(4)
Z	4	4	4	4	2	2
ρ_{calc}/g cm^{-3}	1.422	1.979	2.217	2.431	1.689	1.984
μ/mm^{-1}	0.093	4.016	9.177	10.891	0.764	1.840
F(000)	464.0	1704.0	1000.0	912.0	642.0	1536.0
Radiation source	Mo Kα	Cu Kα	Mo Kα	Mo Kα	Mo Kα	Mo Kα
2θ range/°	3.884 to 61.062	5.85 to 136.836	3.268 to 52.000	4.372 to 61.112	4.276 to 54.246	3.29 to 57.576
Reflns. collected	28997	19212	26772	34815	17941	39537
Independent reflns.	3188 [R_{int} = 0.0677, R_{sigma} = 0.0520]	5151 [R_{int} = 0.0805, R_{sigma} = 0.0863]	3127 [R_{int} = 0.0561, R_{sigma} = 0.0323]	4103 [R_{int} = 0.0225, R_{sigma} = 0.0126]	2673 [R_{int} = 0.1669, R_{sigma} = 0.1094]	6892 [R_{int} = 0.0700, R_{sigma} = 0.0483]
Reflns. Obs. [$I \geq 2\sigma(I)$]	2118	3118	2722	3914	1703	5100
Data/restraints/parameters	3188/0/154	5151/0/407	3127/24/209	4103/0/181	2673/0/196	6892/0/379
GOOF on F^2	1.004	1.017	1.257	1.262	1.014	1.067
R indices [$I \geq 2\sigma(I)$]	R_1 = 0.0470, wR_2 = 0.0908	R_1 = 0.0614, wR_2 = 0.1571	R_1 = 0.0395, wR_2 = 0.0768	R_1 = 0.0171, wR_2 = 0.0305	R_1 = 0.0695, wR_2 = 0.1603	R_1 = 0.0419, wR_2 = 0.0871
R indices [all data]	R_1 = 0.0878, wR_2 = 0.1036	R_1 = 0.1024, wR_2 = 0.1852	R_1 = 0.0485, wR_2 = 0.0790	R_1 = 0.0190, wR_2 = 0.0308	R_1 = 0.1214, wR_2 = 0.1866	R_1 = 0.0700, wR_2 = 0.0972
Largest diff. peak/hole / e Å^{-3}	0.28/-0.25	0.83/-0.36	1.95/-3.97	0.69/-1.25	1.46/-0.85	1.30/-1.08
CCDC Number	1472698	1472699	1472700	1472701	1472702	1472703